Recovery Act:

Geoscience Perspectives in Carbon Sequestration – Educational Training and Research Through Classroom, Field, and Laboratory Investigations

Final Progress Report

Work Performed Under Agreement DE-FE0002416

Submitted by

Missouri University of Science and Technology
Department of Geological Sciences and Engineering
159 McNutt Hall, 1400 North Bishop Ave
Rolla, Missouri 65409-0410

Principle Investigator

David J. Wronkiewicz
Phone: [573-341-4679]
Email: wronk@mst.edu

Contributing Authors

Varun G. Paul, Alsedik M.A. Abousif, and Kyle S. Rybacki

ABSTRACT

The most effective mechanism to limit CO_2 release from underground Geologic Carbon Sequestration (GCS) sites over multi-century time scales will be to convert the CO_2 into solid carbonate minerals. This report describes the results from four independent research investigations on carbonate mineralization: 1) Colloidal calcite particles forming in Maramec Spring, Missouri, provide a natural analog to evaluate reactions that may occur in a leaking GCS site. The calcite crystals form as a result of physiochemical changes that occur as the spring water rises from a depth of more than 190′. The resultant pressure decrease induces a loss of CO_2 from the water, rise in pH, lowering of the solubility of Ca^{2+} and CO_3^{2-}, and calcite precipitation. Equilibrium modelling of the spring water resulted in a calculated undersaturated state with respect to calcite. The discontinuity between the observed occurrence of calcite and the model result predicting undersaturated conditions can be explained if bicarbonate ions (HCO_3^-) are directly involved in precipitation process rather than just carbonate ions (CO_3^{2-}). 2) Sedimentary rocks in the Oronto Group of the Midcontinent Rift (MCR) system contain an abundance of labile Ca-, Mg-, and Fe-silicate minerals that will neutralize carbonic acid and provide alkaline earth ions for carbonate mineralization. One of the challenges in using MCR rocks for GCS results from their low porosity and permeability. Oronto Group samples were reacted with both CO_2-saturated deionized water at 90°C, and a mildly acidic leachant solution in flow-through core-flooding reactor vessels at room temperature. Resulting leachate solutions often exceeded the saturation limit for calcite. Carbonate crystals were also detected in as little as six days of reaction with Oronto Group rocks at 90°C, as well as experiments with forsterite-olivine and augite, both being common minerals this sequence. The Oronto Group samples have poor reservoir rock characteristics, none ever exceeded a permeability value of 2.0 mD even after extensive dissolution of calcite cement during the experiments. The overlying Bayfield Group – Jacobsville Formation sandstones averaged 13.4 ± 4.3% porosity and a single sample tested by core-flooding revealed a permeability of ~340 mD. The high porosity-permeability characteristics of these sandstones will allow them to be used for GCS as a continuous aquifer unit with the overlying Mt. Simon Formation. 3) Anaerobic sulfate reducing bacteria (SRB) can enhance the conversion rate of CO_2 into solid minerals and thereby improve long-term storage. SRB accelerated carbonate mineralization reactions between pCO_2 values of 0.0059 and 14.7 psi. Hydrogen, lactate and formate served as suitable electron donors for SRB metabolism. The use of a $^{13}CO_2$ spiked gas source also produced carbonate minerals with ~53% of the carbon being derived from the gas phase. The sulfate reducing activity of the microbial community was limited, however, at 20 psi pCO_2 and carbonate mineralization did not occur. Inhibition of bacterial metabolism may have resulted from the acidic conditions or CO_2 toxicity. 4) Microbialite communities forming in the high turbidity and hypersaline water of Storrs' Lake, San Salvador Island, The Bahamas, were investigated for their distribution, mineralogy and microbial diversity. Molecular analysis of the organic mats on the microbialites indicate only a trace amount of cyanobacteria, while anaerobic and photosynthetic non-sulfur bacteria of the phyla Chloroflexi and purple sulfur bacteria of class Gammaproteobacteria were abundant.

LIST OF ACRONYMS AND ABBREVIATIONS

CHC – Copper Harbor Conglomerate

DOC - Dissolved Organic Carbon

DNA - Deoxyribonucleic Acid

EDS - Energy Dispersive Spectroscopy

Eh - redox potential or reduction-oxidation potential

EPS - Extracellular Polymeric Substance

Ga - Gigaannum

GCS - Geologic Carbon Sequestration

HTP - High Temperature Pressure

IC - Ion Chromatography

ICP - Inductively Coupled Plasma

K_d - Distribution coefficient

KeV – KiloelectronVolt

K_{sp} - Equilibrium Solubility Product

LMVSS - Lower Mixed Volcanic-Sedimentary Sequence

LOI - Loss on Ignition

Ma - Megaannum

mD - millidarcy

meq/L - milliequivalent/Liter

MCR - Midcontinent Rift

mg/kg - milligrams/kilogram

mg/L - milligram/Liter

mS/cm - milliSiemens/centimeter

mV- milliVolts

NTU - Nephelometric Turbidity Units

OES - Optical Emission Spectroscopy

OTUs - Operational Taxonomic Units

pCO_2 - partial pressure of CO_2

pH - Potential of Hydrogen or Power of Hydrogen

ppm - Parts Per Million

ppt - Parts Per Thousand

psi - Pounds per Square Inch
Q-F-L - Quartz-Feldspar-Lithic (Q-F-L)
R^2 - coefficient of determination
SEM - Scanning Electron Microscopy
SI - Saturation Index
SRB - Sulfur Reducing Bacteria
TDS - Total Dissolved Solids
TSS - Total Suspended Solids
UMVSS - Upper Mixed Volcanic-Sedimentary Sequence
USGS - United States Geological Survey
VPDB - Vienna PeeDee Belemnite, the carbon isotope standard
XRD - X-Ray Diffraction
XRF - X-Ray Fluorescence
16S rRNA – 16S ribosomal ribonucleic acid
$\delta^{13}C$ - Carbon isotopic ratio
µS/cm - microSiemens/centimeter
µm – micrometer (micron)
µM - micromole

ACKNOWLEDGMENTS

The Department of Energy Grant "Geoscience Perspectives in Carbon Sequestration – Educational Training and Research through Classroom, Field, and Laboratory Investigations" (DE-FE0002416), the Missouri S&T Opportunities for Undergraduate Research Experience (OURE), and the Donald Radcliffe trust fund of the Geology and Geophysics Program at Missouri University of Science and Technology kindly provided funding that supported travel and research efforts. The James Foundation of St. James, MO, operators of Maramec Spring Park, kindly provided access to the site and allowed us to collect samples. The late Lucy Wortham James is acknowledged for her visionary understanding of the natural beauty of the Maramec Spring and her desire that it be available for "the enjoyment of the people". We also thank the staff of the Gerace Research Centre, San Salvador Island, for logistics and assistance while we were in the Bahamas, and the Bahamas Environment Science & Technology Commission (BEST) for permission to collect and export microbialite samples.

We thank the Advanced Material Characterization Laboratory (AMCL), Materials Research Center (MRC) and Environmental Research Center (ERC) facilities at Missouri University of Science and Technology for access to analytical facilities. Assistance with instrumentation was provided by F. Scott Miller and Clarissa Wisner (SEM-EDS), Nathan Miller and Honglan Shi (ICP-OES), and Eric Bohannan (XRD). Emitt Witt is also acknowledged for his assistance with sampling microbialites and Kwame Awuah-Offei for assistance with the CO_2 gas-flux measurements at Maramec Spring. LI-COR Instruments is thanked for the use of their portable CO_2 gas analyzer system and John Schumacher of the USGS for use of the portable filtration unit. We are also grateful to Ken MacLeod, Cheryl Kelley, and Shannon Haynes of The University of Missouri's Biogeochemistry IRMS Lab for analysis of, and helping interpret the isotopic data. Melanie Mormile, Jamie Foster, Shreya Ghosh, James Vandike, and Carlos Sanchez-Botero are thanked for insightful discussion related to various topics of this paper. Finally, the following undergraduate students are thanked for their assistance with various subtasks associated with this research effort: Coleen Conrad, Hang Deng, Thomas Herbst, Hanani Tajul Nahar, Rebecca Nuckolls, Airin Price, Joshua Silverstein, and Robert Swain.

TABLE OF CONTENTS

SECTION I. INTRODUCTORY PARAGRAPHS

SECTION II. EXPERIMENTAL METHODS

SECTION III. INVESTIGATION OF CARBONATE MINERAL PRECIPITATION AT MARAMEC SPRING MISSOURI

SECTION IV. EVALUATION OF THE MINERAL AND GEOCHEMICAL ATTRIBUTES OF THE MIDCONTINENT RIFT SEQUENCE FOR CARBON SEQUESTRATION

SECTION V. EFFECT OF ELEVATED CO_2 ON THE ABILITY OF SULFATE-REDUCING BACTERIA TO PRECIPITATE CARBONATE MINERALS: IMPLICATIONS FOR CARBON SEQUESTRATION

SECTION VI. CHARACTERIZATION OF WATER PROPERTIES AND MICROBIALITES IN THE HYPERSALINE ENVIRONMENT OF STORRS' LAKE, THE BAHAMAS

SECTION VII. EDUCATION AND TRAINING IN THE UNDERGRADUATE CURRICULUM: CARBONATE SYSTEMS AND CARBON SEQUESTRATION

EXECUTIVE SUMMARY

The primary *long-term* concern with underground Geologic Carbon Sequestration (GCS) will be the containment of the supercritical liquid, gas phase, and/or aqueous phase components of CO_2. The most effective mechanism to limit this release over multi-century time scales will be to convert the injected CO_2 into solid carbonate minerals as these are immobile and represent the densest form of CO_2. The rate of carbon mineralization will depend on many factors, but principle among these will be the ability of the rock matrix minerals to neutralize the acid bicarbonate fluids and provide alkaline earth ions for mineralization.

Maramec Spring in southeast Missouri emits an average of 3.6×10^8 liters of water/day (9.6×10^7 gallons/day). The water exhibits a milky blue-white color under normal flow conditions, a positive release of CO_2 gas into the atmosphere, a rise in pH in the downstream direction, and slight decreases in Ca and Mg downstream. The blue-white color results from light being scattering off colloidal particles suspended in the turbulent water. Detailed chemical, microscopic, and X-ray diffraction analysis of the colloids revealed the presence of calcite, quartz, clays (kaolinite, illite, and smectite), dolomite, anglesite, and living diatoms. The calcite particles were digested in nitric acid and chemically analyzed to reveal a composition of $Ca_{0.92}Mg_{0.08}CO_3$, while the position of the (104) diffraction angle at 29.92^o 2Θ is suggestive of a more Mg-rich composition of $Ca_{0.84}Mg_{0.16}CO_3$. The isolated calcite grains are devoid of any dissolution pits or corrosion features that would suggest their derivation as weathered particles from the subsurface dolomite strata. The CO_2 loss from the water causes a pH rise and associated lowering of the solubility of Ca^{2+} and CO_3^{2-} towards the calcite phase. The calcite particles continue to grow with time as they move downstream or when water samples are collected and held for several hours.

Modelling the Maramec Spring system using the PHREEQC code and measured water parameters resulted in a calculated undersaturated state with respect to calcite (SI = -0.86). A sensitivity analysis of major input parameters (a_{Ca2+}, alkalinity, temperature, and pH) suggests that mineralization is most sensitive to changes in pH. A change from the measured pH $\approx$ 7.0 at the zone of upwelling to a hypothetical pH value of 7.81 would induce saturation. Actual field pH measurements, however, never reach this value as the highest recorded pH was 7.50 in a downstream direction where calcite formation was already well-underway. The discontinuity between the observed occurrence of calcite and the model result predicting undersaturated conditions can be explained if bicarbonate ions (HCO_3^-) are directly involved in precipitation process rather than just carbonate ions (CO_3^{2-}). The calcite precipitation reaction taking place at Maramec Spring can provide insight into reactions that may occur in a leaking GCS site where aqueous-CO_2 fluids move through fractures from high- to low-pressure zones. The pressure decrease may result in the release of $CO_{2(aq)}$ from the fluid, causing a pH increase, and then the formation of carbonate minerals. These minerals can potentially seal the fractures.

Mineralization reactions at Maramec Spring suggest that calcite precipitation may be initiated when the modeled water parameters still indicate a SI value < 0.0.

The Midcontinent Rift (MCR) system in central North America is composed of several Mesoproterozoic aged stratigraphic units, some of which may be attractive as a GCS target due to their abundance of Ca-, Mg-, and Fe-silicate minerals. The Oronto Group forms the lowermost major sedimentary horizon and contains an abundance of labile mineral constituents including calcite cement, volcanic lithic fragments, feldspars, muscovite, biotite, iron oxides, epidote, clay minerals, and zeolites. One of the major challenges in using the Oronto Group sequence for a GCS site is related to its low porosity and permeability. Occlusion of pore space by calcite cement often results in open-porosity values of $\leq 2\%$ for much of the sequence, although two of the Oronto Group samples examined in the present study had porosities of 8.9% and 7.9%. The latter sample correlates to a 22′ thick section of clastic sandstone that was previously recorded as a potentially high porosity zone by geophysical methods in a deep petroleum exploration well in Kansas (Berendsen et al., 1988).

Rock samples from several MCR stratigraphic units were cut into wafers, polished, and then reacted with CO_2-saturated deionized water, at 90°C, or in flow-through core-flooding reactor vessels with a mildly acidic solution at room temperature, in order to evaluate reactions under simulated GCS conditions. Deionized water was used as the leachant, rather than a brine, to evaluate the influence of dissolving mineral constituents on the reactions. The pore filling cements in the Oronto Group include hematite, albite, silica, etc., but are typically dominated by calcite, which locally exceeds 20% of the overall rock volume. The calcite rapidly dissolved in the experiments as evidenced by microscopic examination of the reacted solids, Ca release to solution, a pH rise, and an increase in rock permeability in the core flooding tests. Dissolution of silicate minerals was also recognized by the presence of their constituents in solution and in examinations of the reacted solids using various microscopy techniques. While overall porosity increased following these reactions, permeability changes were inconsistent, increasing in some samples, but decreasing in others. None of the samples ever exceeded a value of 2.0 mD. Barnes (1990) estimated *conservative* lower limits for using the Cambrian Mt. Simon sandstone as a GCS site at 10% porosity and 33 mD. Although we only tested a limited number of samples in this pilot scale study, our maximum 9% porosity and < 2.0 mD values failed to meet these limits.

The Bayfield Group – Jacobsville Formation sandstones form the upper MCR sedimentary sequence. Samples from this unit averaged 13.4 ± 4.3% porosity and a single sample tested by core-flooding revealed a permeability of ~340 mD. The Bayfield Group – Jacobsville Formation sandstones thus exceed the *conservative* reservoir criteria established by Barnes (1990). While the Bayfield-Jacobsville sequence does not have a stratigraphic cap rock, it is unconformably overlain by the high porosity-permeability sandstones of the Mt. Simon Formation and thus offers addition CO_2 storage volume where the two units come in contact with one another to form a single aquifer unit. Basal volcanic rocks and/or Oronto Group sediments have been tectonically emplaced on top of Bayfield-Jacobsville sequence by thrust faulting in many regions of the MCR including deeply buried sections located in Kansas. This inverted stratigraphy can place alkaline earth enriched Oronto Group sediments and basaltic volcanic rocks with a good capacity for producing carbonate minerals on top of the higher porosity-permeability Bayfield-Jacobsville sandstones. These tectonically juxtaposed sequences offer the best potential for GCS efforts, especially with respect to carbonate mineralization processes that will improve the long term storage potential of CO_2 in underground repositories.

Corrosion experiments conducted with Oronto Group samples often produced leachant solutions with a calculated SI value exceeding the saturation limit for calcite. Carbonate crystals were also produced as alteration phases in two experiments with Oronto Group samples as well as experiments with forsterite-olivine and augite-pyroxene. Both of these minerals are commonly found in the MCR sequence. Mineral precipitation was initiated in as little as six to ten days at 90°C. The rift sedimentary rocks of the Oronto Group thus display great potential to rapidly induce the formation of carbonate minerals during reactions with CO_2 enriched fluids.

Known carbonate mineral precipitating microorganisms, such as the anaerobic sulfate reducing bacteria (SRB), could enhance the rate of conversion of CO_2 into solid minerals and thereby improve long-term storage of CO_2 injected into a subsurface repository. The ability of SRB to induce and accelerate carbonate mineral precipitation under elevated pCO_2 conditions was investigated using laboratory scale testing with bacteria cultures collected from organic-rich sediments from hypersaline Lake Estancia in New Mexico. The SRB culture was inoculated into continuous gas flow and batch reactors experiments under variable headspace pCO_2 contents (0.0059 to 20 psi) while solution pH, redox, sulfide, Ca and Mg concentrations were monitored. The sediment material from the tests was also examined by various microscopy techniques. Reactors exposed to pCO_2 conditions between 0.0059 and 14.7 psi formed Mg-enriched calcite crystals, while the 20 psi pCO_2 reactors did not. Inhibition of bacterial metabolism may have occurred in the 20 psi pCO_2 reactors due to acidic conditions or CO_2 toxicity. The 20 psi reactors did display an increase in sulfide concentration during 10-day experimental run, but the amount of sulfide produced was only about 20% of that produced from 14.7 psi pCO_2 reactors. This data suggests that the bacteria were still viable in the higher pCO_2 environment, but were less active.

Hydrogen, lactate and formate were shown to work as suitable sources of electrons for SRB metabolism, with carbonate mineralization being detected in experiments with all three electron donors. The use of a $^{13}CO_2$ spiked gas source produced carbonate minerals with ~53% of their carbon being derived from the gas-phase source of CO_2. The remaining carbon was derived from the organic electron donors and/or the bicarbonate ions in the leachant. This project has demonstrated that SRB can accelerate the precipitation of carbonate minerals at a more rapid rate than would occur in their absence. The bacteria used in these tests displayed lowered metabolic activity at higher p CO_2 levels, thus the viability of both introduced and native microbial communities in the subsurface will need to be assessed in the presence of high CO_2 levels to evaluate their potential utility in accelerating carbonate biomineralization at a GCS site.

Microbialites are lithified organo-sedimentary structures, usually formed by phototrophic microbial mat communities under high-intensity sunlight environments. The microbialites present in hypersaline water of Storrs' Lake, San Salvador Island, The Bahamas, thus represent a unique type of community because they exist in a high turbidity water column. These microbialites were investigated for their distribution, mineralogy and microbial diversity. Several morphological varieties of microbialites have been identified in this current and previous studies (calcareous knob, plateau-mushroom, cauliflower-top mushroom, pinnacle mound, and multi-cuspate). The plateau-mushroom and pinnacle mound microbialites contained blocky and needle-shaped crystals, calcified cyanobacteria filaments, and remains of exopolymer substances. X-ray diffraction analysis of the microbialite mounds confirmed the presence of both Mg-calcite and aragonite in the plateau-mushroom and pinnacle mound varieties, whereas only Mg-calcite was identified in the other microbialites. A comprehensive molecular analysis of the organic mats on the microbialites using barcoded pyrosequencing techniques identified at least 12 dominant bacterial phyla. Cyanobacteria populations were in low abundance and ranged from ~0.01% of the recovered population in the deeper pinnacle mounds to ~3.2% in the shallow calcareous knobs. Other photosynthetic microbes including green non-sulfur bacteria of the phyla Chloroflexi, and purple sulfur bacteria of class Gammaproteobacteria were abundant. Chloroflexi comprised ~46% of the population in the deeper water cauliflower-top mushroom and pinnacle mound mats, and provide evidence for the dominance of photosynthetic communities in these systems, despite the highly turbid nature of Storrs' Lake. All mat types contained strict anaerobes including sulfate reducing and dehalogenating bacteria that are suspected of playing a role in promoting carbonate biomineralization.

The Maramec Spring system lends itself as a natural outdoor laboratory to introduce college undergraduate students to both field analytical techniques and carbonate chemistry reactions. This spring is located close to the Missouri University of Science and Technology campus and is made accessible as a privately owned park that is operated by the James Foundation in St. James, Missouri. A total of 157 students visited the spring in conjunction with their introductory geochemistry course during the 2010 through 2012 academic years. Students conducted measurements for pH, Eh, conductivity, temperature, alkalinity, Ca-Mg hardness, and turbidity changes in the water. They also discussed the importance of the carbonate minerals identified as colloidal particles in the spring water, the importance of the particles in evaluating the carbon cycle, and potential implications for the sequestration of anthropogenic carbon dioxide. The carbonate platform sequence of The Bahamas was also used as a focal point for students to study the Earth's carbon cycle in our spring field studies course. Students evaluated topics ranging from biologic production of organic ooze, biomineralization of carbonate rocks, karst formation, cementation and dissolution processes in carbonate rocks, and sedimentation processes that have sculpture the islands into their present morphology. A total of 34 students visited the island in an experiential learning environment in two separate trips to the island in the 2010 and 2012 academic years.

SECTION I. INTRODUCTORY PARAGRAPHS

1. GREENHOUSE GASSES AND CARBON SEQUESTRATION STRATEGIES

Atmospheric CO_2 concentrations have risen during the industrial revolution primarily due to human influence and this has likely affected natural climatic patterns (Raynaud et al., 1993; Post et al., 2004). Atmospheric CO_2 and other greenhouse gases absorb infra-red terrestrial radiation reflected from the Earth's surface and reemit this energy into the atmosphere to create what known is as the greenhouse effect. Atmospheric CO_2 emissions increased by approximately 70% between 1970 and 2004 and concentrations reached the 400 ppm benchmark in 2014 (Pacala and Socolow, 2004; http://co2now.org/). Anthropogenic releases of greenhouse gasses are projected to double from the 7.0 gigga-tons carbon/year released in 2000 to approximately 14 gigga-tons/year in 2050 if we continue to increase annual emissions at the present rate.

Although controversies exist about the influence of CO_2 on global climatic change and the proportion of the current CO_2 increase resulting from atmospheric emissions (Cess, 1976; Kump et al., 2000), many industries and government sectors have initialized efforts to reduce their carbon footprint. A variety of options have been considered to minimize the amount of CO_2 released in to the atmosphere, and to capture and sequester the gas by a combination of geochemical, physical, and biological processes (Schlesinger, 1999; Metz et al., 2005; Jun et al., 2013). Geologic carbon sequestration (GCS), in particular, has received considerable attention due to efficiency and available volume of subsurface rock material that can be used to trap and store gasses (Jun et al., 2013). The GCS concept involves injecting supercritical CO_2 into deep underground saline aquifers, coal layers, depleted oil-gas reservoirs, and deep ocean basins. The strategy for injection into deep saline aquifers involves four main trapping mechanisms: 1) physical trapping of a gas or supercritical liquid phase CO_2 by large-scale geologic structures such as low-permeability shale layers, 2) residual trapping of gas or critical liquid phase CO_2 as bubbles that attached to the surface of rock particles due to surface tension between the two phases, 3) solubility trapping of CO_2 that has dissolved into the aqueous phase, and 4) mineral trapping as CO_2 combines with dissolved cations in the aqueous phase to precipitate as solid mineral phases.

A significant portion of physical and residual trapped CO_2 will be converted into the dissolved aqueous-phase component over time, with the dissolved phase likely dominating all components between 20 and 200 years after CO_2 injection (Ennis-King and Paterson, 2003). Aqueous phases resulting from the injection of CO_2 into an aquifer will include $CO_{2\,(aq)}$, $H_2CO_{3\,(aq)}$, HCO_3^-, and CO_3^{2-}. The relative proportions of the various phases will depend on the temperature, salinity, confining pressure, and pH of the fluid. The incorporation of CO_2 into water will also tend to decrease the pH of the resultant solution. One of the *long-term* concerns with the GCS process is centered on the containment of the supercritical liquid, gas phase, and/or aqueous phase components in the subsurface injection site. All three of the previously mentioned components are highly mobile and may leak back to the surface, either very rapidly in the case of a catastrophic failure of a physical barrier or transmission in undetected exploration drill well(s), or more slowly in the case of thinning barriers and/or microfractures which transgress across the physical barrier (Metz et al., 2005). White et al., (2003) provided a review of several studies investigating the leakage rate of CO_2 and at what point it would offset the beneficial effects of GCS. The authors propose using a leakage standard of 0.1%/year as the performance standard but note that such a standard would be very difficult to meet in all cases. A leakage rate of 0.1%/year would result in 10% of the injected gas being released back into the atmosphere in a 110-year period. The capture, processing, transport, and injection of CO_2 into the subsurface will also require energy input and this energy requirement will likely involve the generation of additional CO_2 emissions. It is a reasonable concern that our efforts to reduce atmospheric greenhouse gasses in the present era will place an undue burden on future generations. White et al. note that the U.S. Department of Energy has set a goal for global seepage of less than 0.01%/year, a target goal that would reduce the leakage rate to <1% over the same 110-year period. The most effective means to limit this release over the long-term will likely be to accelerate the rate that injected CO_2 converts into carbonate minerals as these solid minerals represent an immobile and dense form of CO_2 (Goldberg et al., 2001). The rate of carbon mineralization will depend on many factors, but principle among these will be the ability of the rock matrix minerals to neutralize the acid bicarbonate fluids and provide alkaline earth ions for mineralization.

During injection, CO_2 can react with subsurface aqueous fluids to produce carbonic acid ($H_2CO_{3(aq)}$). Carbonic acid and/or its partial dissociation product the bicarbonate ion (HCO_3^-) will in turn, react with many of the primary rock-forming mineral phases. Ion exchange reactions between the acids and minerals will neutralize the acids and release ionic constituents from the minerals such as Ca^{2+}, Mg^{2+}, and Fe^{2+}. These ions can combine with the carbonate ion (CO_3^{2-}) to form carbonate mineral phases. The aqueous fluids in the subsurface GCS sites will also provide the same acid neutralizing capacity and dissolved alkaline earth ions, but the abundance of the necessary components in the fluids are limited by solubility constraints, and will be easily overwhelmed by any appreciable quantity of CO_2 injection. Thus the underground rock system will be the dominant source that provides the long-term neutralization capacity and supply of cations for the carbonate mineralization process.

The first minerals that react with the carbonic acid may include carbonate cements. Carbonate dissolution will initially lead to an increase in the porosity and permeability of a reservoir by opening blocked pores, however, the dissolved carbonate ion would eventually have to be reprecipitated again just to keep the mineralization process at a zero sum. Reactions involving aluminosilicate phases (e.g., feldspar and clay minerals) or Fe-oxides may release alkaline earth and transition metal components that commonly are incorporated as carbonate minerals in natural systems (Gauss, 2005; Benson and Cole, 2008). These reactions also effectively increase the pH of the solution. These dissolved cations can complex with the dissolved carbonate ion to precipitate as a variety of carbonate minerals (e.g., calcite, $CaCO_3$; dolomite, $CaMg(CO_3)_2$; and siderite, $FeCO_3$) in longer term reactions, and in reactions taking place in distal locations from the CO_2 injection wells even while injection is taking place.

One of the initial considerations used for selecting a GCS target site is the porosity and permeability of the host-rock target. A reasonably interconnected porosity of $\geq$ 10% is considered a reasonable target to allow injection without excessive back-pressure buildup. Quartz-rich sandstones are thus often selected as primary targets for GCS due their high porosity-permeability characteristics. Unfortunately, these quartz-rich units generally have low abundances of alkaline earth bearing minerals and thus will have minimal carbonate mineralization potential. Minerals that contain high proportions of alkali and alkaline earth components (e.g., feldspars) often produce clay minerals as alteration products and these clays may precipitate within pores in the rock matrix resulting in a lowered permeability. Thus the selection criteria for picking a GCS site will often include the conflicting interests of selecting between a high-porosity permeability quartz-rich stratigraphic unit, with limited carbonate mineralization potential, *versus* a lower porosity-permeability unit with high carbonate mineralization potential. The first generation of selected CO_2 injection sites have been chosen with the former criteria as a priority item (along with an effective seal rock, and a high water salinity that will render the aquifer as a non-potable water supply). Examples of such quartz-rich sandstones (quartz arenite) include the Sleipner-Hugin-Heather sequence in the North Sea and the Mt. Simon Formation in the Illinois Basin (Greenwood et al., 1994, Driese et al., 1981, respectively). Systems that are selected solely on aquifer properties, and neglect to consider the carbonate mineralization potential, will ultimately fail as a repository site from the perspective of future generations unless leakage can be controlled at a very slow rate (<0.01%).

Mineral precipitation is generally a slow process and it may take centuries or longer for the majority of the injected CO_2 to be converted into solid mineral phases. Xu (2011) ran a reactive transport model simulating the injection of CO_2 under conditions simulating the Texas Gulf Coast region. The model results suggest that 43% of the injected CO_2 would remain as the trapped gas phase, 28% as the aqueous phase, and 29% as solid carbonate minerals in a time frame 1000 years after injection had ceased (without leakage). Thus 71% of the injected CO_2 would still remain in a highly mobile form and be a potential leakage issue even after 1000 years had passed. The scientific community does not currently possess the knowledge base or have the experimental foundation to guarantee against the risk of CO_2 leakage for such a long time interval. Reactions that occur to convert CO_2 into solid minerals may appreciably mitigate against such leakage if they occur, or can be induced to occur, at a fast enough rate. Mineral precipitation reactions will be expected to occur in a more rapid fashion, and consume a higher proportion of the injected CO_2, if the rock material contains a higher proportion of alkali, and especially alkaline earth components. Biologic communities may also be able to harness the thermodynamic energy associated with mineral precipitation reactions, or passively produce carbonate minerals through the chemical modification of their local environment as a result of their life-functions.

The purpose of this study is to describe processes and mechanisms that can influence carbonate mineralization reactions. This report is a compilation of four individual research projects that address issues of carbonate mineralization under potential CO_2 sequestration conditions. Each project formed a dissertation or thesis topic for a different graduate student in the Geology and Geophysics Program at Missouri University of Science and Technology. Each section is written as a stand-alone individual document that is intended for journal publication. Thus there will be some differences in formatting between the sections. Components of each of the four projects also involved undergraduate students in both individual research projects and students enrolled in courses at Missouri S&T who were exposed to experiments involving the carbon cycle.

2. SECTION ORGANIZATION OF DOCUMENT

The current Section I of this report provides a general synopsis of greenhouse gas issues associated with carbon dioxide (CO_2) and societal plans to mitigate against potential climate change. Section II describes the experimental methods used in all of the remaining sections of the report. Section III is the first-of-four topical research portions of this report (Sections III, IV, V, and VI). Each section covers a research project or sub-project led by a different graduate student (the co-authors of this paper) in the Geology and Geophysics Program at the Missouri University of Science and Technology.

Section III of details chemical changes and mineral precipitation events occurring in the Maramec Spring system in Missouri. The spring water is $Ca + HCO_3^-$ rich, and upwells from a depth of 190′ or more. The water experience a loss of CO_2 due to the decreasing confining pressures as the water rises to the surface. Chemical changes occur in the water as a result of the CO_2 loss and induce a series of chemical reactions that ultimately result in the precipitation of colloidal calcite grains. The Maramec Spring system thus serves as a natural analog to evaluate chemical and mineral changes that could occur in a leaking CO_2 repository.

Section IV of this report addresses the potential utilization of the Midcontinent Rift (MCR) basin in the central United States as a potential CGS site. While many of the finer scale details on the geologic characterization of the MCR sequence remain unknown due to limited drilling access into the basin; geophysical evaluation, exposures in the Lake Superior Region, and several deep petroleum exploration wells have provided a general overall synopsis on the basin. Thorleifson et al., (2008) provide a comprehensive evaluation on GCS potential for the MCR in Minnesota and surrounding areas. They conclude that large portions of the MCR basin occur at an adequate depth, have a potential cap-rock and/or faulted marginal traps, and contain Ca^{2+}-, Mg^{2+}-, and Fe^{2+}-rich minerals that can provide ions for carbon mineralization. However, the low permeability of the lower part of the sedimentary (Oronto Group) and volcanic sequences of the rift basin were found to be a limiting factor that may hinder injectability and storage space within the MCR sequence. The purpose of this section of the study was to evaluate the applicability of MCR sediments to sequester CO_2, especially with respect to their distribution of Ca^{2+}-, Mg^{2+}-, and Fe^{2+} bearing phases, the role of released Ca^{2+} and Mg^{2+} ions in inducing the precipitation of solid carbonate minerals, and the effect of exposing calcite cemented pores to a $CO_2 + H_2O$ environment and thus potentially increase the porosity-permeability characteristics of the overall reservoir rock.

Section V investigates the potential role in using microorganisms to accelerate carbonate mineralization process(es). Microorganisms, especially cyanobacteria, bacteria, and marine algae have played a major role in the global cycling of carbon and other elements in the past and they continue to do so today (Fenchel and Blackburn, 1979; Foster and Mobberley, 2010). Seawater, saline lakes, and soils provide many examples of microorganisms forming carbonate deposits (Hammes and Verstrate, 2002). Although most microorganisms will fix atmospheric CO_2 using photosynthetic processes at or near the Earth's surface, many subsurface (and aphotic) microbial communities are also known to induce carbonate mineralization by chemotrophic activity (Dupraz et al, 2013). Accelerating carbonate mineralization reactions may thus potentially be achieved in a subsurface GCS site through the use of microorganisms.

Section VI reports on a detailed examination of the microbialite communities living within Storrs' Lake on San Salvador Island in The Bahamas. Microbialites are living organo-mineralized structures, and the microbialite community present in Storrs' Lake is a hypersaline environment that has been precipitating Ca-carbonate minerals in microbialite mounds for more than 2300 years. The lake system was examined to determine the mineralogy of microbialite mounds, the genetic makeup of their living microbial communities, lake water chemistry, and light penetration into the lake system. Storrs' Lake is an unusual location for microbialites as the lake water is highly turbid as a result of suspended material in the water column.

Section VII describes how the information gained in Sections III through VI, and the acquired instrumentation facilities associated with this project, were used to improve the educational component of our undergraduate curriculum at Missouri University of Science and Technology. Improvement in education was gained in activities that spanned three different levels of student involvement. The first involved a large population of Introductory Geochemistry students who were exposed to research in an organized field-based laboratory assignment at Maramec Spring. The students spend a single field day collecting chemical data from this dynamic spring system that exhibits a positive pH shift and precipitation of colloidal calcite. A total of 157 students were brought out to the spring over a three-year period, with an additional 12 students serving as teaching assistants. The second level of activity involved students enrolled in our Spring Field Studies Courses. The format for this course requires students to pre-read selected papers from the scientific literature and then openly critique those papers and discuss key findings in a weekly discussion session during the semester. Students would then participate in a 10-day long field trip visiting many of the same geologic features and locations that they had read about during the semester. Our Spring Field Studies classes included a visit to the Lake Superior Region – Midcontinent Rift sequence in 2011, and two separate visits to the carbonate platform deposits of San Salvador Island in the Bahamas in 2010 and 2012. A total of 44 students were involved in the three trips over the three-year period. Our third educational component including a relatively small group of eight undergraduate students who were directly involved in research activities. These students conducted experiments and gathered data on small segments of this overall research effort (e.g., pH measurements in association with the Goldich weathering experiments, Section IV). Our long-term plan is to continue with as many of these activities as funding and equipment resources will allow. The information gained for these activities have also been incorporated into the regular lecture portion of our courses.

REFERENCES

Benson, S.M. and Cole, D.R., 2008, CO_2 sequestration in deep sedimentary formations, *Elements,* v. 4, p. 325-331.

Cess, R.D., Potter, G.L., 1984, A commentary on the recent CO_2-climate controversy, *Climatic Change,* v. 6, p. 365-376.

Driese, S.G., Byers, C.W., and Dott, R.H., 1981, Tidal deposition in the basal Upper Cambrian Mt. Simon Formation in Wisconsin, *Journal of Sedimentary Research,* v. 51, p. 367-381.

Dupraz C, Fowler A, Tobias C, Visscher P., 2013, Stromatolitic knobs in Storr's Lake (San Salvador, Bahamas): a model system for formation and alteration of laminae, *Geobiology,* v. 11, p. 527-548.

Ennis-King, J., and Paterson, L., 2003, Role of convective mixing in the long-term storage of carbon dioxide in deep saline formations, *in* Proceedings SPE Annual Technical Conference and Exhibition.

Fenchel, T., Blackburn, T.H., 1979, Bacteria and mineral cycling. Academic Press, Inc. (London) Ltd.

Foster, J.S., Mobberley, J.M., 2010, Past, present, and future: microbial mats as models for astrobiological research, *in* Microbial Mats. Springer, pp. 563-582.

Gauss, I., Azaroual, M., Czernichowski-Lauriol, I., 2005, Reactive transport modelling of the impact of CO_2 injection on the clayey cap rock at Sleipner (North Sea), *Chemical Geology*, v. 217, p. 319-337.

Greenwood, P.J., Shaw, H.F., Fallick, A.E., 1994, Petrographic and Diagenetic Evidence for Diagenetic Processes in the Middle Jurassic Sandstones and Mudrocks from the Brae Area, North Sea, *Clay Minerals*, v. 29, p. 637-650.

Goldberg, P., Chen, Z.-Y., O'Connor, W., Walters, R., Ziock, H., 2001, CO_2 mineral sequestration studies in US, *Journal of Energy and Environmental Research,* v. 1, p. 117-126.

Hammes, F., Verstraete, W., 2002, Key roles of pH and calcium metabolism in microbial carbonate precipitation, *Reviews in Environmental Science and Biotechnology,* v. 1, p. 3-7.

Jun, Y.-S., Giammar, D.E., Werth, C.J., Dzombak, D.A., 2013, Environmental and Geochemical Aspects of Geologic Carbon Sequestration: A Special Issue, *Environmental Science and Technology,* v. 47, p. 1-2.

Kump, L.R., Brantley, S.L., Arthur, M.A., 2000, Chemical weathering, atmospheric CO_2, and climate, *Annual Review of Earth and Planetary Sciences,* v. 28, p. 611-667.

Metz, B., Davidson, O., de Coninck, H., Loos, M. and Meyer, L., 2005, IPCC special report on carbon dioxide capture and storage. Intergovernmental Panel on Climate Change, Geneva (Switzerland). Working Group III.

Pacala, S. and Socolow, R., 2004, Stabilization wedges: solving the climate problem for the next 50 years with current technologies, *Science*, v. 305, p. 968-972.

Post, W.M., Izaurralde, R.C., Jastrow, J.D., McCarl, B.A., Amonette, J.E., Bailey, V.L., Jardine, P.M., West, T.O., Zhou, J., 2004, Enhancement of carbon sequestration in US soils, *Bioscience* v. 54, p. 895-908.

Raynaud, D., Jouzel, J., Barnola, J., Chappellaz, J., Delmas, R., Lorius, C., 1993, The ice record of greenhouse gases, *Science*, v. 259, p. 926-933.

Schlesinger, W.H., 1999, Carbon sequestration in soils, *Science,* v. 284, p. 2095.

Thorleifson, L. H., ed., 2008, Potential Capacity for Geologic Carbon Sequestration in the Midcontinent Rift System in Minnesota, Minnesota Geological Survey Open File Report OFR-08-01, 138 pp.

White, C.M., Strazisar, B.R., Granite, E.J., Hoffman, J.S., Pennline, H.W., 2003, Separation and capture of CO_2 from large stationary sources and sequestration in geological formations—coal beds and deep saline aquifers. *Journal of the Air & Waste Management Association,* v. 53, p. 645-715.

Xu, T., 2011, Reactive Transport Modeling for CO_2 Geological Sequestration, 2011, *Journal of Petroleum Science and Engineering*, v. 78, p. 765-777.

II. EXPERIMENTAL METHODS

1. FIELD SAMPLE COLLECTION SITES AND COLLECTION PROCEDURES

Water and rock samples were collected, and *in situ* water analyses were performed from multiple sites across North America to investigate several topics related to carbon sequestration and carbonate mineralization (Figure 1). These sites included:

1. Maramec Spring, Missouri.
2. The Midcontinent Rift sedimentary-volcanic sequence in the Lake Superior Region and subsurface continuations of the same sequence of rocks in Iowa and Kansas.
3. Hypersaline lake systems at Lake Estancia, New Mexico, and Great Salt Plains State Park in Oklahoma.
4. Microbialite communities in Storrs' Lake, San Salvador Island, The Bahamas.

1.1. Maramec Spring, Missouri

Maramec Spring is Missouri's fifth largest cold-water spring. It is located in Phelps County, Missouri, 11 km southeast of St. James. After the spring water upwells to the surface, it collects into an oval shaped pool with a surface area of approximately 3100 m^2 (33,000 ft^2; Figure 2). Water from the pool then bifurcates into two waterways as it flows northward, with a relatively small portion of the water also being diverted into a third concrete water chute that is used as a trout hatchery. The majority of the pool water, however, flows over a rock dam in the central channel. The three branches eventually rejoin, bifurcate again, and rejoin a final time again as the stream system travels in a series of flowing riffles and slow flowing pool systems. All water and fine particulate material collected for this investigative study were obtained from the Maramec Stream system at different intervals as it flows from its point of initial upwelling from the subsurface to its termination to the south where it merges with the Meramec River. The stream originates at the spring upwelling (sampling location #1; Figure 2) and then is comprised of a series of falls (location #3) rapids (locations #6-8), shallow riffles (location #4), and slow moving water pools (locations #2 and #5). These eight sampling locations are ordered numerically from furthest upstream at the point of spring water upwelling (location #1), to furthest downstream (location #8). Moving downstream from location #1, the cumulative nautical distance from the point of upwelling is: location #2, 60 m; location #3, 105 m; location #4, 290 m; location #5, 530 m; location #6, 845 m; location #7, 1050 m; and location #8, 1295 m. Maramec Stream continues another 65 meters past location #8 before it empties into the Meramec River, thus travels a total distance of 1360 meters. Water samples (filtered and unfiltered, field chemical and physical measurements, and colloidal particles were collected from the site during numerous visits between 2001 and 2012, however the majority of the samples were collected between 2009 and 2012.

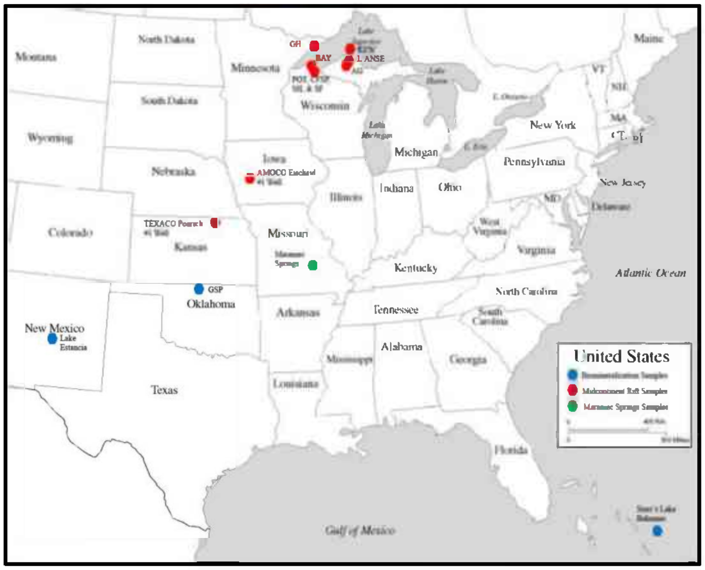

Figure 1. Sample locations for this study: Carbonate mineralization at Maramec Spring (green dot), CO_2 sequestration in the Midcontinent Rift (red dots), and biomineralization of carbonate minerals (blue dots). Abbreviations for sample locations: KEW, Keweenawan Peninsula; L'ANSE, L'Anse (Michigan); AG, Agate Falls; GH, Good Harbor; BAY, Bayfield Peninsula; POT, Potato River Falls; CFSP, Copper Falls State Park; SH, Saxon Harbor; SF, Superior Falls; and GSP, Great Salt Plains. The Amoco Eischeid #1 and Texaco Poersch #1 drill wells are also shown.

Figure 2. Google Earth Image outlining the sampling locations at Maramec Spring from this study. The point of the spring conduit upwelling is located at sampling location #1. Stream flow is from south (bottom of photograph) to north (top of photograph). The roadway in the lower right corner of the photograph is Missouri Highway 8.

1.2. Midcontinent Rift Sequence

Forty eight rock samples from surface outcrops were collected from various locations around the Lake Superior Region (Figure 3) as well as twenty one subsurface petroleum exploration drill core samples from the M.G. Amoco Eischeid #1 well in Iowa and the Texaco Poersch #1, well in Kansas (Figure 1). These samples were used to determine rock petrographic characteristics, bulk geochemistry, clay matrix mineralogy, and to provide samples for corrosion testing experiments with a $CO_2 + H_2O$ atmosphere. The Lake Superior surface samples included collection sites from the Keweenaw Peninsula (MI), the L'Anse area (MI;), Agate Falls Park (MI), Potato River Falls (WI), Copper Falls State Park (WI), the Bayfield Peninsula (WI), Beaver Bay Complex (MN), North Shore Volcanic Group (MN), and Duluth Complex (MN). The Eischeid #1 petroleum exploration well is located approximately 8 kilometers northwest of the buried Iowa Horst, penetrating through about 14,898′ of the rock sequences at the northern end of the Defiance Basin (Figure 1). Samples from this well were provided by the Iowa Geological Survey. Subsurface samples of the MCR sequence were also obtained from the Texaco Poersch #1 petroleum exploration drill well in Kansas (Figure 1). Samples from this well were provided by the Kansas Geological Survey.

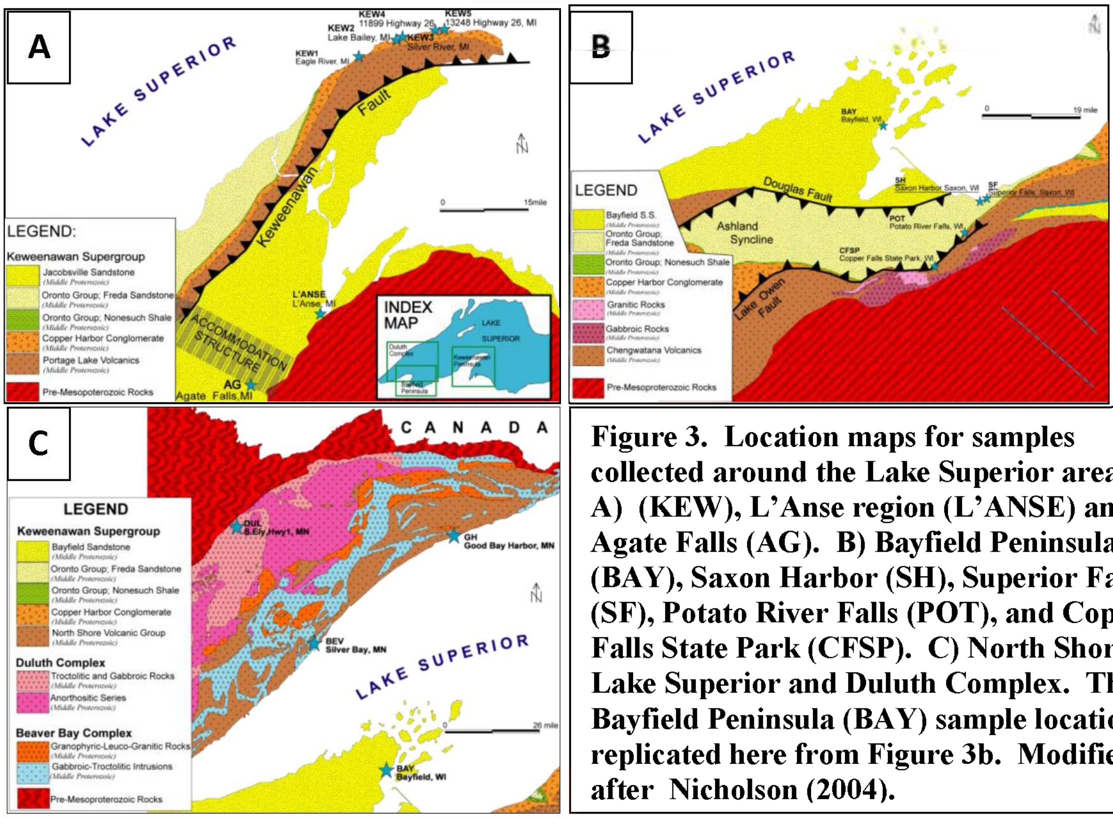

Figure 3. Location maps for samples collected around the Lake Superior area. A) (KEW), L'Anse region (L'ANSE) and Agate Falls (AG). B) Bayfield Peninsula (BAY), Saxon Harbor (SH), Superior Falls (SF), Potato River Falls (POT), and Copper Falls State Park (CFSP). C) North Shore Lake Superior and Duluth Complex. The Bayfield Peninsula (BAY) sample location is replicated here from Figure 3b. Modified after Nicholson (2004).

1.3. Sulfate Reducing Bacteria - Microbial Biomineralization Study

Three hypersaline lake sites were sampled in the microbial biomineralization study to collect samples of microbial communities, for water composition, and mineralogy determination. These sites included the Great Salt Plains Lake in Oklahoma, Lake Estancia in New Mexico, and Storrs' Lake on Sal Salvador Island in The Bahamas. The Great Salt Plains is a 65 km^2 lake in north-central Oklahoma that is a manmade impoundment formed from a concrete spillway built across the Salt Fork of the Arkansas River. The western area of the lake, where samples were collected, is composed of a salty sabkha mud flat (Figure 4a; Reed, 1982). The area derives its salts through the upwelling of groundwater that had previously penetrated through gypsum-bearing strata to the west. Gypsum crystals actively precipitate within the sabkha sediments and a white evaporite crust forms on the sediment surface. Lenses of organic-rich sands are also interstratified within organic-poor sands (Figure 5a). Filtered water, subsurface sediment materials, and core sediment samples were collected during a visit to the site in May 2010. The water samples were collected from seepage at a depth of ~30 cm from a shallow pit dug into the sand, while two sediment profile cores were collected using a one-meter piston core that was hammered into the soft sediment. The core and sediment samples were kept intact by placing them in coolers and transported to the laboratory for further analysis.

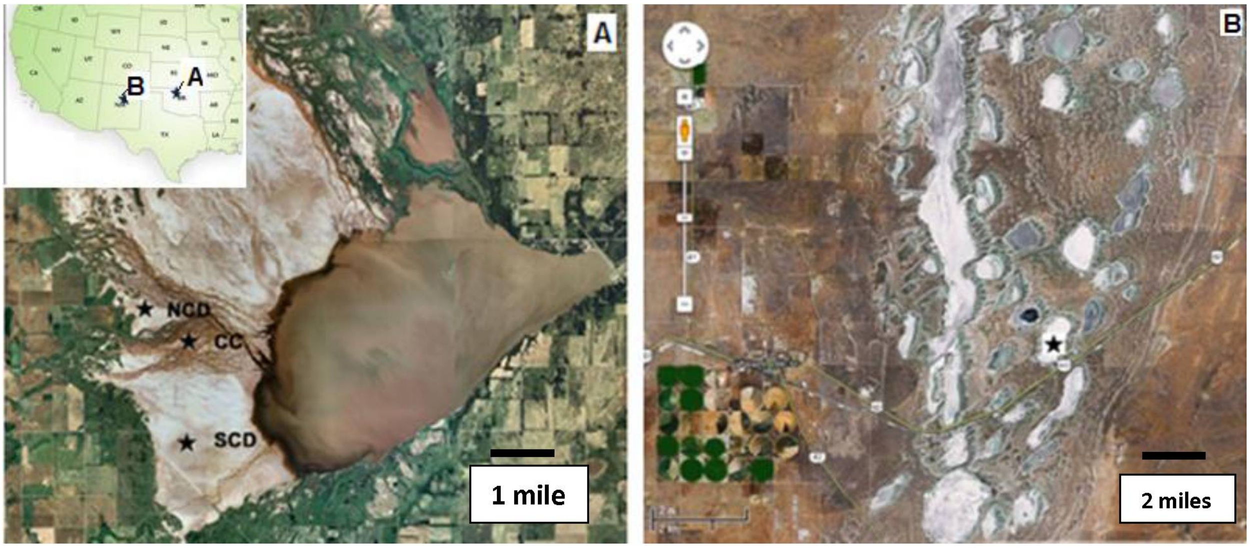

Figure 4. Google maps of Hypersaline lakes: A) Great Salt Plains Lake, Alfalfa County, Oklahoma. SCD-South Crystal Dig, CC-Clay creek, NCD-North Crystal Dig. Samples for this study were collected from SCD [Image from the 2003 NAIP aerial image database http://www2.ocgi.okstate.edu/2003img1/]. B) Lake Estancia and Estancia Basin, Torrance County, New Mexico. Star indicates the location where samples were collected. Inset in A shows the locations of Lake Estancia and Great Salt Plains Lake in the US map.

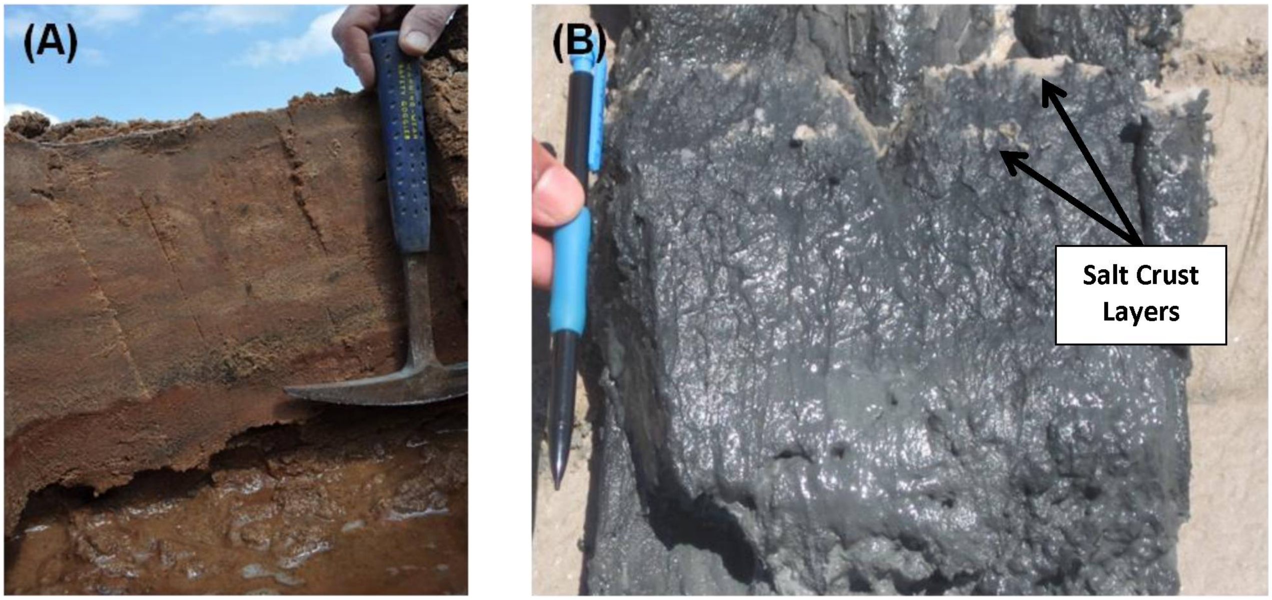

Figure 5. (A) Cross-cut section of sedimentary strata from Great Salt Plains Lake. The stratified sequence displays three weakly developed organic layers (black colored) near the top, middle, and lower sections (the latter just above the point of the hammer). Relatively coarse grained and permeable sections are represented by the lighter layers and the red layers are typically finer-grained and less permeable. (B) A vertical section of the organic- and sulfide- rich sediments of Lake Estancia. Lighter-colored evaporite material with occasional salt crystals are seen at the top surface layer and a second evaporite layer occurs ~5 cm below the surface. The majority of the remaining sediments are composed of the dark, organic-rich material.

Lake Estancia, New Mexico is a closed-drainage, paleoglacial playa lake located at an elevation of approximately 1,890 meters (6,200 feet) and has a surface area of 1,125 km^2. The lake basin was formed during crustal extension and uplift along the margin of the Rio Grande Rift (Szynkiewicz et al., 2009). It once covered a much larger aerial extent during the Pleistocene. A change to a warmer and drier climate eventually led to the desiccation of the lake system starting about 24,000 years before present, thus leaving the large playa on the basin floor. More recent sand blow-out zones have locally removed loose sediments from the valley floor and created numerous small depressions on the order of ~50 feet deep that fill with water during seasonal periods of rainfall (Figure 4b). Carbonates, clays, gypsum, and organic-rich muds occur in the lake sediments; these carbonates and gypsum are also present in the surrounding lower and middle Permian-aged geologic strata (Allen and Anderson, 2000; Szynkiewicz et al., 2009). The water level was ~30 cm in the center of the pond that was sampled during the single visit to the site in May 2010. Salt evaporates were noted at the surface of the submerged sediments, along the dried up lake shore, and in buried sediments beneath layers of organic rich mud (Figure 5b). Filtered water, subsurface sediment materials, and core sediment samples were collected.

Storrs' Lake is located on the eastern portion of San Salvador Island, The Bahamas (Figure 6). This lake formed during the late Holocene sea level rise when a depression on the east side of the island was flooded. Modern evaporitic conditions cause the lake to exhibit variable and seasonally hypersaline conditions (Neumann et al., 1989; Zabielski, 1991). The lake is fairly shallow with maximum depth of approximately two meters. The water is slightly alkaline, and is extremely turbid as a result of planktonic organisms and benthic components which become suspended along with gases released from microbial metabolism (Neumann et al., 1989; Mann and Nelson, 1989). The water exhibits a characteristic reddish-brown color due to this suspended organic material (Figure 7C). Storrs' Lake is one of just two environments known that contain hardened and calcified microbialite mounds that grow in limited light conditions, along with Pavilion Lake, British Columbia, Canada (Laval et al., 2000; Lim et al., 2009).

Storrs' Lake was sampled during three visits in April 2011, June 2012, and June 2013. Both microbialite and water samples were collected in 2011 and 2012, and only water samples were collected in 2013. The year 2011 was relatively dry with the total rainfall for the months of February and March recorded at only ~1.0 cm, while in 2012 and 2013 the lake received a substantial increase in the amount of freshwater inflow due to heavy rainfall. Water samples (~20-50 mL) were collected at different locations along a transect in the western portion of the lake where several different water depth sample profiles were collected. Water depth was measured by using a centimeter-marked PVC pipe with the length between the top surface of the lake sediments and the water surface being noted as the water depth. The transect was started near a man-made conduit inlet to the lake on the western shore to the Cactus Island in the northern portion of the lake (Figures 6C and 7A). This transect was similar to that used by Mann and Nelson (1989, section B-B') and Neumann et al. (1989). For comparison purposes, ocean water was also collected from Dim Bay in 2012 at the beach opposite to the southern extremity of Storrs' Lake.

Living microbial communities were found on the surface of the microbialites mounds and ranged from few millimeters to ~1 cm thick, and were either uniform or sporadic in their distribution on the top surface of the mounds. The offshore 'cheesecake' leathery mats, described by Neumann et al., (1989) were present extensively on the lake soft-sediment bottom between the microbial mounds. Four distinct microbialite morphologies have been previously identified in discreet zones within the lake (Mann and Nelson, 1989; Neumann et al., 1989). Moving from shore to the lake center these include the clotted thrombolite pie mound, crumbly, calcareous knob (up to 15 cm tall), flat-topped plateau laminated stromatolites, and taller and narrower pinnacle mounds (i.e. club-shaped), which can extend up to 70 cm in length. The pie mound and calcareous knob types are often exposed above the water line during periods of low lake levels (Figure 7C) while the plateau and pinnacle mounds occur under deeper and have never been observed above the water level of the lake.

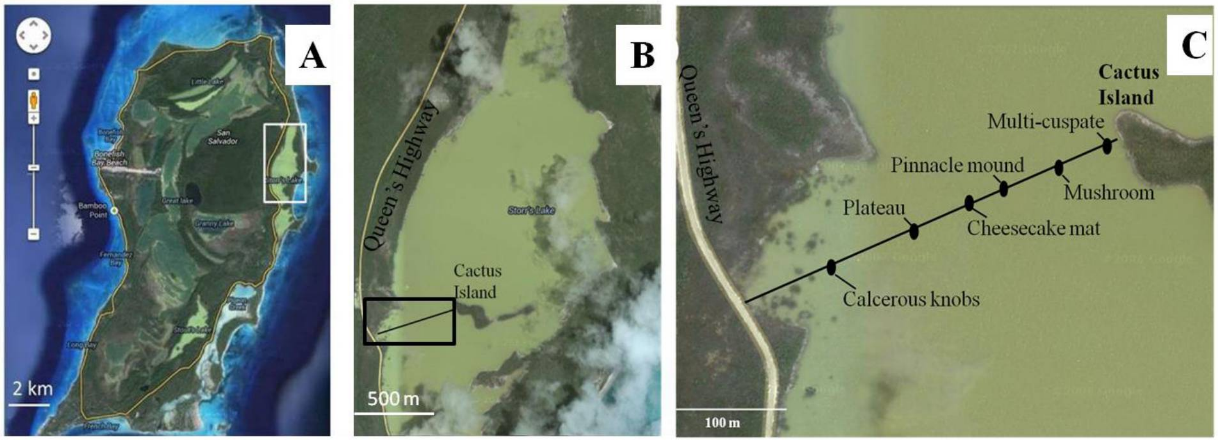

Figure 6. Overview of the collection sites at Storrs' Lake. (A) Google map of San Salvador Island with located noted along the eastern-margin of the island (white box). Bar = 2 km; (B) Magnified image of white box depicting the northern section of Storrs' Lake. The line indicated by the star represents the approximate transect along which the water and microbialite samples were collected Bar = 500 m; (C) Magnified Google map image of the black box in Figure 6b showing the locations, where the different microbialites and microbial mats were sampled in 2011 and 2012.

Figure 7. A) The conduit located on the western shore of Storrs' Lake through which low-turbidity brackish and tannin-rich water enters the lake. B) Image of the lake from the western shore in 2013 displaying two different water turbidity zones with the transition shown by arrows. Distance from shore to the transition zone is ~60 m. Cactus Island forms the shoreline in the far background in right half of photograph. C) Image taken in 2011 of a calcareous knob microbialite with head sticking out of the reddish-brown and high-turbidity lake water.

1.4. Centrifuged Water Sample

Particulate samples were collected by centrifuging four liters of Maramec after transporting the samples back to the Missouri S&T laboratory. Samples were centrifuge for a half-hour, the water was decanted, and the solid contents in the bottom of the vessel were scraped into a petri dish and examined my microscopy techniques. This sample was collected on 9/21/2007.

1.5. Filtered Water Samples

Water samples from all field sites and laboratory experiments for chemical analysis were filtered immediately upon collection using a disposable plastic syringes and 0.45 µm cellulose acetate filter and while simultaneously injecting the filtrate into precleaned 50 mL plastic vials. Rapid filtration and sample collection was vital for many of the samples as changes associated with the loss (CO_2) or gain (O_2) of gaseous components into the water may influence the solubility of various elements. The Maramec Stream water samples were filtered using either a 5.0 µm nylon, 0.45 µm cellulose acetate, and/or 0.02 µm alumina filters. Unfiltered water sample were also sometimes collected giving four filter sizes for the water samples (unfiltered, <5 µm , <0.45 µm, <0.02 µm). For most samples though, only the 0.45 µm cellulose acetate filter was used. All samples were placed into an insulated cooler to prevent warming of the samples and transported back to the laboratory. Samples for cation analysis were acidified with a high-purity nitric acid upon return to the laboratory, while samples for anion analysis were not acidified.

Filters from the 5/13/12 sampling at Maramec Spring were also processed in the field in the usual manner as described above. A second aliquot of water was also collected in a one liter bottle, transported back to the Missouri University of Science and Technology laboratory, placed in an insulated cooler to maintain river water temperatures, and left opened for venting. Filtered water samples were then collected after 12 and 36 hours using the <5 µm , <0.45 µm, <0.02 µm filters. The filters (which are contained in a sealed plastic housing) were then rinsed with deionized water to remove any spring water attached to the particles or filters, dry sparged to remove excess water, refilled with a 5% high-purity nitric acid solution and held for four hours, then syringed pumped with additional acid to flush out and collect the digested material. The acid flushed alumina <0.02 µm filters released the greatest amount of dissolved components so these were reported upon in Section III, with the exception of Al which was reported upon from the 0.45 µm cellulose acetate filters.

Maramec Spring water was also subjected to a third filtration process using a Masterflex peristaltic pump vacuum system and Millipore cellulose filters. This equipment facilitated the processing of large water volumes so that particulate material could be collected from the water samples directly at the field site without the delay of transporting samples back to the laboratory. The particulate material was collected using this system on two different sampling dates. On 8/29/2010 a four liter water sample was filtered on site from sampling location #1 using a 0.22 µm cellulose filter and a mechanical vacuum filtration system. Four liters of water from the sampling locations #1, #5, and #8 were also filtered sequentially using 5.0 µm, 0.45 µm, 0.22 µm, and 0.05 µm cellulose filters on 10/6/2010 and 10/26/2012. All vacuum filtered samples were returned to the Missouri S&T campus, allowed to dry at room temperature, and examined using a scanning electron microscopy- energy dispersive spectroscopy (SEM-EDS and X-ray diffraction analysis (XRD).

1.6. Collection of Microbial Samples

Microbial samples from Great Salt Plains, Lake Estancia, and Storrs' Lake were aseptically collected in duplicate (5 -10 g each) and immediately stored in a nucleic acid preservation solution (LifeGuard Soil Preservation solution, MoBio Laboratories, Carlsbad, CA, USA). The mat samples from Storrs' Lake were transported back to the Gerace Research Centre lab and placed in a freezer within eight hours of sampling. The frozen mats were placed in an insulated cooler for transportation to the Missouri University of Science and Technology labs. Great Salt Plains and Lake Estancia microbial samples were placed in a thermal cooler and kept below 20^{o}C during the field travel. Microbial culture inoculations were collected from the samples in the field, then returned to the Missouri S&T laboratory and placed in a -20°C freezer until they were used for molecular analysis.

1.7. Collection of Rock Samples

Surface outcrop rock samples from the Midcontinent Rift were collected from actively eroding river valleys and lake shore locations whenever possible. These high-energy erosive environments tend to mechanically abrade away the chemically weathered material thus minimizing the influence of element redistribution in a weathering profile. Surface outcrop samples were trimmed in the field using a rock hammer to remove visibly weathered surfaces, if present. The mineralized portions of microbial mound samples from Storrs' Lake were placed into clean water-tight polypropylene containers along with lake water. Samples were then placed in a cooler and transported back to the Gerace Research Centre lab and stored in a refrigerator. These samples were transported back to the Missouri University of Science and Technology labs in an insulated cooler and also placed in a refrigerator upon arrival.

2. CHEMICAL AND PHYSICAL ANALYSIS OF WATER SAMPLES

Water samples for analysis included four different sample matrices. The first set included natural field water samples analyzed *in situ* or collected directly from Storrs' Lake, Great Salt Planes, Lake Estancia, and Maramec Stream. A second set of solutions were generated by the complete dissolution of carbonate mineral samples by acid digestion. The dissolved mineral materials included microbialite samples collected from Storrs' Lake and micron-sized particles collected by filtering water samples from the Maramec Stream system. The third set of water samples were derived from the laboratory corrosion tests with the Midcontinent Rift rock samples that were reacted in a $H_2O + CO_2$ environment at 90^{o}C. These rock samples released some components to solution but were not completely dissolved. The final set of samples were produced in the laboratory with the mineral precipitation experiments using the microbial reactors and involved the reactions of the microbial communities in a synthetic seawater solution.

2.1. *In Situ* Field Analyses of Water Samples for Eh-pH, Conductivity, Temperature, and Dissolved Oxygen

Water samples were analyzed *in situ* for pH and Eh (Accumet AP115 portable pH-Eh meter, conductivity and temperature (WTW Cond 333i), and dissolved oxygen (Accumet AP64 dissolved oxygen meter with an Au/Ag cathode/electrode). Analysis of standards before, during and after measurements indicated an accuracy of ± 0.05 pH units or better for the 7.00 pH standard, and a precision better than ± 0.2 %. An average error percentage of ± 8.2 % and ± 3.2 % was determined for the conductivity probe when checked with 1,008 and 100.8 mS/cm standards, with precisions better than 4.5 % and 7.9 %, respectively. Conductivity measurements at Storrs' Lake were tested against a 100,000 mS/cm standard and were accurate to within 5%. Eh analyses are referenced against an internal platinum standard and temperature was calibration checked using ice water. The dissolved oxygen probe was calibrated by saturating a sponge with deionized water and allowing it to equilibrate in a 100% relative humidity environment which produces an 8 ppm oxygen solution. The dissolved oxygen probe was also immersed in a CO_2 rich/O_2 poor atmosphere. It reported less than 0.12 mg/l of dissolved oxygen in this environment. No drift was observed within the dissolved oxygen probe from location to location with Maramec Spring measurements, however, the accuracy for the probe diminished during Storrs' Lake measurements in 2012, thus only qualitative measurements could be made at that time.

2.2. *Ex Situ* Field Analyses of Alkalinity and Ca-Mg-Hardness

Alkalinity and Ca-Mg hardness were measured on site after extracting water samples for analysis. All of these measurements were made by colorimetric titration by using respective HACH test kits (Loveland, CO, USA). Samples for alkalinity were always given highest priority to allow a measurement to be completed with minimal potential loss of CO_2 from the system. It was not possible to conduct an immediate alkalinity measurements at Storrs' Lake, so samples were placed in a one liter Nalgene bottle filled completely to the brim, capped tightly, and then kept at ambient water temperature until measurements could be made (within 2 to 3 hours). The alkalinity values represent milliequivalent/L concentration (meq/L; millimolar concentration * ionic charge). Ca-Mg hardness measurements for the high-salinity lake water samples required dilutions in 1:20 or 1:100 ratios with deionized water. The Ca-, Mg-, and total- (Ca + Mg) hardness values are expressed in mg/kg of the respective carbonate compound (e.g., $CaCO_3$).

2.3. Turbidity and Light Penetration Measurements for Field Samples

Turbidity-light penetration measurements were quantitatively measured at Storrs' Lake using a Secchi Disk and light intensity loggers from HOBO (Cape Cod, MA, USA). The waterproof HOBO light meters were placed at several locations at the bottom of the lake by attached to metal spikes with monofilament thread and anchoring the buoyant probes at a water height equivalent to the top of the adjacent microbialite probes. The probes were also attached to a floating fishing bobber to allow the units to be relocated and recovered. Data from the probes was recorded by using the HOBOware data processing software program.

Turbidity in the Maramec Spring-Stream system and Storrs' Lake were measured using a HACH 2100P Nephelometric Turbidity Unit (NTU) light scattering turbidimeter, Standards for NTU turbidity measurements indicated an average accuracy error percentage of ± 6.8 %. The settling rate of the particles from Storrs' Lake were determined by collecting lake water samples and testing for turbidity at regular intervals under controlled, enclosed laboratory conditions. A water sample collected in 2012 was also placed in a clean glass vial and allowed to remain undisturbed in the dark chamber of the turbidimeter for a six-month period at room temperature as turbidity values were periodically recorded. A comparison was made between the settling rates of the Storrs' Lake organic particles versus those of the clay minerals illite (illite-bearing shale, Fithian, Illinois) and smectite (Wards Scientific and Clay Mineral Society Standard, STX-1). The clay samples were dispersed in a solution prepared with 5% synthetic seawater – 95% deionized water. The humid external air near the Maramec Spring system combined with the cool temperature of the spring water often caused water condensation on the glass turbidity vessels in the warmer seasonal months, thus preventing accurate measurements from being made during those seasonal periods.

2.4. Total Suspended Solids – Total Dissolved Solids Analysis

A one liter sample of unfiltered water from Maramec Spring was collected on October 6, 2010 at sample location #1 for total dissolved solids (TDS) and total suspended solids (TSS) analysis. TDS and TSS analyses were completed using a 0.45 μm cellulose filter and vacuum filtration. The filter was dried at 103°C for 1 hour and then weighed using a four decimal place balance. The filter was pre-wetted and placed on a pre-cleaned filtration apparatus. After filtration, the filter paper was removed, covered, and allowed to dry at room temperature. After drying the filter paper was further dried in a 103°C oven for 1 hour. TSS was calculated by subtracting the difference in the weight of the dried filter paper both before and after filtration and then dividing by the known volume of water passed through the filter. The filtrate was placed into a pre-weighed 150 mL beaker, covered with a watch glass, and placed in an oven at 90°C until the water was completely evaporated. The temperature was then ramped up to 185°C for 8 hours to remove any residual water. The beaker was allowed to cool at room temperature in a desiccation chamber for 45 minutes, and then was weighed on a four decimal place balance. TDS was calculated by dividing the weight of the solid evaporite material collected in the beaker by the volume of water sample evaporated.

2.5. Inductively Coupled Plasma – Optical Emission Spectroscopy (ICP-OES) Analysis for Cations

All water samples for Inductively Coupled Plasma – Optical Emission Spectrometer (ICP-OES) analysis were acidified using ultra-pure HNO_3 to a pH of ~2 or lower upon return to the laboratory and stored until analysis. The higher salinity Storrs' Lake, Lake Estancia, and Great Salt Plains water samples were diluted prior to analysis at a ratio of 1:10 or 1:100 to bring the solution concentrations within or near the optimum instrumental detection range of 1.0 to 100 ppm.

Both the acidified water samples and any collected acid digested solids were analyzed on a Perkin Elmer Optima 2000DV ICP-OES unit to determine the water chemistry. Resulting solutions were typically analyzed for Ca, Mg, K, Na, Si, Al, Fe, and Mn. The elements B, S, Sr, and Li were also measured for the 2011 Storrs' Lake water samples. Commercially traceable standard solutions (starting concentration of 1,000 ppm) of the different cations were prepared at 100, 10, 1 and 0.1 ppm, with 1% HNO_3 in high-purity deionized water as the diluting agent. The standards were used for calibration and for quality control checks during each run.

Accuracy and precision was calculated for all analysis that allowed calibration of the instruments, by using the measurements from known standards. Accuracy was calculated as the deviation from the known sample concentration while precision was calculated as a standard deviation from the mean value. Analytical results for the standards display a high degree of precision with repeatability often 1% or better relative to the expected value of the standard. The measured accuracies for both the 10 ppm standards were generally 3% or better for Ca, Mg, and Al; 5% or better for Si, K, Na, and Fe; 8% or better for Li, B, and Mn; and 13% or better for Li. The ICP-OES limit for determination is approximately 0.1 ppm though accuracy values often fall to 30% or worse at these low concentration values. Blanks using American Society for Testing and Materials - Type 1 deionized water are also routinely run using the disposable syringes and filters. None of the elements of interest to this study have been detected in the blanks using deionized water. Aluminum contributions from the 0.02 micron alumina filters are sometimes noted, however, especially with more acidic waters. Aluminum determinations thus are not reported from the 0.02 μm filters.

Sulfide ion (S^{2-}) determinations were made using the colorimetric $CuSO_4$ method (Cord-Ruwisch, 1985), by using a Genesys 20 spectrophotometer (Thermo Fisher Scientific, Inc., Rochester, NY, USA). The error range was within ± 7.7 % for sulfide analysis tested with 0.78, 3.13, and 12.5 mM standards prepared with sodium sulfide (Na_2S). Sulfur determinations by ICP-OES were of lower quality, with error percentage ± 45 % for 1 ppm and ± 36 % for 10 ppm standards.

2.6. Ion Chromatography Analysis for Anions

Anions (sulfate and chloride) were analyzed for the Storrs' Lake 2012 and Maramec Spring 2010 water samples using a Dionex DX-120 Ion Chromatography (IC) Unit at VHG Labs (Manchester, NH). Samples for anion analysis were filtered on site using the same disposable 0.45 μm cellulose acetate syringes and filters used for the cation ICP-OES samples. The IC samples were not acidified, however. 100 mL of 1:100 diluted samples (diluted with 0.45 μm filtered, deionized water) were sent to the laboratory for analysis. The maximum error percentage reported by VHG Labs for anion analysis was ± 7.0 %. Analyzed anions included fluoride, chloride, nitrate, phosphate, and sulfate. Minimum detection limits for chloride, nitrate, sulfate, and phosphate are 0.05, 0.1, 0.01, and 0.2 ppm, respectively. Laboratory and field blanks were run in addition to a 5 ppm reference standard. Measured values of the 5.0 ppm standard for chloride, nitrate, phosphate, and sulfate are 4.44, 4.7, 4.8, and 4.6 ppm, respectively, thus all analytical determinations were accurate to within 4 to11%. One sample duplicate was run to determine the repeatability of measurements and precision was determined to be 3% or better. Lab water and field water blanks were processed using American Society for Testing and Materials Type I deionized water. Determined elemental concentrations for all blanks were below the instrument detection limits.

2.7. Saturation Index Modelling Using the PHREEQC Modelling Program

PHREEQ software program (United States Geological Survey, version 3.1.2.8538; Parkhurst and Appelo, 3/3/2014) was used to compare analyzed water parameters to saturation index values. These comparisons were made for the water concentrations at Storrs' Lake, Maramec Spring, and many of the laboratory experiments associated with this project. The output from PHREEQ program gives the saturation index (SI) of various minerals based on the water chemistry and temperature, as well as the minerals that may be expected to precipitate. The saturation index is defined as the log of the ratio of the ion activity product of components in solution divided by the equilibrium solubility product (K_{sp}) of a respective mineral phase.

3. MINERAL AND ELEMENTAL ANALYSIS OF SOLID PHASES

3.1. X-Ray Diffraction (XRD) Analysis

X-Ray Diffraction (XRD) scans were conducted at a two-theta at a scan rate of 2.8° (2-theta; 2θ) per minute, at 0.03 degree step intervals, using a PANalytical X'Pert Pro Multi-Purpose X-Ray Diffractometer with a $Cu_{K\alpha}$ radiation source (wavelength of 1.54 Å). The software program used in the operation of the instrument determined semi-quantitative comparison of the relative percentages among the minerals identified. The software automatically calculated the area of the peaks observed for the different minerals and correlated the area to the relative percentage.

Only minute volumes of particulate material were collected by filtration from Maramec Spring water, thus the particulate material was scanned while still attached to the filter paper. Both the unused sterile filter sheet (blanks) and the filtered Maramec Spring water samples were taped to glass slides before XRD analysis. An analysis of the blank filter plus glass slide mount produced a broad X-ray background centered at approximately 20^{o} 2θ, but did not reveal any sharply defined peaks that would indicate the presence of any crystalline compounds over the 2θ scan range used. Maramec Spring samples were scanned between 6^{o} and 60^{o} 2θ.

Powder X-Ray diffraction was also conducted to investigate the mineral composition of the whole rock MCR samples. These samples were mechanically crushed using a stainless steel "hockey-puck and ring" shaker box crusher for less than 30 seconds, and then sieved to collect the < 64 μm fraction. Samples were continuously crushed until all material passed through the sieve. These samples were packed into press-mount circular aluminum disk holders and the analyzed by XRD. The clay-sized fraction of minerals (< 4 um) from the MCR samples was also isolated from the sample matrix by water gravity separation technique and then analyzed by XRD analysis. Each sample run was prepared by hand crushing using an agate mortar and pestle to isolate approximately 25 g of the sample. The samples were then suspended in a glass beaker with 100 mL of deionized water and decanted to collect the finer suspended fraction. A few drops of sodium hexametaphosphate were added if the materials continued to settle too quickly. The suspended materials were then carefully pipetted from the top portion of the solution and placed on labeled, thermally resistant glass slides where they were left to dry overnight. XRD scans were run on untreated sample slides, slides exposed to an ethylene glycol atmosphere for 12 or more hours (to expand smectite clays), and heat heated samples after a 300°C exposure for one hour. Clay-mount XRD scans were made using the same PANalytical X'Pert Pro system described previously, however, the scans were run only between 2 and 36°.

Microbialite carbonate sediment samples that were collected from Storrs' Lake, as well as sediment samples from Lake Estancia and Great Salt Plains were analyzed for their mineral content using XRD analysis. These microbialite material was hand crushed to a fine powder with a mortar and pestle, rinsed three times with deionized water to remove any soluble sea salts and low density organic particles, then dried overnight in an oven at 55°C prior to analysis. Samples included homogenized microbialites with equal mass sections collected from ~1 cm^3 partitioned replicate sections from random positions within each of the four microbialite heads, and individual samples collected from ~2 cm^3 regions throughout the mounds from various areas in samples. Spikes of an aragonite standard were added to one of the Storrs' Lake samples to check the accuracy on the XRD mineral percentage quantification program.

3.2. Optical Microscopy Analysis

An optical microscope (Nikon Eclipse 50i POL) capable of magnification of up to a 1000X, fitted with a Nikon DS-Fi1 camera and operated by using a NIS-Elements D 3.2 image software was used to visualize particulate material collected from Storrs' Lake and Maramec Spring water samples. The hypersaline water samples from Storrs' Lake was centrifuged at 2,000 rpm and the residue was rinsed with deionized water with a centrifugation step each time to dilute the salt content. After the final rinse, a drop of the solution was placed on a clean microscope slide, a cover slip added on to the top of the solution, and the microorganisms were viewed under the microscope. The Maramec Spring particulate samples were collected by both centrifugation and filtration onto 0.45 and 0.22 μm cellulose acetate filter paper.

The microbialite mound samples from Storrs' Lake were also mounted in epoxy, cut, and polished smooth down to a 0.3 μm finish using alumina and diamond paste compounds. These samples were examined using a 126-X Nikon binocular reflected light microscope to examine fine scale layering features of the microbialite mounds.

The MCR samples were investigated for mineral composition, porosity, and textural maturity (roundness) using a petrographic Nikon 2000 polarized microscope. Selected sections of each sample were trimmed with a diamond wafer saw using deionized water as a lubricant, and then sent to National Petrographic Services, Inc. in Houston for thin section mounting and staining. The stain for the samples included alizarin red-S to test for calcite, sodium cobalt nitrite for detection of potassium feldspar, and staining with barium chloride and rhodizonate to detect plagioclase feldspar. The thin sectioned samples were point counted while viewing under the microscope to examine between 270 to 300 point counts per thin section as a minimum statistical satisfaction of point counting (Dickinson, 1985; Dickinson, 1970). The spacing between any successive points was set to one mm to avoid repeating more than one count on a single grain. The matrix and clay mineralogy was also investigated both petrographically and by using the XRD technique described previously. The quantitative porosity analysis used a blue epoxy that was impregnated into the samples before polishing.

3.3. Scanning Electron Microscopy–Energy Dispersive Spectroscopy Analysis (SEM-EDS)

Solid samples from all facets of the biomineralization, MCR, and Maramec Spring studies were examined using either a Hitachi S4700 SEM or Helios Nanolab 600 Focused Ion Beam Scanning Electron Microscopy – Energy Dispersive Spectroscopy (SEM-EDS) instrument. Samples were mounted on aluminum stubs using a carbon mounting adhesive and then coated with either a charge dissipating carbon or Au-Pd coating. SEM-EDS analysis was conducted using an accelerating voltage of 15 kV, and a working distance of 15 mm under vacuum. For energy dispersive spectroscopy (EDS) the working distance was increased to 20 mm and all other parameters remained constant.

Solid microbialite samples from Storrs' Lake were also imaged for their morphology and texture as well as using the EDS tool to provide a semi-quantitative analysis of the percentage elemental composition of the various phases analyzed. Samples were prepared by isolating material of interest, rinsing with deionized water three times, and placing a portion of the material on top of a clean copper tape pasted on an aluminum stub. The material was then coated with Au-Pd for one to two minutes and the samples were analyzed for their crystal morphology, chemical composition and mineral association.

Hydrated biogenic material like bacteria is normally unstable and will disintegrate under the high vacuum conditions in the SEM, and hence biological samples have to be pre-treated for stabilization. The preparation step began with initially storing the collected samples in 3% glutaraldehyde, which serves as a primary fixing agent. The samples in the glutaraldehyde solution were then added to a 0.45 µm cellulose filter and allowed to dry at room temperature. The sediments were further treated with a graded ethanol series (30%, 40%, 50%, 70%, 80%, 90%, 100% [twice]), with 5 minutes for each treatment. The samples were then rinsed with de-ionized water. Following this step, the samples were subjected to critical point drying by soaking them twice with hexamethyldisiloxane, with 5 minutes for each soak. The dried samples were then sputter coated with Au-Pd and imaged with the SEM.

3.4. X-Ray Fluorescence (XRF) Analysis

X-Ray Fluorescence (XRF) analysis was used to determine the major element chemical composition of the samples as oxide weight percent (SiO_2, Al_2O_3, Fe_2O_3, CaO, MgO, Na_2O, K_2O, MnO, TiO_2, and P_2O_5). The samples were crushed mechanically using the same technique as previously described for the XRD whole rock samples. Approximately 20 g of the crushed samples were sent to the ACME Analytical Laboratory in Vancouver, British Columbia for analysis using their 4X group lithological analyses for the major element oxides. The accuracy for XRF analysis was better than 6.3% for SiO_2, Al_2O_3, Fe_2O_3, CaO, MgO, Na_2O, K_2O, MnO, and TiO_2. The accuracy for P_2O_5 was a little lower at 8.3%. The calculated precision for the analyzed samples was better than 0.2 % for all elements.

3.5. Digestion and Chemical Analysis of Solid Phase Samples

We conducted an elemental analysis on the digested pinnacle mound and plateau type microbialites from Storrs' Lake by ICP-OES in order to help identify the mineralogy of the samples and to get a more precise understanding of the ratio of aragonite to calcite. Approximately 0.25 g of each sample was rinsed with deionized water, dried overnight in an oven at 55°C, weighed to 0.0001 gram accuracy, and then digested in a 10 mL volume solution of 5% high-purity Ultrex HNO_3. The digested solution was filtered through a 0.45 µm cellulose acetate syringe filter and then major and minor element cations (Ca, Mg and Sr) were determined using a Perkin Elmer 2000 DV ICP-OES system. The digestions were performed on identical sample splits from the second set of individual XRD analysis samples. Strontium is an important element with respect to evaluating carbonate mineral polymorph formation as it is preferentially incorporated in the aragonite mineral structure over calcite (aragonite $K_{d\text{-}Sr}$ =1.13 *versus* calcite $K_{d\text{-}Sr}$ = 0.045 to 0.14; Morse and Mackenzie, 1990). Thus, if strontium is present, its concentration can be indirectly used to evaluate aragonite/calcite ratios. Conversely, Mg is often enriched in the calcite phase, but not aragonite.

ICP-OES analyses were also conducted on the Maramec Spring particulate material to determine its chemical composition. The remaining halves of the 0.45 μm and 0.22 μm filters used for TSS and XRD, respectively, were each placed in an ultrasonic cleaner for 30 minutes in 15 mL of a 5% ultra-pure HNO_3 acid solution to remove the particulate material from the filter paper. The filter papers were then re-dried and re-weighed on a four decimal precision balance to determine the amount of material liberated from each filter. Approximately 3 mg of particulate material was liberated from each filter. This particulate material was then further digested using ultra-pure HNO3 diluted to produce a solution pH of 2 or less and analyzed on the ICP-OES. ICP-OES analyses were also conducted on calcite vein material collected from the MCR samples and centrifuged material collected from Maramec Spring to determine Ca/Mg ratios. Several isolated grains were weighed, digested in a 5% ultra-pure HNO_3 acid solution, and analyzed by ICP-OES analysis for each of the samples.

4. LABORATORY BIOMINERALIZATION REACTOR EXPERIMENTS

4.1. Microbialite Enrichment Cultures

Sediment samples from Lake Estancia and Great Salt Plains, and microbial mat samples from Storrs' Lake were cultured in a sulfate-reducing enrichment media to enrich for bacteria capable of performing sulfate reduction following the procedure of Kjeldsen et al. (2007). All five of the different microbial mat samples collected from Storrs' Lake were used to enrich for sulfate reducing bacteria (SRB). The final pH of the medium before addition of the sediments was 7.3. To test sulfate-reducing bacterial community enriched from the study sites, for their carbonate mineral precipitation ability under varying CO_2 levels, small-scale reactors were employed. Two types of reactors were basically used for this purpose and are described below.

4.2. Continuous – Flow Reactor Tests

A continuous reactor method was used for testing the carbonate mineral precipitation ability of SRB community at 400 and 1200 ppm CO_2 concentrations. Sterilized screw-top Nalgene polypropylene bottles, 150 ml, were used for this purpose. The bottles contained either quartz sand (St. Peter Sandstone) or carbonate mudrock (Atlantic crushed coral, World Wide Imports, FL) further crushed into particles <1 mm, as a substrate material that served for a three-fold purpose: (i) to provide surface area for the bacteria to attach, (ii) to simulate interaction with two possible types of subsurface rock material, and (iii) to provide a template for possible carbonate mineral precipitation. The quartz sand was pre-treated treated with 5% HCl solution for two to three hours to remove any carbonate mineral phases. Carbonate mudrock (crushed carbonate marine aquarium gravel) in the other test format provided Ca^{2+} and CO_3^{2-} to the solution. The quartz sand grains were rounded to sub-rounded with a fairly uniform size distribution (100-200 μm), thereby allowing high porosity and permeability. The carbonate mudrock particles had a wider size distribution (25 to 250 μm), but were generally finer than the quartz grains, and hence more compacted with less pore space. The crystal morphology of the crushed carbonate mudrock was a mixture of rugged, angular, rhombohedral, and sub-rounded grains.

The substrate material was topped with artificial seawater, prepared as described by Kester et al. (1967). The final pH of the artificial seawater before addition of any other material was 8.01. The composition of seawater was slightly modified to increase the total sulfate concentration from 40 mM to 100 mM to provide the required sulfate for the SRB as used in the enrichment medium. It is important to note the sulfate added as a salt of calcium, magnesium, or sodium, would lead to an increase in the charge equivalent concentration of the respective cations.

The seawater media was sterilized by autoclaving. After addition of the media to the substrate material, SRB enrichment cultures were added at 10% total volume. Filter-sterilized lactate, 20 mM, was finally amended as the carbon source. Control reactors with quartz sand, but without inoculum were also tested. The reactors were placed in aquarium size tanks (40 cm x 15 cm x 12 cm) that were sealed gastight and supplied with a constant atmosphere of flowing CO_2 at a concentration of either 400 ppm or 1200 ppm (Figure 8). The constant CO_2 atmosphere was maintained by a CO_2 monitoring and controlling device (PPM-3 manufactured by C.A.P., Perris, CA). Food grade CO_2 (Airgas, MO) from a pressurized gas cylinder was connected to the reactors through a solenoid gas pressure regulator. All experiments were conducted in triplicate under ambient room temperature conditions at ~22°C. Solution pH and redox potential (Eh) were measured at regular intervals in the overlying water. Water samples were collected periodically to measure the calcium and magnesium concentration by ICP-OES analysis.

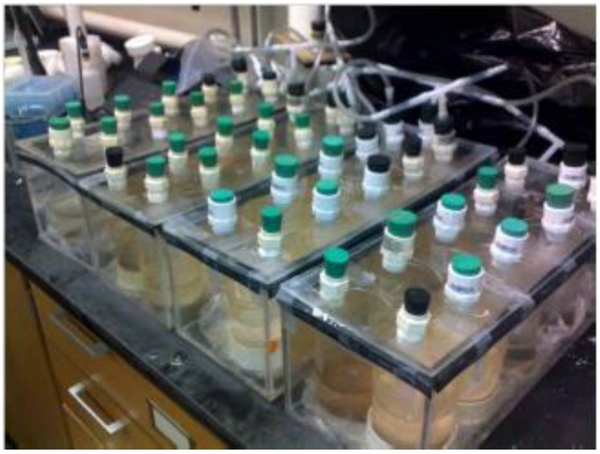

Figure 8. Aquarium tanks used for the continuous flow gas reactors. The solid and liquid reactor components were added in to Nalgene bottles and placed inside the Plexiglas tanks. A CO_2 concentration of 400 or 1,200 ppm was maintained. Water samples were collected through the top ports for analysis.

4.3. Batch Reactor Experiments

Batch reactors were set up in 20mL serum bottles to test for SRB activity under higher CO_2 concentrations than the continuous reactors could use. Only the Lake Estancia enrichment cultures were tested in this format. Two CO_2 headspace pressure conditions in the serum bottle reactors were tested: (i) 14.7 psi (~1,500 ppm CO_2 in water), and (ii) ~20 psi (~2,000 ppm CO_2 in water). It should be noted that the continuous-flow reactors were tested at atmospheric pressures and hence the actual pCO_2 in those reactors much lower than that of the batch reactors. Though the pCO_2 tested here are well below that planned to be injected in to an actual CO_2 sequestration site, these experiments do provide a suitable platform to analyze SRB influence on carbonate mineral precipitation. All serum bottle reactors (20 mL) were run in triplicate, containing either quartz sand or crushed carbonate mudrock as the substrate. In a separate batch of experiments, different electron donors (hydrogen, formate, lactate and acetate) were also tested in batch reactor mode to determine the effect of the different electron donors on carbonate mineral precipitation. The electron donors also served as the carbon sources, except in the case of hydrogen, where the gas phase serves only as the electron donor and the added CO_2 is the only potential source for the carbon required by the bacteria. In the reactors tested for optimal electron donor, only quartz sand was used as substrate. The synthetic seawater used for batch reactors was made anaerobic by boiling, followed by allowing the solution to come to room temperature under a stream of nitrogen gas, and distributing the solution into the serum bottle reactors inside an anaerobic glove bag that had a 90% N_2 and 10% H_2 environment. Each of the bottles were capped with a rubber stopper and crimped with an aluminum seal to make the reactors gastight. After sealing, the bottles were sterilized in an autoclave at 121°C for 20 minutes. After the reactor bottles cooled to room temperature, filter-sterilized, organic electron donors were added to achieve final concentrations of 20 mM in each. Reactors with hydrogen gas were injected with a 10% H_2: 90% N_2 gas mix, through a sterile syringe needle to a constant headspace pressure of ~14.7 or ~20 psi. The hydrogen gas was added along with the CO_2 so that constant headspace pressure was maintained with equal components of all the gases. The headspace gas in the bottles was exchanged with two alternating cycles of vacuum and nitrogen, followed by a third vacuum run. After this, CO_2 gas was introduced to the reactors till the respective pressures were reached. The total liquid volume after addition of all the components was 10 mL.

Three types of control reactors were run with the 1,500 ppm reactors: (i) reactors with no bacterial culture or electron donor (control), (ii) a blank reactor containing only the synthetic seawater (blank), and (iii) a reactor with all components added including the bacterial inoculum, but sterilized (killed control) to determine if the presence of non-viable cells would influence the precipitation process. Care was taken to sample only the liquid portion by gently inverting the serum bottles and collecting the water through a sterilized needle. Similar to the continuous reactors, pH, Eh, calcium and magnesium concentrations were measured from the collected water samples, but only at days 1 and 10. Additionally, sulfide concentrations in the overlying seawater media during both time intervals were measured following a colorimetric $CuSO_4$

method (Cord-Ruwisch, 1985), by using a Genesys 20 spectrophotometer (Thermo Fisher Scientific Inc., Rochester, NY, USA).

The bottom sediment substrate material from serum bottle reactors with quartz sand was analyzed for the production of carbonate minerals. The substrate was collected with a sterile spatula and gently rinsed with deionized water. A portion of the rinsed sediments were added to a microscope slide, then hydrochloric acid (10%) was added while samples were observed under an optical microscope to check for effervescence due to CO_2 release from carbonate minerals. Sediments from reactors that tested positive for CO_2 effervescence were selected for investigating the mineral morphology and elemental composition using more detailed SEM-EDS analysis. In some cases, the sediments were filtered with a 0.45 μm cellulose acetate filter that was then attached to an aluminum stub and viewed under SEM while attached to the filter. If the first vessel of the triplicate set did not reveal the presence of carbonate mineral, then the remaining two reactors were allowed to proceed for a longer time (up to 60 days) and the sediments were examined again at the end of the extended reaction period. Reactors with the carbonate mudrock substrate were not chosen for HCl immersion tests as the carbonate substrate would interfere with the detection of any newly precipitated carbonate minerals.

4.4. Carbon Isotope Analysis in Batch Reactor Experiments

A limited number of biomineralization triplicate batch reactor experiments were run with an isotopically labelled $^{13}CO_2$ gas source. Tracking the source of carbon for the carbonate minerals is important because if the carbon is only derived from the organic material, then no net precipitation of the CO_2 gas phase will occur. This isotopically labeled gas source (Sigma-Aldrich, St.Louis, MO) contained 99.9% $^{13}CO_2$ and was supplied at a ~14.7 psi headspace pressure (concentration of 1,500 ppm) after a series of vacuum and nitrogen gas exchanges. Lactate, formate, hydrogen and acetate were used as electron donors with only quartz sand as the substrate. The extent of mineral sequestration accomplished through the activity of SRB can be determined by positively identifying the carbon source and by quantifying the amount of the labeled isotopic carbon that was incorporated in any precipitated carbonate minerals. The synthetic seawater used for batch reactors was made anaerobic and CO_2 free as described previously and distributing the solution into the serum bottle reactors inside an anaerobic glove bag. Any minerals that were produced in these reactors at the end of the reaction period (10 days) were isolated along with the quartz sand. Both $NaHCO_3$, another possible carbonate source that was used to prepare the artificial seawater media was analyzed to obtain its $\delta^{13}C$ value. Sodium acetate and sodium formate, two of the electron donors tested in the reactors were also analyzed for their $\delta^{13}C$ isotopic signature. Sodium lactate was available only as a liquid form and hence was not analyzed.

All sediments were rinsed three times in deionized water, flushed with air for five minutes, and then analyzed for their $\delta^{13}C$ values. The carbonate minerals produced were carefully portioned off from the quartz sand substrate while viewing under an optical microscope. In certain instances, small amount of quartz sand was included, especially when the carbonate material appeared to be coating the quartz grains. In samples that had no visible carbonate mineral precipitation (determined either through the addition of a 10% HCl treatment or microscopic observation), the quartz sand substrate was directly analyzed. The samples for use in elemental analyzer were weighed in a small capsule made of aluminum foil. The capsule with the weighed sample was then compressed into smaller cubes by using a pair of tweezers to remove any external air that could have been trapped in it.

Stable isotope data were measured by two methods, 1) by using either a Thermo FinneganTM Delta Plus mass spectrometer operated in dual inlet mode with an on-line automated carbonate reaction Kiel III device, or 2) with a Thermo FinneganTM Delta Plus XL operated in continuous flow mode with an online automated Carlo-Erba 1500 elemental analyzer. The Kiel device follows a standard phosphoric acid digestion procedure, where the carbonate material was digested with the acid and the evolved CO_2 gas was measured (Swart et al., 1991; Hoefs, 2009). With the elemental analyzer, the material was combusted under oxygen and high temperature, and the evolved CO_2 gas was measured. Both instruments measured CO_2 gas (masses 44, 45, 46) liberated from the samples, following which, the $^{45}CO_2/^{44}CO_2$ ratios and $^{46}CO_2/^{44}CO_2$ ratios were calculated. The $^{45}CO_2/^{44}CO_2$ ratio is mostly $^{13}CO_2/^{12}CO_2$, but also may also include some $^{12}C^{17}O^{16}O/^{12}CO_2$. The instruments also measured the ^{18}O and ^{17}O values and used these measurements to correct for the ^{17}O by using the $^{46}CO_2/^{44}CO_2$ ratios ($^{12}C^{18}O^{16}O/^{12}CO_2$).

The $\delta^{13}C$ values were calculated according to the formula given below:

$$\delta^{13}C = \frac{(^{13}C/^{12}C_{\text{sample}} - {}^{13}C/^{12}C_{\text{VPDB standard}})}{(^{13}C/^{12}C_{\text{VPDB standard}})} \times \frac{1{,}000}{1} \ldots\ldots\ldots\ldots\ldots\ldots\ldots\ldots(1)$$

The $^{13}CO_2$ values (used to calculate $\delta^{13}C$) determined by the elemental analyzer combustion method measured the 'total carbon', as opposed to the Kiel device for which, only the carbon in the carbonate minerals was measured (CO_2 released from phosphoric acid treatment). The elemental analyzer was better at analyzing higher concentrations of the heavier isotope than the Kiel device, as the latter did not perform well when the ^{13}C levels were high. Since the carbon isotopic composition in the carbonate minerals was the major focus of this experiment, it was important to verify that both instruments analyzed CO_2 evolved only from the carbonate minerals. Although samples were rinsed thoroughly with deionized to remove most low-density organics and bacterial material, further examination was required to verify the material being analyzed. To achieve this goal, three samples with large values of ^{13}C were analyzed with both instruments. Each device quantified the isotopic values from the voltage generated from the evolved gas, and it was possible to manually correct for voltages obtained from the Kiel analysis.

This correction was necessary to relate the ratio of ^{13}C to ^{12}C obtained from the Kiel to that of the elemental analyzer. Comparing the values obtained from both instruments, a maximum variation of ±10% was observed. This comparison indicates that the majority of ^{13}C analyzed was indeed from the carbonate minerals, and any influence from any remnant organic material or bacteria was not large enough to substantially affect the ^{13}C values any more than the random precision associated with each instrument as discussed below.

Data obtained from the isotope analyses were reported relative to the Vienna PeeDee Belemnite (VPDB) standard. Data are expressed as per mil deviations on the VPDB. Replicate measurements of National Bureau of Standards-19 (NBS-19) and acetanilide for each approach yielded an external (instrumental) precision < 0.1‰ for $\delta^{13}C$, but this value is only appropriate for samples where the relative abundance of ^{13}C is comparable to that of the standard (~1.1%). The $^{13}C/^{12}C$ of the NBS-19 carbonate is 1.00195 times that of VPDB. Because the precipitated $CaCO_3$ minerals in the labeled isotopic experiments had ^{13}C abundances of ~50%, precision can be better estimated by comparison among analyses from replicate samples. Coefficients of variation from measurements of replicates run on consecutive days or on the same day were better than 12%, and generally better than 5% (i.e. ± 3,000 to 7,000 ‰) for samples with measured $\delta^{13}C$ values of ~ +26,000 to 60,000 ‰.

The method employed to calculate percentage ^{13}C from the $CaCO_3$ was used by Mitchell et al. (2010), and the finalized solution is shown in equation 2. In natural systems, it is common for carbonates to have ~ 1.11 atomic % ^{13}C (Hoefs, 2009). Any differences within these values occur mostly in the 2nd or 3rd decimal places (< 10 per mil). A carbonate mineral having a ^{13}C value of 1000 ‰ would be 100% enriched over the natural abundance of ^{13}C, or would have twice the natural abundance. It could then be said that a + 1000 ‰ carbonate has about 2.2 atom % ^{13}C, and by extension, a + 2000 ‰ sample has about 3.3 atom % ^{13}C, a + 9000 ‰ sample has about 11.0 atom % ^{13}C, and so on. Simplifying this concept, we arrive at the following equation to calculate atomic % ^{13}C in precipitated $CaCO_3$:

$$[(\delta^{13}C/1000) \times 1.1] + 1.1 \qquad (2)$$

5. CO_2 GAS FLUX EXPERIMENTS

The CO_2 flux measurements were made in the Maramec Spring system water using a portable LI-COR Model LI-8100 gas flux meter and are referenced relative to atmospheric CO_2 as the standard. The CO_2 gas is collected by immersing the open end of a PVC pipe into the water and attaching the opposite end to the sealed LI-COR gas flux meter. All gas flow is subsequently directed across the meter for analysis.

6. HIGH- PRESSURE- TEMPERATURE CORROSION EXPERIMENTS

The high pressure temperature (HPT) experiments were used to mimic potential underground repository conditions in a CO_2 repository where acidified waters produced by gas injection react with a host rock material. Chemical weathering is accelerated under these conditions. The geothermal gradient at the Texaco Poersch #1 well was 19°C/km (Anderson, 1990). The temperature at the top of Units E (7,020′), D (10,510′), and C (14,980′) would be expected to be approximately 41, 61, and 87°C, respectively, within the range of the present set of experiments. The kinetic dissolution rate of silicate minerals generally increases with temperature (Langmuir, 1997), thus the 90°C used in the tests will also accelerate silicate reactions so that longer-term trends can be observed in relatively short term experiments. These higher temperature mineral reactions are also likely valid for any potential repository horizons at lower temperatures as well because the observed alteration mineral sequence at $90^{o}C$ is the same as those found in natural weathering profiles. Higher temperatures commonly accelerate mineral weathering reactions with alteration rates expected to double for every $10^{o}C$ rise in temperature (White, 2013).

Rock or mineral samples were prepared for testing by slicing samples into one to two millimeter thick by one centimeter diameter monoliths on a diamond wafer saw using deionized water as a lubricant. The samples were then polished to a uniform 600 grit finish using Si-carbide paper and water again as a lubricant. The solids were then ultrasonically cleaned in deionized water, dried in an oven at $105^{o}C$, cooled in a desiccator, weighed, and measured, geometrically for the surface area.

Stainless steel Parr^{TM} 4749 general purpose reaction vessels with inner 23ml-Teflon liners were used in the HTP corrosion experiments (Figure 9). The vessels were cleaned in nitric acid and rinsed in deionized water prior to use. Approximately 2-3 g of dry ice was added to a preweighed Teflon-lined vessel which was then hermetically sealed and placed in an oven at 90°C for three days to saturate the inner pore surfaces with CO_2. The vessels were then cooled, opened, and reloaded with reactants (dry ice, 10 milliliters of deionized water, and a wafered sample), then hermetically sealed again, reweighed and again placed in the oven at 50 or 90°C to initiate the experiments. The weight loss of the assembled HTP vessel and contents were monitored periodically, and the experiments were terminated once that weight loss reached one gram or the desired test length had been reached. Tests were terminated by cooling and opening the vessels. Both the pH and Eh were immediately measured using a one milliliter aliquot of water that was transferred to a small plastic vial. Immediate analysis was required because the vessel fluids will actively loose CO_2 once the confining pressure applied by the test vessel was removed. The remaining fluid in the Teflon vessels was then filtered by using a 10 ml Nalgene syringe to inject the fluid through a 0.45-µm Nalgene cellulose acetate filter into a pre-cleaned 30-ml Nalgene bottle. The filtered solution was then acidified with high-purity nitric acid to dissolve any colloidal particles and to prevent mineral precipitation. Fluids were then analyzed by ICP-OES analysis for dissolved elemental contents.

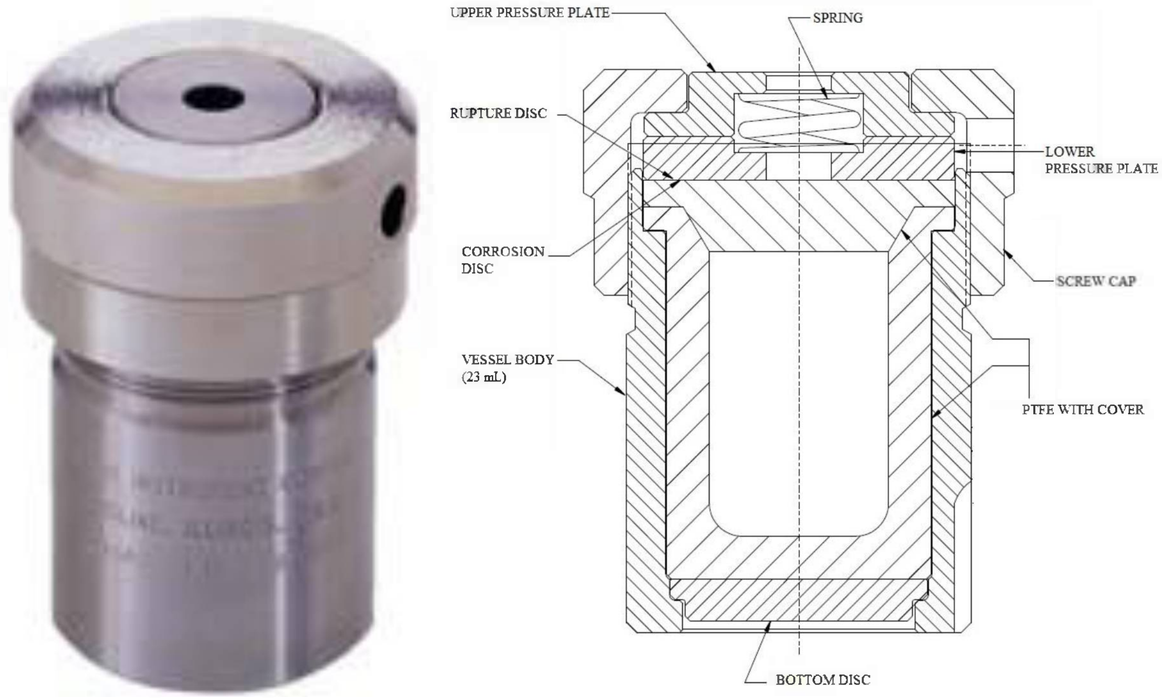

Figure 9. ParrTM 4749 general purpose vessel with Teflon liner.

An actual geologic disposal scenario for CO_2 in the United States will required the waste gasses to be injected into a saline aquifer system that is too saline to be used for a drinking water supply (>10,000 mg/liter TDS). The HPT experiments used deionized water rather than a brine leachant for the following reasons: 1) The tests were being conducted in a non-site specific fashion, thus the potential aquifer chemistry was not known. 2) The experiments were conducted to allow the chemical composition of rocks to dominate the water composition, which happens in natural aquifers. 3) high concentrations of brine components will limit the accuracy of the ICP-OES analytical method as analyzing such solutions would require a high dilution ratios. High brine concentrations tend to mask the release of rock components during testing. There is not a representative data set for water samples collected from the deeper Oronto Group sediments as deeply buried segments of the MCR are not normally used as a source for drinking water (Thorleifson, 2008). The chemical composition of shallower underground waters of the MCR were evaluated from 66 wells that had penetrated through the Cambrian-aged Mt. Simon and MCR Hinckley Aquifers by Lively et al. (1992). This compilation indicates an average Ca concentration of 71 ppm with maximum value of 526 ppm. The Mg concentration averaged 27 ppm with a maximum value of 240 ppm. Sodium averaged 66 ppm with 1870 ppm as the maximum. All other major elements were present in concentrations at <10 ppm average compositions. The total dissolved solids were 7,471 mg/kg maximum, which would classify the water as being brackish but below the threshold for a waste injection well.

The partial pressure of CO_2 in the experimental vessels ($p$$CO_2$ in bars) was calculated from the equation:

$$P_{gas} = \left(\frac{Concentration\ of\ gas}{Total\ volume\ of\ gases}\right) \times pressure\ (bar)$$

The pressure was measured using a Parr^{TM} 4848 reactor controller for the same proportional amounts solid, water, and dry ice that used in Parr^{TM}4749 general purpose reactors. The total measured pressure from the Parr^{TM} 4848 reactor controller were ranged between 69 and 71 bars. The partial pressure of the O_2 was 14.7 bars using the atmospheric concentration of O_2 at 21%. The pressures of the reactor were controlled by the conversion of the CO_2 solid added to the vessels into a gaseous phases. Giammar et al. (2005) estimated the free CO_2 gaseous phase from this equation:

$$m_{CO_{2(free)}} = \left(V_{reactor} - \frac{m_{water}}{\rho_{water\ (P,T)}} - \frac{m_{rock}}{\rho_{rock}}\right) \times \rho_{CO_2}(P,T)$$

Where m is mass in gram, V is volume, and ρ is density in g/cm^3.

The volume of the reactor is 23 cm^3 and the mass of water added was 10 cm^3. The densities of the CO_2 and H_2O at 90°C were measured using the online conversion site http://www.peacesoftware.de/einigewerte/einigewerte_e.html. The density of the low porosity rocks were assigned at 2.8 g/cm^3, and 2.0 g/cm^3 for the high porosity sedimentary rocks (e.g., BAY3). The dissolved phases of CO_2 were measured using the equations of Duan and Sun (2003), which are available as online conversion at http://calc.kl-edi.ac.cn/Pages/Solubility.aspx webpage.

7. CORE FLOODING EXPERIMENTS

Each core sample was prepared for the core flooding experiments with an approximately one inch diameter (r) and 2 inch length (L) core using a diamond core drilling bit with 1.1 inch (2.8 cm) inside diameter and water as a lubricant. The total volume of the samples (Vt) was determined from the equation [$Vt = \pi * r^2 * L$]. The samples were dried at 45°C overnight and then weighed to the nearest 0.01 g to determine the dry weight (Wd). The samples were vacuumed, flooded with deionized water, and then weighted to determine their saturated weight (Ws). Then Φ (porosity) was estimated from the formula:

$\Phi = [(Ws-Wd)/Vt]*10$

A core flooding system was prepared (Figure 10) according to the methodology presented by Wellman et al. (2003). An artificial leachant solution of pH 3.7-3.8 (close to the pH of deionized water saturated with CO_2 at atmospheric pressure) was prepared from using analytical grade nitric acid. Sample cores were cut to lengths of between 0.55 to 1.25 inches (1.4 to 3.2 cm) depending on the expected porosity (high porosity sample were cut to greater lengths). The samples were sealed to the external Acrylic core tube using a viscous and water insoluble epoxy along with a rubber ring to prevent any preferential leakage between the rock sample and the Acrylic tube wall housing the sample. The fluid pump and the tubing were washed with DIW to reduce the contamination from NaCl brine, which often adheres to the test vessel components from previous runs. The core holder could tolerate a maximum pressure of 500 psi. Samples for core flooding tests were selected to represent a wide array of rock types ranging from high porosity and low calcite cement (e.g., BAY2, 22.1% porosity and 0% calcite), moderate porosity and high calcite cement (e.g., KEW3-1, 8.9% porosity and 10.0% calcite), low porosity and high calcite cement (e.g., KEW-1, 1% porosity and 15.9% calcite) and low porosity and low calcite cement POT8 (both <1% porosity, 0% calcite).

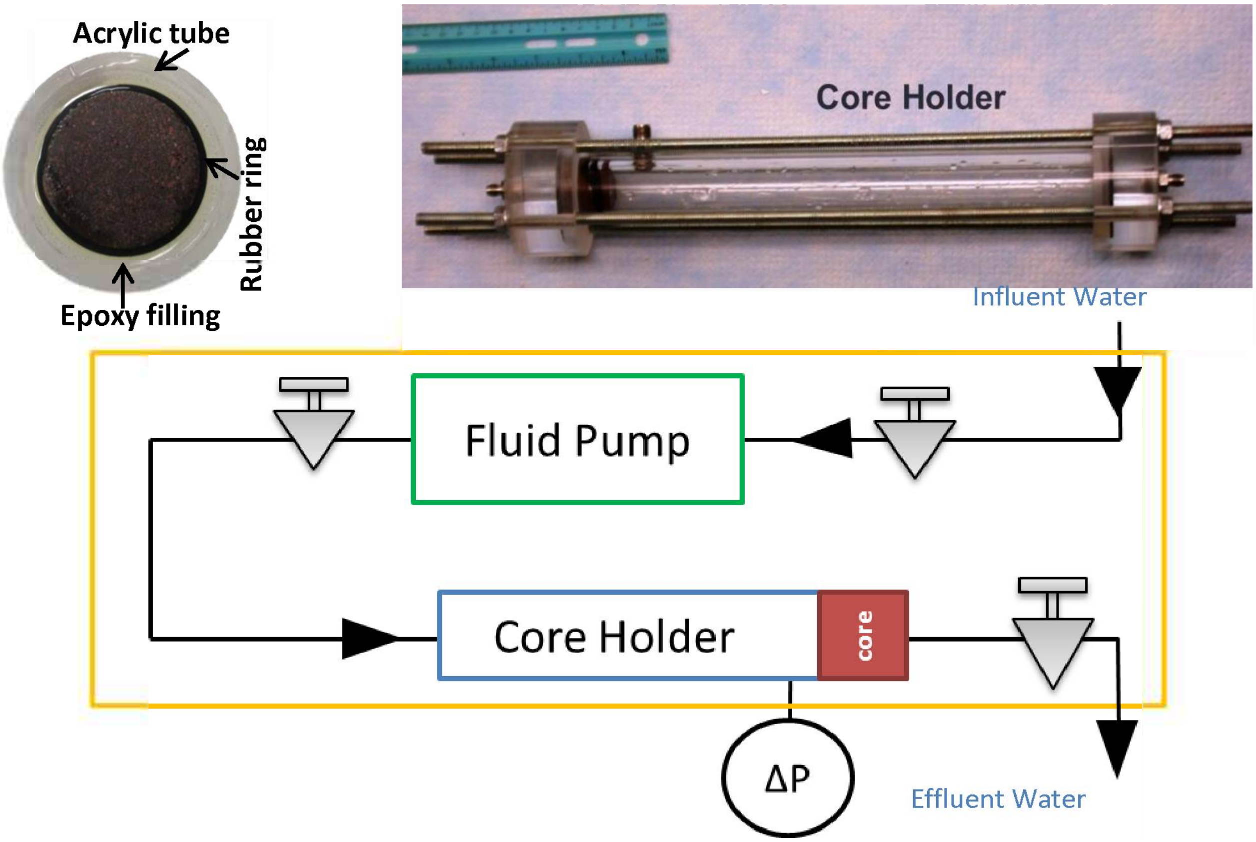

Figure 10. Photograph and schematic diagram for the core flooding experiment test apparatus.

The initial permeability was compared with the final to determine whether or not flooding with the acidified fluids had any effect on the sample properties. The initial and final permeability was also estimated by continuously evaluating the backpressure on the system. Non-steady flow represented either a pressure decrease resulting from the widening of the pore openings (e.g., calcite pore cement dissolution or pressure induced fracturing) or a pressure increase through the blockage of the pore space by migrating particles that block the narrow restricted pores.

Solution samples were collected from the syringe pump along with a wash sample to check for background contamination (especially sodium). The effluent fluid was periodically analyzed for pH and alkalinity, as well as collecting samples for ICP-OES analysis of cations. A final sample was also collected from the core holder tube, just above the sample, to determine the actual chemical composition of the leachant fluid prior to its passing through the core sample at the end of the experimental run (influent).

8. RELATIVE RATES OF MINERAL WEATHERING – GOLDICH REACTIONS

A suite of single mineral samples and a few rock samples were tested by immersion in a nitric acid leachant solution prepared to a pH of approximately 3.78 (1.66 x 10^{-4} M). Solutions at pH of 3.78 represent both the minimum value expected in organic-acidic soils and the pH following saturation of deionized water with a pure CO_2 gas at atmospheric pressure. These experiments were used to simulate the effect of carbonic acid exposure on mineral dissolution rates, the nitric acid was used rather than carbonic acid to allow pH measurements to be made without allowing the acid component to volatilize and transfer into a gas phase. Nitric acid also is stronger than carbonic and more fully dissociates to release H^+ ions into solution for reaction. Large and rapid increases in pH are an indication of rapid chemical reactivity as the exchange of $nH^+ \Leftrightarrow M^+$, where M^+ corresponds to any metal cation (e.g., Na^+, K^+, Ca^{2+}, Mg^{2+}, Fe^{2+} etc.). Minerals that react more rapidly with acids promote carbonate mineral formation more rapidly because they have a greater buffering capacity for neutralizing acids and they will also release Ca^{2+}, Mg^{2+} and Fe^{2+} ions that can complex with CO_3^{2-} to form carbonate mineral phases (e.g., $CaCO_3$, $MgCO_3$, $CaMg(CO_3)_2$, $FeCO_3$).

The mineral samples were prepared by crushing followed by sieving to collect the -200 mesh sized fraction (<74 µm). A 0.20 gram batch of each powdered sample was added into a precleaned 250 ml polyethylene vial to which, 200 ml of HNO_3 solution was added. Experiments were conducted at a room temperature in closed vials, however, the atmosphere above the test solution in the vials was periodically replenished with fresh air each time the vessels were opened and pH measurements were made. Solution readings for the first pH sample were taken following two hours of exposure, and then readings were repeated, after approximately doubling the length of time for the previous reactions up to the point where pH readings were taken approximately one month apart. The pH meters used in the testing were routinely calibrated with standards to ensure that accurate and repeatable pH measurements were being made. Samples reacted include the following groups:

a) A series of nine mineral end members similar to those used in Sam Goldich's 1938 classic study on natural weathering rates of minerals including: forsterite Mg-rich olivine, pyroxene-augite, amphibole-hornblende, two orthoclase feldspars, quartz, and plagioclase feldspar (three feldspars representing a nearly pure $NaAlSi_3O_8$ albite phase, Na-rich oligoclase, and Ca-rich bytownite).
b) Eight clay minerals representing a potential range of matrix materials present in sedimentary rocks or those formed from the alteration of aluminosilicate minerals. Seven of these were obtained from "Source Clay Minerals Repository" standards and include: Na-montmorillonite (Wyoming bentonite), Ca-montmorillonite (STX-1), nontronite H33a), hectorite (H34), kaolinite "well-crystallized" (KGa-1), kaolinite "poorly crystallized" (KGa-2), and illite (IMT-1). The eighth clay mineral tested, glauconite, was obtained from the mineral collections at Missouri S&T.
c) A suite of three minerals that are often found as cementing materials in sandstones (calcite, hematite, plus the previously mentioned quartz), chlorite (often found as a matrix or cementing material in low-grade metamorphic rocks including the MCR), and epidote (often found as a hydrothermal alteration phase in the MCR.
d) Two rock samples from the Midcontinent Rift sequence; Hematite cemented Jacobsville Sandstone from Alger County Michigan and Portage Lake Volcanic basalt from Bessemer, Wisconsin.
e) Two additional "blank tests", with 200 ml HNO_3 but no mineral or rock samples were run as controls.

9. DNA EXTRACTION AND 16S rRNA GENE ANALYSIS

To determine the microbial community composition of the microbialites in Storrs' Lake, Great Salt Plains, and Lake Estancia, a barcoded 16S rRNA gene analysis was performed in triplicate using a barcoded pyrosequencing approach developed by Genomic DNA (UltraClean™ Soil DNA Isolation Kit, MoBio Laboratories, Carlsbad, CA, USA). The Storrs' Lake samples included from four microbial mats associated with the calcareous knobs, plateau, mushroom and pinnacle mound microbialites, as well as a fifth sample representing the cheesecake microbial mat. All sediments were aseptically portioned from the top few layers of the core collected from both these environments. The sediments from the cores of microbialites were portioned from samples stored at room temperature in the dark for nine to ten months, by using sterile spatulas. DNA was also extracted from enrichment cultures (triplicates) obtained from Lake Estancia sediments that were sub-cultured for at least over six generations. The DNA samples obtained from the triplicate extractions from each sample were combined together separately according to the sample type. A total of eight DNA samples were then subjected to analysis by sequencing (five microbial mats from Storrs' Lake, two sediments each from Lake Estancia and Great Salt Plains, and one SRB enrichment sample developed from Lake Estancia). The extracted DNA, from the different sources, was shipped to MoGene, LC (St. Louis, MO, USA) for further analysis using a Quant-iT Picogreen dsDNA Assay kit (Invitrogen, Carlsbad, CA) and PCR-amplified by using barcoded primers targeting the V1-V3 region of the 16S rRNA gene. The bacterial primers used were the 27-Forward AGRGTTTGATCMTGGCTCAG (Weisburg et al., 1991) and 518-Reverse CGTATTACCGCGGCTGCTGG (Muyzer et al., 1993). The primers incorporated the Titanium Lib-A adaptor sequences and barcode sequences specific for the individual samples.

The polymerase chain reaction (PCR) mixture included 1X Master mix (MOLZYM Mastermix 16S Basic, Molzym, Bremen, Germany), 0.2 µM each of the MID forward and reverse primers, 0.51 U Taq DNA polymerase (MolTaq, Molzym), 30 ng of the template DNA, and DNA-free water for a final volume of 25 µL. Conditions for PCR were 96°C for 5 min, 25 cycles of 95°C for 10 sec, 56°C for 30 sec and 72°C for 30 sec, followed by a single cycle of 72°C for 5 min. The amplicons were then purified with a 1.8% agarose gel purification run (QIAquick Gel Extraction kit, Qiagen, Chatsworth, CA). The purified amplicons were examined with an Agilent Bioanalyzer DNA 7500 (Agilent, Santa Clara, CA) to determine concentration and assess the size of the products. The amplicon libraries were normalized, pooled and then pyrosequenced with Titanium chemistry (454 GS-FLX, Roche, Branford, CT, USA).

The bioinformatics software program QIIME was used for processing, cluster analysis, and classification of the raw sequences (Caporaso et al., 2010). High quality reads were separated based on the multiplex identifier and analyzed for phylogenetic origin by comparison to reference database Greengenes (DeSantis et al., 2006). The ChimerSlayer program available in QIIME was used to perform Chimera check. Community analysis and comparison of the mat types were performed phylogenetically by using Unifrac jackknifed environmental clustering that compare distances between communities (Lozupone & Knight, 2005). QIIME was also used to calculate the alpha diversity index parameters, such as Chao1, Shannon and observed species. The program randomly generated a subset of sequences (termed 'equalized'), and 10 iterations were run for each diversity indices. The sequencing reads obtained from Storrs' Lake were submitted to NCBI sequencing read archive (SRA) with accession number SRP031628.

REFERENCES

Allen, B.D. and Anderson, R.Y., 2000, A continuous, high-resolution record of late Pleistocene climate variability from the Estancia basin, New Mexico. *Geological Society of America Bulletin,* v. 112, p. 1444-1458.

Anderson, R.R., 1990, Review of the Precambrian geologic history of the central United States and the Midcontinent Rift system: in The Amoco M.G. Eischeid #1 deep petroleum test Carroll County, Iowa, Preliminary Investigations, Special Report Series #2, (R.R. Anderson ed.) Iowa Department of Natural Resources, p. 1-25.

Caporaso, J.G., Kuczynski, J., Stombaugh, J., Bittinger, K., Bushman, F.D., Costello, E.K., Fierer, N., Pena, A.G., Goodrich, J.K. and Gordon, J.I., 2010, QIIME allows analysis of high-throughput community sequencing data. *Nature Methods,* v. 7, p. 335-336.

Cord-Ruwisch, R., 1985, A quick method for the determination of dissolved and precipitated sulfides in cultures of sulfate-reducing bacteria. *Journal of Microbiology and Methods,* v. 4, p. 33-36.

DeSantis, T.Z., Hugenholtz, P., Larsen, N., Rojas, M., Brodie, E.L., Keller, K., Huber, T., Dalevi, D., Hu, P. and Andersen, G.L., 2006, Greengenes, a chimera-checked 16S rRNA gene database and workbench compatible with ARB, *Applied and Environmental Microbiology,* v. 72, p. 5069-5072.

Dickinson, W.R., 1970, Interpreting detrital modes of graywacke and arkose: *Journal of Sedimentary Research*, v. 40, p. 695-707.

Dickinson, W.R., 1985, Interpreting Provenance Relations from Detrital Modes of Sandstones, *in* Zuffa, G.G., ed., Provenance of Arenites, v. 148, Springer Netherlands, p. 333-361.

Duan, Z.H. and Sun, R., 2003, An improved model calculating CO_2 solubility in pure water and aqueous NaCl solutions from 273 to 533 K and from 0 to 2000 bar, *Chemical Geology,* v. 193, p. 253-271.

Giammar, D.E., Bruant Jr, R.G. and Peters, C.A., 2005, Forsterite dissolution and magnesite precipitation at conditions relevant for deep saline aquifer storage and sequestration of carbon dioxide, *Chemical Geology*, v. 217, p. 257-276.

Goldich, S.S., 1938, A study in Rock Weathering. *Journal of Geology,* v. 46, p. 17–58.

Hoefs, J., 2009, Stable Isotope Geochemistry, 6th ed. Springer, Berlin, Heidelberg.

Kester, D.R., Duedall, I.W., Connors, D.N. and Pytkowicz, R.M., 1967, Preparation of artificial seawater, *Limnology and Oceanography,* v. 12, p. 176-179.

Kjeldsen, K.U., Loy, A., Jakobsen, T.F., Thomsen, T.R., Wagner, M. and Ingvorsen, K., 2007, Diversity of sulfate-reducing bacteria from an extreme hypersaline sediment, Great Salt Lake (Utah), *FEMS Microbial Ecology,* v. 60, p. 287-298.

Langmuir, D., 1997, Aqueous Environmental Geochemistry, Prentice Hall, New Jersey.

Laval, B., Cady, S.L., Pollack, J.C., McKay, C.P., Bird, J.S., Grotzinger, J.P., Ford, D.C. and Bohm H.R., 2000, Modern freshwater microbialite analogues for ancient dendritic reef structures, *Nature,* v. 407, p. 626-629.

Lim, D.S., Laval, B.E., Slater, G., Antoniades, D., Forrest, A.L., Pike, W., Pieters, R., Saffari, M., Reid, D., Schulze-Makuch, D., Andersen, D. and McKay, C.P., 2009, Limnology of Pavilion Lake, BC, Canada-Characterization of a microbialite forming environment, *Fundamental and Applied Limnology Archiv für Hydrobiologie,* v. 173, p. 329-351.

Lively, R., Jameson, R., Alexander, E. and Morey, G., 1992, Radium in the Mt. Simon-Hinckley aquifer, east-central and southeastern Minnesota, Minnesota Geological Survey Information Circular 36, 58 pp.

Lozupone, C. and Knight, R., 2005, UniFrac: a new phylogenetic method for comparing microbial communities, *Applied and Environmental Microbiology,* v. 71, p. 8228-8235.

Mann, C.J. and Nelson, W.M., 1989, Microbialitic structures in Storr's Lake, San Salvador Island, Bahama Islands, *Palaios,* v. 4, p. 287-293.

Mitchell, A.C., Dideriksen, K., Spangler, L.H., Cunningham, A.B. and Gerlach, R., 2010, Microbially enhanced carbon capture and storage by mineral-trapping and solubility-trapping, *Environmental Science and Technology* v. 44, p. 5270-5276.

Morse, J.W. and Mackenzie, F.T., 1990, Geochemistry of Sedimentary Carbonates, Elsevier.

Muyzer, G., De Waal, E.C. and Uitterlinden, A.G., 1993, Profiling of complex microbial populations by denaturing gradient gel electrophoresis analysis of polymerase chain reaction-amplified genes coding for 16S rRNA, *Applied Environmental Microbiology,* v. 59, p. 695-700.

Neumann, C., Bebout, B., McNeese, L., Paull, C. and Paerl, H., 1989, Modern stromatolites and associated mats: San Salvador, Bahamas, *in* Proceedings of the Fourth Symposium on The Geology of Bahamas (Mylroie J.E., ed.), p. 243-254.

Nicholson, S.W., Dicken, C.L., Foose, M.P., and Mueller, J.A.L., 2004, Integrated Geologic Map Databases for the United States: The Upper Midwest States, Minnesota, Wisconsin, Michigan, Illinois, and Indiana, v. 1.1, US Geological Survey, Open Flie Report 2004-1355, http://pubs.usgs.gov/of/2004/1355/.

PHREEQ software program (United States Geological Survey, version 3.1.2.8538; Parkhurst, D.L. and Appelo, C.A.J. (3/3/2014).

Reed, J., 1982, Preliminary projections of the effects of chloride-control structures on the Quaternary aquifer at Great Salt Plains, Oklahoma, U.S. Geological Survey Report # WRI 80-120, 45 pp.

Swart, P.K., Burns, S.J. and Leder, J.J., 1991, Fractionation of the stable isotopes of oxygen and carbon in carbon dioxide during the reaction of calcite with phosphoric acid as a function of temperature and technique. *Chemical Geology, Isotope Geosciences Section,* v. 86, p. 89-96.

Szynkiewicz, A., Moore, C.H., Glamoclija, M. and Pratt, L.M., 2009, Sulfur isotope signatures in gypsiferous sediments of the Estancia and Tularosa Basins as indicators of sulfate sources, hydrological processes, and microbial activity. *Geochimica et Cosmochimica Acta,* v. 73, p. 6162-6186.

Thorleifson, L.H., ed., 2008, Potential Capacity for Geologic Carbon Sequestration in the Midcontinent Rift System in Minnesota, Minnesota Geological Survey Open File Report OFR-08-01, 138 pp.

Weisburg, W.G., Barns, S.M., Pelletier, D.A., and Lane, D.J., 1991, 16S ribosomal DNA amplification for phylogenetic study, *Journal of Bacteriology,* v. 173, p. 697-703.

Wellman, T.P., Grigg, R.B., McPherson, B.J., Svec, R.K. and Lichtner, P.C., Evaluation of CO_2-brine-reservoir rock interaction with laboratory flow tests and reactive transport modeling, Paper SPE 80228 *in* Proceedings International symposium on oilfield chemistry 2003, Society of Petroleum Engineers, Houston, Texas.

White, W. M., 2013, Geochemistry, John Wiley & Sons.

SECTION III. INVESTIGATION OF CARBONATE MINETRAL PRECIPITATION AT MARAMEC SPRING MISSOURI

1 INTRODUCTION

1.1 Maramec Spring Site and Sampling Locations

Maramec Spring is Missouri's fifth largest cold-water spring. It is located in Phelps County, Missouri, 11 km southeast of St. James. The water emanating from many springs in the Missouri Ozarks region, although moderately clear, generally retains a milky blue-white color due to the presence of fine-grained colloidal particles (Figure 1). This color is present under most water flow conditions except during flood stages when enough additional particulate material is incorporated in the water column to impart a brownish color and increase the overall water turbidity. These springs are enriched in Ca and Mg, which are derived from the dissolution of the largely dolomitic strata in the spring recharge area. While the precipitation of carbonate minerals is common in many spring systems, especially in warm hydrothermal waters and cave systems, the carbonate minerals typically occur as hardened substrates that deposits directly on available surfaces. To the authors' knowledge, no studies have ever been conducted to identify the mineralogy of these suspended colloidal particles in this or any other spring system.

After the spring water upwells to the surface, it collects into an oval shaped pool with a surface area of approximately 3100 m^2 (33,000 ft^2; Figure 1). Water from the pool then bifurcates into two major channels as it flows northward, with a third relatively small artificial concrete channel that is used to raise trout from the park hatchery. The majority of the pool water, however, falls over a rock dam in the central channel. The three branches eventually rejoin, bifurcate again, and rejoin a final time again as the stream system travels in a series of flowing riffles and slow flowing pool systems. This stream has not been assigned any formal name on the USGS 7.5' Maramec Spring topographic map, but is herein informally referred to as the *Maramec Stream*. The entire course of the stream system travels ~1360 meters until *Maramec Stream* eventually flows into and joins with the *Meramec River*.

All water and fine particulate material collected for this investigative study were obtained from the Maramec Stream system at different intervals as it flows from its point of initial upwelling from the subsurface to its termination to the south where it merges with the Meramec River (Section II-Figure 2). The stream originates at the spring upwelling (sampling location #1; Figure 1) and then is comprised of a series of falls (location #3) rapids (locations #6-8), shallow riffles (location #4), and slow moving water pools (locations #2 and #5). These eight sampling locations are ordered numerically from furthest upstream at the point of spring water upwelling (location #1), to furthest downstream (location #8). Further details on these sampling locations are given in Section II of this report. The trout water channel begins downstream of sampling location #3 and recombines with the main channel upstream of location #4. Thus, sampling locations #4-8 may be influenced by organic material from a concentrated fish population. Notable, but relatively insignificant ephemeral spring seeps also enter the Maramec Stream system downstream of sampling location #5 but are inconsequential with regards to the overall volume of water. Additional water may be added by springs that flow directly into Maramec Stream sediments, but none are visible from the stream banks. Sampling location #9 is located on the Meramec River above its point of confluence with Maramec Stream.

1.2 Regional Geology

The Gasconade and Eminence Formation dolomites ($CaMg(CO_3)_2$) host many well developed karst features (e.g., sinkholes, caves, springs, etc.) across central and southern Missouri, including Maramec Spring (Orndorff et al., 2006). The Ordovician-aged Gasconade is on average 100 meters (330 feet) thick, varies in color from light gray to buff, is generally finely crystalline, and moderately to thickly bedded. The unit is unofficially broken into the "lower Gasconade" and "upper Gasconade." The lithological feature for this distinction is the abundance of chert within the "lower Gasconade," while the "upper Gasconade" is relatively chert free. The Gasconade also contains one prominent sandstone member (Gunter Sandstone) that marks the base of this unit and the contact between the underlying Eminence Formation (Thompson, 1991). The Gunter Sandstone averages 10 meters (33 feet) in thickness, varies in color from white to reddish-brown, is medium grained, and is thinly bedded with some minor cross-bedding. It is generally a quartz-rich sandstone, but in some places it may grade into a sandy dolomitic unit. The Gunter is often a major aquifer for water wells throughout Missouri due to its higher permeability. The Cambrian-aged Eminence Formation is a light grey colored cherty dolomite that is greater than 60 meters >200 feet) in thickness.

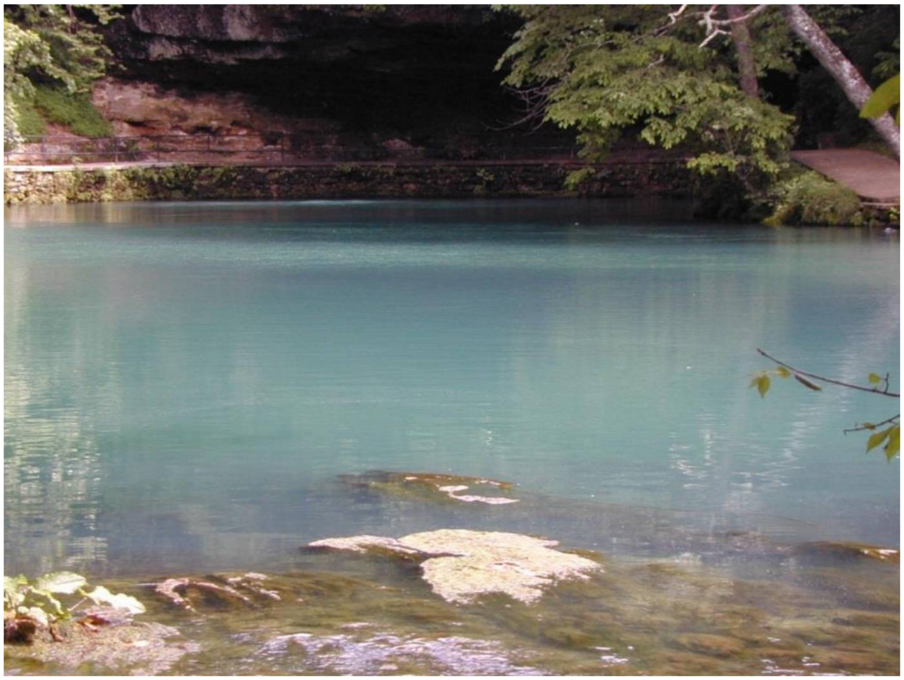

Figure 1. Photograph of Maramec Spring from sampling location #3 looking towards location #1. A zone of gentile upwelling from the spring outflow is just visible in the far end of the pool. The water outflow was low to moderate during this visit. Note the milky blue-white color of the water due to light scattering from the colloidal particles.

1.3 Hydrology of Maramec Spring and Stream System

Maramec Spring expels an average of 3.6 x 10^8 liters of water/day (9.6 x 10^7 gallons/day) from a large open sub-vertical conduit that is collared in the Gasconade dolomite and transgresses through at least the upper 30 meters (100 feet) of the underlying Eminence. The discharge ranges from 1.6 to 31.1 m^3/sec (56 to 1,100 ft^3/sec), with an average discharge of 4.4 m^3/sec (155 ft^3/sec). The recharge area of the spring is estimated to encompass 800 square km (310 square miles) to the south and west of the spring (Unklesbay and Vineyard, 1992; Vandike, 1996). The spring conduit has been entered and mapped by SCUBA divers over a distance of approximately 945 meters (1700 feet), and a depth of 58 meters (190 feet), but this survey of course investigated only a minuscule portion of the underwater spring system that likely goes to greater depths.

The hydrology of Maramec Spring has been extensively studied by Vandike (1996) and references cited therein. Much of the interest in the Maramec Spring system was in response to a liquid fertilizer pipeline break that contaminated the waters with ammonia in November of 1981. These studies were focused on an evaluation of water quality and hydrologic modeling parameters (Vandike, 1985, 1996; Wicks and Hoke, 2000). The geochemical processes occurring in the Maramec Spring system also were the focus of a MS thesis research at Missouri University of Science and Technology, from which the new data for this current report is derived (Rybacki, 2010).

1.4 Overview of Carbonate Precipitation Mechanisms

Calcium carbonate precipitation kinetics is of great importance to scientists and engineers. Calcium carbonate precipitation from supersaturated solutions is known to reduce the permeability and porosity in reservoir rocks, the efficiency of water softening devices, and clog the piping of residential and commercial water systems utilizing hard water (Heydari, 2000). The calcium concentration ([Ca^{+2}]) in solution (Dove and Hochella, 1993), CO_2 loss (Dreybrodt et al., 1997; Zhang and Grattoni, 1998), and solution pH (Wilson, 1975; Cohen and McConnaughey, 2003) are considered to be the three dominant factors influencing calcium carbonate precipitation. Groundwater usually contains dissolved CO_2 in quantities 10 to 100 times greater than atmospheric levels, especially for water transgressing through carbonate strata (Lebron and Suarez, 1996). In experimental studies, a decrease in solution pH is commonly observed during the experimental crystallization of calcium carbonate. This pH change is attributed to the loss of CO_2 from the system (Reddy and Nancollas, 1971; Lakshtanov and Stipp, 2010). Theoretically, one mole of CO_2 should be removed (as $CO_3^{2-)}$ for every mole of calcium carbonate precipitated (Zhang and Grattoni, 1998). Since pH can easily be measured *in situ*, many researchers use pH as a proxy to estimate for the amount of calcium carbonate precipitated from solution.

Several studies propose that the degree of calcium supersaturation in solution, with respect to calcite, is the dominant factor influencing calcium carbonate crystallization in aqueous systems (Kamkha et al., 1989; Dove and Hochella, 1993; Gómez-Morales et al., 1996a; Teng et al., 2000; Dickinson et al., 2002; Lakshtanov and Stipp, 2010). In this scenario conductivity can be used as a proxy, in addition to pH, to measure the relative change in [Ca^{+2}] over time. Gómez-Morales et al. (1996b) were able to measure induction times using pH and [Ca^{+2}], but found [Ca^{+2}] was not as sensitive an indicator to the induction of calcite crystallization as was pH.

Laboratory crystallization experiments can produce all three polymorphs of calcium carbonate (i.e. calcite, aragonite, and vaterite), though the most commonly occurring polymorph is calcite (Reddy and Nancollas, 1976). Swinney et al. (1982) experimentally determined that hard waters are softened more efficiently by the precipitation of rhombohedral calcite rather than by aragonite; vaterite was never observed. This is attributed to the variation in crystal habits between calcite and aragonite, i.e. the aragonite crystals take up more space reducing the efficiency of the water softener. Vaterite was only observed precipitating in unseeded supersaturated solutions where concentrations were extremely high (Gómez-Morales et al., 1996a).

Not only are the rates of precipitation of all the polymorphs of calcium carbonate important, but so are the transformation rates from one polymorph to another. Polymorphic transformations are believed to occur by the dissolution of the parent phase(s), aragonite or vaterite, and the growth of the more stable phase, generally calcite (Ogino et al., 1990). Calcite growth is also believed to be the rate limiting step in the polymorphic transformation, and not the dissolution of the less stable polymorph. Transformation rates between all polymorphs are slowed in the presence of Li^+.

The growth of calcium carbonate crystals from solution is predominantly studied in one of two ways. The first and most common way is with the addition of calcite seed crystals, which act as nucleation sites. Seed crystals are usually euhedral, transparent, approximately 10µm in size (Reddy and Nancollas, 1971), and retain their euhedral shapes throughout calcium carbonate growth (Goodarz-nia and Motamedi, 1980). The second, but much less common method is the spontaneous nucleation of calcium carbonate from supersaturated solutions in the absence of seed crystals. The calcium carbonate precipitation mechanics appear to be the same for both the seeded crystallization and spontaneous nucleation experiments. Spontaneous nucleation occurs almost instantaneously and is not ideal for studying the ***rates*** of calcium carbonate precipitation since extremely high saturation indices are necessary to initiate spontaneous nucleation. Spontaneous nucleation of calcium carbonate is ideal for estimating the ***amount*** of calcium carbonate precipitated from solution since there is no crystalline material prior to induced crystallization. Numerous authors have proposed that calcium carbonate precipitation in a seeded experiment is surface area controlled with growth rates being proportional to the number of available growth sites (Reddy and Nancollas 1971; Nancollas and Reddy 1971; Reddy and Gillard, 1981; Ogino et al., 1990; Dove and Hochella, 1993). This surface area control may also represent the rate limiting step for calcite crystal growth (Nancollas and Reddy, 1971; Zhang and Grattoni, 1998).

The effect of competing species (e.g., Mg, Mn, Sr, Si, SO_4^{-2}, PO_4^{-3}, and dissolved organic carbon) on the precipitation of calcium carbonate is of great industrial importance. Of these potential growth inhibitors, Mg (Reddy and Nancollas, 1976), Si (Lakshtanov and Stipp, 2010), PO_4^{-3} (Reddy and Nancollas, 1973, Nancollas, 1979), and dissolved organic carbon (DOC) (Lebron and Suarez, 1996) appear to have the most dramatic effects on influencing the rate of calcium carbonate precipitation. DOC and PO_4 are known to affect crystal growth by attaching to and reducing the number of potential adsorption sites on crystal surfaces (Reddy and Nancollas, 1973; Dove and Hochella, 1993; Lebron and Suarez, 1996). Contaminants are also observed to affect which polymorph of calcium carbonate may precipitate from supersaturated solutions, the crystallization induction rate, as well as the transformation rate between polymorphs. For example, the activity of silica has been established as an influence on which polymorph precipitates and the rate of induction (Lakshtanov and Stipp, 2010).

Some studies propose that the formation of an amorphous phase of calcium carbonate occurs prior to crystallization in the presence of certain contaminants (Reddy and Nancollas, 1976; Söhnel and Mullin, 1982). The presence of PO_4 appears to produce amorphous shapes and jagged edges during calcite growth (Dove and Hochella, 1993). The crystalline calcite precipitated from supersaturated solutions with Mg present was preceded by an amorphous calcium carbonate phase and then conversion to a crystalline form similar to calcite crystals observed to grow in the absence of Mg. The size of the calcite crystals also appear to be correlated to the amount of impurities incorporated within the calcite crystal structure with higher impurity contents resulting in smaller crystal dimensions (Söhnel and Mullin, 1982). Gebauer et al. (2008) also observed an amorphous phase that preceded the crystalline phase and proposed that stable calcium carbonate clusters grow through the binding of Ca^{+2} and CO_3^- ions to form an amorphous phase. These non-crystalline clusters would then eventually convert into a thermodynamically stable calcium carbonate polymorph. All steps associated with ion binding were anticipated to be pH dependent.

The exact role of kinetics and thermodynamics in calcium carbonate precipitation is not well understood. In calcite precipitation there is an initial rapid growth surge of calcium carbonate that eventually slows to follow kinetic rate equations (Nancollas and Reddy, 1971). The most commonly proposed rate limiting steps are CO_2 production (Dreybrodt et al., 1997; Zhang and Grattoni, 1998), the number of available growth sites (Dove and Hochella, 1993; Zhang and Grattoni, 1998), system flow characteristics (Dreybrodt et al., 1997), and $[Ca^{+2}]$ saturation levels (Dove and Hochella, 1993). Most researchers are in agreement that the most important thermodynamic factor is the $[Ca^{+2}]$ in solution, but the most important kinetic factor is still debated. For example, Kamkha et al. (1989) and Dickinson et al. (2002) had differing views about kinetic factors. Kamkha et al. (1989) suggested that the solution pH, specifically the pH influence on $[HCO_3^-]$ controlled the kinetics of calcium carbonate precipitation, but Dickinson et al. (2002) proposes that the kinetics of the growth reactions were controlled by CO_2 release. The genetic linkage between CO_2 release and $[HCO_3^-]$ suggests that both authors may be correct.

The $[Ca^{+2}]$ in solution is intuitively the most plausible kinetic factor affecting calcium carbonate crystallization when open systems are exposed to a CO_2 rich atmosphere. Varying the $[Ca^{+2}]$ relative to the saturation level within a system has a profound effect on growth rates and mechanisms of calcium carbonate formation. In solutions with saturation levels greater than one but less than two, calcite exhibits two different types of growth morphologies. Calcite growth is initially dominated by surface nucleation and coalescence but transitions into a spiral growth morphology over time. In undersaturated solutions but close to equilibrium, both surface dissolution and precipitation of calcium carbonate appear to occur simultaneously (Dove and Hochella, 1993).

Theoretically, one mole of CO_2 is produced for every mole of calcium carbonate precipitated. Thus, the rate at which CO_2 can be produced and removed from an aqueous system can also be a rate limiting step for calcium carbonate precipitation. In natural settings aquatic organisms may have a positive effect on the rate of calcium carbonate precipitation as they consume CO_2 for their vital processes (Lebron and Suarez, 1996). Dreybrodt et al. (1997) studied the effect of enzymes on the $HCO_3^- + H^+ \rightarrow H_2O + CO_2$ reaction rate to determine if CO_2 production could be enhanced. They observed that this reaction was enhanced in the presence of the enzymes, suggesting a linkage of CO_2 removal and carbonate precipitation. The exact role the enzymes play is not well understood (Zhang and Grattoni, 1998).

When comparing all these studies, it becomes apparent that the calcium carbonate precipitation rate laws need to be carefully selected and applied (Teng et al., 2000). Analyzing the change in bulk chemistry of a system may not be the most accurate way to derive rate laws of calcium carbonate precipitation (i.e. discrepancies between rate law equations from studies of different scales). For example, Goodarz-nia and Motamedi (1980) observed an interesting phenomenon during their experimental precipitation of calcium carbonate that was not noted in any other study. They observed that the overall crystal size increased with time until approximately 50 minutes after initial precipitation. After this time, the crystal sizes were observed to decrease, rather than continuing to grow. They could not explain this phenomenon, which could have been the result of the system reaching equilibrium, achieving slightly undersaturated conditions, or transformation from one polymorphous phase to another with lower equilibrium solubility values.

1.5 Study Objectives

The purpose of the present study is to: (1) identify the mineral speciation of the colloidal mineral phase(s) present in Maramec Spring water that imparts the milky blue-white color to the water column, (2) determine if this phase(s) are actively precipitating from solution due to physical and chemical changes as the spring water rises to the surface, and (3) determine potential mechanisms for colloid mineral formation. Calcium carbonate precipitation and dissolution processes are also of extreme importance with respect to CO_2 sequestration. A good understanding of carbonate system behavior under varying natural conditions is necessary to enhance CO_2 sequestration attempts. Natural analogs such as Maramec Spring act as natural laboratories to study carbonate precipitation and dissolution (i.e. sedimentation and karstification). These spring systems represent and mimic processes that may occur when a CO_2 sequestration repository develops a leaking seal rock and the changes that occur when CO_2 rich fluids move upwards through geologic strata. Knowledge gained from these studies can thus be applied to CO_2 sequestration programs.

2 RESULTS

2.1 Solution and Gas Phase Analysis of the Spring Water

Spring water pH values measured at the point of upwelling (location #1) show only a minimal variation, averaging 7.02 ± 0.15 pH units, with a range from 6.78 to 7.39 for 21 visits to the site between 2001 and 2012 (Figure 2; Table 1). Measurements made at the location of spring water upwelling (location #1) often failed to produce a stable pH reading due to non-equilibrium conditions, in which case a median value was used as an estimate. Although the pH varied from one sampling date to another, there was no apparent correlation in the pH at the location of upwelling relative to season or recent rainfall events. A small but statistically significant increase in pH was always observed as the Maramec Spring water moved downstream away from the point of upwelling. The average pH increase for 17 different sampling dates where we extended the sampling out to location #5 was 0.21 ± 0.10 pH units. Extending the sampling distance out to #8 we observed a pH increase between locations #1 and #3 that averaged 0.31 ± 0.12 for six different dates. Spring water from location #1 was also collected on 4/13/12 and held at a near-constant temperature in a ventilated container. The pH was measured at 0, 1, 3, 14, 27, and 40 hours, with values of 7.04, 7.14, 7.16, 7.31, 7.71, and 7.93, respectively. The resulting pH rise occurred in a sub-linear fashion with time and there was no evidence of a decrease in rate with time. Two additional measurements were made on Meramec River water, at a site just upstream from the confluence with Maramec Stream. The recorded pH values at that location were 8.08 and 8.32. Eh values are observed to decrease slightly downstream with only minor variability, and these were inversely correlated with the measured pH increase (Figure 3). The average Eh value at sampling location #1 was +3 ± 11 mV. These values decreased an average of -10 ± 6 mV between locations #1 and #5 and an average of -19 ± 16 mV between locations #1 and #8. The corresponding two measured Meramec River Eh vales were -41 and -60 mV.

The temperature of the upwelling spring water at location #1 was remarkably constant having an average range of 13.6 ± 0.6 ^{o}C (Figure 4; Table 1). The lowest temperatures were measured during the early spring months whereas the highest were from the late summer and autumn. In addition to the seasonal changes, we also note a short-term decrease of ~0.5 ^{o}C in the upwelling spring water in the following a heavy seasonal rain while the water outflow had noticeably increased. The temperature of the water also equilibrated with that of the atmosphere as the water moved downstream. An increase was generally observed downstream during testing as most of our sampling dates were conducted in the warmer months of the year.

Unlike the spatial variability observed in pH, Eh, and temperature values for the Maramec Stream system, conductivity was relatively consistent throughout the sampling reach for any individual sampling date (Table 1). The conductivity measurements did vary from day-to-day, however, and tended to be higher on days following local rain events with an overall range for all dates falling between 180.6 and 361.0 µS/cm.

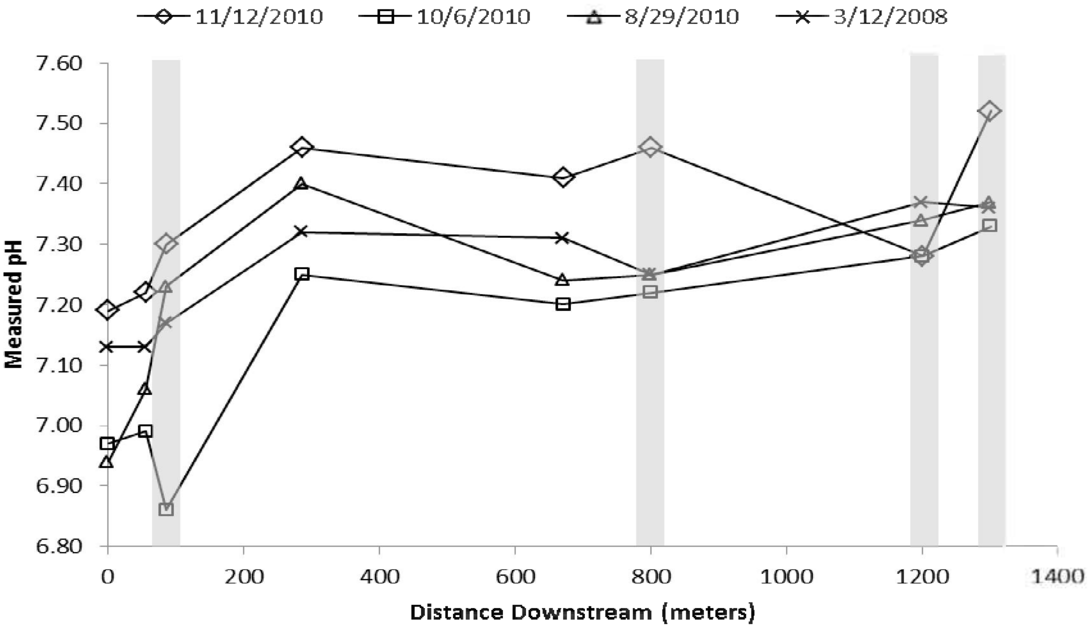

Figure 2. Measured pH values of the Maramec Spring and Stream water from four sample dates. Overall, pH values increase in the downstream direction. Shaded regions indicate areas where small waterfalls or rapids are located.

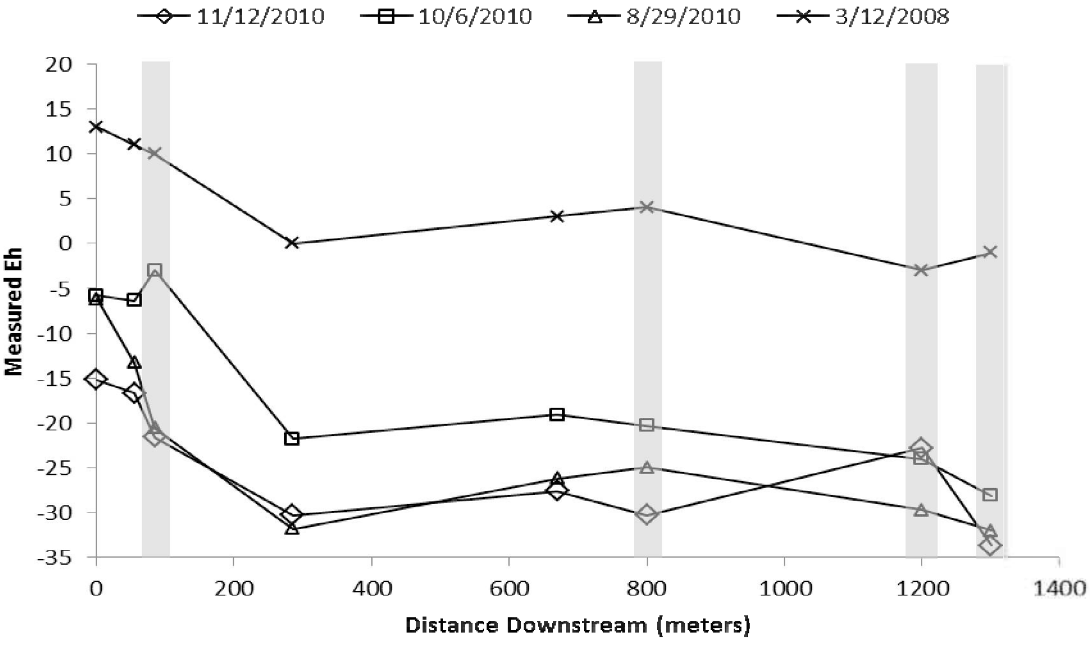

Figure 3. Measured Eh values (in millivolts) of Maramec Spring and Stream water from four sampling dates. Eh values are inversely correlated to measured pH values, decreasing in the downstream direction. Shaded regions indicate areas where small waterfalls or rapids are located.

Table 1. On site measurements for various water parameters at Maramec Spring. The site was visited a total of 21 dates, but only a representative suite of sampling date is presented here. Alkalinity is measured in milliequivalents/liter ((moles/L) * valence charge).

Date/site	Water Condition	pH	Temp °C	Eh mV	Conductivity µS/cm	Alkalinity meq/L	Dissolved Oxygen mg/L
6/19/09							
1	High flow-turbid	6.78	13.8	+25	145		
3		6.80	13.9	+21	145		
5		6.83	14.2	+19	145		
6/25/09							
1	Normal	6.84	13.9	+18	173		
2		6.86	14.0	+16	173		
3		6.93	13.9	+15	173		
4		7.03	14.0	+10	174		
5		7.03	14.2	+10	173		
7/07/09							
1	Normal	6.80		+8			
2		6.90		+5			
3		6.97		+7			
4		7.02		+1			
8/29/10							
1	Normal	6.94	14.1	-6	320	144	4.55
2		7.06	14.3	-13	319	131	4.40
3		7.23	14.2	-21	321	error	6.68
4		7.40	14.5	-32	320	149	7.10
5		7.24					
8		7.37		-32			
11/12/10	Normal						
1		7.19	14.0	-15	361	153	4.77
2		7.22	14.3	-17	360	154	4.27
3		7.30	14.1	-22	361	153	6.75
4		7.46	14.3	-30	361	146	6.29
5		7.41	14.3	-28	361	146	5.58
6		7.46	14.3	-30	361	147	6.91
7		7.28	14.6	-23	361	151	6.44
8		7.52	14.4	-34	361	140	7.26
4/16/2011							
1		6.88	12.9	-3			
5		6.99		-7			
4/17/2011							
1		6.94	12.4	-7			
5		7.13		-12			
4/13/2012	Light rain						
1		7.10	13.0	+8	229	118	
2		7.03	13.4	+8	229	114	
4		7.40	13.4	-11	228	110	
5		7.32	13.1	-6	226	115	
4/14/2012	Rain						
1		7.04	13.7	+2	259	116	
2		7.19	13.8	+8	260	118	
4		7.40	14.0	-10	259	121	
5		7.19	14.4	+6	263	121	

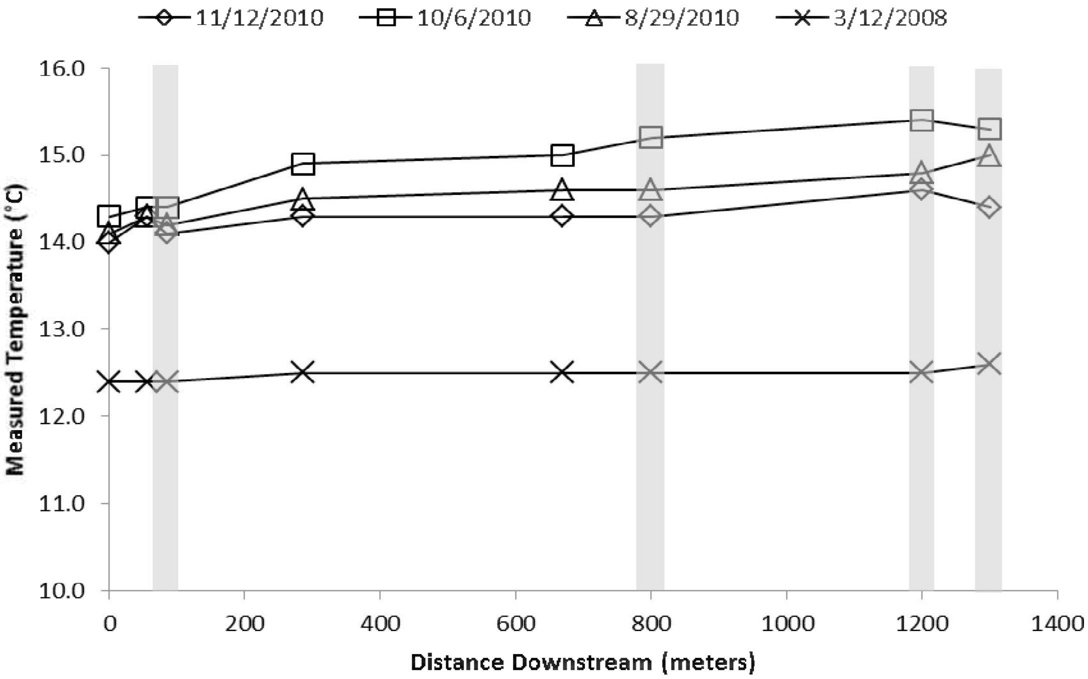

Figure 4. Measured Maramec Spring and Stream water temperature for four sampling trips. Temperature increases in the downstream direction, away from the point of upwelling. Shaded regions indicate areas where small waterfalls or rapids are located.

The turbidity of the Maramec Spring and Stream waters could not be measured accurately during most of the warm seasonal visits to the site moisture condensation on the light scattering turbidity vials after they were filled with the cool spring water. Successful turbidity measurements were made on March 12, 2008 and November 11, 2010. Measured turbidities for locations #1-#8 on March 12 were 7.53, 7.54, 7.67, 7.53, 7.74, 8.48, 8.24, and 7.78 Nephelometric Turbidity Units (NTU), respectively, while the corresponding values on November 11th were 0.50, 0.87, 4.06, 0.96, 1.10, 2.48, 1.09, and 0.97. The November 11, 2010, turbidity measurements continued for each site after the samples were collected from the spring water and held in the glass turbidity vials. These water aliquots measured after 1, 3, 5, and 240 minutes. The measured turbidity values decreased an average of 24% between the first sampling and the 240 minute sample. The vials were then shaken after the last reading to determine if any particulate material had settled to the bottom of the sample containers. After agitating the vessels we noted that turbidity had increased an average of 76% relative to the unshaken measurements taken just moments before, and also increased an average of 34% relative to the measurements taken when the samples were first collected. This overall pattern indicates that particles were being produced and settling within the glass measuring tube during the 240 minute holding period.

Total Suspended Solids (TSS) and Total Dissolved Solids (TDS) contents were also determined from spring water collected during a normal non-flood condition sampling on October 6th 2010. The TSS value for collected particulate material in a 0.45 µm filter was 1.93 mg/liter while the

TDS value (which will include any colloidal material passing through the filter) was 205 mg/liter. The Visitor Center at Maramec Park displays a video entitled “The Hidden World Beneath Maramec Spring Park”. This video shows SCUBA divers as they descend into the depths of the Maramec cave system up to approximately 200′ foot depths. The turbidity of the water is still apparent even in the in the deeper and totally dark portions of the cave (ignoring cave floor sediments suspended by the swimming motion of the divers). Thus, from the movie documentary, it appears that precipitation of the calcite colloids must be initiated in even deeper portions of the cave below a 200′ depth, or alternatively, the turbidity must result from only suspended quartz particles as these are likely to be derived as a weathering residue from the dissolving dolomite within the cave passage.

The flux of CO_2 gas from the spring water was measured at three different sampling locations using a LI-COR CO_2 gas analyzer on 6/19/2009. This sampling date occurred three days following a heavy rain event. Flux values at sampling locations #1, #3, and #5 were: 17.5 ± 3.3, 8.5 ± 3.9, and 2.6 ± 6.1 μmoles CO_2/m^2sec, respectively (Figure 5). These values are relative to the local atmosphere of 1.14 μmoles CO_2/m^2sec (360 ppm). Thus, CO_2 concentration in the air directly above the pool water was enriched in CO_2 15-fold relative to the average atmosphere. Dissolved oxygen contents were measured on two sampling dates (Table 1). Water upwelling at the spring opening displayed dissolved oxygen contents of 4.6 to 4.8 mg/kg. Dissolved oxygen increased downstream as the waters had the time to come to equilibrium with the ambient atmosphere. The highest recorded oxygen concentration was a value of ~7.3 mg/kg recorded at location #8 on 11/12/2010.

Alkalinity (acid buffering capacity) measurements were determined in the field using a HACH colorimetric titration kit. The analyzed alkalinity measurements varied from day to day showing an overall range of approximately 110 to 155 meq/L over four different sampling dates (Table 1). Variation in alkalinity values on any one sampling date were relatively small and did not display and consistent trend in a downstream direction.

ICP-OES analysis of the Maramec Stream water was performed on unfiltered as well as water samples that were filtered on site on four different sampling dates. Calcium was the most abundant cation observed in solution. The lowest Ca concentration at the zone of upwelling (locations #1 or #2) was 16.5 mg/kg on 6/25/2009, while the highest was 48.0 mg/kg on 4/16/2011. Average concentrations for the 8/29/2010 sampling for locations #1-4 were Ca = 33.0 ± 0.1 mg/kg (Figure 6 and Table 2). Filtering the water did not have any significant effect on the Ca concentrations, thus the filtered water samples had a composition that was indistinguishable from the unfiltered (Figures 6 and 7). This similarity was noted for both the syringe and vacuum filtered water samples. There was a very slight decrease noted in Ca and Mg concentrations in the downstream direction on any one sampling dates, however, these changes typically were near or less than analytical accuracy determinations (1-2% for Ca and 6% for Mg) and were not consistent for all filter sizes. Overall changes in water chemistry were different from one sampling date to another. The second highest concentration cation was Mg with a mean concentration of 19.7 ± 0.1 mg/kg. Si, K, and Na were always detected in minor amounts and had mean concentrations of 4.2 ± 0.0, 1.7 ± 0.0, and 1.4 ± 0.0 mg/kg, respectively. The concentrations of Al, Fe, and Mn were measured, but always were at or below the ICP-OES analytical detection limit of 0.1 mg/kg (Figure 7).

Anion analyses were performed on unfiltered water collected from sampling locations #1-8 on November 11, 2010 (Table 2). The anions determinations showed very little variation along the entire stream reach. Measured chloride concentrations were between 6.0 and 6.3 mg/kg, nitrate between 3.1 and 3.2 mg/kg, and sulfate between and 4.3 and 4.5 mg/kg. Fluoride and phosphate were measured, but fell below the ion chromatography instrument detection limits of 0.05 and 0.2 mg/kg, respectively.

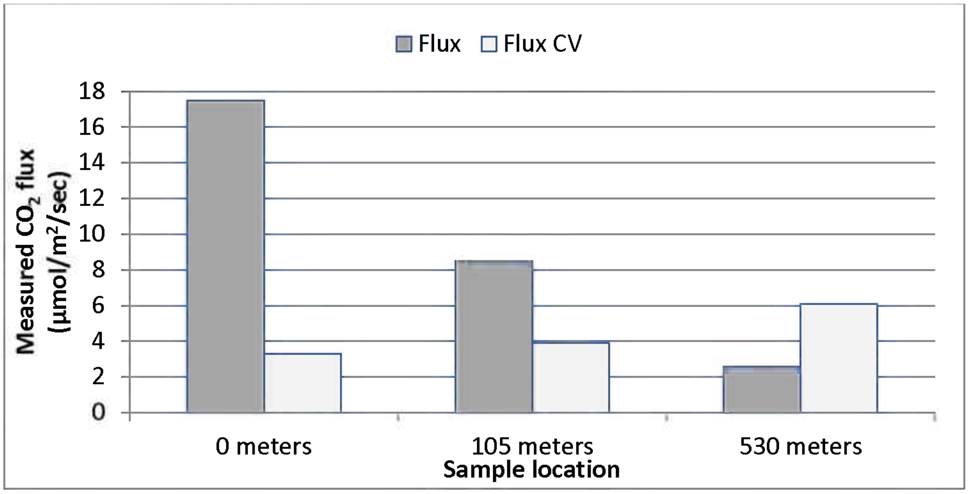

Figure 5. Measured CO_2 flux at Maramec Spring in the upwelling pool area (0 m, location #1) and downstream locations #3 (85 m) and #5 (670 m) on 6/19/2009, three days after a heavy rain event. The spring water turbidity and flow rate were increased relative to normal flow conditions. The relatively high coefficient of variation (CV) noted at location #5 is believed to result from the photosynthetic activity of aquatic algae.

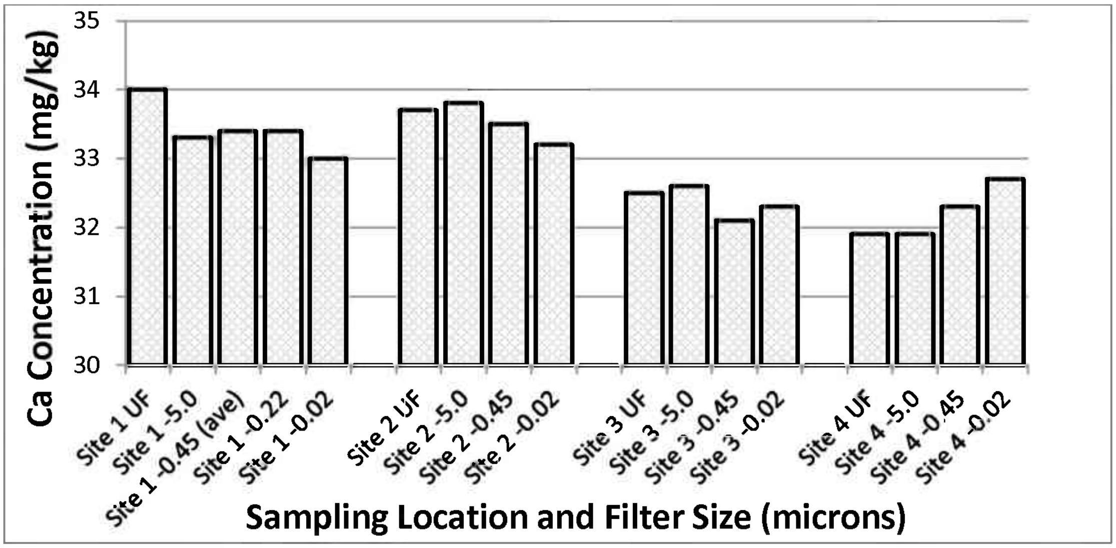

Figure 6. Measured calcium by ICP-OES of for unfiltered (UF) and various filtered water samples (5.0, 0.45, and 0.02 µm) collected from sampling locations #1-4 on 8/29/2010. Note that there is no appreciable concentration change associated with filter size and only a minor decrease in measured [Ca^{+2}] can be observed in the downstream direction.

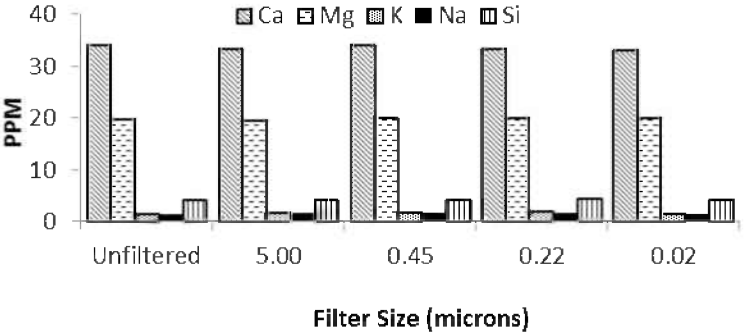

Figure 7. ICP-OES analytical results from unfiltered and syringe filtered spring water (5.0, 0.45, 0.22, and 0.02 µm filters) from sampling location #1 collected 8/29/2010. Note that filtering does not appear to have any significant effect on the water chemistry.
Table 2. Cation and anion results from filtered and unfiltered water samples. Values in mg/kg. Solutions were also analyzed for Mn, F, and PO_4^{3-} with concentrations always below detection limits of 0.1, 0.05, and 0.2 mg/kg respectively.

2.2 Analysis of Colloidal Particles Isolated by Centrifuging

The suspended particulate material recovered by centrifuging from Maramec Spring water has been identified as a carbonate mineral by immersion in a 5% HCl solution and observing CO_2 bubble production under a microscope as the grains dissolved. The isolated particles were also analyzed by SEM-EDS and determined to have a rhombohedral form with crystal sizes of approximately 6.5 µm in their long-axis direction (Figure 8). These particles were slightly larger than typical colloids (0.001 to 1.0 µm), though it is likely that they continued to grow between their time of collection and final mounting, and thus may have been smaller at their time of collection. An elapsed time of ~24 hours had passed between the time they were collected, centrifuged, pipetted onto an aluminum SEM mounting stub (along with a few drops of spring water), and then finally dried completely in the ambient air. These particles produced ghost crosses as very finely crystalline calcite grains precipitated along the crystal corners in contact with the class slide (Figures 8a and b). Semi-quantitative SEM-EDS compositional results on the larger central crystals revealed a Ca:Mg molar percentage ratio of 95 to 5%, although the EDS detection system is only semi-quantitative and thus these values are only approximate. Biogenic filaments and diatoms were also observed during SEM-EDS analysis.

Table 2. Cation and anion results from filtered and unfiltered water samples. Values in mg/kg. Solutions were also analyzed for Mn, F, and PO_4^{3-} with concentrations always below detection limits of 0.1, 0.05, and 0.2 mg/kg respectively.

Date Location #	Filter (µm)	Ca	Mg	Si	K	Na	Al	Fe	Cl^-	NO_3^-	SO_4^{2-}
6/25/2009											
2	Unfiltered	16.0	11.5	4.0	1.5	0.6	0.2	0.1			
2	-5.0	16.5	11.2	3.9	1.5	0.6	0.1	<0.1			
2	-0.45	16.3	11.4	3.8	1.5	0.6	<0.1	<0.1			
2	-0.02	16.3	11.4	3.7	1.5	0.6	<0.1	<0.1			
5	Unfiltered	16.3	11.5	3.9	1.5	0.6	0.1	0.1			
5	-5.0	16.6	11.4	3.9	1.5	0.6	<0.1	<0.1			
5	-0.45	16.0	11.2	3.7	1.5	0.6	<0.1	<0.1			
5	-0.02	16.3	11.4	3.7	1.5	0.6	<0.1	<0.1			
7/07/09											
2	Unfiltered	25.8	14.2	4.7	1.7	1.0	<0.1	<0.1			
2	-5.0	25.7	13.7	4.7	1.7	0.8	<0.1	<0.1			
2	-0.45	25.2	14.0	4.6	1.7	0.9	<0.1	<0.1			
2	-0.02	25.4	13.8	4.5	1.7	0.9	<0.1	<0.1			
8/29/2010											
1	Unfiltered	34.0	19.9	4.3	1.5	1.4	<0.1	<0.1			
1	-5.0	33.3	19.5	4.3	1.8	1.4	<0.1	<0.1			
1	-0.45	33.4	19.8	4.3	1.7	1.4	<0.1	<0.1	6.2	3.2	4.4
1	-0.22	33.4	19.9	4.3	1.9	1.5	<0.1	<0.1			
1	-0.02	33.4	20.0	4.3	1.5	1.4	<0.1	<0.1			
2	Unfiltered	33.7	19.7	4.3	1.6	1.4	<0.1	<0.1			
2	-5.0	33.8	19.9	4.2	1.6	1.4	<0.1	<0.1			
2	-0.45	33.5	19.9	4.2	1.6	1.4	<0.1	<0.1	6.3	3.2	4.4
2	-0.02	33.2	19.9	4.2	1.6	1.4	<0.1	<0.1			
3	Unfiltered	32.5	19.3	4.3	2.2	1.4	<0.1	<0.1			
3	-5.0	32.6	19.9	4.3	1.9	1.4	<0.1	<0.1			
3	-0.45	32.1	19.5	4.2	1.9	1.4	<0.1	<0.1	6.1	3.2	4.3
3	-0.02	32.3	19.7	4.2	1.7	1.4	<0.1	<0.1			
4	Unfiltered	31.9	19.5	4.2	1.7	1.4	<0.1	<0.1			
4	-5.0	31.9	19.4	4.2	1.6	1.4	<0.1	<0.1			
4	-0.45	32.3	19.5	4.2	1.6	1.4	<0.1	<0.1	6.1	3.2	4.4
4	-0.02	32.7	19.8	4.2	1.7	1.4	<0.1	<0.1			
4/16/2011											
1	Unfiltered	47.4	27.0	7.2	2.6	2.1	<0.1	<0.1			
1	-5.0	47.9	26.4	7.0	2.6	2.0	<0.1	<0.1			
1	-0.45	47.1	26.5	7.0	2.6	2.0	<0.1	<0.1			
1	-0.02	47.2	25.9	6.9	2.8	2.1	<0.1	<0.1			
2	Unfiltered	48.0	26.3	6.9	2.6	2.0	<0.1	<0.1			
2	-5.0	48.4	26.0	7.0	2.6	2.0	<0.1	<0.1			
2	-0.45	48.3	26.4	6.9	2.6	2.0	<0.1	<0.1			
2	-0.02	47.1	26.4	7.1	2.6	2.1	<0.1	<0.1			
5	Unfiltered	46.6	26.3	6.9	2.9	2.0	<0.1	<0.1			
5	-5.0	46.8	26.0	6.9	2.9	2.1	<0.1	<0.1			
5	-0.45	48.1	26.4	6.9	2.9	2.1	<0.1	<0.1			
5	-0.02	47.4	26.3	6.9	2.9	2.1	<0.1	<0.1			
8	Unfiltered	46.4	25.9	6.8	2.5	2.0	<0.1	<0.1			
8	-5.0	47.1	26.2	6.8	2.6	2.0	<0.1	<0.1			
8	-0.45	47.1	26.0	6.8	2.6	2.0	<0.1	<0.1			
8	-0.02	47.3	26.7	6.9	2.6	2.1	<0.1	<0.1			

Table 2 (cont.)

Date Location #	Filter (µm)	Ca	Mg	Si	K	Na	Al	Fe	Cl^-	NO_3^-	SO_4^{2-}
4/13/12											
1	Unfiltered	30.8	17.9	3.9	1.3	1.2	<0.1	0.1			
1	-0.45	30.9	17.8	4.0	0.7	1.5	<0.1	0.1			
1	-0.02	29.6	17.7	4.0	1.3	1.2	<0.1	<0.1			
4/14/12											
1	Unfiltered	28.9	17.3	3.9	1.3	1.2	<0.1	0.1			
1	-0.45	29.7	17.2	3.9	0.5	1.7	<0.1	0.1			
1	-0.02	28.7	17.3	3.9	1.3	1.2	<0.1	0.1			

2.3 Analysis of Colloidal Particles Isolated by Vacuum Filtration

Particulate material was also collected from spring water by filtration using 5.0 µm, 0.45 µm, 0.22 µm, 0.10 µm, and 0.05 µm Millipore cellulose filters in succession. Yellow particles were observed on both the 5.0 and 0.45 µm filter fractions, being most prominent on the latter during higher water flow and former during low flow conditions (Figure 9). Most of the yellow particles were larger than 0.45 µm as none of this material was visible on the 0.22 or 0.05 µm filters. The 0.45 and 0.22 µm filters collected the largest volume of material.

The particles trapped on the various filter paper sizes were also examined by SEM-EDS analytical techniques. It is important to note that when analyzing small particles using EDS that the resultant X-ray counts may not be generated solely from the particulate material of interest, but also from the surrounding and/or underlying material. The SEM-EDS analysis of an unused cellulose filter mounted on a SEM Al-stub produced EDS peaks for O, C, and Si, while Al peaks were derived from the Al mounting stub, plus Au and Pd from the electrical conductance coating used in the SEM. A much larger variety of particles were observed on the filters as opposed to those recovered by centrifuging. The filter-recovered material also varied greatly in quantity, color, and morphologic features between the various filter sizes (Figures 9 and 10). The particles collected on the 5 µm filter included elongated fibers (Figure 10a) and tubular structures (Figure 10b). Both the filamentous and tubular, and displayed only peaks for Si and Al, both of which were present in the substrate and thus may be responsible for most, if not all of this spectral signal. A rectangular phase (Figure 10c) was found to be enriched in sulfur and also contained lead as identified by EDS spectra of the $L_{\beta 1}$ and $L_{\beta 2}$ lines at 12.61 and 12.62 KeV, respectively. There appeared to be a bimodal size distribution of the particulate material collected upon these filters (Figure 10d) as finer particles were often trapped within the filter pore spaces and then overlain by the larger particles. The 0.05 µm filter trapped the smallest amount of material. The phases collected on this filter have a rectangular outline and are observed to cluster together (Figure 10e). The finer grained material (0.5 µm to 1 µm diameter particles) which fills the pores of the 0.45 and 0.22 µm filters also displays sharp peaks for S as does the rectangular particulate material collected on the 0.05 µm filter. Weak peaks for iron were also detected. Filtered samples collected from sampling locations #5 and 8 on November 11, 2010 were enriched in a Ca, and/or Ca+Mg phase. The Ca-enriched phase consists of particulate material with rhombohedral morphologies with sharp crystal faces and rarely pitted surfaces, and thus appears to be calcite.

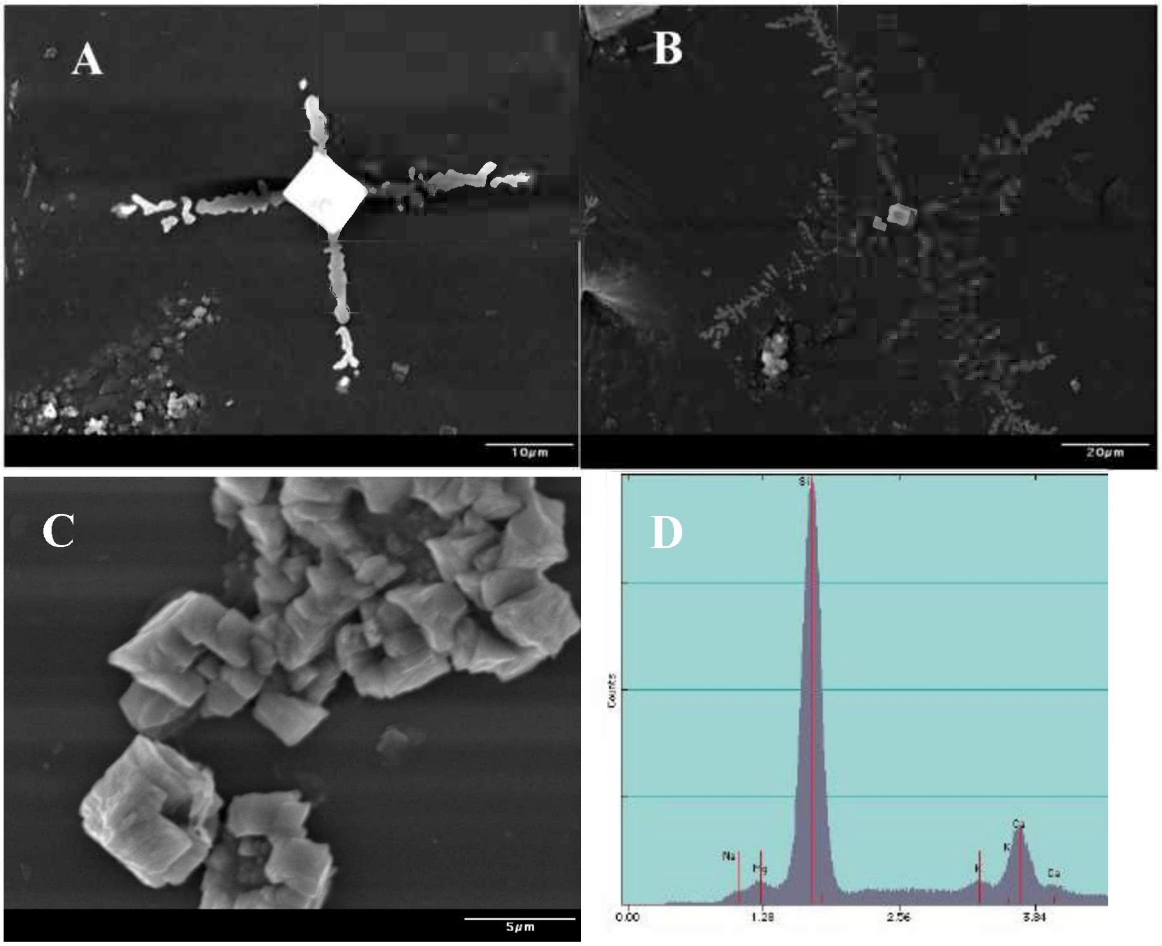

Figure 8. Crystals collected *via* centrifuging of Maramec Spring water at sampling location #1 on 9/21/2007. (A) Rhombohedral crystals acting as a nucleation point for further calcite growth as a ghost cross as the small amount of solution accompanying the centrifuged particles dried on the glass slide. (B) A larger dendritic structure with a rhombohedral carbonate crystal as a nucleus. (C) A cluster of rhombohedral carbonate crystals with agglomerations approximately 6 µm in diameter being composed of individual crystallites ranging from 1 to 3 µm in diameter. (D) SEM-EDS spectra from larger rhombohedral crystal from image in Figure 8A. The peaks for Si and K are derived from the underlying glass substrate that the samples are resting upon.

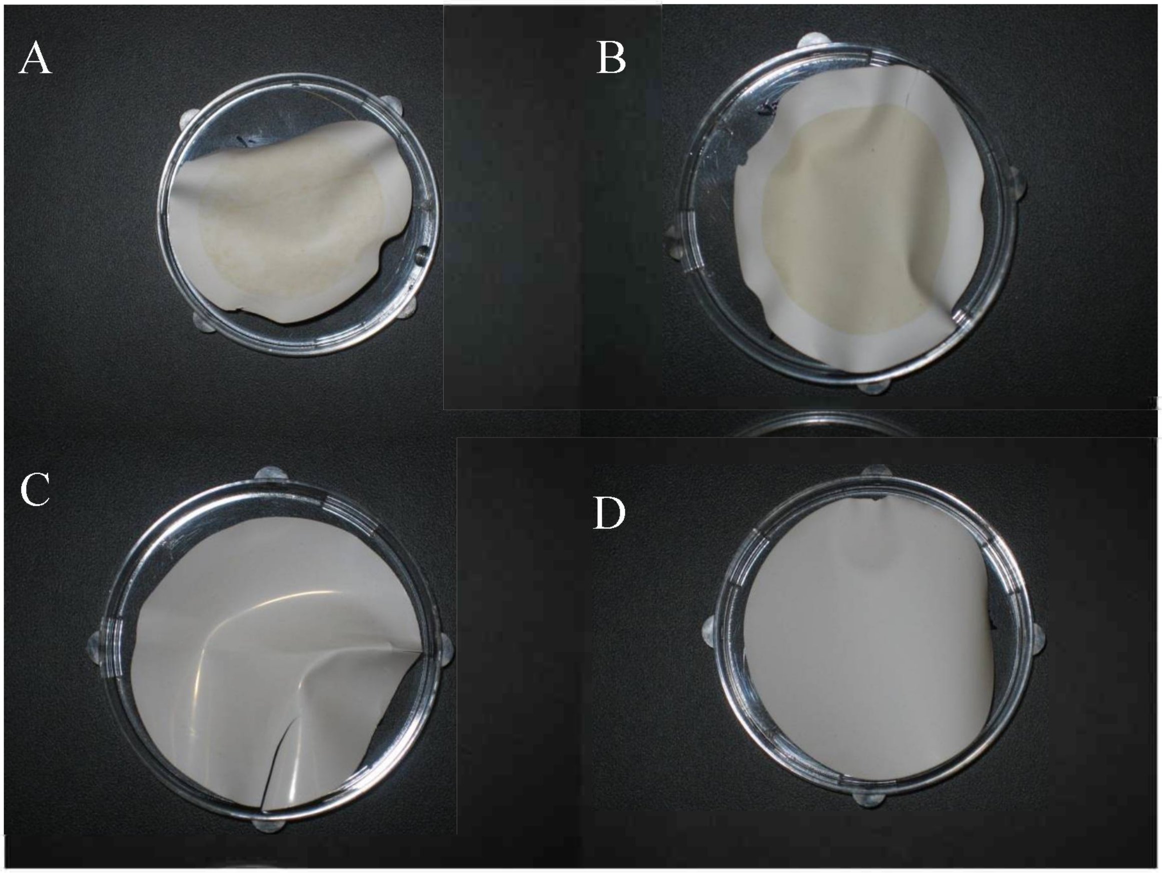

Figure 9. Particulate material collected on the (A) 5.0 µm, (B), 0.45 µm, (C) 0.22 µm, and (D) 0.05 µm cellulose filters from sampling location #1 on 10/6/2010. A yellow particulate phase was collected on the 5.0 µm, and 0.45 µm filters (A and B), but is not observed on the 0.22 µm or 0.05 µm (C and D) filters. The diameter of the plastic container holding the filters is 47 mm.

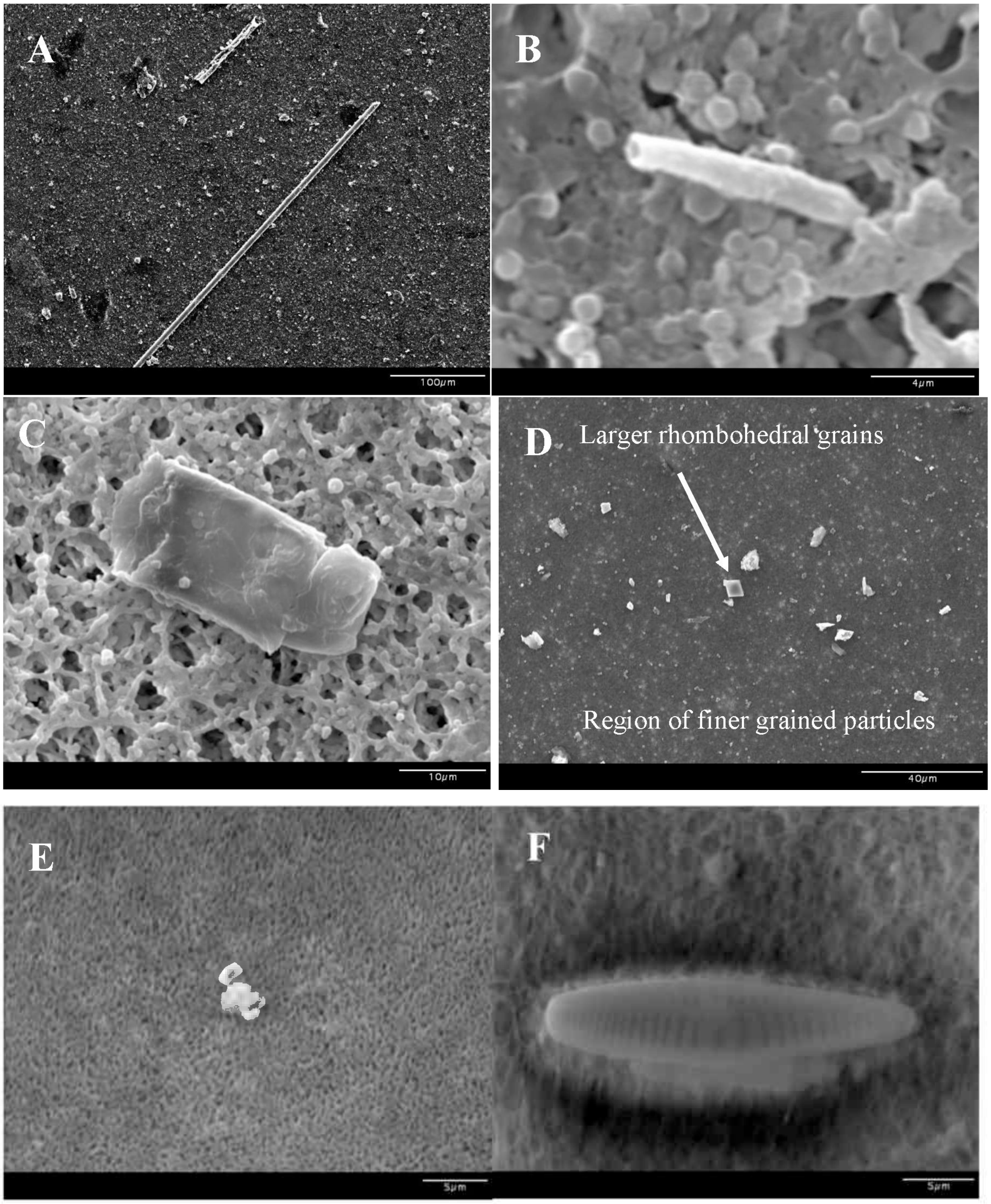

Figure 10. Material collected on cellulose filters by sequential vacuum filtration on 10/6/2010 from sampling location #1. (A) Filaments on 5.0 µm filter. (B) elongate tubular structure on 5.0 µm filter. (C) Subhedral blocky sulfur- and lead-enriched particulate material on 5.0 µm filter. (D) Bi-modal size distribution on 0.22 µm filter with larger grains displaying Ca-enriched and rhombohedral forms and finer grained material lodged into filter pores, (E) Cluster of Ca-enriched particulate material collected on the 0.05 µm filter. (F) Asymmetric Si-rich diatom captured in 0.22 µm filter.

2.4 X-Ray Diffraction Analysis of Colloidal Particles

X-ray diffraction (XRD) analysis was conducted on the 5.0, 0.45, 0.22, and 0.10 μm filters collected from sampling locations #1, #5, and #8 as well as an unused blank cellulose filters. The filters were affixed to an X-ray amorphous glass slide for stability. Unused blank 0.22 and blank 0.45μm cellulose filters mounted on glass slides produced a broad background peak centered at ~20° 2θ that could easily be distinguished from small, though sharp and narrow peaks associated with the crystalline phases trapped on the filters (Figures 11 a and b). XRD peaks were collected from 13 filters; 12 of these representing the 11/12/2010 sampling date where four different filter sizes were used at three different locations. The remaining sample was collected using a 0.22 μm filter at location #1 on 8/29/2010. The particles caught on the filter paper produced peaks occurring at 2Θ diffraction angles of approximately 6.3°, 8.8°, 9.3, 12.4°, 20.8°, 24.8°, 25.7°, 26.6°, 27.5°, 29.9°, 30.9°, 33°, 36.6°, 39.5°, 40.3°, 42.5°, 50.1, and 51°. Not every peak was apparent on every filter and most of the peaks displayed very small heights above the filter background, especially those at 2Θ angles >31°. The low peak heights result from the small proportion of particles recovered on the filter paper. The 29.9° 2Θ peak was the most common, occurring in 11 of the 13 filter papers. The 26.6° peak often was the most prominent in some filters, but it was absent in others.

2.5 Inductively Coupled Plasma – Optical Emissions Spectroscopy

The ICP-OES analysis of acid digested particles recovered by centrifuging plus those trapped on the vacuum filter material revealed differences in the compositions between the digested particles from the different collection methods and filter sizes, though this likely results from the digestion of different types of particles that were isolated by the different methods (Figure 12; Table 3). Analytical results from several white rhombohedral shaped particles that were recovered by the centrifuge technique, isolated, and digested revealed a composition with a Ca:Mg atomic ratio of 92 to 8%. This was comparable to the SEM-EDS result from a centrifuge recovered grain that revealed a Ca:Mg ratio of 95 to 5%. The digested 0.45 μm particulate material (enriched in yellow particles) contained Si, Al, and Fe as the major components, while Ca, Si, Al, Fe, and K were the major components detected in the leachate from the 0.22 μm particulate material. Mg and Na were also detected as trace constituents from most particles. The Ca:Mg molar ratio for the digested particles from the 0.45 μm filter was 78:22, while the ratio for the digested particles from the 0.22 μm filter was 50:50, These digestion results represent the entire assembly of soluble and acid leachable components captured on the filters as individual grains could not be isolated for digestion.

Table 3. Results from 5% nitric acid digestion of colloidal particles. Centrifuge collected particles were rinsed in deionized water, isolated by hand picking under a microscope, dried, weighed, then acid digested. Filtered particles (0.45 and 0.22 µm were collected by vacuum filtration in the field, rinsed with deionized water, dried, weighed, and then immersed in acid. Syringe filter samples (0.02 µm for all elements except for Al where 0.45 µm filter was used) were collected for location #1 on site (0 hr.), and then after 12 and 36 hour holding periods. Filters were rinsed in deionized water, flushed with air, and then soaked in acid for four hours. Values in upper rows are in mg/kg, lower rows are in moles/kg. ICP-OES detection limits are 0.1 ppm, however accuracy falls to ~30-50% for analyses <1.0 mg/kg.

Site#/Date	Sample Type	Ca	Mg	Si	K	Na	Al	Fe	Mn
#1 - 6/25/09	Centrifuge	4.2	2.4	0.4	0.4	0.1	0.7	0.3	<0.1
“	“	$1.05x10^{-4}$	$9.87x10^{-5}$	$1.42x10^{-5}$	$1.02x10^{-5}$	$4.35x10^{-6}$	$2.59x10^{-5}$	$5.37x10^{-6}$	$<4.3x10^{-6}$
#1 - 8/29/10	+0.45 µm filter particles	2.7	0.5	2.1	1.1	0.4	1.3	0.8	<0.1
“	“	$6.74x10^{-5}$	$2.06x10^{-5}$	$7.48x10^{-5}$	$2.81x10^{-5}$	$1.74x10^{-5}$	$4.82x10^{-5}$	$1.43x10^{-5}$	$<4.3x10^{-6}$
#1 - 8/29/10	-0.45 + 0.22µm filter particles	1.3	0.8	7.2	1.4	0.7	3.4	2.1	<0.1
“	“	$3.24x10^{-5}$	$3.29x10^{-5}$	$2.56x10^{-4}$	$3.58x10^{-5}$	$3.04x10^{-5}$	$1.26x10^{-4}$	$3.76x10^{-5}$	$<4.3x10^{-6}$
#1 – 4/13/12	Particles +0.02 µm filter, 0 hr.	0.03	0.01	0.07	0.01	<0.01	0.05	0.03	<0.01
“		$7.49x10^{-7}$	$4.11x10^{-7}$	$2.49x10^{-6}$	$2.56x10^{-7}$	$-4.35x10^{-7}$	$1.85\ x10^{-6}$	$5.37x10^{-7}$	$<4.35x10^{-7}$
#1 – 4/13/12	Particles +0.02 µm filter, 12 hr.	0.21	0.03	0.15	0.02	<0.01	0.04	0.03	<0.01
“		$5.24x10^{-6}$	$1.23x10^{-7}$	$5.34x10^{-6}$	$5.12x10^{-7}$	$-4.35x10^{-7}$	$1.48\ x10^{-6}$	$5.37x10^{-7}$	$<4.35x10^{-7}$
#1 – 4/13/12	Particles + 0.02 µm filter, 36 hr.	1.36	0.56	0.19	0.10	<0.01	0.03	0.01	<0.01
“		$3.39\ x10^{-5}$	$2.30x10^{-5}$	$6.76x10^{-6}$	$2.56x10^{-6}$	$-4.35x10^{-7}$	$1.11\ x10^{-6}$	$1.79x10^{-7}$	$<4.35x10^{-7}$

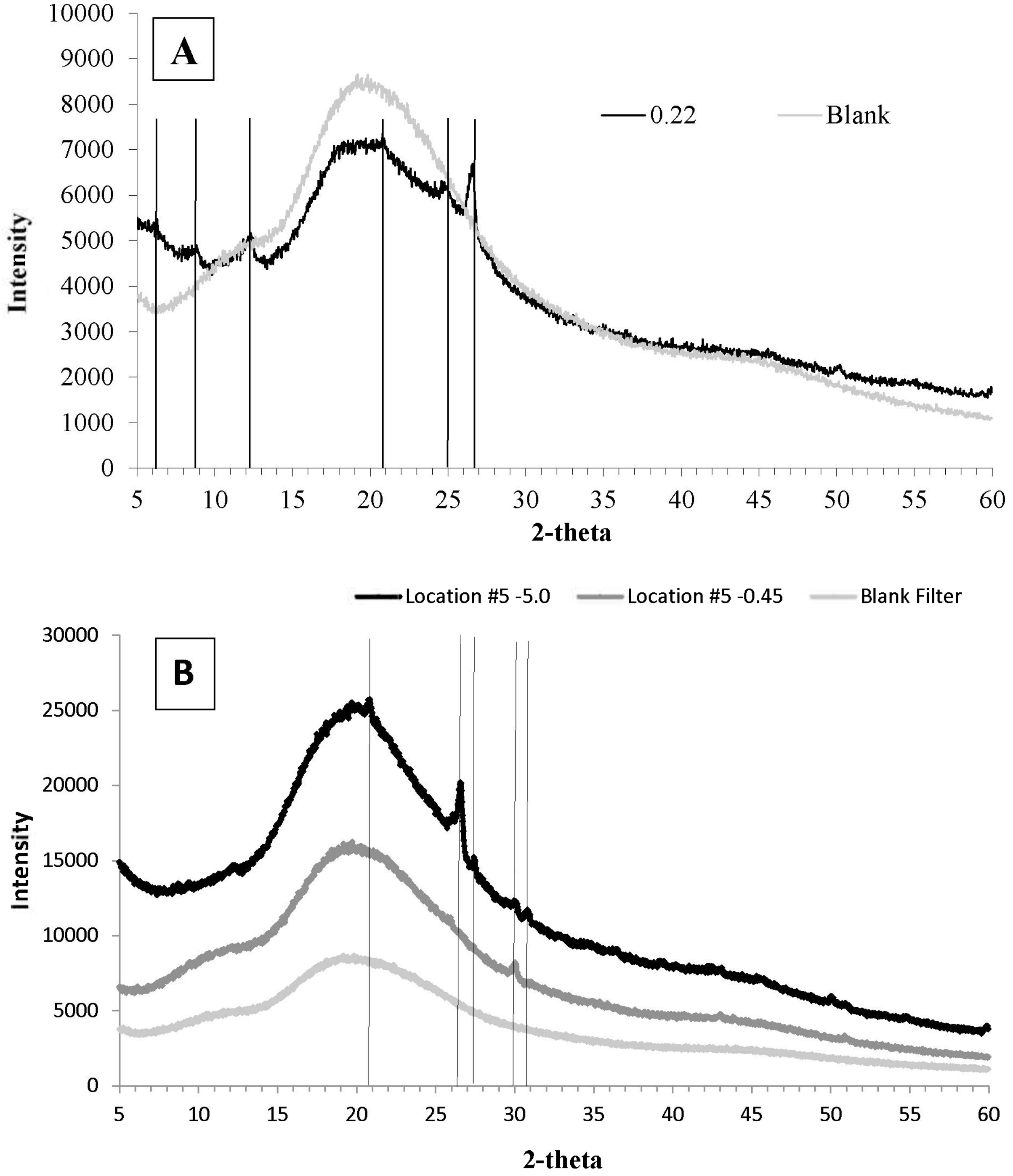

Figure 11. (A) XRD diffraction spectra for particulate material collected on a 0.22 µm filter from sampling location #1 on 8/29/2010. Minor peaks are marked at 2θ angles of 6.3°, 8.8°, 12.4°, 20.8°, 24.8°, and 26.6°. (B) XRD spectra for particulate material collected from sampling location #5 on a both a 5.0 and 0.45 µm filter on 11/12/2010. Peaks are marked at 2θ angles of 20.8°, 26.6°, 27.5°, 29.9°, and 30.9°. "Blank" in both figures refers to XRD spectra collected from an unused filter.

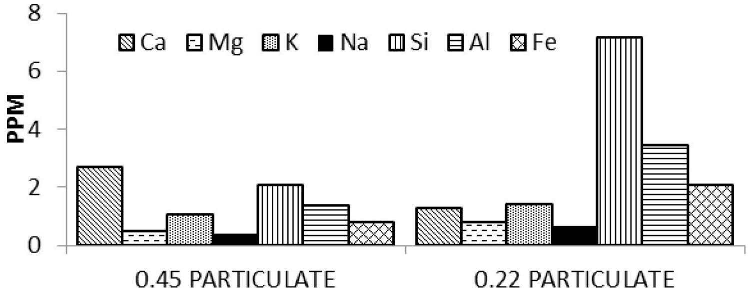

Figure 12. ICP-OES analysis of the nitric acid digestion of particulate material collected on the 0.45 µm and 0.22 µm cellulose filters at sampling location #1 on 10/6/2010. Note the varying composition between the two filter sizes.

3 DISCUSSION

3.1 Genesis of Carbonate Colloids Within the Maramec Spring System

Physical and chemical changes occurring in the Maramec Spring system as water upwells from the subsurface result in the precipitation of colloidal particles that impart a characteristic milky blue-white color to the water. The rhombohedral morphology of the crystals, white color, reaction with a 5% HCl solution. Digestion of centrifuge collected crystals and analysis by ICP-OES indicates a Mg calcite composition with a Ca: Mg ratio of 92 to 8 mole %. The 92:8 molar ration of Ca to Mg is considerably different from the Maramec Spring water from which the crystals precipitated, the latter of which has a 50:50 molar ratio and thus is reflective of the composition of the Gasconade and Eminence Formation dolomites through which the spring conduit is known to transgress (Vandike, 1996). SEM-EDS analyses of the 5.0 µm and 0.45 µm filters from sampling locations #5 and #8 (11/12/2010), and centrifuged samples from location #1 (9/21/2007) also provide evidence for a rhombohedral calcite phase with approximately 5 mole% Mg. The calcite appeared to be the dominant material in the centrifuged samples, but was less abundant in the vacuum filtered samples. Calcite was not detected on the filters from the vacuum filtered samples from location #1 on 10/6/2010.

Vacuum filters used to process Maramec Spring water were analyzed by XRD analysis. The most ubiquitous peak generated in the XRD spectra was that occurring at ~29.9° 2Θ position. This peak occurred in 11 of the 12 filter samples collected on 11/12/2010, but was not detected on the 8/29/2010 sample. The 29.9° 2Θ peak correlates with Mg calcite, which is also supported by the presence of Mg in the dissolved centrifuge particles (Figure 8; Table 3). The 29.9° calcite peaks were larger for samples collected from locations #5 and #8, relative to location #1. A size distribution analysis also indicates the calcite peaks were most prominent on the 0.45 µm filters, always present on the 5.0 and 0.22 µm filters, present on the 0.05 µm filter only at location #1, but absent in the 0.05 µm filters at locations #5 and #8. All of these patterns are consistent with the colloidal particles progressively growing to larger dimensions in a downstream and being dominated by particles with diameters between 5.0 and 0.45 µm.

Carbonate minerals are often identified from their (104) diffraction peak angle during XRD analysis as this is the most prominent peak generated in a random oriented specimen. The (104) peak is located at a 2Θ position of ~29.4° for pure calcite, but the peak position progressively shifts to higher and higher 2Θ angles (smaller and smaller interplanar atomic distances, or d-spacings) as smaller radii Mg ions substitute for Ca into the calcite crystal structure (i.e. lattice distortion). The relationship between Mg content and d-spacing is linear at least for lower Mg content calcites and thus the diffraction peak position can be used to estimate Mg content (Goldsmith and Graf 1958; Goldsmith et al., 1961). The (104) diffraction peaks were evaluated for eight filter samples with large enough peaks to be positioned accurately. These ranged from 29.89 to 30.01° 2Θ, with an average peak position at 29.92°. These diffraction angles correlate to d_{104} spacings with a range from 2.990 to 2.978Å, and an average of 2.986Å. The d_{104} spacings, in turn, correlate to Mg contents ranging from 14 to 18, and averaging 15.7 mole%. The extrapolated XRD Mg contents were roughly double the 8 mole % Mg value determined from the ICP-OES analysis of the acid digested centrifuge particles and triple the ~5 mole Mg % determined by SEM/EDS analysis. The SEM/EDS analyses determinations are the least accurate of the three methods and will not be discussed further. The XRD method is usually preferred over the digestion and chemical analysis procedure as the former procedure allows for the determination of Mg concentrations for only the calcite phase, as these can be distinguished from the interference caused by other Mg phases by their diffraction angles (Ries, 2011). However, the digestion procedure used here determined a Ca:Mg ratio that was lower than the XRD procedure, not higher, thus any interference contributions from the digestion of other Mg-bearing phases does not appear to be an issue. The cause for the difference in compositional determinations by the two methods has thus not been resolved. Possibilities for the discrepancy include contaminants other than Mg contributing to the smaller d-spacing in the calcite structure, the small crystal size and or rapid precipitation rates of calcite leading to distorted d-spacings that resemble Mg-calcite, and/or Mg-contents in calcite vary over time due to the dynamic nature of the Maramec Spring system (the centrifuged and filtered samples were collected on different dates).

The presence or absence of carbonate minerals other than calcite in the Maramec Spring system is difficult to discern due to low XRD peak heights and/or overlapping peak positions with other mineral phases. Small peaks for dolomite were detected at ~30.9° and possibly 50.8° 2Θ in the 5.0 µm filter from location #5 (Figure 11c) and the 0.45µm filter from location #8. The dolomite was likely derived as small colloidal particles eroded from the walls of the Gasconade and Eminence Formations that make up the cave system. Vaterite and aragonite are two polymorphous compounds with calcite. Although vaterite is rarely preserved in the geological record, it often is encountered as a transient phase during incipient carbonate mineralization (Lakshtanov and Stipp, 2010). Aragonite is often encountered in marine, hydrothermal and cave systems often coprecipitating with Mg-calcite. Several of the more prominent XRD peaks for both of these carbonate minerals overlap with peaks for kaolinite and quartz (both of which are present). For example, the three most prominent XRD peaks for vaterite occur at 24.8°, 27°, and 32.8° 2Θ. The first two overlap with peaks for kaolinite and quartz, respectively, while the third matches with the major peak for anglesite ($PbSO_4$) as discussed in the next section. Thus we were unable to determine if vaterite, or anglesite, or both were present in the system by XRD analysis. No crystals with morphologies resembling the common forms of vaterite (rosettes or platelets) or aragonite (acicular needles) were noted during SEM analysis making their presence in the system unlikely.

The available evidence suggests that the colloidal calcite is precipitating in the spring water rather than being derived from the cave walls as weathering detritus. This evidence includes the Ca-rich ($Ca_{92}Mg_{08}$) composition of the colloidal particles, rather than the dolomite composition ($Ca_{50}Mg_{50}$) which is the dominant mineral in the Gasconade and Eminence Formations. The well-formed euhedral shaped crystals with sharp edges and corners (Figure 8) also favors a colloidal precipitation mechanism rather a weathering residue because the sharp edges and corners would tend to be physically abraded due to impact collisions during transport and dissolution pits common in many weathered calcite samples are absent on the faces of the colloidal calcite.

The precipitation rate of colloidal crystals as the water ascends within the dark cave passage favors a non-biogenic origin for carbonate crystal formation. The absence of sunlight in the deeper passages where mineralization must first appear would exclude any photosynthetic communities from participating in the mineralization process and the low total sulfur content of the water (4.4 mg/kg) would similarly limit the participation of sulfate reducing microbial communities. Any motile microorganism community would also be constantly be flushed upwards and out of the cave by the highly energetic water flow and the cave wall surfaces in the deeper portions of the cave do not harbor any large-scale biologic communities capable of precipitating minerals at any significant scale that would account for the turbidity of the spring water at the site of upwelling. Our interpretation of a non-biogenic origin for the colloids does not exclude biomineralization processes occurring once the water reaches the surface pool. Maramec Spring harbors a rich community of aquatic plants that may utilize carbonate or silica crystals as a tensile strength skeletal material. We have also detected diatoms as members of the microscopic community living in the pool water (Figure 10f).

Multiple factors that can influence calcium carbonate precipitation have been proposed. Wilson (1975) described eight environmental factors that can encourage the precipitation of $CaCO_3$. They are: an increase in temperature, increased evaporation, influx of Ca supersaturated water to $CaCO_3$ nucleation sites, upwelling from higher pressure to lower pressure regions, mixing of waters with high $[CO_3^{-2}]$ and low $[Ca^{+2}]$ with sea water, organic processes, bacterial decay producing ammonia, rising pH with an associated increased carbonate concentration, and CO_2 - removal via photosynthetic processes. Available evidence suggests that the Maramec Spring system experiences three of these factors: upwelling from higher pressure to lower pressure region, rising pH with an associated increased carbonate concentration, and CO_2 removal (although by a physical process rather than by photosynthesis). Theoretically, as the spring water upwells from depth within the conduit there will be a decrease in pressure. This pressure decrease would effectively reduce confining pressure holding CO_2 in solution and allow its escape from the water into a gaseous phase that is released into the atmosphere. Measurements collected *in situ* at Maramec Spring and Stream system support this hypothesis in the CO_2 flux measurements that show that CO_2 being degassed at the point of upwelling at Maramec Spring and continuing but at decreasing flux rates downstream (Figure 5).

A chemical reaction depicting the precipitation of a $CaCO_3$ mineral in association with CO_2 loss from an aqueous system is depicted in reaction (1) (Langmuir, 1997).

$$CaCO_3 + CO_2(g)\uparrow + H_2O \leftrightarrow Ca^{+2} + 2HCO_3^- \qquad (1)$$

Reaction equation (1) is a cumulative equation that may more accurately be expressed as a series of three consecutive reactions (2-4) that are linked by the common species $CO_{2(aq)}$ and H^+; and Le Chatelier's Principle.

$$CO_{2(g)}\uparrow \leftrightarrow CO_{2(aq)} \qquad (2)$$
$$H_2O + CO_{2(aq)} \leftrightarrow H^+ + HCO_3^- \qquad (3)$$
$$CaCO_3 + H^+ \leftrightarrow Ca^{+2} + HCO_3^- \qquad (4)$$

$$CaCO_3 \leftrightarrow Ca^{+2} + CO_3^{2-} \qquad (5)$$

With the chemical reactions depicted in equation (2), the process of $CO_{2(g)}$ loss from a system would be reflected in the reaction to be driven from right to left. The $CO_{2(aq)}$ loss from reaction (2) may be balanced by reaction (3) also moving from right-to-left. The net result of the shifts in equations (2) and (3) are the transfer and release of CO_2 aqueous to CO_2 gas phase, and the consumption of H^+ ions (pH increase) and bicarbonate. Both the evolution of CO_2 gas and a pH increase are consistent with the changes observed in the Maramec system as water moves in a downstream direction. The consumption of H^+ ions in equation (3) also will drive the reaction depicted in equation (4) from right to left, resulting in the precipitation of a $CaCO_3$ solid and consumption of Ca^{2+} and an additional bicarbonate ion.

Theoretically, if all these reactions all proceed at the same rate, then there would be no measured change in pH (i.e. reaction (3) balances reaction (4)) and one mole of $CaCO_3$ would be precipitated for every mole of CO_2 (g) released from the water system once the saturation point had been reached for the solid phase. The reaction depicted in equation (5) could also produce the same net result of $CaCO_3$ precipitation and no pH change. If equation (3) is forced to the left at a faster rate than equation (4), then an increase in solution pH $CaCO_3(s)$ precipitation will occur, and this is observed in the Maramec system. Reaction (4) is also still be linked to $CO_2(g)$ release in equation (2) but not in a 1:1 quantitative fashion. The measured CO_2 flux from the water (Figure 5), pH increase along the Maramec Stream reach (Figure 2), and the milky-white colloidal precipitates in the water system (Figures 1, 8, and 10d) all support a reaction process where reaction equations (2) through (4) proceed from right to left, and reaction (3) proceeds at a faster rate than (4). When the water system is saturated to supersaturated in calcium with respect to calcite, then the degassing of CO_2 from solution depicted in reaction (1) will be the rate limiting step for calcium carbonate precipitation (Lebron and Suarez, 1996, Dreybrodt et al., 1997; Zhang and Grattoni, 1998). Calcium carbonate precipitation may also occur according to reaction (5) when the ion activity of $Ca^{+2} * CO_3^{2-}$ reaches or exceeds the equilibrium solubility product. Reaction (5) does not induce a change in pH, but will be favored by a pH rise, which in turn leads to the transformation of $HCO_3^- \leftrightarrow CO_3^{2-} + H^+$, with the excess proton being consumed in reactions with OH^- ions. Reaction (5) also represents the driving calculation equation for calcite precipitation in the PHREEQC and other equilibrium models.

The observed temperature increase along the Maramec Spring branch during warmer seasonal months, water turbulence as it cascades over small falls and rapids, and photosynthetic activity by aquatic organisms may all contribute to additional CO_2 loss while the water is in entrained within the Maramec Stream system (Figure 4). The abundance of the colloids in the upwelling Maramec Spring water at location #1, however, indicates that the pressure loss and associated chemical changes in the water as it rises up conduit has already induced the chemical changes necessary to cause mineralization by the time the water has reached the surface. The formation of these Mg calcite colloids in the rising conduit water also suggests that mineralization is likely occurring *via* a non-biologic precipitation process as the ultimate causative factor is the pressure decrease during the ascent of the spring water to the surface.

Unlike the pH increase measured along the Maramec Spring and Stream reach, many experimental laboratory studies have observed a pH decrease upon the initial onset of calcium carbonate precipitation (Reddy and Nancollas, 1971; Lakshtanov and Stipp, 2010). This disagreement arises because reactions (3) and (4), while moving right to left, both may influence the solution pH of the system. In reaction (4a), moving right to left, hydrogen ions are produced, thus lowering solution pH. Conversely, in reaction (3) hydrogen ions are consumed and solution pH increases. Calcium carbonate precipitation from supersaturated solutions may cause reaction (4a) to move from right to left temporarily at a faster rate than reaction (3) proceeds. In this case, a temporary pH decrease may occur, but of course cannot continue indefinitely as continued acidification would eventually reverse the process and lead to calcite dissolution. In the case of supersaturated solutions, the reaction depicted in (4a) may also be the rate limiting step. In an attempt to maintain chemical equilibrium reactions (1), (2), and (3) are forced to move to the left in response to reaction (4a). We would also expect calcium carbonate crystallization to occur very rapidly at first (i.e. when reaction (4) is the rate limiting step), and then slow as the solution approaches equilibrium (Kamkha et al., 1989; Dove and Hochella, 1993; Gómez-Morales et al., 1996b; Teng et al., 2000; Dickinson et al., 2002; Lakshtanov and Stipp, 2010).

A comparison of all experimental results suggests that calcium carbonate precipitation in Maramec Spring is induced by CO_2 degassing as the driving mechanism rather than due to $[Ca^{+2}]$ solution increase. Evidence for this conclusion includes the measured CO_2 gas being volatized from the water (Figure 5), pH rise (Figure 2), near constant to slight decrease in $[Ca^{+2}]$ in the downstream direction. The CO_2 degassing results from the pressure decrease that results during the ascent of the spring water to the surface, a depth change that exceeds 58 meters (190 feet). Such a depth change would correlate to a pressure decrease of approximately six atmospheres. The loss in CO_2 induces a step-wise series of reactions starting with a pH rise, which allows the transformation of HCO_3^- to CO_3^{2-}, which allows the solution ion activity product of $Ca^{2+} * CO_3^{2-}$ to theoretically reach the saturation level with respect to calcite, although a $SI \geq 0.0$ could not be calculated based on the measured spring water chemistry and temperature (Section 3.3).

3.2 Non-Carbonate Colloidal Material from Maramec Spring

The colloidal particles collected by vacuum filtration of the Maramec Spring water displayed a much wider variability in mineralogy and chemistry than the particles collected by centrifuging. The particles collected by centrifuge were also slightly larger, though we believe that this is a result of continued growth of the crystals after the samples were removed from the spring system up until the time they were centrifuged and dried on a mounting block (Figure 8). The particulate material collected by sequential filtering universally displayed SEM-EDS spectral peaks for Si and Al. Unfortunately, these two elements were also present in the filter paper and Al-SEM mounting blocks, respectively, The very minute sizes of the vacuum captured particles commonly results in X-ray generation areas during EDS analysis that are larger than the particles themselves. Thus the EDS spectra signals often include overlapping and underlying substrate material along with the sample target. Thus the presence or absence of Si and Al cannot be confirmed nor denied in these particles.

XRD analyses of the vacuum filtered particles commonly revealed the presence of two relatively prominent peaks for quartz at 2θ angles of 20.8°, 26.6°, and a series of subdued peaks occurring at 36.6°, 39.5°, 40.3°, 42.5°, and 50.1° 2θ . The 26.6° peak was often the largest displayed for all minerals identified on the filters (Figure 11). The samples collected on 11/12/2010 displayed large peaks for quartz on the 5.0 μm filters, but none on the smaller filter sizes. Filter papers collected at locations #5 and #8 also displayed a greater abundance of quartz than the samples from location #1. The 8/29/2010 sampling only included a 0.22 μm filter and this also displayed large peaks for quartz. The quartz particle sizes thus appear to be >5 μm as none of the grains were passed onto the smaller filter sizes in the sequential vacuum filtering procedure. The origin of the quartz is unknown but they may be derived as: weathering residue from the dissolution of the Gasconade and Eminence dolomites and thus transported through the underwater cave passages as detritus; soil particles that were washed into the cave and have transgressed the entire cave system; inorganically precipitated quartz from the spring water; phyto-planktonic diatoms, possibly the genus *Navicula* (Figure 10f); and/or silica secreted by the water plants in Maramec pool. A detrital particle origin is favored for these quartz grains as biogenic and low-temperature precipitates of silica are often dominated by amorphous silica with only minor and poorly ordered quartz (Gregg et al., 1977). Thus biogenic recently precipitate silica would to give rise to only broad and low-amplitude XRD peaks for quartz and no distinctive peaks from the amorphous silica.

The XRD spectra for particulate material collected on a 0.22 μm filter on 8/29/2010 revealed peaks at 6.3°, 8.8°, 12.4°, 20.8°, 24.8°, and 26.6° 2Θ (Figure 10a). The 20.8° and 26.6° peaks result from quartz being present. The remaining diffraction peaks at 6.3°, 8.8°, 12.4°, and 24.8° are commonly associated with preferred oriented mounts of phyllosilicate minerals, especially for chlorite (6.3°, 12.6°, 18.9°, 25.2°), illite (8.8°, 17.9°, 26.8°, 36.1°), kaolinite (12.4°, 24.9°, 37.8°, 51.3°), and/or smectite (5.7-7.1°, 11.5-14.3°, 17.4-21-7°, 23.4-28.8°). Peak positions for the smectite clays display a wider range of 2Θ angles due to the substitution of different ions in the interlayer positions in the clay structure and the ability of the smectite to shrink and swell with water loss or gain. The first peak position listed for each of the individual phyllosilicate is usually the strongest (001) reflection, and may be the only peak detected when only minor amounts of a mineral are present. Illite is likely present based on the rather diagnostic 8.8° peak position and its common occurrence in Missouri soils. Peaks for the remaining three phyllosilicates are difficult to distinguish from one another without conducting more advanced XRD treatment runs on heated or ethylene glycol-treated samples. We were not able to capture and isolate enough sample material to perform such analyses. It is likely that the remaining phyllosilicate peaks were generated from kaolinite and smectite. The Gasconade dolomite and other sedimentary sequences in Missouri host economically-viable kaolinite deposits located in paleo-sinkholes and caves (Keller et al., 1954). Some of these deposits are located just a 15 km north (9 miles) from Maramec Spring. The Gasconade likely also contains minor quantities of kaolinite and fine-grained quartz throughout its stratigraphic succession. Most of the kaolinite was ultimately derived from the weathering of feldspar minerals in the Precambrian basement rocks of Missouri during its distant geologic past. By contrast, chlorite is not commonly found in any quantity in Missouri strata.

The size distribution of the clays is also unknown, other than a portion of them are larger than the 0.22 μm filter from which they were captured on 8/29/2010. The phyllosilicate peaks that were detected on the 8/29/2010 XRD scans were relatively prominent (Figure 11a), but were absent to relatively subdued on the filter samples collected on 11/12/2010 samples (Figure 11b and c). This contrasting pattern of the two sampling dates suggests that the suspension of clay minerals in the Maramec system is an episodic event that is induced by rainfall in the recharge area, and even minor increases in flow may induce subtle changes in particle transport dynamics. There was no visual increase in water turbidity or color on 8/29/2010, thus the influx of particles into spring will not be noticed by the casual observer following minor increases in water discharge. Vandike (1996) noted that the spring system discharge at Maramec Spring often increases within four to six hours after the initiation of a heavy rain event, though this flow increase is induced by the pressure head of the newly arrived meteoric water at distal locations and not the influx of new water at the spring opening. It often takes several days for the new meteoric water to arrive at the spring, and the mass center of the water recharge pulse typically reaches the spring 12 to 15 days after the rain event. An increase in water flow had been recorded at the United States Geologic Survey-Cook Station Gauge on the Meramec River nine days before our 8/29/2010 sampling. Cook Station is located only six miles east of the eastern boundary of the Maramec Spring recharge area determined by Vandike (1996), thus any new influx of water at Cook Station is likely to be mirrored by an influx of water into the Maramec Spring recharge area. The increase in water flow at Cook Station was first recorded at 10:15 CDT 8/20/2010 when the water began to rise above its base of 0.71 m^3/sec (25 ft^3/sec; Figure 13). By 16:00 CDT on 8/21/2010 the water flow had more than doubled, cresting at 1.56 m^3/sec (55 ft^3/sec), then receding for the next five days until the original 0.71 m^3/sec was reached. It is likely that Maramec Spring was experiencing a period of increased water discharge and associated turbulence on 8/29/2010 that was a result of the same 8/20 to 8/21/2010 water influx event at Cook Station if the mass center recharge travel time for Maramec Spring requires 12 to 15 days (Vandike, 1996). This period of increased flow may have been enough to erode small amounts of clay sediment from the cave floors and walls, or transport surface soil derived clays through the entire cave system from their point of surficial water influx in the recharge zone, or both.

The 11/12/2010 filtration sampling at Maramec Spring occurred when there was a prolonged period with a constant 0.82 m^3/sec (29 ft^3/sec) and no significant increase in water flow for more than 30 days at the Cook Station gauge. While the XRD peaks for phyllosilicates minerals were subdued for the 11/12/2010 sampling relative to the 8/29/2010 collection, the peaks for quartz were still pronounced for both sampling periods (Compare Figures 11a and c). Thus, the transport behavior of quartz appears to differ from that of the phyllosilicates through the Maramec Spring system. This is good supporting evidence that the clay minerals detected on 8/29/2010 sampling were derived from distal surficial material that was washed into the cave from soils in the recharge area. Clay minerals easily remain suspended in a water column with small amounts of turbulence, while clay minerals already deposited as a sediment layer are more difficult to dislodge due to the strong electrostatic attraction between the individual clay particles. The darker brown colored water produced during very high flow events will likely involve the same surface soil influx, plus cave sediments that may be scoured out by the flood waters. Future sampling of the flood waters may shed further light on the processes affecting transport of solid particles through this cave system.

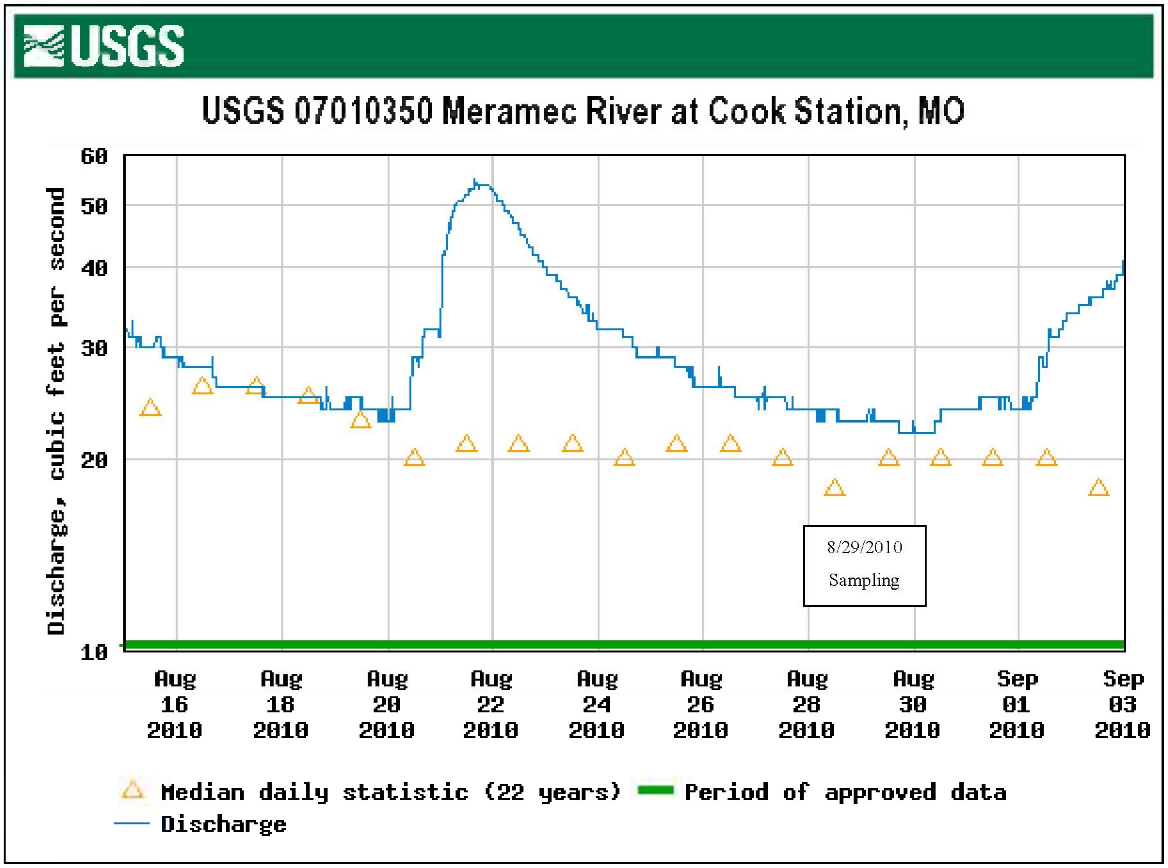

8/29/2010 Sampling

Figure 13. Water discharge in ft^3/second as recorded at Cook Station USGS Gage Station just prior to and after the 8/29/2010 sampling event. A doubling of water flow is noted on August 21-22. Cook Station is located ~10 km (6 miles) east of the eastern boundary of the Maramec Spring recharge area.

Identifying minerals responsible for generating peaks for minor mineral can be difficult when only one major peak is present, or without correlating compositional data generated by SEM-EDS and/or digestion results from the solids. One potential phase matching some of these peaks may be related to the relatively large cubic-rectangular particles (Figure 10c) or clusters of cubic particles (Figure 10e) that revealed a SEM-EDS spectral peak for sulfur and lead. The chemical composition, rectangular morphology (orthorhombic), plus the 27.5° and 33° 2Θ XRD angles are all consistent with these particles being the mineral anglesite ($PbSO_4$). Southern Missouri is host to numerous lead-zinc mineral deposits, thus it is not surprising to find isolated lead minerals disseminated throughout the local geologic strata. Finding these minerals in high enough concentrations to produce an identifiable XRD signal from filtered spring however is a surprising find. Lead as an element has a high electron density, thus a relatively small concentration of lead bearing minerals could be expected to produce a relatively pronounced XRD signal. Positive confirmation of this mineral phase would be provided by the analysis of the unfiltered water samples for lead. The 33° peak also corresponds to one of the three most prominent peaks for the carbonate mineral vaterite (the remaining two most prominent peaks overlap with kaolinite and quartz). Thus vaterite is also a potential phase represented by this XRD spectra, however, we have not been able to find any crystals with a morphological resemblance to vaterite during SEM analysis of the filter and centrifuge particles.

The 9.3° 2Θ angle would correlate with a larger d-spacing resembling the dimensions of the (001) spacing on a phyllosilicate mineral, however, no specific phyllosilicate matches this exact peak position. The large diffraction spacing may also correlate to an unknown organic substance.

One remaining minor XRD peak at a 2Θ position of 25.7° remains unidentified. Both the large and finer particulate grains also displayed peaks for Si and Al during SEM-EDS analysis with a small peak for Fe. These possibly represent Fe-rich clays, however the Si and Al signals may also be derived from the filter paper and Al-SEM block, in which case the Fe may be the result of the presence of iron oxides, hydroxides, and/or oxyhydroxides.

3.3 Geochemical Modeling of the Maramec Spring System Water

Calcium carbonate precipitation is attributed to binding between Ca^{+2} and CO_3^- ion, resulting in amorphous calcium carbonate clusters which then transform into crystalline calcite (Gebaur et al., 2008). Despite the confirmed presence of colloidal calcite in the Maramec Spring water, we have not been able to successively run a computer model using the water composition that also correlates with the observed mineral formation. Model runs using the PHREEQC-Version 3 were used to calculate saturation index values ($SI = \log [(a\mathrm{Ca} * a\mathrm{CO_3}^{-2})/K_{sp})]$ for calcite, aragonite, dolomite, quartz, chalcedony (fine needle quartz), and amorphous silica ($SiO_{2(am)}$). Input data parameters used in the modal run are shown in Tables 1, 2, and 4, while the calculated SI values determined by the model are also shown in Table 4. The PHREEQC code calculates a SI value of -0.86 and -0.41 for calcite at locations #1 and #4, respectively ($SI < 0.0$ indicates undersaturated conditions). The model also indicates that undersaturated conditions exist for aragonite and dolomite, with dolomite undersaturation of course being a requirement to maintain the opening of the cave-water conduit passage. The model also predicts saturation with respect to quartz for location #1 water ($SI = 0.0$), a slight undersaturation at location #4 ($SI = -0.02$), and undersaturated conditions for chalcedony and amorphous silica for all water samples. Quartz has been identified in the XRD analyses of the particles collected in the filters (Figure 11a).

Although the PHREEQC code *calculates* undersaturated conditions for calcite in the Maramec system water, the calculations also demonstrate that the changing conditions moving from location #1 to #4 are also causing changes in the solution that move it closer to the saturation point. Thus we can assume that if we are at saturation at location #1, which we must be as calcite has been recovered there, then the changes in water chemistry moving from location #1 to #4 will also to continue to promote the precipitation of additional calcite. Furthermore, if the changes in water chemistry occurring from location #1 to #4 are the same as those occurring during the ascent of water from the subsurface to the spring outlet at location #1, then the water ascent will also be inducing chemical changes that promote calcite precipitation.

We conducted a sensitivity analysis of the various water parameters that may be responsible for inducing calcite mineralization by alternately changing one of the key water chemistry parameters to achieve a calculated SI = 0.0 in the PHREEQC model, while alternatively holding all other parameters constant at their measured values in water samples:

Temperature: Calcite solubility is inversely proportional to temperature, thus an increase in temperature will lower the K_{sp} for calcite, potentially inducing crystal formation. The solution temperature also has an influence on two additional parameters that are worth reviewing as they can also then influence the solubility of carbonate minerals. 1) Increasing temperature will lower the solubility of the $CO_2(aq)$ phase, leading to CO_2 volatilization, and potential rise in pH that can promote mineralization. 2) An increase in temperature will also increase the CO_3^{2-} / HCO^{3-} alkalinity ratio, also a factor in promoting calcite formation. According to our sensitivity analysis model, however, an unrealistically high temperature increase to 82°C would be required to change the SI = 0.0 for calcite at location #1 (optimized parameter Temp-1 in Table 4). And at this temperature dolomite would be the solubility limiting phase with a SI = +0.16. Furthermore, the great mass of the surrounding rock material will insulate against temperature changes thus the system can be considered as nearly isothermal. Our temperature measurements at site #1 averaged 13.6 ± 0.6°C for recordings made during the spring, summer and fall months indicating a relatively constant temperature for the discharged water at the spring site.

Small increases in water temperature are noted as the Maramec Stream water moves downstream from location #1 to location #8 over a distance of 1360 meters. This temperature increase typically is in the range of 0.5 to 1.0°C during the warmer summer months. A sensitivity analysis conducted using the PHREEQC code with location #1 water rising from 14.1 to 15.1°C would result in only a minute SI change from -0.86 to -0.85. The corresponding changes in the activities of dissolved aqueous CO_2 species with this one degree temperature increase would be: CO_3^{2-} increase from 8.367×10^{-7} to 8.585×10^{-7} molal; HCO_3^- decrease from 2.638×10^{-3} to 2.637×10^{-3} molal; and $CO_{2(aq)}$ decrease from 8.081×10^{-4} to 7.927×10^{-4} molal. Thus an increase in temperature as water moves downstream in the Maramec Stream system during the warmer season months would induce several changes in the water composition, though small, would all favor continued carbonate mineralization.

Table 4. Results of PHREEQC Modeling of Maramec Spring and Stream Water Runs. The saturation index for calcite would be calculated as (SI = log [(aCa*$a$$CO_3^{-2}$)/$K_{sp}$]), where precipitation should occur when SI ≥ 0.0. The model uses K_{sp} values at 287 K and one atmosphere for: calcite $10^{-8.43}$, aragonite $10^{-8.27}$, dolomite $10^{-16.83}$, quartz $10^{-4.15}$, chalcedony $10^{-3.68}$, and amorphous silica $10^{-2.80}$. The "Optimized Parameter" row refers to changes adjusted on the water chemistry to force a SI = 0.0 for calcite. Optimized parameters used in the sensitivity analysis are shaded in the data columns.

Optimized Parameter	None-1	None-4	Temp-1	Ca-1	Alkalinity-1a	Alkalinity-1b	pH-1	pH-4
Sampling Date	8/29/10	8/29/10	8/29/10	8/29/10	8/29/10	8/29/10	8/29/10	8/29/10
Location	#1	#4	#1	#1	#1	#1	#1	#4
Ca mg/kg	34.0	31.9	34.0	340	34.0	34.0	34.0	31.9
Mg mg/kg	19.9	19.5	19.9	19.9	19.9	19.9	19.9	19.5
$SiO_{2(aq)}$ mg/kg	4.3	4.2	4.3	4.3	4.3	4.3	4.3	4.2
alkalinity meq/L	144	149	144	144	186	1600	144	149
pH	6.94	7.40	6.94	6.94	6.94	6.94	7.81	7.81
Temperature °C	14.1	14.5	82	14.1	14.1	14.1	14.1	14.5
SI calcite	-0.86	-0.41	0.00	0.00	-0.76	0.00	0.00	0.00
SI aragonite	-1.01	-0.56	-0.11	-0.15	-0.92	-0.15	-0.15	-0.15
SI dolomite	-1.76	-0.83	+0.16	-1.04	-1.57	-0.05	-0.03	-0.02
SI quartz	0.00	-0.02	-0.87	0.00	0.00	0.00	0.00	-0.02
SI chalcedony	-0.46	-0.48	-1.15	-0.46	-0.46	-0.46	-0.46	-0.48
SI amorphous silica	-1.34	-1.35	-1.83	-1.34	-1.34	-1.34	-1.34	-1.36

Alkalinity: Alkalinity attributed to CO_3^{2-}, has an important role in controlling the solubility carbonate minerals. We considered the possibility that alkalinity contents were higher in the subsurface waters relative to the measured surface water composition, and/or alkalinity loss was significant in the collected surface waters due to CO_2 loss before they could be analyzed (even though the alkalinity measurements were given a high priority in field sampling and were completed within 15 to 30 minutes of sample collection). It is important to note here that the Maramec Spring water was clearly not at equilibrium and it was exhibiting a loss of CO_2 and an associated pH rise as solutions were moving downstream (Figures 3 and 4), and in spring water solutions collected and held in a vessel (pH change from 7.04 to 7.71 over 40 hours). An estimate potential instability of the solutions resulting from CO_2 loss can be made by comparing the charge equivalence balance of the water. This calculation for location #1 reveals a total cation charge excess over anion charge by 0.772 x 10^{-3} charge equivalents (molal concentration * ionic charge). If the missing 0.772 x 10^{-3} negative charge equivalent is added back the measured alkalinity as bicarbonate, then the corrected alkalinity value would be increased from 2.878 x 10^{-3} m to 3.650 x 10^{-3} m, or 144 to 183 meq/L. Using this higher alkalinity value for the Maramec Spring water in the PHREEQC calculation still predicts an undersaturated solution with respect to calcite (SI = -0.76; optimized parameter alkalinity-1a in Table 4).

Our alkalinity determinations were also conducted using the colorimetric titration method and may not be as accurate as the potentiometric titrations using a Gran end point determination (Anderson, 2002). Our measured range in alkalinities was 131 to 149 meq/L for three locations measured on 8/29/2010 and were represented by bicarbonate alkalinity (Table 2). Our values were also similar to the average value of 149 ± 35 meq/L (range 101 to 215 meq/L) recorded by the USGS between 1993 and 1995 (Vandike (1996). According to our sensitivity analysis calculations, an increase in alkalinity to ~1600 meq/L would be required to saturate with respect to calcite, or an increase of more than 10-fold of what we currently are seeing in the Maramec Spring water (optimized parameter alkalinity-1b in Table 4).

<u>Calcium activity:</u> The presence of Ca and similar alkaline earth cations is a controlling factor in determining the saturation state with respect to calcite. We determined a Ca^{2+} concentration for the Maramec Spring of 34.0 and 31.9 for unfiltered water at locations #1 and #4 and our measured values were slightly higher than the 1993-1995 USGS data (average 27.8 ± 4.4 mg/kg). Our sensitivity analysis study indicates that the PHREEQC calculations will require a Ca concentration increase to 340 mg/kg, or a 10-fold increase in Ca to achieve calcite saturation while holding all other parameters constant (optimized parameter Ca-1 in Table 4).

<u>Solution pH:</u> The pH value may be the most important parameter controlling carbonate speciation and calcite saturation at the conditions of the Maramec Spring system. These waters certainly contains a high enough Ca^{2+} ion activity and enough total alkalinity to be saturated with respect to calcite, the only issue that prevents the PHREEQC code from determining a SI ≥ 0.0 results from the neutral to mildly alkaline conditions that in turn produce a molar CO_3^{2-}/HCO_3^- activity ratio that is too low to produce saturated conditions for calcite. A pH increase will have an indirect but important effect of converting HCO_3^- into CO_3^{2-}. The CO_3^{2-}/HCO_3^- ratio calculated for the water composition at location #1 was 8.367 x 10^{-7}/2.368 x 10^{-3}, thus CO_3^{2-} comprises only 0.0317% of the total of the two species at a pH 6.94, and the SI at this point equals -0.86. The corresponding values at location #4 are 2.518 x 10^{-6}/2.724 x 10^{-3}, with CO_3^{2-} comprising 0.0924% of the total of the two species at a pH 7.40, and the SI at this point equaling -0.41. Holding the alkalinity and Ca values constant for both locations, but raising the pH to 7.81, results in a change in the alkalinity species molar ratio to 6.427 x 10^{-6}/2.705 x 10^{-3}. The CO_3^{2-} carbonate ion now makes up 0.2370% of the total, and the SI = 0.0 at both locations #1 and #4 (optimized parameters pH-1 and pH-4 in Table 4). A pH value of 7.50 had been recorded at location #8 on 10/4/2007, and this was the highest Maramec water value measured.

Two additional factors affecting the saturation point are worth consideration, but we have yet to quantitatively evaluate their influence at this point. Both of these factors would produce a more soluble calcite phase and thus make the Maramec system fall to even lower SI values that it presently does in the PHREEQC model. The first factor relates to the Mg content of the calcite grains (~8 mole % Mg as detected by digestion and solution analysis of centrifuge collected solids and ~16 mole% as determined by a shift in the calcite d_{104} spacing). Increased Mg content should produce a calcite phase that has a higher soluble than a relatively low-Mg calcite phase (Morse et al., 2006; Ries, 2011), thus an even a higher ion activity product ($a\mathrm{Ca}^{2+}$ * $a\mathrm{CO}_3^{2-}$) should be required to attain saturation state. The second feature of the colloids grains requiring a higher ion activity product relates to the minute size of the colloids. Very fine grained crystalline materials exhibit higher solubility constants than their coarser-grained counterparts due to a higher-proportion of defect-type structural positions located at crystalline corners and edges. These sites are more easily dissolved that ions located at flat crystal faces. Having a higher proportion of surface corners + edges / flat faces thus results in a higher solubility for the colloidal phases.

Fritz and Eady (1985) were able to induce the precipitation of calcite from undersaturated solution with respect to calcites (SI = -0.04 to -0.23) by hydraulically forcing fluids through a Ca-bentonite membrane. Precipitated occurred when the local microenvironment adjacent to the bentonite layer established a layer of ions along the high-pressure side of the clay membrane that was higher than the bulk solution. Eventually the activity of the ions in the microenvironment exceeded the saturation limits for calcite and precipitation occurred. XRD results from this present study indicate that the Maramec Spring water contains the clay minerals kaolinite, illite, and probably smectite (bentonite) clays as well. Kaolinite appears to be the dominant clay mineral present. While clay minerals commonly can concentrate dissolved ions around their charged surfaces, the kaolins are least efficient at this process as they have weakest surface layer charge. The clays suspended in the Maramec Springs water would also only be completely suspended in water, as opposed to the membrane layer geometry used in the Fritz and Eady study, thus it is unlikely that concentration of charged ions would achieve high enough levels to reach a SI = 0 value. None-the-less, it is interesting to think of the potential for the surfaces if the clays to act as nucleation centers to initiate the precipitation of calcite. Dissolution of the centrifuged captured calcite grains revealed the presence of trace amounts of Al, K, Si, and Fe (Table 3) with these elements being the predominant components in many clay minerals.

The participation of HCO_3^- in the mineralization process, rather than strictly CO_3^{2-} as is used in the computer codes, may also be invoked as a potential mechanism that explains the different results between the experimental results that clearly show calcite is being precipitated, and the computer code simulation that that predicts calcite precipitation can't be happening. The hypothesis proposed here is that the carbonate ion (CO_3^{2-}) is the *desired specie* for the reaction and not the *required specie*. Thus, as the pressure decreases in conjunction with the fluid ascent in the spring conduit, both the carbonate and bicarbonate species (HCO_3^-) are becoming involved in the precipitation reaction. The negatively charged HCO_3^- should be attracted to the Ca^{2+} ions as depicted in reaction equation (4). We do not have any experimental protocol to determine if HCO_3^- can be directly involved in mineral precipitation as depicted, as opposed to CO_3^{2-} (equation 5), but theoretically the HCO_3^- should become involved in calcite precipitation reactions for neutral to mildly alkaline solutions where CO_3^{2-} contents are relatively low (Zilberbrand, 2003) and pH increases are being observed (Morse et al., 2003). Carbon-hydrogen bonding distortions, consistent with the presence of HCO_3^- clusters, have also been detected by NMR spectroscopy within the structure of synthetic, natural biogenic, and abiogenic calcites (Feng et al., 2006).

4 CONCLUSIONS

The physical and chemical changes occurring in the Maramec Spring system water as it rises from the subsurface induces the precipitation of Mg calcite colloidal particles (Ca:Mg molar ratio = 92:8). Precipitation continues as the water moves down the Maramec Stream system. The colloidal particulate material forms as a result of pressure loss (and warming of water in the stream), CO_2 degassing, and an associated rise in solution pH. The pH increase causes a transformation of alkalinity speciation and an increase in the CO_3^{2-}/HCO_3^- ratio. An increase in CO_3^{2-} should eventually increase the ion activity product $Ca^{2+} * CO_3^{2-}$ to a point where saturation is achieved with respect to calcite. Calcite precipitation in the Maramec Spring and Stream system is being achieved, however, at a point where the calculated SI values were between -0.86 and -0.41. The observed calcite precipitation is thus in conflict with the predicted PHREEQC saturation model for the Maramec system. A sensitivity analysis of the modelling parameters indicates that carbonate mineralization is most susceptible to a pH increase. Although a pH rise has been observed in the spring water, it still is not sufficient to reach a SI = 0.0 in the model. Rapid loss of alkalinity components before they could be measured could be responsible for a part of this discrepancy, however the participation of HCO_3^- in the mineralization process, rather than strictly CO_3^{2-} is the most plausible explanation to account for the differences between the precipitation reactions producing calcite and the computer code calculations.

Our discovery of Mg calcite colloids as a precipitated product in the upwelling water of Maramec Spring suggests that the milky blue-white color of the spring water is a result of light reflection or scattering off of the calcite colloids. The presence of silica-bearing minerals such as quartz, illite, kaolinite and possibly smectite clay, as well as a sulfur-lead phase in the spring water was also confirmed by SEM-EDS, XRD, and ICP-OES analysis and these minerals may also contribute to light scattering in the water. Fine grained particles are often associated with light scattering or sorption effects in acidic water systems that produce a bluish-white coloration, but these typically are produced by colloidal silica or sulfur particles (Ohsawa et al., 2002, 2010; Yuuji et al., 2003). The relatively consistent color of the water during all but the highest flood stage events also favors the colloidal calcite being the primary phase responsible for the cloudy discoloration, though the quartz particles commonly encountered may also play a role in the light scattering process. Low solubility detrital particles of clays and quartz most likely are derived as a weathering residue from the dissolution of the Gasconade or Eminence dolomites, or any other carbonate rock or derivative soil that the Maramec Spring aquifer recharge system transgresses through. Deposition and erosion of the detrital particles onto the subaqueous cave conduit floors and walls certainly occurs, with the amount and particle size distribution being dependent on the hydrologic transport properties of the particles (grain diameter, grain shape, density, surface charge), water turbulence, and water flow rate through the cave. These same hydrologic transport properties would of course also influence the rate of resuspension of these particles, and thus the cloudiness of the Maramec Spring pool should vary in accordance to the rate of water flow through the system. The blue-white color and low, but visible turbidity is the normal condition of the spring. The only exceptions are noted under very high water flow rates caused by heavy seasonal rains. These induce a notable increase in turbidity and a change to brown colored water occurs. We believe this latter change is the result of the resuspension of the detrital sediments but we have yet to collect water samples from such a high-discharge stage event to confirm this hypothesis.

Theoretically, the Maramec Spring system could provide some insight on natural systems acting as both CO_2 sources and reservoirs. The CO_2 dissolved in Maramec Spring water is being introduced into groundwater system in the recharge portion of the spring system due to the absorption of CO_2 from the atmosphere, soil gases, and the dissolution of the carbonate bedrock that hosts the spring system. This CO_2 is transported though the spring system in solution as $H_2CO_3(aq)$, HCO_3^-, CO_3^{-2}, and $CO_2(aq)$. Some of this CO_2 is then released back into atmosphere as a gas at the point of spring upwelling. This natural system provides a valuable analog into the solution chemistry processes that may influence CO_2 precipitation as carbonate phases following a decrease in pressure. Such reactions may also induce carbonate precipitation reactions in areas where future CO_2 repositories develop leaks along fractures or drill wells. Mineral precipitation can naturally seal these fractures by progressive blockage of the fracture openings. The chemical and physical parameters driving such precipitation occur naturally in response to the decrease in pressure on the fluid as it rises. The carbonate mineralization occurring at Maramec Spring, however, occurs as a colloidal suspension rather than a precipitate on the walls of the spring conduit. The latter process would be required in order for a self-sealing fracture process to occur. The high turbulence of the water during its ascent to the surface certainly may influence this mode of mineral precipitation but we are unaware if other factors may be involved.

The process involving carbonate mineralization at Maramec Spring also provides an analogue to evaluate other natural colloidal carbonate precipitation events such as sudden development of turbulent aqueous white clouds of aragonite needles, or “whiting events” that are observed to occur periodically in carbonate platform settings such as the Red Sea or Bahamas (Robbins et al., 1996; Morse et al., 2003). Various hypotheses for the precipitation mechanisms for the whiting events range from the suspension of bottom sediment by schools of fish, water turbulence that suspends very fine needles that act as nucleation sites for carbonate minerals, or algal blooms that induce mineralization as a consequence of biologic processes. The Maramec Spring system is quite different from an oceanic system: Maramec Spring has a lower salinity, lower Mg/Ca molal ratios, near constant temperature, greater depth and associated pressure decrease associated with upwelling water, and precipitates only calcite as opposed to aragonite dominated-lesser calcite whiting events). Despite their many difference, the Maramec Spring system is still a fresh water whiting event that apparently occurs without any biologic intervention. Although seed crystals have not been found as nucleation centers within the calcite grains, the microscopy investigations of the present study are preliminary and it is possible that higher resolution microscopy investigations may detect such seed crystals in the future. The detection of small amounts of Al, Si, K, and Fe in the digestion fluids produced from the centrifuged calcite particles permits the contribution of clay minerals (illite, kaolinite, smectite), iron oxides or oxy-hydroxides, and/or quartz as nucleation seed material. A study of the water parameters in these different systems may give insight into which chemical or physical parameters leads to colloid particle nucleation in both systems.

All reactions at the Maramec Spring system lends itself as a natural outdoor laboratory to introduce college undergraduate students to both field geochemical analysis techniques and carbonate chemistry. We have taken advantage of this opportunity to introduce 157 students to the spring as a laboratory exercise during the 2010 through 2012 academic years. Students measured and examined the water chemistry and evaluated the importance of the carbonate minerals in the carbon cycle and implications for the sequestration of anthropogenic carbon dioxide.

REFERENCES

Anderson, C.B., 2002, Understanding Carbonate Equilibria By Measuring Alkalinity in Experimental and Natural Systems, *Journal of Geoscience Education*, v. 50, p. 389–403.

Cohen A.L. and McConnaughey T.A., 2003, Geochemical Perspective on Coral Mineralization. Chapter 6, *in*: Biomineralization. Dove PM, Weiner S, deYoreo JJ (eds.) Reviews in Mineralogy and Geochemistry v. 54, pp 151-187.

Dickinson, S.R., Henderson, G.E., and McGrath, K.M., 2002, Controlling the Kinetic versus Thermodynamic Crystallization of Calcium Carbonate, *Journal of Crystal Growth*, v. 244, p. 369–378.

Dove, P.M. and Hochella, M.F., 1993, Calcite Precipitation Mechanisms and Inhibition by Orthophosphate: In Situ Observations by Scanning Force Microscopy, *Geochimica et Cosmochimica Acta*, v. 57, p. 705–714.

Dreybrodt, W., Eisenlohr, L., Madry, B., and Ringer, S., 1997, Precipitation Kinetics of Calcite in the System $CaCO_3$-H_2O-CO_2: The Conversion to CO_2 by the Slow Process of $H^+ + HCO_3^- \rightarrow CO_2 + H_2O$ as a Rate Limiting Step, *Geochimica et Cosmochimica Acta*, v. 61, p. 3897–3904.

Feng, J., Lee, Y.J., Reeder, R.J., and Phillips, B.L., 2006, Observation of Bicarbonate in Calcite by NMR Spectroscopy, *American Mineralogist*, v. 91, p. 957-960.

Fritz, S.J. and Eady, C.D., 1885, Hyperfiltration-Induced Precipitation of Calcite, *Geochimica et Cosmochimica Acta*, v. 49, p. 761–768.

Gebauer, D., Völkel, A., and Cölfen, H., 2008, Stable Pronucleation Calcium Carbonate Clusters, *Science*, v. 322, p. 1819–1822.

Goldsmith, J.R. and Graf, D.L., 1958, Relation Between Lattice Constants and Composition of Ca-Mg Carbonates, *American Mineralogist*, v. 43, p. 84-101.

Goldsmith, J.R., Graf, D.L., and Heard, H.C., 1961, Lattice Constants of the Calcium-Magnesium Carbonates, *American Mineralogist*, v. 46, p. 453-457.

Gómez-Morales, J., Torrent-Burgués, J., López-Marcipe, A., and Rodríguez-Clemente, R., 1996a, Precipitation of Calcium Carbonate from Solutions with Varying Ca^{2+}/carbonate ratios, *Journal of Crystal Growth*, v. 166, p. 1020–1026.

Gómez-Morales, J., Torrent-Burgués, J., and Rodríguez-Clemente, R., 1996b, Nucleation of Calcium Carbonate at Different Initial pH Conditions, *Journal of Crystal Growth*, v. 169, p. 331–338.

Goodarz-nia, I. and Motamedi, M., 1980, Kinetics of Calcium Carbonate Crystallization from Aqueous Solutions, *Journal of Crystal Growth*, v. 48, p. 125–131.

Gregg, J.M., Goldstein, S.T., and Walters, L.J. Jr., 1977, Occurrence of Strained Quartz in the Siliceous Frustules of Cultured Freshwater Diatoms, *Journal of Sedimentary Petrology*, v. 47 p. 1623-1629.

Heydari, E. 2000, Porosity Loss, Fluid Flow, and Mass Transfer in Limestone Reservoirs: Application to the Upper Jurassic Smackover Formation, Mississippi, *American Association of Petroleum Geologists Bulletin*, v. 84, p. 100-118.

Kamkha, M.A., Sibiryakov, P.B., and Bizyaev, V.L, 1989, Effect of pH on the Kinetics of Mass Crystallization of Calcium Carbonate, *Kinetics and Catalysis*, v. 30, p. 62–67.

Keller, W.D., Westcott, J.F., and Bledsoe, A.O., 1954, The Origin of Missouri Fire Clays, *in Second National Conference on Clays and Clay Minerals*, Univ. of Missouri, Columbia, Missouri, Oct. 15-17, 1953, Publication #327, p. 7–46.

Lakshtanov, L.Z. and Stipp, S.L.S., 2010, Interaction Between Dissolved Silica and Calcium Carbonate: 1. Spontaneous Precipitation of Calcium Carbonate in the Presence of Dissolved Silica, *Geochimica et Cosmochimica Acta*, v. 74, p. 2655–2644.

Langmuir, D., 1997, *Aqueous Environmental Geochemistry*, Prentice-Hall, New Jersey, 600 p.

Lebron, I. and Suarez, D.L., 1996, Calcite Nucleation and Precipitation Kinetics As Affected by Dissolved Organic Matter at 25°C and pH > 7.5, *Geochimica et Cosmochimica Acta*, v. 60, p. 2765–2776.

Morse, J.W., Gledhill, D.K., and Millero, F.J., 2003, $CaCO_3$ Precipitation Kinetics in Waters from the Great Bahama Bank: Implications for the Relationship Between Bank Hydrochemistry and Whitings, *Geochimica et Cosmochimica Acta*, v. 67, p. 2819–2826.

Morse, J.W., Andersson, A.J., and Mackenzie, F.T., 2006, Initial Responses of Carbonate-Rich Shelf Sediments to Rising Atmospheric pCO2 and ''Ocean Acidification'': Role of High Mg-calcites, *Geochimica et Cosmochimica Acta*, v. 70, p. 5814–5830.

Nancollas, G.H., 1979, The Growth of Crystals in Solution, *Advances In Colloidal Interface Science*, p. 215–252.

Nancollas, G.H. and Reddy, M.M., 1971, The Crystallization of Calcium Carbonate: II. Calcite Growth Mechanism, *Journal of Colloid and Interface Science*, v. 37, p. 824–830.

Ogino, T., Suzuki, T., and Sawada, K., 1990, The Rate and Mechanism Polymorphic Transformation of Calcium Carbonate in Water, *Journal of Crystal Growth*, v. 100, p. 159–167.

Orndorff, R. C., Weary, D.J., and Harrison, R.W., 2006, The Role of Sandstone in the Development of an Ozark Karst System, South-Central Missouri, *Geological Society of America, Special Paper 404*, p. 31–38.

Ohsawa, S., Kawamura T., Takamatsu, N., and Yusa, Y., 2002, Rayleigh Scattering by Aqueous Colloidal Silica as a Cause for the Blue Color of Hydrothermal Water, *Journal of Volcanology and Geothermal Research*, v. 113, p. 49-60.

Ohsawa, S., Saito, Yoshikawa, S., Mawatari, H., Yamada, M., Amita, K., Takamatsu, N., Sudo, Y., and Kagiyama, T., 2010, Color Change of Lake Water at the Active Crater Lake of Aso Volcano, Yudamari, Japan: Is it in Response to Change in Water Quality Induced by Volcanic Activity?, *Limnology* v. 11, p. 207–215.

PHREEQC Interactive version 3.1.2.8538, United States Geological Survey, D.L. Parkhurst and C.A.J. Appelo, Released March 3rd, 2014.

Reddy, M.M. and Gilliard, W.D., 1981, Kinetics of Calcium Carbonate (Calcite)-Seeded Crystallization: Influence of Solid/Solution Ratio on the Reaction Rate Constant, *Journal of Colloid and Interface Science*, v. 80, p. 171–178.

Reddy, M.M. and Nancollas, G.H., 1971, The Crystallization of Calcium Carbonate I. Isotope Exchange and Kinetics, *Journal of Colloid and Interface Science*, v. 36, p. 166–172.

Reddy, M.M and Nancollas, G.H., 1973, Calcite Crystal Growth Inhibition by Phosphates, *Desalination*, v. 12, p. 61–73.

Reddy, M.M. and Nancollas, G.H., 1976, The Crystallization of Calcium Carbonate: IV. The Effect of Magnesium, Strontium and Sulfate Ions, *Journal of Crystal Growth*, v. 35, p. 33–38.

Ries, J.B., 2011, Skeletal Mineralogy in a High-CO_2 World, *Journal of Experimental Marine Biology and Ecology*, v. 403, p. 54–64.

Robbins, L.L, Yates, K., Shinn, G., and Blackwelder, P. 1996, Whitings on the Great Bahama Bank: A microscopic solution to a macroscopic mystery. *Bahamas Journal of Science* v. 4, p. 2-6.

Rybacki, K.S., 2010, Calcium Carbonate Precipitation Mechanisms and Geochemical Analysis of Particulate Material Found Within the Waters of Maramec Spring, St. James, Missouri. Missouri University of Science and Technology MS Thesis, 47 pages.

Söhnel, O. and Mullin, J.W., 1982, Precipitation of Calcium Carbonate, *Journal of Crystal Growth*, v. 60, p. 239–250.

Swinney, L.D., Stevens, J.D., and Peters, R.W., 1982, Calcium Carbonate Crystallization Kinetics, *Industrial & Engineering Chemistry Fundamentals*, v. 21, p. 31–36.

Teng, H.H., Dove, P.M., and De Yoreo, J.J., 2000, Kinetics of Calcite Growth: Surface Processes and Relationships to Macroscopic Rate Laws, *Geochimica et Cosmochimica Acta*, v. 64, p. 2255–2266.

Thompson, T.L., 1991, *Paleozoic Succession in Missouri, Part 2 – Ordovician System*: Missouri Department of Natural Resources, Division of Geology and Land Survey, Report of Investigations 70, part 2, 292 p.

Unklesbay, A.G. and Vineyard, J.D., 1992, *Missouri Geology: Three Billion Years of Volcanoes, Seas, Sediments, and Erosion*, University of Missouri Press, Columbia, 189 p.

Vandike, J.E., 1985, Hydrogeologic Aspects of the November, 1981 Liquid Fertilizer Pipeline Break on Groundwater in the Maramec Spring Recharge Area, Phelps Country, Missouri, *Missouri Speleology*, v. 25, p. 93–101.

Vandike, J.E., 1996, *The Hydrology of Maramec Spring*, Water Resources Report No. 55, Missouri Department of Natural Resources, Division of Geology and Land Survey, Water Resources Report No. 55, 104 p.

Wicks, C.M. and Hoke, J.A., 2000, Prediction of the Quality and Quantity of Maramec Spring Water, *Groundwater*, v. 38, p. 218–225.

Wilson, J.L., 1975, *Carbonate Facies in Geologic History*, Springer-Verlag, Berlin, 471 pages.

Yuuji, O., Shinji, O., Nobuki, T., 2003, A colorimetric and Geochemical Study of the Coloration Factor of Hyper-Acid Active Crater Lakes, *Japanese Journal of Limnology*, v. 64, p. 1-10.

Zhang, Y. and Grattoni, C.A., 1998, Comment on "Precipitation Kinetics of Calcite in the System $CaCO_3$-H_2O-CO_2: The Conversion to CO_2 by the Slow Process of $H^+ + HCO_3^- \rightarrow CO_2 + H_2O$ as a Rate Limiting Step" by W. Dreybolt, L. Eisenlohr, B. Madry, and S. Ringer, *Geochimica et Cosmochimica Acta,* v. 62, p. 3789–3790.

Zilberbrand, M., 2003, Degassing Water Around Air Bubbles Entrapped in the Vadose Zone as a Mechanism of Carbonate Precipitation – A Hypothesis, *Journal of Sedimentary Research*, v. 73, p. 491-497.

SECTION IV. EVALUATION OF THE MINERAL AND GEOCHEMICAL ATTRIBUTES OF THE MIDCONTINENT RIFT SEQUENCE FOR CARBON SEQUESTRATION

1 INTRODUCTION

1.1 Geologic Sequestration of Carbon Dioxide

Geologic sequestration involves injecting supercritical-phase CO_2 into a deep saline aquifer to prevent its return to the atmosphere. The acidity of the aquifer water will increase as CO_2 is injected and dissolves into the aquifer. Concentrations of dissolved carbon dioxide ($CO_{2(aq)}$) carbonic acid ($H_2CO_{3(aq)}$), bicarbonate (HCO_3^-), and carbonate (CO_3^{2-}) will increase in solution (Berner and Lasaga, 1983), with their relative proportions depending largely on pH, but also on temperature, salinity, and pressure. Dissolution of CO_2 into water and the formation of various aqueous species are controlled by the following equations:

$$CO_2 + H_2O \rightleftharpoons \underset{\textit{carbonic acid}}{H_2CO_{3(aq)}} \qquad (1)$$

$$H_2CO_{3(aq)} \rightleftharpoons H^+ + \underset{\textit{bicarbonate}}{HCO_3^-} \qquad (2)$$

$$HCO^{3-} \rightleftharpoons H^+ + \underset{\textit{carbonate}}{CO_3^{2-}} \qquad (3)$$

Water + rock + CO_2 aqueous specie reactions will occur as the pH of the solution decreases (Berner and Lasaga, 1983; Holland, 1984; Meybeck, 1987). The calcite ($CaCO_3$) cement commonly observed in Midcontinent Rift (MCR) rocks exposed in the Lake Superior region will readily react with the acid in such a scenario. Since this calcite cement is often the major pore filling material, its dissolution will serve to open the primary pore space in the MCR rocks and increase their permeability. This increase will allow the aqueous fluids to permeate further into the surrounding pore spaces and react with silicate and oxide minerals as their surfaces become exposed. Dissolving carbonate minerals to aid in the precipitation of carbonate minerals in the overall concept of carbonate mineralization is of course a zero gain scenario due to the generation of new sources of CO_2 gas. In order to be an effective process, the volume of carbonate minerals dissolved during the dissolution of carbonate cement must be exceeded by the volume of preexisting pore space accessed by the newly opened pores + the volume of new pore space generated by the dissolution of silicate and oxide rock components.

$$H^+ + CaCO_3 \rightleftharpoons Ca^{2+} + H_2CO_{3(aq)} \qquad (4)$$

The dissolution of Ca-, Mg- and ferrous Fe-bearing silicates from the MCR sedimentary and volcanic rocks represent a vast source of Ca^{2+}, Mg^{2+}, and Fe^{2+}, which when combined with the carbonate ion (CO_3^{2-}), may produce a variety of carbonate minerals (Meybeck, 1987; Gunter et al., 1993; Bachu et al., 1994; Giammar et al., 2005). Ferric iron phases such as hematite (Fe_2O_3) are commonly encountered as cement in many subsurface rocks, and these may also be involved in carbonate mineralization reactions if the iron can be reduced to the Fe^{2+} state by reducing agents present in the system. The reactions involving silicate and carbonate minerals will also act neutralize carbonic acid produced in near-field reactions close to the point of CO_2 injection (Figure 1). The pH of the groundwater will increase as a result of these neutralizing reactions with the minerals, with acid protons (H^+) being exchanged with metallic ions (e.g., Na^+, K^+, Ca^{2+}, Mg^{2+}, Fe^{2+}, etc.). These acid neutralizing reactions may promote carbonate mineral formation in far-field settings at locations that are remotely located from the injection point of CO_2, and/or in near-field settings after injection of CO_2 has ceased and long enough time periods have passed to allow acid neutralization. As a result of the pH increase, the solubility of released cations will decrease and mineral precipitation would eventually occur (Giammar et al., 2005; Knauss et al., 2005; Palandri and Kharaka, 2005; Xu et al., 2005). Several of the more common mineral phase reactions are depicted in reactions 5-8:

$$CO_3^{2-} + Ca^{2+} \rightleftharpoons CaCO_3 \qquad \textit{(calcite/aragonite)} \qquad (5)$$

$$CO_3^{2-} + Mg^{2+} \rightleftharpoons MgCO_3 \qquad \text{(magnesite)} \qquad (6)$$

$$2CO_3^{2-} + Ca^{2+}\ Mg^{2+} \rightleftharpoons CaMg(CO_3)_2 \qquad \textit{(dolomite)} \qquad (7)$$

$$CO_3^{2-} + Fe^{2+} \rightleftharpoons FeCO_3 \qquad \textit{(siderite)} \qquad (8)$$

Carbonate ions may precipitate as carbonate minerals as pressure decreases when water moves upwards, much like the processes that occur in hydrothermal systems (Katz et al., 2006). The same mineralization process may occur during a reduced pressurization stage following the cessation of CO_2 injection or as water move upwards through fractures. Experiments conducted on the fractured Ogachi granodiorite in Japan found that a significant amount of Ca^{2+} was dissolved into solution after the injection of supercritical-phase CO_2 at 200°C and 6 MPa (870 psi). After the temperature declined to 100°C, the dissolved carbonate ions began to complex with dissolved alkaline earth elements and precipitate as carbonate minerals (Ueda et al., 2005).

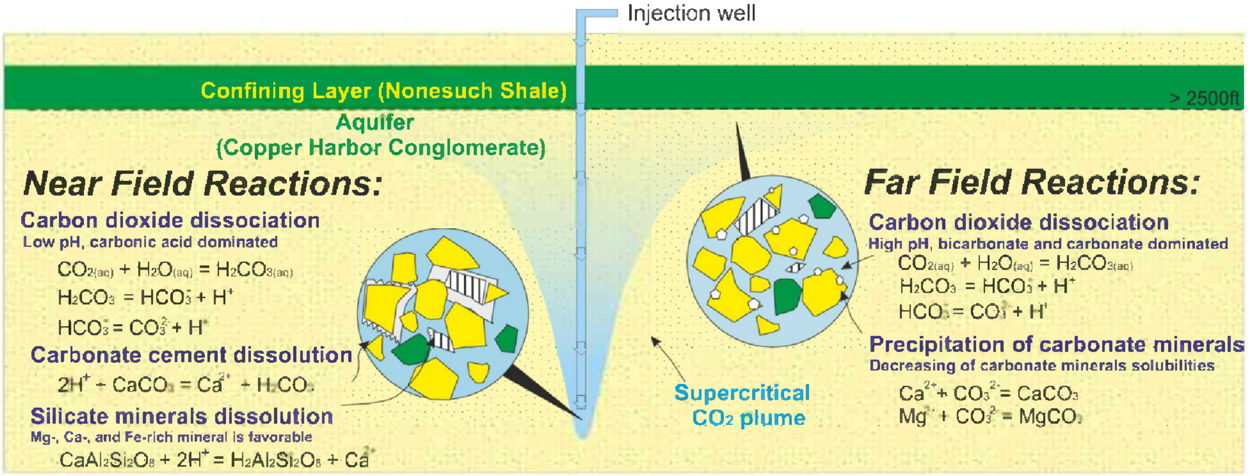

Figure 1. Hypothetical model of CO_2 sequestration in the MCR clastic sediments. This shows the geochemical reactions that could occur at the injection site (near-field reactions) and more distal locations (far-field reactions).

1.2 Structural Elements of the Midcontinent Rift (MCR)

The MCR is a Mesoproterozoic (1115 to 1050 Ma) volcanic and sedimentary rock sequence that has formed within a series of rifted basins across the Midcontinent of North America (Woollard, 1943; Thiel, 1956; King and Zietz, 1971; Behrend et al., 1988; Miller, 2007). Surface exposures of the MCR rocks are encountered only in the region around western Lake Superior while the subsurface configuration can be easily traced below younger covering rocks using both Bouguer gravity and magnetic geophysical surveys (Stein et al., 2011).

The geometry of MCR basins were controlled by regional extensional stresses (Green, 1983; Cannon and Hinze, 1992; Paces and Miller, 1993; and Cannon, 1994). The initial extension phase began as a triple junction at what is now Lake Superior. This extension was associated with a rising mantle plume and crustal thinning. The southwestern MCR arm extends 1300 km from the center of Lake Superior to Kansas. The southeastern arm stretches from Michigan to Ohio, approximately 700 km, and its geophysical signature terminates against the Grenville orogenic front. The Lake Nipigon dike and sill province to the north of Lake Superior represents the third failed arm of the rift triple junction. Dickas and Mudrey (1997) have separated the western and eastern arms into five major zones based upon structural accommodation zones. These are represented in a southwest-to-northeast-to-southeast arcuate direction by the Kansas, Iowa, Superior, Mackinaw, and Maumee Zones, with the first three zones being investigated in the present study (Figure 2). The Kansas Zone is completely buried by Paleozoic and younger sediments and geophysical signatures of subsurface features suggest the presence of a central uplifted horst (the Kansas Horst). The Iowa Zone is also buried by younger sediments and also contains a central uplifted horst (the Iowa Horst). Numerous sedimentary basins can be defined within this Iowa Zone including the Wellsburg, Ankeny, and Shenandoah basins that lie to the southeast of the central horst; the Duncan and Defiance basins that lie to the northwest of central horst, and the Mineola Graben and Stratford basin that are basins developed on top of the central horsts (Anderson, 1990). The Superior Zone is exposed at the surface in the Lake Superior region, while buried sections are also found to the southwest and are subdivided into the St. Croix Horst, Twin City Basin, and Ashland Syncline.

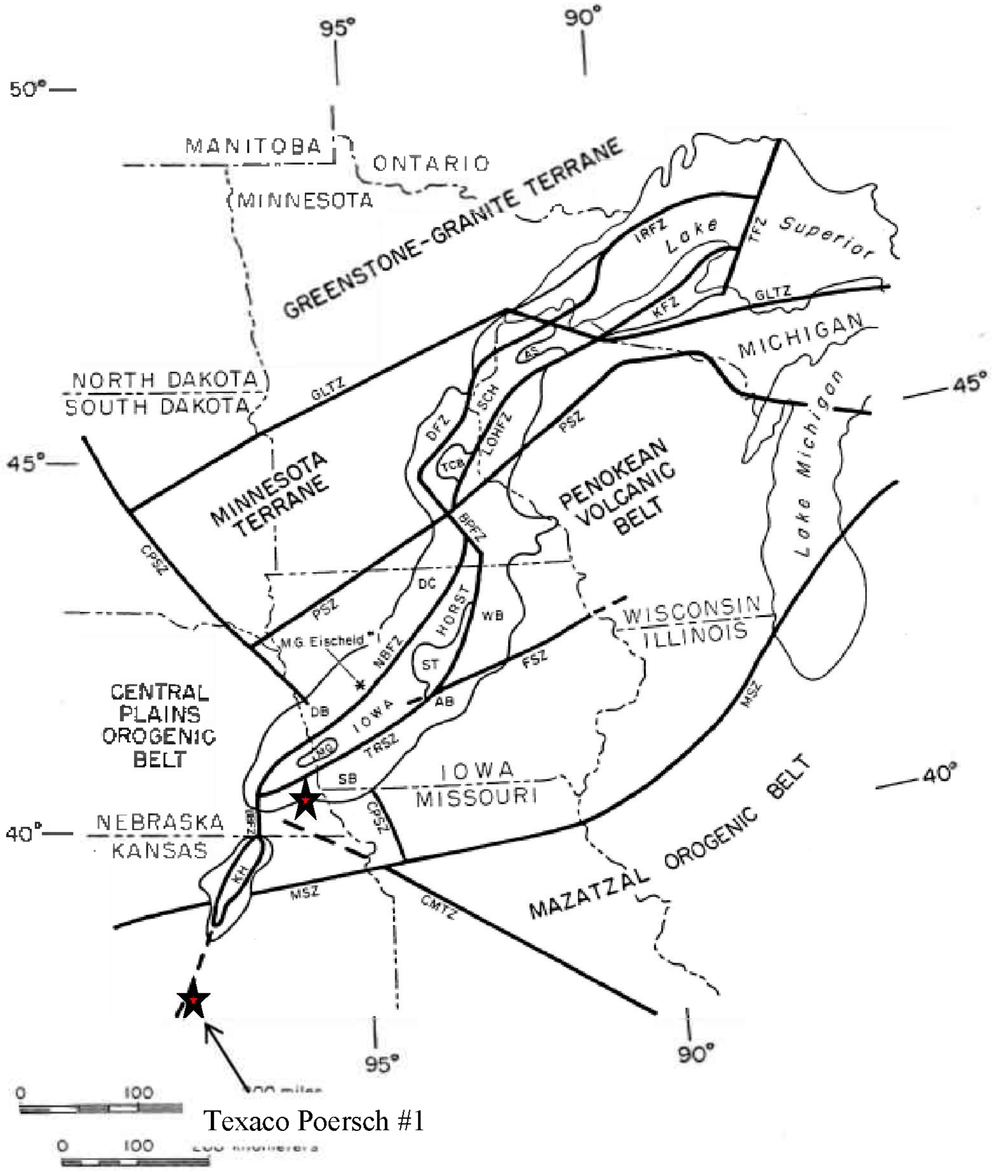

***Figure 2 - Caption on following page.**

Figure 2 (previous page). The main structural elements of the southwestern arm segment of MCR showing three zones from southwest to northeast; the Kansas, Iowa, and Lake Superior Zones, these being separated by the Central Missouri Tectonic Zone (CMTZ), Belle Plaine Fault Zone (BPFZ), and Thiel Fault Zone (TFZ) (Dickas and Mudrey (1997). The Kansas Zone displays a central uplifted Kansas Horst (KH). The Iowa Zone is further divided into the Wellsburg (WB), Ankeny (AB), Shenandoah (SB), Duncan (DC), Defiance (DB), and Stratford Basins (ST), as well as the Mineola Graben (MG) (Anderson, 1990). The southwestern portion of the Superior Zone is subdivided into the St. Croix Horst (SCH), Twin City Basin (TCB), and Ashland Syncline (AS). Additional tectonic features defining basin boundaries include the Isle Royale Fault Zone (IRFZ), Keweenaw Fault Zone (KFZ), Douglas Fault Zone (DFZ), Lake Owen-Hastings Fault Zone (LOHFZ), Northern Boundary Fault Zone (NBFZ), Thurman-Redfield Structural Zone (TRSZ), Big Blue Fault Zone (BBFZ), Great Lakes Tectonic Zone (GLTZ), Central Plains Suture Zone (CPSZ), Penokean Structure Zone (PSZ), Mazatzal Suture Zone (MSZ), and Fayette Structural Zone (FSZ). Drill core locations for the Texaco Poersch #1 Well in Kansas and the M.G. Eischeid #1 Well in Iowa are also marked with star symbols. Modified after Anderson (1990).

1.3 Stratigraphy and Stratigraphic Correlations of the Rift Basins

Thin and discontinuous basal sedimentation intervals accompanied the initiation of rifting and basin subsidence. These sequences were deposited directly on top of pre-MCR basement rocks and are represented by the Nopeming Formation in Minnesota, the Bessemer Quartzite in Wisconsin and other laterally stratigraphic units (Figure 3; Green, 1982a and b). The Nopeming is mature quartz arenite with a basal pebbly horizon that was deposited in a braded river environment (Ojakangas and Morey, 1982). The early sedimentary deposits were covered by a thick sequence of reversed and normal polarity Mesoproterozoic tholeiitic volcanic flows. These filled the central rift axis to form a huge lava plateau that was locally incised and interlayered with minor clastic infilling sediments during volcanically quiet intervals (Green, 1982b). The volcanic sequence, being composed of multiple flow horizons, reach a cumulative thickness of up to 20 kilometers. Increasingly higher proportions of sedimentary rocks began to fill the basin as volcanic activity began to wane and finally cease. The crustal rocks within the rift continued to sag downwards as a result of the weight of the volcanic rock load, emptying of magma chambers from below, and the thermal subsidence associated with hot spot abatement. The generally fining-upward prograding wedge of sediments represented by the Oronto Group was then deposited. These include the basal Copper Harbor Conglomerate (CHC), followed by the lacustrine siltstone-shale deposits of the Nonesuch Formation, and finally the extensive fluvial deposits of the Freda Formation (Anderson, 1990).

Regional tectonic forces changed from extension to compression after the Freda Formation was deposited due to the initiation of the Grenville Orogeny along the eastern seaboard of the paleo-

North American Continent (Cannon, 1994). Previous down-dropped grabens were converted into uplifted horsts in some locations and previously deposited Oronto Group sediments were eroded from the top of these horsts. Fluvial deposits of the Bayfield Group-Jacobsville Formation were deposited at the horst flanks with a higher maturity level than that of the older sequences (Figure 3; Anderson, 1990). Since these latest sediments were reworked from previous deposits, they were produced as chemically mature sediments up to the point where quartz arenite has sometimes formed (Ojakangas and Morey, 1982).

Seismic, magnetic, and gravitational surveys of the MCR sector in Kansas suggest the presence of a thrust fault that tectonically emplaced older volcanic sequences on top of younger sedimentary rocks giving a sense of reverse stratigraphy (Behrend et al., 1988; Woelk and Hinze, 1991). Younger extensional sediments were overlain by the older volcanic rocks, and the younger compressional sediments were overlain by an older extensional sediments (Anderson, 1990). Interpretations of the seismic and the gravitational profiles indicate these thrust faults bound the central horst with an angle between 15° and 75°. The juxtaposition of the normally impermeable-natured early-rift stage extensional rocks on top of the relatively permeable late stage sedimentary rocks could provide a possible sedimentary-structural trap for sequestration of carbon dioxide.

1.3.1 Volcanic Successions

Initial sedimentary deposits were rapidly and progressively overlain by a series of massive volcanic flows composed of four main eruptive episodes (Figure 3; Ojakangas and Morey, 1982; Miller, 2007). The first magmatic stage (1,115 to 1,107 Ma) is reverse magnetic polarized and composed of mafic to ultra-mafic olivine-rich basalts that were directly sourced from a mantle plume, although significant crustal melt contamination had affected the earlier flows from this stage. The second magmatic stage (1,107 to 1,102 Ma) is a period of relatively minimal volcanism that is characterized by normal to reversed polarized magnetism. Volcanism was often felsic in nature, as opposed to the mafic volcanism that dominates the earlier and later MCR sequences, and was accompanied by vertical subsidence that allowed the previously discussed immature sandstones to accumulate in small basins. The main magmatic stage (1,102 to 1,092 Ma; Portage and Porcupine Volcanics of WI and MI, plus the Chengwatana Volcanics and North Shore Volcanic Group in MN) is a normal polarized magmatic event with basal tholeiitic basalts, followed by olivine basalt and lesser, though locally abundant felsic volcanics (Miller, 2007). The fourth and final magmatic pulse (1,094 to 1,086 Ma) produced normal polarized basalt volcanism associated with interstratified alluvial, fluvial, and lacustrine deposits that became more abundant upwards as volcanism waned (e.g., the traps of the Keweenawan Peninsula).

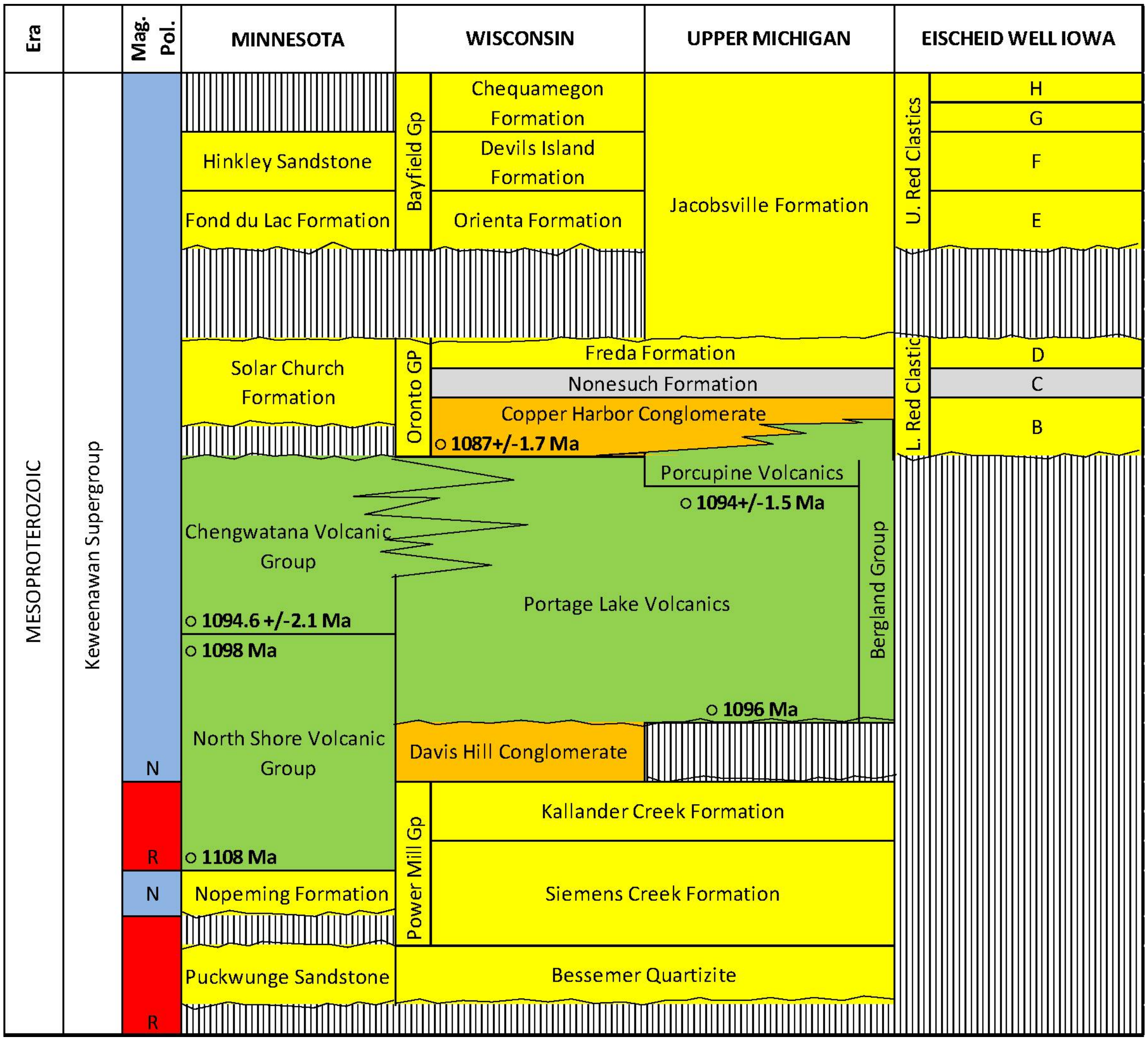

Figure 3. The Keweenawan Supergroup and its nomenclature in Minnesota, Wisconsin, Michigan, and Iowa (Modified from Cannon and Nicholson, 1992; Anderson (1997).

1.3.2 Oronto Group and Equivalent Stratigraphic Units

Although cessation of volcanism occurred at 1086 Ma, subsidence of the central basin continued to occur as evidenced by the thick accumulation of the Oronto Group sediments. The Oronto Group is a clastic dominated sedimentary sequence, and was the main focus of the present study. Both Craddock (1972) and White (1972) have described the Oronto Group in west central Wisconsin as being comprised of three formations deposited in stratigraphic succession: the basal CHC, the Nonesuch Formation, and the Freda Formation (Figure 3). The CHC is a fining upward sequence of immature conglomerate to lithofeldspathic sandstone, and siltstone. This formation is approximately 2130 m (7000 ft.) thick with a lower portion developed as an alluvial fan deposit and the upper portions forming as meandering stream deposits (Daniels, 1982;

Elmore, 1984). The overlying Nonesuch Formation is a 75-210 m (250-700 ft.) gray-to-black organic-rich shale and shaly siltstone. Elmore et al. (1989) and Suszek (1997) described the depositional environment of this formation, based on bacterial and algal contents as a restricted lacustrine deposit although Pratt et al. (1991) suggests that the Nonesuch may have an estuarine origin based upon organic molecules that resemble those found in marine fossils. The Freda Formation sandstone is the upper-most unit in the Oronto Group. This sequence is composed of approximately 3500 m (1150 ft.) of cyclic sandstone, siltstone, and mudstone that was deposited in a braided river system (Daniels, 1982). The Solar Church Formation is encountered only in the subsurface in Minnesota and is considered to be broadly correlative to the Oronto Group.

In the Iowa sector, the Lower Red Clastic Group (equivalent to the Oronto Group) is designated the units of B, C, and D (Witzke, 1990). The primary difference between the Unit B and the CHC is the dominace of the sandy quartzose facies in Unit B (Daniels, 1982; Ludvigson et al., 1990). Units C and D in the Iowa sector have similar lithologic characteristics to the Nonesuch and Freda Formations, respectivly (Anderson, 1990; Witzke, 1990). Unit C is characterized by the abundant siltstone and shale, and contains abundant vein and pore-filling calcite cement along with structurally deformed mineral grains. Unit D is is an upward fining sequence of sandsone similar to the Freda Formation.

1.3.3 The Bayfield-Jacobsville Sandstones and Equivalent Stratigraphic Units

The Bayfield Group-Jacobsville Formation sequence unconformably overlies the Oronto Group. This sequence is interpreted to have been deposited during a compressive tectonic phase associated with the Grenville Orogeny. The Bayfield Group and Jacobsville Formation are also stratigraphically equivalent units to the Fond du Lac-Hinkley Formations in Minnesota, (Figure 3; Ojakangas and Morey, 1982). The Bayfield is formally subdivided into three formations. The lowermost unit is the Orienta Formation sandstone, which constitutes 575 m (1880 ft.) of red-lithofeldspathic sandstone-siltstone-shale facies. The fining upward nature of the succession suggests a meandering river origin (Anderson, 1990; Ojakangas et al., 2001). The Orienta is conformably overlain by the Devils Island Formation sandstone, which is the thinnest stratigraphic unit of the sequence (~90 m). The Devils Island sandstone is a buff colored and highly mature due to its being formed by reworking older sediments in eolian and lacustrine environments (Tryhorn and Ojakangas, 1972). The Chequamegon sandstone is the youngest unit and lies conformably upon the underlying sandstones. This unit is a highly mature, porous, and permeable quartz-arenite with a total thickness of approximately 150 m (Ojakangas, 1986).

Witzke (1990) assigned the names Unit E, Unit F, and Unit G for the Upper Red Clastics in the M.G. Eischeied #1 Well in Iowa, while Unit H was later added by Anderson (1990). Unit E is sandstone-dominated with an abundance of lithic fragments. Unit F is cycles between very fine to fine grained gray sandstone with lesser red and brown siltstone and shale. Unit G is red-brown fine to medium-grained sandstone intercallated with minor shale and siltstone. Unit H is light redish-brown very course-grained sandstone with some micaceous shale to sandy siltstone intervals. The mineral and textural maturation of the Upper Red Clastic Group is less than that for the Lower red Clastic Group (Units B, C, and D). That is reverse of the pattern displayed for the Oronto and Bayfield Group sequence exposed in the Lake Superior region where the Bayfield Group is more mature when compared with the underlying Oronto Group sediments (Ojakangas and Morey, 1982; Ojakangas, 1986; Ludvigson et al., 1990; Ojakangas et al., 2001).

The Phanerozoic Sequence unconformably overlies the Keweenawan Supergroup, although much of this sequence has been eroded away in the Lake Superior region (Anderson, 1990, 1992, and 1997). About 914 m (~3000′) of Phanerozoic sediments are preserved in the penetrated section of the Eischeid #1 Well, in Iowa. The Cambrian sequence lying on top of the MCR sediments constitutes approximately 196 m (640′) of glauconitic arenaceous to argillaceous facies sandstone, similar to those found in the basal Mt. Simon-Lamotte Formations and then overlying carbonate-rich rocks similar to the Eau Claire-Bonneterre Formations.

1.4 Attributes of the Midcontinent Rift (MCR) for CO_2 Sequestration

Aquifer attributes that make a sedimentary succession favorable for carbon sequestration have been summarized by Bachu (2000, 2002) and Thorleifson (2008). These considerations when applied to the MCR sequence include the following assessment:

Favorable Attributes of the MCR for CO_2 Sequestration:

- The disposal depth generally exceeds 760 m (2500′) outside of the Lake Superior area. At these depths the injected CO_2 will be in a supercritical state (Buchanan and McCauley, 1987; Doughty and Pruess, 2004). The density of the supercritical CO_2 phase is between 0.27 kg/m^3 and 0.32 kg/m^3 and will take up less space than gaseous phase CO_2. The diffusion rate of supercritical CO_2, especially through tight pore spaces, is faster than both gaseous and liquid phases. Finally, the greater depths of sequestration may reduce the risk of contaminating drinking water aquifers that occur at shallower depths.
- The CHC is stratigraphically overlain by about 250 m (820′) of fine grained Nonesuch Formation sediments, which represent a potential stratigraphic trap for migrating fluids and gasses. The faulted margins of the basins could also create structural traps.
- Most of these units, particularly the Oronto Group and underlying volcanic rocks, are composed of silicate and oxide minerals that contain abundant quantities of Ca^{2+}, Mg^{2+}, Fe^{2+} and other cations that could play an important role in long-term carbon sequestration by complexing with dissolved CO_3^{2-} to form solid carbonate minerals.
- The proximal distribution of stationary coal-fired power plants and the existing pipe line infrastructure will reduce the cost of transport associated with sequestration in the MCR. The maximum distance that liquid-phase CO_2 can be transported through a pipeline without additional CO_2 recompression is about 300 km (Figure 4).
- The Bayfield Group and laterally equivalent units are the most permeable sections of the MCR, but these lack a stratigraphic trap rock in the Lake Superior region. Some portions of the equivalent strata in the Iowa and Kansas rift segments have been tectonically overlain by

volcanic sequences and older sediments due to thrust faulting. Volcanic sequences may have significant porosity along fractured and vesicular-amygdaloidal flow tops and bottoms, thus their reliability as a stratigraphic trap must take these horizons into account.

- The exploration activities associated with mineral and petroleum resources within the MCR sedimentary rocks outside the Lake Superior region are minimal and thus there is a low drilling density intruding the MCR sequence. This feature will reduce the possibility of CO_2 leakage to back into the atmosphere through drill wells that have not been recorded.

Non-favorable Attributes of the MCR CO_2 Sequestration:

- The generally impermeable nature of the Oronto Group rift clastic rocks could hinder both CO_2 injectability and limit gas storage volume (Thorleifson et al., 2008). This is the major factor limiting the use of the MCR sequence for CO_2 disposal. Porosity estimations of the MCR clastic sedimentary rocks in all drilled wells are summarized in Table 1. Porosities vary from location to location, depth in the drill cores, and by the method(s) used to determine them, but often fall below 1 or 2% for many of the deeper Oronto Group sediments and their equivalent stratigraphic units. The main porosity limiting factors result from the precipitation of fine grained clays, Fe-oxides, and especially calcite between the detrital grains. There is a general absence of direct porosity and permeability measurements in the MCR sequence beneath Minnesota as well as other states (Thorleifson et al., 2008). Studies of the Kansas section have revealed local zones of higher porosity (Berendsen et al., 1988).
- The fine-grained Nonesuch Formation with shale rich horizons is a potential trap rock. However, the lateral continuity of the unit characteristics is well-known only in limited segments of the MCR basin.
- The complexity associated with the tectonic history of the MCR may be an advantage or a disadvantage to CO_2 sequestration. Leakage may potentially occur along tectonically induced fractures. Tectonic activity may also produce structural traps along fault planes and domes, as they often do in hydrocarbon occurrences. Segments of the MCR in Kansas have tectonically juxtaposed of the normally impermeable-natured early-rift stage extensional rocks (Oronto Group equivalents) on top of the relatively permeable late stage sedimentary sandstones. These provide an attractive target for sequestration of carbon dioxide.
- The most porous and permeable aquifers in the MCR (i.e. the Bayfield Group-Jacobsville Formation) are characterized by low Ca^{2+}, Mg^{2+}, and Fe^{2+} contents that reduce the potential to induce carbonate mineralization. The Bayfield Group and its equivalent stratigraphic units have a wide lateral extent and are overlain by Phanerozoic arenaceous or argillaceous sediments that will likely have limited stratigraphic sealing capacity as evidenced by widespread formation of the basal Mt. Simon Formation sandstone. This would of course render the Bayfield-Jacobsville sequence as a continuous aquifer unit with the Mount Simon sandstone, thus both could be used as a combined GCS unit where the Mount Simon is overlain by an effective trap rock.

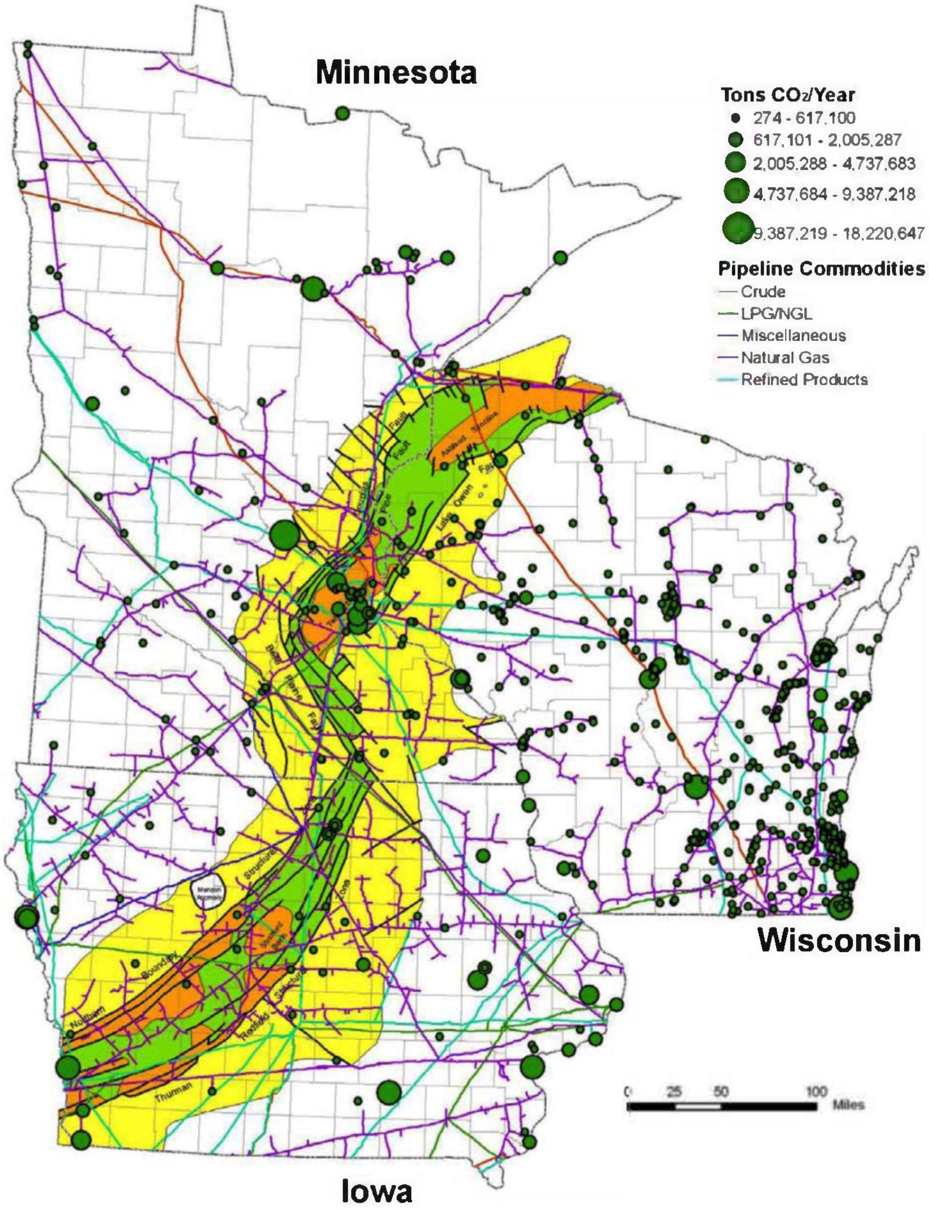

Figure 4. Stationary power plants, pipeline distribution, and the extent of MCR sediments in MN, IA, and WI (Thorleifson, 2008). The yellow color represents the presence of the Bayfield Group at the top of the sequence, whereas orange represents the presence of the Oronto Group at the top. The stratigraphy in the immediate vicinity of the Lake Superior region is exposed at the surface, whereas stratigraphic units approximately 50 miles or more southwest from Duluth, Minnesota are buried beneath Phanerozoic and/or younger sequences.

Table 1. Summary of measured porosity (P) in volume percent and permeability (*K*) in millidarcys. Data is segregated into method used for collection including laboratory flooding tests, downhole geophysics, and thin-section point counting. Depths for measurement intervals are noted. Compiled from data by Thorleifson (2008).

Borehole	St. Amour # 1-29 Test and Hickey Creek	Terra-Patrick #7-22	M.G. Eischeid #1	Ray McCallum A-1	Rhinehart Farms A-1	Texaco Poersch #1
Location	Michigan, Upper Peninsula	NW Wisconsin	West-Central Iowa	Southwest Iowa	Southwest Iowa	Northeast Kansas
Porosity-Permeability by Laboratory Flood Test			8835-15,106′ 27 samples P = 1.9% avg., range 0.3-3.8% 26 samples $K \approx 10^{-3}$ avg.	3014′ P = 8.87% $K = 10^{-3}$	3069-3080′ 4 samples P = 9.1% avg., range 6.3-11.6% $K = 10^{-2}$ mD avg. range 10^{-2} to 10^{-4}	
Permeability Measurement by Downhole Geophysics		2500-3000′ P = 7-10% 3000-4500′ P ≈0-10% >4500′ P = 3% avg.	>11,450′ P = 2.3% avg., range 1-6%			~4500-11,296′ P = <2% except 11,055′-10,077 where P ≤ 15%
Permeability by Thin Section Point Count	2500 to > 4500′ P = 0.6% avg., range 0-3.3%		2500-3000′ P = 6% 3000-4500′ P = 1-2.5% 4500-15,000′ P = 0-1%			

1.5 Chemistry of Carbonate Mineral Reactions

Many factors can play a role in carbonate mineral equilibria, including pH, temperature, pressure, mineralization inhibitors (e.g., phosphate, organic matter, and sulfate), and alkalinity (Walter, 1986; Morse and Mackenzie, 1990; Morse, 2003). The ionic activity of the respective mineral constituents is an essential factor in carbonate equilibria reactions. The saturation state of carbonate minerals is defined by the solubility product of carbonate minerals (equilibrium constant; K_{sp}) and the saturation index (SI) of carbonate minerals can be expressed as:

$$\mathrm{SI}_{mineral} = \log \frac{a_{Me^{2+}} \times a_{CO_3^{2-}}}{K_{sp}}$$

where (a) is ionic activity in mole/kg, (Me^{2+}) is any two-plus valance state cation, and (K_{sp}) is the equilibrium solubility product. If SI = 0.0, the solution will be in equilibrium, if SI < 0.0, the solution will be undersaturated and if SI > 0.0, the solution will be supersaturated and will eventually precipitate carbonate minerals (Morse and Mackenzie, 1990; Morse, 2003).

The relative concentration of the dissolved inorganic carbon species will vary as a function of solution pH (Figure 5). At low pH values (< 6.4), carbonic acid ($H_2CO_{3(aq)}$) is the dominant specie. At intermediate pH (between 6.4 and 10.3) bicarbonate (HCO_3^-) will dominate. The carbonate ion (CO_3^{2-}) is the dominant aqueous specie when the pH exceeds 10.3. These equivalence points and concentrations of all aqueous carbon dioxide species can vary with temperature, pressure, CO_2 content, salinity, etc.

Carbonate minerals are generally divided into either the calcite group (a six-fold coordinated structure in the hexagonal crystal system) or aragonite group (a nine-fold coordinate structure in the orthorhombic crystal system (Figure 6; Railsback, 2011). Large radii cations (e.g., Sr^{2+}, Pb^{2+}, and Ba^{2+}) fit more easily into the nine-fold coordinated structure (around the oxygen in the carbonate anion), while smaller radii cations (e.g., Mg^{2+}, Co^{2+}, Zn^{2+}, Fe^{2+}, Mn^{2+}, and Cd^{2+}) preferentially fit into the six-fold crystal structure. Only Ca can be found in appreciable quantities in both (calcite and aragonite). The most soluble carbonate minerals are recognized at the end members of each group and thus their precipitation is less favored from a thermodynamic perspective.

In general, Ca^{2+} and Mg^{2+} are the two most common cations found during carbonate mineralization and by analogy will be the most important cations in any geochemical investigations about mineral sequestration. Calcium carbonate is commonly represented by the calcite and aragonite polymorphs. Vaterite, hydrated calcium carbonate (e.g., monohydrocalcite and ikaite), and amorphous calcium carbonate also occur during incipient mineralization processes, but are relatively uncommon in the geologic rock record.

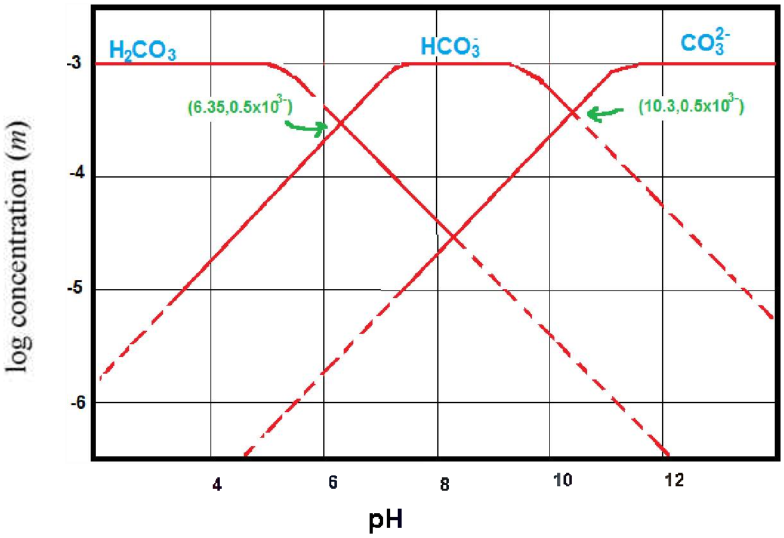

Figure 5. The molal concentration of the common aqueous carbonate species as a function of changing pH in the solution.

The substitution of Ca^{2+} by Mg^{2+} in calcite is common. Therefore, calcite is grouped into low Mg-calcite (Mg< 4 mole %), high Mg-calcite (Mg >11 mole %) varieties, plus disordered and ordered dolomite (Mg =50 mole %; Boggild, 1930). The solubility of high Mg-calcite is greater than that of low Mg-calcite as illustrated in Figure 6 and Table 2 (Morse and Mackenzie, 1990). Poorly ordered dolomite ($(Mg,Ca)(CO_3)_2$;or proto-dolomite) is found on rare occasions precipitating in modern near-surface environments hypersaline lagoons and sabkhas (Bush, 1973; Machel and Mountjoy, 1986), but very commonly is produced during Mg-metasomatism reactions involving limestone. The solubility of Mg-bearing calcite increases proportionally with the Mg-content while the solubility of dolomite increases as the crystallinity of dolomite decreases.

Potassium and sodium are likely to be less important in most geologic mineral sequestration processes because their respective carbonate mineral phases are highly soluble in natural systems. While dawsonite [$(NaAlCO_3(OH)_2$] precipitation is commonly predicted in computer simulations in CO_2 rich systems, it is rarely recognized in natural systems, or even the lab syntheses from NaCl, $NaHCO_3$, and Al minerals (Kaszuba et al., 2005).

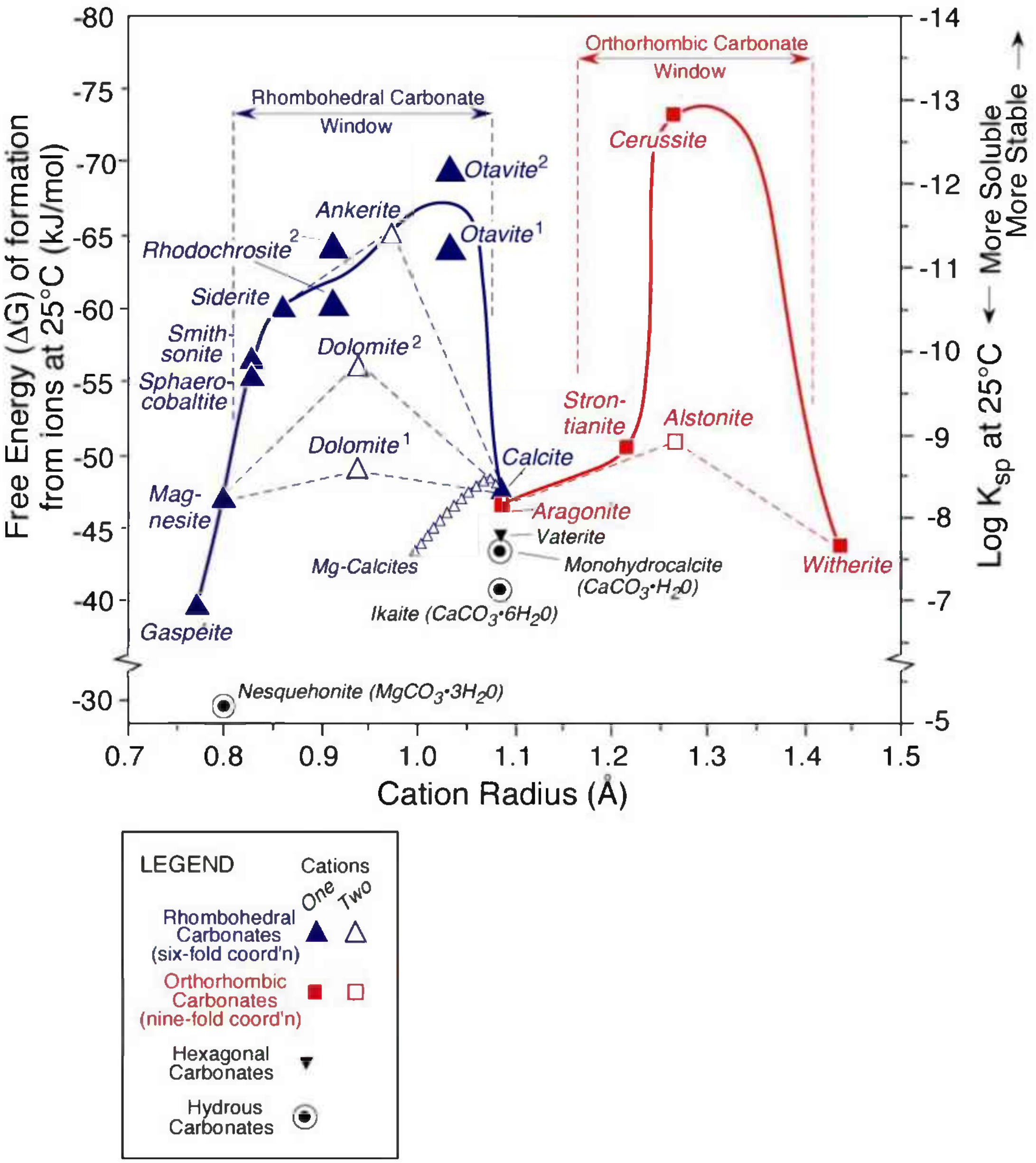

Figure 6. Summary of carbonate mineral stability based on their ionic radii, solubility product, and free energy of formation (Railsback, 2011).

Table 2. Summary of Ca and Mg carbonate minerals with their corresponding solubility products (K_{sp}) and occurrence (Railsback, 2011).

Mineral	K_{sp} (25°C)	Sedimentary Occurrence
Low Mg Calcite ($Mg_{0.04}Ca_{0.96}CO_3$)	3.16E-09	Some biomineralization; dominant in ancient limestone
Medium Mg Calcite ($Mg_{0.04-0.12}Ca_{0.96-0.88}CO_3$)	3.16E-09 to 5.01E-09	Marine sediments via biomineralization and precipitation
High Mg Calcite ($Mg_{0.12-0.25}Ca_{0.88-0.75}CO_3$)	5.01E-09 to 3.16E-08	Marine sediments via biomineralization and precipitation
Aragonite ($CaCO_3$)	5.01E-09	Common. Marine and terrestrial sediments
Vaterite ($CaCO_3$)	1.25E-08	Rare occurrence, biomineralization
Monohydrocalcite ($CaCO_3.6H_2O$)	3.16E-08 to 2.51E-08	Rare occurrence in caves, lakes, and low-temperature deposits
Disordered Dolomite ($Mg_{0.5}Ca_{0.5}CO_3$)	~6.30E-09	Metastable
Ordered Dolomite ($Mg_{0.5}Ca_{0.5}CO_3$)	~2.51E-09	Ancient limestone and dolomite
Magnesite ($MgCO_3$)	~6.30E-09	Lake sediments (as an alteration phase of hydromagnesite)
Ikaite ($CaCO_3.6H_2O$)	7.94E-08	Rare occurrence in cold water marine tufa.
Barringtonite ($MgCO_3.2H_2O$?)		
Nesquehonite ($MgCO_3.3H_2O$)	~1.00E-05	Diagenesis product in lake sediments
Lansfordite ($MgCO_3.5H_2O$)		
Artinite ($Mg_2(CO_3)(OH)_2.3H_2O$)		
Hydromagnesite ($Mg_5(CO_3)_4(OH)_2.4H_2O$)		Ephemeral lakes and speleothems
Dypingite ($Mg_5(CO_3)_4(OH)_2.6H_2O$)		

The Fe^{2+} ion may complex with CO_3^{2-} to precipitate siderite ($FeCO_3$). Iron is commonly encountered as Fe^{3+} phases in subsurface oxidized settings as various ferric-oxide, -hydroxide, and mixed oxide-hydroxide phases (Meyer, 1984). Mineral sequestration of CO_3^{2-} in siderite will thus require the reduction of ferric to ferrous iron, which can be caused by the presence of reducing agents such as H_2S, organic material, etc. (Palandri and Kharaka, 2005; Murphy et al., 2011).

An effective mineral sequestration process is dependent, primarily, on the dissolution of Ca-, Mg-, and Fe silicate or oxides and/or the presence of significant quantities of these ions in groundwater brines. The rate of dissolution for Ca-, Mg-, and Fe silicate or oxides can be accelerated by increasing the surface area of the host rocks, temperature, and acidification (Golubev and Pokrovsky, 2006; Huijgen et al., 2006). One of the most efficient cation sources for any carbonate mineralization process is forsterite-olivine (5.86 tons to sequester one ton of carbon), followed by serpentine (7.69 tons to sequester one ton of carbon), basaltic glass (8.76 tons to sequester one ton of carbon), wollastonite (9.68 tons to sequester one ton of carbon), and then anorthite (23.1 tons to sequester one ton of carbon; Oelkers et al., 2008).

Pressure may also influence carbonate solubility. There is inverse relationship between the dissolved CO_2 and the carbonate mineralization, so, the degasing of CO_2 from the water is one of important factors that may promote carbonate mineralization (Ryan, 2014). The degasing of CO_2 could be a result of a pressure decrease, temperature increase, or photosynthetic activity. The solubility product of the carbonate minerals as a function of pressure as the following:

$$\mathrm{K}_{cc} = \frac{Me^{2+} \times CO_3^{2-}}{PCO_2}$$

where: (K_{cc}) is a solubility product of the carbonate mineral, (PCO_2) partial pressure of CO_2; (Me^{2+}) is any two-plus valance state cation such as Ca^{2+}.

Carbonate minerals display an inverted solubility relationship with temperature, whereby an increase in temperature will result a lower K_{sp} value. Temperature also has an influence on two additional parameters that are worth reviewing as they can also then influence the solubility of carbonate minerals. 1) Increasing temperature will lower the solubility of the $CO_{2(aq)}$ phase, leading to CO_2 volatilization and a potential rise in pH that can promote mineralization. 2) An increase in temperature will also increase the CO_3^{2-} / HCO^{3-} alkalinity ratio, also a factor in promoting mineralization. The release of CO_2 gas as a volatile component will also be dependent on the confining pressure of the surrounding hydrostatic or lithostatic medium.

1.6 Study Objectives

The primary purpose of this study is to evaluate the applicability of using the MCR sediments to sequester CO2, especially with respect to forming carbonate mineral phases. More specific goals are to:

1. Evaluate the MCR samples collected in the field or subsurface drill core samples to determine their distribution of Ca^{2+}-, Mg^{2+}-, and Fe^{2+}- in carbonate, silicate and oxide minerals, based on both petrographic study and bulk chemical analysis of the samples.
2. Evaluate the potential for and rate of Ca carbonate cement dissolution that would result following CO_2 injection and associated carbonic acid formation. Dissolution of pore-blocking cements may increase the primary porosity-permeability characteristics of the rock samples.
3. Evaluate the potential for the dissolution of Ca- and Mg-silicates and oxides that would result following CO_2 injection and associated carbonic acid formation. These minerals will provide the dissolved alkaline earth components that are generally needed for the precipitation of carbonate minerals. The dissolution rate of silicate minerals is expected to be much slower than that for the carbonates. Porosity may even decrease following silicate mineral dissolution in response to the formation of alteration minerals such as clays and dislodging of soluble grains that are transported to and block the narrow pore-throats between clastic grains.
4. Evaluate the potential for carbonate mineral precipitation as a result of dissolution and acid neutralization reactions following CO_2 injection. These reactions will occur in a repository setting in more distal far-field locations from the injection well(s) and/or near the injection well(s) over longer time intervals following the cessation of CO_2 injection.
5. Evaluate the potential for long-term carbonate mineralization using the PHREEQ modelling code and compare modeling results to mineral-water reactions observed experimental corrosion tests using water-rock-CO_2 reactions.

2 RESULTS AND DISCUSSION

2.1 Sample Collection Locations

Forty-eight rock samples from surface outcrops were collected from various locations around the Lake Superior Region as well as twenty-one subsurface petroleum exploration drill core samples from the M. G. Eischeid #1 Well in Iowa and the Texaco Poersch #1, Well in Kansas. These samples were used to determine rock petrographic characteristics, bulk geochemistry, clay matrix mineralogy, and to provide samples for corrosion testing experiments with $CO_2 + H_2O$. The surface outcrop samples were collected from actively eroding river valleys and lake shore locations, environments that tend to mechanically abrade away chemically weathered material thus minimizing chemical weathering effects. All surface outcrop samples were also trimmed in the field using a rock hammer to remove visibly weathered surfaces, if present. The Lake

Superior surface samples (Figure 7) included collection sites from the Keweenaw Peninsula (MI), the L'Anse area (MI;), Agate Falls Park (MI), Potato River Falls (WI), Copper Falls State Park (WI), the Bayfield Peninsula (WI), Beaver Bay Complex (MN), North Shore Volcanic Group (MN), and Duluth Complex (MN).

Sediment samples were collected from the Copper Harbor Conglomerate (CHC; lower Oronto Group) at five locations within the Keweenawan Peninsula of Michigan (designated as KEW samples; Figure 7a). The CHC is the basal section of the Oronto Group and is composed largely of conglomerate and coarse grained sandstones (Figure 8a). All of the CHC samples used in this study were preferentially sampled from sandstone- or siltstone-rich horizons within the predominantly coarser-grained conglomeratic beds. Additional CHC samples were collected from the Potato River Falls and at Copper Falls State Park areas in Wisconsin (labeled POT, CFSP; Figure 7b). Both of these latter exposures have been tilted by tectonic forces to a nearly vertical orientation to expose a continuous cross-section of the Oronto Group sediment profile.

The Nonesuch Formation is a fine-grained siltstone and shale unit located stratigraphically within the middle of the Oronto Group sediment sequence. Samples of the Nonesuch were collected form the Potato River Falls and Copper Falls State Park areas in Wisconsin (labeled POT and CFSP, Figures 7b and 8b)

The Freda Formation rock samples were reddish-brown in color, medium-to-fine-grained sandstones that are enriched in lithic and/or arkosic fragments and locally contained clay-rich, silt-rich, to sandy facies. The Freda sandstone is also typically more friable than the underlying CHC and sandstone-rich lenses in the Nonesuch, and thus tends to erode more easily. Samples from the Freda Formation were collected from four locations (Figure 7b): Potato River Falls, Copper Falls State Park, Oronto Creek near Saxon Harbor along the boundary between Wisconsin and the Upper Peninsula of Michigan, and Superior Falls, Wisconsin (Figure 8c).

The Bayfield Group-Jacobsville Formation sequence overlies the lower Oronto Group sedimentary rocks with an angular unconformity, indicating that a significant length of time had passed between the deposition of the two units. Samples of the Jacobsville were collected from the L'ANSE and Agate Falls Park (AF) areas in Michigan (Figure 7a). Rock exposures here consist of medium- to coarse-grained red to buff colored sandstone that is often cross-bedded and locally displays a distinctive white spotted coloration pattern due to Fe mobilization around local organic-rich reduction zones. The Bayfield Group (WI) sequence is stratigraphically equivalent to the Jacobsville. All Bayfield samples were collected from the type locality along the Bayfield Peninsula, Wisconsin (BAY; Figure 7b). The Jacobsville-Bayfield samples are typically medium-grained sands, friable, and highly permeable, although localized low-permeability zones are found.

A thick sequence of North Shore Volcanic Group (NSVG) basalt is exposed in Good Harbor Bay, Minnesota. A sample was collected from a lens-shaped unit of brown-to-reddish colored and fine grained sandstone-siltstone that occurs as an interflow sediment layer between two successive lava flows (Figures 7c and 8d). The outflow of water exposed in the road cut throughout the sediment horizon indicates significant permeability of the interflow sedimentary rocks. Samples were also collected from an anorthositic mega-xenolith from the Silver Bay area and a pyroxene-rich gabbro from the Beaver Bay complex east of Ely Minnesota.

The Eischeid #1 petroleum exploration well is located approximately 8 kilometers northwest of the buried Iowa Horst, penetrating through about 14,898′ of the rock sequence at the northern end of the Defiance Basin (Figure 2). Samples from this well were provided by the Iowa Geological Survey. Rift sediments were grouped into the Upper Red Clastics (which correlates with the Bayfield Group exposed near Lake Superior) and the Lower Red Clastics (which correlates with the Oronto Group). The Lower Red Clastics were classified into Units B, C, and D while the Upper Red Clastics were divided into Units E, F, G, and H (Figure 9a). No volcanic or plutonic sections were intersected in the Eischeid #1 Well section.

Three different samples were collected from the core interval that penetrated Unit E of the Eischeid #1 Well (Figure 9a; the Orienta Formation equivalent). All three samples exhibited traces of calcite cement, high plagioclase to K-feldspar ratios, and approximately 11% open porosity. The E2-2 sample was a laminated-to-low-angle stratified brownish red, well-cemented fine-grained sandstone, while E2-3 was a massive, brownish red, coarse-grained sandstone, and E2-4 was a stratified brownish red to white and mottled color medium-grained sandstone. Three samples were also collected from the Unit D (which correlates to the Freda sandstone exposed in the Lake Superior region). The Unit D exhibited low porosity and calcite cement. Sample D4-1 was a red tabular to trough cross-bedded fine grained sandstone, D4-2 was a thick laminated sandstone with mudstone intercalations, while D4-3 was a red colored and well-cemented silty sandstone. Five samples were collected from Unit C2 (which correlates to the Nonesuch Formation). The Unit C is characterized by abundant calcite cement within a black shale-siltstone-sandstone sequence. Sample C2-1 was a light gray calcareous and very-fine grained laminated sandstone, C2-2 was similar, but fine-to-medium-grained, C2-3 and C2-4 were composed of intercalated sandstone-siltstone-shale layers, and C2-5 was a massive to laminated calcareous and very fine-grained sandstone.

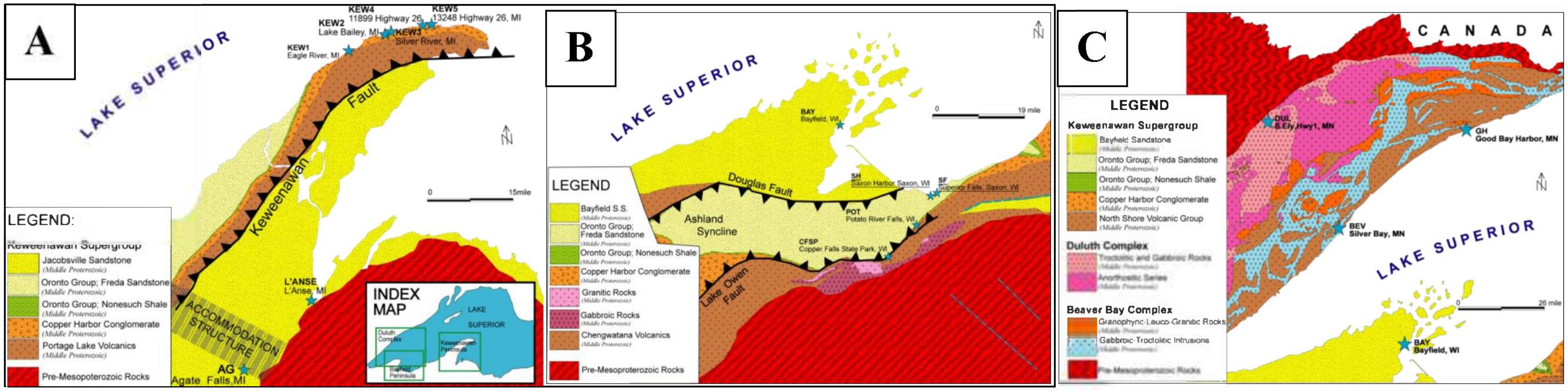

Figure 7. Location maps for surface samples collected in the Lake Superior region. A) Sampling locations on the Keweenawan Peninsula (KEW), L'Anse region (L'ANSE), and Agate Falls (AG). Inset diagram shows regional location for all three maps. B) Sampling locations for the Bayfield Peninsula (BAY), Saxon Harbor (SH), Superior Falls (SF), Potato River Falls (POT), and Copper Falls State Park (CFSP). C) Sampling locations near the North Shore of Lake Superior and Duluth Complex. Also shown is the location of the Bayfield Peninsula (BAY) sample from Figure 7b. Maps have been modified after USGS file of Nicholson et al. (2004).

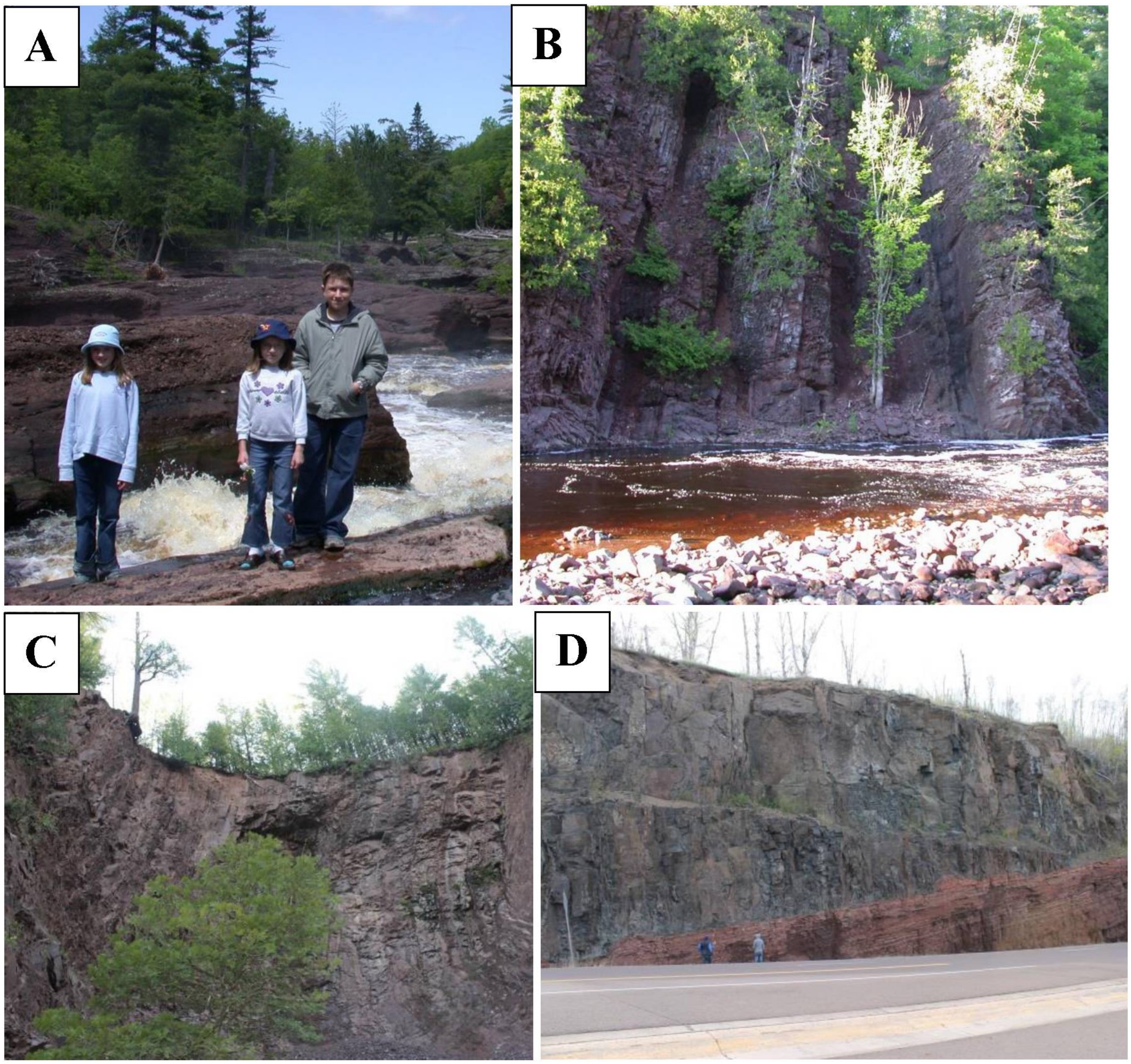

Figure 8. Outcrop exposures of Oronto Group sediments exposed around Lake Superior. A) Subhorizontal Copper Harbor Conglomerate beds along the Black River of Michigan showing alternating sandy (darker red) and conglomeratic facies (lighter red). Sedimentary layer contacts are dipping in the direction of the river flow. B) Vertically tilted section of the Nonesuch Formation at Copper Falls State Park (location for sample CFSP-3) showing alternating dark shale and lighter red siltstone-sandstone facies rocks. C) Vertically tilted Freda sandstone at Superior Falls, Montreal River, Michigan-Wisconsin border (location for sample SF1 through SF4). D) Near-horizontal section of the North Shore Volcanic Group section and interflow clastic rocks (red color) located on highway MN61, at the road cut of Grand Marais historical site, Good Bay Harbor, MN (location for sample GH-C).

Subsurface samples of the MCR sequence were also obtained from the Texaco Poersch #1 petroleum exploration drill well in Kansas (Figure 9b). The well section contained a significant thickness of Precambrian MCR clastic and igneous rocks in a faulted basement block segment. The well first encountered the MCR sequence at a drilling depth of 2846′ and remained within that sequence for the entire remaining depth to 11,300′ (Berendsen et al., 1988). Samples from this well were provided by the Kansas Geological Survey. Geophysical imaging indicates that faulting on the flanks of the central horst have juxtaposed the older volcanic sequence on top of the younger clastic rocks in a stratigraphic succession that is inverted to that of normal sequence exposed in surface outcrops near Lake Superior (Woelk and Hinze, 1991). The MCR sequence in this core has been differentiated from top to bottom into: upper gabbroic intrusive (2846-3150′), basalt flows (3150-4140′), upper mixed volcanic-sedimentary sequence (UMVSS; 4140-5719′), a second basalt dominated sequence (5719-7039′), pegmatite (7036-7039′), lower mixed volcanic-sedimentary sequence (LMVSS; 7039-7429′), and a thick underlying clastic dominated section which has been further subdivided into the Upper (7429-8806′), Middle (8806-10,840′), and Lower Sedimentary Sequences (10,840-11,300′). Samples selected for testing in the present study were collected from the lower clastic dominated sections and clastic interflow sediments. These include two red siltstone-shale samples from the UMVSS, two feldspathic sandstones from the Upper Sedimentary Sequence, two feldspathic sandstones from the Middle Sedimentary Sequence, and one fractured feldspathic sandstone from the Lower Sedimentary Sequence.

2.2 Petrographic Analysis of the Midcontinent Rift (MCR) Rocks

Thin-sectioned samples from both MCR sedimentary rocks collected from both Lake Superior region and deep drilling wells in Iowa and Kansas were studied using a Nikon 2000 polarized microscope. The petrographic investigations were used to identify the mineral composition, fabric, porosity, grain form, roundness, grain contact features, surface texture, matrix, cementation, and diagenetic features. Only a summary of these results are presented here, while more details can be found in Abousif (2014).

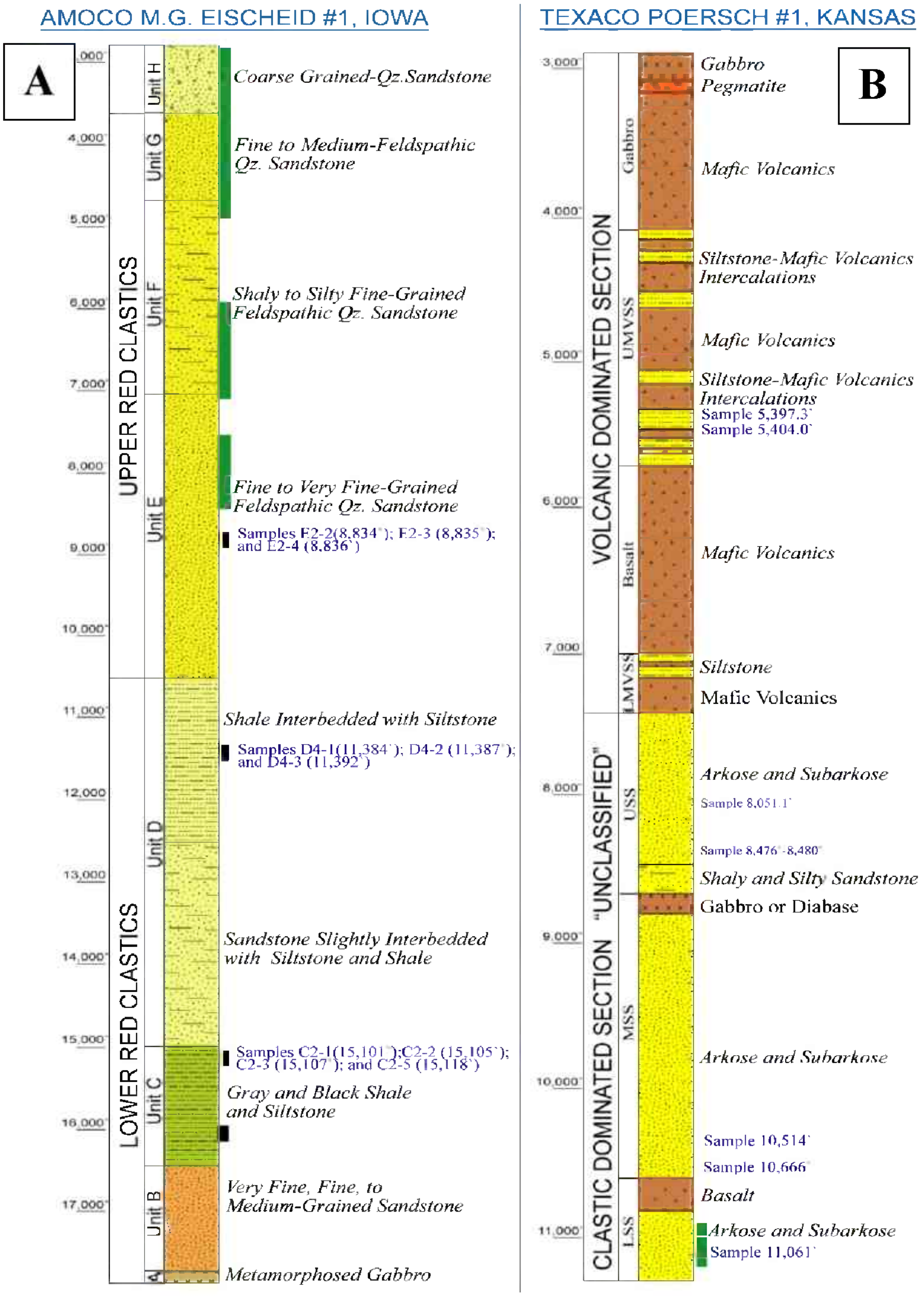

Figure 9. Stratigraphy of deep drilling wells penetrating MCR in A) Iowa and B) Kansas. The black line pattern represents locations where samples were collected for this study; the green lines represent additional sampling horizons with relatively high porosity-permeability; Upper mixed volcanic-sedimentary sequence (UMVSS); Lower mixed volcanic-sedimentary sequence (LMVSS); Upper Sedimentary Sequence (USS), Lower Sedimentary Sequence (LSS).

2.2.1 Oronto Group Sequence

2.2.1.1 The Copper Harbor Conglomerate (CHC) and Equivalent Stratigraphic Units

All CHC samples were selectively collected from the finer grained sand-dominated lenses and have been sampled to selectively avoid larger pebble to boulder-sized clasts, which often can comprise up to 50 volume percent or more of the samples. Grain and matrix mineralogy for ten CHC samples collected from the Keweenawan Peninsula and Potato Falls areas were dominantly composed of volcanic lithic fragments. Quartz-Feldspar-Lithic (Q-F-L) percent ratios for the sand-sized grains varied from lithic dominated $Q_{01}F_{02}L_{97}$ to those expressing more varied clast lithologies ranging from $Q_{38}F_{32.5}L_{29.5}$ to $Q_{11}F_{42.5}L_{46.5}$, (Figures 10a and 11; and Table 3). The feldspar compositions were generally dominated by plagioclase over K-feldspar, but ratios did vary from K-Feldspar rich 0.71/1 to plagioclase rich 2.4/1. The lithic fragments were almost exclusively lithic-volcanics (98.9%). Other trace grain components include muscovite $[KAl_2(Si_3Al)O_{10}(OH,F)_2]$, epidote $[Ca_2(Al,Fe^{3+})_3Si_3O_{12}(OH)]$, semi-opaque Fe oxide(s), and unidentified heavy minerals. The lithic volcanic clasts displayed variable types of igneous rock textures (e.g., porphyritic, trachytic, and granophyric). Based on matrix content, sorting, and mineral grain roundness features (Table 4), the Keweenawan Peninsula samples were classified as being texturally immature to sub-mature, while the samples from the Potato Falls section were texturally more mature than samples from the Keweenawan Peninsula.

The total silt- and clay-sized matrix content of the CHC samples varied from zero to about 25 volume % (Table 3). Semiquantitative XRD analysis of the clay-sized fraction revealed that chlorite $[(Mg,Fe)_3(Si,Al)_4O_{10}\text{-}(OH)_2.(Mg,Fe)_3(OH)_6]$ was the dominant component (up to ~75% of total), with locally abundant illite $[K_{1.5\text{-}1.0}Al_4(Si_{6.5\text{-}7.0},Al_{1.5\text{-}1.0}O_{20})(OH)_4$; up to ~23%], and minor smectite (~7% maximum; Figure 12a; Table 5). The non-clay minerals in the matrix fraction included quartz (SiO_2), K-feldspar, calcite, and laumontite ($Ca\ (AlSi_2O_6)_{2,4}H_2O$; a zeolite mineral).

The CHC samples were influenced by extensive post-depositional alteration including the effects of diagenesis, metamorphism, and hydrothermal alteration. Calcite was a common cementation agent and vein fracture filling component comprising between 6.6 to 23.5 volume percent of the Keweenawan Peninsula samples (Figure 11; Table 3). Opaque Fe-oxides also were present as pore-filling cement and sometimes occurred as a meniscus around the grains. Additionally, the feldspar and lithic grains were often highly altered. Compaction features varied from sample to sample and were reflected in the presence of concave-convex and line contacts between sand grains. Most post-depositional processes led to a decrease the porosity-permeability of the sandstones, however some quartz grains responded to tectonic stresses by fracturing, a feature that may increase porosity and permeability.

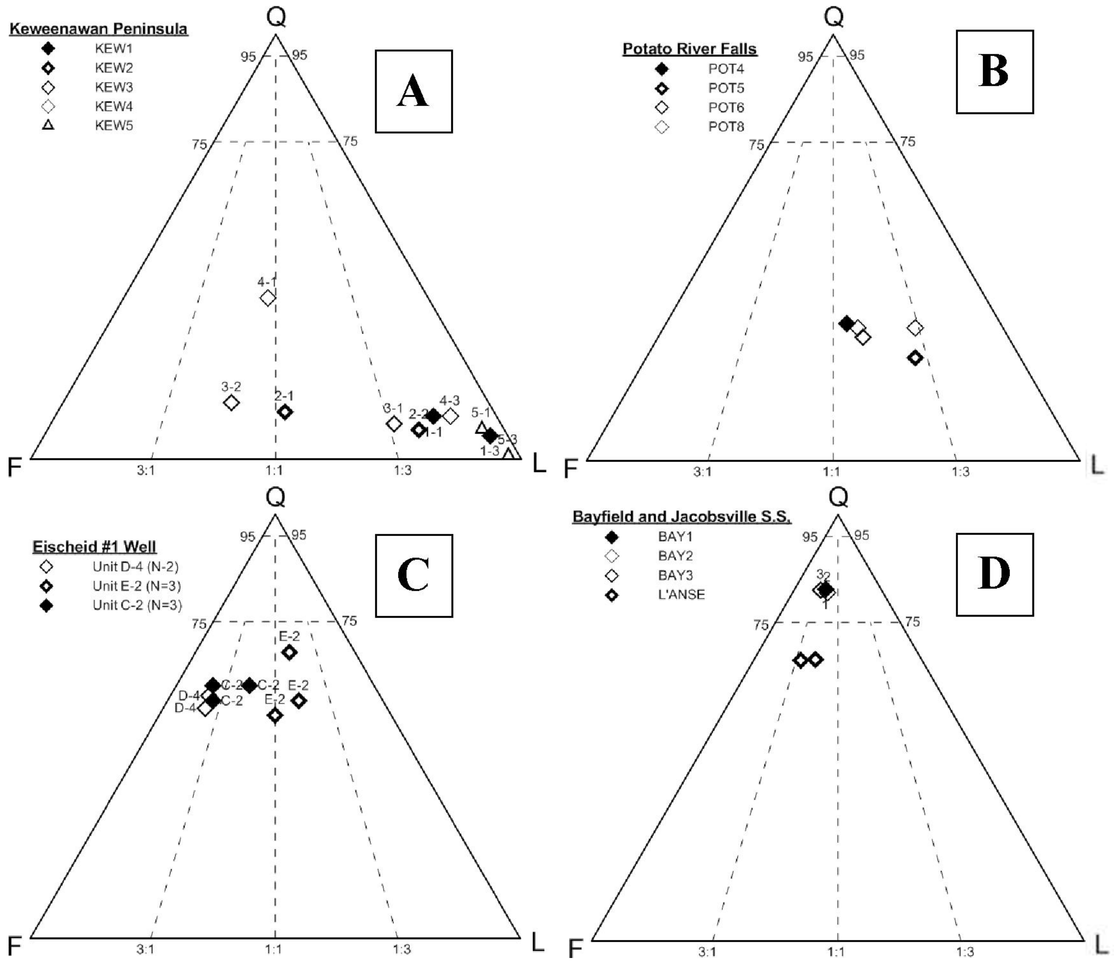

Figure 10. Triangular plot of quartz, feldspar, and lithic fragments (Q-F-L) based on point counting of 300 points per thin section. A) Samples of Copper Harbor Conglomerate collected from the Keweenawan Peninsula, MI. B) Potato River Falls samples of Nonesuch Formation. C) Samples from the Eischeid #1 Well in Iowa (Anderson, 1990). D) Samples from the Bayfield Group – Jacobsville Formation sequence.

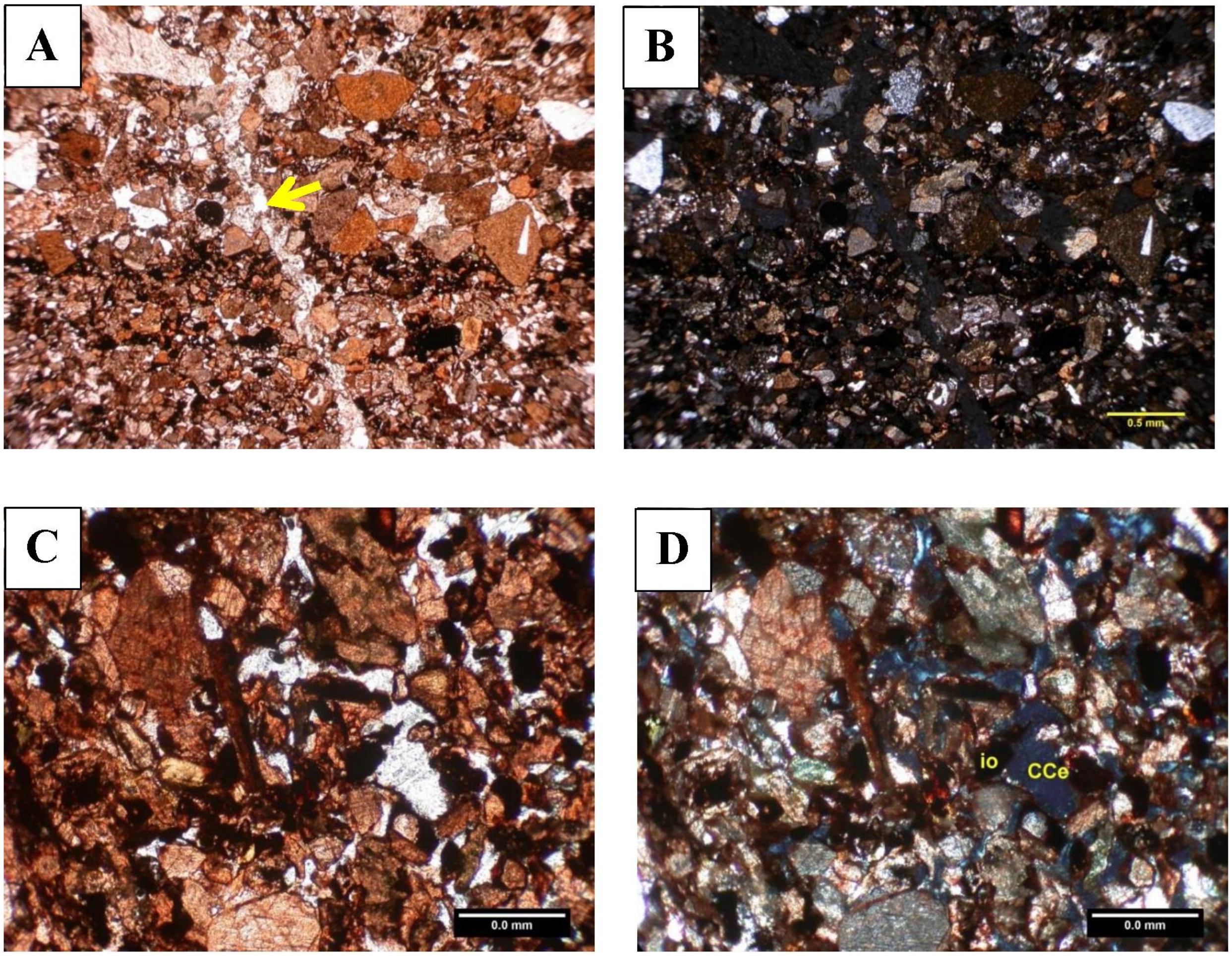

Figure 11. Thin sections of the Copper Harbor Conglomerate samples showing poorly sorted and mixed lithology sedimentary rocks. (A) Plane-polarized light image for KEW1-1 sample with fracture vein-filled by calcite shown with arrow. (B) Cross-polarized light for KEW1-1 sample. (C) Plane-polarized light image of KEW3-2 sample. (D) Cross-polarized image of KEW3-2 sample; Fe oxide "io", and calcite cement "CCe".

Table 3. Percentage of mineral components of surface outcrop samples from Oronto Group. Analysis is based upon 300 counts per thin section sample. Qz is quartz, Plag is plagioclase feldspar, K-spr is K-feldspar, L is lithic fragment, OQ is opaque mineral oxides, M is mica, HM is heavy minerals (e.g., zircon), Ep is epidote, Uk is unknown, SM is silty matrix, CM is clayey matrix, IO is iron oxide cement, CCe is carbonate cement, and P is porosity; * reflects porosities where samples displayed evidence of grain dislodgement "plucking" during sample preparation. CHC is Copper Harbor Conglomerate.

Sample ID	UNIT	Qz	Plag	K-spr	L	OQ	M	HM	Ep	Uk	SM	CM	IO	CCe	P	Total
KEW1-1	CHC	6.0	4.6	3.0	45.7	4.0	0.3	0.3	0.3	0.0	8.3	0.3	10.3	15.9	1.0	100.0
KEW2-1	CHC	7.0	10.6	15.0	28.8	1.7	0.0	0.3	0.3	1.3	5.6	0.3	8.3	14.6	5.3	100.0
KEW2-2	CHC	5.0	6.7	6.0	55.3	0.7	0.0	0.0	0.3	0.3	5.0	1.0	8.3	8.7	2.7	100.0
KEW3-1	CHC	5.0	6.1	7.1	42.5	3.9	0.0	0.0	0.4	1.1	6.4	1.8	6.4	10.4	8.9	100.0
KEW3-2	CHC	5.7	11.4	11.1	14.8	7.0	0.0	0.3	0.3	3.0	17.4	7.0	6.7	11.1	4.0	100.0
KEW4-1	CHC	23.8	12.8	7.7	18.5	2.3	0.0	0.0	0.0	0.7	11.7	4.7	6.7	8.1	3.0	100.0
KEW5-1	CHC	5.3	2.3	1.0	65.7	0.7	0.0	0.3	0.3	0.0	3.7	1.0	2.3	14.7	2.7	100.0
KEW5-3	CHC	0.7	1.1	0.7	79.4	0.4	0.0	0.0	0.4	0.0	2.2	1.8	4.8	6.6	1.8	100.0
POT4	Nonesuch	21.1	11.6	8.8	24.0	3.4	1.0	0.0	2.4	0.0	9.0	3.4	12.6	0.3	2.4	100.0
POT5	Nonesuch	28.2	13.0	14.3	32.0	0.7	0.3	0.0	2.4	0.0	0.0	5.7	0.0	0.0	3.4	100.0
POT6	CHC	25.3	18.0	7.8	36.5	4.0	0.4	0.0	2.6	1.1	0.0	1.3	2.2	0.0	0.8	100.0
POT8-1	Freda	28.9	5.3	22.7	32.9	6.8	0.0	0.0	3.4	0.0	0.0	0.0	0.0	0.0	0.0	100.0
POT8-2	Freda	28.4	9.6	17.2	36.1	4.7	0.0	0.0	2.8	0.0	0.0	0.0	0.0	0.0	1.2	100.0
Average		**14.6**	**8.7**	**9.4**	**39.4**	**3.1**	**0.2**	**0.1**	**1.2**	**0.6**	**5.3**	**2.2**	**5.3**	**7.0**	**2.9**	**100.0**
Stdev.		**10.7**	**4.6**	**6.2**	**17.8**	**2.2**	**0.3**	**0.1**	**1.2**	**0.8**	**5.1**	**2.2**	**4.0**	**6.0**	**2.2**	**0.0**
KEW1-3	CHC	3.7	1.7	0.7	60.9	0.0	0.3	0.0	0.0	0.3	0.0	0.0	0.7	16.7	15.0*	100.0
KEW4-3	CHC	5.4	2.7	2.3	43.0	4.7	0.0	0.0	0.0	0.3	2.0	1.3	4.7	23.5	10.1*	100.0

Table 4. Percentage of grain forms, roundness, contact and surface texture of surface outcrop samples from Oronto Group samples. Analysis is based upon 300 counts per thin section sample. Elg is elongated, Eq is equant, VA is very angular, A is angular, SA is sub-angular, SR is sub-rounded, R is rounded, WR is well rounded, F is fractured contact, S is sutured contact, CC is concave-convex contact, L is line contact, P is point contact, Fl is floated grain, C is corroded surface, Fr is fractured surface, and Po is polished surface.

	Grain form			Roundness						Grain contact						Surface texture		
	Elg - Eq	**Elg**	**Eq**	**VA**	**A**	**SA**	**SR**	**R**	**WR**	**F**	**S**	**CC**	**L**	**P**	**Fl**	**C**	**Fr**	**Po**
KEW1-1	6.8	43.2	50.0	0.0	14.6	46.4	31.8	7.3	0.0	1.0	0.5	48.5	27.8	15.5	6.7	35.4	12.5	52.1
KEW1-3	13.0	50.5	36.5	0.0	10.1	40.7	46.2	2.5	0.5	0.0	13.5	41.5	17.0	3.5	24.5	12.1	4.0	83.9
KEW2-1	4.0	47.5	48.5	0.0	33.5	30.5	27.0	9.0	0.0	2.0	9.6	49.5	22.2	11.6	5.1	35.0	13.5	51.5
KEW2-2	1.8	77.0	21.2	1.3	12.6	22.4	61.0	1.8	0.9	3.6	2.7	25.1	10.3	5.8	52.5	22.9	5.4	71.7
KEW3-1	4.8	39.6	55.6	0.0	27.8	34.8	26.7	10.7	0.0	2.1	9.1	35.3	27.3	19.8	6.4	45.7	7.0	47.3
KEW3-2	0.0	43.6	56.4	0.0	46.6	21.5	18.4	13.5	0.0	4.9	6.7	32.5	32.5	20.9	2.5	49.7	6.7	43.6
KEW4-1	2.0	33.3	64.6	0.0	35.0	22.3	27.9	14.7	0.0	0.5	0.0	36.9	26.3	32.3	4.0	46.0	6.1	48.0
KEW4-3	0.0	46.6	53.4	0.0	31.0	25.3	24.1	19.5	0.0	1.1	1.1	18.9	12.6	35.4	30.9	48.0	0.6	51.4
KEW5-1	2.2	42.3	55.5	0.0	31.0	30.1	33.2	5.8	0.0	2.6	2.6	49.3	25.1	16.3	4.1	15.9	0.0	84.1
KEW5-3	0.4	10.7	88.9	0.0	11.1	7.1	7.1	74.7	0.0	0.0	1.8	4.0	8.4	8.9	76.9	15.1	1.3	83.6
POT4	7.7	30.9	61.4	3.2	16.8	36.1	33.4	10.5	0.0	1.3	2.7	46.8	19.3	20.6	9.3	22.4	19.1	58.5
POT5	3.8	36.9	59.3	0.6	15.1	42.5	28.2	13.6	0.0	0.0	0.3	57.6	29.0	8.6	4.5	31.2	24.2	44.6
POT6	1.5	41.7	56.8	0.0	9.8	21.6	40.6	28.0	0.0	1.6	1.0	48.0	44.9	6.5	5.0	30.8	20.3	48.9
POT8-1	6.1	27.9	66.0	0.0	6.5	24.3	30.2	38.4	0.6	0.0	1.4	53.0	31.2	12.1	2.3	27.9	16.9	55.2
POT8-2	1.6	31.2	57.2	0.0	12.3	22.3	29.8	35.6	0.0	0.0	2.4	57.7	28.0	11.1	0.8	26.8	20.4	52.8

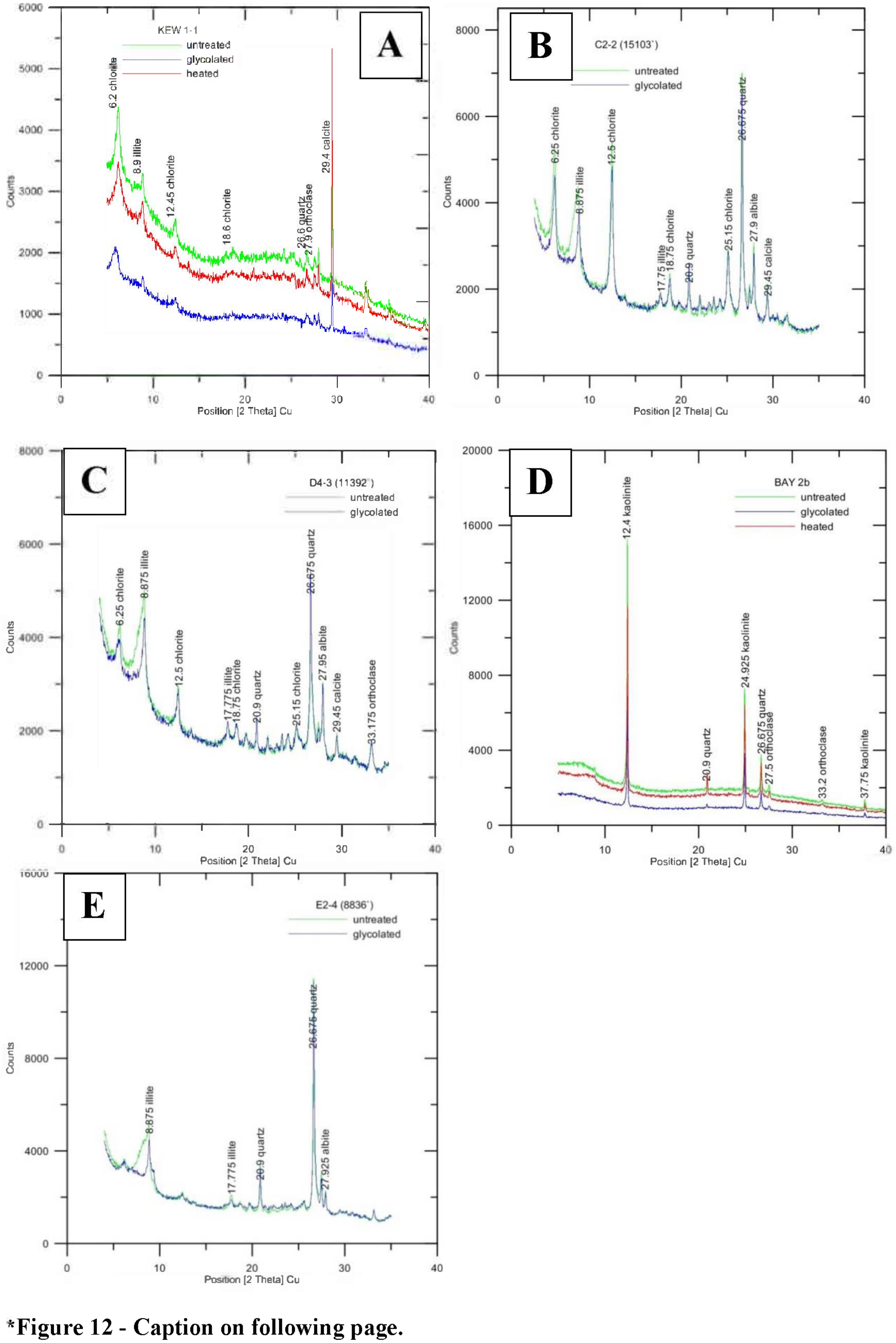

***Figure 12 - Caption on following page.**

Figure 12 (previous page). X-Ray Diffraction spectra from the clay-sized matrix fraction of sediments. A) Copper Harbor Conglomerate at Eagle River Falls sample KEW1-1 peaks for chlorite, illite, quartz, orthoclase, and calcite. B) Unit C2-2 sample from Eischeid #1 Well in Iowa displaying peaks for chlorite, illite, quartz, orthoclase, and albite. C) Unit D4-3 sample of Eischeid #1 Well with peaks for chlorite, illite, quartz, orthoclase, albite, and calcite. D) Bayfield Group BAY2 sample showing peaks for kaolinite, quartz, and orthoclase. E) Unit E (E2-4) sample of Eischeid #1 Well displaying peaks for illite, quartz, and albite.

The primary intergranular porosity of many of the MCR sections examined has been significantly reduced by the presence of carbonate cement. Throughout this text the terms "***original porosity***" will be used to describe the syndepositional intergranular porosity, even for pores that are now filled with calcite or other diagenetic minerals. The term "***residual porosity***" will be used to describe the percentage of petrographically identified porosity that was still open and visible in the samples during thin section examination. Porosity resulting from grain dislodgement "plucking" or sample fracturing that occurred during the cutting and/or polishing of the thin section samples was noted where pores were simply too large to not have been filled in by fine sediments and/or where the roundness and dimensions of the pores match well with clastic grains in the thin section. Porosity of this type is noted separately.

The "residual porosity" for the CHC sediments varied from 1.0 to 8.9% and averaged 3.7± 2.3% for eight samples that did not exhibit signs of "grain-plucking". Calcite filled fractures and pores for the same eight samples range from 6.6 to 15.9%, and averaged 11.3 ± 3.2% of the total sample volume. Thus the "original porosity" for these CHC sandstone-rich lenses averaged 14.9 ± 3.9% of the total sample volume. The large pebble to boulder sized fragments were deliberately avoided during sample collection thus the above porosity determinations are representative of only the sandy matrix portion of the CHC. Although percentage of large clasts is highly variable from outcrop to outcrop, they typically comprise ~50 volume percent of the outcrops along the Keweenawan Peninsula. Assuming that these larger clastic fragments do not contain any significant porosity, one can estimate a "residual porosity" and "original porosity" for the CHC "whole rock sequence" in the Keweenawan Peninsula at approximately 1.8 and 7.5% respectively. The CHC sections exposed at Potato Falls and Copper Harbor State Park displayed considerably lower percentages of residual porosity and calcite cement.

Table 5. Summary of minerals identified by the XRD analysis of the clay-sized fine-grained matrix portion of clastic sediments collected from the MCR.

Stratigraphic Unit	Sample ID	Phylosilicate Minrals						Non-clay Minerals					
		Kaolinite	Chlorite	Smectite	Illite	Zinwaldite		Calcite	Orthoclase	Laumontite	Albite	Dolomite	Quartz
BAYFIELD GP.	BAY2b	x							x				x
	BAY1	x							x				x
	BAY3	x							x				x
Jacobsville Fm	L'ANSE1	x			x				x				x
E Unit	E2-2	x?			x						x		x
	E2-3	x?			x						x		x
	E2-4	x?			x						x		x
CHC	KEW1-1		x		x			x	x				x
	KEW4-1		x		x			x	x				x
	KEW4-3		x					x	x				x
	KEW1-3		x					x	x				x
	KEW2-1		x					x	x	x			x
	KEW2-2		x					x	x	x			x
	KEW3-2		x					x	x				x
	KEW5-1		x					x	x				x
	KEW5-2		x					x	x				x
Nonesuch Fm	C2-2		x		x			x			x		x
	C2-3		x		x						x		x
	C2-4		x		x						x		x
	C2-5		x		x			x	x	x			x
Freda Fm	D4-1		x		x			x	x		x		x
	D4-2		x		x			x	x		x		x
	D4-3		x		x			x	x		x		x
	POT8-1		x	x	x			x	x	x			x
	CFSP2		x	x	x					x			x
UNCLASSIFIED	5396`		x										x
	5400`		x					x			x		x
	8052.5`		x			x		x			x		x
	8476-8480`		x			x		x			x		x
	10509`		x			x		x			x		x
	10666`		x								x		
	11061.5`		x								x	x	

2.2.1.2 The Nonesuch Formation and Equivalent Stratigraphic Units

Two Nonesuch Formation samples were examined by thin section from the Potato River Falls section. These samples were feldspathic-lithic arenites with Q-F-L compositions of $Q_{32.2}F_{31.1}L_{36.6}$. and $Q_{24.1}F_{21.2}L_{54.6}$. and were texturally immature to sub-mature (Figures 10b and 13; Tables 3 and 4). The plagioclase to K-feldspar ratio was approximately 1/1. Lithic fragments were almost exclusively the lithic-volcanic variety (98.4%). Other clastic components included opaque oxides, mica, and epidote (the latter formed from altered clastic grains). Iron oxide was the main cementing material (12.6%) and carbonate cement constituted only 0.3% of the total counted grains. The silty and clayey matrixes constituted 9.0% and 3.4% of the total counts respectively. Post-depositional alteration features also included alteration of feldspar and lithic volcanic grains. The degree of compaction was moderate with the vast majority of the grains displayed a concave to convex to line contact. Quartz grains were also fractured. The porosity counts represent about 2.4% and 3.4% for the POT4 and the POT5 samples, respectively (Table 3). None of the Nonesuch Formation rocks were analyzed by XRD analysis in the present study, however Li et al. (1995) found Fe-rich chlorite and mixed layer illite-smectite (phengite) in the sediments recovered from the White Pine Mine in Michigan. Li et al. interpreted these minerals as being derived from detrital and early burial diagenetic reactions, with both having survived the later hydrothermal overprint that accompanied copper mineralization.

Unit C of the Lower Red Clastics in the Amoco M. G. Eischeid #1 Well is interpreted to be an equivalent unit to the Nonesuch Formation of Oronto Group. This unit was classified as a lithic feldspathic arenite to feldspathic arenite with an abundance of calcite cement (Anderson, 1990; Figures 10c and 14; Table 6). The Q-F-L point counts for three Unit C samples averaged approximately $Q_{58}F_{18}L_{24}$ with mica and epidote also being detected. The average matrix composition from the clay size materials of Unit C detected by XRD was 49% chlorite, 41% illite, and 9% mixed layer illite/smectite layers along with detected XRD peaks for albite and calcite (Figure 12b).

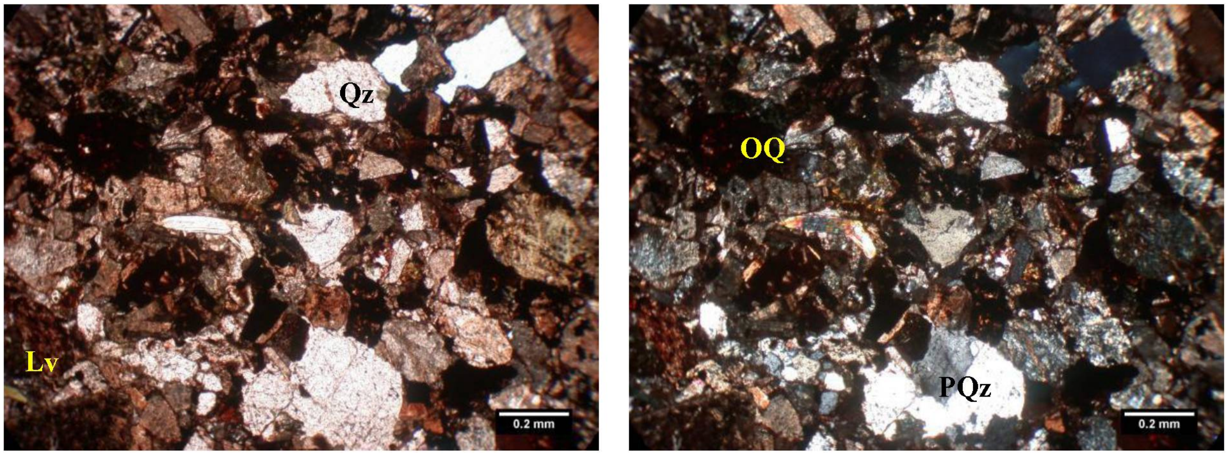

Figure 13. Thin section of Nonesuch Formation (POT4) showing monocrystalline-quartz grains (MQ), K-feldspar (K-spr), volcanic lithic fragments (Lv), and opaque mineral oxides (OQ). Plane-polarized light image (left) and cross-polarized image (right).

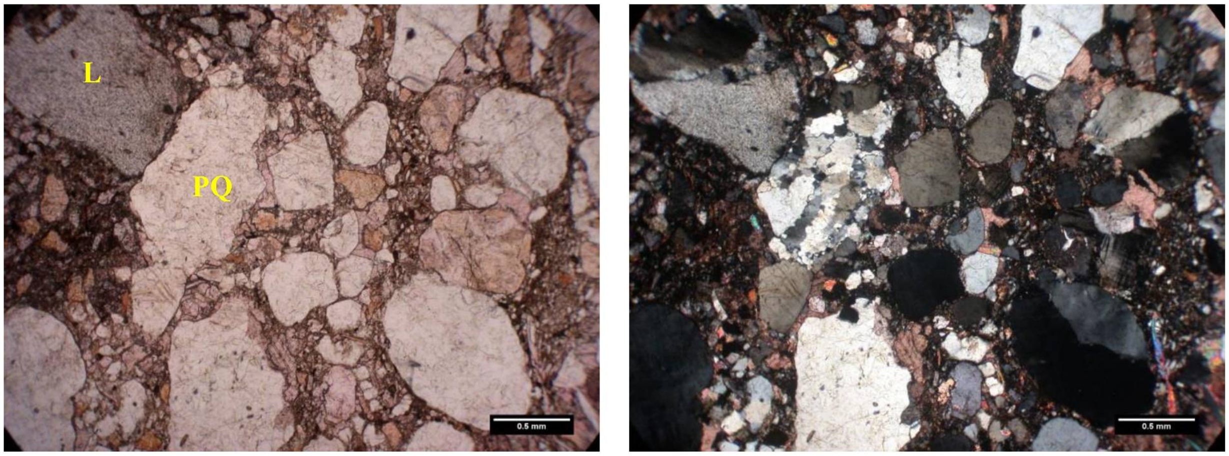

Figure 14. Thin section of unit C2 (15,107′) showing monocrystalline-quartz grains (MQ), polycrystalline-quartz (PQ), lithic fragments (L). Plane-polarized light image (left) and cross-polarized image (right).

Table 6. Petrographic investigation results based on 250 point counts from the Amoco M. G. Eischeid #1 samples, Iowa (Barnes, 1990). Qz is quartz, K-spr is K-feldspar, Plag is plagioclase, L is lithic fragment, HM is heavy minerals, M is matrix, IO is iron oxide cement, CC is carbonate cement, and Ab. C is albite cement. Only trace amounts of pore space were reported for these samples.

Unit	Depth (ft.)	Qz	K-spr	Plag	L	HM.	Mtrx.	Ab. C	CC	IO
E2	8,834.3	52	10	6	25	0	0	2	1	4
E2	8,835.6	51	16	7	23	1	0	1	0	0
E2	8,836.5	56	4	7	16	5	0	4	trace	7
D4	11,387.5	36	5	17	5	6	4	0	1	26
D4	11.392.6	38	12	14	6	11	1	0	6	12
C2	15,101.9	40	3	14	10	trace	0	0	33	0
C2	15,107.6	42	13	13	7	3	3	0	17	0
C2	15,109.0	40	12	10	5	14	3	0	15	0

2.2.1.3 The Freda Formation Sandstone and Equivalent Stratigraphic Units

Two samples from the Freda Formation collected from the Potato River Falls location were examined in thin section. These samples displayed Q-F-L distributions of $Q_{31.1}F_{17.7}L_{51.1}$ and $Q_{31.1}F_{29.4}L_{39.5}$ (Table 3; sample POT8, Figure 10b). The plagioclase to K-feldspar ratios were 1/4.3 and 1/1.8. Lithic fragments were represented by ~80% as lithic volcanic and 20% lithic sedimentary. The mineralogy of the clay-sized fraction matrix displayed abundant chlorite (~43%), smectite (~42%), and a trace of illite and laumontite (Table 5). Compaction of the samples appeared to be significant as more than half the grains displayed concave-convex contacts. A significant amount of the feldspathic grains were also altered. The grain shapes ranged between rounded to sub-rounded and the sample was medium to course-grained and texturally mature (Table 4). The residual porosity ranged between 0.0 and 1.2% and calcite was not detected as a cementing agent.

Unit D of Amoco M. G. Eischeid #1 is equivalent to the Freda sandstone of the Oronto Group. Point counting of two thin sections from the Unit D samples gave Q-F-L values that averaged approximately $Q_{56}F_{36}L_{8}$ along with minor heavy minerals (Figures 10c and 15; Table 6). Monocrystalline quartz was the dominant clast type with iron oxide as the dominant cement material (Figure 15; Anderson, 1990). The clay-sized matrix fraction averaged 64% illite, 27% mixed layer illite/smectite, 9% chlorite. The non-clay minerals, represented in the XRD spectra, were quartz, albite, K-feldspar, and calcite (Figure 12c).

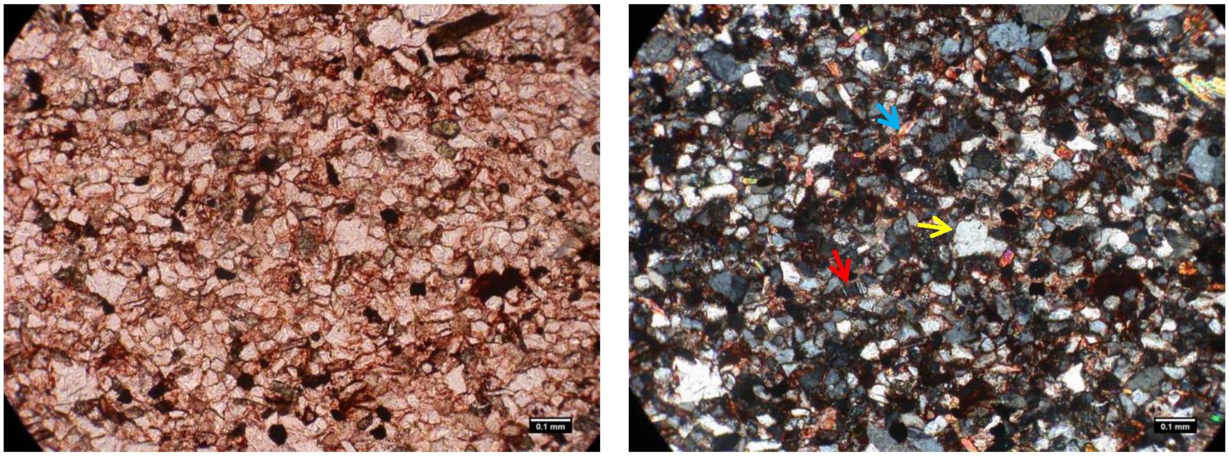

Figure 15. Thin section of Unit D (D4) showing monocrystalline-quartz grains (yellow arrow), plagioclase (red arrow), and muscovite (blue arrow). Plane-polarized light image (left) and cross-polarized image (right).

2.2.2 The Bayfield - Jacobsville Sandstones and Equivalent Stratigraphic Units

Three samples were examined from the Bayfield Group in Wisconsin and two more from the stratigraphically equivalent Jacobsville Formation in Michigan. The Q-F-L point counts for the Bayfield samples averaged approximately $Q_{82.5}F_{11}L_{6.5}$, while the two Jacobsville sample were more lithic- and feldspar-rich at approximately $Q_{66}F_{23}L_{11}$ (Figures 10d, 16, and 17; Table 7). Mica, microcline, and heavy minerals were additional minor mineral components. Lithic sedimentary grains were sourced from ~75% sedimentary and 25% volcanic provenance areas. Silt- and clay-sized matrix material comprise 1 to 7.3% of the samples, with the clay-sized material containing kaolinite as the predominant clay mineral with traces of illite (~5%) and chlorite (~7%) observed in the Jacobsville samples (Figure 12d; Table 5). Quartz, K-feldspar, and opaque mineral oxides were also detected in the clay-sized matrix fraction. The plagioclase to K-feldspar feldspar ratio was 1:18.

Post-depositional alteration features included the weathering of feldspar grains, greenish discoloration along cleavage planes, the precipitation of authigenic kaolinite clay in pores, and the formation of concave-convex compression line contacts (Table 8). The quartz grains were also heavily fractured in some samples as a result of applied tectonic stress. The “residual porosity” varied from 8.2 to 19.7% and averaged 13.4 ± 4.3% for four samples that did not exhibit evidence for “grain-plucking” during thin section preparation. The direct measurement of the primary porosity by water flooding on one sample corroborated with the point count results giving a core sample porosity values of 17.5%. Calcite filled fractures and pores for the same four samples averaged only 0.6%. Thus the "original porosity" for these CHC sandstone-rich lenses originally comprised upwards of 14.0 ± 3.9% of the total sample volume.

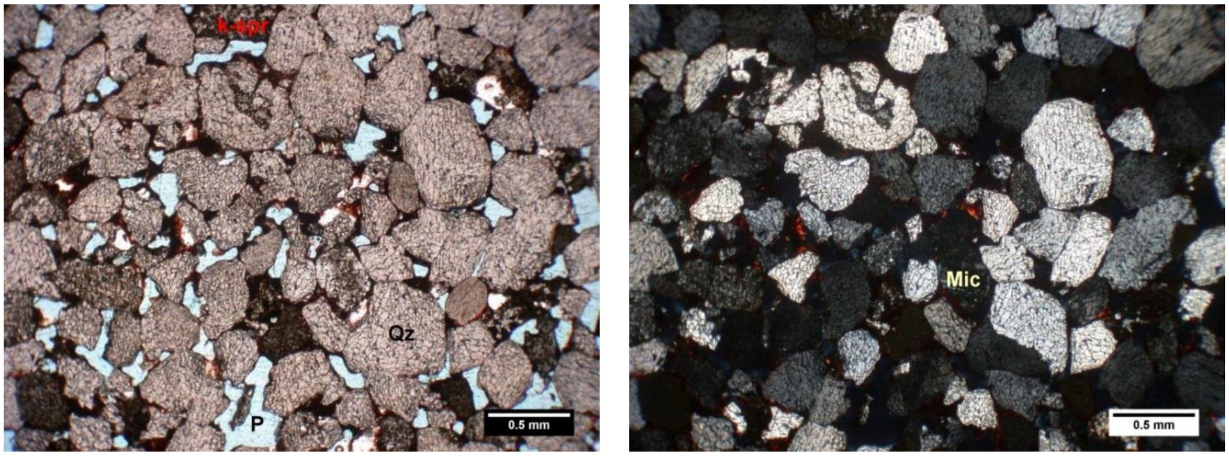

Figure 16. Thin section of Bayfield Formation BAY1 sample showing well sorted, monocrystalline-quartz "Qz", porosity "P", and microcline "Mic". Plane-polarized light image (left) and cross-polarized image (right).

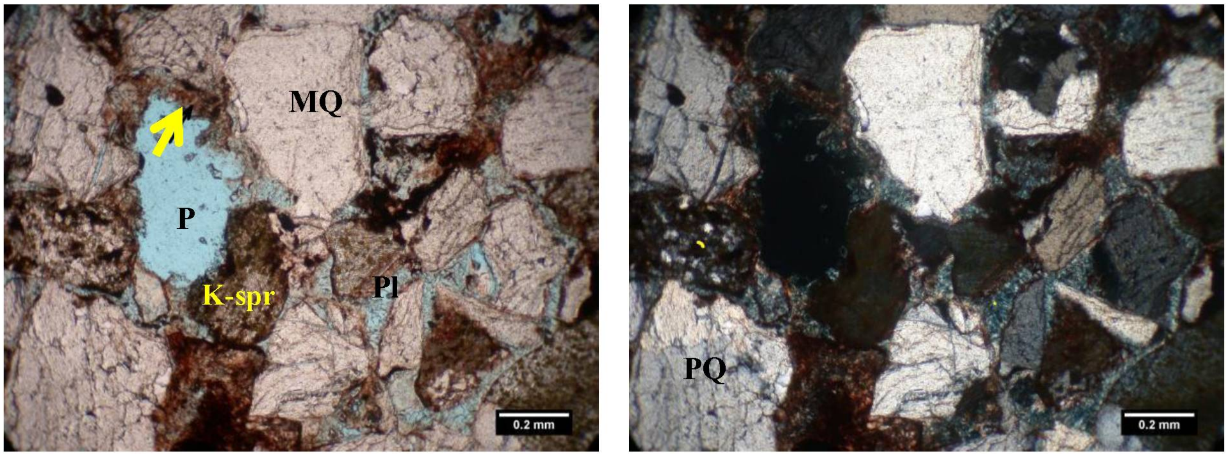

Figure 17. Thin section of Jacobsville Formation (L'ANSE 1)showing monocrystalline-quartz (MQ), polycrystalline-quartz (PQ), K-feldspar (K-spr), diagenetic clay (arrow), authigenic pore lining clay (Pl), and porosity (P). Plane-polarized light image (left) and cross-polarized image (right).

Table 7. Percentage of mineral components from surface outcrop samples of Bayfield Group and its equivalent stratigraphic units. Analysis is based upon 300 counts per thin section sample. Qz is quartz, Plag is plagioclase feldspar, K-spr is K-feldspar, L is lithic fragment, OQ is opaque mineral oxides, M is mica, HM is heavy minerals, Ep. is epidote, Uk is unknown, SM is silty matrix, CM is clayey matrix, IO is iron oxide cement, CC is carbonate cement, and P is porosity. "*" sample with grains dislodged by sample preparation thus not a true porosity.

Sample ID	UNIT	Qz	Plag	K-spr	L	OQ	M	HM	Ep.	Uk.	SM	CM	IO	CC	P	Total
BAY1	Bayfield	61.5	7.0	1.3	4.7	0.0	0.0	0.0	0.0	0.0	0.7	0.3	4.7	0.0	19.7	100
BAY2	Bayfield	64.5	7.7	0.3	5.0	0.0	0.3	0.0	0.0	0.0	3.0	4.3	0.0	0.0	14.7	100
BAY3	Bayfield	50.8	0.3	7.3	3.3	0.0	0.0	0.1	0.0	0.0	2.7	1.3	1.0	0.0	*32.2	100
L'ANSE1	Jacobsville	50.0	8.6	10.1	7.3	2.8	0.0	0.0	0.0	0.0	1.6	4.5	2.4	1.7	11.0	100
'ANSE2	Jacobsville	51.2	5.5	11.2	9.6	3.0	0.0	0.0	0.0	0.0	2.3	4.7	3.5	0.8	8.2	100

Table 8. Percentage of grain forms, roundness, contact and surface texture from surface outcrop samples of Bayfield Group and its equivalent stratigraphic units. Analysis is based upon 300 counts per thin section sample. Elg. is elongated, Eq. is equant, VA is very angular, A is angular, SA is sub-angular, R is rounded, WR is well rounded, F is fractured contact, S is sutured contact, CC. is concave-convex contact, L is line contact, P is point contact, Fl. is floated grain, C is corroded surface, Fr. is fractured surface, and Po is polished surface.

Sample ID	Grain form			Roundness						Grain contact						Surface texture		
	Elg. - Eq.	Elg.	Eq.	VA	A	SA	SA	R	WR	F	S	CC.	L.	P	Fl.	C	Fr.	Po.
BAY1	8.1	19.3	72.6	0.4	8.1	22.0	39.5	18.8	11.2	8.1	1.8	26.5	53.4	9.8	0.4	14.9	81.9	3.2
BAY2	5.6	31.0	63.4	0.5	8.4	19.5	33.0	25.6	13.0	3.7	2.8	43.9	39.3	5.6	4.7	16.4	79.9	3.7
BAY3	6.9	24.5	68.6	0.0	3.7	15.4	34.6	22.9	23.4	2.1	4.8	48.9	32.4	9.6	2.2	14.9	83.0	2.1
L'ANSE1	15.0	13.8	71.2	0.8	7.7	12.6	27.1	36.6	15.2	1.1	3.6	39.8	34.3	14.7	6.5	24.3	71.7	4.0
L'ANSE2	15.4	15.1	69.5	1.2	7.5	13.9	28.0	35.8	13.6	2.0	3.2	43.3	36.9	10.1	4.5	25.8	72.3	1.9

Unit E of the Eischeid #1 Well in Iowa is stratigraphically equivalent to the Orienta sandstone of the Bayfield Group. This unit was a moderately sorted fine to medium-grained sandstone (Anderson, 1990). The proportional composition of the main constituents averaged $Q_{58}F_{31}L_{11}$ for the three samples along with minor amounts of heavy minerals (Figures 10c and 18; Table 6). Albite, Fe-oxide, and calcite cements were the main diagenetic minerals. The fine grained matrix fraction was dominated by quartz, illite, with minor albite. The XRD peaks for chlorite were substantially subdued when compared to chlorite peaks for the Unit C and D sections (Figure 12e). The illite peak at the 8.8° two-theta position displayed shoulder-broadening to lower angle positions, suggesting the presence of mixed layer illite-smectite clays. A substantial increase in the glycolated signature of a 5.2 degree two-theta peak also suggests the presence of smectite. Smectite is often used as a drilling mud, thus it is possible that this material is present as a contaminant introduced during drilling rather than as a mineral present in the original sedimentary rock. The main diagenetic feature in the Unit E was the development of relatively minor amounts of Fe-oxide, albite, and calcite cement.

2.2.3 Texaco Poersch #1 Well

The Texaco Poersch #1 Well does not correlate directly to the MCR stratigraphic sections exposed in the Lake Superior region, thus its stratigraphic relationships need to be discussed separately. Several thin section samples were collected from an unnamed stratigraphic unit within the clastic-dominated portion of the Texaco Poersch #1 Well, in Kansas (Figure 9b). These samples were collected as well drill cutting fragments, and the lithological descriptions were determined by Berendsen et al. (1988). The samples contained a significant amount of plagioclase feldspar in arkosic to subarkosic proportions. Microcline (K-feldspar) and quartz grains were found in low abundance while volcanic lithic fragments were also recognized. The Lower Sedimentary Sequence (11,050' – 11,090') was relatively fine grained while the Upper Sedimentary Sequence is a pebbly course to medium-grained sandstone. Fractured quartz grains were also recognized, likely reflecting exposure to tectonic stresses applied on the grains. Calcite was not detected in any of the thin sections that were examined.

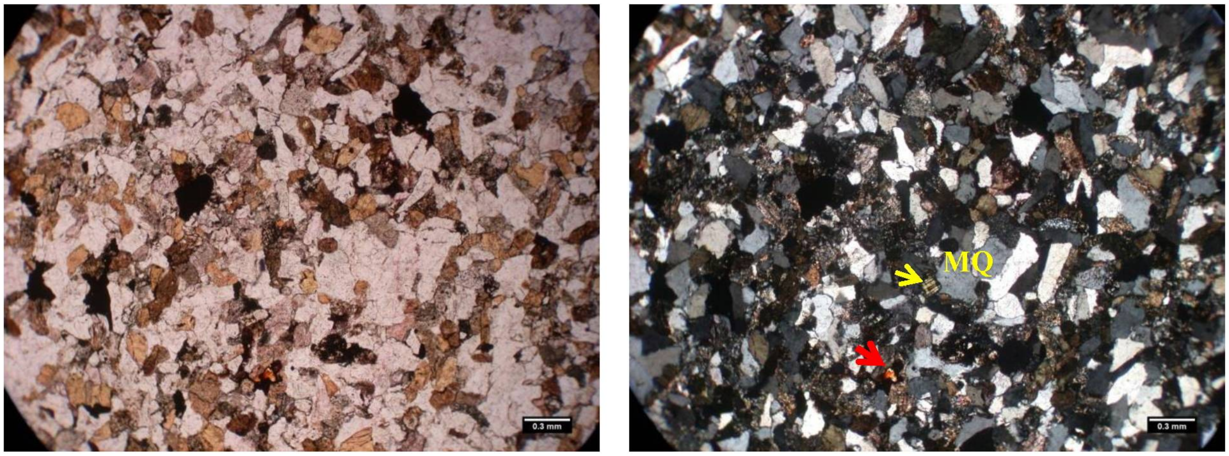

Figure 18. Thin section of Unit E (E2-4 sample) showing monocrystalline quartz grains (MQ), Heavy mineral (red arrow), and K-feldspar (yellow arrow). Plane-polarized light image (left) and cross-polarized image (right).

The XRD analysis of the clay-sized matrix fraction form the Texaco Poersch #1 samples in the present study displayed significant peaks for both clay and non-clay minerals (Figure 19). The Upper Mixed Sedimentary-Volcanic Sequence samples (UMVSS in Figure 9; 5,396′ and 5,400′) and the Middle Sedimentary Sequence samples (8052.5′, 8476-8480′, and 10,514′) had a similar mineral composition and clay content. Peaks for Ni-Mg-rich chlorite (nimite [$(Ni,Mg,Fe)_5Al(Si_3Al)O_{10}(OH)_8$]), phlogopite, [$KMg_3AlSi_3O_{10}(F,OH)_2$], Li-rich illite [zinnwaldite, $KLiFe(AlSi_3)O_{10}(OH,F)_2$], quartz, dolomite, calcite and albite were detected in both units. The Middle Sedimentary Sequence sample (10,666′) displayed large peaks for chlorite with the non-phyllosilicate minerals being represented by albite and dolomite. The Lower Sedimentary Sequence sample (11,061′) displayed only minor chlorite peaks, with larger peaks for albite and dolomite. Thin section point count analysis from two well cutting samples that were measured in this present study revealed porosity values of only 0.2% in the sample collected from the 8051.5′ (Upper Sedimentary Sequence; 7429-8806′), while the porosity was 7.9% in the Lower Sedimentary Sequence sample from 11,061′ (10,840-11,300′; Figure 9). The latter measurement corroborates a key finding of Berendsen et al. (1988) where a 22′ thick section of relatively high porosity sandstone (up to 15%) was detected by down-hole resistivity and neutron density analysis between 11,055 and 11,077′.

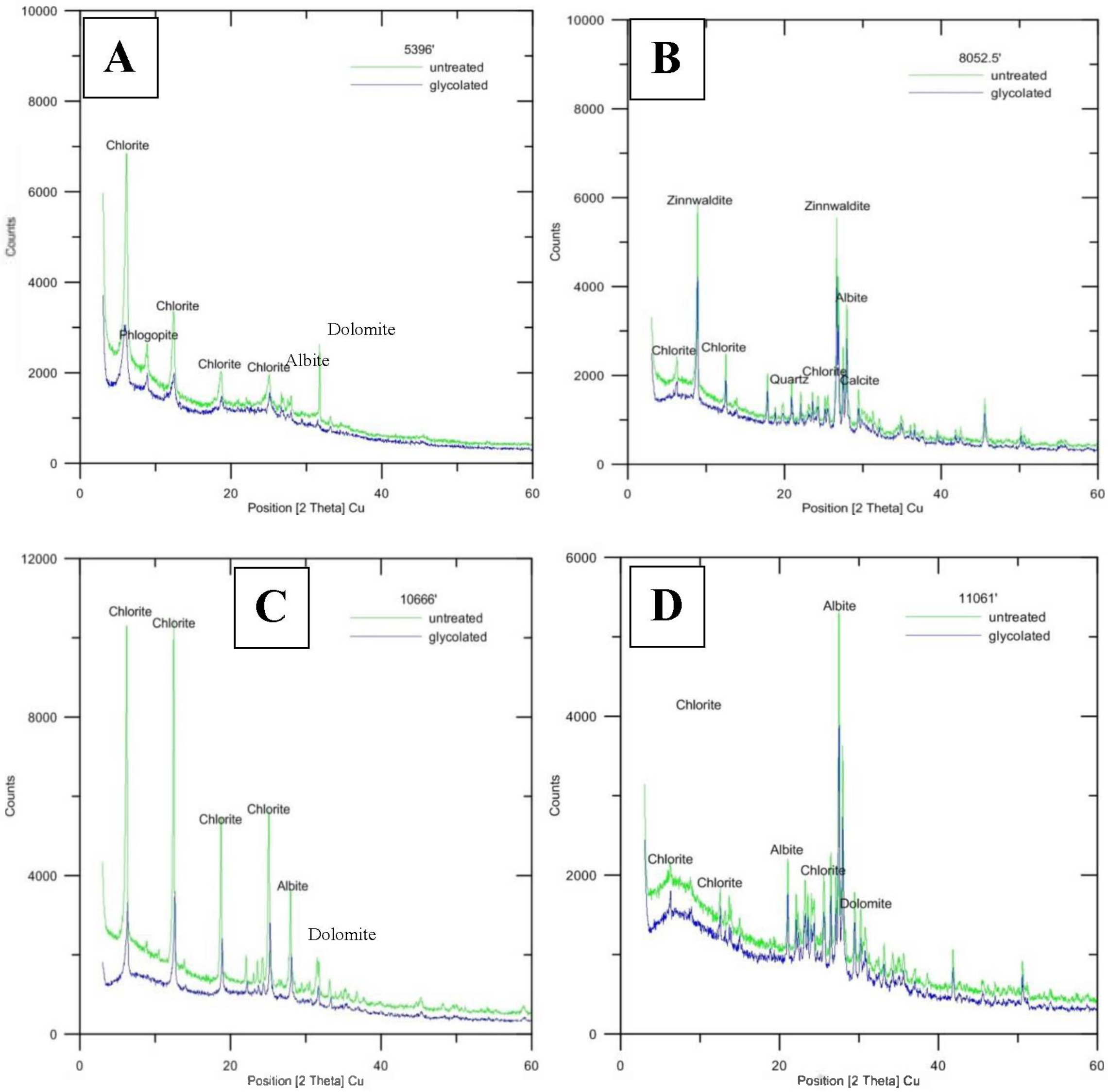

Figure 19. X-Ray Diffraction spectra from the clay-sized matrix fraction of sediments from the Texaco Poersch #1 Well in Kansas. A) Sample from 5396′ depth showing peaks for chlorite, phlogopite, albite, and dolomite. B) Sample from 8052.5′ depth showing peaks for chlorite, zinnwaldite, quartz, albite and calcite. C) Sample from 10,666′ depth showing peaks for chlorite, albite, and dolomite. D) Sample from 11,061′ depth showing peaks for chlorite, albite, and dolomite.

2.2.4 Midcontinent Rift Volcanic and Plutonic Rocks

The Keweenawan-age volcanic rocks of the MCR represent one of the largest igneous provinces in the world. Tholeiitic basalts are the major rock type although a complete compositional range exists between picrite and rhyolite. Consanguineous plutonic sequences display the same range in composition from ultramafic peridotite to felsic granites. The vast majority of the plutonic rocks have plagioclase-rich gabbro to troctolite compositions (Green, 1982a; Klewin, 1987; Klewin and Berg, 1991; Klewin and Shirey, 1992). Petrographic investigations of the Duluth Complex intrusive igneous rocks revealed the presence of up to 45% olivine along with alteration products of secondary oxides and serpentine. Clinopyroxene and secondary chlorite represent another 40%, plagioclase 8%, hornblende 3%, along with minor sericite and Fe-Ti oxides (Weiblen and Morey, 1980; Southwick et al., 1988).

2.3 Major Element Composition of the Midcontinent Rift Sequence Rocks

The chemical compositions of the major oxides (SiO_2, Al_2O_3, Fe_2O_3, CaO, MgO, Na_2O, K_2O, MnO, TiO_2, and P_2O_5) were investigated by XRF chemical analysis. The accuracy was better than 6.3% for all major oxides except the P_2O_5, which was better than 8.3%. Precision as determined by triplicate analysis of the same sample was better than 0.14% for all elements.

2.3.1 Oronto Group

A chemical analysis of samples collected from the Oronto Group and equivalent stratigraphic sections revealed the presence of a high concentration of both alkaline earth metals (i.e. CaO and MgO) and Fe (Figure 20; Table 9). The underlying volcanic and plutonic rocks displayed similar compositions (Figures 21e and f). The interaction of these elements with aqueous CO_2 species as they are released from altering rock material may promote carbonate mineralization. The combined average CaO + MgO concentrations were highest in the CHC and Nonesuch Formations (7.9 to 10.4%), then progressively decreased upsection through the Freda (4.1 wt.%), and Bayfield-Jacobsville Formations (0.6% wt.%). Carbonate minerals, which are recognized as carbonate cement in the petrographic investigations, can also produce high Loss on Ignition (LOI) values, although clay minerals and other silicates may contribute to a portion of this weight loss upon heating (Tables 3 and 5). LOI values roughly correlate to CaO + MgO concentrations, with the highest values in the CHC and Nonesuch, then progressively decreasing upsection through the Freda and Bayfield-Jacobsville Formations (Table 9).

The average of the major elements for 13 CHC samples from the Keweenawan Peninsula, was approximately 54 wt.% SiO_2, 10.4 wt.% alkaline earth metals (CaO + MgO), 11 wt.% Al_2O_3, 9 wt.% Fe_2O_3, and 6.1 wt.% alkali metals (Na_2O and K_2O; Figures 20a and b; Table 9). The high CaO content could be sourced from plagioclase, which was abundant in the volcanic rock fragments as well as the calcite cement material. Additional sources of Ca, Mg, and Fe could be from chlorite, mafic, and opaque mineral oxides. The average chemical composition of the alkaline earth metal oxides from the 3 CHC samples collected at the Potato River Falls and Copper Falls State Park locations were similar to those of the Keweenawan Peninsula with 56 wt.% SiO_2, 7.6 wt.% alkaline earth metals (CaO + MgO), 12 wt.% Al_2O_3 and Fe_2O_3, and 4.6 wt.% alkali metals (Na_2O + K_2O).

Eight samples from the Nonesuch Formation (Potato River Falls and Copper Falls State Park locations) and eight additional samples from Unit C in the Amoco M. G. Eischeid #1 Well are also similar in average composition to the CHC samples except that Al_2O_3 contents are slightly higher in the Nonesuch (13 wt. %; Figures 20c and d) and the alkaline earth metals are higher in the Unit C samples (approximately 12.2 wt. %; Tables 9 and 10).

Nine samples collected from the Freda Formation contained approximately 4.1% combined CaO + MgO (Figure 20e; Table 9), while alkali metal oxides were also about 3.8 wt.%. The Al and Fe-oxides were 11 and 5 wt.%, respectively. The correlative Unit D of the Eischeid #1 Well exhibited slightly higher alkaline earth metal oxides and alkali metal oxides relative to the Freda, at 4.5 and 5.4 wt.%, respectively (Figure 20f; Table 10; 3 samples analyzed). The Al_2O_3 content was 12 wt.% and the Fe oxide was about 4.8 wt.%. The SiO_2 constituted about 69 wt. % of the samples, and this was the highest percentage reported in the Oronto Group for the major element oxides.

2.3.1 Bayfield Group, Jacobsville Formation, and Unit E of the Eischeid #1 Well

Results from the major element XRF analysis conducted on three Bayfield Group and Jacobsville Formation samples displayed high average SiO_2 concentrations (88 wt.%) and relatively low concentrations for all other oxides (Figure 21a; Table 9). These included four samples from the Lake Superior shoreline along the Bayfield Peninsula, one sample from the Agate Falls location, and two from L'Anse. The high Si content reflects the quartz-dominated nature of this mature sedimentary sequence. The alkaline earth metals were present at an average concentration of only 0.6 wt.%, while the alkali metals were present 2.6 wt.%, with the majority being K_2O. The Al_2O_3 content was also relatively low at 4.9 wt.%, and reflected the presence of minor amounts of kaolinite clays (Table 5). The Bayfield and Jacobsville sandstones from Agate Falls were similar in overall chemical composition. The two samples collected from L'Anse, Michigan were depleted in Si relative to the Bayfield and Jacobsville-Agate Falls samples, and displayed correspondingly higher concentrations of Al, Fe, Ca, Mg, K, and Ti oxides (Table 9).

The SiO_2 content for three samples from Unit E of the Eischeid #1 Well averaged approximately 81% (Table 10) and were found to be most comparable to the Bayfield L'Anse samples in chemical composition (Tables 9 and 10). The average alkaline earth metal content was approximately 1.7 wt.% and the alkali metal oxide content was 4.2 wt.% (Figure 21c; Table 10). The chemical determinations confirm the petrographic characteristics of the Upper Red Clastics unit, which indicated the presence of texturally mature and quartz-rich sandstone. Sample E2-4 (8,834′) had a CaO concentration of only 0.7 wt. %, this correlating with the minor amount of calcite cement that was identified during petrographic thin section analysis (Table 7).

Table 9. XRF chemical composition results from surface outcrop rocks from the Lake Superior Region; The values in oxide wt. %; LOI is Loss on Ignition.

	SiO_2	Al_2O_3	Fe_2O_3	CaO	MgO	Na_2O	K_2O	MnO	TiO_2	P_2O_5	LOI
KEW1-1	55.7	12.68	8.49	6.14	1.89	3.59	3.83	0.09	1.42	0.14	6.11
KEW1-2	58.1	10.85	6.53	7.81	1.62	3.10	3.67	0.11	1.07	0.11	7.05
KEW1-3	51.8	9.19	4.15	14.70	1.36	2.43	3.28	0.09	0.49	0.07	12.34
KEW2-2	48.5	12.18	8.99	9.56	3.56	3.74	2.46	0.12	1.80	0.18	8.63
KEW3-S	50.2	12.62	14.56	4.30	3.49	3.35	2.18	0.14	4.72	0.26	3.61
KEW3-1	45.3	10.57	9.45	13.33	3.23	3.02	1.79	0.12	1.61	0.18	11.41
KEW4C	58.1	12.04	12.59	0.52	4.57	1.86	4.57	0.13	1.83	0.22	3.65
KEW4S	57.0	10.95	9.60	3.02	4.67	0.49	5.89	0.15	1.67	0.24	6.04
KEW4-1	62.7	9.86	5.24	5.97	2.44	1.46	3.91	0.06	1.00	0.14	6.74
KEW4-2	56.6	12.13	12.22	0.87	5.00	1.70	4.64	0.15	1.95	0.40	3.88
KEW4-3	50.2	7.88	8.70	11.85	3.77	0.88	3.11	0.11	1.80	0.17	11.57
KEW5-1	53.5	12.99	5.80	7.94	2.64	3.67	3.87	0.08	1.08	0.21	8.19
KEW5-2	50.9	14.51	7.08	5.75	4.52	2.46	4.80	0.08	1.15	0.19	8.30
Average	**53.7**	**11.42**	**8.72**	**7.06**	**3.29**	**2.44**	**3.69**	**0.11**	**1.66**	**0.19**	**7.50**
Stdev.	**4.6**	**1.70**	**2.93**	**4.27**	**1.17**	**1.05**	**1.10**	**0.03**	**0.97**	**0.08**	**2.85**
POT6	52.2	13.01	14.98	1.95	4.53	1.87	3.71	0.13	2.19	0.21	3.97
POT7	59.3	11.65	11.38	1.62	4.59	2.03	3.17	0.13	1.31	0.17	3.56
CFSP4	55.9	10.96	11.12	6.86	3.28	1.30	1.59	0.14	1.53	0.19	7.01
Average	55.8	11.87	12.49	3.48	4.13	1.73	2.82	0.13	1.68	0.19	4.85
Stdev.	2.9	0.85	1.76	2.40	0.60	0.31	0.90	0.00	0.37	0.02	1.54
POT1	53.1	16.10	12.12	2.19	4.39	1.65	2.67	0.19	1.27	0.19	5.95
POT2	49.3	13.04	12.38	7.49	4.12	2.08	1.23	0.20	1.82	0.21	7.69
POT3	54.3	14.35	12.83	2.69	4.62	1.88	1.87	0.19	1.64	0.20	5.04
POT4	54.0	12.68	13.77	4.06	4.23	2.04	1.39	0.16	1.77	0.21	4.78
POT4b	55.0	14.81	11.74	2.01	5.03	1.95	3.31	0.17	1.46	0.22	4.49
POT5	55.8	12.30	13.85	2.19	4.41	1.81	3.67	0.12	1.87	0.21	3.42
POT5b	53.5	13.39	13.00	1.60	6.35	2.01	3.48	0.18	1.57	0.18	4.59
CFSP3	57.9	10.64	9.92	6.43	1.58	2.82	2.71	0.10	0.96	0.14	6.20
Average	**54.1**	**13.41**	**12.45**	**3.58**	**4.34**	**2.03**	**2.54**	**0.16**	**1.55**	**0.20**	**5.27**
Stdev.	**2.3**	**1.57**	**1.18**	**2.08**	**1.24**	**0.33**	**0.89**	**0.03**	**0.29**	**0.02**	**1.22**

Table 9. (cont.)

	SiO_2	**Al_2O_3**	**Fe_2O_3**	**CaO**	**MgO**	**Na_2O**	**K_2O**	**MnO**	**TiO_2**	**P_2O_5**	**LOI**
POT8-1	54.5	12.16	12.40	5.93	3.31	0.16	1.10	0.15	2.13	0.19	7.46
POT8-2	70.2	9.29	6.74	4.57	1.42	0.11	0.77	0.06	1.02	0.15	5.24
CFSP1	55.5	16.63	10.50	1.47	3.31	0.45	3.61	0.20	1.42	0.11	6.79
CFSP2	76.1	8.97	3.72	2.44	1.07	0.78	1.54	0.09	0.85	0.05	3.72
SF1	75.5	11.20	2.02	0.89	1.06	2.33	3.51	0.03	0.60	0.13	2.01
SF2	74.7	9.58	1.65	3.42	0.94	2.03	2.16	0.07	0.70	0.12	3.88
SF3	79.0	9.37	1.66	1.34	0.95	1.78	2.42	0.05	0.67	0.12	2.33
SF4	70.6	12.25	4.12	1.01	1.79	2.13	3.57	0.06	0.82	0.16	3.10
SH	72.9	10.22	5.31	0.37	1.53	1.63	3.67	0.06	0.92	0.15	2.32
Average	**69.9**	**11.07**	**5.35**	**2.38**	**1.71**	**1.27**	**2.48**	**0.09**	**1.01**	**0.13**	**4.09**
Stdev.	**8.4**	**2.28**	**3.66**	**1.78**	**0.90**	**0.84**	**1.09**	**0.05**	**0.46**	**0.04**	**1.88**
BAY-1	92.2	3.37	1.45	0.03	0.13	0.07	1.77	0.02	0.12	0.02	0.96
BAY-2b	92.5	3.47	1.18	0.02	0.04	0.11	2.03	0.05	0.16	0.03	0.77
BAY-3	92.2	2.98	1.26	0.01	0.05	0.07	1.91	0.01	0.28	0.02	0.79
BAY-2a	93.4	2.98	0.90	0.02	0.05	0.09	1.76	0.01	0.25	0.01	0.48
AF	91.6	2.74	1.01	0.05	0.09	0.04	2.06	<0.01	0.20	0.03	0.65
L'ANSE1	76.9	9.34	3.50	0.33	1.59	0.14	4.03	0.04	0.46	0.09	3.00
L'ANSE2	76.8	9.26	3.60	0.30	1.58	0.14	4.04	0.03	0.48	0.10	2.98
Average	**87.9**	**4.88**	**1.84**	**0.11**	**0.50**	**0.09**	**2.51**	**0.03**	**0.28**	**0.04**	**1.38**
Stdev.	**7.0**	**2.81**	**1.09**	**0.13**	**0.68**	**0.03**	**0.97**	**0.01**	**0.13**	**0.03**	**1.03**

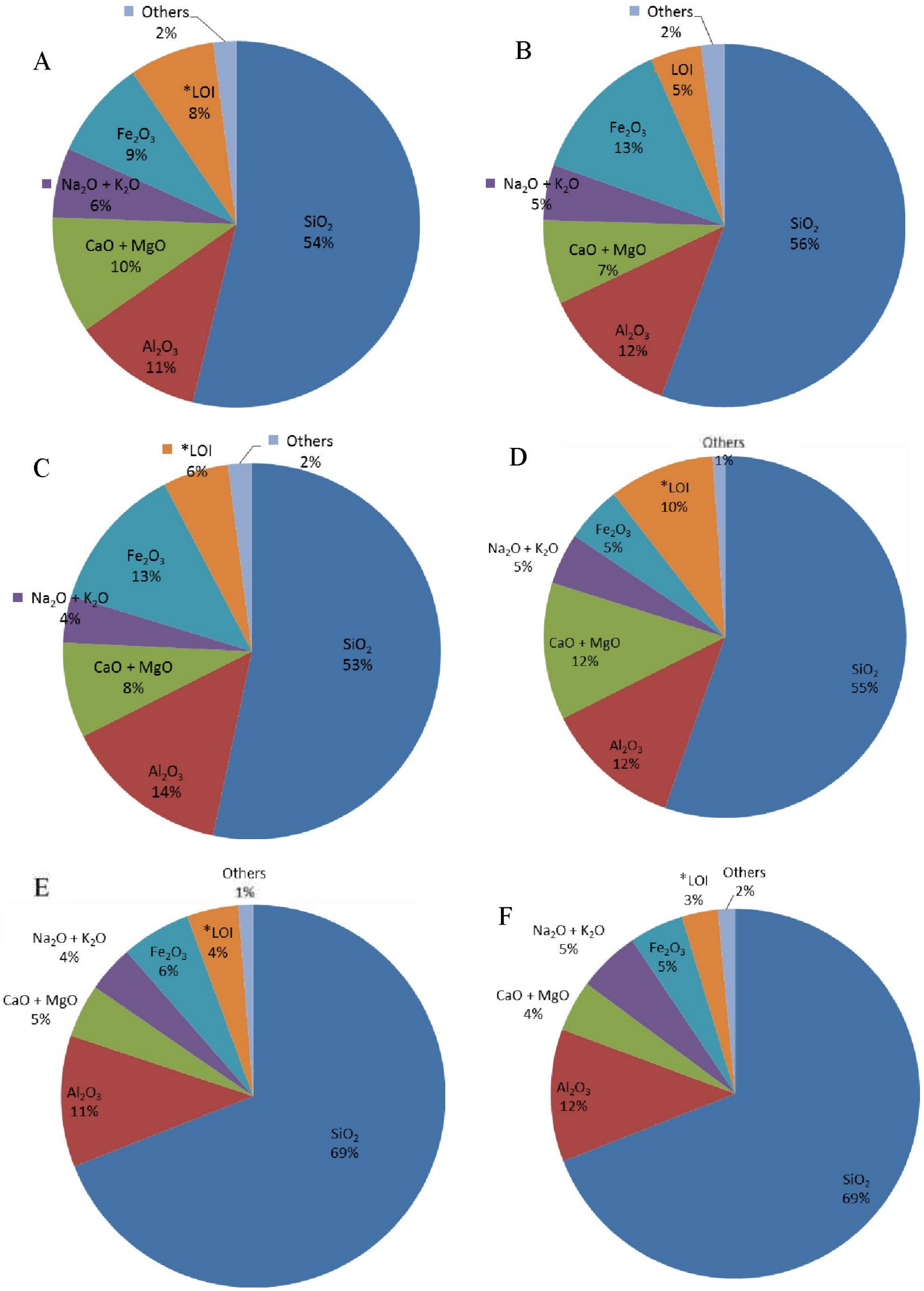

Figure 20. Average major oxide composition of Oronto Group samples: A) CHC Keweenawan Peninsula, B) CHC Potato River Falls and Copper Falls State Park, C) Nonesuch Formation Potato River Falls, D) Unit C of Eischeid #1 Well, E) Freda Formation Potato River Falls, Copper Falls State, Saxon Harbor Bay, and Superior Falls, F) Unit D of Eischeid #1 Well. "Others" includes TiO_2, P_2O_5, and Ba. LOI represents Loss on Ignition.

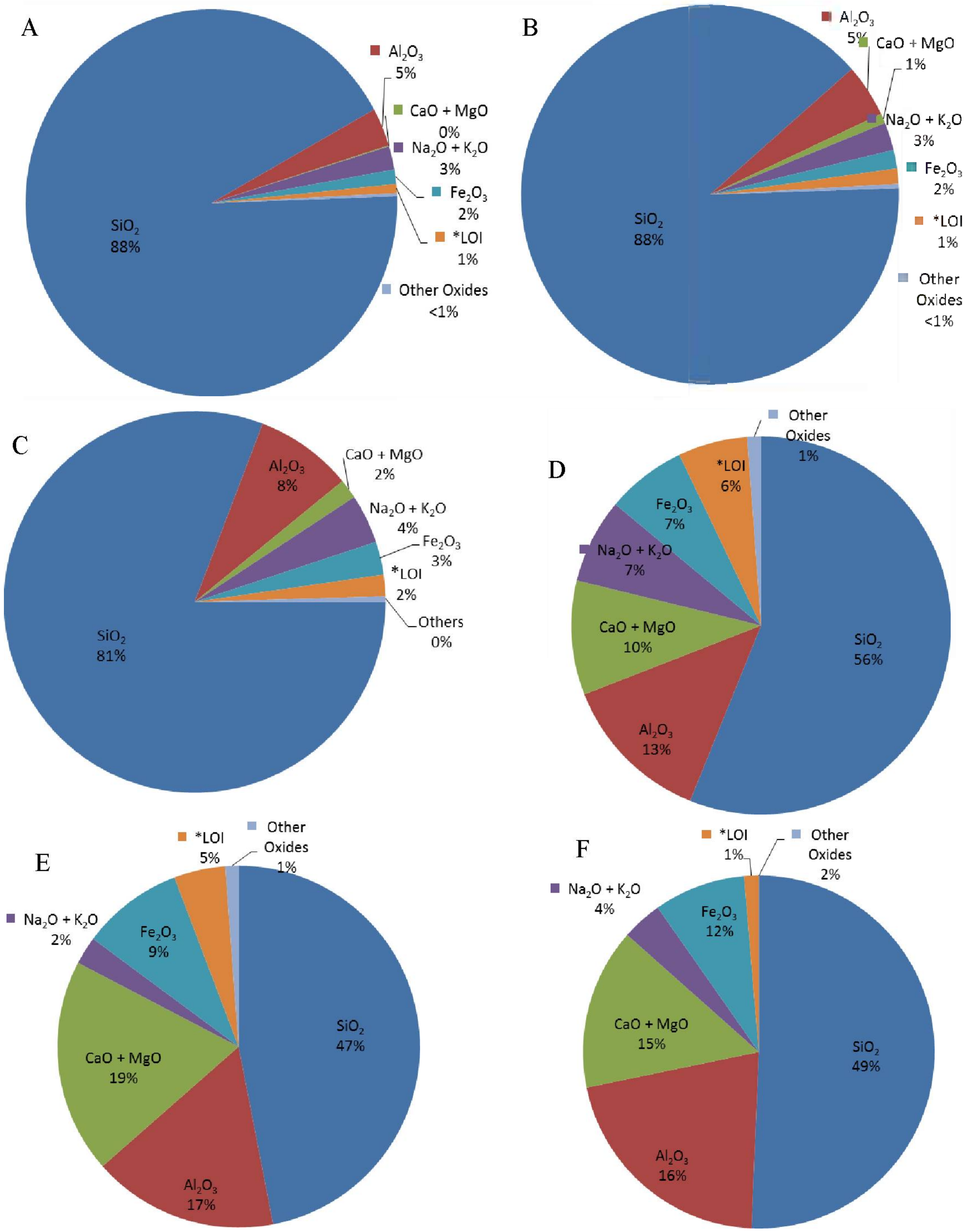

Figure 21. Average major oxide element composition of: (A) Bayfield Group, (B) Jacobsville sandstone, (C), Unit E of Eischeid #1 Well, (D), Texaco Poersch #1 Well, (E), the North Shore Volcanic Group (NSVG) including compositions from Brannon (1984), and (F) Beaver Bay Complex including data from Miller and Chandler (1997). "Others" includes TiO_2, P_2O_5, and Ba. LOI represents Loss on Ignition).

2.3.2 Texaco Poersch #1 Well, Kansas

Results from the XRF analysis of samples from the Texaco Poersch #1 Well in Kansas display variable, but generally enriched concentrations of both Ca and Mg oxides and a relatively low SiO_2 content (Figure 21d; Table 11). Higher Na_2O and K_2O concentrations reflect the presence of feldspathic, igneous lithic fragments, and/or clay enriched components. The Ca, Mg, and Fe oxide contents were also enriched, which reflected the mafic nature of the source rocks for these sediments (Berendsen et al., 1988; Figure 11b). Although sections of the Texaco Poersch #1 have not been positively correlated stratigraphically to MCR sequence lithologies exposed in the Lake Superior region, the average chemical composition of the samples analyzed here resembled those of the CHC and Nonesuch Formations in the Oronto Group suggesting the two units may be time correlative, or at least are sourced from similar provenance materials (e.g., compare Figures 20a-c to Figure 21d). A similar assessment was made by Berendsen et al.

Numerous basalt flows, immature arkosic sandstones, and one gabbroic intrusive unit also occur within the stratigraphic succession intersected in the Texaco Poersch #1 Well. The basalt and gabbroic samples are generally enriched in Fe, Ca, and Mg relative to the associated sedimentary horizons from the same well (Table 11). The 5396′ sedimentary sample most closely resembles the composition of the basalt samples, thus indicating the chemically immature nature of this unit.

2.3.3 Midcontinent Rift Volcanic and Plutonic Rocks

The North Shore Volcanic Group (NSVG) was dominated by tholeiitic basalts along with minor, but locally abundant components of felsic volcanism. Brannon (1984) found that several samples taken from Good Bay Harbor, MN, exhibited a significant enrichment in their alkaline earth element contents (~19 oxide wt.% ; Table 12) and had relatively low alkali element concentrations (Figure 21e). The NSVG was also characterized by the presence of interflow sedimentary rock units that also contain high alkaline earth element contents (11.49 oxide wt.%). Additional components included SiO_2 (52.2 wt. %), Al_2O_3 (17.0 wt. %), K_2O and Na_2O (3.0 wt. %), and Fe_2O_3 (4.2 wt. %).

The average chemical composition of the intrusive Silver Bay anorthosite and Lax Ely Gabbro were determined in this study. The Lax Lake Gabbro, Blesner Lake Gabbro, Victor Head Diabase, Beaver River Diabase, Silver Bay Gabbro, and upper Manitou Gabbro compositions were all determined by Miller and Chandler (1997). These intrusive units all exhibit an enrichment of alkaline earth metal oxides (15 wt.% average). The mafic nature of the Beaver Bay complex samples is also reflected in their low in SiO_2 content (Figure 21f; Table 12). A small portion of the intrusive sequence rocks are more felsic in nature and may reach up to 73 wt.% SiO_2, 0.7 wt.% alkaline earth elements, and 5.8 wt.% alkali elements.

Table 10. XRF results from sedimentary clastic rock samples collected from Eischeid #1 Well in Iowa. The values are in wt.%; LOI is Loss on Ignition.

	SiO_2	Al_2O_3	Fe_2O_3	CaO	MgO	Na_2O	K_2O	MnO	TiO_2	P_2O_5	LOI
C2-1	48.1	5.76	0.99	22.92	0.55	0.94	2.57	0.10	0.17	0.13	18.11
C2-2	72.1	11.00	3.13	2.77	1.70	2.50	2.22	0.04	0.90	0.31	2.79
C2-3	62.6	14.15	6.62	1.83	3.95	2.28	2.68	0.07	1.27	0.23	3.87
C2-4	58.5	16.49	7.67	0.97	4.87	1.82	3.57	0.07	0.94	0.19	4.92
C2-5	61.1	15.26	6.47	1.80	4.66	2.09	2.96	0.07	0.96	0.20	4.56
C1-6	39.3	8.42	3.56	22.95	1.85	1.75	1.79	0.09	0.57	0.13	19.25
C1-7	53.7	14.91	6.93	6.14	3.94	1.84	3.22	0.07	0.81	0.16	8.32
C1-8	47.0	11.67	4.90	14.19	2.77	1.87	2.57	0.08	0.74	0.16	13.44
Aver.	**55.3**	**12.21**	**5.03**	**9.20**	**3.04**	**1.89**	**2.70**	**0.07**	**0.80**	**0.19**	**9.41**
Stdev.	**9.7**	**3.47**	**2.16**	**8.87**	**1.46**	**0.43**	**0.52**	**0.02**	**0.30**	**0.06**	**6.21**
D4-1	71.3	10.65	5.04	2.63	1.12	2.62	2.41	0.07	1.59	0.26	2.23
D4-2	69.5	10.84	4.14	3.83	1.18	2.60	2.75	0.08	0.95	0.20	3.67
D4-3	65.7	13.16	5.06	2.73	1.88	2.91	2.98	0.08	0.95	0.19	3.50
Aver.	**68.8**	**11.55**	**4.75**	**3.06**	**1.39**	**2.71**	**2.71**	**0.08**	**1.16**	**0.22**	**3.13**
Stdev.	**2.3**	**1.14**	**0.43**	**0.54**	**0.34**	**0.14**	**0.23**	**0.00**	**0.30**	**0.03**	**0.64**
E2-2	82.8	6.99	2.11	1.57	0.44	0.82	2.58	0.04	0.34	0.07	1.87
E2-3	77.9	9.37	3.35	0.76	0.84	1.04	3.59	0.05	0.31	0.10	1.92
E2-4	80.9	8.41	2.92	0.70	0.65	0.91	3.51	0.04	0.22	0.08	1.64
Aver.	**80.5**	**8.26**	**2.79**	**1.01**	**0.64**	**0.92**	**3.23**	**0.04**	**0.29**	**0.08**	**1.81**
Stdev.	**2.0**	**0.98**	**0.51**	**0.40**	**0.16**	**0.09**	**0.46**	**0.00**	**0.05**	**0.01**	**0.12**

Table 11a. XRF results from sedimentary clastic rock samples from Texaco Poersch #1 Well in Kansas. The values in wt.%; LOI is Loss on Ignition.

Depth (ft.)	SiO_2	Al_2O_3	Fe_2O_3	CaO	MgO	Na_2O	K_2O	MnO	TiO_2	P_2O_5	LOI
5396′	49.7	15.30	7.89	4.08	9.04	2.90	2.90	0.17	1.73	0.26	5.71
5400′	22.2	7.41	17.15	26.17	2.38	2.73	0.49	0.11	1.57	0.21	20.18
8052.5′	71.6	12.55	2.17	2.91	0.51	3.43	4.15	0.04	0.27	0.07	2.41
8476-8480′	72.5	11.48	2.68	3.24	1.10	4.26	2.39	0.06	0.37	0.1	2.36
10,666′	48.9	15.41	13.21	3.36	6.34	6.47	0.46	0.33	1.27	0.24	3.83
10,509.5′	66.2	10.54	2.25	7.37	0.34	3.25	3.53	0.09	0.44	0.10	5.68
11,061.5′	62.3	18.13	2.64	1.50	0.17	4.46	9.34	0.01	0.16	0.06	1.35
Aver.	**56.20**	**12.97**	**6.86**	**6.95**	**2.84**	**3.93**	**3.32**	**0.12**	**0.83**	**0.15**	**5.93**
Stdev.	**16.44**	**3.32**	**5.68**	**8.02**	**3.22**	**1.20**	**2.78**	**0.10**	**0.62**	**0.08**	**6.02**

Table 11b. XRF results from mafic volcanic and intrusive rock samples, plus immature sedimentary arkosic units collected from the Texaco Poersch #1 Well in Kansas (data from Berendsen et al., 1988). The values are in wt.%; LOI is Loss on Ignition.

Depth (ft.)	Lithology	SiO_2	Al_2O_3	Fe_2O_3	MnO	TiO_2	CaO	MgO	Na_2O	K_2O	LOI
2860-2870′	Gabbro	43.1	16.27	11.57	0.21	1.35	10.21	8.93	1.53	3.16	3.99
3720-3730′	Basalt	42.5	14.68	13.09	0.20	1.05	7.95	14.92	1.12	1.31	3.20
4760-4770′	Basalt	46.5	15.15	13.68	0.21	2.63	8.12	5.53	2.99	2.61	3.19
6130-6140′	Basalt	46.4	14.89	12.68	0.21	2.09	8.21	6.61	2.28	4.26	2.92
7180-7190′	Basalt	42.9	14.02	16.93	0.24	2.97	7.14	5.84	2.50	4.99	3.18
8330-8340′	Arkose	58.9	13.07	3.13	0.05	0.58	7.98	9.17	2.68	3.55	0.83
8730-8740′	Gabbro	42.2	14.48	16.33	0.29	2.77	8.00	6.12	1.79	4.93	3.34
6780-6790′	Basalt	44.8	16.10	13.58	0.21	1.62	8.91	8.14	2.04	1.98	2.09
9590-9600′	Arkose	66.0	12.68	1.89	0.21	0.32	1.90	0.46	2.30	12.76	1.97
10,730-10,740′	Basalt	49.6	15.12	11.54	0.27	1.55	5.37	6.30	3.74	4.84	2.40

Table 12. XRF results from assorted igneous rock units and immature sediments exposed in the Lake Superior Region. GH-C, clastic sediment samples collected from the NSVG sedimentary interflow units; GH-B, North Shore Volcanic Group basalt; LLG, Lax Lake Gabbro; BLG, Blesner lake Gabbro; VHD, Victor Head Diabase; BBD, Beaver River Diabase; SBG, Silver Bay Gabbro; UMG, Upper Manitou Gabbro; BEV1 through BEV3, Silver Bay Anorthosite. The LLG, BLG, VHD, BBD, SBG, and UMG data are from Miller and Chandler (1997). All remaining analyses are from the present study. The values are in wt.%; LOI is Loss on Ignition.

	SiO_2	Al_2O_3	Fe_2O_3	CaO	MgO	Na_2O	K_2O	MnO	TiO_2	P_2O_5	LOI
GH-C	52.2	17.06	4.18	9.17	2.32	2.42	0.58	0.06	0.98	0.09	9.51
GH-B	46.5	15.65	10.15	10.15	8.84	2.24	0.27	0.17	1.12	0.11	4.69
LLG	47.7	16.2	12.5	9.7	4.8	2.74	0.78	0.19	2.27	0.24	1.17
BLG	49.5	18.6	9.4	10.21	3.63	3.8	0.7	0.14	1.7	0.14	2.85
VHD	49.7	15.9	11.2	9.5	5.3	2.57	0.68	0.15	1.71	0.25	1.39
BBD	48	16.7	10.5	10.4	7.8	2.3	0.35	0.17	1.31	0.14	1.71
SBG	49.5	12.4	15.4	7.8	3.6	2.85	1.17	0.23	3.25	0.47	1.42
UMG	48.3	16.3	11.6	10.2	5.7	2.58	0.56	0.18	1.64	0.14	0.99
BEV1	50.2	29.52	1.14	13.16	0.6	3.59	0.19	0.01	0.12	0.01	0.8
BEV2	50	30.44	0.78	13.63	0.35	3.34	0.19	0.01	0.11	<0.01	0.63
BEV3	50.8	28.77	1.2	12.47	0.63	3.82	0.22	0.02	0.14	<0.01	0.75

2.4 High Pressure-Temperature (HPT) Simulated Near-Field Chemical Reactions

The injection of CO_2 into a subsurface repository will result in the acidification of the subsurface aqueous groundwater near the injection point(s) (near field) due to the formation of carbonic acid. This acid will change the equilibrium conditions of the aquifer to the point where aquifer cements and clastic grains may react with the acid and dissolve. As these minerals react with the acid, they can neutralize the acidic solution while exchanging and releasing alkali and alkaline earth components for acidic protons. Acid neutralization reactions would be expected to more effective in the far field regions or over the longer time periods. Carbonate mineralization reactions may be induced by the released alkaline earth elements and increasing pH. In order to replicate these water + rock + CO_2 interactions, we selected 64 samples from the MCR rocks that were sliced into one to two millimeter thick wafers, polished them to a 600 grit finish, and reacted with deionized water + CO_2 at high pressure-temperature (HTP) conditions. The reactants were placed at 90°C in Teflon-vessels for various lengths of time between 2 and 246 days. Leachate fluids were collected and checked for pH, Eh, and major element release.

2.4.1 Oronto Group

HPT testing on the samples from the Oronto Group and its equivalent stratigraphic units revealed a general trend of sample weight loss during the corrosion reactions (up to 1.21%) although a few samples gained a small amount of weight, likely corresponding to the formation of hydrous or carbonate phases. The pH taken from the blank sample experiments (deionized water + CO_2 dry ice) ranged between 3.8 and 4.0. The pH range of the leachate solutions after reaction with the rock samples included in the experiments ranged between 5.0 and 6.4 (Table 13a). The higher pH values reflect more extensive neutralization of the carbonic acid due to reactions with the host rock minerals, however all samples with the CHC samples induced a significant positive increase in pH during reaction. The Eh of the leachate solutions ranged between +31 and +73 mV.

The ions concentration data displays variable release amounts from each individual sample (Table 13b). Elemental release, and rate of release, is dependent on many factors including test duration, surface area of the solid, temperature, element of interest, corrosion resistance of the solid mineral materials. In addition, precipitation reactions involving the formation of alteration minerals on the reacted samples or test vessel components will be reflected in the reacted solids, but the released components would not appear in the solution.

The released Si concentration varied from between 26 and 141 ppm for the CHC, 70 and 121 ppm for the Nonesuch, and 28 and 164 ppm for the Freda Formation samples (Table 13b). Although Si may be derived from the corrosion of quartz, it is more likely being derived from hydrolysis reactions with of feldspars, pyroxenes, and other silicate minerals as quartz is relatively inert in the presence of acidic weathering solutions (Dove and Crerar, 1990; Bennett, 1991; Dove, 1999). The concentration of Si was also converted into molal concentration, and then normalized to the surface area of the sample, and reaction duration and expressed as moles/cm^2.day elemental release. The initial concentration of SiO_2, obtained from the XRF analysis of the CHC solid samples was used in these calculations (54 - 56 wt.% SiO_2; Table 9). Normalized release rates of Si were low for all samples: between 4.62×10^{-6} and 2.06×10^{-5} moles/cm^2.day for the CHC, 5.96×10^{-6} 4.01×10^{-5} moles/cm^2.day for the Nonesuch, and 1.55×10^{-7} and 4.87×10^{-5} moles/cm^2.day for the Freda sandstone (Figures 22 through 24, respectively; Tables 13c and d).

Table 13a. HTP corrosion test solution data for Oronto Group samples and its equivalent stratigraphic units following reaction in a $CO_2 + H_2O$ system at 90°C. KEW, POT8, and CFSP are Copper Harbor Conglomerate; POT2, POT4, and POT5 are Nonesuch Formation; SF and SH are Freda sandstone; C2 is Unit C; and D4 is Unit D.

Sample ID	Location	Surface area (cm^2)	% weight loss/gain	pH final	Eh (mV)	Time (days)
Copper Harbor Conglomerate						
KEW1-1	Keweenaw P., MI	5.6	-0.48%	6.08	+50	6.0
KEW4-2	Keweenaw P., MI	4.8	-0.20%	5.87	+67	87.8
KEW5-1	Keweenaw P., MI	5.6	-0.45%	5.00	+31	101.9
CFSP4	Copper F. P., WI	5.0	+0.12%	5.78	+68	48.8
Nonesuch Formation						
POT2	Potato R. F., WI	5.0	-0.80%	6.43	+33	43.0
POT4	Potato R. F., WI	4.3	-0.03%	6.22	+67	25.0
POT5-1	Potato R. F., WI	6.0	-0.65%	6.42	+72	34.0
Freda Formation						
SF1-1	Superior F., WI	8.5	-0.08%	5.78	+68	59.9
SF3-1	Superior F., WI	12.1	-0.12%	5.86	+65	59.9
SH1	Saxon H., WI	11.8	+ 0.02%	5.38	+91	59.9
SF1-2	Superior F., WI	10.1	-0.02%	6.16	+47	59.9
SF3-2	Superior F., WI	12.4	-0.06%	5.82	+67	59.9
SH2	Saxon H., WI	11.7	-0.00%	5.38	+93	59.9
Eischeid #1 Well – Unit C						
C2-1	Eischeid #1, IA	6.3	-1.21%	6.24	+45.7	26.5
C2-2	Eischeid #1, IA	6.2	-0.87%	5.77	+58.2	43.0
C2-3	Eischeid #1, IA	7.0	+0.01%	5.65	+80.8	26.5
C2-5	Eischeid #1, IA	4.5	-0.46%	5.71	+84.0	14.0
Eischeid #1 Well – Unit D						
D4-1	Eischeid #1, IA	7.2	-0.79%	5.85	+53	43.0
D4-2	Eischeid #1, IA	3.8	-0.94%	6.00	+66.5	18.0
POT8-2	Potato R. F., WI	4.8	-0.08%	5.80	+78	25.0

Table 13b. Chemical composition of leachate solutions collected after opening the HPT vessels for Keweenawan Supergroup samples (KEW), Potato River Falls (POT), Copper Falls State Park (CFSP), Superior Falls (average of two duplicates; SF), Saxon Harbor (average of two duplicates; SH), Unit C (C2), and Unit D (D4). Values are in ppm (mg/kg).

Formation	Sample	Si	Al	Fe	Ca	Mg	K	Na	Mn
CHC	KEW1-1	26.0	< 0.1	< 0.1	702	39.0	17.0	4.3	7.8
	KEW4-2	64.0	< 0.1	< 0.1	796	166	23.0	4.8	3.2
	KEW5-1	74.0	< 0.1	< 0.1	915	134	22.0	12.0	3.1
	POT5-1	51.0	< 0.1	< 0.1	600	120	19.0	7.7	0.1
	CFSP4	141	< 0.1	< 0.1	282	109	51.0	1.0	10
Nonesuch and Unit C	POT2	70.0	< 0.1	< 0.1	459	128	32.0	4.4	0.1
	POT4	121	< 0.1	< 0.1	230	81.0	15.0	2.9	17
	C2-1	28.3	< 0.1	0.1	267	35.3	16.3	15.9	0.1
	C2-2	44.6	< 0.1	0.1	377	8.8	5.5	5.5	1.2
	C2-3	44.6	< 0.3	0.8	44.6	27.8	9.3	14.1	1.5
	C2-5	10.8	< 0.1	0.1	176	13.8	8.5	13.7	0.8
Freda and Unit D	POT8-2	164	< 0.1	< 0.1	230	16.0	29.0	5.4	2.1
	SF1-1	41.2	< 0.1	< 0.1	223	36.7	9.0	18.4	2.0
	SF1-2	37.3	< 0.1	< 0.1	159	29.7	8.2	16.0	0.6
	SF3-1	41.2	< 0.1	< 0.1	288	37.6	6.8	15.9	1.7
	SF3-2	27.9	< 0.1	< 0.1	168	20.3	5.9	12.9	0.3
	SH-1	36.7	< 0.1	< 0.1	67.0	32.2	9.5	13.2	1.7
	SH-2	37.0	< 0.1	< 0.1	58.0	29.0	8.4	12.2	2.2
	D4-1	68.1	< 0.1	0.1	452	14.8	12.0	12.3	4.0
	D4-2	36.3	< 0.1	0.1	486	7.0	7.6	5.6	3.5

Table 13c. The molal concentration (mole/kg) of leachate solutions collected after Oronto Group samples after HTP testing.

	Si	Al	Fe	Ca	Mg	Na	K	Mn
Copper Harbor Conglomerate								
KEW1-1	9.26E-04	<3.71E-06	<1.79E-06	1.75E-02	1.60E-03	1.10E-04	7.39E-04	1.42E-04
KEW4-2	2.28E-03	<3.71E-06	<1.79E-06	1.99E-02	6.83E-03	1.23E-04	1.00E-03	5.82E-05
KEW5-1	2.63E-03	<3.71E-06	<1.79E-06	2.28E-02	5.51E-03	3.07E-04	9.57E-04	5.64E-05
POT5-1	1.82E-03	<3.71E-06	<1.79E-06	2.99E-03	3.17E-04	4.86E-04	<4.35E-06	1.82E-06
CFSP4	5.02E-03	<3.71E-06	<1.79E-06	2.72E-03	4.11E-05	1.30E-03	4.35E-04	1.82E-04
Nonesuch Formation and Unit C								
POT2	2.49E-03	<3.71E-06	<1.79E-06	3.19E-03	1.81E-04	8.18E-04	<4.35E-06	1.82E-06
POT4	4.31E-03	<3.71E-06	<1.79E-06	2.02E-03	1.19E-04	3.84E-04	7.39E-04	3.09E-04
C2-1	1.01E-03	<3.71E-06	<1.79E-06	6.67E-03	1.45E-03	4.07E-04	7.09E-04	1.82E-06
C2-2	1.59E-03	<3.71E-06	<1.79E-06	9.40E-03	3.62E-04	1.41E-04	2.39E-04	2.18E-05
C2-3	1.59E-03	1.11E-05	1.43E-05	1.11E-03	1.14E-03	3.61E-04	4.05E-04	2.73E-05
C2-5	3.85E-04	<3.71E-06	<1.79E-06	4.39E-03	5.68E-04	3.50E-04	3.70E-04	1.46E-05
Freda Formation and Unit D								
POT8-2	5.84E-03	<3.71E-06	<1.79E-06	5.74E-03	6.58E-04	1.38E-04	1.26E-03	3.82E-05
D4-1	2.42E-03	<3.71E-06	<1.79E-06	1.13E-02	6.09E-04	3.15E-04	5.22E-04	7.28E-05
D4-2	1.29E-03	<3.71E-06	<1.79E-06	1.21E-02	2.88E-04	1.43E-04	3.31E-04	6.37E-05
SF1-1	1.47E-03	<3.71E-06	<1.79E-06	5.57E-03	1.51E-03	4.71E-04	3.91E-04	3.64E-05
SF1-2	1.33E-03	<3.71E-06	<1.79E-06	3.98E-03	1.22E-03	4.09E-04	3.57E-04	1.09E-05
SF3-1	1.47E-03	<3.71E-06	<1.79E-06	7.18E-03	1.55E-03	4.07E-04	2.96E-04	3.09E-05
SF3-2	9.93E-04	<3.71E-06	<1.79E-06	4.19E-03	8.35E-04	3.30E-04	2.57E-04	5.46E-06
SH-1	1.31E-03	<3.71E-06	<1.79E-06	1.67E-03	1.32E-03	3.38E-04	4.13E-04	3.09E-05
SH-2	1.32E-03	<3.71E-06	<1.79E-06	1.45E-03	1.19E-03	3.12E-04	3.65E-04	4.00E-05

Table 13d. Surface area normalized release results from solutions collected from Oronto Group sample high-pressure-temperature corrosion test vessels. Values in moles/cm^2.d.

Moles/cm^2.d	Si	Al	Fe	Ca	Mg	Na	K	Mn
Copper Harbor Conglomerate								
KEW1-1	2.76E-05	<1.10E-07	<5.33E-08	5.21E-04	4.78E-05	3.27E-06	2.20E-05	4.23E-06
KEW4-2	5.41E-06	<8.79E-09	<4.25E-09	4.71E-05	1.62E-05	2.91E-07	2.37E-06	1.38E-07
KEW5-1	4.62E-06	<6.49E-09	<3.14E-09	4.00E-05	9.66E-06	5.38E-07	1.68E-06	9.89E-08
POT5-1	8.90E-06	<1.82E-08	<8.78E-09	1.47E-05	1.55E-06	2.38E-06	<2.13E-08	8.92E-09
CFSP4	2.06E-05	<1.52E-08	<7.34E-09	1.11E-05	1.69E-07	5.35E-06	1.78E-06	7.46E-07
Nonesuch Formation and Unit C								
POT2	1.16E-05	<1.72E-08	<8.33E-09	1.49E-05	8.42E-07	3.81E-06	<2.02E-08	8.47E-09
POT4	4.01E-05	<3.45E-08	<1.67E-08	1.88E-05	1.11E-06	3.57E-06	6.88E-06	2.88E-06
C2-1	6.04E-06	<2.22E-08	<1.07E-08	3.99E-05	8.70E-06	2.44E-06	4.25E-06	1.09E-08
C2-2	5.96E-06	<1.39E-08	<6.72E-09	3.53E-05	1.36E-06	5.28E-07	8.97E-07	8.19E-08
C2-3	8.56E-06	5.99E-08	7.72E-08	6.00E-06	6.17E-06	1.94E-06	2.18E-06	1.47E-07
C2-5	6.10E-06	<5.88E-08	<2.84E-08	6.97E-05	9.01E-06	5.56E-06	5.87E-06	2.31E-07
Freda Formation and Unit D								
POT8-2	4.87E-05	<3.09E-08	<1.49E-08	4.78E-05	5.49E-06	1.15E-06	1.05E-05	3.19E-07
D4-1	7.83E-06	<1.20E-08	<5.78E-09	3.64E-05	1.97E-06	1.02E-06	1.69E-06	2.35E-07
D4-2	1.89E-05	<5.42E-08	<2.62E-08	1.77E-04	4.21E-06	2.09E-06	4.83E-06	9.31E-07
SF1-1	3.33E-07	<8.43E-10	<4.07E-10	1.27E-06	3.43E-07	1.07E-07	8.9E-08	8.28E-09
SF1-2	2.54E-07	<7.09E-10	<3.43E-10	7.61E-07	2.34E-07	7.83E-08	6.82E-08	2.09E-09
SF3-1	2.34E-07	<5.92E-10	<2.86E-10	1.15E-06	2.47E-07	6.49E-08	4.72E-08	4.94E-09
SF3-2	1.55E-07	<5.78E-10	<2.79E-10	6.53E-07	1.3E-07	5.14E-08	4E-08	8.51E-10
SH-1	2.14E-07	<6.07E-10	<2.93E-10	2.74E-07	2.17E-07	5.53E-08	6.77E-08	5.07E-09
SH-2	2.18E-07	<6.12E-10	<2.96E-10	2.39E-07	1.97E-07	5.15E-08	6.03E-08	6.61E-09

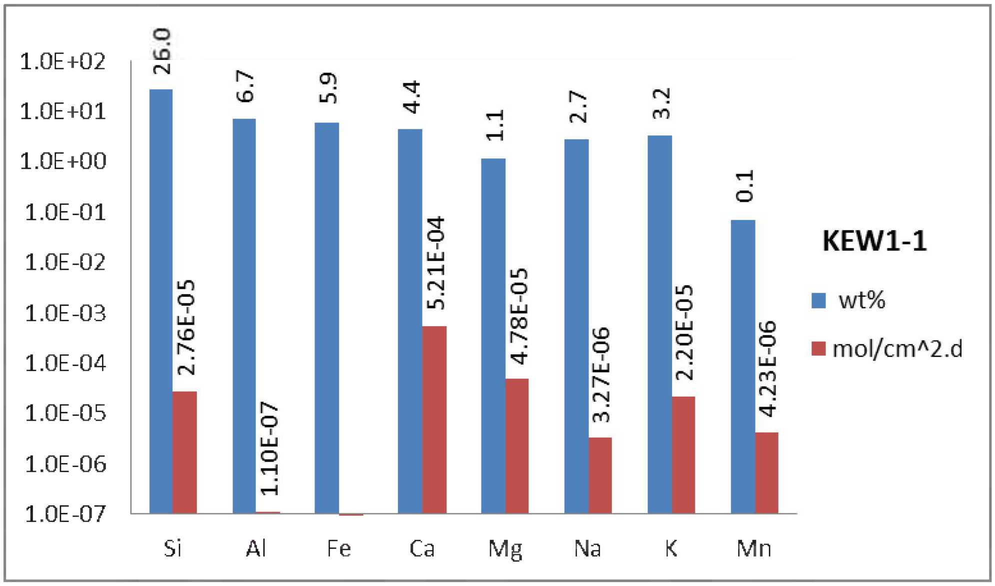

Figure 22. Comparison between the dissolution rate (red bars, in mole/m^2.sec) and the concentration of elements in the solid (blue bars, as element wt.% in the solid) for KEW1-1 sample (CHC) showing that the highest release rate is associated with Ca, even though Si, Al, and Fe are present in greater concentrations in the solid. Dissolution testing was conducted at 90^{o}C $H_2O + CO_2$ solution for 6 days.

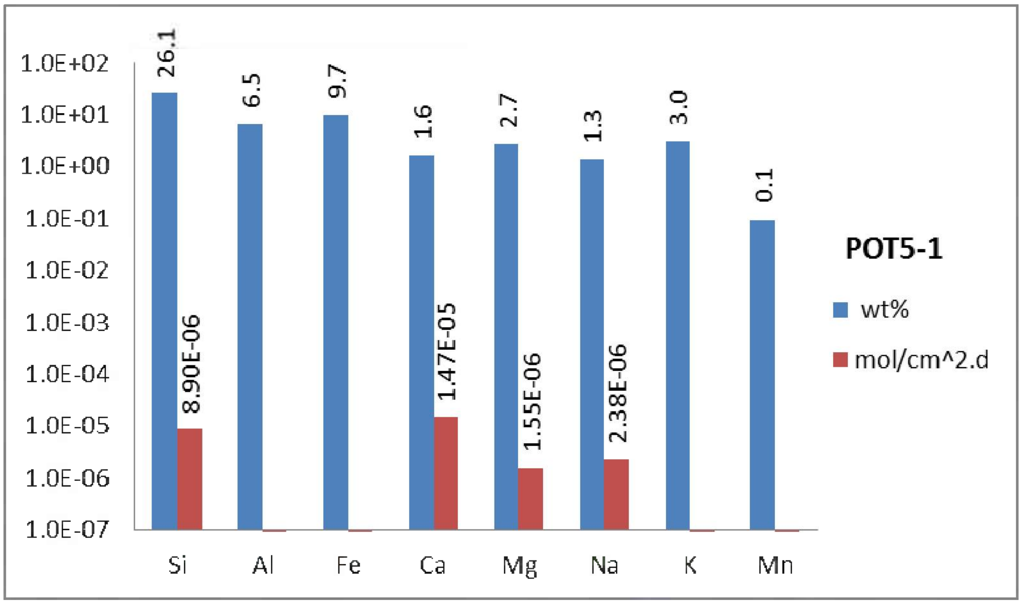

Figure 23. Comparison between the dissolution rate (red bars, in mole/m^2.sec) and the concentration of elements in the solid (blue bars, as element wt. % in the solid) for POT5-1 (Nonesuch Formation). The fastest release rate is associated with Ca. Dissolution testing was conducted at 90^{o}C $H_2O + CO_2$ solution for 34 days.

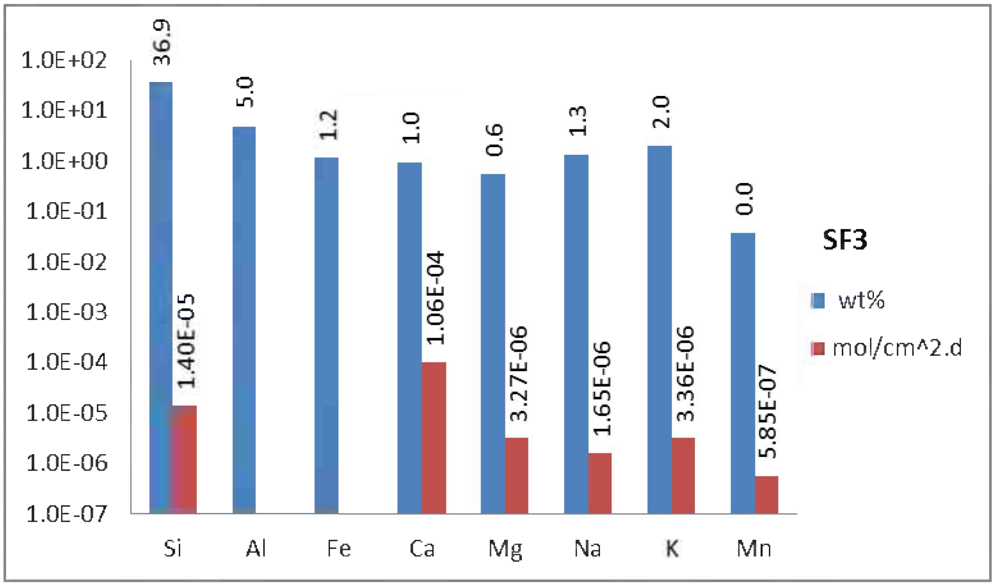

Figure 24. Comparison between the dissolution rate (red bars, in mole/m^2.sec) and the concentration of elements in the solid (blue bars, as element wt. % in the solid) for SF3-1 and SF3-2 samples (Freda Formation). The fastest release rate is associated with Ca. Dissolution testing was conducted at 90°C H_2O + CO_2 solution for 59 days.

The highest concentration release of Ca at 915 ppm came from the CHC sample KEW5-1 sample, while the lowest was from the CFSP4 sample at 282 ppm. The Ca release from the Nonesuch Formation and the Unit C samples ranged between 45 (sample C2-3) and 459 ppm (POT2). The Freda sandstone leachate fluids had a Ca concentrations ranging between 451 and 486 ppm (Table 13b). Calcium is important for geologic sequestration because of its ability to react with carbonate to produce calcite, aragonite, vaterite, or other mixed composition of alkali and alkaline earth carbonate minerals. Most Oronto Group samples released the highest amount of Ca into the solution as a result of the presence of abundant calcite cementation and vein infilling (Section 2.2.1). Silicate minerals such as plagioclase feldspars, clays, epidote, pyroxenes and amphiboles may contribute to the release as well. The high dissolution rate of calcite cement suggests that additional porosity could be created in these rock units as a result of CO_2 acidification. Samples taken from the CHC also displayed very high normalized Ca release rates. For example, the release rate was approximately 5.2×10^{-4} moles/cm^2.day for the KEW1-1 (Figure 22a) sample and 4.71×10^{-5} moles/cm^2.day for the KEW4-2 sample (Table 13d). The molal release rate of the Ca was approximately 10-times greater than the release of either Mg or Si, especially for the samples that contained a high percentage of calcite cement (e.g., 15.9% calcite for KEW1-1; Table 13c). The Nonesuch Formation and Unit C samples exhibited Ca release rates that ranged between 6.0×10^{-6} and 6.97×10^{-5} moles/cm^2.day (Figure 23, Nonesuch only). The Freda sandstone sample also displayed high release rates for Ca at 2.39×10^{-7} to 1.77×10^{-4} moles/cm^2.day (Figure 24).

Magnesium concentrations ranged between 39 and 166 ppm for the CHC, 9 and 128 ppm for the Nonesuch, and 7 to 37 ppm for the Freda Formation samples (Table 13b). In order to determine the Ca:Mg ratio of the cement material, we isolated calcite cement from the KEW1 and KEW4 samples by crushing and hand picking under a microscope, weighed them, digested the samples in a 5% nitric acid solution, and then analyzed the solution by ICP-OES. The average mole fraction of Ca:Mg in the cement was 99.5/0.5. Thus the cement material in Keweenawan Peninsula samples was dominated by low Mg-calcite and any release of Mg to solution is more likely to be dominated by the dissolution rate of silicate minerals such as the pyroxene, amphibole, and mica group minerals. Magnesium is important because it can be involved in the precipitation of dolomite [$CaMg(CO_3)_2$] or magnesite ($MgCO_3$) after complexing with CO_3^{2-}. Normalize release rates of Mg were between 1.69×10^{-7} to 4.78×10^{-5} moles/cm^2.day for the CHC, 8.42×10^{-7} to 9.17×10^{-6} moles/cm^2.day for the Nonesuch (including Unit C-Eischeid #1 Well), and 1.30×10^{-7} to 5.49×10^{-6} moles/cm^2.day for the Freda sandstone (and Unit D Eischeid #1 Well; Figures 22 through 24, respectively; Tables 13c and d). Overall, molal Mg release rates were ~10-fold lower than Ca for the CHC and Freda sandstones, while release rates for the two elements were more comparable for the Nonesuch Formation samples.

Little correlation existed between the amounts of K and Na in the rock samples versus the amount released into the solution (Tables 9 and 13b). Potassium and sodium are often released from feldspars, phyllosilicates, zeolites, and potentially other minerals during corrosion *via* ion exchange processes with H^+ ions or other alkali and alkaline earth elements present in solution. Thus the process that leads to their release into solution could contribute to the acid buffering capacity of the rock. The CHC samples released Na to levels that maximized at 1 to 12 ppm, while K was at 17 to 51 ppm. The Nonesuch and Unit C samples released Na to a level of 4 to 16 ppm, while K was between 5.5 and 32 ppm. The Freda sandstone and the Unit D samples (9 samples) released between 5.4 and 18 ppm Na, and between 5.9 and 29 ppm K. Normalized release rates ranged from $5.50 \text{ X } 10^{-6}$ to $5.14 \text{ X } 10^{-8}$ and $2.20 \text{ X } 10^{-5}$ to $4.20 \text{ X } 10^{-8}$ moles/cm^2.d for the same two elements (Figures 22 through 24, respectively; Tables 13c and d).

Aluminum, Mn, and Fe release was generally low for all Oronto Group samples, with Al and Fe concentrations often falling below the analytical detection limit of the ICP-OES instrument (Table 13b). The low concentrations for these elements are likely due to their rapid incorporation into alteration phases. Because both Mn and Fe exhibit significantly lower solubilities in non-acidic conditions and with their oxidized forms (Mn^{4+} and Fe^{3+}), we can conclude that the reactions during the tests were not highly reducing nor acidic, a conclusion supported by the Eh-pH measurements made after the tests were terminated (Table 13a).

2.4.2 Bayfield Group, Jacobsville Formation, and Unit E Eischeid #1 Well

All test samples collected from the Bayfield Formation and its equivalent stratigraphic units displayed only minor weight changes during HPT testing, except for the Eischeid #1 Well sample E2-2, which lost 1.24% of its sample weight. The pH increased from approximately 3.8 (value from the blank tests) to between 4.8 to 5.9 following ion exchange reactions with the rock that buffer against H^+ (Table 14a). The Eh of the leachate solution ranged from +14 to +128 mV.

Silica release from the Bayfield, Jacobsville, and Unit E samples ranged between 19 and 64 ppm with normalized release rates were between 1.18×10^{-6} and 2.46×10^{-5} moles/cm^2.day (Figure 25, Eischeid sample E2-4 only; Tables 14b through d). The release of Al, Mn, and Fe was also very low from these samples likely due to the formation of low-solubility commonly alteration phases. Although Si may be derived from the corrosion of quartz, it is more likely being derived from hydrolysis reactions with of feldspars, pyroxenes, and other silicate minerals as quartz is relatively inert in the presence of acidic weathering solutions (Dove and Crerar, 1990; Bennett, 1991; Dove, 1999). Evidence supporting such a trend can be found in the lower release concentrations of Si being associated with the Bayfield Group-Jacobsville-Unit E samples, relative to the Oronto Group, even though the former had much higher percentages of quartz grains as determined by point count analysis of thin sectioned samples and SiO_2 contents as determined by XRF analysis.

Calcium release was significantly lower for the Bayfield and Jacobsville samples when compared to the Unit E samples from the Eischeid Well, while Ca release was lower in all three sequences compared to the Oronto Group (Tables 13b and 14b). The most likely cause for this difference in Ca release is the lower calcite cement concentrations in the Bayfield and Jacobsville sequences. One exception to this trend is the E2-2 sample from the Eischeid Well which had a leachant concentration of 497 ppm (normalized release 5.37×10^{-5} moles/cm^2.day). Petrographic studies indicate that the Unit E samples and Jacobsville-Bayfield all contained low amounts of calcite (<1.7%), with the three Bayfield samples examined not containing any detectible calcite (Table 7). The Ca contents revealed by XRF analysis indicate that the seven Bayfield-Jacobsville samples contained an average of 0.11 ± 0.13% Ca, while the three Unit E samples contained 1.01 ± 0.40% Ca (Tables 9 and 10). Corresponding normalized Ca release rates were ~3.19×10^{-6} moles/cm^2.day for the one Bayfield BAY3 sample; between 7.31×10^{-7} and 1.75×10^{-6} moles/cm^2.day for the three Jacobsville samples, and between 6.56×10^{-6} and 5.37×10^{-5} moles/cm^2.day for the three Unit E samples (Figure 25; Tables 14c and d).

Table 14a. Sampling and HTP test data for Bayfield sample (BAY), L'Anse (L'ANSE), Agate Falls (AG), and Eischeid #1 Well (Unit E) samples following reaction in a $CO_2 + H_2O$ system at 90°C. BAY is Bayfield Group; L'ANSE and AF are Jacobsville Formation sandstones.

Sample ID & depth	Location	Surface area (cm^2)	% weight loss/gain	pH final	Eh (mV)	Time (days)
Bayfield Group						
BAY 3	Bayfield, WI	6.6	-0.38%	5.39	+86.0	19.8
Jacobsville Formation						
L'ANSE1	L'Anse, MI	10.0	-0.09%	4.78	+14.0	37.8
AG-1	Agate Falls, MI	11.6	-0.12%	5.06	+109.9	59.9
AG-2	Agate Falls, MI	12.6	-0.17%	5.59	+79.3	59.9
Eischeid #1 Well – E Unit						
E2-2 (8,834′)	Eischeid #1, IA	4.5	-1.24%	5.90	+53.5	50.0
E2-3 (8,835′)	Eischeid #1, IA	4.5	+0.10%	4.96	+127.5	6.0
E2-4 (8,836′)	Eischeid #1, IA	4.7	-0.08%	5.06	+104.4	50.0

Table 14b. Chemical composition of leachate solutions collected after opining the HPT vessels for Bayfield sample (BAY), L'Anse (L'ANSE), Agate Falls (AG), and Eischeid #1 Well (Unit E) samples following reaction in a $CO_2 + H_2O$ system at 90°C. Values are in ppm (mg/kg).

ppm	Si	Al	Fe	Ca	Mg	K	Na	Mn
Bayfield Group								
BAY3	30.0	1.3	17.0	4.0	18.0	10.0	3.7	10.0
Jacobsville Formation								
L'ANSE1	64.0	<0.1	27.0	9.4	28.0	7.3	1.0	1.0
AG-1	30.4	1.8	1.8	27.5	11.4	24.4	1.6	2.1
AG-2	25.0	0.1	0.1	22.5	9.7	21.2	1.4	1.3
Eischeid #1 Well – E Unit								
E2-2 (8,834′)	50.5	<0.1	<0.1	497	3.7	4.8	4.4	0.6
E2-3 (8,835′)	18.6	<0.1	0.3	26.5	1.4	4.5	4.5	1.1
E2-4 (8,836′)	48.6	0.2	<0.1	63.3	3.2	7.7	7.8	2.3

Table 14c. The molal concentration (mole/kg) of leachate solutions collected after Bayfield Group samples HTP corrosion testing for Bayfield sample (BAY), L’Anse (L’ANSE), Agate Falls (AG), and Eischeid #1 Well (Unit E) samples following reaction in a $CO_2 + H_2O$ system at 90°C.

	Si	Al	Fe	Ca	Mg	Na	K	Mn
Bayfield Group								
BAY3	1.07E-03	3.71E-04	2.36E-03	4.17E-04	1.65E-04	4.35E-04	4.60E-04	6.73E-05
Jacobsville Formation								
L’NAS 1	2.28E-03	<3.71E-05	1.79E-06	6.62E-04	3.87E-04	3.18E-04	7.16E-04	1.82E-05
AG-1	1.08E-03	6.67E-05	3.22E-05	6.74E-04	4.69E-04	6.96E-05	6.24E-04	3.82E-05
AG-2	8.90E-04	<3.71E-06	<1.79E-06	5.52E-04	3.99E-04	6.09E-05	5.42E-04	2.37E-05
Eischeid #1 Well – E Unit								
E2-2	1.80E-03	<3.71E-06	<1.79E-06	1.22E-02	1.52E-04	1.91E-04	1.23E-04	1.09E-05
E2-3	6.62E-04	<3.71E-06	5.37E-06	6.50E-04	5.76E-05	1.96E-04	1.15E-04	2.00E-05
E2-4	1.73E-03	7.41E-06	<1.79E-06	1.55E-03	1.32E-04	3.39E-04	1.97E-04	4.19E-05

Table 14d. Surface area normalized release results from solutions collected from Bayfield Group after high-pressure-temperature corrosion testing. Values are in moles/cm^2.d.

Moles/cm^2.d	Si	Al	Fe	Ca	Mg	K	Na	Mn
BAY3	8.17E-06	2.84E-06	1.81E-05	3.19E-06	1.26E-06	3.33E-06	3.52E-06	5.15E-07
L’NASE1	6.03E-06	<9.80E-08	4.74E-09	1.75E-06	1.02E-06	8.40E-07	1.89E-06	4.82E-08
AG-1	1.56E-06	9.60E-08	4.64E-08	9.71E-07	6.75E-07	1.00E-07	8.98E-07	5.50E-08
AG-2	1.18E-06	<4.91E-09	<2.37E-09	7.31E-07	5.29E-07	8.07E-08	7.18E-07	3.14E-08
E2-2	7.93E-06	<1.63E-08	<7.90E-09	5.37E-05	6.71E-07	8.44E-07	5.41E-07	4.82E-08
E2-3	2.46E-05	<1.38E-07	2.00E-07	2.42E-05	2.14E-06	7.28E-06	4.28E-06	7.45E-07
E2-4	7.32E-06	3.13E-08	<7.57E-09	6.56E-06	5.57E-07	1.43E-06	8.33E-07	1.77E-07

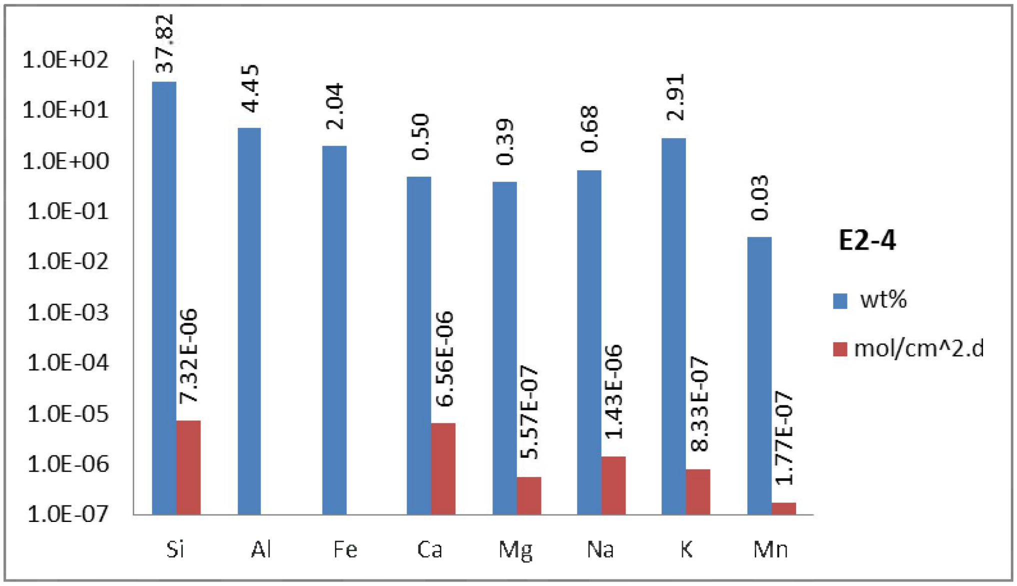

Figure 25. Comparison between the dissolution rate (red bars, in mole/m^2.sec) and the concentration of elements in the solid (blue bars, as element wt. % in the solid) for E2-4 (Unit E of Eischeid #1 Well, IA). The fastest release rate is associated with Ca. Dissolution testing was conducted at 90^{o}C H_2O + CO_2 solution for 50 days.

Magnesium release concentrations were moderately low for the Bayfield Group and Jacobsville Formation samples, with release concentrations ranging between 10 and 28 ppm (Table 14b). The Eischeid Well samples had the lowest Mg release values for all samples tested, with release concentrations ranging between 1.4 and 3.7 ppm for three samples. The normalized Mg release rate was also lower than that of Ca and ranged between 5.29×10^{-7} and 2.14×10^{-6} moles/cm^2.day (Table 14d). Potassium and Na release values were comparable to many of the Oronto Group samples, with K concentrations ranging from 4.5 to 24 ppm, and Na ranging from 1.0 to 7.8 ppm. Overall iron release was generally high in the BAY3 (17 ppm) and L'ANSE1 (27 ppm) samples, while all other samples had concentrations of <1.8 ppm. Aluminum contents were very low (<1.8 ppm) for all samples, indicating that Al was relatively insoluble under our experimental conditions.

2.4.3 Texaco Poersch #1 Well, Kansas

No clear stratigraphic correlation exists between the Texaco Poersch #1 Well in Kansas and either the Eischeid Well in Iowa or the surface outcrops of MCR rocks in the Lake Superior region. Therefore, the Poersch #1 leachate solutions cannot be directly correlated to the Oronto nor Bayfield Groups. Fourteen samples from the Poersch Well were reacted in the HTP tests. All of the samples exhibited some weight loss during testing, ranging from 0.22 to 1.26% (Table

15a). The leachate pH values were variable, but all solutions displayed a rise in pH from the initial ~3.8 starting leachant value to final values of between 5.7 to and 6.1, while Eh values ranged from +48 to +82 mV.

Both the Ca and Mg release concentrations for the Poersch #1 samples were highly variable with Ca tending to dominate the release patterns for all samples with the exception of the well sample from 5,397.3′ (Table 15). Calcium contents tended to be high in most samples obtained at depths of 8000′ or more, with concentrations ranging from 242 to 566 ppm. The Mg concentrations were much lower in these deeper samples, ranging from 1 to 32 ppm. The high Ca:Mg ratios would likely signify the abundance of calcite over dolomite cement. Both calcite and dolomite peaks were identified in the XRD analyses (Figure 19) for this group of samples and these minerals are the likely source of the majority of the released Ca and Mg. The XRD spectra also displayed well-developed peaks for the Mg-rich mica phlogopite in the upper volcanic-dominated sequence. Phlogopite represents a potential source for Mg. Both Al and Fe concentrations were very low, most were below the detection limit of 0.1 ppm, a factor likely related to the low solubility of alteration phases containing these components.

The lowermost clastic-dominated sequence for the Poersch #1 samples (8,051′ to 11,061′) was characterized by low Si release rates (<2.28E-06 moles/cm^2.d; Table 15c). The K and Na release from these deeper sections of the well (> 8000′) were lower than the K and Na released from the shallower core segments (Table 15b).

In the Texaco Poersch #1 samples, the normalized release rate of Ca was generally found to be high (e.g., nearly 100 fold more than that in K, Na, Mg, and Si; Figure 26; Table 15c and d). The arkosic nature of the lower clastic-dominated sequence would normally have resulted in the release of more K and Na, relative to Ca if silicate minerals were responsible for this release. However, it appears that the Ca and Mg were being released from dissolving carbonate cements. The release of Fe, Al, and Mn were generally below the ICP-OES instrumental detection limit.

Table 15a. Sampling and HTP test data for Texaco Poersch #1 Well samples following reaction in a $CO_2 + H_2O$ system at 90°C.

Sample ID	Location	Surface area (cm^2)	% weight loss/gain	pH final	Eh (mV)	Time (days)
5,397.3′a	Poersch #1 Well, KS	9.9	-0.42%	5.94	+47.6	43.0
5,404′a	“	9.5	-0.22%	5.73	+82.0	22.0
8,051.1′a	“	7.8	-1.26%	5.79	+59.3	95.0
8,476′-8,480′a	“	8.9	-1.20%	6.03	+64.9	18.0
10,514′a	“	7.8	-0.92%	5.87	+75.0	14.0
10,666′a	“	10.8	-0.97%	5.84	+76.3	22.0
11,061′a	“	7.0	-0.96%	5.85	+74.8	3.0
5,397.3′b	“	10.0	-0.28%	6.12	+51.7	26.5
5,404′b	“	9.6	-0.17%	n/a	n/a	36.0
8,051.1′b	“	7.1	-0.73%	5.78	+75.4	3.0
8,476′-8,480′b	“	8.6	-1.17%	5.81	+72.7	6.0
10,514′b	“	9.3	-1.19%	5.80	+59.0	95.0
10,666′b	“	9.6	-0.74%	5.90	+72.0	14.0
11,061′b	“	7.1	-1.26%	5.77	+60.9	71.0

Table 15b. Chemical composition of leachate solutions collected after opining the high-pressure vessels for the Poersch #1 Well samples. Values are in ppm (mg/kg).

ppm	Si	Al	Fe	Ca	Mg	K	Na	Mn
5,397.3′a	48.6	<0.1	<0.1	54.2	240	19.6	99.9	0.1
5,397.3′b	45.8	<0.1	<0.1	159	120	13.1	63.6	3.4
5,404′a	48.9	0.2	<0.1	110	48.6	16.6	41.9	1.9
8,051.1′a	76.4	<0.1	<0.1	513	2.4	4.7	7.1	3.0
8,051.1′b	11.8	<0.1	<0.1	342	1.6	2.8	2.5	2.3
8,476-8,470′a	37.4	<0.1	<0.1	502	4.9	2.8	4.9	4.1
8,476-8,480′b	20.9	<0.1	<0.1	518	4.8	2.0	3.5	3.5
10,514′a	16.4	<0.1	<0.1	419	1.1	1.8	3.0	3.6
10,514′b	51.3	<0.1	<0.1	497	1.5	2.6	7.4	4.5
10,666′a	21.5	<0.1	<0.1	242	25.9	3.7	15.1	5.7
10,666′b	25.4	<0.1	<0.1	361	32.6	3.5	15.1	8.6
11,061′a	9.2	<0.1	0.3	363	1.2	2.3	4.3	1.4
11,061′b	39.5	<0.1	<0.1	566	1.1	3.5	7.8	1.5

Table 15c. The molal concentration (mole/kg) of leachate solutions collected from the Kansas Poersch #1 Well samples HTP corrosion testing.

	Si	Al	Fe	Ca	Mg	K	Na	Mn
5,397.3′a	1.73E-03	<3.71E-06	<1.79E-06	1.35E-03	9.89E-03	5.01E-04	4.35E-03	<1.82E-06
5,397.3′b	1.63E-03	<3.71E-06	<1.79E-06	3.95E-03	4.95E-03	3.35E-04	2.77E-03	6.19E-05
5,404′a	1.74E-03	7.41E-06	<1.79E-06	2.75E-03	2.00E-03	4.25E-04	1.82E-03	3.46E-05
8,051.1a	2.72E-03	<3.71E-06	<1.79E-06	1.28E-02	9.87E-05	1.20E-04	3.09E-04	5.46E-05
8,051.1′b	4.20E-04	<3.71E-06	<1.79E-06	8.53E-03	6.58E-05	7.16E-05	1.09E-04	4.19E-05
8,476 to 8,470′a	1.33E-03	<3.71E-06	<1.79E-06	1.25E-02	2.02E-04	7.16E-05	2.13E-04	7.46E-05
8,476 to 8,480′b	7.44E-04	<3.71E-06	<1.79E-06	1.29E-02	1.97E-04	5.12E-05	1.52E-04	6.37E-05
10,514′a	5.84E-04	<3.71E-06	<1.79E-06	1.05E-02	4.53E-05	4.60E-05	1.30E-04	6.55E-05
10,514′b	1.83E-03	<3.71E-06	<1.79E-06	1.24E-02	6.17E-05	6.65E-05	3.22E-04	8.19E-05
10,666′a	7.66E-04	<3.71E-06	<1.79E-06	6.04E-03	1.07E-03	9.46E-05	6.57E-04	1.04E-04
10,666′b	9.04E-04	<3.71E-06	<1.79E-06	9.00E-03	1.34E-03	8.95E-05	6.57E-04	1.57E-04
11,061′a	3.28E-04	<3.71E-06	5.37E-06	9.06E-03	4.94E-05	5.88E-05	1.87E-04	2.55E-05
11,061′b	1.41E-03	<3.71E-06	<1.79E-06	1.41E-02	4.53E-05	8.95E-05	3.39E-04	2.73E-05

Table 15d. Surface area normalized release results from solutions collected from the Kansas Poersch #1 Well samples after high-pressure-temperature corrosion testing. Values are in moles/cm^2.d.

Moles/m^2 .sec	Si	Al	Fe	Ca	Mg	K	Na	Mn
5,397.3′a	4.70E-07	<1.01E-09	<4.87E-10	3.68E-07	2.69E-06	1.36E-07	1.18E-06	<4.95E-10
5,397.3′b	7.12E-07	<1.62E-09	<7.82E-10	1.73E-06	2.16E-06	1.46E-07	1.21E-06	2.70E-08
5,404′a	9.64E-07	4.1E-09	<9.92E-10	1.52E-06	1.11E-06	2.35E-07	1.01E-06	1.92E-08
8,051.1a	4.25E-07	<5.79E-10	<2.80E-10	2.00E-06	1.54E-08	1.88E-08	4.82E-08	8.53E-09
8,051.1′b	2.28E-06	<2.01E-08	<9.73E-09	4.64E-05	3.58E-07	3.89E-07	5.91E-07	2.27E-07
8,476 to 8,470′a	9.62E-07	<2.68E-09	<1.29E-09	9.05E-06	1.46E-07	5.17E-08	1.54E-07	5.39E-08
8,476 to 8,480′b	1.67E-06	<8.31E-09	<4.02E-09	2.90E-05	4.43E-07	1.15E-07	3.41E-07	1.43E-07
10,514′a	6.19E-07	<3.93E-09	<1.9E-09	1.11E-05	4.8E-08	4.88E-08	1.38E-07	6.95E-08
10,514′b	2.39E-07	<4.86E-10	<2.35E-10	1.62E-06	8.08E-09	8.71E-09	4.22E-08	1.07E-08
10,666′a	3.73E-07	<1.81E-09	<8.72E-10	2.94E-06	5.19E-07	4.61E-08	3.20E-07	5.05E-08
10,666′b	7.79E-07	<3.19E-09	<1.54E-09	7.75E-06	1.16E-06	7.71E-08	5.66E-07	1.35E-07
11,061′a	1.81E-06	<2.04E-08	2.96E-08	5.00E-05	2.72E-07	3.24E-07	1.03E-06	1.40E-07
11,061′b	3.23E-07	<8.51E-10	<4.11E-10	3.24E-06	1.04E-08	2.06E-08	7.79E-08	6.27E-09

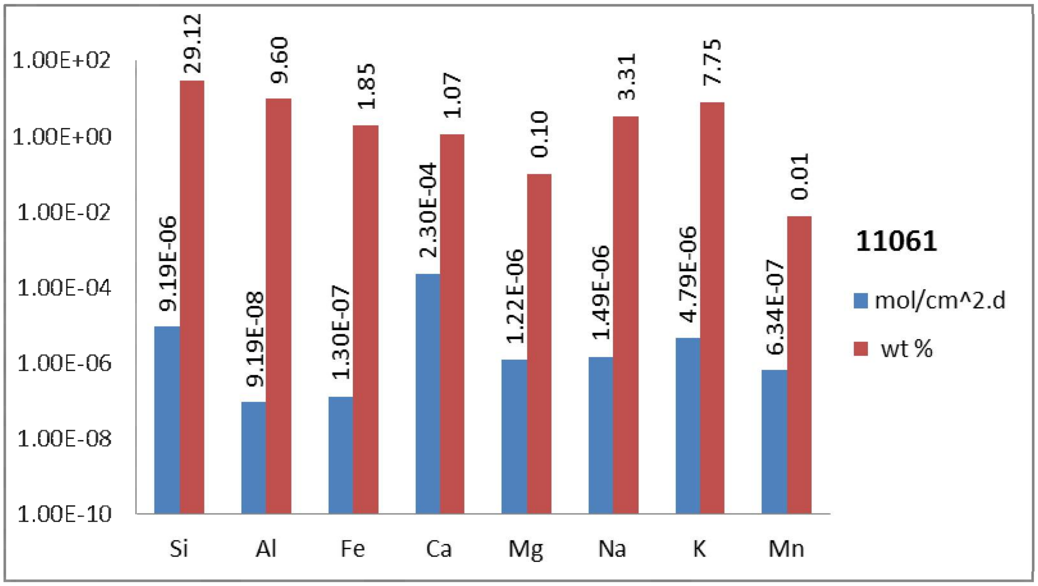

Figure 26. Comparison between the dissolution rate (blue bars, in mole/m^2.sec) and the concentration of elements in the solid (red bars, as element wt. % in the solid) for the 11,061′A and B samples from the Texaco Poersch #1 Well. Dissolution testing was conducted at 90°C in a H_2O + CO_2 solution for 71 days.

2.4.4 Midcontinent Rift Volcanic and Plutonic Rocks

Only a limited suite of igneous rocks were tested in the corrosion tests, these including plutonic intrusive sequences of the Beaver Bay and Duluth Complexes, extrusive basalt flows from Good Harbor Bay, and closely associated interflow clastic sediments from the same location. Many of these units represent provenance sources for detrital clastic rocks in the MCR sedimentary rocks. Samples taken from the MCR igneous rocks sequence exhibited significant alteration during high temperature-pressure corrosion testing, especially the two Good Harbor Bay basalt samples, which experienced weight losses of 1.18 and 3.78%. One of the Good Harbor Bay clastic interflow sediment samples gained 0.42% of its weight during testing. The pH of the tested samples increased significantly from the initial pH of 3.8 to between 5.0 and 6.1. Solution Eh values ranged from +44 to +124 millivolts with the Silver Bay samples recording the higher values (Table 16a).

The Si released from the clastic interflow GHC-1 samples (sedimentary clastic bed sandwiched between flow basalts) exceeded 120 ppm (Table 16b). The other samples had Si release values below 90 ppm. As discussed previously, the Si concentration in the leachate solution likely reflects release from feldspars, pyroxenes, amphiboles, rather than quartz. The rate of Si release varied between 1.78×10^{-7} to 1.09×10^{-6} moles/cm^2.day (Table 16d). Both the DUL and BEV gabbroic samples were characterized by low Ca release concentrations relative to the basalt sample. Due to the mafic nature (i.e. Mg-Fe-rich) of these volcanic units, the Mg concentration was relatively high in all but the BEV samples. The release rate of Ca and Mg was between 3.29×10^{-7} and 2.68×10^{-6} moles/cm^2.day. Iron was also released in high concentrations, especially from the basaltic GHB samples, but eventually precipitated as hematite rust on the inside surfaces of the Teflon vessels. The concentration of K varied between 0.5 and 4.7 ppm while Na was between 3.8 and 24 ppm. The rate of the alkali metal release was less than 4.15×10^{-8} moles/cm^2.day for K and less than 1.01×10^{-7} moles/cm^2.day for Na (Table 16d). Aluminum concentrations were below the ICP-OES analytical detection limit of 0.1 ppm. The normalized release rates of Ca, Mg, and Si were relatively high in the basalt sample with Ca being the highest at 2.30E$\times10^{-4}$ moles/cm^2.day (Figure 27; Table 16c and d). A significant portion of the MCR clastic sedimentary grains were found to be composed of mafic lithic fragments derived from volcanic basalts. Therefore, these mafic-dominated volcanic sequences represent a good source for Ca and Mg. These two elements are often incorporated into carbonate minerals following alteration of the sediments and/or volcanic rocks.

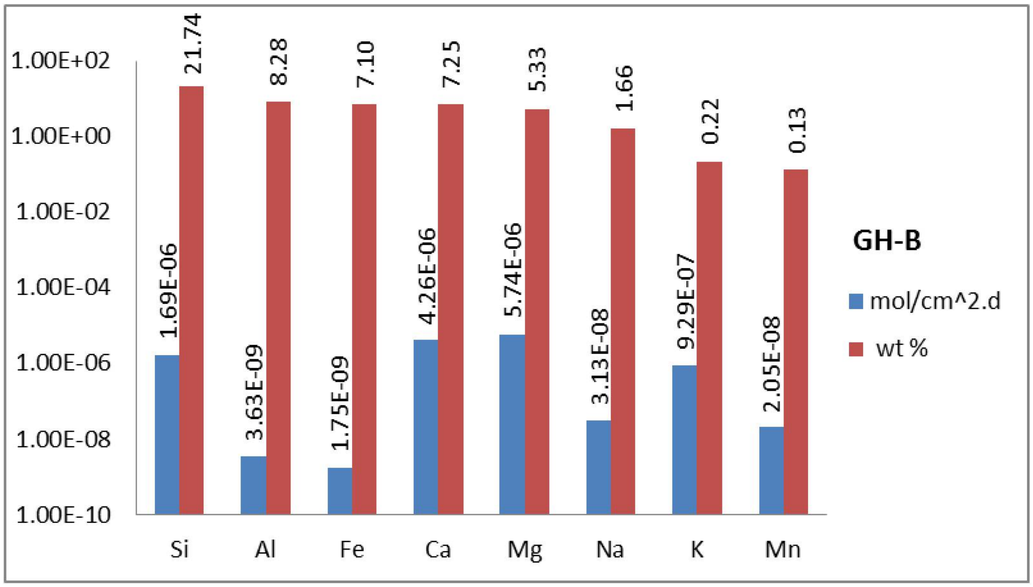

Figure 27. Comparison between the dissolution rate (red bars, in mole/m^2.sec) and the concentration of elements in the solid (blue bars, as element wt. % in the solid) for the North Shore Volcanic Group basalt GH-B sample. The fastest release rate is associated with Ca. Dissolution testing was conducted at 90°C H_2O + CO_2 solution for 59 days.

Table 16a. Sampling and HTP test data for MCR igneous rocks samples following reaction in a $CO_2 + H_2O$ system at 90°C. BEV is Beaver Bay Complex; DUL is Duluth Complex; GHB is Good Harbor Bay basalt (North Shore Volcanic Group); GHC is Good Harbor Bay clastic interflow sediment.

Sample ID	**Location**	**Surface area (cm^2)**	**% weight loss/gain**	**pH Final**	**Eh (mV)**	**Time (Days)**
BEV1	Silver Bay, MN	-	-	5.00	+124.4	10.0
BEV2	Silver Bay, MN	5.0	-	-	+103.6	43.0
DUL-1	Hwy 1, Ely, MN	5.7	-0.15%	5.92	+60.9	59.9
DUL-2	Hwy 1, Ely, MN	5.6	-0.21%	5.84	+64.7	59.9
GHB-1	Good Harbor Bay, MN	17.0	-3.78%	6.12	+48.7	59.9
GHB-2	Good Harbor Bay, MN	17.1	-1.18%	5.87	+64.0	59.9
GHC-1	Good Harbor Bay, MN	9.4	+0.42%	5.93	+60.4	59.9
GHC-2	Good Harbor Bay, MN	8.8	-0.07%	6.22	+44.1	59.9

Table 16b. Chemical composition of leachate solutions collected after opening the vessels containing MCR igneous rocks samples. Values are in ppm (mg/kg). BBC is beaver Bay Complex; NSVG-IC is North Shore Volcanic Group – clastic interflow sediments.

ppm	**Si**	**Al**	**Fe**	**Ca**	**Mg**	**K**	**Na**	**Mn**
BEV1	27.1	<0.1	0.4	17.3	7.0	1.9	3.8	<0.1
BEV2	54.0	<0.1	<0.1	31.4	16.0	2.2	5.9	<0.1
DUL-1	90.2	< 0.1	< 0.1	39.4	192	3.9	7.2	0.4
DUL-2	74.8	< 0.1	< 0.1	38.2	135	4.7	6.7	0.4
GHB-1	52.6	< 0.1	< 0.1	225	184	1.4	24.0	1.8
GHB-2	44.2	< 0.1	< 0.1	124	101	1.1	19.6	0.5
GHC-1	124	< 0.1	< 0.1	289	66.7	0.7	19.5	1.2
GHC-2	125	< 0.1	< 0.1	279	67.0	0.5	14.4	1.8

Table 16c. The molal concentration (mole/kg) of leachate solutions collected from MCR igneous rocks samples after HTP testing.

	Si	Al	Fe	Ca	Mg	K	Na	Mn
GHB-1	1.87E-03	<3.71E-06	<1.79E-06	5.60E-03	7.55E-03	3.58E-05	1.04E-03	3.28E-05
GHC-1	4.42E-03	<3.71E-06	<1.79E-06	7.20E-03	2.74E-03	1.79E-05	8.48E-04	2.18E-05
GHB-2	1.57E-03	<3.71E-06	<1.79E-06	3.08E-03	4.17E-03	2.81E-05	8.53E-04	9.10E-06
GHC-2	4.45E-03	<3.71E-06	<1.79E-06	6.96E-03	2.76E-03	1.28E-05	6.26E-04	3.28E-05
DUL-1	3.21E-03	<3.71E-06	<1.79E-06	9.83E-04	7.90E-03	9.97E-05	3.13E-04	7.28E-06
DUL-2	2.66E-03	<3.71E-06	<1.79E-06	9.53E-04	5.54E-03	1.20E-04	2.91E-04	7.28E-06

Table 16d. Surface area normalized release results from solutions collected from MCR igneous rocks samples after opining the HPT vessels. Values in moles/cm^2.d.

Moles/m^2.s	Si	Al	Fe	Ca	Mg	K	Na	Mn
GHB-1	2.13E-07	<4.21E-10	<2.04E-10	6.37E-07	8.59E-07	4.07E-09	1.19E-07	3.72E-09
GHC-1	9.08E-07	<7.62E-10	<3.68E-10	1.48E-06	5.64E-07	3.68E-09	1.74E-07	4.49E-09
GHB-2	1.78E-07	<4.19E-10	<2.02E-10	3.48E-07	4.71E-07	3.18E-09	9.63E-08	1.03E-09
GHC-2	9.77E-07	<8.14E-10	<3.93E-10	1.53E-06	6.05E-07	2.81E-09	1.38E-07	7.19E-09
DUL-1	1.09E-06	<1.26E-09	<6.07E-10	3.33E-07	2.68E-06	3.38E-08	1.06E-07	2.47E-09
DUL-2	9.19E-07	<1.28E-09	<6.18E-10	3.29E-07	1.91E-06	4.15E-08	1.01E-07	2.51E-09

2.5 Accelerated Weathering Reactions – Goldich Series Reactions

The amount of elemental release into the solution during mineral corrosion is dependent upon the stability of the mineral exposed to weathering fluids, with this stability in turn, dependent upon the atomic structure and composition of the mineral, temperature, redox conditions, and fluid composition. To test these parameters we reacted:

1) Powdered samples of individual mineral grains in a series of acid neutralization reactions (Goldich series reactions).
2) Polished wafers of minerals in the HPT reaction chambers.

2.5.1 Relative Rates of Mineral Weathering

A suite of finely powdered single mineral samples (-200 mesh) plus powdered rock samples were tested by immersion in a nitric acid leachant solution prepared to a pH of approximately 3.78 (1.66 x 10^{-4} M). A Solution at pH of 3.78 represent both the minimum value expected in organic-acidic soils and the approximate pH following saturation of deionized water with a pure CO_2 gas phase at atmospheric pressure. The experiments were used to simulate the effect of carbonic acid $H_2CO_{3(aq)}$ exposure on mineral dissolution rates. Using nitric acid rather than carbonic acid allows for frequent opening of the vessels for pH measurements as the former does not readily volatilize and transfer into a gas phase. The tests are termed the Goldich reaction series after Samuel Goldich who was one of the pioneers in the study of weathering rates on minerals (Goldich, 1938). These experiments were also conducted at room temperature and pressure.

Results from the Goldich (1938) series tests indicate mineral reaction trends in the following decreasing order of reactivity; olivine reacted the fastest, followed in sequence by hornblende, pyroxene, orthoclase feldspar, Ca-plagioclase (bytownite), Na-plagioclase, and finally quartz (Figure 28a). Increases in pH are an indication of chemical reactivity as the exchange of $nH^+ \Leftrightarrow M^{n+}$, where M^{n+} corresponds to any metal cation (e.g., Na^+, K^+, Ca^{2+}, Mg^{2+}, Fe^{2+}, etc., and n is generally equal to 1 or 2). Minerals that react more rapidly with acids, and have higher proportions of M^{2+} cations, have a greater buffering capacity for neutralizing acidic solutions. These minerals may also promote carbonate mineral formation both by increasing the solution pH and releasing Ca^{2+}, Mg^{2+} and Fe^{2+} ions that can complex with CO_3^{2-} to form carbonate mineral phases (e.g., $CaCO_3$, $MgCO_3$, $CaMg(CO_3)_2$, $FeCO_3$). As the minerals react, the pH will rise over that of the blank tests, indicating chemical buffering of the acids is taking place. The pH values eventually peak for the more reactive minerals indicating that an effective consumption of acids has occurred. Overall, the silicate mineral reaction rates closely followed the Goldich stability trend (Figures 28 and 29). For example, the olivine reaction peaked at a pH = 8.46 in one week, and the Ca-rich feldspar peaked at a pH = 5.53 in 105 days. The solution contacting the quartz sample exhibited no apparent change in the pH indicating no detectible reaction with the acidified leachant. The only exceptions to the Goldich reaction trends were found in the hornblende reacting faster than pyroxene, and the orthoclase feldspar reacting faster than both the Ca- and Na-rich plagioclase.

Feldspars are an abundant mineral in the MCR sedimentary and igneous sequences, and an even more important contributor to alkali and alkaline element release due to their relatively rapid alteration rates (Goldich, 1938). We therefor tested several additional feldspar compositions to gain more knowledge on their alteration behavior. Ca-rich plagioclase was more reactive than Na-rich plagioclase feldspar as expected (Figure 28b). The two K-feldspar samples that were tested exhibited widely different reactivities, with the orthoclase sample exhibiting a much higher than expected reaction rate, while the Georgia K-feldspar sample reacted at a lower rate and rate that was similar to the Na-rich plagioclase.

Although not studied by Goldich in his reaction series, the common hydrothermal alteration mineral epidote [$Ca_2Al_2Fe^{3+}(Si_2O_7)(SiO_4)(OH)$] is found in rocks throughout the MCR system. Epidote displayed a fairly significant amount of reaction with the leachant solution, rapidly buffering the solution pH to a value of approximately 6.3 after 96 hours (4 days) and then continuing to display a slow rise in pH until a value of 6.8 was reached after 1512 hours (63 days; Figure 28c). The reaction of epidote will also release Ca^{2+} and Fe^{3+} to solution, potentially sequestering CO_2 in $CaCO_3$ and $FeCO_3$ mineral phases if the Fe can be reduced.

Calcite, hematite (Fe_2O_3), and quartz often occur as cement materials in sandstones. The calcite reacted quite readily with the acid solution to produce a high pH solution within a few hours of testing and reached a value of 8.78 in only two days (Figure 28c). The rapid reaction of calcite cement in sandstones and other rock types will enhance the porosity and permeability of rocks that are cemented by this material. By contrast, hematite was only slightly reactive in the tests, with a long-term pH rise only increasing from the initial 3.78 to 4.20 after 336 hours (14 days) of testing. Combined results thus suggest that both hematite and quartz cement (previously discussed above; Figure 28a) should behave in a relatively inert manner under the mildly acidic conditions used in the present series of tests, with quartz being the most inert cement material. An increase in the solubility of Fe would be aided under more reducing conditions where ferric to ferrous iron transformation (Fe^{3+} to Fe^{2+}) would occur. Increasing salinity will also increase Fe solubility. An enrichment of dissolved Fe^{2+} would promote siderite precipitation ($FeCO_3$).

Clays are often present as pore-filling minerals in sandstones and are abundant in the impermeable shale layers that may represent trap rocks in a CO_2 injection repository. Some may even be generated as intermediate alteration phases following the reaction of acid species with some of the primary igneous minerals discussed in the preceding paragraphs. For the clay minerals, the order of decreasing reactivity is from fastest to slowest:

hectorite > Na-montmorillonite > illite > nontronite > Ca-montmorillonite > glauconite > kaolinite

The solution in contact with kaolinite displayed only a minimal pH rise above the blank test value reflecting its inert behavior to acids (Figure 28c). Natural clay minerals may often display highly variable chemical compositions thus some caution should be used in extrapolating the results from these experiments to other mineral systems without giving careful consideration to variations in mineral composition.

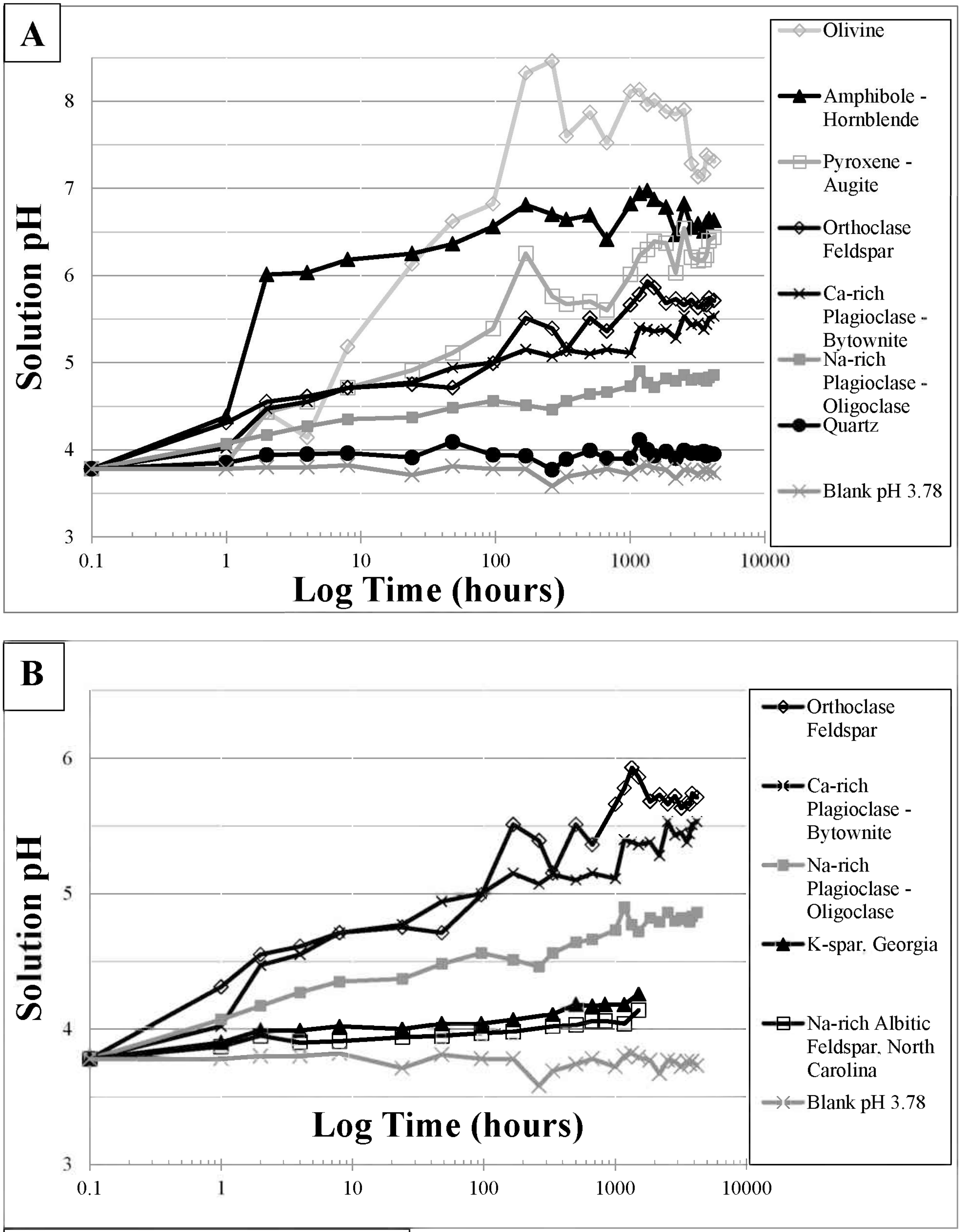

* Figure 28 - Caption on following page

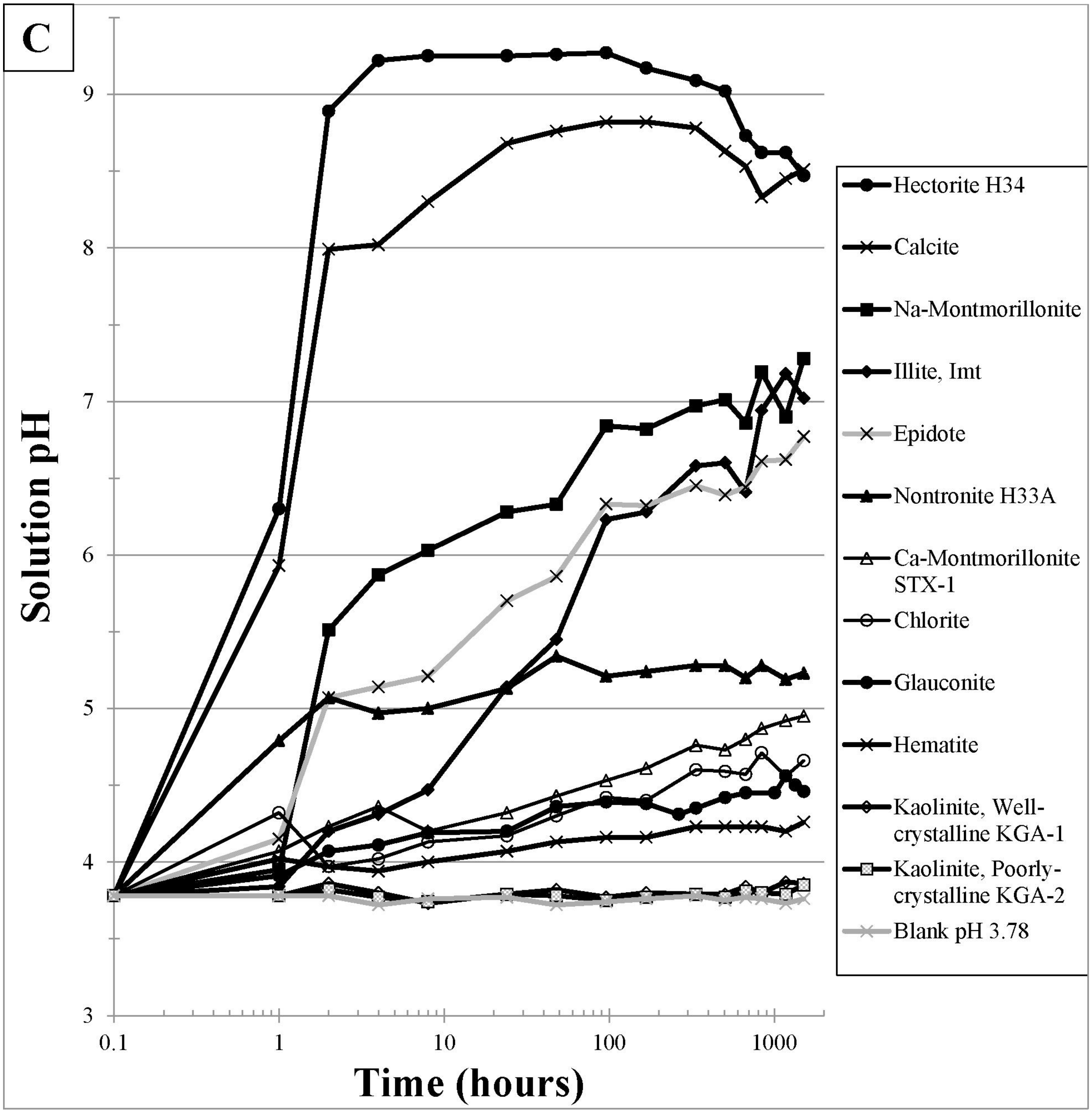

Figure 28. Relative ordering of Goldich series mineral reaction rates following immersion in nitric acid solution at starting pH = 3.78. Blank test pH trend is the lowest for all samples and plots at the bottom. A) (previous page) Plot of reactivity of common igneous minerals tested by Goldich, B) (previous page) Relative reactivity of additional feldspar minerals reactions. C) Relative reactivity of clays, several which are common matrix materials in the MCR, plus calcite and hematite, which occur as cements, and finally epidote as a common hydrothermal alteration mineral phase.

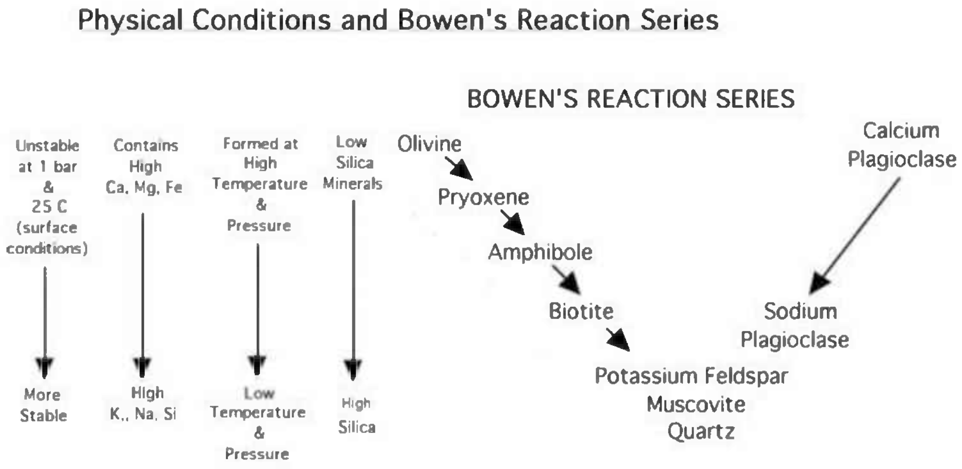

Figure 29. Relative ordering of mineral crystallization during the cooling and solidification of a hypothetical igneous body according to Bowen. The Goldich weathering series (Goldich, 1938) predicts that minerals will weather at rates that are inversely correlated to their crystallization temperatures as noted at the far left side of the figure.

2.5.2 High Pressure and Temperature Corrosion Testing of Individual Minerals

Two of the mineral phases that were reacted as powdered samples in the Goldich series experiments were also subjected to the HPT testing at 90°C to evaluate their potential for producing carbonate minerals as alteration phases. Both optical microscopy analysis of the altered sample of olivine (forsterite Mg_2SiO_4) and augite pyroxene ($CaMgSi_2O_6$) produced patches of a white precipitate. SEM-EDS analysis of the alteration phases on the olivine sample revealed the presence of rhombohedral magnesite after 10 days of exposure ($MgCO_3$; Figure 30). This finding agrees with that of Giammar et al. (2005) who identified magnesite as an alteration product following the reaction of forsterite in a CO_2 plus water environment. Low-Mg calcite crystals with a rhombohedral morphology were also found as precipitated crystals on altered augite samples following their reaction for 10 days in the HPT testing apparatus (Figure 31).

Lasaga et al. (1994) determined the theoretical length of time required for a hypothetical one mm sphere of different minerals to dissolve in a constant pH = 5 solution. His calculations follow the Goldich reaction series, but add a quantitative component to the evaluations (Figures 29 and 32a). Our experimental data match very well with the model calculations provided by Lasaga (Figures 32a and b). Both quartz and kaolinite were largely innert in the experiments, with the pH values remaining near the starting leachant solution, in a manner that correlates with the predicted behavior by Lasaga. Similarly, feldspar minerals reacted with K-feldspars (microcline) reacting the slowest. The plagioclase feldspar series minerals react faster than the K-feldspars, and also display increasing reactivity in correlation with the Ca/Na ratio of the plagioclase. Thus albite ($Na_{0.9-1.0}Ca_{0.0-0.1}Al_{1.0-1.1}Si_{2.9-3.0}O_8$), was the least reactive plagioclase mineral followed by oligoclase ($Na_{0.7-0.9}Ca_{0.1-0.3}Al_{1.1-1.3}Si_{2.7-2.9}O_8$; data from this study), andesine ($Na_{0.5-0.7}Ca_{0.3-0.5}Al_{1.3-1.5}Si_{2.5-2.7}O_8$; Lasaga model), and finally bytownite ($Na_{0.1-0.3}Ca_{0.7-0.9}Al_{1.7-1.9}Si_{2.1-2.3}O_8$). The pyroxenes ($(Mg,Fe,Ca)_2Si_2O_6$) were the next most reactive phase, with enstatite and diopside being evaluated in the Lasaga study, and augite being reacted in the present study). The pyroxenes were followed by fosteritic olivine (Mg_2SiO_4), and finally calcite as the most reactive phases. The only deviation that we noted between the Lasaga model and our experimental data was with the mineral epidote ($Ca_2(Al,Fe)Al_2O(SiO_4)(Si_2O_7)(OH)$) where Lasaga predicted epidote to be a durable mineral phase on par with the reactivity of K-feldspar, while we found it to be more reactive with an acid neutralizing capacity similar to the pxroxene group of minerals.

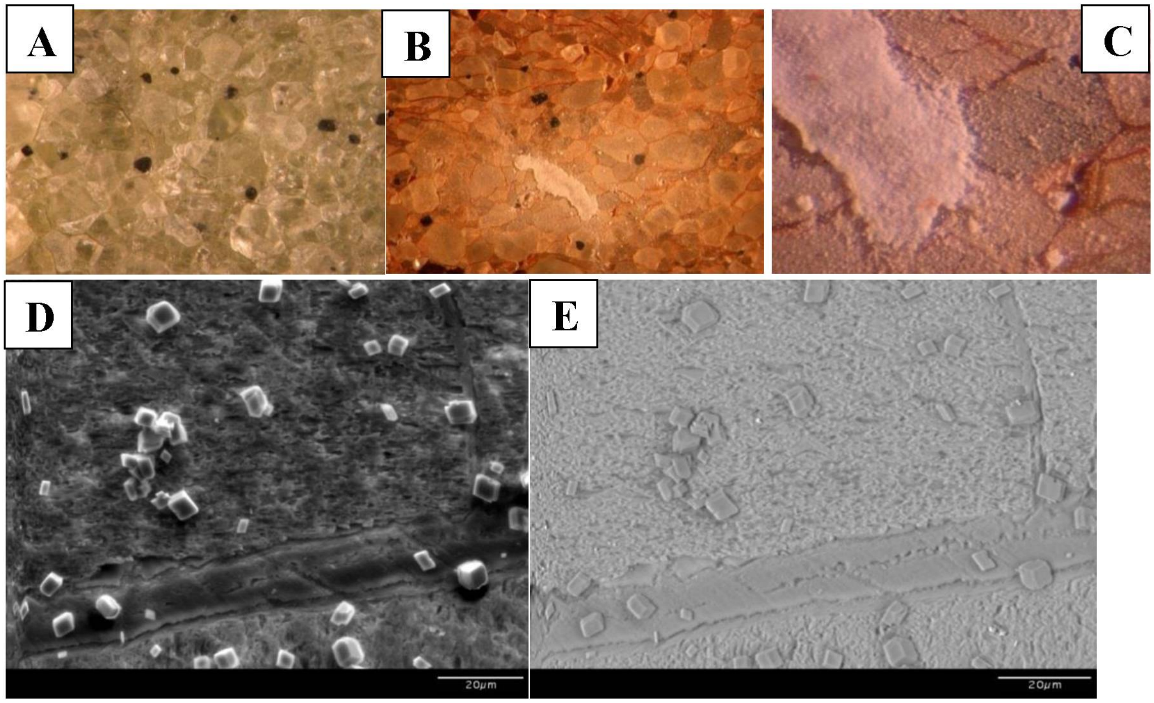

Figure 30. Images of mineral samples and alteration phases following reaction in a CO_2 + H_2O environment at 90°C for 236 hours (9.8 days). A) Unreacted olivine. Sample also contains enstatite pyroxene and black chromite-magnetite. B) Reacted surface showing red hematite and white patch of magnesite ($MgCO_3$). C) Higher magnification image of magnesite crystals from image B. D) Scanning Electron Microscope image of rhombohedral magnesite on altered olivine sample. E) Backscattered electron image of rhombohedral magnesite.

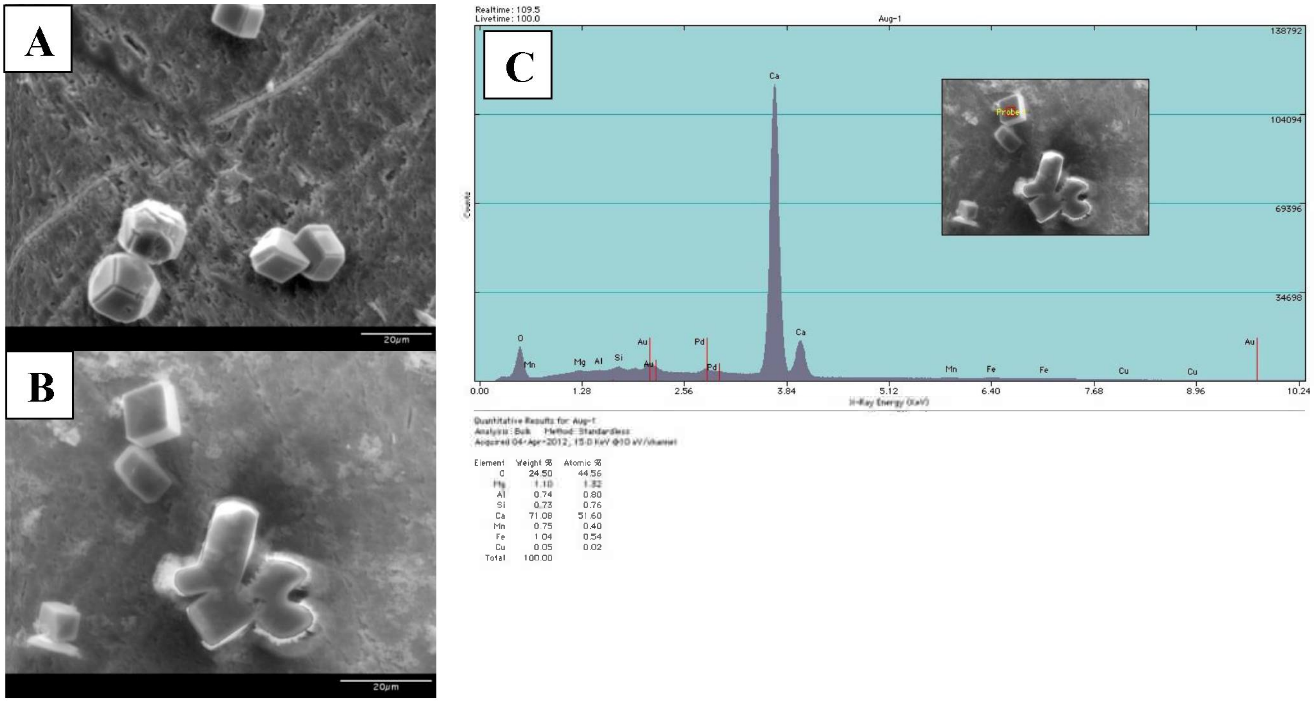

Quantitative Results for: Aug-1
Analysis: Bulk Method: Standardless
Acquired 04-Apr-2012, 15.0 KeV @10 eV/channel

Element	Weight %	Atomic %
O	24.50	44.56
Mg	1.10	1.32
Al	0.74	0.80
Si	0.73	0.76
Ca	71.08	51.60
Mn	0.75	0.40
Fe	1.04	0.54
Cu	0.05	0.02
Total	100.00	

Figure 31. SEM-EDS analysis of low-Mg calcite crystals formed on reacted augite-pyroxenes at 90°C for 236 hours (9.8 days). A) SEM image of alteration crystals with complex surface growth features. B) Rhombohedral calcite crystals. C) EDS analysis of rhombohedral grain displaying Ca + O composition suggesting the presence of calcite.

2.6 Experimental Parameters Affecting Mineral Reaction Rates

Mineral reaction rates are dependent on numerous factors including reaction time, exposed surface area, leachant volume, temperature, pressure, and fluid composition. Twenty-one samples of the POT4 Nonesuch Formation we prepared and reacted under variable test conditions to evaluate these factors in the HPT corrosion experiments (Table 17). Reaction times varied from 2 to 246 days. Sixteen duplicates were sliced into monoliths, polished to a 600-grit finish, cleaned, and dried for the corrosion testing in 10 ml of water. Another subset of samples were crushed in an agate mortar and pestle then sieved to collect the 100 mesh (0.149 mm) to 60 mesh (0.250 mm) size fraction in order to investigate the effect of increasing the exposed surface area on dissolution rates. Three monolith samples were also tested at 50°C to investigate the effect of temperature, as a comparison against the standard 90°C experiments. One monolith sample was also reacted with half the water volume (5 ml) allowing the sample to be only partially submerged in the leachant fluid.

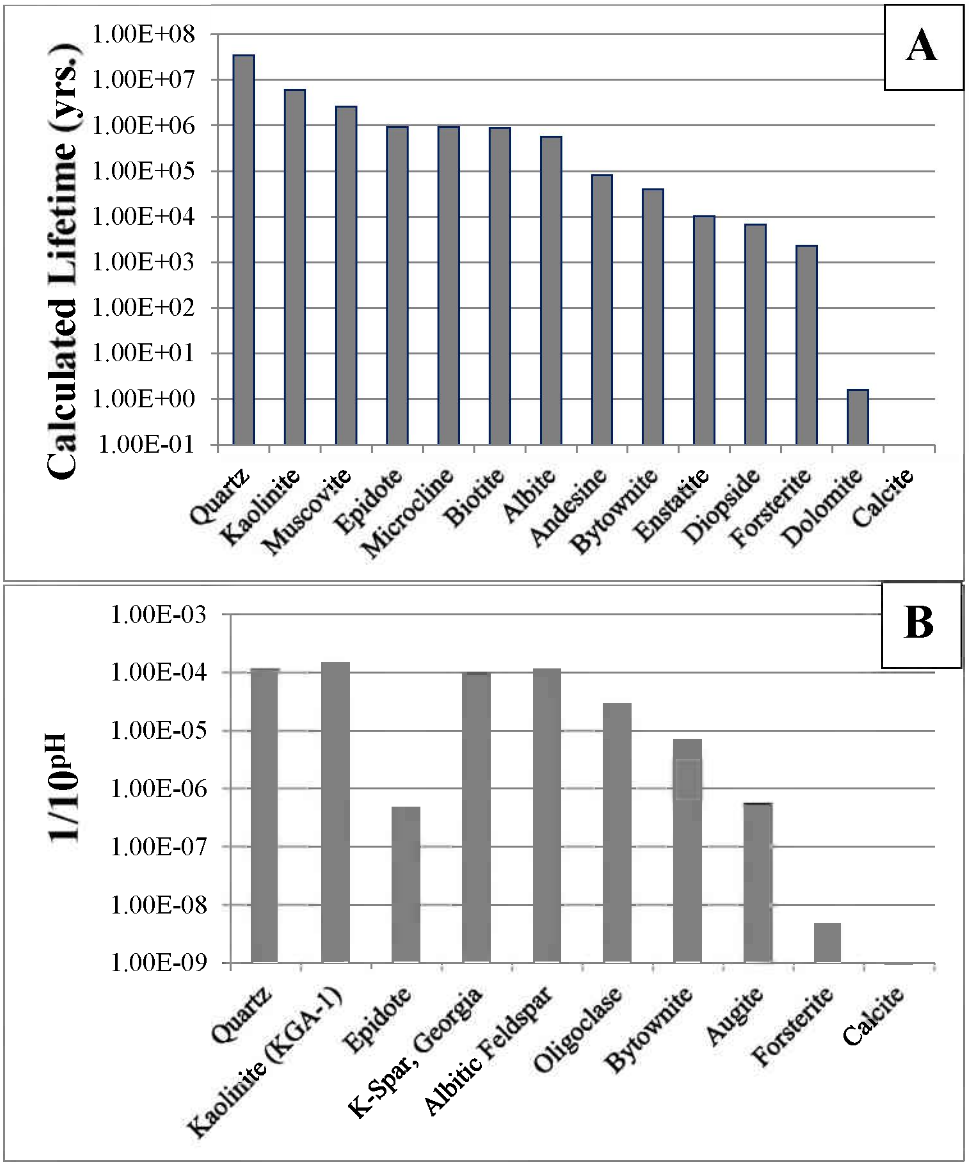

Figure 32. Relative reaction rates of minerals during weathering. A) Calculated lifetime of minerals in years, data from Lasaga et al. (1994). The bar for calcite plots as the width of the horizontal boundary line on the 1.00E-01 year position. B) Relative acid neutralization rate plotted as $1/10^{pH}$ for minerals reacted in nitric acid at starting leachant value pH=3.78. The pH value plotted is the recorded value after 168 hours exposure to the starting leachant fluid. The pH value for calcite peaked at 8.68 after 24 hours, so the 24 hour pH value was used the calculation was taken at 7 days * $1/10^{8.68}$. Lasaga et al. (1994) evaluated muscovite, biotite, diopside, and dolomite, but these were not reacted in the present set of experiments.

The POT4 sample was a feldspar and volcanic lithic fragment rich sandstone with a heterogeneous grain size distribution composed of 72.3% sand, 9% silt, and 3.4% clay sized detrital grains. Cement was represented largely by Fe oxides (12.6%), with minimal carbonate (0.3%), while open pores comprised the remaining 2.4% of the sample. The sample contained relatively high MgO and CaO concentrations (4.23 and 4.06 wt.%; Table 9) while petrographic point count analysis revealed a Q-F-L ratio of $Q_{31}F_{32}L_{36}$ (Table 3). The plagioclase to K-feldspar ratio was 1.3 : 1 and accessory minerals included opaque oxides (3.4%), mica (1.0%), and epidote (2.4%). The low amount of carbonate cement and abundance of lithic fragments makes this a good sample to investigate the effect of corrosion on the silicate minerals in the MCR.

2.6.1 Reaction Time Effect on Reaction Rates

All of the samples displayed increased pH values with time from the CO_2 saturated blank sample, which represents a starting leachant fluid with a pH of approximately 3.8, to a final leachant pH of ~6.2 after 246 days of reaction at 90°C. The samples displayed a moderately high linear correlation between the pH and log reaction time (R^2=0.70) and the 50°C samples appear to display a slightly higher acid neutralization rate (i.e. a higher slope compared with regular samples), although these lower temperature data show more scatter. Carbonic acid is produced as CO_2 dissolves in the aqueous solution inside the vessels. The pH rise with time reflects the acid (H^+) buffering capacity of the solid rock samples, with the minerals in the rock either dissolving or exchanging ions as they react with the acidified fluid (Figure 33). The pH rise, in turn, may induce the precipitation of dissolved components in longer term reactions. The formation of carbonate minerals represents a potential long term mechanism for isolating anthropogenic CO_2.

A moderately high positive correlation exists between the Si concentration and time (R^2=0.63; Figure 34). Quartz reacts relatively slowly in these solutions so the release of Si to solution more likely reflects the hydrolysis reactions affecting feldspars, pyroxenes, and other aluminosilicate phases (Figure 28a). The normalized Si release is low when compared to Mg, K, and Na, suggesting that some of the Si that was released from the samples was being preferentially retained and/or re-precipitated back onto the samples as an alteration phase(s) (Table 17).

The Ca concentration is weakly correlated to the reaction time (R^2=0.19; Figure 35). The rapid release and high concentrations of Ca likely reflects the rapid dissolution of calcite cement. Even though the calcite cement only comprises 0.3% by volume of the POT4 sample, it still appears to have a significant effect on the release of Ca. The Ca concentration still appears to climb in the longer term reactions, possibly signifying contributions from aluminosilicate phases such as plagioclase feldspar (anorthite variety $CaAl_2Si_2O_8$; Tables 3 and 17). Magnesium, being sourced largely from silicate minerals (the mole fraction of Ca:Mg in the cement was only 99.5/0.5), would alternatively be expected to display slower rates and more linear release into solution. The Mg release to solution displays a strong positive relationship with the reaction time and progressively increases with time (R^2=0.77; Figure 36).

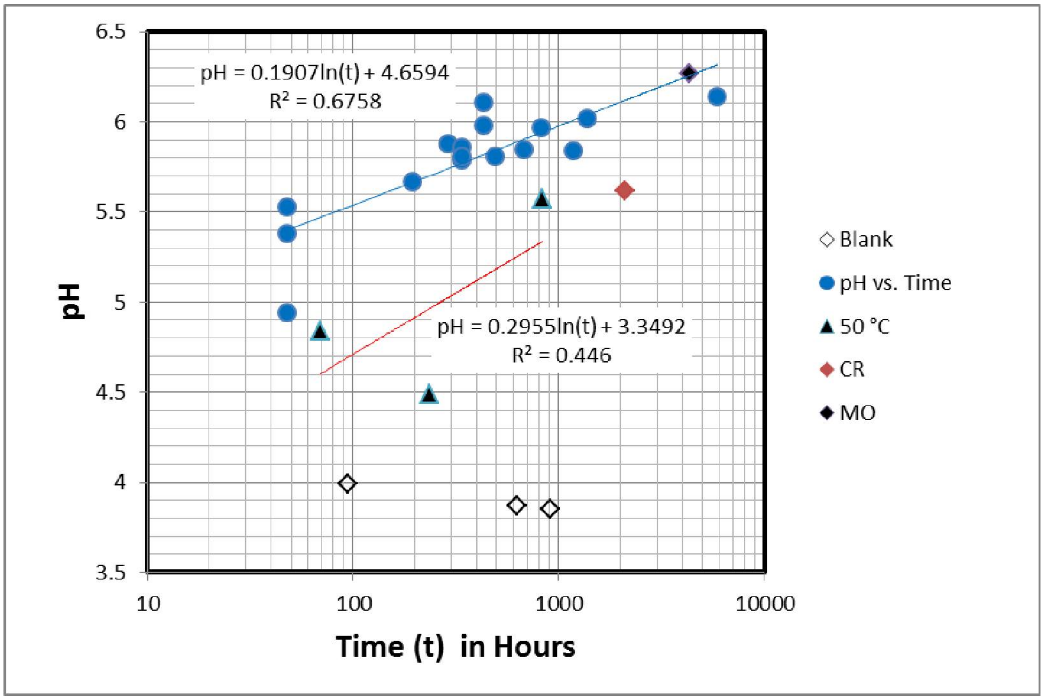

Figure 33. Variation in solution pH as a function of increasing reaction time for the Nonesuch Formation POT4 sample. Standard reactions in blue circles contain a wafered rock sample reacted in a $CO_2 + H_2O$ environment at 90°C. Test variables include higher surface area (crushed; CR), lower temperature (50°C), and sample mounting (wafered sample with lower fluid amount; MO) for (details in Table 17).

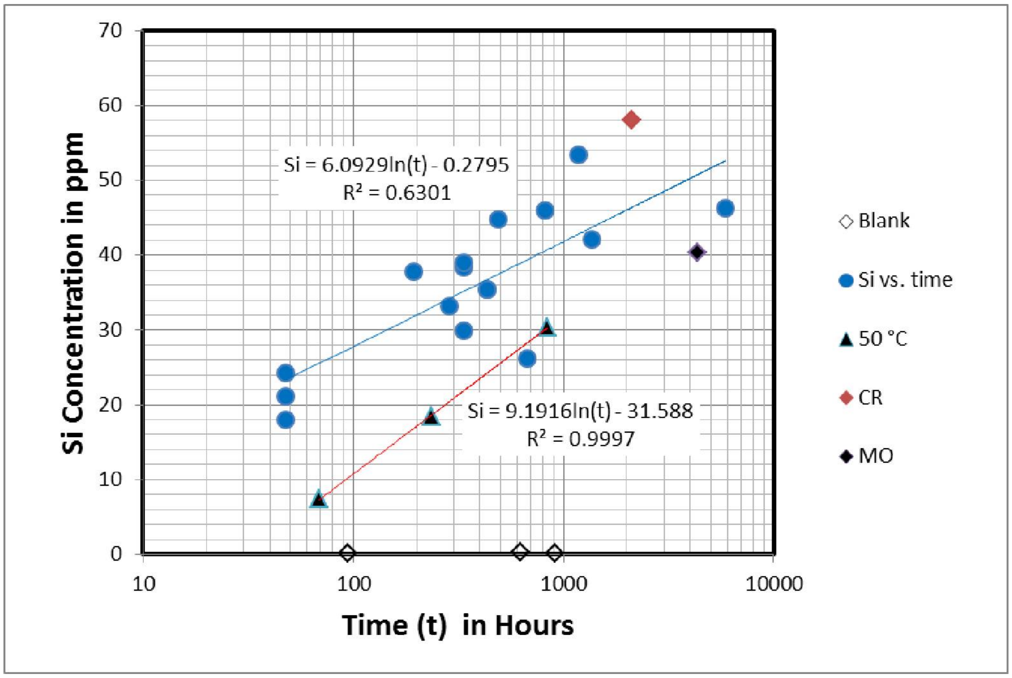

Figure 34. Silicon concentration with reaction time for the Nonesuch Formation POT4 sample. Symbols and reaction conditions are the same as described for Figure 33.

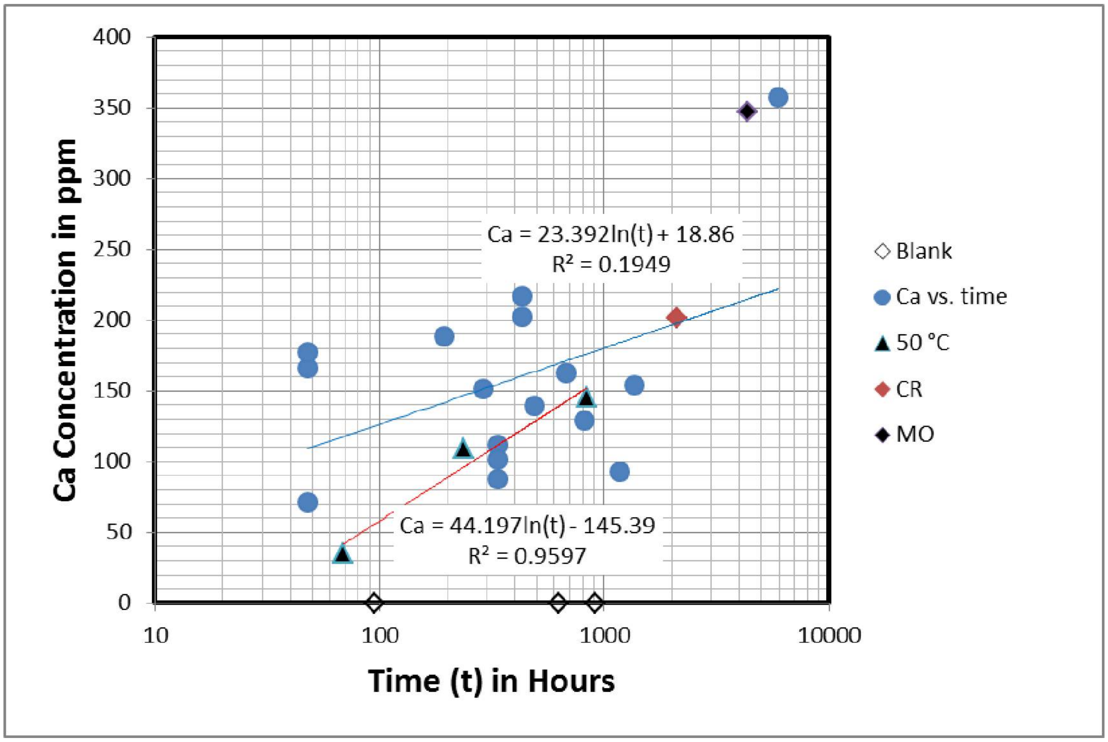

Figure 35. Calcium concentration with reaction time for the Nonesuch Formation POT4 sample. Symbols and reaction conditions are the same as described for Figure 33.

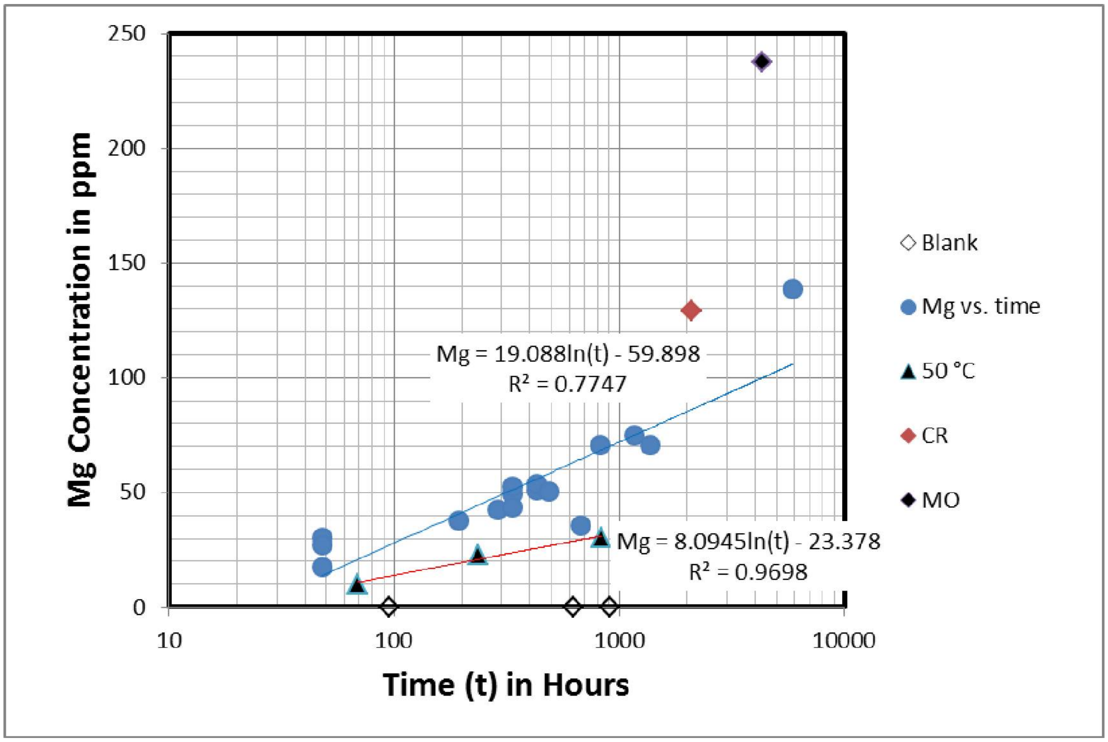

Figure 36. Magnesium concentration with reaction time for the Nonesuch Formation POT4 sample. Symbols and reaction conditions are the same as described for Figure 33.

Table 17. ICP-OES results from solution collected after opening the high-pressure vessels for the POT4 samples. Values are in ppm (mg/kg). Al and Fe were analyzed and were at or below the analytical detection limit of 0.1 ppm for all samples.

Sample	Time (hours)	Si	Ca	Mg	K	Na	Mn
T1	48 (2 days)	21.2	166	30.4	7.0	0.6	1.2
T2	48 (2 days)	24.2	71.8	17.3	7.6	0.7	1.9
T3	48 (2 days)	18.0	178	27.1	7.1	0.6	1.2
T4	194 (8 days)	37.9	189	37.6	6.0	<0.1	2.7
T5	288 (12 days)	33.3	152	42.4	8.6	0.2	<0.1
T6	336 (14 days)	38.4	112	49.2	9.6	1.4	0.2
T7	336 (14 days)	39.0	102	52.9	8.5	0.8	<0.1
T8	336 (14 days)	29.9	87.7	43.5	8.0	0.8	<0.1
T9	432 (18 days)	35.5	203	50.8	9.4	1.0	<0.1
T10	432 (18 days)	35.5	217	53.8	10.5	1.1	<0.1
T11	488 (20 days)	44.8	139	50.5	9.1	1.0	1.1
T12	675 (28 days)	26.2	163	35.4	7.3	1.0	<0.1
T13	819 (34 days)	46.0	129	70.9	6.3	1.1	<0.1
T14	1175 (50 days)	53.6	93.1	74.8	8.1	1.0	0.1
T15	1367 (60 days)	42.1	154	70.6	9.8	1.7	<0.1
T16	5913 (246 d)	46.3	357	139	12.0	3.6	4.1
Blank1	95 (4 days)	<0.1	<0.1	<0.1	<0.1	<0.1	<0.1
Blank2	627 (26 days)	0.22	<0.1	<0.1	<0.1	<0.1	<0.1
Blank3	915 (38 days)	0.11	<0.1	<0.1	<0.1	<0.1	<0.1
Crushed	2112 (88 days)	58.0	201	129	8.0	2.7	4.6
Mounted	4343 (181 d)	40.3	348	238	32.9	5.5	2.6
At 50°C	69 (3 days)	7.5	35.2	9.9	3.8	0.8	1.1
At 50°C	236 (10 days)	18.4	109	22.9	3.0	1.0	2.8
At 50°C	833 (35 days)	30.3	145	30.0	3.0	1.0	3.6

The release of K, Na, and some of the Ca is believed to result from the hydrolysis of feldspars through the exchange of alkali and alkaline earth elements in the solids with the H^+ ions in the acidic solution. The release of K and Na displays a moderate to weak correlation with reaction time (potassium R^2=0.35 and sodium R^2=0.52; Figures 37 and 38, respectively). Potassium shows a positive temperature dependence, Na data does not. The Na release from the samples is also relatively low, thus there may be some scatter of data related to the lower analytical accuracy as the concentrations in solution approach the ICP-OES analytical detection limits.

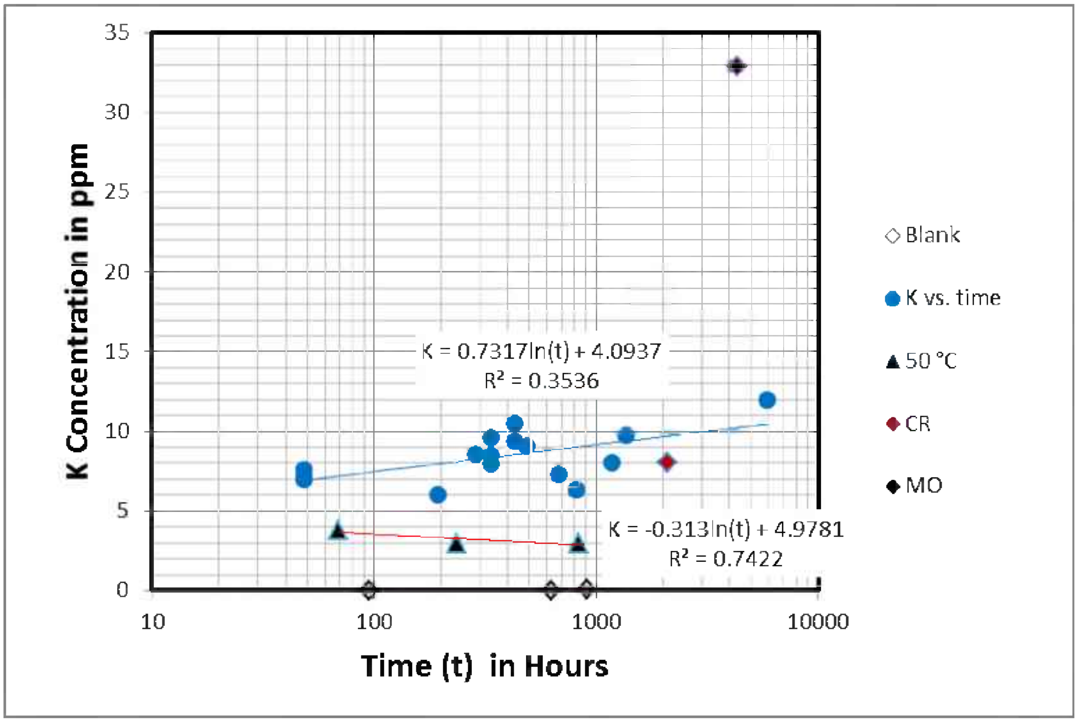

Figure 37. Potassium concentration with reaction time for the Nonesuch Formation POT4 sample. Symbols and reaction conditions are the same as described for Figure 33.

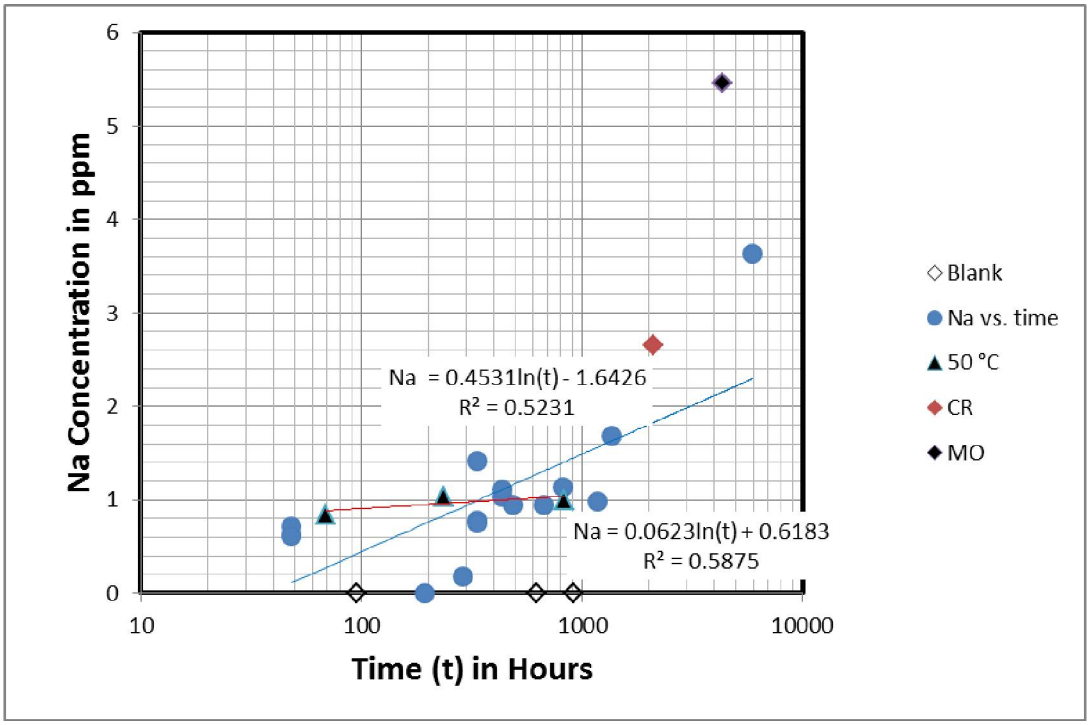

Figure 38. Sodium concentration with reaction time for the Nonesuch Formation POT4 sample. Symbols and reaction conditions are the same as described for Figure 33.

2.6.2 Temperature Effect on Reaction Rates

A limited suite of three experiments were conducted at 50°C so that a comparison could be made as to the effect of reaction temperature between the 50 and 90°C elemental release rates. The average geothermal gradient in the Iowa sector of the MCR has been estimated at between 16 to 19°C/km (Anderson, 1990; Hegarty et al., 2007). Therefore, if the thermal conductivity of the MCR sequence was homogeneous, the 50°C temperature would correlate to a depth of 3.1 km (10,170′) while the 90°C temperature would correlate to 5.6 km (18,372′; assuming a temperature for near-surface rocks of 10°C).

The overall pH is lower in the 50°C samples than it is for the 90°C samples, reflecting the slower reactions between the aqueous solution and the mineral phases at lower temperature. The variation in the trends seems to indicated that the pH is increasing at a faster rate with reaction time for the 50°C tests (slope of +0.29) relative to the 90°C tests (slope of +0.19), however there is a great amount of scatter in the data, especially for the lower temperature experiments.

Overall, the solubility and kinetic dissolution rates of the silicate minerals also increase as the temperature is increased. Both the 50 and 90°C trends show good linear correlations with reaction time, with the 90°C Si release concentrations being approximately 400% higher in the short term tests after ~70 hours, but this effect is decreasing with longer reaction times to the point where the Si release is only 25% higher after ~800 hours of testing (Figure 34). The increase in Si release rates observed these experimental results is similar or slightly accelerated relative to experimentally determined solubility trends reported for the various feldspar minerals (Berman, 1988; Shock and Helgeson, 1988; Shock et al., 1989; Arnorsson and Stefansson, 1999). For example the dissolution of anorthite feldspar ($CaAl_2Si_2O_8$) increases approximately 1000-fold as temperature increases between zero and 90°C (pK changes from between 23.75 to 21.25 at 0°C to 19 to 19.25 at 90°C). Albite plagioclase ($NaAlSi_3O_8$) and K-feldspar ($KAlSi_3O_8$) show similar temperature dependent trends (pK for albite is between 20 to 23.5 at 0°C and between 16 to17 at 90°C; K-feldspar is 24 to 26 at 0°C and between 19 and 19.5).

Opposite to the silicates, the solubility of Ca and Mg with respect to carbonate minerals is non-linear and is inversely proportion to temperature. The pattern of Ca release for the 90°C tests displays a lot of scatter ($R^2 = 0.19$; Figure 35) and thus do not define any distinctive trend with reaction time. In contrast, Mg release is linear with reaction time and shows a much higher degree of correlation ($R^2 = 0.77$; Figure 36). A plausible cause for this difference may be related to the presence of rapidly dissolving low-Mg calcite that released a large proportion of the Ca in solution, while silicate minerals were releasing Mg, Si, and some additional Ca. Some of the data scatter for Ca may also be related to the preferential precipitation of Ca into secondary carbonate minerals as reactions progressed into longer time intervals. Indeed, many of the lower Ca concentrations are related to the longer-term test intervals. The average concentration of Mg from the samples reacted at 50°C was also lower than that of the 90°C samples, however, for Ca there was more overlap between the 50 and 90°C data.

Sodium and potassium release concentrations were generally flat and/or displayed a moderate amount of data scatter over time (Figures 37 and 38). The concentration of K was notably lower for the 50°C experiments relative to the 90°C samples, while the Na release trends display complete overlap between the two test temperatures. The concentrations of both Al and Fe from the leachate solution were generally below the ICP-OES detection limit of 0.1 ppm, while Mn concentrations were always below 4.6 ppm and did not display any consistent reaction trends with time (Table 17).

2.6.3 Sample Solid Surface Area Effect on Reaction Rates

A single sample of the Nonesuch POT4 sample was mechanically crushed and sieved to collect the +100 mesh (0.149 mm) to -60 mesh (0.250 mm) size fraction in order to examine the effect of increasing surface area on the reaction rates. One gram of the crushed sample was reacted in 10 ml of water to provide a higher sample surface area / leachant volume test environment. The pH of the leachant solution following reaction with the high surface area crushed sample was about 5.7, which was slightly lower than the experiments with the lower surface area wafered samples (Figure 33, "CR" sample). This lower pH value was unexpected, as the greater surface area of the crushed sample should have resulted in a more rapid acid neutralization capacity for the sample, and hence a higher pH value. The pH of the mounted sample (MO, reacted with 5 ml rather than 10 ml of water (and with the sample only partially submerged) displayed a similar pH as the reaction trend plot for the remaining monolith samples reacted with twice the water amount. There thus appeared to be no discernable effect of exposing the samples to less fluid by reacting them in partially unsaturated conditions.

The effect of the increased surface area for the crushed sample had a notable effect of helping to increase the rate of Si, Mg, and Na release as compared to the standard wafered sample experiments (Figures 34, 36, and 38). The release concentrations for these three elements were higher than the overall trend of the wafered 90°C samples by 12, 40, and 4.5 ppm, respectively. By contrast, Ca and K were released at rates that were similar to the rates of the wafered 90°C samples (Figures 35 and 37). The concentrations of Al and Fe were too low to reveal any specific release patterns.

Both surface area and the geomorphology of a mineral grain can influence the rate of dissolution. A smaller grained particle has a higher proportion of atoms located at kinks, steps, and terraces on the crystal surface. Atoms in these positions will have fewer coordinating ions of an opposite charge, thus making these atoms located at points of dislocation more soluble (Berner and Morse, 1974; Railsback, 2011). The cleavage in the minerals (surface roughness) increases the proportion of positive kinks, steps, and terrace located atoms. A feldspar crystal from a reacted sample of POT4 displayed monoclinic or triclinic cleavage morphology with two preferential dissolution regions; one at the corners of the three intersecting cleavage planes and the other occurring along the edges of two of the cleavage planes (Figure 39). The preferred dissolution of the crystal at these locations resulted in the formation of a serrated edges and rounded corners. By contrast, only a few dissolution pits can be found on the flat crystal faces of the same sample, indicating that they were less reactive in the leachant solution.

The alteration and dissolution of pore filling calcite cement in the MCR samples from the HPT experiments is also characterized by the development of preferential dissolution along cleavage planes and grain boundary contacts with other mineral phases (Figures 40 and 41). The development of these preferential dissolution pathways could enhance the primary porosity of the Oronto Group sediments when these pores are blocked by surrounding zones that have pores filled by calcite cement. This acid induced opening of pores should occur in a rapid fashion (hours) as calcite and other carbonate cement tends to react quickly with acids (Figure 28). Fluids penetrating through these preferred pathways will migrate into the sample matrix much more rapidly than if the corrosion front had occurred in a more uniform manner. Fluid penetration into the rock sample will be even more rapid if dissolution front intersects open but isolated pore space within the sample matrix. In such a process, the fluids would rapidly dissolve along a cleavage plane or grain boundary, then very rapidly move through an open pore, penetrate another blocked pore filled with calcite, then rapidly jump through a second open pore, in a hop-scotch like progression. The preferential dissolution along boundaries between calcite and other minerals (Figure 41) also indicates that acid attack on any alkaline earth silicates or Fe-oxides may initiate fairly rapidly in the corrosion sequence as these contact points will be the locations of the earliest penetration of fluids. Acid ion exchange reactions weathering the silicate and oxide grains may be subdued at first, since the reaction rate of calcite in is much more rapid, and the presence of calcite will neutralize the acids.

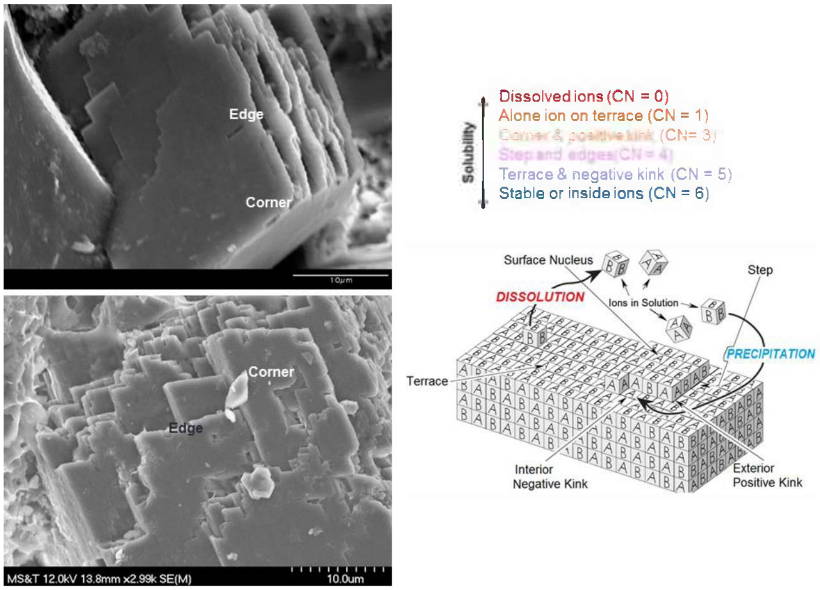

Figure 39. Left top and bottom, photomicrographs of POT4 sample reacted at 90°C for 25 days showing selective dissolution of feldspars along the most vulnerable kink edge and corner sites. (Right) schematic diagram showing the equilibrium scenario between the dissolution at high energy dislocation sites and precipitation at low-energy sites, modified from Railsback (2011).

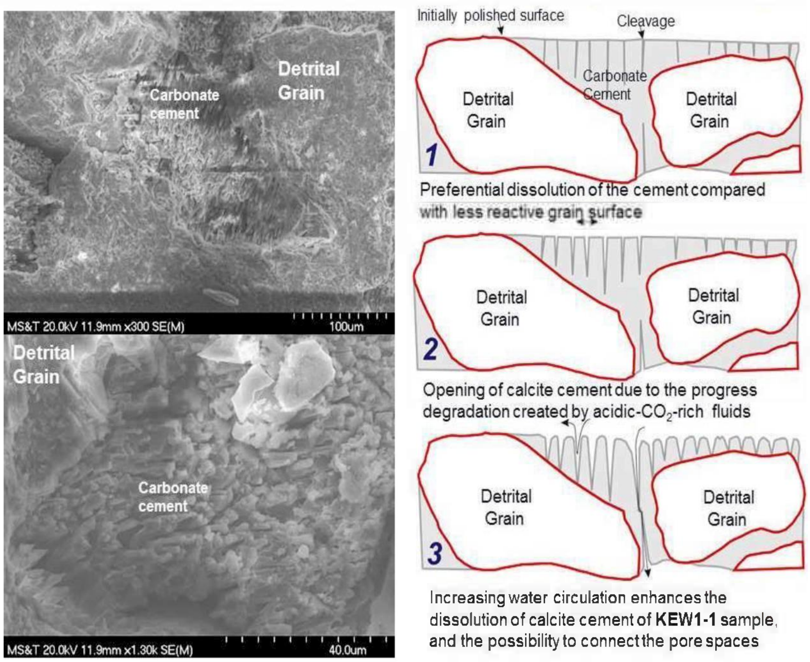

Figure 40. Photomicrograph of KEW1-1 sample (Copper Harbor Conglomerate) reacted for 143 hours at 90°C in a deionized water + CO_2 environment. The dissolution of calcite cement is enhanced along the parallel cleavage plane surfaces. The increase in the surface area created by preferential penetration of acidic fluids along cleavage planes will further accelerate calcite dissolution by increasing the surface area.

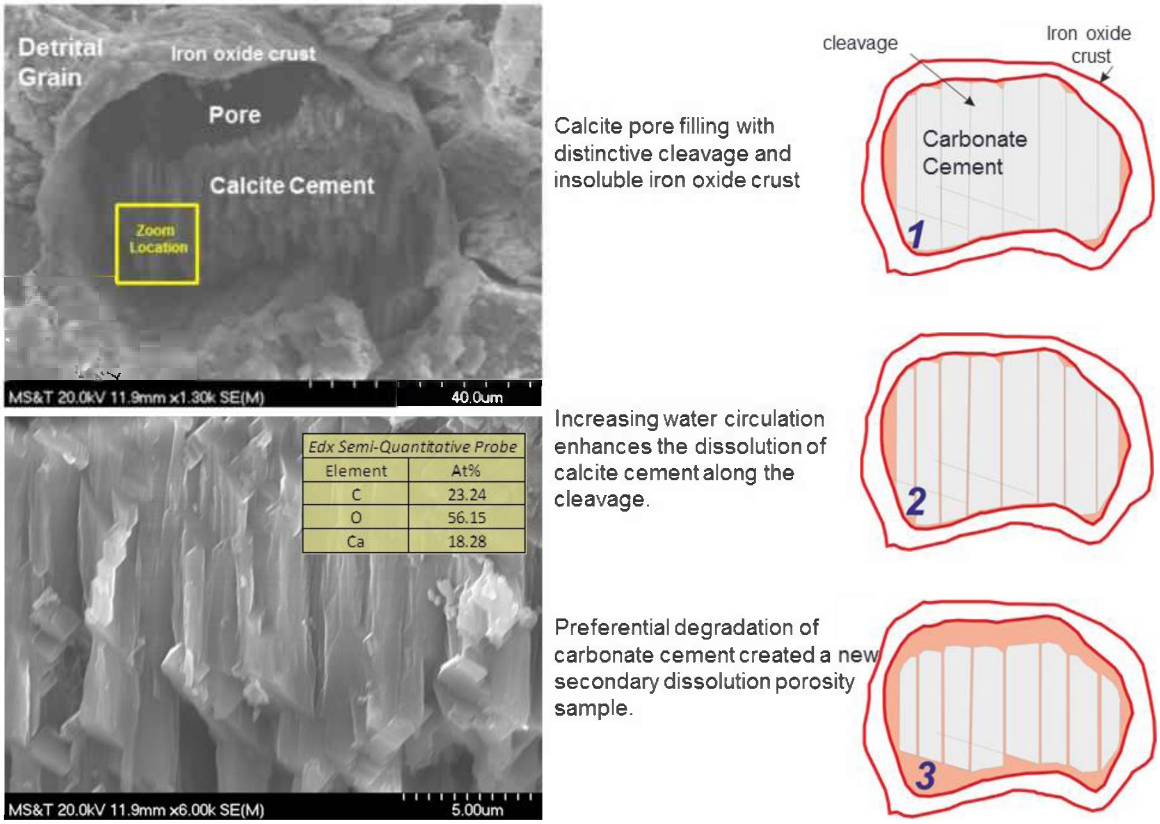

Edx Semi-Quantitative Probe

Element	At%
C	23.24
O	56.15
Ca	18.28

Calcite pore filling with distinctive cleavage and insoluble iron oxide crust

Increasing water circulation enhances the dissolution of calcite cement along the cleavage.

Preferential degradation of carbonate cement created a new secondary dissolution porosity sample.

Figure 41. Photomicrograph of KEW1-1 sample reacted at 90°C for six days. Dissolution of carbonate cement occurred preferentially along calcite cleavage planes and the pore boundaries where the cement was in contact with detrital grains and/or detrital grains covered with Fe-oxides.

2.6.4 Redox Conditions

The Eh-pH diagram (Figure 42) illustrated that most of the solutions contacting the reacting POT4 samples were located within the crystalline stability field for hematite (Fe_2O_3) once the reactions had progressed for a significant length of time. Therefore, any Fe^{2+} that may have been released from dissolving samples should have eventually been converted to the Fe^{3+} state and precipitated as hematite or some other ferric-iron hydroxide or oxy-hydroxide phase(s) once the Fe concentration had reached the saturation level. The iron concentration of final leachate solution was, normally, below the detection limit of the instrument (<0.1 ppm) and Fe coatings were noted on some of the Teflon reaction vessels indicating that Fe was being released from the samples in a soluble and mobile form, but precipitated as an Fe^{3+} phase during the testing interval (Figure 43). Although we expect that MCR rocks will influence pH changes in an actual disposal setting as they do in our HPT experiments, we are not so sure that we have fully replicated the redox conditions for any potential subsurface repository setting. The Eh values will likely be controlled by the massive volume of rock material where iron silicate and/or Fe-oxide minerals are abundant. Microbial populations and associated redox reactions may also play a role, although this biologic influence will be minimal in most subsurface reactions where nutrients are limited.

2.6.5 CO_2 Generated During Calcite Dissolution

A significant amount of secondary CO_2 may be generated as calcite and other carbonate minerals dissolve following the injection of CO_2 into a subsurface repository containing carbonate minerals. To determine the volume of this gas phase produced we reacted a 0.1 gram sample of calcite in a 5% of HNO_3 solution with the atmosphere chamber above the reaction vessel connected to a sealed water filled U-tube that was in turn connected to a volumetric chamber. The reaction of the calcite thus produced gas phase CO_2 that displaces an equivalent volume of water that can then be measured. The 0.1 gram sample of calcite was completely consumed after two minutes of reaction, producing 0.93 ml of CO_2 gas at an average rate of 0.43 ml/min at atmospheric pressure, The stoichiometric balance of components indicates that the 0.1g of calcite ($CaCO_3$) initially occupies a volume as a solid of 0.0369 cm^3 (calcite density = 2.71 g/cm^3) and would produce 0.044 g of a CO_2 gas phase following dissolution. The increase in the volume ratio between the gas phase *versus* the solid calcite was 25-fold when the gas was at atmospheric pressure.

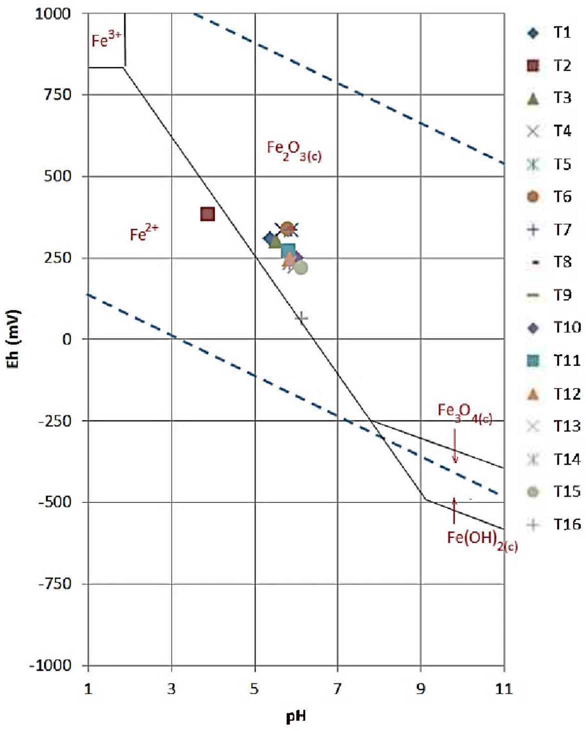

Figure 42. The characteristics of the fluid composition of the leachate fluids collected after testing POT4 sample. Reaction conditions were at 90°C and 65-70 bars pressure.

Figure 43. Teflon liner with only CO_2 and H_2O (to the left) and a Teflon liner containing GHB (Good Harbor Basalt) sample (to the right), showing a precipitation of Fe^{2+} mineral phases on the walls of the Teflon liner.

No readily discernable correlation existed between the Mn concentrations and reaction time, though a large portion of the samples had concentrations of Mn that were below detection limits of the ICP-OES instrument, especially for most of the longer term reacted samples (R^2=0.03; Figure 44). Manganese, like Fe, will exhibit a decrease in solubility when the respective metal ions are fully oxidized. The oxidation of Mn requires higher redox potentials that Fe, so it appears that the longer term experiments had sufficiently provided enough electron acceptors to fully oxidize, and cause the precipitation of both Fe and Mn minerals. For Mn, this results in the conversion of higher solubility Mn^{2+} and Mn^{3+}, into fully oxidized and low solubility Mn^{4+} phases.

2.7 Core Flooding Experiments

Core flooding experiments were conducted to show the effect of the CO_2-rich fluids on the aquifer properties, and specifically permeability under an induced pressure head. Six samples were reacted in the core flooding experiments ranging from the high porosity-permeability Bayfield (BAY2) sample, the moderate porosity and calcite cemented CHC (KEW3-1) and non-calcite Freda samples (POT8-2), and the moderate porosity-permeability 11,061.5′ Texaco Poersch #1 sample (Table 18). The core flooding experiments exposed a wafered rock sample to a pressurized container filled with nitric acid acidified water (pH=3.8) at ambient room temperature. The starting leachant fluid was prepared to a pH value approximately equivalent to that of deionized water exposed to a pure CO_2 atmosphere. The relative permeability of the rock is evaluated in real time by measuring pressure changes as the rock reacts with the leachant fluid, fluid effluent rates, and the solution chemistry.

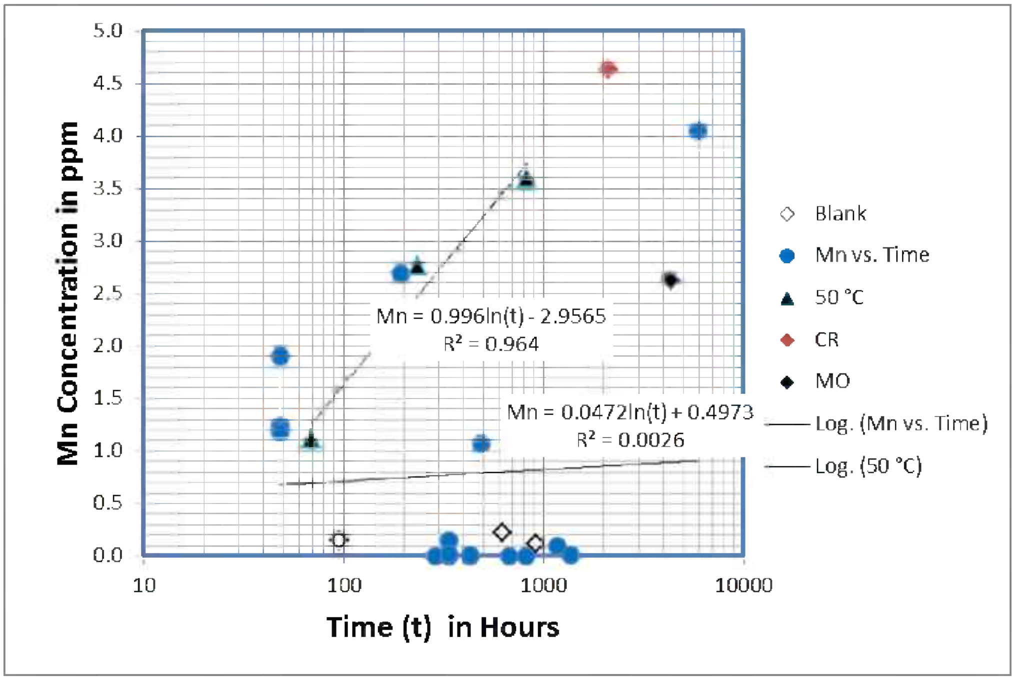

Figure 44. Manganese concentration with reaction time for the Nonesuch Formation POT4 sample. Symbols and reaction conditions are the same as described for Figure 33.

Table 18. Summary of samples used in the core flooding experiments. The symbol "P" represents the porosity determined by petrographic analysis, "CCe" represents volume percent calcite cement also determined by petrographic analysis. Thickness of rock sample testes in core flooding experiment is given in centimeters.

		Carbonate Cement Content	
		Low	High
Porosity	Low	**POT8-2** (P=1.2%; CCe =0.0%) 1.27 cm.	**KEW1-1** Sample (P=1.0%; CCe =15.9 %) 1.65 cm. **KEW3-2** Sample (P=4.0%; CCe =11.1%) 2.29 cm.
	Moderate/High	**Texaco Poersch #1 - 11,061.1'** (P=7.9%; CCe= minor reaction with HCl, only dolomite detected by XRD analysis) 1.91 cm. **BAY2** Sample (P=32.2%; CCe =0.0%) 3.18 cm.	**KEW3-1** Sample (P=8.9%; CCe =10.4%) 1.65 cm.

The Bayfield BAY2 sample represents a mature quartz arenite composition sandstone with a high initial porosity (14.7%) and no detectible calcite cement. Impregnation of the highly permeable sandstone pores by the epoxy mounting along the outer edge of the sample core during mounting caused some blockage that was accounted for by estimating a smaller disk diameter in the permeability calculation. The initial measured permeability was ≈340 mD and did not appreciably change during testing indicating that the sample reacted minimally with the acid leachant during testing. The BAY2 sample was also reacted at different flow rates between 0.25 and 1.0 ml/minute by varying the headspace pressure. A steady-state fluid pressure was achieved in approximately two minutes and the backpressure remained at a low and constant value throughout the entire 8 to 14 minute testing interval for all flow rates tested (Figure 45). This continuous steady-state flow with low backpressure is a characteristic of a good aquifer rock that offers minimal resistance to flowage of water, or for injected CO_2.

The initial and final pH of the influent and effluent fluids was 3.7 and 3.8, respectively. The limited change indicates minimal reaction between the quartz-dominated rock sample with the leachant fluid. This feature was also reflected in the low concentrations of dissolved constituents in the effluent (Table 19). Sodium was the only element present and was likely derived as a trace contaminant from previous experiments with Na-brine fluids. Sodium tends to adsorb to plastic test vessel components and is difficult to completely remove without very extensive pre-test rinse cycles.

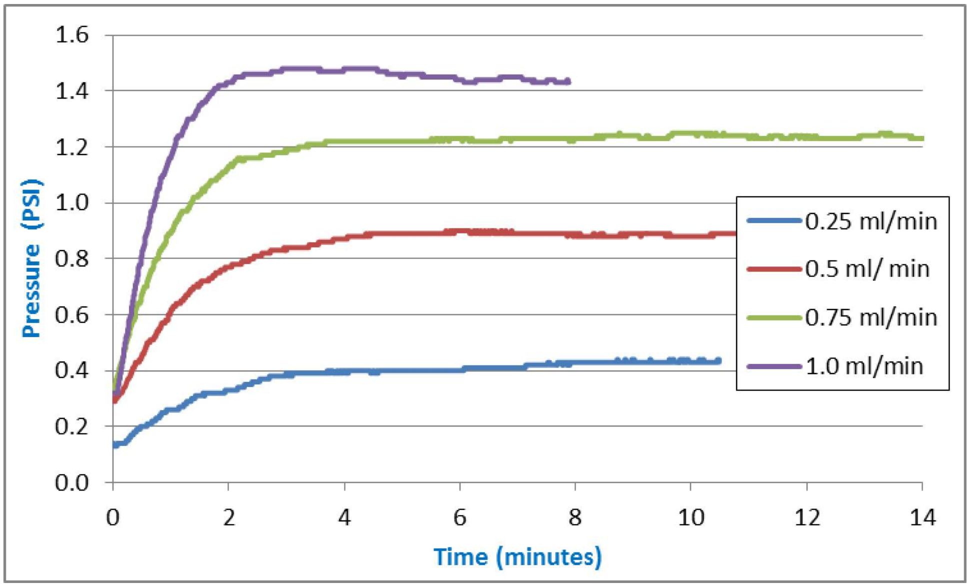

Figure 45. Steady flow (dp/dt = 0) for sample BAY2 in the core flooding experiment with breakthrough after approximately two minutes of flooding. The rapid attainment of steady-state flow after the initial two-minute period indicates that no changes in the rock permeability had occurred during the testing interval.

Table 19. Chemical composition of the core flooding experiment influent and effluent fluids for the BAY2 sample (in ppm). A high initial Na concentration was a result of contamination from previous experiments with the pump that used a Na-brine fluid.

	Time min.	Ca	Mg	K	Na	Mn	Fe	Si	Al
Blank		<0.1	<0.1	<0.1	<0.1	<0.1	<0.1	<0.1	<0.1
Influent	30	<0.1	<0.1	<0.1	0.2	<0.1	<0.1	<0.1	<0.1
Effluent	10	0.9	<0.1	<0.1	23.1	<0.1	<0.1	<0.1	0.8
	15	<0.1	<0.1	<0.1	7.1	<0.1	<0.1	<0.1	0.5
	30	<0.1	<0.1	<0.1	2.1	<0.1	<0.1	<0.1	0.5

The Texaco Poersch #1 Well sample from the 11,061.5′ depth contained abundant feldspar and minor carbonate cement (dolomite) with a moderate petrographic porosity (7.9%). Minor peaks for dolomite, chlorite, and albite were identified during the XRD analysis of the segregated clay-sized particle fraction of this sample. Four stages of fluid break-through were recognized during the core flooding test with this sample (Figure 46). The first stage occurred between 1 and 8 minutes, in which the pressure buildup occurred. The second stage occurred between 8 and 45 minutes and was characterized by a steady flow (dp/dt=0). This was followed by the third stage where there was an abrupt decrease in pressure, likely resulting from the activation of a fracture or the final dissolution and breakthrough of mineral cements that were blocking the pores in the sample. The fracture hypothesis is favored due to the very rapid decrease in pressure that was observed. The final stage of reaction (from 45 to ~105 minutes) was characterized by a transient flow, in which the pressure increased very gradually over time (dp/dt>0). This minor increase in pressure may continuous blockage of pores or fractures in the sandstone due to dislodging of fine particles by the fluid, movement of the particles in the sample, and subsequent blockage of the relatively narrow pore throats where several grains may come in contact. Expansion of clay particles may also produce a similar blockage, however, no expansive clays were detected in the XRD analysis of this sample. The average fluid permeability during the second stage was 1.01 mD. This jumped to 1.29 mD during the abrupt pressure decrease, and then gradually fell back to 1.12 mD during the final flow stage.

The solution pH increased from a starting 3.8 to 5.7 after 100 minutes of testing. The chemical composition of the effluent fluid displayed an increase in alkalinity (from 3 to 20 mg/L) and Ca (from <0.1 to 5 ppm) during the first 100 minutes. Increases in Si, Fe, and K also are noted but were relatively subdued (Table 20). The increase in alkalinity, pH and Ca concentration all reflect dissolution of the calcite cement in the sample while the other components reflect the dissolution of silicate and/or oxide minerals.

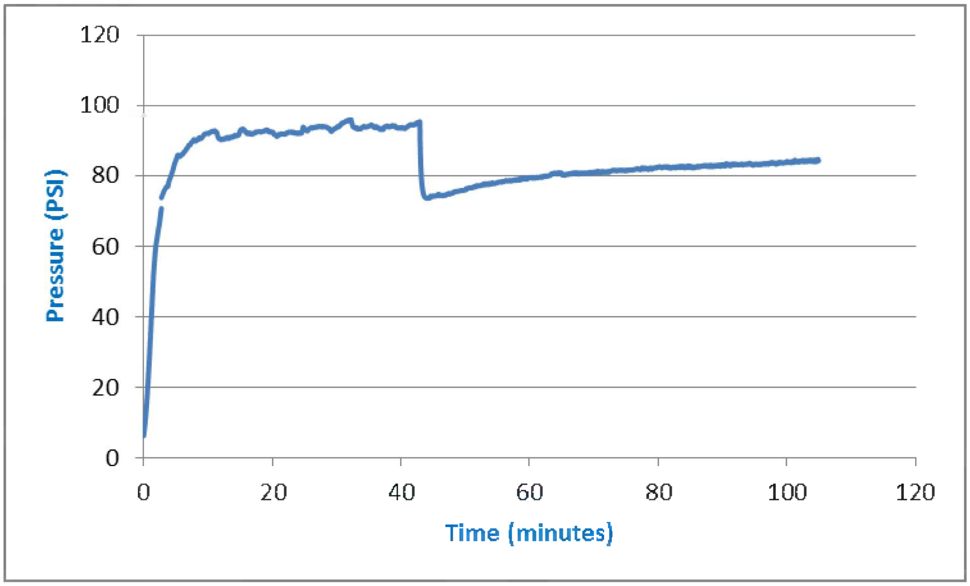

Figure 46. The pressure curve for the 11,061.5′, Texaco Poersch #1 core flooding experiment indicating initial breakthrough after eight minutes, steady flow until 45 minutes, and then an abrupt pressure drop, and final transient flow until ~110 minutes.

Table 20. The chemical composition of the 11,061.5′, Texaco Poersch #1 sample influent and effluent water (in ppm). Initial Na is a result of pump contamination.

	Time min.	**pH**	**Ca**	**Mg**	**K**	**Na**	**Mn**	**Fe**	**Si**	**Al**
Blank		3.8	<0.1	<0.1	<0.1	<0.1	<0.1	<0.1	<0.1	<0.1
Influent	120	3.8	<0.1	<0.1	<0.1	3.9	<0.1	<0.1	<0.1	<0.1
Effluent	60	5.8	4.9	<0.1	<0.1	8.3	<0.1	<0.1	0.1	<0.1
	80	5.8	4.9	<0.1	<0.1	4.2	<0.1	<0.1	0.1	<0.1
	100	5.7	5.0	<0.1	<0.1	4.0	<0.1	<0.1	0.1	<0.1
	120n	5.7	3.6	<0.1	0.5	7.5	<0.1	0.4	0.1	<0.1

The CHC KEW3-1 sample contained an abundance of calcite cement (10.4%) and relatively high petrographic porosity (8.9%). This sample thus represents a horizon in the CHC that would be amenable to CO_2 injection and where the acidified fluids would be expected to enhance the porosity and permeability by dissolving calcite. The permeability rose ~30% during testing, from approximately 0.92 mD to 1.2 mD over the 125 minutes of testing of this sample in the core flooding experiment. Unlike the steady-state flow achieved in the BAY2 sample, the KEW3-1 sample exhibited transient increase in flow (and associated back-pressure decrease) with time (dp/dt <0) suggesting that the dissolution of the calcite cement and a progressive increase in porosity and permeability were occurring upon exposure of the sample to the acidified leachant solution (Figure 47).

The chemical composition of the effluent fluid displayed an increase in the following components over the three hour test interval: alkalinity (from ~3 to ~9 mg/L), pH (from 3.7 to ~ 5.7), Ca (from <0.1 to 7.5 ppm), K (from <0.1 to 0.9 ppm), and Si (from <0.1 to 0.3 ppm; total solution volume was ~325 ml; Table 21). The increase in alkalinity, pH and Ca concentration all reflect the dissolution of calcite cement, whereas the more subdued increase in K and Si concentrations reflect the contribution from altering silicate minerals, likely K-feldspar. The total weight of the sample also decreased by 11% during testing, suggesting that most of the calcite contained in the 1.65 cm. long segment of core had been dissolved during the two hours of testing as the weight loss was approximately the same mass of the calcite calculated to be in the sample before corrosion testing was initiated. This experimental result demonstrates that a repository containing calcite cement with some primary interconnected porosity will experience rapid pore widening and permeability-porosity increases following injection of CO_2. The reactions of this sample removed most of the calcite (10.4 volume percent) in a 1.65 cm thick sample in two hours.

The CHC KEW3-2 sample is a lithic-feldspathic arenite that contained a significant amount of calcite cement (11.1%) and moderate petrographic porosity (4.0%). The flow rate with this sample was ramped up from one ml/min to two ml/min during the first three minutes of testing. The pressure curve displayed a transient flow pattern with a positive pressure gradient, opposite to the pattern of sample KEW3-1 (dp/dt>0; Figure 48). The resulting permeability started off at a moderately high 2.00 mD at the onset of the pressure stabilization after five minutes and decreased slightly 1.79 mD over the 53 minutes testing period. A gradual decrease in porosity probably results from the blockage of narrow pore throats.

The pH of the effluent water from sample KEW3-2 increased from the starting leachant value of 3.8 to a value of 6.2 after about 40 minutes of testing (Table 22). Dissolution of the calcite cement was the likely cause of the rapid increase in released Ca, which peaked after 10 minutes, followed by a decline as the easily accessible calcite in the pores was progressively dissolved away. Magnesium was only detected in the 10 minute sample, paralleling the high Ca release and reflecting our measurement of calcite that revealed only ~0.5 mole % Mg. The concentration of Si was at a maximum of 2.8 ppm at 40 minutes, but did not display any consistent trend over time. Sodium and potassium concentrations were high with the former probably reflecting contamination from previous pump tests with brines.

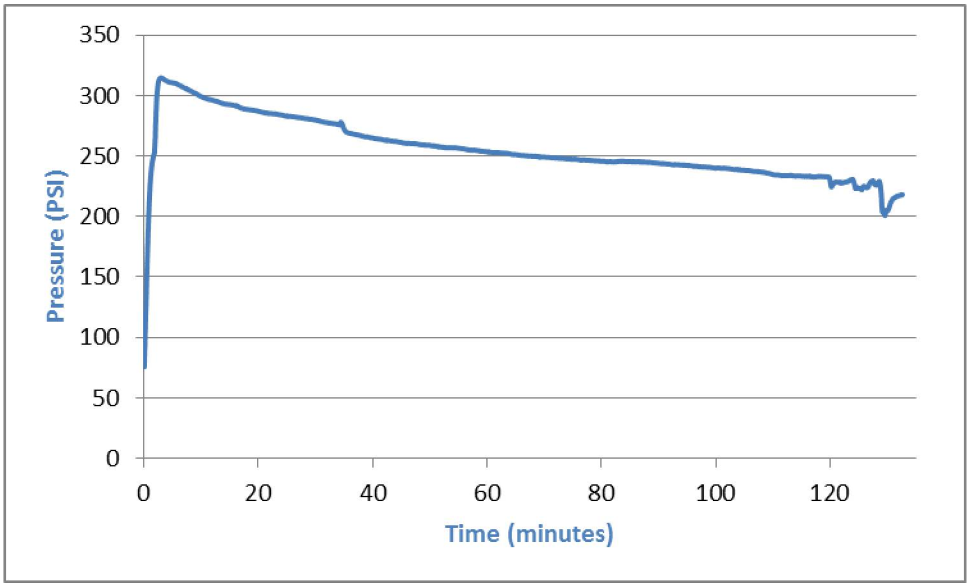

Figure 47. Transient flow (dp/dt <0) recognized in KEW3-1 sample core flooding experiment, indicating initial breakthrough after several minutes and gradual enhancement in sample porosity and permeability (reflected by a gradual long-term decrease in backpressure) associated with dissolution of calcite cement during ~125 minutes.

Table 21. Chemical composition of the influent and effluent water, in ppm, for the KEW3-1 sample core flooding experiments. Calcium makes up a significant portion of the dissolved material and is likely derived from calcite. The high initial Na concentration is likely due to residual contamination inside the pump from previous experiments.

	Time min.	pH	Alkalinity	Ca	Mg	K	Na	Mn	Fe	Si	Al
Blank				<0.1	<0.1	<0.1	<0.1	<0.1	<0.1	<0.1	<0.1
Influent	125	3.66	0 to 3	<0.1	<0.1	<0.1	<0.1	<0.1	<0.1	<0.1	<0.1
Effluent	30	5.80		3.9	<0.1	0.9	3.4	<0.1	<0.1	0.3	<0.1
	60	5.73		5.4	<0.1	0.8	1.4	<0.1	<0.1	0.3	<0.1
	125	5.70	9	6.1	<0.1	0.5	0.5	<0.1	<0.1	0.2	<0.1

The increasing pressure gradient behavior over time for sample KEW3-2 (Figure 48) was unexpected and did not correlate to the increasing pH and dissolved Ca + Mg content, both being suggestive of an increase in porosity-permeability following calcite dissolution. A lowering of the backpressure was expected, opposite to the observed pattern. A possible explanation for this trend would invoke the blockage of restricted pore throats by migrating particles within the sample. Mineral particles (e.g., clays) could have been liberated and suspended from zones where calcite was dissolving, and then became trapped in the narrow pore passages where grain boundaries come closest together. Sample KEW3-2 contained the highest proportion of silt and clay material (17.4 and 7.0 volume %, respectively; Table 3) for all the CHC samples thus there is a significant potential in this sample for particle migration.

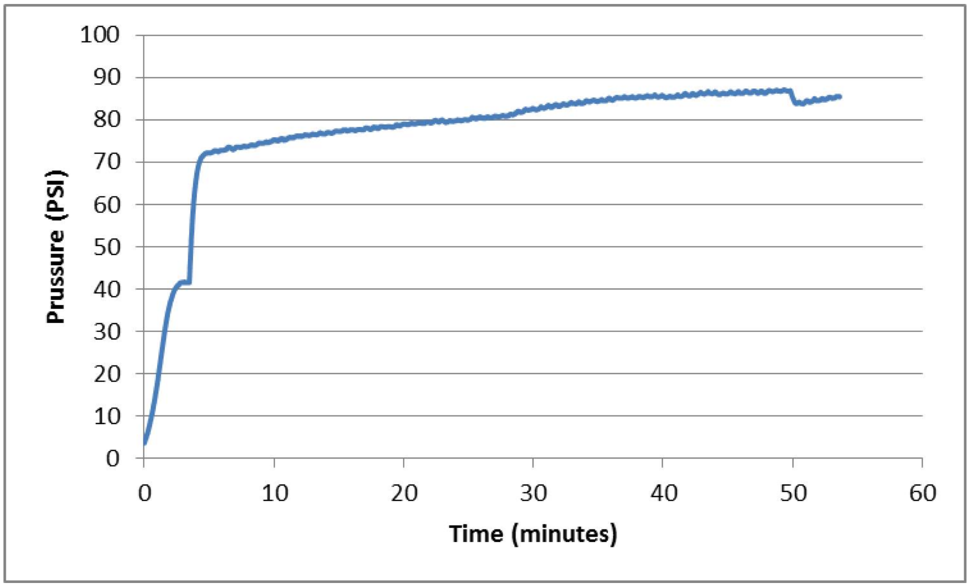

Figure 48 Transient flow (dp/dt>0) recognized in KEW3-2 sample core flooding experiments displaying an increase in backpressure over time.

Table 22. Chemical composition of the influent and effluent water, in ppm, for the KEW3-2 sample core flooding experiment. Ca comprises the most significant portion of the released components while the high initial Na concentration is likely due to contamination inside the pump from previous runs with brine fluids.

	Time min.	pH	Si	Fe	Ca	Mg	K	Na	Mn	Al
Blank			<0.1	<0.1	<0.1	<0.1	<0.1	<0.1	<0.1	<0.1
Influent	53		<0.1	<0.1	<0.1	<0.1	14	3.6	<0.1	<0.1
	10		0.5	<0.1	56.4	1.1	2.8	101	<0.1	<0.1
	20	5.7	0.3	<0.1	11.0	<0.1	1.2	47.1	<0.1	<0.1
	30	5.6	0.3	<0.1	4.4	<0.1	0.7	22.9	<0.1	<0.1
	40	6.2	2.8	<0.1	2.2	<0.1	0.4	9.0	<0.1	<0.1
	50		<0.1	<0.1	2.5	<0.1	0.4	6.2	<0.1	<0.1

The CHC sample KEW1-1 was selected as a low porosity (1.0% by petrographic point counting) and high calcite cement (15.9%) core flooding experiment. This sample was exposed to the maximum pressure limit of 500 psi without any fluids being extruded through the sample after three minutes of testing. The experiment was terminated in order to avoid over pressurizing the system and damaging the equipment.

The POT8-2 sample was a feldspathic lithic arenite collected from the Freda Formation at the Potato River Falls location. This sample displayed a low initial petrographic porosity (1.2%) and no observable calcite cement during petrographic analysis. The flow rate used in this experiment was one ml/min. The pressure curve reflected a gradual increase of back pressure over time (transient flow; dp/dt>0). Therefore the permeability of the aquifer decreased over time from 0.190 mD after five minutes to 0.175 mD after about 30 minutes of testing. The experiment was terminated after 33 minutes following the development of a fracture in the sample as noted by a sharp decrease in pressure (Figure 49).

The pH of the effluent fluid from the POT8-2 sample rapidly increased to 6.4 during the first 13 minutes and then was constant thereafter (Table 23). The effluent water contained Si concentrations between 0.26 ppm and 0.5 ppm. Calcium was approximately 3.0 ppm in the samples except for a 26 ppm pulse of Ca release at six minutes. The K concentration was approximately one ppm in the effluent samples except the sample collected after about six minutes (3.5 ppm). Sodium ranged between 2.8 ppm and 5.1 ppm, and again the sample collected after six minutes displayed a high Na pulse (13.2 ppm). The closely associated POT8-1 sample was characterized by the presence of smectite clay (42% of the total clays), chlorite (43%) and traces of illite and zeolite (Table 3). All these mineral components could represent a possible source of the cations released into the effluent water. The pulse release at six minutes suggests the rapid attack and removal of a mineral component(s) in the sample. This pulse likely involved the dissolution of silicate minerals as the pulse involved more than just Ca being released. Solutions were filtered using a 0.45 μm filter upon collection, so this pulse is not the result of particulate material, unless the particles were <0.45 μm in diameter. The pulsed release after six minutes also coincided with the attainment of a steady-state backpressure, thus indicating breakthrough of fluids through the sample had stabilized at a relatively steady, but slow rate.

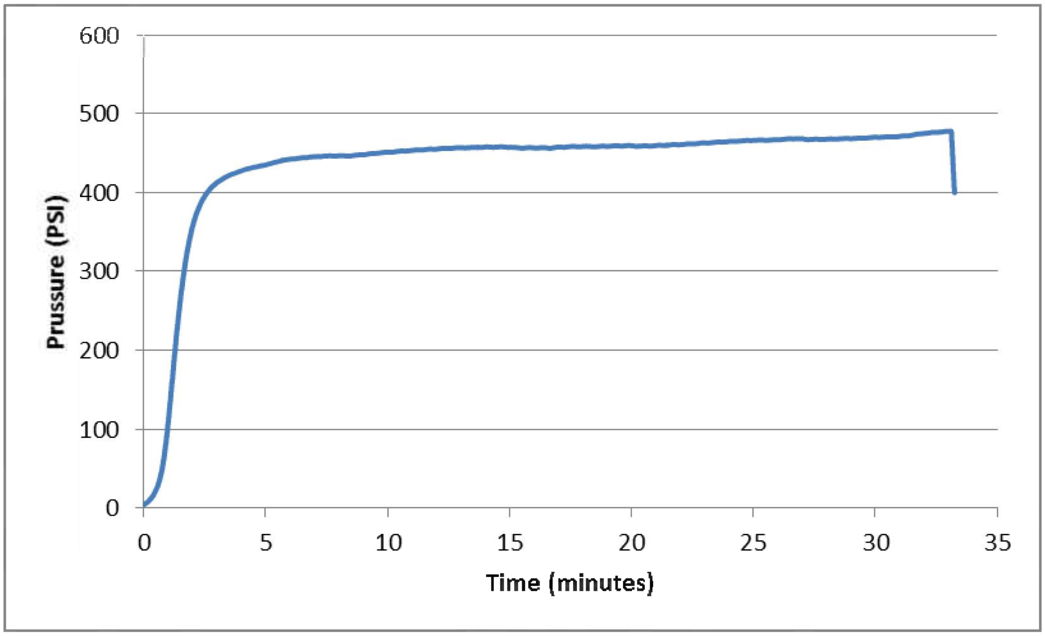

Figure 49. The pressure curve for the POT8-2 sample in the core flooding experiment indicated an initial breakthrough in 3-4 minutes, and slowly increasing transient flow until the sudden decrease in pressure after 33 minutes.

Table 23. Chemical composition of the core flooding experiment influent leachant and effluent fluids (in ppm) for the POT8-2 sample. A high initial Na and K concentration was, probably, created by contamination from previous brine runs.

	Time min.	pH	Si	Fe	Ca	Mg	K	Na	Mn	Al
Blank			<0.1	<0.1	<0.1	<0.1	<0.1	<0.1	<0.1	<0.1
Influent	35	3.8	<0.1	<0.1	<0.1	<0.1	0.4	0.4	<0.1	<0.1
Effluent	6	5.7	0.5	<0.1	25.6	0.5	3.5	13.2	<0.1	<0.1
	13	6.4	0.4	<0.1	3.5	<0.1	1.2	5.1	<0.1	<0.1
	19	6.3	0.3	<0.1	3.1	<0.1	1.0	3.9	<0.1	<0.1
	24		0.3	<0.1	3.1	<0.1	1.0	3.4	<0.1	<0.1
	29	6.4	0.3	<0.1	3.1	<0.1	0.9	3.0	<0.1	<0.1
	34		0.3	<0.1	3.2	<0.1	0.9	2.8	<0.1	<0.1

Porosity variations and different dissolution rates within and between minerals may have a large impact on permeability at spatially small scales. Porosity-permeability factors are often heterogeneous, and may become more-so as corrosive fluids migrate along preferential regions of a sample and expand these regions to create a channelized flow zone within specific regions of the rock sample (Wellman et al., 2003). A three mm thick cylindrical core section of the KEW1-1 sample was sliced, polished, and then reacted in the 90°C HPT testing environment with H_2O + CO_2 for 43 days. Upon completion of the corrosion test, the sample was impregnated with blue stained epoxy to preserve porosity features, and then cut along its cylinder c-axis. Detailed high resolution microscopic point counting was conducted on reacted sample using a microfilm projector. The sample displayed a high degree of porosity heterogeneity, with alternating high- and low porosity zones occurring as porous and calcite-cemented course-grained lamina (e.g., zone A; Figure 50B) with less porous-Fe oxide cemented-fine grained lamina (e.g., zone B). The sample lost approximately 1.8% of its original weight during testing. The Ca concentration in the leachate fluid at the end of the corrosion testing was 496 ppm; the Mg was 114 ppm. The final pH of the collected fluids was 6.2, indicating a significant dissolution within the sample as the initial pH in the CO_2-rich atmosphere of the tests was approximately 3.8.

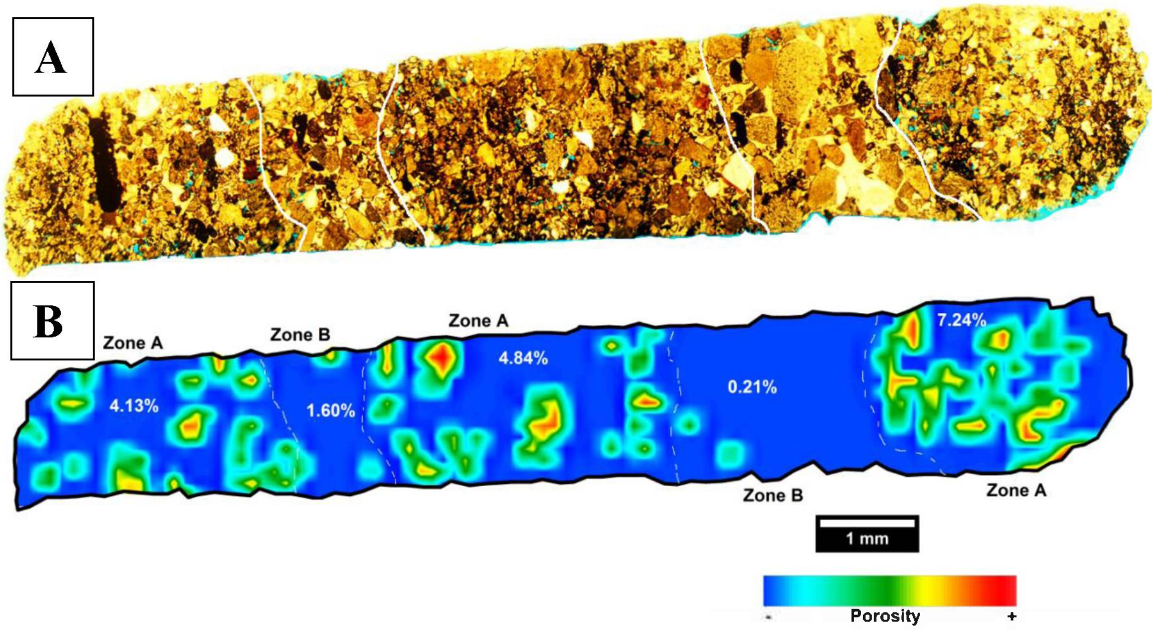

Figure 50. Image of the KEW1-1 sample after exposure to 90°C environment with H_2O and CO_2 for 1032 hours (43 days). Sample disk is approximately 2.5 cm long and 3 mm thick. (A) Plane-polarized optical image showing laminations and heterogeneous porosity distribution. The sample had been impregnated with blue-epoxy to fill the open pore spaces. (B). Color enhanced image showing the zonation of porosity zonation and the average of porosity for each zone. The warm colors (red to green) represent the highest porosity and most favorable flow paths through the sample.

2.8 Far Field Geochemical Reactions Causing Mineral Precipitation

2.8.1 SEM-EDS Microanalysis

A primary goal for long-term geologic sequestration of CO_2 is the immobilization of injected CO_2 in a subsurface repository as mineral phases. The incorporation of CO_2 into solid minerals represents an immobilized from of the sequestered carbon that will remain in place for geologic time scales. The experimental goal of this study sought to produce carbonate minerals through the geochemical reactions between MCR rock samples and a $H_2O + CO_2$ reaction environment. The most effective way to ensure that MCR sedimentary and volcanic rocks can produce carbonate minerals is to examine the reacted sample surfaces using a combination of SEM-EDS microanalysis, solution analysis, and geochemical modelling. SEM-EDS analysis of the CHC samples KEW1-1 and KEW 5-1 revealed the presence of numerous 4 to 6 μm diameter calcium carbonate crystals that likely had precipitated during the alteration of these samples. The calcium carbonate crystals were rhombohedral and had a Ca-C-O composition in ratio of approximately 1:1:3, both features which are characteristic of calcite (Figure 51a-c). The crystals were euhedral and there were no signs of dissolution pits occurring on their surfaces, indicating that these were newly formed crystals. Any calcite present as an original constituent of the rock, and present during test initiation, would likely show the formation of dissolution pits as a result of the acidified carbonic acid-rich solution contacting the samples during shorter term tests. In longer term reactions, the reactions between the rock samples and the aqueous fluid would neutralize the acids and allow carbonate minerals to form.

Two samples displayed the formation of carbonate minerals, KEW1-1 and KEW 5-1, these being reacted for a total of 143 and 2,446 hours, respectively (6 and 102 days). The precipitation of the calcite minerals in such a short time period confirms that carbonate mineralization will likely be initiated in very short time periods in a potential MCR GCS site. The MCR rocks that were tested in these experiments contain an abundance of alumino-silicate minerals that quickly reacted with the carbonic acid solution in the test vessels to neutralize the solution pH and release Ca^{2+} ions into solution, both factors which will induce carbonate mineral formation. The final bulk solution pH for the KEW1-1 sample was 6.1 and the Ca concentration was 702 ppm. For the KEW5-1 sample the final pH was 5.0 and the Ca concentration was 915 ppm. We expect that the solution in the microenvironments in the pore spaces may achieve even higher pH values and Ca contents than the bulk solution that was measured. Since both experimental solutions were still mildly acidic when the tests were terminated, we would also expect that continued carbonate mineralization would occur in longer term tests as the solutions were further neutralized through reactions with the rock minerals. These tests thus simulate longer-term and/or more distal reactions where the buffering capacity of the groundwater system and associated rocks have neutralized acids formed in association with CO_2 injection.

In addition to calcite forming as precipitated alteration phases, sample POT4 had developed rounded alteration precipitates (Figure 51d) with a chemical composition of (in mole %) of 10% Na, 10% Al, 26% Si, and 52% O, with trace Fe and Mg. The relatively small size of the crystals precludes an accurate chemical determination as the EDS response signal likely included an analysis from the surrounding and/or underlying substrate in the sample. The composition and occurrence of this phase on altering basaltic rock fragments is consistent with the presence of the zeolite group mineral analcime ($NaAlSi_2O_6.H_2O$). Analcime commonly displays a trapezohedron morphology, but may also exhibit platy, cubic, and rounded forms.

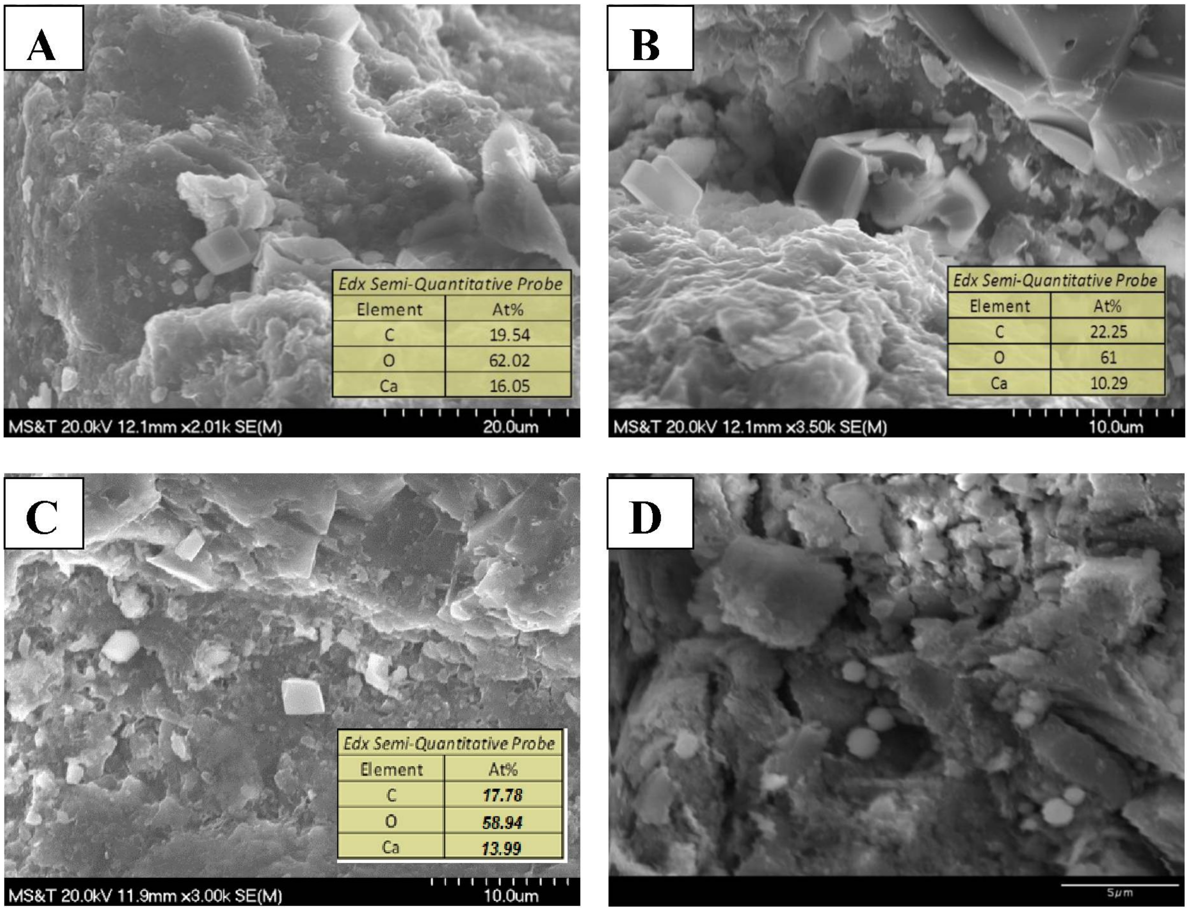

Figure 51. Midcontinent Rift sediment samples displaying precipitated alteration minerals following reaction in a CO_2 + DIW environment at 90°C. A) Calcite crystals identified from EDS microanalysis and rhombohedral morphology from CHC sample KEW5-1 reacted for 2446 hours (101.9 days). B) Additional calcite crystals on sample KEW5-1. C) Calcite crystal on CHC sample KEW1-1 sample reacted for 143 hours (six days). D) Rounded crystals on Nonesuch Formation sample POT4 reacted for 4343 hours (180.9 days). The rounded phase is tentatively identified as analcime based on its morphological characteristics and chemical composition.

2.8.2 Geochemical Modeling of Carbonate Mineral Precipitation

The results of the solution data generated by the HPT experiments were used to estimate the saturation state of the chemical species in the solutions using the PHREEQC – Interactive Version 3 - Geochemical Modeling Software program. Saturation indexes of the minerals ($SI = \log [(aM^+ * aX^-)/K_{sp})]$) were determined by the program where a SI = 0.0 represents a saturated state for the solution and a SI > 0.0 indicates a supersaturated solution. Partial pressures of gasses inside the experimental test vessels were calculated using the procedures outlined in the experimental methods (Section II; part 6). The calculated pressure used in the model was 70 bars, partial pressure of O_2 was 14.7 bars, volume of water was 10 cm^3, volume of rock was ~1.5 cm^3, while the remaining gas space volume was ~11.5 $cm^{3.}$ The densities of the CO_2 and H_2O phases at 90°C were determined using the online conversion calculator found at http://www.peacesoftware.de/einigewerte/einigewerte_e.html. The density of the low porosity sedimentary rock samples were assigned a value of 2.8 g/cm^3, while the higher porosity samples such as BAY2 sample were assigned a density value of 2.0 g/cm^3. The amount of the gaseous phase CO_2 that dissolves into the fluid to cause saturation was calculated using the methods of Duan and Sun (2003), which are available as online conversion at http://calc.kl-edi.ac.cn/Pages/Solubility.aspx.

The chemical input data were represented by the results from the pH, Eh, and ICP-OES chemical analysis from the solution for each individual experiment. The input data for the PHREEQC software is provided in Tables 13 to 16. The model results calculated when using a fixed pH as measured in the test vessels would generally display a negative SI values for minerals, even though many of the minerals were detected as alteration phases during SEM-EDS examinations of the reacted solids. Thus a floating pH model was used in the calculations. The floating pH model calculates an expected pH based on the total species concentration and charge that is entered in the chemical data input.

Modeling of the leachate solution provides an estimate of the mineral phases that could precipitate during the HPT testing and were not recognized under the SEM-EDS microanalysis. PHREEQC modeled results indicate that the solutions produced by reacting the CHC samples were supersaturated with respect to several carbonate minerals (i.e., aragonite, calcite, dolomite, and rhodochrosite, $MnCO_3$; Table 24). Calcite is the stable polymorph controlling Ca-carbonate solubility at near-surface Earth conditions, with aragonite being the stable polymorph at higher temperatures and pressures (Plumber and Busenberg, 1982). Aragonite often forms as a metastable phase, however, due to kinetic inhibitions for calcite formation and/or the increasing solubility of calcite in conjunction with increasing Mg concentration (Figure 6). Needle shaped grains indicative of the presence of aragonite were not detected on any of the HTP reacted samples.

Talc, quartz, and chalcedony were also determined to be supersaturated in the solutions contacting the KEW4-2 and KEW5-1 samples. The manganese oxides had a positive saturation indexes for hausmannite (Mn_3O_4) and pyrochroite ($Mn(OH)_2$). The determination of a supersaturated state for calcite matches with the observed calcite formation as an alteration phase on the KEW1-1 and KEW5-1 samples (Figure 51).

Solutions in contact with the Potato River Nonesuch and CHC samples (POT2-5) were also determined by the PHREEQC model code to be supersaturated with respect to aragonite, calcite, and dolomite, while the Freda Formation sample tested (POT8-2) produced a solution that was undersaturated with respect to these phases (Table 24). Hausmannite and pyrolusite were also predicted to control the Mn-oxide solubility.

The Unit C2 samples from the Eischeid #1 Well in Iowa produced solutions that were undersaturated with respect to carbonate minerals, except for sample C2-1, which was supersaturated with respect to calcite, and C2-2 which was supersaturated with respect to both aragonite and calcite. Quartz and Mn oxides were supersaturated in experiments with C2-2 and C2-3 samples, while Fe oxides and hydroxide minerals were supersaturated in all the Unit C2 samples. The Unit D4 sample solution was supersaturated with respect of aragonite, calcite, and rhodochrosite. The release of Mn and Fe resulted in a calculated supersaturated state for oxides containing these elements in the Unit C2 samples (Table 24).

Table 24. The saturation index values (SI) of the leachate solutions of samples collected from HPT experiments with the Keweenawan Peninsula (KEW), Potato River (POT), Copper Falls State Park (CFSP), and the Units C and D samples of the Eischeid#1 Well. The negative values represent undersaturated solutions while positive values represent supersaturated solutions. Calcite crystals were detected as alteration minerals on samples KEW1-1 and KEW5-1 (Figure 51).

	Aragonite ($CaCO_3$)	**Calcite ($CaCO_3$)**	**Dolomite ($CaMg(CO_3)_2$)**	**Rhodochrosite ($MnCO_3$)**	**Siderite ($FeCO_3$)**	**Quartz (SiO_2)**	**Talc ($Mg_3Si_4O_{10}(OH)_2$)**	**Hausmannite (Mn_3O_4)**	**Manganite (MnO(OH))**	**Pyrochroite ($Mn(OH)_2$)**	**Pyrolusite ($MnO2:H_2O$)**	**Hematite (Fe_2O_3)**	**Goethite (Foe(OH))**
KEW1-1	0.90	1.01	1.06	0.86	-	-0.20	-3.68	6.53	-1.68	-8.16	7.43	-	-
KEW4-2	1.14	1.24	2.11	0.62	-	0.19	0.33	5.81	-1.93	-8.40	7.19	-	-
KEW5-1	1.23	1.34	2.15	0.63	-	0.25	0.41	5.85	-1.91	-8.38	7.20	-	-
POT8-2	-0.20	-0.10	-1.05	-0.23	-	0.59	-3.52	3.26	-2.78	-9.25	6.34	-	-
CFSP4	0.24	0.35	0.59	0.75	-	0.59	0.03	6.20	-1.79	-8.26	7.32	-	-
POT2	0.65	0.75	1.25	-1.09	-	0.23	-0.62	0.68	-3.63	-10.1	5.48	-	-
POT4	0.00	0.10	0.05	0.85	-	0.46	-1.33	6.50	-1.70	-8.17	7.42	-	-
POT5-1	0.86	0.96	1.53	-1.02	-	0.09	-0.98	0.91	-3.56	-10.0	5.55	-	-
C2-1	-0.01	0.10	-0.38	-1.44	-8.17	-0.17	-5.17	-0.40	-4.00	-10.5	5.12	14.01	5.87
C2-2	0.23	0.33	-0.67	-0.29	-8.13	0.03	-5.94	3.05	-2.85	-9.32	6.27	14.08	5.91
C2-3	-1.80	-1.70	-3.79	-1.17	-7.74	0.02	-9.21	0.44	-3.71	-10.2	5.40	14.88	6.31
C2-5	-0.48	-0.38	-1.56	-0.80	-8.30	-0.59	-8.94	1.57	-3.34	-9.81	5.77	13.75	5.75
D4-1	0.44	0.54	-0.10	0.34	-8.08	0.21	-4.13	4.95	-2.21	-8.68	6.90	14.18	5.96
D4-2	0.50	0.61	-0.32	0.31	-8.08	-0.06	-6.03	4.93	-2.22	-8.69	6.89	14.22	5.98

The samples collected from the Bayfield Group-Jacobsville Formation and the Eischeid Well Unit E sequences were generally calculated to be undersaturated with respect to carbonate minerals (Table 25). The only exception was for E2-2 sample which was determined to be supersaturated for both aragonite and calcite. This sample contained calcite cement prior to the reactions as determined by petrographic analysis (Table 3). The L'ANSE1, E2-2, and E2-4 samples also were supersaturated with respect to quartz. The Fe oxide and hydroxides minerals (hematite and goethite) were supersaturated along with the Mn oxides (i.e., hausmannite and pyrolusite). Phyllosilicate minerals were predicted to precipitate; including gibbsite (precursor to phyllosilicates), kaolinite, illite, Ca-montmorillonite, and muscovite for the leachate solutions of the BAY3, E2-4, AG1, and AG2 samples.

Solutions were commonly predicted to be supersaturated with respect to aragonite, calcite, and rhodochrosite in the leachate fluids produced by reactions with the Kansas Poersch#1 Well using the PHREEQC model (Table 26). Dolomite was also predicted to be supersaturated in the solutions produced in reactions with the 5,397.3′A and B samples. Other predicted occurrences for silicate minerals were represented by quartz (in 5,397.3′A and B, 8,051.1′A, and 10,514′B) and chalcedony (in 8,051.1′A). Hausmannite and pyrolusite were predicted to be supersaturated in all leachate solutions collected from the reacted Poersch#1 Well samples. Solutions from the 11,061′A sample also displayed a positive saturation index for both goethite and hematite.

The leachate solutions of MCR igneous rock samples under HTP experimental conditions were obtained from samples collected from the Duluth complex (DUL), Beaver Bay complex (BEV), and North Shore Volcanic Group (GHB and GHC). These samples were also modeled for the alteration mineral occurrence using the PHREEQC geochemical model (Table 27). Carbonate minerals were predicted to be undersaturated for the solutions generated from the BEV, DUL, and GHB samples. The only exception was the GHB2 sample, which was predicted to be supersaturated for both calcite and dolomite. The clastic interflow unit for the NSVG included both the GHC1 and GHC2 samples. Both of these produced solutions with supersaturation indexes for calcite, aragonite, and dolomite. Quartz was predicted to be supersaturated in reaction fluids with all MCR igneous rock samples except BEV1, and chalcedony was supersaturated in the fluids for the DUL1, DUL2, GHC1, and GHC2 samples. The Mn oxides were again represented by predicted formation of hausmannite and pyrolusite, with the single exception of the BEV1 sample, although this sample did produce a fluid that was supersaturated with respect to hematite and goethite.

Table 25. The saturation indexes (SI) of the leachate solutions of samples collected from the Bayfield Peninsula (BAY), L'Anse area (L'ANSE), Agate Falls (AG), and the Unit E of the Eischeid#1 Well. The negative values represent undersaturated solutions while positive values represent supersaturated solutions.

	Aragonite ($CaCO_3$)	Calcite ($CaCO_3$)	Dolomite ($CaMg(CO_3)_2$)	Rhodochrosite ($MnCO_3$)	Siderite ($FeCO_3$)	Quartz (SiO_2)	K-feldspar ($KAlSi_3O_8$)	Albite ($NaAlSi_3O_8$)	Chalcedony (SiO_2)	Talc ($Mg_3Si_4O_{10}(OH)_2$)	Hausmannite (Mn_3O_4)	Manganite ($MnO(OH)$)	Pyrochroite ($Mn(OH)_2$)	Pyrolusite ($MnO_2:H_2O$)	Hematite (Fe_2O_3)	Goethite ($FeO(OH)$)	Chlorite(14A) ($Mg_5Al_2Si_3O_{10}(OH)_8$)	Ca-Montmorillonite [$Ca_{0.16}Al_{2.3}Si_{3.6}O_{10}(OH)_2$]	Gibbsite ($Al(OH)_3$)	Illite $K_{0.6}Mg_{0.2}Al_{2.3}Si_{3.5}O_{10}(OH)_2$	Kaolinite ($Al_2Si_2O_5(OH)_4$)
BAY3(-Al)	-3.1	-3	-5.1	-0.6	-6.5	-0.2	-	-	-0.4	-9.8	2.09	-3.2	-9.6	5.95	17.3	7.5	-	-	-	-	-
BAY3(+Al)	-2.7	-2.6	-4.2	-0.2	-6.3	-0.2	-0	-2.2	-0.4	-8.6	3.28	-2.8	-9.2	6.34	17.7	7.71	-6.7	7.52	4.09	5.57	9.01
L'ANSE1	-2.6	-2.5	-4.2	-1.5	-6.2	0.18	-	-	-0	-7.5	-0.5	-4	-10	5.1	17.8	7.78	-	-	-	-	-
E2-2	0.5	0.6	-0.6	-0.5		0.08	-	-	-0.1	-6.4	2.51	-3	-9.5	6.09	-	-	-	-	-	-	-
E2-3	-2.6	-2.5	-5.9	-1.8	-8.5	-0.4	-	-	-0.6	-15	-1.5	-4.4	-11	4.74	13.5	5.61	-	-	-	-	-
E2-4	-1.6	-1.5	-4.0	-1.0		0.06	-2.4	-4.1	-0.2	-10	1.09	-3.5	-10	5.62	-	-	-16	1	1.24	-0.6	3.74
AG-1	-2.2	-2.1	-4.3	-1.2	-7.5	-0.1	-1.8	-4.7	-0.4	-10	0.18	-3.8	-10	5.31	15.4	6.55	-14	3	2.11	1	5.06
AG-2	-2.4	-2.3	-4.7	-1.6	-8.8	-0.2	-3.5	-6.4	-0.5	-11	-0.9	-4.2	-11	4.96	12.7	5.22	-18	-0.4	0.79	-2.5	2.26

Table 26. The saturation indexes (SI) of the leachate solutions of samples collected from the Texaco Poersch #1 Well. The negative values represent undersaturated solutions while positive values represent supersaturated solutions.

	Aragonite ($CaCO_3$)	Calcite ($CaCO_3$)	Dolomite ($CaMg(CO_3)_2$)	Rhodochrosite ($MnCO_3$)	Siderite ($FeCO_3$)	Quartz (SiO_2)	Talc ($Mg_3Si_4O_{10}(OH)_2$)	Hausmannite (Mn_3O_4)	Manganite ($MnO(OH)$)	Pyrochroite ($Mn(OH)_2$)	Pyrolusite ($MnO2:H_2O$)	Hematite (Fe_2O_3)	Goethite ($FeO(OH)$)
5,397.3′ A	-0.45	-0.35	0.26	-1.24	-	0.07	-1.1	0.08	-3.83	-10.3	5.28	-	-
8,051.1′ A	0.5	0.6	-0.82	0.22	-	0.26	-6.37	4.48	-2.37	-8.84	6.75	-	-
8,476′-8,480′ A	0.48	0.58	-0.54	0.34	-	-0.05	-6.71	4.86	-2.24	-8.71	6.87	-	-
10,514′ A	0.29	0.4	-1.48	0.2	-	-0.41	-10.4	4.46	-2.38	-8.85	6.74	-	-
10,666′ A	-0.18	-0.07	-0.81	0.2	-	-0.29	-6.56	4.4	-2.39	-8.87	6.72	-	-
11,061′ A	0.15	0.26	-1.66	-0.28	-7.67	-0.66	-11.5	3.07	-2.84	-9.31	6.28	14.98	6.36
5,397.3′ B	-0.15	-0.04	0.1	0.15	-	0.04	-2.6	4.27	-2.44	-8.91	6.68	-	-
8,051.1′ B	0.73	0.83	-0.64	0.21	-	-0.55	-9.72	4.5	-2.36	-8.83	6.75	-	-
8,476′-8,480′ B	0.5	0.6	-0.53	0.28	-	-0.3	-7.77	4.64	-2.32	-8.79	6.8	-	-
10,514′ B	0.45	0.56	-1.11	0.36	-	0.09	-7.8	4.89	-2.23	-8.7	6.88	-	-
10,666′ B	0.22	0.33	-0.09	0.57	-	-0.22	-5.29	5.51	-2.03	-8.5	7.09	-	-
11,061′ B	0.62	0.72	-0.97	0.46	-	-0.02	-8.24	5.27	-2.1	-8.58	7.01	-	-

Table 27. The saturation indexes (SI) of the leachate solutions of samples collected from Silver Bay (Beaver Bay Complex; BEV), Ely city area (Duluth complex; DUL), and Good Harbor Bay (North Shore Volcanic Group; GHB and GHC). The negative values represent undersaturated solutions while positive values represent supersaturated solutions.

	Aragonite ($CaCO_3$)	Calcite ($CaCO_3$)	Dolomite ($CaMg(CO_3)_2$)	Rhodochrosite ($MnCO_3$)	Siderite ($FeCO_3$)	Quartz (SiO_2)	Talc ($Mg_3Si_4O_{10}(OH)_2$)	Hausmannite (Mn_3O_4)	Manganite ($MnO(OH)$)	Pyrochroite ($Mn(OH)_2$)	Pyrolusite ($MnO2{:}H_2O$)	Hematite (Fe_2O_3)	Goethite ($FeO(OH)$)
BEV1	-2.83	-2.73	-5.53	-	-8.36	-0.19	-12.2	-	-	-	-	13.68	5.71
DUL-1	-0.82	-0.72	-0.45	-0.83	-	0.33	-0.94	1.41	-3.39	-9.86	5.72	-	-
DUL-2	-1.02	-0.92	-0.98	-0.99	-	0.25	-2.25	0.97	-3.54	-10	5.57	-	-
GHB-1	0.12	0.23	0.68	-0.03	-	0.1	-1.53	3.64	-2.65	-9.12	6.47	-	-
GHB-2	-0.47	-0.36	-0.51	-0.86	-	0.02	-3.55	1.2	-3.46	-9.93	5.65	-	-
GHC-1	0.1	0.2	0.07	-0.31	-	0.47	-1.68	2.88	-2.9	-9.37	6.21	-	-
GHC-2	0.08	0.19	0.06	-0.13	-	0.48	-1.61	3.47	-2.7	-9.18	6.41	-	-

A conceptualized Three-Box model was developed to show the three different zones of reaction that may exist during the injection of CO_2 or following the cessation of the injection processes into MCR rocks (Figure 52). This model is based on the results of the reaction tests with samples collected from the MCR and follows a natural progression as acidic fluids produced by CO_2 injection are neutralized by reactions involving the minerals. These acid neutralization reactions often involve ion exchange between the acidified fluids and the host rock minerals, releasing ions such as Ca^{2+}, Mg^{2+}, and Fe^{2+} into solution. Both the acid neutralization process and the release of alkaline earth components can induce the precipitation of carbonate minerals in a kinetic process that will be favored by a function of increasing distance from the point of the CO_2 subsurface injection well(s) and/or increasing reaction time.

Box 1of the model shows the initial stage where the forward dissolution of calcite is occurring in response to the presence of the acidified fluid (Figure 52). The acid neutralizing capacity due to the alkalinity of the aqueous groundwater fluid (largely HCO_3^-) should be quickly overwhelmed due to CO_2 injection to the point where the MCR rock matrix minerals will begin to react to counteract the carbonic acid generation. Carbonate minerals such as calcite are most susceptible to acid attack and their dissolution will largely control reactions and chemical conditions as represented in the Box 1 segment. Measured dissolution rates for calcite ranged from 4.0×10^{-5} to 5.21×10^{-4} moles/cm^2.day in the 90°C static dissolution tests. This is equivalent to the dissolution of 1.60 to 20.09 mg per day for every cm^2 of exposed calcite surface area relative to the 10 ml of leachant fluid in the test vessel. The average volume proportion of calcite cement in the Keweenawan MCR samples was 13% (ranging from 6.6 to 23.5%), therefore one cm^3 of Keweenawan rocks should have 0.13 cm^3 of calcite, which represents 353 mg of calcite (calcite density 2710 mg/cm^3). The 0.13 cm^3 volume of cement would be completely dissolved in 16 to 220 days under the static test conditions of the HPT experiments where the acid is being progressively neutralized. The reaction rates are even more rapid under dynamic flow-through testing conditions. The core flooding experiment on sample KEW3-1 lost a total weight equivalent to nearly its entire inventory of calcite in only two hours of testing, resulting in a whole rock porosity-permeability increase of 30% (Figure 47).

The movement of the dissolution front through the calcite grains will also preferentially penetrate along cleavage surfaces and grain boundaries with the clastic particles, allowing the exposed surface area of calcite to increase more rapidly than if dissolution were occurring along a uniform reaction front. The effective porosity will be enhanced as one segregated pore is connected to another as fluids penetrate through the newly created pore space along zones of higher mineral stain (Figures 40 and 41). The pressure resulting from the injection processes will also likely enhance the fluid penetration through cleavage openings or even by generating new fractures through the cemented zones. The calcite-rich sample KEW5-1 displayed a fluid breakthrough in the three cm thick sample and the start of calcite dissolution within three minutes of the test initiation in the core flooding experiment (Figure 48).

The dissolution of alumino-silicate phases is expected to be relatively minor as long as remnants of calcite remain in the vicinity of the reaction front as the kinetic rate of calcite dissolution is many orders of magnitude greater than even relatively fast reacting olivine and pyroxene minerals (Figures 29, 32, and 52). Reactions in Box 2 thus represent the reaction progress once the removal of all nearby carbonate mineral phases has been completed in the upstream direction to fluid flow. The continued injection of CO_2 without the presence of the rapidly dissolving carbonate minerals may result in groundwater pH values falling to values between 3 and 4. Dissolution of the alumino-silicate and oxide rock minerals will begin to show an increase in reaction rates. These minerals should react preferentially in the order and rates predicted by Goldich (1938; Figure 29) and Lasaga et al. (1994; Figure 32a), and confirmed in the present experiments in this study (Figure 32b). The preferential order of reaction will be olivine, pyroxene, epidote, and Ca-plagioclase as representing the faster reacting phases, while Na-plagioclase, K-feldspars, and quartz will react more slowly. Actual reaction rates will vary as a function of temperature, exposed mineral surface area, mineral composition and solution acidity. We also expect that most of these minerals will be reacting at the same time, just not at equivalent reaction rates. Ion exchange reactions between the H^+ ions in the acidic solution and the alumino-silicate and oxide minerals containing Ca^{2+}, Mg^{2+}, Fe^{2+}, K^+, Na^+, and other components will neutralize the acidic solution and increase the salinity of the fluid.

The Box 3 simulation represents the part of the reactions where the calcite and alumino-silicate minerals have effectively reacted with the carbonic acid in solution to the point where the increase in solution pH and Ca^{2+} ion concentration (and/or other alkaline earths) has neutralized the carbonic acid and increased fluid activity of Ca to the point where carbonate mineralization

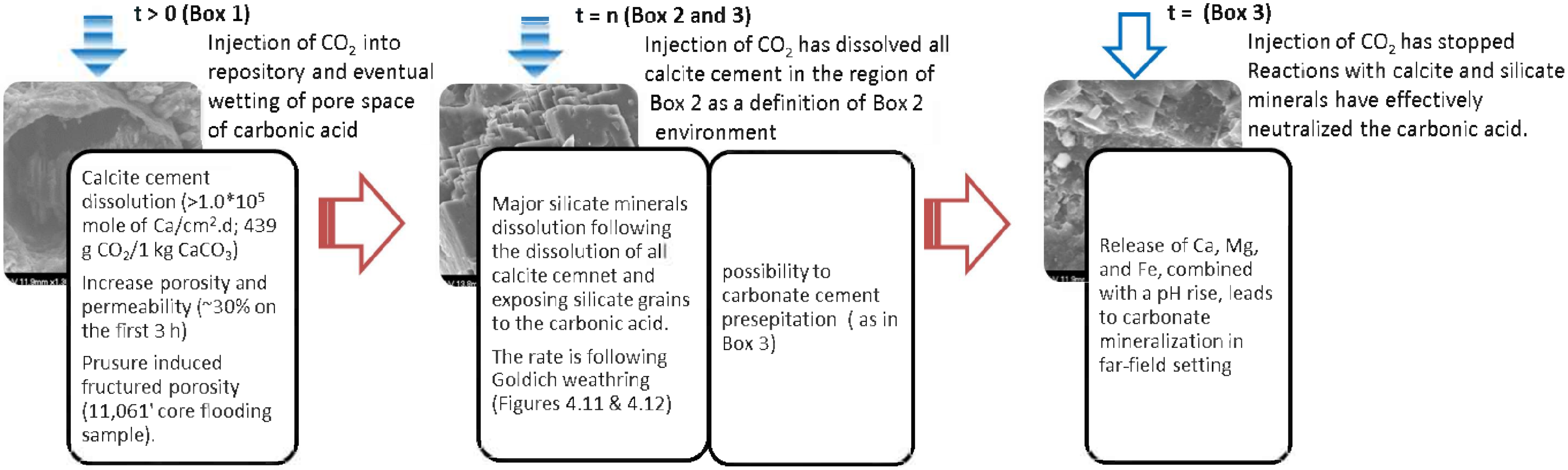

t > 0 (Box 1)

Injection of CO_2 into repository and eventual wetting of pore space of carbonic acid

Calcite cement dissolution (>1.0*10^5 mole of Ca/cm^2.d; 439 g CO_2/1 kg $CaCO_3$)

Increase porosity and permeability (~30% on the first 3 h)

Prusure induced fructured porosity (11,061' core flooding sample).

t = n (Box 2 and 3)

Injection of CO_2 has dissolved all calcite cement in the region of Box 2 as a definition of Box 2 environment

Major silicate minerals dissolution following the dissolution of all calcite cemnet and exposing silicate grains to the carbonic acid.

The rate is following Goldich weathring (Figures 4.11 & 4.12)

possibility to carbonate cement presepitation (as in Box 3)

t = (Box 3)

Injection of CO_2 has stopped Reactions with calcite and silicate minerals have effectively neutralized the carbonic acid.

Release of Ca, Mg, and Fe, combined with a pH rise, leads to carbonate mineralization in far-field setting

Figure 52. Conceptual box model displaying the various geochemical processes that follow the injection of supercritical CO_2 in the subsurface MCR rocks as a function of distance from the injection well and/or time.

begins to occur (Figure 52). Such a scenario may occur with increasing travel distance and or time of fluids from the CO_2 injection well(s). Similar reactions may also occur when there is a reduction in the rate of CO_2 injection or following cessation of CO_2 injection entirely. These precipitated carbonate minerals will effectively immobilize the injected CO_2 on geologic time scales.

3 CONCLUSIONS

Increasing concern about anthropogenic induced climate change has resulted in numerous investigations into finding suitable and cost effective methods into reducing greenhouse gas emissions and finding ways to dispose of greenhouse gasses from large stationary power sources such as ethanol and coal fired power plants. Subsurface GCS into deep saline aquifers is one disposal option being considered. Many of the targeted geologic formations for CO_2 disposal, such as the Mount Simon-Lamotte basal Cambrian sandstone, possess favorable aquifer characteristics including high porosity-permeability and large storage volumes (Barnes et al., 2009). A common feature in rocks that possess these favorable aquifer characteristics is a high-degree of mineralogical maturity resulting from the quartz-rich nature of the sandstones. Unfortunately these same sandstones often have minimal concentrations of alkaline earth bearing silicate minerals (e.g., olivine, pyroxene, chlorite, etc.). These silicates can release Mg^{2+}, Ca^{2+}, and other metallic cation components into solution, which when complexed with the carbonate ion (CO_3^{2-}) will form solid carbonate minerals. The same mineral dissolution process releasing the cations will also neutralize the carbonic acid in the groundwater. The containment of sequestered carbon in highly mature - quartz rich GCS targets will therefore be heavily reliant on the impermeable nature of the cap rock sequence(s) to keep the injected CO_2 and aquifer water in place for time periods that will exceed multiple centuries or longer.

A previous study conducted by the Minnesota Geological Survey had noted that the Precambrian-aged MCR sequence possesses favorable depth, thickness, and seal rock characteristics (for the lower Oronto Group), and also has a minimal number of exploration test holes that would pose a risk for leakage (Thorleifson, 1989). This study concluded, however, that the MCR was far less suitable for CO_2 sequestration than many other sites under consideration due to its complex tectonic history and low porosity-permeability characteristics. The report also noted that there was insufficient data and knowledge on much of the detailed geology of the MCR sequence. This purpose of this present study is to provide bench-scale laboratory testing data on the MCR sequence that can be used to more fully evaluate this sequence as a GCS target.

The Bayfield Group and Jacobsville Formation sandstones, plus their likely equivalent stratigraphic horizons in the Iowa Eischeid #1 Well (Unit E to H horizons) are the uppermost sedimentary sequence in the MCR. These sandstones are chemically and mineralogically mature, possess favorable porosity and permeability characteristics, but generally lack an effective seal rock as they are often covered unconformably by Cambrian-aged sandstones. The mineral and chemical compositions of the sandstones varied with location and were represented by quartz-arenite to feldspathic quartz-arenite. Samples from all areas contained a high proportion of SiO_2 (77-93%), reflecting their quartz-rich nature, and had limited alkaline earth contents (MgO + CaO) of only 0.6% for Lake Superior and 1.7% for the Eischeid #1well samples. Residual porosity values for the Bayfield-Jacobsville samples averaged 13.4 ± 4.3% while an additional 0.6% of the paleo-pore space was filled with calcite. A single Bayfield sample was tested in the core flooding apparatus with mildly acidic deionized water and revealed a porosity of 17.5% and a permeability of ≈ 340 mD. The Unit E through H sections of the Iowa Eischeid #1 Well contain up to 6% porosity (Ludvigson et al., 1990; Witzke, 1990). The Bayfield-Jacobsville sandstone is locally overlain by basal Cambrian sandstones of the Mount Simon-Lamotte sandstone, with the latter also being evaluated as a GCS target (McKay, 1990; Barnes et al., 2009). The Bayfield-Jacobsville sandstones thus offer additional reservoir capacity towards efforts to use the basal Cambrian sandstones of the Midcontinent region as a GCS site. Their low alkaline earth contents indicate they will have minimal capacity to induce the formation of carbonate minerals. Results from equilibrium saturation modeling studies using the PHREEQC code and leachant water compositions obtained from the CO_2 +H_2O experiments with all Bayfield-Jacobsville samples indicate that the solutions were undersaturated with respect to carbonate minerals with the exception while one Unit E sample from the Eischeid #1 Well in Iowa. Carbonate phases were also not detected on the surfaces any of the samples that were reacted in the experiments.

The Oronto Group sediments (CHC, Nonesuch Formation, and Freda Formation) and their laterally equivalent stratigraphic units represent a more challenging target for CO_2 sequestration due to their low porosity-permeability characteristics. The Oronto Group samples collected from Lake Superior region contained open porosity values that were ≈2.9 ± 2.2%. The petrographic determinations of the CHC samples from this and other studies are typically conducted from sections made from sand-sized sediments, and avoiding the larger pebble to boulder sized fragments. Thus the field porosity values for the conglomeratic units will often be less than the petrographic determinations in a proportion roughly equivalent to the volume percent of the larger clasts present in the rock sequence. Low porosity values are also a characteristic of the MCR samples in both the Poersch #1 Well in Kansas (Berendsen et al., 1988)) and samples at depths >8000′ in the Eischeid #1 Well in Iowa (Ludvigson et al., 1990). A significant portion of the paleo-porosity space in these rocks has been filled in with calcite cement, exceeded 20 % in some samples, and averaging 7.0 ± 6.0% for the 13 Lake Superior region Oronto Group samples analyzed in this study. While only trace amounts of calcite were detected in the Poersch #1 Well in Kansas, three samples from Unit C in the Eischeid #1 Well in Iowa tested in the present study contained between 15 to 33% calcite. Ludvigson et al., (1990) also found calcite as a common constituent throughout most of the Eischeid core, especially in the Unit C and D sections where it has essentially occluded all pore space. Barnes (1990) has suggested that this calcite was deposited early in the diagenetic history of the Unit C sediments as the cement has preserved much of the open pore space and normally ductile mica grains were found to be relatively undeformed.

Two of the MCR samples examined in this this study displayed anonymously high porosity values. The CHC sample KEW3-1 (collected in Esrey Park on the Keweenawan Peninsula of Michigan) had 8.9% open porosity plus an additional 10.4% of the pore space filled with calcite cement. The sample was collected from a sandy lens within a conglomeratic unit, so the actual rock porosity should approximate half of this value as larger pebbles and cobbles with very limited porosities comprise ~50% of the observed rock outcrop. A sample collected from the Poersch #1 Well in Kansas at the 11,061′ depth horizon was found to contain 7.9% open porosity and only trace amounts of calcite cement. The relatively high porosity determination for this sample corroborates a key finding of Berendsen et al. (1988) where a 22′ thick section of relatively high porosity sandstone (up to 15%) was detected by down-hole resistivity and neutron density analysis between 11,055 and 11,077 feet.

Oronto Group sediments were typically enriched in lithic volcanic rock fragments that were eroded from the surrounding rock mass during the time of MCR sediment deposition. Sedimentary rocks recovered from deeply buried MCR sections in Kansas and Iowa also reveal an abundance of lithic fragments (Berendsen, 1988; Ludvigson, 1990). Feldspar, micas, epidote, chlorite, illite, smectite, and Fe-oxides were also identified as common mineral constituents in these rocks. Chemical analyses of Oronto Group samples display enrichment in the alkaline earth oxides (between 5 and 12 wt.% CaO + MgO) suggesting that these rock units would have great potential for immobilizing injected CO_2 by reacting with the groundwater fluids to precipitate carbonate minerals.

High temperature and pressure $CO_2 + H_2O$ experiments (90°C and 65-70 bars) conducted with MCR-Oronto Group samples produced leachate fluids with high Ca concentrations. Calcium release rates were 10-times higher than the release rate of other rock components suggesting that most of the Ca was derived from the preferential dissolution of calcite cement. Microscopic examination of reacted calcite grains indicates that they preferentially dissolve along cleavage planes and the boundary zones between the calcite cement and adjacent pore walls. This dissolution pattern suggests that the leading edge of a reaction front penetrating into calcite filled pores will advance into the rock at a faster rate than the bulk solution as the leading edge of the dissolution front bypasses the slower dissolving portions of the calcite grains.

Although the dissolution of calcite will initially work against a net goal of precipitating carbonate minerals as a mechanism for immobilizing CO_2, this dissolution front will increase the porosity-permeability characteristics of the overall rock mass by connecting isolated pores and increasing the exposed surface area of silicate minerals to groundwater fluids. The eventual dissolution of silicate and oxide minerals from the CHC rock matrix will also create additional space for carbonate minerals to precipitate. Evidence for such a process occurring in the past has been recognized during the analysis of thin sections from the Iowa Eischeid #1 Well where original detrital grains have been replaced by calcite producing rock sections with up to a combined 33% calcite pore infilling + calcite replacement texture (Barnes, 1990).

Three CHC samples were tested in the core flooding experiments with a pH = 4 leachant solution to evaluate the effect of dissolving calcite cement on the reservoir properties of the rock samples. Sample KEW3-1 was the only one of the three that displayed an increase in permeability during testing, from 0.92 to 1.2 mD, as a result of calcite dissolution over a two-hour testing period. One sample did not display any measurable permeability, while another displayed an overall decrease in permeability during testing, from 2.00 to 1.73 mD over a 53 minute period. A single sample from the 11,061.5′ depth of the Poersch #1 Well in Kansas several fluctuations in permeability during testing, with a variation between 1.01 to 1.29 mD over a 105 minute interval. A fine-grained siltstone sample from the Freda Formation displayed a lower permeability value and a slight decline from 0.190 to 0.175 mD over a 33 minute testing period. None of the samples displayed a permeability values above 2.0 mD, thus all should be considered as having poor reservoir characteristics. The decrease observed during the permeability tests for several of the samples likely resulted from acid-resistant small grains being dislodged from regions where calcite was dissolving. Once released, these grains will become entrained in the moving water, and then can become lodged in the narrow pore throats separating the larger diameter pore regions from each other. Another potential cause for this reduction in permeability may involve the swelling of clay minerals.

Because carbonate minerals will react many orders of magnitude faster than silicates, and neutralize acidic solutions in the process, we expect that overall silicate and oxide mineral dissolution will proceed at a very slow rate as long as any residual carbonate material is present. An exception to this pattern may include the exchangeable ions from interlayer sites in clay minerals or ions weakly adsorbed onto the surfaces of oxides. Once the carbonates are completely dissolved, however, the pH of the fluid should decrease in response to carbonic acid formation from injected CO_2. Dissolution rates of the silicate and oxide minerals would then be accelerated as they become more involved in acid neutralization reactions. The leachate solutions from the HTP CO_2 +H_2O experiments contained elevated concentrations and release rates for Mg, K, Na and Si as a result of the dissolution of silicate minerals processes. A portion of the Ca release is also occurring from silicate minerals, in addition to the release from calcite. The high Mg contents likely reflect the alteration of amphiboles, pyroxenes, and/or chlorite (MCR calcite contains only ~0.5 mole% Mg), while Na and K release are likely dominated by feldspar alteration. Water-rock reactions involving the exchange of H^+ ions from a carbonic acid rich solution, with alkali and/or alkaline earth components from the rock-forming silicate minerals will increase the pH and salinity of any associated water system, both factors of which tend to favor the precipitation of carbonate minerals.

The saturation state of the leachate fluids produced by HTP 90°C reactions with the Oronto Group samples was evaluated using the PHREEQC equilibrium saturation code. Solutions were calculated to be supersaturated with respect to calcite for 11 of the 14 samples tested from the Oronto Group and equivalent stratigraphic units in the Eischeid #1 Well. Similarly, 9 of the 12 experiments from the Poersch #1 samples also produced supersaturated solutions, as did 3 of 4 experiments with the North Shore Volcanic Group basalts or interflow clastic sediments. Since these tests were initiated with deionized water, they demonstrate the ability of the mineral materials in the MCR sediments to rapidly react with the CO_2 +H_2O fluids to produce a saturated fluid. The groundwater in an actual CO_2 injection scenario would have had thousands of years or longer to come to pseudo-steady state equilibrium with the reacting rock material and produce a brine fluid capable of inducing carbonate mineralization reactions on a time scale even more rapid than we observe in these experiments. Newly precipitated calcite crystals were detected on two of the reacted MCR samples, one in as little as six days, and the second following 102 days of reaction. Both of the experimental solutions had SI values >1.0. We were also able to induce the formation of carbonate minerals during reactions with both olivine-forsterite and pyroxene-augite in less than 10 days of reaction time. These two minerals are common constituents in the MCR igneous rocks and lithic volcanic clasts in MCR sedimentary rocks.

In summary, the chemical composition of the Oronto Group rocks of the MCR, and any groundwater in contact with them, will provide excellent potential for inducing the formation of carbonate minerals if a GCS site were to be located within in this stratigraphic unit. The formation of solid mineral phases containing CO_2 will be the most reliable method for immobilizing CO_2 for timescales that should easily span multiple centuries and may even extend into geologic time scales. Corrosion experiments conducted with Oronto Group rock samples, CO_2, and deionized water at 90°C often produced a leachant solution that was supersaturated with respect to carbonate minerals, while calcite crystals were also produced as alteration minerals. The most critical factor preventing the use of the MCR sequence for CO_2 sequestration is related to the low porosity and permeability of the Oronto Group sediments. Occlusion of pore space by calcite cement generally results in porosity values $\leq 2\%$. Two of the Oronto Group samples examined in the present study however had 8.9% and 7.9% open porosity values, the latter sample correlates to a 22′ thick section of clastic sandstone that was previously recorded as a potentially high porosity zone by geophysical methods (Berendsen et al., 1988). Calcite is highly reactive in a mildly acidic carbonic acid solution, thus the injection of CO_2 into a hypothetical MCR repository would result in the dissolution of calcite cement and potentially improve the porosity-permeability characteristics. Core flooding and static corrosion experiments simulating exposure to a CO_2 + H_2O fluid readily induced the dissolution of the calcite cement as well as lesser amounts of the silicate rock forming minerals. While overall porosity increased, permeability changes were inconsistent, increasing in some samples, decreasing in others, but never exceeding a value of 2.0 mD. A rock system with porosity values at <9% and permeability values of <2.0 mD would make poor reservoir. Any attempt to inject CO_2 into the Oronto Group sediments for GCS purposes would have to overcome these poor reservoir characteristics. The upper MCR sedimentary sequence of the Bayfield Group – Jacobsville Formation averages 13.4 ± 4.3% porosity and a single sample tested in the core flooding apparatus exhibited a permeability of ~340 mD. This unit thus has good reservoir characteristics for GCS. While the Bayfield-Jacobsville sequence does not have a stratigraphic cap rock, it does form a continuous aquifer unit where it comes in contact with the unconformably overlying Mt. Simon Formation and thus offers addition CO_2 storage volume for efforts to use the Mount Simon sandstone as a GCS unit.

Basal volcanic rocks and/or Oronto Group sediments have been tectonically emplaced on top of Bayfield-Jacobsville sequence by thrust faulting in many regions of the MCR including deeply buried sections located in Kansas. This inverted stratigraphy can place alkaline earth enriched Oronto Group sediments and basaltic volcanic rocks with a good capacity for producing carbonate minerals on top of the higher porosity-permeability Bayfield-Jacobsville sandstones. These tectonically juxtaposed sequences offer the best potential for GCS efforts, especially with respect to carbonate mineralization processes that will improve the long term storage potential of CO_2 in underground repositories.

REFERENCES

Abousif, A.M.A., 2014, Mineral and geochemical attributes of the Midcontinent Rift sequence: An application for deep CO_2 sequestration: Missouri University of Science and Technology, Ph.D. Dissertation (in preparation).

Anderson, R.R., 1990, Review of the Precambrian geology history of the central United States and the Midcontinent Rift system, *in* The Amoco M.G. Eischeid #1 Deep Petroleum Test Carroll County, Iowa, Preliminary Investigations, Special Report Series #2, R.R. Anderson (ed.), Iowa Department of Natural Resources, p. 1-25.

Anderson, R.R., 1992, The Midcontinent Rift of Iowa: University of Iowa, Iowa City, Ph.D. dissertation, 324 pp.

Anderson, R.R., 1997, Keweenawan Supergroup clastic rocks, *in* The Midcontinent Rift of Iowa, Middle Proterozoic to Cambrian Rifting, Central North America, Ojakangas, R.W., Dickas, A.B., Green, J.C. (eds.), Geological Socciaty of America Special Papers, v. 312, p. 211 –230.

Arnorsson, S.N.A. and Stefansson, A.S., 1999, Assessment of feldspar solubility constants in water in the range 0 to 350°C at vapor saturation pressures, *American Journal of Science*, v. 299, p. 173-209.

Bachu, S., 2000, Sequestration of CO_2 in geological media: criteria and approach for site selection in response to climate change, *Energy Conversion and Management*, v. 41, p. 953-970.

Bachu, S., 2002, Sequestration of CO_2 in geological media in response to climate change: road map for site selection using the transform of the geological space into the CO_2 phase space, *Energy Conversion and Management*, v. 43, p. 87-102.

Bachu, S., Gunter, W., and Perkins, E., 1994, Aquifer disposal of CO_2: Hydrodynamic and mineral trapping, *Energy Conversion and Management*, v. 35, p. 269-279.

Barnes, D.A., 1990, Sandstone petrology from conventional core in the M.G. Eischeid #1 Well, Carroll County, Iowa, *in* The Amoco M.G. Eischeid #1 Deep Petroleum Test Carroll County, Iowa, Preliminary Investigations, Special Report Series #2, R.R. Anderson (ed.), Iowa Department of Natural Resources, p. 113-118.

Barnes, D.A., Bacon, D.H., and Kelley, S.R., 2009, Geological sequestration of carbon dioxide in the Cambrian Mount Simon Sandstone: Regional storage capacity, site characterization, and large-scale injection feasibility, Michigan Basin, *Environmental Geosciences*, v. 16, p. 163-183.

Behrend, J., Green, A., Cannon, W., Hutchinson, D., Lee, M., Milkereit, B., Agena, W., and Spencer, C., 1988, Crustal structure of the Midcontinent Rift system: Results from GLIMPCE deep seismic reflection profiles, *Geology*, v. 16, p. 81-85.

Bennett, P.C., 1991, Quartz dissolution in organic-rich aqueous systems, *Geochimica et Cosmochimica Acta*, v. 55, p. 1781-1797.

Berendsen, P.M., Borcherding, R.M., Doveton, J., Gerhard, L., Newell, K.D., Steeples, D., and Watney, W.L., 1988, Texaco Poersch #1, Washington County, Kansas-preliminary geologic report of the pre-Phanerozoic rocks: Kansas Geological Survey, Open-file Report 88-22.

Berman, R.G., 1988, Internally-consistent thermodynamic data for minerals in the system Na_2O-K_2O-CaO-MgO-FeO-Fe_2O_3-Al_2O_3-SiO_2-TiO_2-H_2O-CO_2, *Journal of Petrology*, v. 29, p. 445-522.

Berner, R.A. and Lasaga, A.C., 1983, The carbonate-silicate geochemical cycle and its effect on atmospheric carbon dioxide over the past 100 million years, *American Journal of Science*, v. 283, p. 641-683.

Berner, R.A. and Morse, J.W., 1974, Dissolution kinetics of calcium carbonate in sea water; IV, Theory of calcite dissolution, *American Journal of Science*, v. 274, p. 108-134.

Boggild, O.B., 1930, The shell structure of the mollusks: *K. Danske Vidensk. Selskabs Skrifter*, Copenhagen, v. 2, p. 232-325.

Brannon, J.C., 1984, Geochemistry of successive lava flows of the Keweenawan North Shore Volcanic Group, Washington University St Louis, MO, Ph.D. Dissertation, 312 pp.

Buchanan, R., and McCauley, J., 2010, Roadside Kansas: A Traveller's Guide to Its Geology and Landmarks, 2nd edition, Kansas Geological Survey, 376 pp.

Bush, P., 1973, Some aspects of the diagenetic history of the sabkha, Abu Dhabi, the Persian Gulf, Holocene carbonate sedimentation and diagenesis, *in* A Shallow Epicontinental Sea, B.H. Purser (ed.), Springer, p. 395-407.

Cannon, W.F., 1994, Closing of the Midcontinent Rift-A far field effect of Grenvillian compression, *Geology*, v. 22, p. 155-158.

Cannon, W.F. and Hinze, W.J., 1992, Speculations on the origin of the North American Midcontinent Rift, *Tectonophysics*, v. 213, p. 49-55.

Cannon, W.F. and Nicholson, S.W., 1992, Revisions of stratigraphic nomenclature within the Keweenawan Supergroup of northern Michigan, U.S. Geological Survey, Bulletin 1970A, 21 pp.

Craddock, C., 1972, Late Precambrian Regional Geologic Setting: Geology of Minnesota: A Centennial Volume, Minnesota Geological Survey, p. 281-291.

Daniels, P.A., 1982, Upper Precambrian sedimentary rocks: Oronto Group, Michigan-Wisconsin, *in* R.J. Wold and W.J. Hinze (eds.), Geology and Tectonics of the Lake Superior Basin, Geological Society of America, Memoir 156, p. 107-133.

Dickas, A.B. and Mudrey, M.G., 1997, Segmented structure of the middle Proterozoic Midcontinent Rift System, North America, *in* Middle Proterozoic to Cambrian Rifting, Central North America, R.W. Ojakangas, A.B. Dickas, and J.C. Green (eds.), Geological Socciaty of America Special Papers, v. 312, p. 37-46.

Doughty, C. and Pruess, K., 2004, Modeling supercritical carbon dioxide injection in heterogeneous porous media, *Vadose Zone Journal*, v. 3, p. 837-847.

Dove, P.M., 1999, The dissolution kinetics of quartz in aqueous mixed cation solutions: *Geochimica et Cosmochimica Acta*, v. 63, p. 3715-3727.

Dove, P.M. and Crerar, D.A., 1990, Kinetics of quartz dissolution in electrolyte solutions using a hydrothermal mixed flow reactor, *Geochimica et Cosmochimica Acta*, v. 54, p. 955-969.

Duan, Z. and Sun, R., 2003, An improved model calculating CO_2 solubility in pure water and aqueous NaCl solutions from 273 to 533 K and from 0 to 2000 bar, *Chemical geology*, v. 193, p. 257-271.

Elmore, R.D., Milavec, G.J., Imbus, S.W., and Engel, M.H., 1989, The Precambrian Nonesuch Formation of the North American Mid-Continent Rift, sedimentology and organic geochemical aspects of lacustrine deposition, *Precambrian Research*, v. 43, p. 191-213.

Elmore, R.D., 1984, The Copper Harbor Conglomerate: A late Precambrian fining-upward alluvial fan sequence in northern Michigan, *Geological Society of America Bulletin*, v. 95, p. 610-617.

Giammar, D.E., Bruant Jr, R.G., and Peters, C.A., 2005, Forsterite dissolution and magnesite precipitation at conditions relevant for deep saline aquifer storage and sequestration of carbon dioxide, *Chemical Geology*, v. 217, p. 257-276.

Goldich, S.S., 1938, A study in Rock Weathering, *Journal of Geology*, v. 46, p. 17–58.

Golubev, S.V. and Pokrovsky, O.S., 2006, Experimental study of the effect of organic ligands on diopside dissolution kinetics, *Chemical Geology*, v. 235, p. 377-389.

Green, J.C., 1982, Geology of Keweenaw extrusive rocks, *in* R.J. Wold and W.J. Hinze (eds.), Geology and Tectonics of the Lake Superior Basin, Geological Society of America, Memoir 156, p. 47-56.

Green, J.C.,1983, Geologic and geochemical evidence for the nature and development of the middle Proterozoic (Keweenawan) Midcontinent Rift of North America, *Tectonophysics*, v. 94, p. 413-437.

Gunter, W.D., Perkins, E.H., and McCann, T.J., 1993, Aquifer disposal of CO_2-rich gases: Reaction design for added capacity, *Energy Conversion and Management*, v. 34, p. 941-948.

Hegarty, K.A., Foland, S.S., Cook, A.C., Green, P.F., and Duddy, I.R., 2007, Direct measurement of timing: Underpinning a reliable petroleum system model for the Mid-Continent Rift system, *American Association of Petroleum Geologists Bulletin,* v. 91, p. 959-979.

Holland, H.D., 1984, The Chemical Evolution of the Atmosphere and Oceans, Princeton University Press, 587 pp.

Huijgen, W.J.J., Witkamp, G.-J., and Comans, R.N.J., 2006, Mechanisms of aqueous wollastonite carbonation as a possible CO_2 sequestration process, *Chemical Engineering Science*, v. 61, p. 4242-4251.

Katz, D.A., Eberli, G.P., Swart, P.K., and Smith, L.B., 2006, Tectonic-hydrothermal brecciation associated with calcite precipitation and permeability destruction in Mississippian carbonate reservoirs, Montana and Wyoming, *AAPG Bulletin*, v. 90, p. 1803-1841.

Kaszuba, J.P., Janecky, D.R., and Snow, M.G., 2005, Experimental evaluation of mixed fluid reactions between supercritical carbon dioxide and NaCl brine: Relevance to the integrity of a geologic carbon repository, *Chemical Geology*, v. 217, p. 277-293.

King, E.R. and Zietz, I., 1971, Aeromagnetic study of the midcontinent gravity high of central United States, *Geological Society of America Bulletin*, v. 82, p. 2187-2208.

Klewin, K.W., 1987, The Petrology and geochemistry of the Keweenawan Potato River Intrusion, northern Wisconsin, Northern Illinois University, Ph.D. dissertation, 376 pp.

Klewin, K.W. and Berg, J.H., 1991, Petrology of the Keweenawan Mamainse Point lavas, Ontario: Petrogenesis and continental rift evolution, *Journal of Geophysical Research*: Solid Earth, v. 96, p. 457-474.

Klewin, K.W. and Shirey, S.B., 1992, The igneous petrology and magmatic evolution of the Midcontinent Rift system, *Tectonophysics*, v. 213, p. 33-40.

Knauss, K.G., Johnson, J.W., and Steefel, C.I., 2005, Evaluation of the impact of CO_2, co-contaminant gas, aqueous fluid and reservoir rock interactions on the geologic sequestration of CO_2, *Chemical geology*, v. 217, p. 339-350.

Lasaga, A.C., Soler, J.M., Ganor, J., Burch, T.E., and Nagy, K.L., 1994, Chemical weathering rate laws and global geochemical cycles, *Geochimica et Cosmochimica Acta*, v. 58, p. 2361-2386.

Li, G., Mauk, L., and Peacor. D.R., 1995, Preservation of clay minerals in the Precambrian (1.1 GA) Nonesuch Formation in the vicinity of the White Pine Copper Mine, Michigan, *Clay and Clay Minerals*, v. 43, p. 361-376.

Ludvigson, G., McKay, R., and Anderson, R., 1990, Petrology of Keweenawan sedimentary rocks in the MG Eisched# 1 drillhole, The Amoco M.G. Eischeid #1 deep petroleum test Carroll County, Iowa, Preliminary Investigations, Special Report Series #2, R.R. Anderson (ed.), Iowa Department of Natural Resources, p. 77-112.

Machel, H.-G. and Mountjoy, E.W., 1986, Chemistry and environments of dolomitization—a reappraisal, *Earth-Science Reviews*, v. 23, no. 3, p. 175-222.

McKay, R.M., 1990, Regional aspects of the Mount Simon Formation and the placement of the Mount Simon-Pre-Mt. Simon sedimentary contact in the Amoco M.G. Eischeid #1 Drillhole, , *in* The Amoco M.G. Eischeid #1 Deep Petroleum Test Carroll County, Iowa, Preliminary Investigations, Special Report Series #2, R.R. Anderson (ed.), Iowa Department of Natural Resources, p. 59-66.

Meybeck, M., 1987, Global chemical weathering of surficial rocks estimated from river dissolved loads, *American Journal of Science*, v. 287, no. 5, p. 401-428.

Meyer, H., 1984, The influence of impurities on the growth rate of calcite, *Journal of Crystal Growth*, v. 66, p. 639-646.

Miller, J.D., 2007, The Midcontinent Rift in the Lake Superior Region: A 1.1 Ga Large igneous province, Large Igneous Province Commission, accessed November, 2013, http://www.largeigneousprovinces.org/07nov

Miller, J.D. and Chandler, V.W., 1997, Geology, petrology, and tectonic significance of the Beaver Bay Complex, northeastern Minnesota, Middle Proterozoic to Cambrian Rifting, Central North America, R.W. Ojakangas, A.B. Dickas, and J.C. Green (eds.), Geological Socciaty of America Special Paper 312, p. 73-96.

Morse, J.W., 2003, Formation and Diagenesis of Carbonate Sediments, *in* Holland, H. D., and Turekian, K. K., (eds.), Treatise on Geochemistry, Volume 7, Oxford, Pergamon, J.W. Morse and F.T. Mackenzie, p. 67-85.

Morse, J.W. and Mackenzie, F.T., 1990, Geochemistry of Sedimentary Carbonates, Developments in Sedimentology 48, Elsevier, 706 pp.

Murphy, R., Lammers, K., Smirnov, A., Schoonen, M.A.A., and Strongin, D.R., 2011, Hematite reactivity with supercritical CO_2 and aqueous sulfide, *Chemical Geology*, v. 283, p. 210-217.

Nicholson, S.W., Dicken, C.L., Foose, M.P., Mueller, J., 2004, Preliminary integrated geologic map databases for the United States: Minnesota, Wisconsin, Michigan, Illinois, and Indiana, Version 1.1, U.S. Geological Survey Open-File Report 2004-1355, http://pubs.usgs.gov/of/2004/1355/

Oelkers, E.H., Gislason, S.R., and Matter, J., 2008, Mineral carbonation of CO_2, *Elements*, v. 4, p. 333-337.

Ojakangas, R., 1986, Reservoir characteristics of the Keweenawan Supergroup, Lake Superior region: Precambrian petroleum potential, Wisconsin and Michigan, *Geoscience Wisconsin*, v. 11, p. 25-31.

Ojakangas, R., Morey, G., and Green, J., 2001, The Mesoproterozoic midcontinent Midcontinent Rift system, Lake Superior region, USA, *Sedimentary Geology*, v. 141, p. 421-442.

Ojakangas, R.W., and Morey, G., 1982, Keweenawan sedimentary rocks of the Lake Superior region: a summary, *in* R.J. Wold and W.J. Hinze (eds.), Geology and Tectonics of the Lake Superior Basin, Geological Society of America, Memoir 156, p. 157-164.

Paces, J.B. and Miller, J.D., 1993, Precise U-Pb ages of Duluth Complex and related mafic intrusions, northeastern Minnesota: Geochronological insights to physical, petrogenetic, paleomagnetic, and tectonomagmatic processes associated with the 1.1 Ga Midcontinent Rift System, *Journal of Geophysical Research, Solid Earth*, v. 98, no. B8, p. 13997-14013.

Palandri, J.L. and Kharaka, Y.K., 2005, Ferric iron-bearing sediments as a mineral trap for CO_2 sequestration: Iron reduction using sulfur-bearing waste gas, *Chemical Geology*, v. 217, p. 351-364.

PHREEQC software program (United States Geological Survey, version 3.1.2.8538; Parkhurst, D.L. *and* Appelo, C.A.J. (3/3/2014).

Plumber, L. and Busenberg, E., 1982, The solubilities of calcite, aragonite and vaterite in CO_2–H_2O solutions between 0 and 90°C, and an evaluation of the aqueous model for the system $CaCO_3$–CO_2–H_2O, *Geochimica et Cosmochimica Acta*, v. 46, p. 1011-1040.

Pratt, L.M., Summons, R.E., and Hieshima, G.B., 1991, Sterane and triterpane biomarkers in the Precambrian Nonesuch Formation, North American Midcontinent Rift, *Geochimica et Cosmochimica Acta,* v. 55, p. 911-916.

Railsback, L.B., 2011, Surface features on a growing or dissolving crystal, *in* Some Fundamentals of Mineralogy and Geochemistry. http://www.gly.uga.edu/railsback/Fundamentals/815XtalKinksSteps03SF.pdf

Ryan, P., 2014, Environmental and Low Temperature Geochemistry, John Wiley & Sons. 416 pp.

Shock, E.L., and Helgeson, H.C., 1988, Calculation of the thermodynamic and transport properties of aqueous species at high pressures and temperatures: Correlation algorithms for ionic species and equation of state predictions to 5 kb and 1000 C, *Geochimica et Cosmochimica Acta*, v. 52, p. 2009-2036.

Shock, E.L., Helgeson, H.C., and Sverjensky, D.A., 1989, Calculation of the thermodynamic and transport properties of aqueous species at high pressures and temperatures: Standard partial molal properties of inorganic neutral species, *Geochimica et Cosmochimica Acta*, v. 53, p. 2157-2183.

Southwick, D.L., Morey, G.B., and McSwiggen, P.L., 1988, Geologic Map (Scale 1: 250,000) of the Penokean Orogen, central and eastern Minnesota, and accompanying text. Minnesota Geological Survey, Report of Investigations 37, 32 pp.

Stein, S., Van der Lee, S., Jurdy, D., Stein, C., Wiens, D., Wysession, M., Revenaugh, J., Frederiksen, A., Darbyshire, F., and Bollmann, T., 2011, Learning from failure: The SPREE Mid-Continent Rift Experiment, *GSA Today*, v. 21, no. 9, p. 5-7.

Suszek, T., 1997, Petrography and sedimentation of the middle Proterozoic (Keweenawan) Nonesuch Formation, western Lake Superior region, Middle Proterozoic to Cambrian Rifting, Central North America, R.W. Ojakangas, A.B., Dickas, and J.C. Green (eds.), Geological Socciaty of America Special Papers., v. 312, p. 195-210.

Thiel, E., 1956, Correlation of gravity anomalies with the Keweenawan geology of Wisconsin and Minnesota, *Geological Society of America Bulletin*, v. 67, p. 1079-1100.

Thorleifson, L.H., ed., 2008, Potential capacity for geologic carbon sequestration in the Midcontinent Rift system in Minnesota, Minnesota Geological Survey Open File Report OFR-08-01, 138 pp.

Tryhorn, A. and Ojakangas, R., 1972, Sedimentation and petrology of the upper Precambrian Hinckley Sandstone of east-central Minnesota, *in* Geology of Minnesota: A centennial Volume, P.K. Sims and G.B. Morey (eds.), Minnesota Geological Survey, p. 431-435.

Ueda, A., Kato, K., Ohsumi, T., Yajima, T., Ito, H., Kaieda, H., Metcalfe, R., and Takase, H., 2005, Experimental studies of CO_2-rock interaction at elevated temperatures under hydrothermal conditions, *Geochemical Journal*, v. 39, p. 417-425.

Walter, L.M., 1986. Relative efficiency of carbonate dissolution and precipitation during diagenesis: a progress report on the role of solution chemistry, Roles of organic matter in mineral diagenesis, D.L. Gautier (ed.), Society for Sedimentary Geology, Special Publication 38, p. 1–12.

Weiblen, P.W. and Morey, G., 1980, A summary of the stratigraphy, petrology, and structure of the Duluth Complex, *American Journal of Science*, v. 280-A, p. 88-133.

Wellman, T.P, Grigg, R.B., McPherson, B.J., Svec, R.K., and Lichtner, P.C., 2003, Evaluation of CO_2-brine-reservoir rock interaction with laboratory flow tests and reactive transport modeling, Society of Petroleum Engineers International Symposium on Oilfield Chemistry, paper 80228.

White, W.S., 1972, The base of the upper Keweenawan, Michigan and Wisconsin, *U.S. Geological Survey Bulletin*: 1354-F, p. F1-F23.

Witzke, B., 1990, General stratigraphy of the Phanerozoic and Keweenawan sequence, *in* The Amoco M.G. Eischeid #1 Deep Petroleum Test Carroll County, Iowa, Preliminary Investigations, Special Report Series #2, R.R. Anderson (ed.), Iowa Department of Natural Resources, p. 39-57.

Woelk, T.S. and Hinze, W.J., 1991, Model of the Midcontinent Rift system in northeastern Kansas, *Geology*, v. 19, p. 277-280.

Woollard, G.P., 1943, Transcontinental gravitational and magnetic profile of North America and its relation to geologic structure, *Geological Society of America Bulletin*, v. 54, p. 747-789.

Xu, T., Apps, J.A., and Pruess, K., 2005, Mineral sequestration of carbon dioxide in a sandstone–shale system, *Chemical Geology*, v. 217, p. 295-318.

SECTION V. EFFECT OF ELEVATED CO_2 ON THE ABILITY OF SULFATE-REDUCING BACTERIA TO PRECIPITATE CARBONATE MINERALS: IMPLICATIONS FOR CARBON SEQUESTRATION

1. INTRODUCTION

The greenhouse effect of CO_2 gas is a well-known phenomenon and the recent increase in the atmospheric CO_2 level, due primarily to burning of fossil fuels is affecting global climate (Socolow et al., 2004). The atmospheric CO_2 levels have recently crossed the 400 ppm threshold (pCO_2 of 0.0059 psi), leading to an increased urgency to reduce our anthropogenic carbon footprint (Monastersky, 2013). Geologic carbon sequestration (GCS), injection of CO_2 gas in the subsurface, has been investigated and practiced as a potential means of curbing the concentration of the gas in the atmosphere (Dupraz et al., 2009a). It is predicted that up to 60% of point source CO_2 released could be sequestered in the subsurface by using GCS (Jun et al., 2013). However, a potential problem associated with the concept of underground carbon sequestration is the leakage of CO_2 back to the surface due to the high pressures created in the subsurface. Leakage is possible through pores and fractures in the cap rock (White et al., 2003), and drill holes. An ideal combination of trap and storage rock units is essential to contain the gas in the subsurface (Benson and Cole, 2008). It would be beneficial if the CO_2 could be converted into solid phase carbonate minerals, thereby providing a more permanent and stable form of storing the gas (i.e. mineral sequestration). Several investigations have shown that the interaction of CO_2 with the rocks in the subsurface could lead to precipitation of minerals, such as siderite ($FeCO_3$), calcite or aragonite ($CaCO_3$), magnesite ($MgCO_3$) or others carbonate mineral phases (Giammaar et al., 2005; Metz et al., 2005; Oelkers et al., 2008; Jun et al., 2013).

A natural way of sequestering CO_2 as minerals and accelerating the kinetics of such reactions can be achieved through microbial metabolism. Seawater, saline lakes, soils, and other geological formations provide well-documented evidence of the presence of microorganisms and their role in carbonate mineralization (Hammes and Verstraete, 2002). Subsurface environments also harbor indigenous bacteria capable of interacting with injected CO_2 (Pedersen, 2000). To achieve mineral sequestration of the gas through microbial activity, however, the microbes involved will need to be able to survive the extreme subsurface conditions in addition to the toxicity induced by the large amount of CO_2 injected. Alternatively, known and tested microorganisms can be inoculated into the subsurface to achieve mineral sequestration.

Sulfate-reducing bacteria (SRB) are commonly found in anaerobic to partially aerobic conditions (Jonkers et al., 2005) and play an important role in the cycling of carbon and sulfur in marine and hypersaline environments (Canfield and Des Marais, 1993). Carbonate mineral precipitation can be induced by SRB activity as the microorganisms favorably modify pH, alkalinity and/or calcium activity, while reducing sulfate to sulfide (Castanier et al., 1999; Baumgartner et al., 2006; Deng et al., 2010). Additionally, reduction of sulfate would potentially release calcium ions bound in minerals like gypsum and indirectly promote calcium carbonate precipitation (Kah et al., 2001). In many modern marine environments, carbonate mineral precipitation has been closely associated with bacterial sulfate reduction (Allison and Briggs, 1991; Van Lith et al., 2000). Strains of SRB have also been suggested to cause dolomite ($CaMg(CO_3)_2$) and high-Mg calcite precipitation under laboratory conditions (Warthmann et al., 2000; Van Lith et al., 2003; Deng et al., 2010) and in microbial mats forming stromatolites (Visscher et al., 1998).

Lake Estancia is located in central New Mexico (Figs. 1A and B; and Section II Figure 4). The lake is a closed-drainage, hypersaline, playa located in the Estancia Basin, at an elevation of approximately 1890 meters (6,200 feet) and has a surface area of 1125 km^2 (Allen and Anderson, 2000). The lake was initially formed during crustal extension and uplift along the eastern flanking margin of the Rio Grande Rift tectonic provenance (Szynkiewicz et al., 2009). The lake was perennial during the Pleistocene as it was constantly fed by ground and surface water runoff. A change to a warmer and drier climate eventually led to the desiccation of the lake system about 24,000 years before present, thus leaving the large playa on the basin floor. More recent sand blow-out zones have locally removed loose sediments from the valley floor and created numerous segmented small depressions that fill with water during seasonal periods of rainfall (Fig. 1B). Sediment and water samples for this study were collected from one of these sub-basins. The water level was low during the sampling date (12:45 pm MST, May 29th, 2010), with only a shallow water film covering the central portion of the lake and salt evaporates occurring in dry areas (Fig. 1C). Calcareous clays, and gypsiferous sediments occur as layered evaporate deposits in the lake sediments, and these minerals are also present in the surrounding Lower and Middle Permian geologic strata (Allen and Anderson, 2000; Szynkiewicz et al., 2009). Two sediment profile cores were collected from Lake Estancia using a piston core that was pushed into the soft sediment. The top surface of the cores consisted of a thin white salt crust, followed beneath by a thicker layer of organic-rich material (Fig. 1C). A second thin layer of white salts crystals was present ~5 cm below the surface, then again below the dark, organic material dominated the remainder of the ~ 50 cm core section.

The objective of the current study was to investigate the carbonate mineral precipitation ability of a SRB-enriched community isolated from hypersaline Lake Estancia, when exposed to atmospheric and elevated pCO_2 levels. The potential implications of CO_2 injection on amended or indigenous SRB communities in the subsurface are provided with respect to long-term mineral sequestration of carbon dioxide.

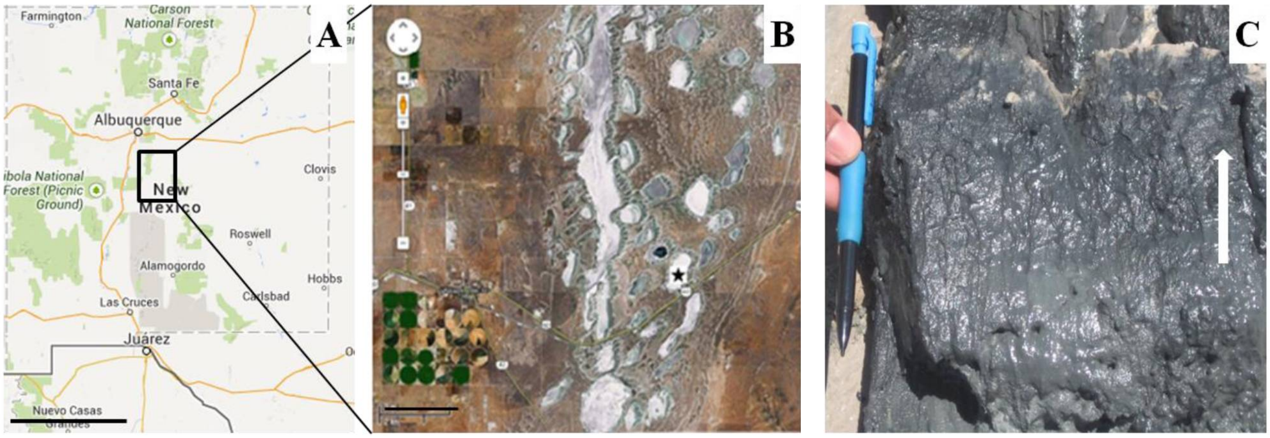

Fig. 1. A) Google map of the southwestern region of US showing the state of New Mexico, bar = 200 km; B) Enlarged Google map image of the region selected in Fig. 1A, showing Lake Estancia and Estancia Basin, Torrance County, New Mexico, bar = 5 km. Star indicates the location where samples were collected; C) A scooped up vertical section of the organic- and sulfide- rich sediments with the white arrow pointing towards the stratigraphic top. Lighter-colored material with occasional salt crystals is seen at the top layer and is repeated ~5 cm below the surface. Majority of the remaining sediments show the dark, organic-rich material.

2. RESULTS

2.1. Lake Estancia Water and Sediment Characterization

The temperature of the shallow water pool filling the depression sampled at Lake Estancia was 31.6°C (12:45 pm MST, May 29th, 2010). The corresponding conductivity value was 118 mS/cm, and a pH of 7.9. Water samples were processed on site by injecting samples through 0.45 µm cellulose acetate syringe filters and storing the filtrates in 50 mL acid-cleaned polyethylene vials. The solutions were subsequently analyzed back in the laboratory for cation composition by ICP-OES. The Ca, Mg, K and Na concentrations were 586, 1800, 1364 and 17,197 mg/kg respectively. It was necessary to dilute the lake water samples 100:1 prior to ICP-OES analysis to bring the elemental concentrations within analytical range and prevent the buildup of salts on instrument components. This dilution caused Si, Al, Fe and Mn concentrations to fall below their detection range of 0.1 ppm during the ICP-OES analyses. The undiluted concentration of these elements in the water would thus be < 10 ppm.

Sediments located between the top crust and up to a depth of ~10 cm in the core (Fig. 1C) were collected, rinsed with deionized water to remove soluble salts, dried in an oven at 55°C overnight, and then homogenized. These sediments were then analyzed by X-ray Diffraction (XRD) analysis using a monochromatic Cu K_α radiation source, and scanned from 10 to 70 degrees two-Θ at a scan rate of 0.45 degrees per minute and a 0.03 degree step interval. Quartz, calcite, and dolomite were detected as major mineral phases in sediments (both white crust and organic material) as determined by their two-Θ peak position values (26.6°, 29.4° and 30.9°, respectively) from the XRD analyses (Fig. 2). The sediment samples also reacted with a 5% hydrochloric acid solution releasing CO_2 bubbles, confirming the presence of carbonate minerals The 30.9° two-Θ peak position corresponds to both true dolomite and a disordered dolomite. A truly ordered dolomite can be identified by an additional two-Θ peak at 35.3°. No such peak was observed, thus the presence of a well-ordered dolomite cannot be confirmed. Optical examinations also revealed the presence of cubic halite and/or sylvite crystals. Sediments were rinsed with deionized water prior to XRD analysis to remove this material.

2.2. Enrichment Culture Results

Sediment samples from Lake Estancia were extracted from the piston cores upon return to the lab and cultured in a medium to enrich for bacteria capable of performing sulfate reduction (Kjeldsen et al. 2007). The final pH of the medium before addition of the sediments was 7.3. The individual media components were mixed together with deionized water. The medium was made anaerobic by boiling and cooling under an atmosphere of N_2:CO_2 (80:20) and subsequent placement in an anaerobic glove bag that was maintained under a constant N_2:H_2 (90:10) atmosphere. Resazurin reagent was used as an indicator of anaerobic conditions in the medium. The reduced medium was distributed in 30 mL serum bottles, capped with butyl rubber stoppers and aluminum crimps, and autoclaved. An inoculum size of 10% final medium volume was used for subculturing every two weeks to one month and the cultures were maintained at room temperature.

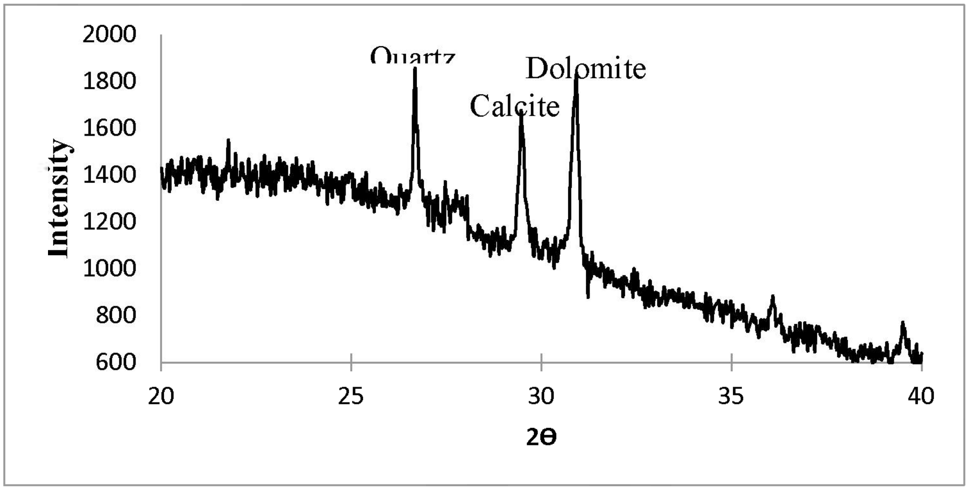

Fig. 2. XRD pattern of the sediments collected from Lake Estancia showing intensity peaks for quartz, calcite and dolomite.

The enrichment cultures for SRB from Lake Estancia were successfully grown in serum bottles and sulfate reduction activity was confirmed in all cultures by visual observation for black metal sulfide precipitates. The cultures were subjected to six consecutive subcultures with each new batch re-inoculated over an interval of two weeks to one month. The successfully grown SRB enrichment cultures were then used for microbial diversity analysis and in the reactor experiments.

2.3. Microbial Diversity Experiment Results

Microbial diversity in the sediments and SRB enrichments that were developed from the lake samples were analyzed by using a barcoded pyrosequencing approach. Samples were collected for genomic DNA extraction from the organic-rich, top five centimeters of the sediment cores and stored at room temperature in the dark for up to ten months before extracting the microbial cultures for DNA extract. Details on the sample preparation, culture medium, and data processing are given in Section II-9, "DNA Extraction and 16S rRNA Gene Analysis".

The quantity of genomic DNA isolated from both the sediment material of Lake Estancia and the SRB enrichment produced from the sediment was extremely low (<0.1 ng/µl). The amplicon products obtained from genomic DNA were analyzed by pyrosequencing. A total of 15,167 sequences were recovered from the barcoded pyrosequencing of the partial (V1-V3 region) of the 16S rRNA gene from two samples (Table 1). The average read length of the sequences was 471 bp, with 11,745 sequence reads, while the enrichments had a lower number of reads (3,422). Alpha diversity values were calculated using QIIME software (Caporaso et al., 2010). The program was used to randomly generate a subset of sequences (termed equalized), and 10 iterations were run for each diversity indices. Chao1 values and Shannon index estimates of species richness had values of 592 and 4.77, respectively for sediments; and 225 and 1.57, respectively for enrichments. The distribution of species, as seen by the equitability value, was 0.53 in the sediments and 0.22 in the enrichments.

The bacterial populations in the sediments collected from the field were not very diverse (Table 1), with about 3.5% of the entire bacterial population regarded as unclassified. The class, KB1 was abundant in the sediments (~21%), but the highest representation in this sample was from the family Oxalobacteraceae, comprising ~57% of the entire population. The families, Comamonadaceae and Burkholderiales, and the order Bacteroidales were among the other significant populations present. The enrichment culture produced from the Lake Estancia sediment population was dominantly made up of the family, Desulfobacteraceae (~87%), which includes several SRB members. Families, including members of Halanaerobiaceae, Halobacteroidaceae, Enterobacteriaceae, and candidate class, KB1, were among the other bacterial members present, each representing between 1.0 to 2.5% of the entire population. It is important to note that the families, Desulfobacteraceae, Halanaerobiaceae and Halobacteroidaceae were only detected in the enrichments and not the lake sediments.

Table 1. Bacterial 16S rRNA gene diversity analysis of the two lake sediments and one enrichment culture by pyrosequencing method. Percentage of major taxa identified are also shown. *o: order, c: class, f: family.

	Sediments	**SRB enrichments**
# of Sequence Reads	11,745	3422
Equalized Sequences	2,425	
Chao1	592	225
Chao1 (95% confidence [LL/UL])	538/647	206/244
Shannon Index	4.77	1.57
Equitability	0.53	0.22
TAXA PERCENTAGE*		
Unclassified bacteria	3.52	4.53
f_ Propionobacteriaceae	2.97	0.53
o_ Bacteroidales	0.04	0.00
f_ Halanaerobiaceae	0.00	2.54
f_ Halobacteroidaceae	0.00	1.20
c_ KB1	21.17	2.25
o_ HMMVPog-54	0.00	0.00
Unclassified Proteobacteria	0.08	0.12
o_ Burkholderiales	3.61	0.00
f_ Comamonadaceae	10.95	0.09
f_ Oxalobacteraceae	57.11	0.20
f_ Desulfohalobiaceae	0.00	0.15
f_ Desulfobacteraceae	0.00	87.14
f_ Enterobacteriaceae	0.54	1.26
f_ Spirochaetaceae	0.00	0.00
Total Coverage	**100.00**	**100.00**

2.4. Continuous Gas Flow Experiment Results

The continuous gas flow reactors were tested at (i) 400 ppm (pCO_2 of 0.0059 psi), and (ii) 1200 ppm (pCO_2 of 0.018 psi) headspace CO_2 concentrations in sterilized Nalgene polycarbonate jars containing either acid-treated quartz sand or crushed carbonate mudrock particles. Fifteen grams of substrate, 45 ml of artificial seawater, 20 mM lactate, and 5 mL of bacterial culture solution were added to each vessel. All reactors were then placed into controlled atmosphere chambers with a constant atmosphere at either 400 ppm (0.0059 psi pCO_2) or 1200 ppm (0.018 psi pCO_2)

flowing CO_2. Vessels were monitored periodically for pH, Eh, Ca, and Mg analysis. Further details on the experimental procedure can be found in Section II-4, “Laboratory Biomineralization Reactor Experiments”.

The continuous gas flow mode reactors operated at 0.0059 and 0.018 psi pCO_2 conditions with the SRB cultures display changes in the pH, Eh and Ca concentrations in the artificial seawater. The reactors were allowed to remain undisturbed for 24 h before the leachant samples were drawn out for analyses. The starting leachant values were calculated based on known data. The starting pH of the artificial seawater solution was measured to be 8.00, Eh of approximately -42 mV, with a Ca and Mg concentration of 900 and 1584 ppm, respectively. These values are considered as the time zero value for control reactors. Calculated values for the starting leachant solution with bacterial enrichment using 90:10 mixture are 7.96, -39 mV, 820 and 1524 ppm, for the pH, Eh, Ca and Mg concentration, respectively (Table 2).

Table 2. Calculated starting inoculated seawater leachant values for the background reactors (control and blank) and the reactors with enrichment medium. These solutions were produced by mixing 90% synthetic seawater with 10% of the inoculum enrichment media or sterilized inoculum media for the blank reactors.

Parameters	**Starting leachant values of artificial seawater leachant**	
	Control and Blank Without bacterial enrichment	**With bacterial enrichment**
pH	8.00	7.96
Eh (mV)	-42	-39
Ca (ppm)	900	820
Mg (ppm)	1584	1524
Sulfide (mM)	~1.5	~5.0

2.4.1. Reactors With 0.0059 psi pCO_2

Samples were left undisturbed for 24 hours after addition of all components to allow the particles to settle and no readings were taken during this day. The first measurements were taken after 24 hours (day-1 results). Experiments at 0.0059 psi pCO_2 (headspace CO_2 at 400 ppm) displayed a drop in pH value between the start of the experiments and day-3. This pH decrease was from the starting pH ≈8.0; to 7.9, 7.8 and 7.6 in the control, carbonate mudrock, and quartz sand reactors, respectively (Fig. 3A). In the control reactor with no bacterial enrichment, but quartz sand substrate, the pH after day-3 remained at 7.8 ± 0.1 until the end of the 43 day run. For carbonate mudrock reactors, the pH increased back to 8.0 by day-9, then dropped again to 7.4 between days 13 and 22, then increased gradually thereafter reaching a final value of 7.7 on day-43. The quartz sand reactor displayed a near parallel trend to the experiment with the carbonate mudrock; after the initial decrease from ~8.0 for the leachant to 7.4 on day-7, the pH rose slightly to 7.5 on day-13. The value then decreased to a low of 7.2 on day-27, followed by a sharp rise to a final pH of 7.7 on day-43. The error range as seen with the pH 7.00 standard is ± 0.03 units; thus, the pH changes observed with the reactor samples are statistically valid.

The redox conditions, measured as Eh values, remained fairly stable throughout the reaction period in the control reactor; Eh initially rose from an initial starting value of -40 mV to -30 mV on day-13, and remained more or less unchanged until day-43 (Fig. 3B). The carbonate mudrock reactors remained fairly steady at -40 mV up to day-12, and then rose to -17 mV on day-16. The conditions continued to slowly increase to -12 mV until day-22, followed by a steady decrease till a final value of -24 mV was reached on day-43. The quartz sand substrate reactors initially showed a drastic fluctuation in their initial Eh values from -40 mV for the starting leachant to +31 mV on day-1 and then to -21 mV on day-3. The Eh increased, but with minor variations, until it reached +5 mV on day-27, followed by a steady drop to -23 mV on day-43, coinciding with the pH trend for these reactors.

The day-1 leachant Ca concentration in the control reactor was 956 ppm, which is higher than the theoretical Ca leachant concentration at day-zero, i.e., 900 ppm, thus creating a Ca concentration imbalance (Fig. 3C). Similarly, the carbonate mudrock and quartz sand reactors also had higher Ca concentration (1110 and 985 ppm, respectively) on day-1 than the theoretical starting value of 820 ppm. While the instrument had a ± 7.1% analytical accuracy, i.e., ± 71 ppm variation, the day-1 values were still higher than day-zero in the reactors with bacterial enrichment. The additional Ca was likely contributed by the dissolution of Ca-carbonates that had precipitated in the enrichment media either through bacterial or chemical activity. In the control reactor, the day-1 concentration of 956 ppm was more or less maintained for most of the entire 43 days of testing, with only intermittent increases of 1013 ppm on day-15, and 1032 ppm on day-31, though these changes are close to the ± 71 ppm instrumental accuracy. The leachant in both the carbonate mudrock and quartz sand reactors displayed a 30% and 32% drop, respectively in their Ca concentration from day-1 to day-43, respectively.

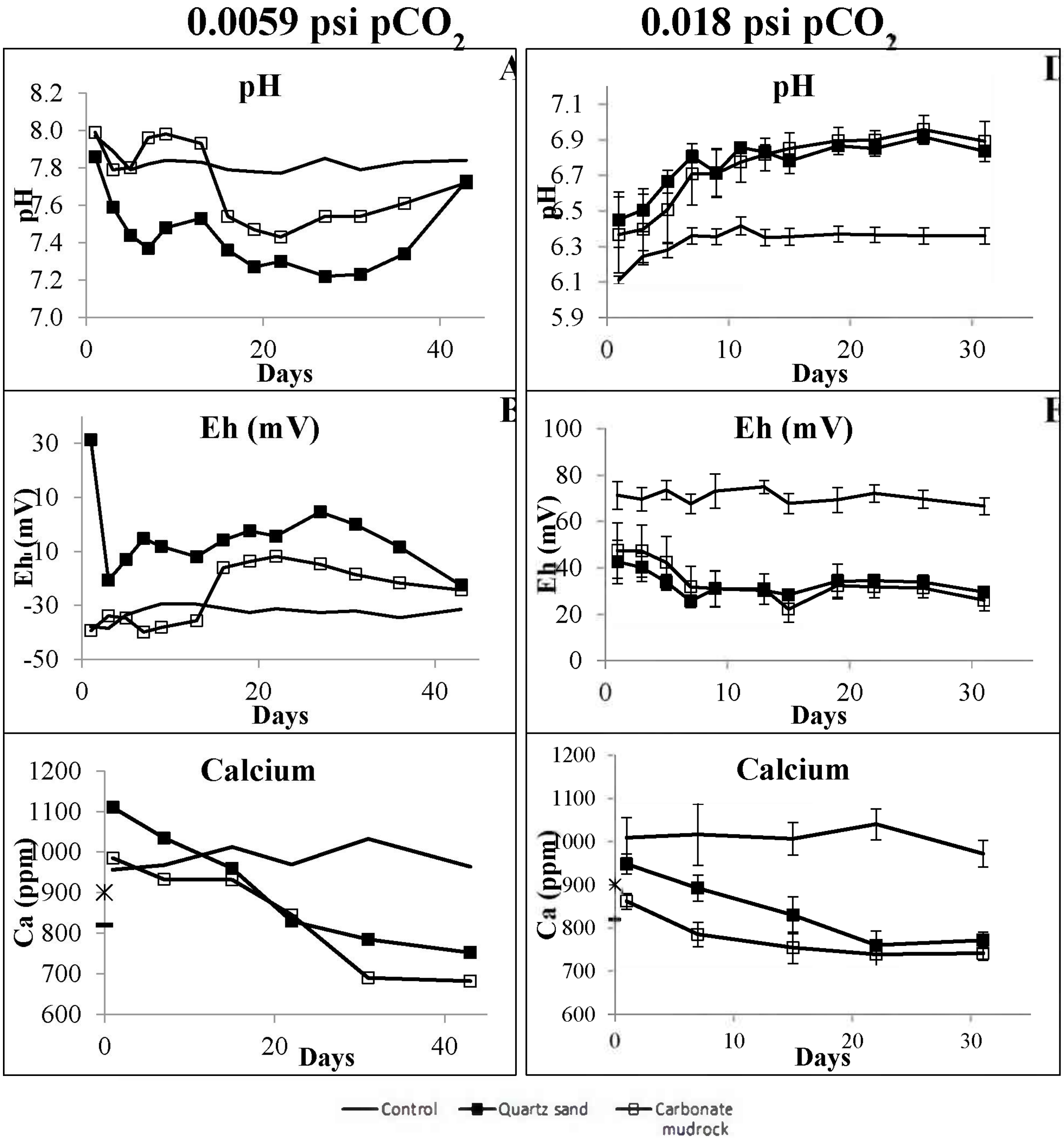

Fig. 3. Results obtained from 0.0059 psi pCO_2 and 0.018 psi pCO_2 reactors with Lake Estancia enrichment cultures showing pH, Eh and Ca concentration values. Control reactors contained only artificial seawater and quartz sand substrate, but no bacterial inoculum was added. The data from the 0.0059 psi pCO_2 were obtained from a single set of reactors (A, B and C), while those from the 0.018 psi pCO_2 were from experiment conducted in triplicate (D, E and F). The error bars in the case of the latter show the standard deviation from the triplicate readings.

The Mg concentration in the leachant had an increase in its value on day-1 (1643 ppm) from a day-zero (1584 ppm) in the case of the control, though this variation was within the ± 88 ppm instrument variation. In this reactor, the leachant decreased from 1643 ppm on day-1 to 1470 ppm on day-22, but finally ended up at 1515 ppm on day-43. The carbonate mudrock reactor displayed a similar decrease from 1455 ppm on day-1 to 1358 ppm on day-7, after which, it remained unchanged. However, the reactor with quartz sand displayed fluctuating changes in the first 22 days (1776 to 1632 ppm), followed by a relatively stable value in the range of 1668 to 1692 ppm till day-43. Also, in the case of quartz sand reactor, the theoretical Mg concentration on day-zero (1524 ppm) was lower than that of day-1 (1776 ppm), indicating that additional Mg must have been contributed by the dissolution of possible Mg-carbonate minerals added from the enrichment media.

In order to check for the formation of carbonate minerals in the 0.0059 psi CO_2 reactors, we added a 10% HCl solution to an isolated portion of the sediments to check for effervescence of CO_2 gas. Visual observation of the quartz sand sediments and carbonate mudrock reactors revealed the presence of grains were loosely fused together by a cement that reacted with the HCl solution, indicating that carbonate mineral precipitation had occurred. In both carbonate mudrock- and quartz sand-containing reactors, the sediments were also held together by a slimy material, indicating extracellular polymeric substance (EPS) production by the bacteria. Though carbonate cementation and/or adherence to EPS were confirmed by visual observation, the sediment particles were only loosely bound to each other and were easily separated from each other by applying minor pressure from a probe.

2.4.2. Reactors With 0.018 psi pCO_2

The continuous gas flow reactors at 0.018 psi pCO_2 were run in triplicates; the leachant values discussed below are the average of triplicate measurements. The injection of CO_2 caused all reactors to express a decrease from a starting pH of ~8.0 to 6.1, 6.5, and 6.4 on day-1 in the control, carbonate mudrock and quartz sand reactors, respectively (Fig. 3D). Following this initial decrease in pH, all reactors experienced an overall increase in the values: the control reactors stabilized after reaching up to 6.4 after seven days, while reactors with carbonate mudrock and quartz sand increased in a near continuous trend to a final value of 6.8 and 6.9, respectively on day-31. A blank reactor with only the artificial seawater was also run. The constant CO_2 supply at 0.018 psi also caused the pH to drop in the blank reactor from the initial leachant pH value of ~8.0 to 5.2 at day-1, 4.8 on day-3, and 4.4 after 10 days.

Before CO_2 injection, the starting Eh value of the leachant was -40 mV, while the day-1 values increased in all reactors; +71 mV in the control reactors, +43 and +47 mV, respectively, in the carbonate mudrock and quartz sand reactors. Control reactors exhibited a steady oxidized state (+70 mV), whereas the reactors containing bacteria became slightly more reducing over the reaction time. The average change in Eh from day-1 to day-31 was +43 mV to +30 mV for the carbonate mudrock reactors, and +47 mV to +26 mV for the quartz sand reactors (Fig. 3E).

Similar to the 0.0059 psi pCO_2 reactors, the Ca concentration of the leachant was 900 ppm for control and 820 ppm for enrichment-added reactors. This was lower than the average day-1 values (862 to 1009 ppm) in all reactors. The average Ca concentration in the control reactors saw a small drop, 1009 ± 47 to 972 ± 31 ppm, during the course of the reaction, except on day-22 when an increase up to 1040 ± 36 ppm was observed (Fig. 3F). The overall decrease in average values, however, was within the standard deviation for each triplicate experiment run at any one reaction time. The analytical accuracy for Ca as determined using ICP-OES standards was ±71 ppm. The average Ca concentration from day-1 to day-22 decreased; 862 ± 24 to 739 ± 36, respectively, for the carbonate mudrock reactors, and 948 ± 31 to 760 ± 45 ppm, respectively, for the quartz sand containing reactors.

The Mg concentration in the control reactors followed a sinusoidal pattern, decreasing initially from an average of 1676 ± 267 ppm on day-1 to 1547 ± 123 ppm on day-7, followed by an increase to 1665 ± 206 ppm for day-22, and finally decreasing to 1601 ± 82 ppm on day-43. The overall variability between triplicate experiments was quite large and masked any trends in Mg concentration with time. The ICP-OES accuracy analysis on commercial standards (± 88 ppm) also contributed to these fluctuations. The Mg concentration in the carbonate mudrock reactors decreased from 1947 ppm on day-1 to 1845 ppm on day-7. The changes following day-7 were within the ± 88 ppm analytical accuracy of the instrument. The quartz sand reactors displayed a slight, insignificant decrease in their Mg concentrations, with day-1 values averaging 1643 ± 72 ppm and ending at an average of 1623 ± 30 ppm.

Sediments collected from the quartz sand reactors revealed the presence of carbonate minerals when reacted with HCl. As noted previously with the 0.0059 psi reactors, those vessels containing bacterial inoculum exhibited EPS production. Sediments in the quartz sand reactors were adhering together, further indicating that mineral precipitation forming cement and/or EPS binding had occurred.

2.5. Batch Reactor Experiment Results

Batch reactors were set up in 20mL glass serum bottles to test for SRB activity under higher pCO_2 conditions than the continuous gas flow reactor vessels could accommodate. Two CO_2 headspace pressure conditions were tested: (i) pCO_2 of 14.7 psi, and (ii) pCO_2 of 20 psi. All serum bottle reactors (20 mL) were run with either quartz sand or crushed carbonate mudrock substrate (5.0 g), 9 ml artificial seawater, and 1 mL of the SRB enrichment culture. A separate set of batch of experiments was also conducted with different electron donors (hydrogen, formate, lactate and acetate) and quartz sand as the substrate. Solution pH, Eh, Ca and Mg were analyzed. Dissolved sulfide was also measured using the colorimetric $CuSO_4$ method. Details on the experimental procedure can be found in Section II-4, “Laboratory Biomineralization Reactor Experiments”.

2.5.1. Batch Reactors With 14.7 psi pCO_2

Three types of background reactors were analyzed to evaluate the changes in water and mineral chemistry occurring in the respective reactors. The ‘control’ reactors containing only quartz sand and artificial seawater did not show any statistically significant changes in the pH values (Fig. 4A): The pH in all reactors decreased from their starting value of ~8.0 to ~6.9 on day-1 following CO_2 addition. The ‘control’ reactors remained at ~ 6.9 during the 10 day period, with relatively high standard deviation values of up to ± 0.12 pH units. Even in the ‘blank’ reactors with only the artificial seawater, the average pH value dropped to ~6.9 on day-1 and remained unchanged thereafter. In the ‘killed control’ reactors containing bacterial cultures that were heat sterilized immediately after inoculation, the average pH decreased from ~ 6.8 to ~ 6.7, but exhibited high standard deviation of up to ± 0.13 units. In the carbonate mudrock reactors the average pH increased from 6.2 ± 0.1 on day-1 to 6.4 ± 0.1 on day-10, whereas in the quartz sand containing reactors, the pH remained at ~7.0 throughout the reaction period.

An initial rise in the Eh values was observed in all reactors following CO_2 injection. For example, the starting calculated Eh value of- 40 mV rose to around +37 mV on day-1 in the ‘control’ reactor. The overall changes in the redox conditions in all the background reactors were minimal between day-1 and 10 (Fig. 4B): for example ‘blank’, and ‘killed control’ reactors displayed only small redox changes of +34 mv to +33 mV, and + 31 mV to + 32 mV, respectively, the ‘control’ reactors remained unchanged at + 37 mV. The reactors with carbonate mudrock exhibited very small, but significant decreases in Eh values, dropping from + 36 mV on day-1 to + 30 mV on day-10. Very small changes were also observed in the quartz sand reactors as well, with + 32 mV on day-1 to reach a final value of + 27 mV on day-10.

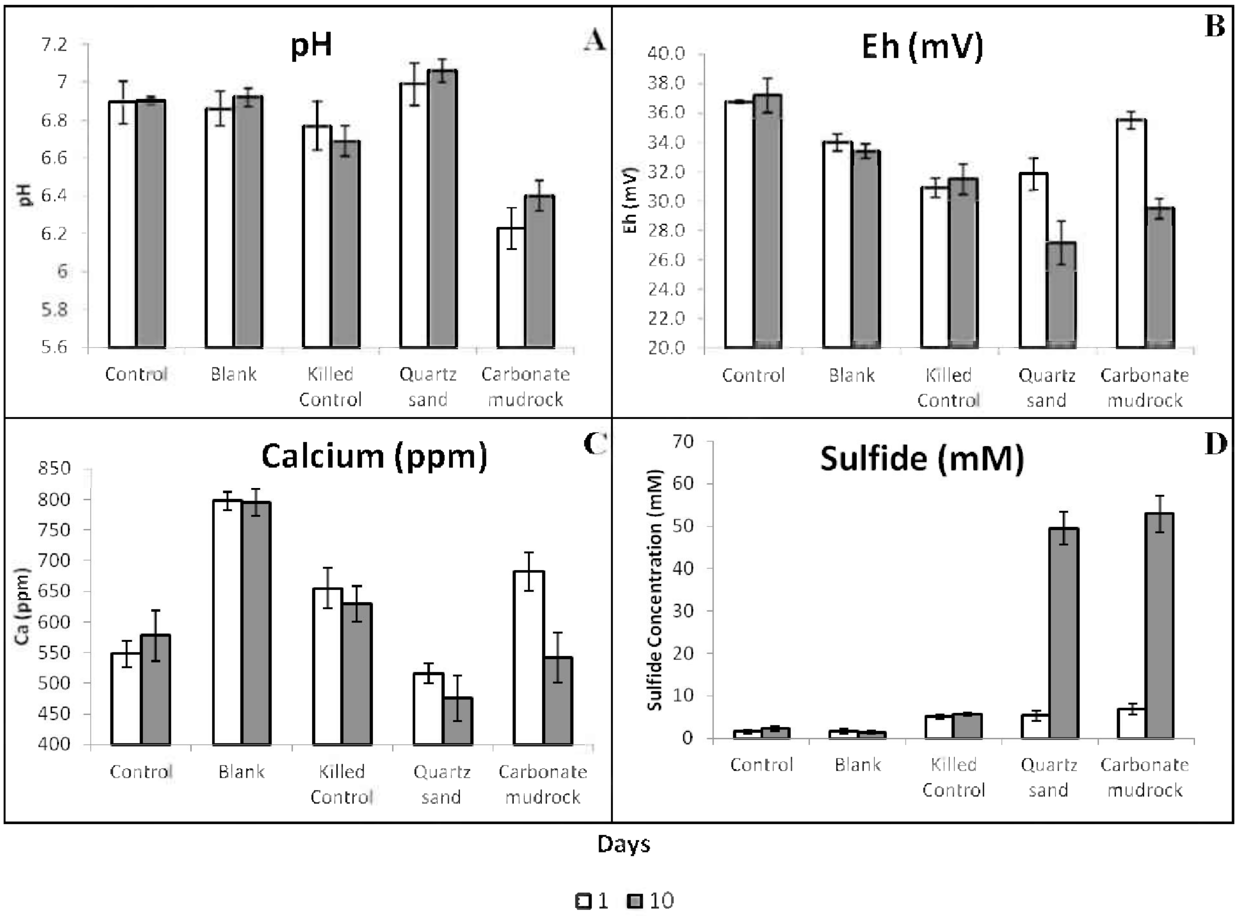

Fig. 4. Changes in (A) pH, (B) Eh in mV, (C) sulfide in mM, and (D) Ca in ppm concentration, from day-1 (white bars) to day-10 (shaded bars) in batch reactors run exposed to 14.7 psi pCO_2. 'Control' reactors had only the artificial seawater and quartz sand grains, but no bacteria; 'Blank' reactors contained only artificial seawater; and 'Killed Control' had bacteria, quartz sand and artificial seawater, but were autoclaved at 121°C after addition of all these components. Error bars indicate standard deviation from triplicate readings.

The calculated starting Ca concentration of 820 ppm in case of the inoculated leachant without the inoculation mix, and 900 ppm for the enrichment-amended leachant, had a drop in their values ranging from 548 to 800 ppm on day-1 in all reactors tested. The Ca concentration in the 'control' reactor increased from 548 ± 22 on day-1 to 578 ± 41 ppm on day-10, however this was well within the standard deviation exhibited within each triplicate set of experiments (Fig. 4C). The concentration in the 'blank' reactors remained unchanged at ~800 ppm. While the 'killed control' reactors decreased from 655 ± 33 to 629 ± 29 ppm, the standard deviation was high and caused the changes to be insignificant. The day-1 Ca concentration in the blank reactors was on an average 250 ppm higher than the quartz 'control' reactors. This indicates that the quartz sand substrate, the only material additionally included in the 'control' reactor that is absent in the 'blank' reactor, may have served as a possible nucleation site for the adsorption of calcium ions or precipitation of Ca-bearing minerals. The Ca values dropped significantly in the inoculated carbonate mudrock reactors as well, with a concentration of 682 ± 31 ppm on day-1 to a final concentration of 542 ± 40 ppm on day-10. The corresponding changes in the quartz sand reactors though decreased from 516 on day-1 to 476 ppm on day-10, although the standard deviation values for day-10 triplicate experiments was larger than any observed trend at ± 57 ppm.

The 'control' and 'blank' reactor results for Mg did not display any change within statistical variability, with an average day-1 and day-10 with values of 1291 ± 15 and 1281 ± 40 ppm, for the 'control', and 1324 ± 5 and 1330 ± 82 ppm for the 'blank' reactor, respectively. The 'killed control' reactor dropped 40 ppm from a day-1 Mg value of 1320 ppm. While the carbonate mudrock experiment displayed an increase from ~1300 to ~1350 ppm, the quartz sand reactors remained unchanged at 1240 ppm. The Mg concentration in all reactors tested, revealed large standard deviation values (± 38 to ± 82 ppm) on day-10, and thus the changes observed in average values between the 1st and 10th days were not significant.

The starting dissolved sulfide concentration in the leachant is considered to be ~1.5 mM, while the corresponding concentration for the reactors with bacterial enrichment is ~5.0 mM (Table 2). Only minor changes in the sulfide concentrations were seen in the background reactors from day-1 to day-10 (Fig. 4D). An increase in the dissolved sulfide concentration would be expected to occur as sulfate-reduction progresses, thus serving as a positive indicator for the presence of SRB. In addition to the sulfate ions in the seawater leachant solution, the bacterial enrichment media used for inoculation would have additionally contributed to the total concentration of both sulfate and sulfide ions in the solution. The 'control', 'blank', and 'killed control' reactors revealed respective changes of only 1.5 ± 0.5 to 2.3 ± 0.7 mM, 1.6 ± 0.6 to 1.3 ± 0.4 mM, and 5.1 ± 0.5 to 5.6 ± 0.3 mM. All the changes in the sulfide concentration in these three reactors were within the standard deviation limits and the percentage analytical error (1.6% with a 12.5 mM standard, i.e., 0.2 mM). In contrast, the reactors containing bacterial cultures displayed a large increased in sulfide concentration during the 10 day experimental runs, positively indicating SRB activity. The carbonate mudrock- and quartz sand- containing reactors showed an average increase from 6.8 ± 1.4 mM to 52.9 ± 4.3 mM, and 5.3 ± 1.1 mM to 49.5 ± 3.9 mM, respectively from day-1 to 10.

2.5.2. Batch Reactors With 20.0 psi pCO_2

The pH in the 20.0 psi pCO_2 control reactors with no bacterial inoculum drop from the starting leachant pH of ~8.0 to 5.2 at day-1 and remained at that value through the remaining 10 day experiments (Fig. 5A). During this time period, the carbonate mudrock- and the quartz sand reactors experienced an average pH increase of only 0.07 units relative to their day-1 values of ~6.2 and ~5.5. These increases are only slightly larger than the accuracy range of the pH probe (± 0.03). The standard deviation of up to ± 0.08 units for the triplicate batch reactor experiments indicates that the variability between samples is larger than the observed changes over time. Redox conditions in the control reactors also remained unchanged, with values remaining at +117 mV (Fig. 5B), though the pre-CO_2 injection redox value of the leachant was -40 mV. Carbonate mudrock reactors displayed only a minor increase from +91 mV on day-1 to +96 mV on day-10. Quartz sand reactors also exhibited little change, increasing from +100 mV to +103 mV in 10 days.

As noted in the 14.7 psi reactors, the Ca concentration in the 20 psi reactors also decreased from the starting leachant value of 900 ppm to 713 ppm on day-1 in the control reactors. The average Ca concentration increased slightly in the control, 713 to 731 ppm, and quartz sand reactors, 594 to 610 ppm, while a decrease was observed in the carbonate mudrock reactors, 682 to 642 ppm (Fig. 5C). The changes in Ca values were insignificant because of the large standard deviation (as high as ± 38 ppm). It is also important to note that the day-1 Ca value in the inoculated quartz sand reactors was significantly lower than in the control reactors. The presence of bacteria or other organic and inorganic components added as part of the inoculum in the quartz sand reactor tests could have bound the Ca ions available in the solution, leading to decreased values initially.

The Mg concentration in the 20 psi pCO_2 reactors had high standard deviation values, ~40 to 125 ppm, similar to the 14.7 psi pCO_2 reactors. There was an increase in the Mg value from the theoretical leachant value of 1584 ppm to a measured day-1 value of 1785 ppm in the control reactor. Reactors with bacterial enrichment also experienced such an increase between test initiation and day-1 values though large standard deviation values rendered the changes insignificant. For example, the quartz sand containing reactors increased from 1796 ± 62 to 1835 ± 85 ppm. The average Mg concentration in the carbonate mudrock reactors remained steady at ~1750 ppm, though the standard deviation at day-10 was ± 125 ppm.

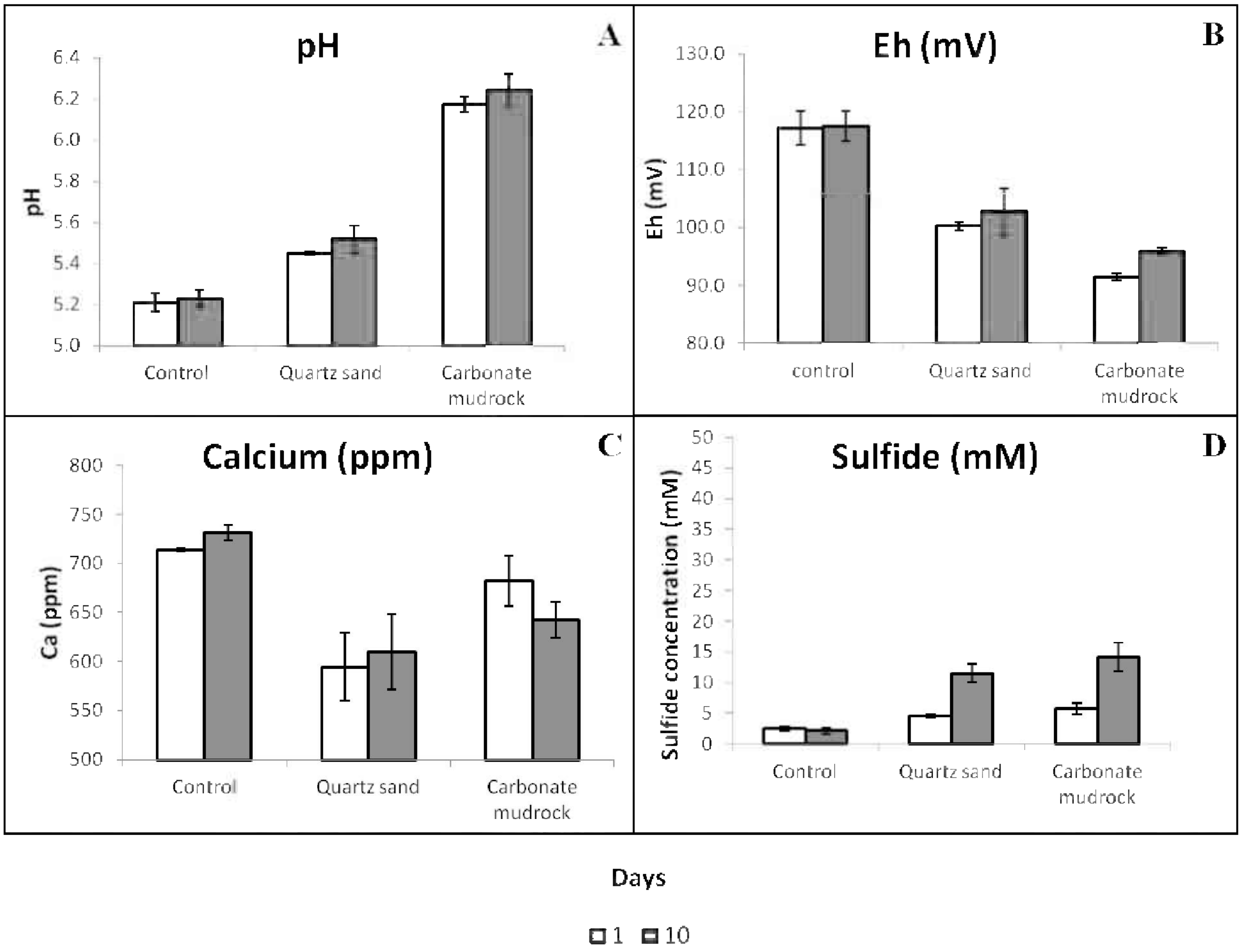

Fig. 5. Changes in (A) pH, (B) Eh in mV, (C) sulfide in mM, and (D) Ca in ppm concentration, from day-1 (white bars) to day-10 (shaded bars) in batch reactors run at 20 psi pCO_2. Control reactors were run with artificial seawater and quartz sand with no bacterial culture amended. Error bars indicate standard deviation obtained from triplicate readings.

The sulfide concentration increased in both the quartz sand and carbonate substrate reactors over time, however, the increase was less than that observed previously in the 14.7 psi reactors (Fig. 5D). For example, in the carbonate mudrock reactors, an average increase in sulfide concentration from ~6 mM on day-1 to ~14 mM on day-10 was observed. All changes were significant with the analytical error being ± 0.2 mM. Carbonate mineral production was not observed in the quartz sand reactors at the end of the reaction period (day-10) and even after extending some of the experiments to 60 days. The cementing of quartz grains resulting from either mineral precipitation or binding by EPS material that was observed in the previously discussed 14.7 psi pCO_2 reactors was not observed in these higher 20 psi pCO_2 reactors.

2.5.3. Electron Donor Batch Reactors Tested at 14.7 psi pCO_2

The control and lactate-fed reactors behaved in a similar manner as the 'control' and quartz sand reactors, as described in Section 3.5.1. The pH values remained steady around ~6.9 in the control reactors (Table 3). Generally, the pH increased in all the reactors with the highest average increase of 0.11 units seen in both formate- and hydrogen-fed reactors. All the pH values in reactors on day-1 had a high standard deviation, as much as ± 0.13 units in the formate-fed reactors. Although the instrumental accuracy was ± 0.03 units, the standard deviation between the triplicate analyses exceeded the observed average change with time, thus these changes cannot be treated as significant. Acetate reactors displayed only a minor decrease in their Eh values (+38 to +37 mV). Formate and lactate reactors each exhibited a drop from +30 to +26 mV and +32 to +27 mV, respectively, while the hydrogen reactors decreased from +39 to +36 mV.

The theoretical starting leachant Ca concentration of 900 ppm before CO_2 injection dropped to 549 ppm in the control reactor on day-1. The corresponding starting leachant concentration of 820 ppm in reactors with bacterial enrichment changed to values in the range of 476 to 868 ppm by day-1 (Table 3). The decrease in Ca concentration was largest in the hydrogen-fed reactors with a 171 ppm decrease from day-1 to final reaction time. The control reactors exhibited only a minor increase in the Ca concentration, from 549 to 578 ppm, but this change was within statistical variability observed between triplicate sets of experiments (maximum of 42 ppm). The ICP-OES instrumental accuracy was ± 71 ppm for Ca. Formate-, acetate-, hydrogen- and lactate-containing reactors all exhibited only minor decreases in Ca concentration. Formate-fed reactors decreased from 798 ±11 to 751 ± 21 ppm, lactate from 516 ± 17 to 476 ± 30 ppm, and acetate decreased from 894 ± 33 to 868 ± 67 ppm. On the other hand, the reactors that were supplied with hydrogen displayed a statistically significant drop in their Ca values, decreasing from 734 ± 28 ppm on day-1 to 564 ± 46 ppm on day-10. The Mg concentration in all reactors showed only minor and statistically insignificant decreases, with the highest drop of 13 ppm from a day-1 value of 1362 ppm seen in the acetate reactors.

Large and statistically significant increases in sulfide production were observed in all reactors that were inoculated with bacteria, with the smallest increase of 2.9 to 39.0 mM observed in acetate-fed reactors, and the highest increase of 4.1 to 56.7 mM observed in hydrogen-fed reactors. All reactors with formate, lactate, or hydrogen as electron donors produced carbonate minerals during the 10 day reactions. Reactors with acetate as the electron donor and the control reactors did not show any carbonate mineral production.

Table 3. Initial (day-1) and final (day-10) values of pH, Eh (mV), sulfide (mM) and Ca (ppm) concentration in batch reactors at 14.7 psi pCO_2 and fed with different electron donors including formate, lactate, acetate and hydrogen. Values shown are averages and standard deviation from triplicate readings. Starting leachant values in the artificial seawater leachant, control reactors, and reactors with bacterial inoculation are in Table 2.

	pH		Eh (mV)		Calcium (ppm)		Sulfide (mM)		Carbonate mineral formation
	Day-1	Day-10	Day-1	Day-10	Day-1	Day-10	Day-1	Day-10	
Control	6.91 (±0.12)	6.90 (±0.02)	+36.8 (±0.1)	+37.2 (±1.1)	549 (±13)	578 (±42)	1.6 (±0.4)	2.3 (±0.5)	NO
Formate	7.03 (±0.13)	7.15 (±0.06)	+30.3 (±3.9)	+25.7 (±0.7)	798 (±11)	751 (±21)	4.5 (±0.1)	46.9 (±0.3)	YES
Lactate	6.99 (±0.12)	7.06 (±0.05)	+31.8 (±1.1)	+27.2 (±1.2)	516 (±17)	476 (±30)	5.3 (±1.1)	49.5 (±3.5)	YES
Acetate	6.84 (±0.10)	6.76 (±0.07)	+37.7 (±4.8)	+36.9 (±3.1)	894 (±33)	868 (±67)	2.9 (±0.1)	38.9 (±0.6)	NO
Hydrogen	6.76 (±0.12)	6.88 (±0.02)	+39.4 (±5.2)	+35.9 (±3.4)	734 (±28)	564 (±46)	4.1 (±0.1)	56.7 (±0.3)	YES

2.6. Carbonate Mineral Phases and Their Composition

The quartz sand used as substrate were chosen as the focal point to examine for secondary carbonate mineral growth based as this substrate was made carbonate-free before testing with an acid wash. The experiments conducted with the 0.0059, 0.018 and 14.7 psi pCO_2 reactors all produced carbonate minerals, as identified by their effervescence when viewing under a microscope and immersing samples in a 10% HCl solution. The carbonate phases were mostly attached to the quartz grains and exhibited varied morphologies when examined by SEM analysis (Figs. 6A-E). A twinned hexagonal prismatic crystal was observed in the 0.0059 psi reactors (Fig. 6A) while dumbbell and rhombohedral shaped grains were found attached on the surface of quartz sand grains in the 0.018 psi reactors. Carbonate minerals found on the surface of quartz sand grains in the 14.7 psi reactors were mostly blocky and appeared to be fused with each other (Fig. 6D). Similar morphologies were observed in the carbonate minerals found in reactors with lactate, formate and hydrogen, with mixed morphology clusters of rhombohedral and dumbbell shaped crystals attached to the surfaces of quartz grains. Examination of ~25 precipitates through SEM-EDS analysis indicated low-Mg concentrations that ranged from 0.9 to 3.5 atomic percent (Fig. 6E). The low-Mg values and the commonly occurring rhombohedral crystal form suggest that the minerals are calcite. The 20 psi reactors did not show any carbonate mineral effervescence through HCl addition, and hence were not analyzed with the SEM. The carbonate mineral precipitates on the surface of quartz grains also appeared to be loosely bonded to each other and to the quartz grains by the EPS produced by the bacteria. Large amounts of EPS were not observed under SEM, probably due to its instability under the high vacuum conditions of SEM. However, occasional remains of fibrous, EPS-like material were identified in the 14.7 psi reactors (Fig. 6F).

2.7. Carbon Isotopic Signature of the Precipitated Carbonate Minerals

Reactor vessel experiments have several potential sources of carbon that can become incorporated into carbonate minerals. These include the organic carbon sources, CO_2 gas, and the relatively small amount of aqueous carbonate phases such as HCO_3^- that are dissolved in the artificial seawater. In order to evaluate the potential source(s) of precipitated carbon in the reactors, experiments were conducted using an isotopically labeled 99.9% $^{13}CO_2$ gas phase. The reactors for the stable isotope tests were run in an identical manner as the 14.7 psi pCO_2 headspace quartz substrate batch reactors described in the previous section except for the CO_2 source. Carbonate minerals were analyzed for $\delta^{13}C$ content using both a Thermo FinneganTM Delta Plus mass spectrometer following phosphoric acid decrepitation and a Thermo FinneganTM Delta Plus XL with an online automated Carlo-Erba 1500 elemental analyzer that measures the 'total carbon'. Data obtained from the isotope analyses were reported relative to the Vienna PeeDee Belemnite (VPDB) standard. Additional details on the carbon isotope analyses can be in Section II-4.4, "Carbon Isotope Analysis in Batch Reactor Experiments".

Reactors that were supplied with formate, hydrogen or lactate produced carbonate minerals that had a high $^{13}CO_2$ isotopic signature (Table 4). The average $\delta^{13}C$ in carbonate minerals from triplicate reactors obtained from experiments with the electron donors was approximately +47,000 ‰. The standard deviation was high in all three experiments with the different electron donors, with the highest deviation seen in the case of lactate (42,244 ±13,749 ‰). Acetate-fed reactors and the control reactors did not produce any carbonate minerals and correspondingly no $^{13}CO_2$ could be detected in the analysis of these samples. The percentage carbon from the carbonate minerals produced in the reactors (% ^{13}C in Table 4) was calculated by using the method described by Mitchell et al. (2010). On average, ~53% of the carbon in the carbonate minerals was derived from the $^{13}CO_2$ gas phase. The carbonate minerals in the lactate-fed reactors had the lowest percentage ^{13}C among the three electron donors, with a value of 47.6 ± 15.1%, whereas both formate-fed and hydrogen-fed reactors had 54.9 ± 6.7% and 55.4 ± 15.1% ^{13}C, respectively. The isotopic composition ($\delta^{13}C$) of the electron donors, acetate and formate, supplied to the reactors were -24.62 and -32.55‰, respectively. The $NaHCO_3$ used in preparing the artificial seawater provided the majority of the bicarbonate ions in the leachant and thus is a potential source of carbon in any carbonate minerals that may be produced. The $NaHCO_3$, also possessed a low $\delta^{13}C$ value (-6.28‰) and thus is not a significant source of ^{13}C in the experiments. Carbonate mudrock substrate represented a naturally precipitated carbonate material and the $\delta^{13}C$ for this sample was -0.75‰.

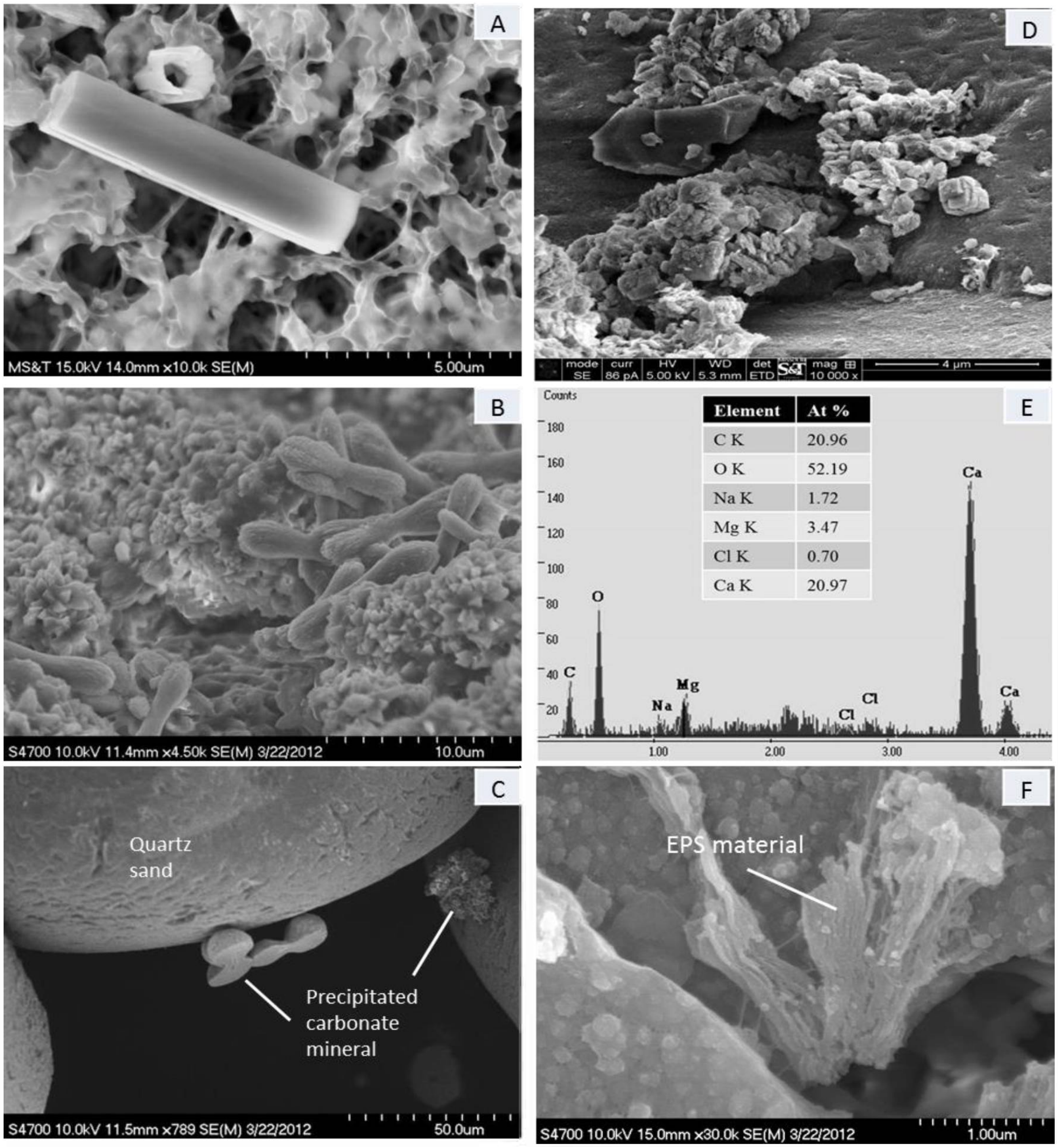

Element	At %
C K	20.96
O K	52.19
Na K	1.72
Mg K	3.47
Cl K	0.70
Ca K	20.97

Fig. 6. Scanning electron microscopy-energy dispersive spectroscopy (SEM-EDS) analysis showing crystal formed in reactors. A) Twinned hexagonal crystal of calcium carbonate on a cellulose-acetate filter paper background obtained from 0.0059 psi pCO_2 reactor. B) Dumbbell shaped cluster of rhombohedral carbonate crystals from 0.018 psi reactors. C) Dumbbell shaped carbonates that appear to be halved (center of image) and clumped cauliflower assembly of carbonates (right center) from 0.018 psi reactor. D) Agglomeration of rhombohedral carbonate crystals attached to quartz grain from 14.7 psi reactors. E) Semi-quantitative EDS elemental composition of the hexagonal crystal in Fig. 6A. Similar spectra were observed for other carbonate minerals in the 0.018 and 14.7 psi reactors. F) Possible EPS material from 14.7 psi reactor. EDS analysis indicates the presence of carbon, oxygen, and trace amounts of phosphorus.

Table 4. Results of isotopic analysis of carbonate sediments in reactors supplied with the different electron donors and labeled $^{13}CO_2$ gas. Values shown are average and standard deviation from three separate triplicate reactors. Control reactors and reactors with acetate did not produce carbonate minerals, thus no isotope signature was detected during analysis. ^{T} % ^{13}C from the carbonates was calculated using the equation given by Mitchell et al. (2010): $[(\delta^{13}C/1000) \times 1.1] + 1.1$.

Electron Donor	$\delta^{13}C$		% $^{13}C^T$	
	Average	**Std. Dev**	**Average**	**Std. Dev**
Formate	+ 48,896	6,094	54.9	6.7
Hydrogen	+ 49,402	13,717	55.4	15.1
Lactate	+ 42,244	13,749	47.6	15.1

3. DISCUSSION

3.1. Bacterial Cultivation and Diversity

The microbial population analyzed by using the barcoded pyrosequencing of the 16S rRNA gene revealed that the diversity and species richness in the Lake Estancia sediments was low (Table 1). The sediments did not possess detectable amounts of Desulfobacteraceae nor Desulfohalobiaceae, two taxa that contain several members of SRB. Oxalobacteraceae includes several aerobic, anaerobic and nitrogen fixers but no known SRB (Garrity et al., 2005), and was the dominant bacterial family in the sediments, comprising ~57% of the taxa. The enrichments developed from the lake sediments exhibited a low diversity because these samples selectively encouraged the growth of only the SRBs. The family Desulfobacteraceae was the dominant member with ~87% of the entire bacterial population in the enrichments (Table 1). Interestingly, Desulfobacteraceae was absent in the sediments from which the enrichments were produced. This family might have been too low to be detected by gene analysis in the sediments, but when subjected to favorable conditions, the SRB population was able to grow and increase substantially with each sub-culturing. Oxalobacteraceae had drastic reduction to 0.20% in their percentage after the enrichment for SRB. Other bacterial taxa were also identified in smaller percentages in the enrichment (e.g., Halanaerobiaceae, Halobacteroidaceae and Enterobacteriaceae). The primary information obtained from the microbial diversity studies is that the bacterial culture used in the reactor experiments was a mixed population, with Desulfobacteraceae being the dominant group. Though only bacterial diversity was analyzed through these studies, archaea members, such as methanogens, might have been present in these hypersaline sediments (Zhilina, 1986).

At least five to six generations of sub-cultures were cultivated from the lake sediments with the enrichment media before being tested in the reactors. It would have been ideal to test a pure bacterial culture to precisely relate the bacteria with the carbonate mineral precipitation activity and extend the process for possible GCS. However, when considering application of these or similar bacteria on an actual subsurface sequestration site, it should be noted that a plethora of microbial population would already be present in such environments (Krumholz, 2000; Ménez et al., 2007). Therefore, maintaining a pure culture would be extremely difficult in a fairly open system, such as a subsurface aquifer.

3.2. Microbial Influence on the Rate Of Carbonate Mineral Precipitation

The production of secondary carbonate minerals was successfully achieved in reactors that contained active SRB population and within a 14.7 psi pCO_2 atmosphere. In the 0.0059 psi pCO_2 reactors, the pH values observed were slightly higher in the tests with carbonate mudrock than those with quartz sand, but the pattern tended to converge during the later stages of the reaction (Fig. 3A). The initial drop followed by the rise in pH with lactate as the electron donor, describes to a certain extent the effect of the activity of SRB as shown by Morse and Mackenzie (1990), and Gallagher et al. (2012). The presence or absence of carbonate did not influence this initial decrease and latter increase in pH. Also, this trend was not observed in the 0.018 psi reactors, where the pH over the 31 day measurements showed a direct increase (Fig. 3D). The higher pCO_2 appeared to have modified the previously observed, SRB-influenced pH trend under atmospheric conditions. Therefore, it is important to consider all of the testing conditions when comparing any previous SRB-related carbonate precipitation studies with the current experiments.

Carbonate mineral precipitation was observed in the 14.7 psi reactors within a 10 day period, while it took a longer time for the reactors at 0.018 and 0.0059 psi, requiring at least 31 and 43 days, respectively. Neither the 'control' nor the 'killed control' reactors revealed any calcium carbonate precipitation, indicating that live SRB activity was required in inducing mineral precipitation. The actively metabolizing bacteria induced a quicker, albeit less pronounced pH change at 14.7 psi (Fig. 4A), when compared to the lower pCO_2 reactors. Previous investigations of carbonate mineral precipitation using a SRB community under different CO_2 concentrations indicated that the mineral formation occurred only in a 20% CO_2 atmosphere, but not under a 5% or 10% atmosphere (Ménez et al., 2007). Though elevated pCO_2 would be expected to inhibit SRB and in turn carbonate mineral precipitation process, such a CO_2 increase only accelerated the chemical changes seen in the reactors tested in our experiments. The availability of excess dissolved CO_2 was quickly converted to carbonate ions due to the pH/alkalinity change induced by bacterial activity. In the current experiments, increased CO_2 concentrations required less time for the precipitation of carbonate minerals. Though alkalinity could not be measured due to the low volume of sample available, an increase in the alkalinity would also be expected as more dissolved CO_2 in the artificial seawater solution is converted to carbonate (CO_3^{2-}) species.

Another contributing factor to the delayed reaction of the continuous gas flow reactors (0.0059 and 0.018 psi reactors) is the presence of oxygen in the media and the headspace in the aquarium tank set-up. Since SRBs are mostly anaerobic with few species exhibiting tolerance to oxygen, the activity of bacteria would have been lowered in the case of continuous gas flow reactors. On the other hand, conditions were made anaerobic in the batch reactors (14.7 and 20 psi), allowing faster growth of the SRBs and producing necessary conditions for favoring carbonate mineral precipitation. This response to oxygen substantiated that SRB community used in the current study were likely tolerant to oxygen, but were more efficient under anoxic conditions. Though the CO_2 concentration was high, anaerobic conditions favored the growth of SRB, leading to the high degree of sulfide production seen in those reactors. The balance between pCO_2 and the presence of oxygen is therefore of vital importance to the functioning of the SRB community in terms of carbonate mineral precipitation.

At 20 psi pCO_2 headspace pressure, the bacterial activity was inhibited due to the acidic conditions induced by the high amounts of CO_2. Though a rise in the sulfide levels was seen in the 20 psi reactors between day-1 and day-10, the increase was not as high as those seen in the 14.7 psi reactors (Fig. 4D). This inhibition either indicates that CO_2 at pressures of 20 psi is toxic to this particular bacterial population or that the pH tolerance of the microorganisms tested was above that observed in the 20 psi reactors, i.e. ~6.2 (Fig. 5A).

Both types of reactors, continuous gas flow and batch mode, displayed varying trends in all the parameters measured. While several changes in pH, Eh and elemental concentrations were significant and valid, few cases exhibited a wide range of fluctuation caused either by the error range of the instrument or the large standard deviation values derived from triplicate measurements. A detailed description of all the changes in the measured parameters is provided in the results section; some of the anomalies are discussed in the following paragraph.

In the continuous gas flow reactors tested, the pCO_2 was maintained at a set level (0.0059 psi or 0.018 psi) throughout the experiment period, whereas the batch reactors were injected just once with the desired pCO_2 (14.7 psi or 20 psi). The starting seawater leachant pH of ~8.0 on dropped to anywhere from 5.2 to 7.9 on day-1 following CO_2 injection in all the reactors. The conversion of gaseous CO_2 to carbonic acid in the leachant solution is responsible for the observed drop in the initial pH values. In the continuous gas flow control reactors, the day-1 Ca and Mg concentration in the artificial seawater were higher than the calculated starting leachant values. For example, in the 0.018 psi control reactors, the starting leachant and day-1 Ca values were 900 and 1009 ± 47 ppm, respectively. This and similar anomalies demand a source for the additional Ca and Mg in the day-1 leachant solutions. The major reason for this difference is the analytical accuracy of the ICP-OES instrument for Ca and Mg, i.e. ± 71 and ± 88 ppm, respectively. Other probable contributors could be evaporation of the sampled leachant solution before analysis leading to a concentration of the ions, or minor human errors that could have occurred during the 1:100 dilution of the sample with 1% HNO_3.

Another anomaly was observed when comparing the pH values of reactors containing carbonate mudrock and quartz sand as the base material. The CO_2 supplied to these reactors should have been buffered by the carbonate material, and thus, the day-1 pH should be higher than that seen in the quartz sand reactors. All reactors followed this trend except for the 14.7 psi reactors, where quartz sand reactors showed unexpectedly higher day-1 pH values than the carbonate mudrock reactors, with respective values of ~7.0 and ~6.2 (Fig. 4A).

3.3. Electron Donors

The type of electron donors utilized by the SRBs plays an important role in creating optimum conditions for carbonate mineral precipitation. For example, through laboratory and modeling studies, Gallagher et al. (2012) tested a known, pure strain of SRB (*Desulfovibrio* sp.) under atmospheric conditions, and found that pH and alkalinity changes favoring mineral precipitation varied with the type of electron donor supplied. Accordingly, electron donors, such as hydrogen, formate and acetate caused an increase in the pH, whereas lactate, glycolate and ethanol caused a decrease in pH. In our experiments, we found that hydrogen, formate and lactate led to an increase in pH under 14.7 psi pCO_2, whereas, acetate-fed reactors developed a slight decrease in the pH (average value of 6.84 to 6.76) overtime (Table 3). Carbonate mineralization occurred only in reactors that experienced an average increase in pH. Comparing our results with those of Gallagher et al. (2012), it appears that the type of electron donor consumed and the related changes in the chemistry of the surrounding environment probably depend on the SRB community tested. While they tested a pure SRB strain of genus *Desulfovibrio*, we tested a whole community that included other bacteria, but was dominated by the SRB family, Desulfobacteraceae. Furthermore, the experiments conducted by Gallagher et al. (2012) were under atmospheric pCO_2, while our experiment investigated the behavior of SRBs at several different elevated pCO_2 contents (14.7 and 20 psi CO_2). Therefore, the optimal carbon source/electron donor requirement in terms of carbonate mineral precipitation appears to vary with external environmental conditions and thus requires further investigation.

It is currently unknown as to why the use of acetate did not lead to a pH increase and carbonate mineral precipitation at 14.7 psi pCO_2, while previous studies have shown SRB utilization of acetate to induce a pH rise (Braissant et al., 2007; Gallagher et al., 2012). Perhaps other microorganisms in the culture were competing with the SRBs for acetate as an energy source (Table 1). The enrichments that were used in the reactor tests contained almost 87% of Desulfobactereaceae, in addition to other bacteria, such as members of the candidate class, KB1 (whose metabolic role has not been characterized) and families, Halanaerobiaceae and Halobacteroidaceae. The sulfide production noted in acetate-fed reactors was also slightly lower on day-10 (38.9 mM), when compared to other energy sources tested (e.g., hydrogen- 56.8 mM, formate- 46.9 mM), indicating that sulfate-reduction was less active when acetate was fed as the electron donor. The electron donor utilization by SRBs is highly variable from species and even strains with the same species. Members of the family, Desulfobactereaceae have been shown to exhibit varied utilization of acetate and other electron donors (Widdel, 1988; Garrity et al., 2005; Gallagher et al., 2012).

Hydrogen gas is an important electron donor for bacterial communities and is a component that is locally abundant in basaltic or metamorphic rocks (Nealson et al., 2005). Several subsurface bacterial communities also utilize hydrogen as their primary electron donor (Reith, 2011). Dissolved hydrogen concentrations as low as 60 µM in basaltic aquifers have been found to support a variety of lithoautotrophic and heterotrophic bacteria (Stevens and McKinley, 1995). The dissolved hydrogen concentration used in our current study was 78 µM (in the 14.7 psi pCO_2 reactors), thus the microbial community we used should be able to metabolize efficiently by using hydrogen as the energy source. Bacteria that use hydrogen as an electron donor also must consume CO_2 or another organic substrate for their carbon requirement (Van Houten et al., 1994). Most SRB that are able to use hydrogen are also able to make use of formate as the electron donor (Widdel, 1988). While lactate and formate also served as good electron sources for the bacterial community tested here, injection of either or both of these components would add to the operation cost of a CO_2 sequestration program. Other options would be to include alternate, cheaper organic sources that could be utilized efficiently by the bacteria. Sulfate reducers have been shown to be able to efficiently utilize organic electron donors, such as molasses, hydrocarbons, and sewage wastes (Liamleam and Annachhatre, 2007). Future research has to be directed towards expanding the list of SRB population that could make use of these cheaper organic sources for SRB-related commercial applications. Additionally, other subsurface materials should be investigated to identify rock sources containing organic compounds that could support microorganisms capable of enhancing CO_2 mineralization.

3.4. Carbonate Mineral Precipitation Mechanism

The lake sediments contained quartz, calcite and dolomite through XRD analysis (Fig. 2). The source of the carbonate minerals could be due to (i) direct or indirect microbial-influenced precipitation, (ii) deposition of detrital particles eroded from surrounding regions, (iii) precipitation following evaporative concentration of dissolved ions, or (iv) a combination of two or more of these factors. In the current reactor experiments with SRB enriched from Lake Estancia sediments, low-Mg calcite was the only carbonate mineral that was identified. If the SRB community is considered to be directly involved in carbonate mineral precipitation in the reactors, then it is likely that the bacterial cell structure played a direct role in initiating and propagating the precipitation of the mineral (Bosak and Newman, 2003). This involvement of bacterial cells also substantiates the point that the pH increase alone does not solely influence precipitation of carbonate minerals, but rather a combination of the factors (pH, alkalinity, availability of organic matrix template, etc.).

Previous studies have shown the direct role of bacterial cells in precipitation by initiating nucleation on membranes or cell walls (Bosak and Newman, 2003; Van Lith et al., 2003). Our findings reported the presence of dumbbell shaped carbonate crystal morphology, which has been previously attributed to SRB activity (Warthmann et al., 2000; Van Lith et al., 2003). The growth of dumbbell shaped dolomite crystals appears to occur at the polar ends of bacterial cells (Fig. 6B). Once the nucleation of the crystals began, the dumbbell shape grows in size (Fig. 6C), and eventually developed into a cauliflower shaped crystals. Thus, Lake Estancia-SRB may have used their cell walls as a site for calcium carbonate mineral build up. However, crediting the bacterial activity as the sole reason for producing dumbbell shaped calcite should be treated with caution. Similar crystal morphologies were also produced in the laboratory without any living material, but through addition of varying concentrations of organic material and Mg in the test solution (Meldrum and Hyde, 2001). The study reported Mg percentages in precipitated calcite as high as 22%, and the presence of organic additives, such as malic acid and citric acid, stabilized the calcite crystal structure. The precipitated secondary calcite in the present experiments had a low atomic percentage of Mg (0.9 to 3.5%), indicating that Mg was incorporated into those structures.

Exopolymers produced by the bacteria positively influence the mechanism of carbonate mineral precipitation (Braissant el al., 2007). It has been shown that EPS could serve as nucleation sites for carbonate mineral precipitation to occur (Dupraz and Visscher, 2005; Visscher and Stolz, 2005). In the reactors tested here, slimy material was seen loosely associated with the bottom sediments and appeared to partially bind the sediment grains together. The dumbbell, rhombohedral and other carbonate crystals that were observed through SEM appeared to be precipitated on a substrate and the mineral growth most probably supported by the EPS (Figs. 6B and D).

3.5. Sources of Carbon in the Precipitated Carbonate Minerals

Carbon is present naturally as two stable isotopic forms: ^{12}C (98.93%) and ^{13}C (1.07. In the atmosphere, CO_2 is present at a concentration of 400 ppm (Monastersky, 2013). The δ^{13}C value (ratio of ^{13}C to ^{12}C, relative to a standard, expressed in per mil, ‰), of earth's atmosphere is currently around -8.0 ‰. The influence of bacteria or other living material (e.g., plants) affects the isotopic fractionation of the carbon. In the case of SRB, the fractionation was shown to depend on several factors, including enzymatic pathways used to consume the organic substrate or CO_2, and the type and growth rate of the bacterial strain (Londry and Des Marais, 2003). In some of the SRB strains tested, the carbon incorporated as biomass was isotopically heavier than the available carbon sources by 8 to 9 ‰.The isotope experiments conducted in the current study focused on evaluating the transfer of $^{13}CO_2$ supplied initially as a gaseous phase through the bacterial reactor system supplied with different electron donors.

Carbonate minerals precipitated in the reactors with hydrogen, lactate or formate supplemented with labeled $^{13}CO_2$ exhibited similar, and very high δ^{13}C values (Table 4). Also, the average percentage ^{13}C in the carbonate material was similar in all the reactors that had carbonate mineralization occurring. Acetate-fed reactors experienced a pH decrease and did not produce any carbonate minerals. The $\delta^{13}C$ values were highly variable even within the triplicate reactors of the entire electron donors tested. For example, reactors fed with lactate had $\delta^{13}C$ ranging from ~29,000 ‰ to ~60,000 ‰. The large standard deviation values could have occurred possibly due to (i) differential usage of the electron donors by the bacteria, (ii) the density of microbial culture within each of the triplicate reactors, (iii) the amount of carbonate minerals precipitated from the electron donor *vs.* those from the original CO_2 atmosphere, and (iv) the weight of the carbonate minerals analyzed during each sample run. In the isotopic measurements, it was observed that as the weight of the analyzed sediment sample increased, the $\delta^{13}C$ values obtained were lower. For example, in the case of the triplicate reactors with formate as the electron donor, the starting weight of each sample was 0.413, 1.022 and 10.204 mg, respectively. The corresponding $\delta^{13}C$ values showed decreasing values of 53,806, 50,806 and 42,075 ‰, respectively. Also important to note that the starting weight of the analyzed material did not entirely comprise of carbonate mineral, but also included the quartz sand base substrate. Though this trend was not consistent with all reactors and their respective weights, the difference in values observed relative to the weight of the material measured could account for the high standard variation.

In the hydrogen-fed reactors, the source of carbon in the carbonate minerals would have been from the $^{13}CO_2$ atmosphere or the bicarbonate ions supplied as $NaHCO_3$ in the artificial seawater as no other organic carbon material was provided. On the other hand, the reactors supplied with formate and lactate as the organic electron donors would have received the carbon from the organic material, the $^{13}CO_2$, the bicarbonate ion from the artificial seawater or from all three sources. As described in the methodology section, analysis of the sediments by using the Kiel device, in which only the carbonate minerals were analyzed, indicated that the contribution of ^{13}C in the bacterial cells was minimal (< 10%). Therefore, the possible sinks for more than 90% of the carbon in the headspace would then be the carbonate minerals, the CO_2 released as a final product of bacterial organic matter degradation, or one of the three ion species in the leachant, i.e., carbonic acid, bicarbonate or carbonate species.

It can be discerned from the $\delta^{13}C$ and $\%^{13}C$ values that almost half of the carbon in the carbonate minerals were derived from the $^{13}CO_2$ spiked gas supplied in headspace of the test vessels (Table 4). The absence of carbonate mineral precipitation in the 'control' reactors without inoculation, or 'killed control' reactors at 14.7 psi pCO_2, without live bacterial cells, is direct evidence that mineralization took place through the activity of bacterial community in the reactors inoculated with the bacterial communities (with the exception of the acetate experiments which did not produce carbonate minerals). It is expected that the pH and alkalinity increases induced by the SRB community caused an increase in the absorption of carbonate ions in the solution from the supplied labeled $^{13}CO_2$ gaseous atmosphere (Mitchell et al., 2010). An increase or decrease in the supplied sulfate and electron donor concentration would potentially alter the rate of sulfate reduction, in turn affecting the pH changes that plays a dominant role in proportioning the carbonate species. Mitchell et al. (2010) observed that when using ureolytic bacteria at higher

CO_2 levels, varying the pCO_2 and the concentration of urea affected the rate of calcite precipitation and the isotopic signature of the calcite minerals that were precipitated. The pCO_2 of the gas, the type of electron donor, and the rate of sulfate-reduction are all factors that can affect the equilibration between the carbonate ion species in the gaseous, liquid and solid phases.

3.6. Application of Bacterial Activity in Geological Sequestration of CO_2

Employing SRB enriched from hypersaline environments for investigating mineral sequestration of CO_2, as in the current experiments, is advantageous; the interpretation of chemical changes would be more relevant to compare the functioning and limitations of the community in a high salinity environment, typical of a subsurface CO_2 injection site. Indigenous SRB population that would already be adapted to such extreme conditions, if stimulated properly by application of suitable electron donors and sulfate sources, would be one of the ideal bacterial communities to enhance the mineral sequestration of CO_2. Therefore, both indigenous and artificially amended population can be used to achieve the goal. However, several issues need to be addressed in terms of microbial survival and viability, including the conditions already existing in the subsurface and those induced during and after CO_2 injection.

The acidic conditions induced by CO_2 injection is a major concern for any microbially enhanced carbonate mineral sequestration in the subsurface. High pCO_2 also alters membrane fluidity and affects a range of intra-cellular functions in the bacterial cell, leading to death or lowered metabolic rate (Oulé et al., 2006; Wu et al., 2010). Even in our experiments, it was determined that the activity of the SRB-dominated community was lowered or restricted at <20 psi pCO_2. In general, the bacteria's ability to shield themselves from the low pH or CO_2 toxicity through the production of EPS and biofilm could ensure better survival and enhanced activity (Santillan et al., 2013). In a previous study, increased biofilm production was achieved when the bacteria was exposed to high pCO_2 (Mitchell et al., 2009).

In addition to the effects of high CO_2, the pressure has important roles in the metabolic activity of SRB, or any surface bacteria exposed to subsurface conditions. Since these parameters were not investigated in the current experiments, the effects could only be speculated, as done here briefly. The effect of pressure can be considered in two aspects: pressure due to overlying rocks and the pressure due to injected CO_2. Both these types of pressures may have a negative effect on the bacterial activity. In cases where the sequestration sites are not too deep, the rapid pressure change due to CO_2 injection may be more of a problem to bacterial survivability than lithostatic pressure of the overlying rocks. Most sequestration processes consider pumping CO_2 as a liquid while it transforms to supercritical phase (critical point at 31.1°C and 73 atm.) as it enters the formation (Benson and Cole, 2008). The volume of CO_2 in the supercritical phase is lower, and thereby allowing much larger quantities to be stored in the subsurface. It has been shown that the survival of microorganisms is extremely unlikely when exposed to supercritical CO_2

concentrations (Werner and Hotchkiss, 2006). However, this study helps illustrate the limits of bacterial tolerance to small increases in pCO_2 or the low pH conditions induced by CO_2 addition.

An increased temperature with depth would be another parameter that would hinder bacterial activity. The natural geothermal gradient of the subsurface rock layers and the proximity to a heating source are two big factors that control the temperature of the formation. At shallower depths, where the temperature is not high enough to be inhibitory, the bacteria could metabolize and induce carbonate mineral precipitation. Under room temperature and elevated pCO_2 conditions (20 psi CO_2 headspace), ureolytic bacteria were able to induce carbonate mineral precipitation as well (Mitchell et al., 2010). An increase of temperature from 30°C to 38°C did not induce any notable change in the bacteria's influence on the mineral sequestration capacity (Dupraz et al., 2009b).

A key component to consider in microbially assisted CO_2 sequestration in the subsurface is the mineral composition of the rock units and reactivity with CO_2 and the microorganisms. In the current investigation, we focused on two such materials commonly found in the subsurface: quartz and carbonate minerals. In the subsurface, addition of CO_2 to pure quartz sandstone will have no major effect on the rock units, since the sandstone is generally non-reactive with CO_2 and the carbonic acid that forms as the gas bonds with water molecules (Baines and Worden, 2004). However, many siliciclastic sedimentary rocks are associated with aluminosilicates, oxides and carbonate cements. CO_2 can react with the first two of these phases to induce solid phase carbonate mineral formation, whereas reaction with the carbonate cements will cause dissolution, leading to increased porosity and permeability. Quartz sand has been further shown to provide protection for the bacteria by housing the microorganisms, where the bacteria can effectively attach and synthesize biofilm. The higher surface area available in the quartz substrate for biofilm formation was suggested as a key mechanism that helps shield the bacteria from CO_2 toxicity (Santillan et al., 2013). In our experiments, the quartz sand grains were loosely fused together in all the reactors that produced carbonate minerals. The fused grains were easily broken off with slight application of force.

While the carbonate mudrock sediments were not considered for SEM analysis, the pH changes, Eh conditions, sulfide (only in 14.7 psi reactors), and Ca concentration changes in the carbonate mudrock reactors followed a parallel trend to the quartz sand experiments, indicating that secondary carbonate mineral precipitation was likely to have occurred in the carbonate mudrock reactors as well (Figs. 3, 4, and 5). The presence of calcite has been shown to reduce the stress on bacterial cells by serving as a buffer for the CO_2 gas (Wu et al., 2010), and likely allowed SRBs to accommodate to the stressful conditions. Injection of CO_2 would initially lead to carbonate mineral dissolution from the mudrock, and therefore the porosity and permeability may increase initially. The addition of CO_2 to the 0.018 psi reactors, for example, caused the dissolution of the carbonate mudrock, and a subsequent increase in the Ca and Mg concentrations in the day-1 seawater leachant solution (Fig. 3D). In the subsurface, such increased porosity and permeability could allow movement of the CO_2 further in the rocks that contain calcite cements. The bacterial activity could later precipitate secondary carbonate minerals by using the Ca and Mg ions previously dissolved. The presence or absence of any organic or biological material that is able to adsorb these elements would also influence the concentration of the ions in the subsurface aquifer. Other rock types such as basaltic or metamorphic should be tested to monitor the interaction between the minerals, CO_2 gas and the microorganisms.

In a GCS system the sites near the CO_2 injection well would receive a large influx of injected CO_2. The pCO_2 in this region would be high enough to deactivate or cause cell death and thus, effective SRB activity or associated carbonate mineral precipitation would be unlikely in such proximal locations to the CO_2 injection wells. Additionally, pH would also likely be low due to carbonic acid formation and extensive dehydration may be expected if the injected CO_2 is a dry gas. In a recent analysis of the microbial population in a subsurface GCS study injecting 500 t of CO_2, a significant decrease (~83%) in the bacterial population was observed within two days of CO_2 arrival at 50 m from the injection site (Morozova et al., 2010). However, the microbial population recovered over time, increasing up to 23 and 40%, in one and five months, respectively. In general, as the CO_2 migrates through the subsurface to more distal sites located further away from the injection point, the concentration of CO_2 would eventually become lower and solution pH values would be expected to rise as a function of the acid buffering capacity of the surrounding rock material. In addition to the distal ends of the reservoir, the buoyant CO_2 supercritical and/or gas phase would also rise towards the interface between the upper surface of the reservoir layer and the lower surface of the seal rock (Benson and Cole, 2008). As the CO_2 would be injected at a controlled rate, sufficient time and bacterial activity could cause the carbonate mineral precipitation to seal the top and distal ends, thus minimizing or even preventing the leakage of gas. Furthermore, the biofilm and EPS production by the bacteria, similar to that shown in the current experiments, would help to prevent the leakage of the gas by biologically sealing the top and distal ends of the reservoir. Eventually over time, the CO_2 injected would reach an equilibrium stage, when the bacteria can gradually convert the remaining CO_2 into solid carbonate mineral phases through the chemical changes induced. Our investigations help to demonstrate that the microbial populations accelerate the kinetics of mineral precipitation. It was also observed that the higher the pCO_2, the more rapid the carbonate mineral precipitation was achieved; though up to a certain point until the CO_2 content became too high (between 14.7 to 20 psi pCO_2) for the bacteria to effectively induce mineralization.

Using SRB for GCS is advantageous because, along with CO_2, SO_2 gas from power plants can also be injected, instead of scrubbing the latter. SO_2, in addition to sulfate, could be utilized by SRB as an electron acceptor (Dasu and Sublette, 1989), and thus the amount of SO_2 that needs to be removed from the power plants prior to subsurface injection can be minimized, if not entirely pumped into the subsurface. Most subsurface aquifers also contain sulfate derived from natural rock reservoir that could be used by the bacteria. A potential problem of employing SRB in the subsurface is the production of sulfides due to bacterial activity. These sulfides cause souring of the wells and could be inhibitory to the bacteria at high concentrations, though the inhibition has been shown to be reversible when favorable conditions return (Reis et al., 1992; Van Houten et al., 1994). Sulfides released from the SRB reaction could be sequestered by reaction with the metals in the subsurface rocks to form metal sulfides, especially with iron to form pyrite (FeS_2) as iron oxides are common minerals in most rocks. Artificial supplementation of metals, such as iron, or those naturally present as trace elements in the gas could be used as a viable option to reduce the sulfide levels (Poulton et al., 2004; Wilkin and DiGiulio, 2010). It should be noted that co-injection of SO_2 would cause additional acidity and would hence need to removed or transferred to a different oxidized or reduced form (Knauss et al., 2005).

4. CONCLUSIONS

The SRB-dominated community from Lake Estancia was capable of producing and accelerating carbonate mineralization reactions relative to control tests without microbes being present. Microbial metabolic reaction increased the solution pH and likely provided nucleation sites for mineral formation up to 14.7 psi pCO_2. The majority of the SRB in the enrichments that were able to induce carbonate mineralization belonged to the family, Desulfobactereaceae. The full range of activity of the SRB community in terms of inducing carbonate mineralization was limited due to toxic effects and/or low pH effected by the amount of CO_2 injected (headspace pCO_2 of 20 psi). However, at lower pCO_2 (0.0059 psi to 14.7 psi), mineral sequestration of the gas was successfully achieved. The ability of SRB to synthesize EPS and induce carbonate mineral precipitation could be potentially be used in GCS applications where, in addition to trapping CO_2 in immobile solid phases, the mineral phases could also seal microfractures in overlying trap rocks and seal pores at the distal ends of the reservoir. Hydrogen, lactate and formate served as suitable energy sources for the SRB community. Isotope studies indicated that the carbon precipitated in the carbonate minerals is derived from both the CO_2 gas and the organic electron donor, thus confirming that the pH and probably alkalinity have been favorably modified for carbonate mineral precipitation through bacterial activity. The study provides a good proxy for investigating the activity of SRBs under elevated CO_2 concentrations and their positive or negative influence on CO_2 reservoir characteristics. Observations obtained from this study could be applied to interpret the effect on the indigenous SRB population in the subsurface as well. Future research would have to be geared towards testing the bacteria under higher temperatures and pressures to simulate an actual GCS practice. The ability of SRB and other bacterial groups to induce and accelerate carbonate mineralization under extreme conditions offers an exciting and promising area to study possible naturally occurring processes to enhance GCS, and ensure the long-term storability of the gas in the subsurface.

REFERENCES

Allen, B.D. and Anderson, R.Y., (2000), A continuous, high-resolution record of late Pleistocene climate variability from the Estancia basin, New Mexico. *GSA Bulletin* **112**, 1444-1458.

Allison, P.A. and Briggs, D.E., (1991), *Taphonomy: releasing the data locked in the fossil record*. Plenum Press, New York.

Baines, S.J. and Worden, R.H., (2004), The long-term fate of CO_2 in the subsurface: natural analogues for CO_2 storage. *Geological Society, London, Special Publications* **233**, 59-85.

Baumgartner, L.K., Reid, R.P., Dupraz, C., Decho, A.W., Buckley, D., Spear, J., Przekop, K.M. and Visscher, P.T., (2006), Sulfate reducing bacteria in microbial mats: changing paradigms, new discoveries. *Sed. Geol.* **185**, 131-145.

Benson, S.M. and Cole, D.R., (2008), CO_2 sequestration in deep sedimentary formations. *Elements* **4**, 325-331.

Bosak, T. and Newman, D.K., (2003), Microbial nucleation of calcium carbonate in the Precambrian. *Geology* **31**, 577-580.

Braissant, O., Cailleau, G., Dupraz, C. and Verrecchia, E.P., (2003), Bacterially induced mineralization of calcium carbonate in terrestrial environments: the role of exopolysaccharides and amino acids. *J. Sed. Research* **73**, 485-490.

Braissant, O., Decho, A.W., Dupraz, C., Glunk, C., Przekop, K.M. and Visscher, P.T., (2007), Exopolymeric substances of sulfate-reducing bacteria: Interactions with calcium at alkaline pH and implication for formation of carbonate minerals. *Geobiology* **5**, 401-411.

Canfield, D.E. and Des Marais, D.J., (1993), Biogeochemical cycles of carbon, sulfur, and free oxygen in a microbial mat. *Geochim. Cosmochim. Acta* **57**, 3971-3984.

Caporaso, J.G., Kuczynski, J., Stombaugh, J., Bittinger, K., Bushman, F.D., Costello, E.K., Fierer, N., Pena, A.G., Goodrich, J.K. and Gordon, J.I., (2010), QIIME allows analysis of high-throughput community sequencing data. *Nat. Methods* 7, 335-336.

Castanier, S., Le Métayer-Levrel, G. and Perthuisot, J.P., (1999), Ca-carbonates precipitation and limestone genesis - the microbiogeologist point of view. *Sed. Geol.* **126**, 9-23.

Cord-Ruwisch, R. (1985) A quick method for the determination of dissolved and precipitated sulfides in cultures of sulfate-reducing bacteria. *J. Microbiol. Methods* **4**, 33-36.

Dasu, B.N. and Sublette, K.L., (1989), Microbial removal of sulfur dioxide from a gas stream with net oxidation to sulfate. *Appl. Biochem. Biotechnol.* **20**, 207-220.

Deng, S., Dong, H., Lv, G., Jiang, H., Yu, B. and Bishop, M.E., (2010), Microbial dolomite precipitation using sulfate reducing and halophilic bacteria: Results from Qinghai Lake, Tibetan Plateau, NW China. *Chem. Geol.* **278**, 151-159.

DeSantis, T.Z., Hugenholtz, P., Larsen, N., Rojas, M., Brodie, E.L., Keller, K., Huber, T., Dalevi, D., Hu, P. and Andersen, G.L., (2006), Greengenes, a chimera-checked 16S rRNA gene database and workbench compatible with ARB. *Appl. Environ. Microbiol.* **72**, 5069-5072.

Dupraz, C., and Visscher, P.T., (2005), Microbial lithification in marine stromatolites and hypersaline mats. *Trends in Microbiol.* **13**, 429-438.

Dupraz, S., Parmentier, M., Ménez, B. and Guyot, F., (2009a), Experimental and numerical modeling of bacterially induced pH increase and calcite precipitation in saline aquifers. *Chem. Geol.* **265**, 44-53.

Dupraz, S., Ménez, B., Gouze, P., Leprovost, R., Bénézeth, P., Pokrovsky, O.S. and Guyot, F., (2009b), Experimental approach of CO_2 biomineralization in deep saline aquifers. *Chem. Geol.* **265**, 54-62.

Gallagher, K., Kading, T., Braissant, O., Dupraz, C. and Visscher, P., (2012), Inside the alkalinity engine: the role of electron donors in the organomineralization potential of sulfate-reducing bacteria. *Geobiology* **10**, 518-530.

Garrity, G. M., Brenner, D. J., Krieg, N. R., Staley, J, T., (2005), Bergey's Manual of Systematic Bacteriology, Volume Two: The Proteobacteria. New York, New York: Springer.

Giammar, D.E., Bruant Jr. R.G., Peter C.A., (2005), Forsterite dissolution and magnesite precipitation at conditions relevant for deep saline aquifer storage and sequestration of carbon dioxide. *Chemical Geology* **217**, 257– 276.

Haas, B.J., Gevers, D., Earl, A.M., Feldgarden, M., Ward, D.V., Giannoukos, G., Ciulla, D., Tabbaa, D., Highlander, S.K., Sodergren, E., Methe, B., DeSantis, T.Z., Human Microbiome Consortium, Petrosino, J.F., Knight, R. and Birren, B.W., (2011), Chimeric 16S rRNA sequence formation and detection in Sanger and 454-pyrosequenced PCR amplicons. *Genome Research* **21**, 494-504.

Hammes, F. and Verstraete, W., (2002), Key roles of pH and calcium metabolism in microbial carbonate precipitation. *Rev. Environ. Sci. Biotechnol.* **1**, 3-7.

Hoefs, J. (2009) *Stable isotope geochemistry*. 6th ed. Springer, Berlin, Heidelberg

Jonkers, H., Koh, I.O., Behrend, P., Muyzer, G. and De Beer, D., (2005), Aerobic organic carbon mineralization by sulfate-reducing bacteria in the oxygen-saturated photic zone of a hypersaline microbial mat. *Microbiol. Ecol.* **49**, 291-300.

Jun, Y.S., Giammar, D.E., Werth, C.J., and Dzombak, D.A., (2013), Environmental and Geochemical Aspects of Geologic Carbon Sequestration: A Special Issue. *Environ. Sci. Technol.* **47**, 1-2.

Kah, L.C., Lyons, T.W. and Chesley, J.T., (2001), Geochemistry of a 1.2 Ga carbonate-evaporite succession, northern Baffin and Bylot Islands: implications for Mesoproterozoic marine evolution. *Precambrian Res.* **111**, 203-234.

Kester, D.R., Duedall, I.W., Connors, D.N. and Pytkowicz, R.M., (1967), Preparation of artificial seawater. *Limnol. Oceano.* **12**, 176-179.

Kjeldsen, K.U., Loy, A., Jakobsen, T.F., Thomsen, T.R., Wagner, M. and Ingvorsen, K., (2007), Diversity of sulfate-reducing bacteria from an extreme hypersaline sediment, Great Salt Lake (Utah). *FEMS Microbiol. Ecol.* **60**, 287-298.

Knauss, K.G., Johnson, J.W. and Steefel, C.I., (2005), Evaluation of the impact of CO_2, co-contaminant gas, aqueous fluid and reservoir rock interactions on the geologic sequestration of CO_2. *Chem. Geol.* **217**, 339-350.

Krumholz, L.R. (2000) Microbial communities in the deep subsurface. *Hydrogeol. J.* **8**, 4-10.

Liamleam, W. and Annachhatre, A.P., (2007), Electron donors for biological sulfate reduction. *Biotechnol. Adv.* **25**, 452-463.

Londry, K.L. and Des Marais, D.J., (2003), Stable carbon isotope fractionation by sulfate-reducing bacteria. *Appl. Environ. Microbiol.* **69**, 2942-2949.

Meldrum, F.C. and Hyde, S.T., (2001), Morphological influence of magnesium and organic additives on the precipitation of calcite. *J. Cryst. Growth* **231**, 544-558.

Ménez, B., Dupraz, S., Gérard, E., Guyot, F., Rommevaux Jestin, C., Libert, M., Jullien, M., Michel, C., Delorme, F. and Battaglia-Brunet, F., (2007), Impact of the deep biosphere on CO_2 storage performance. *Geotechnol. Sci. Report* **9**, 150-163.

Metz, B., Davidson, O., de Coninck, H., Loos, M. and Meyer, L., (2005), IPCC special report on carbon dioxide capture and storage. *Intergovernmental Panel on Climate Change, Geneva (Switzerland)*. Working Group III.

Mitchell, A.C., Phillips, A.J., Hiebert, R., Gerlach, R., Spangler, L.H. and Cunningham, A.B., (2009), Biofilm enhanced geologic sequestration of supercritical CO_2. *Int. J. Greenhouse Gas Control* **3**, 90-99.

Mitchell, A.C., Dideriksen, K., Spangler, L.H., Cunningham, A.B. and Gerlach, R., (2010), Microbially enhanced carbon capture and storage by mineral-trapping and solubility-trapping. *Environ. Sci. Technol.* **44**, 5270-5276.

Monastersky, R., (2013), Global carbon dioxide levels near worrisome milestone. *Nature* **497**, 13.

Morozova, D., Wandrey, M., Alawi, M., Zimmer, M., Vieth, A., Zettlitzer, M. and Würdemann, H., (2010), Monitoring of the microbial community composition in saline aquifers during CO_2 storage by fluorescence in situ hybridisation. *Int. J. Greenhouse Gas Control* **4**, 981-989.

Morse, J.W. and Mackenzie, F.T., (1990), *Geochemistry of sedimentary carbonates.* Elsevier. Amsterdam.

Muyzer, G., De Waal, E.C. and Uitterlinden, A.G., (1993), Profiling of complex microbial populations by denaturing gradient gel electrophoresis analysis of polymerase chain reaction-amplified genes coding for 16S rRNA. *Appl. Environ. Microbiol.* **59**, 695-700.

Nealson, K.H., Inagaki, F. and Takai, K., (2005), Hydrogen-driven subsurface lithoautotrophic microbial ecosystems (SLiMEs): do they exist and why should we care? *Trends Microbiol.* **13**, 405-410.

Oelkers, E.H., Gislason, S.R. and Matter, J., (2008), Mineral carbonation of CO_2. *Elements* **4**, 333-337.

O'Flaherty, V., Lens, P., Leahy, B. and Colleran, E., (1998), Long-term competition between sulphate-reducing and methane-producing bacteria during full-scale anaerobic treatment of citric acid production wastewater. *Wat. Res* .**32**, 815-825.

Oule, M., Dickman, M. and Arul, J., (2010), Microbicidal effect of pressurized CO_2 and the influence of sensitizing additives. *European J. Sci. Res.* **41**, 570-582.

Palumbo-Roe, B. and West, J., (2013), Evaluation of the potential impacts of an influx of CO_2 on subsurface microbial populations using a thermodynamic approach. *British Geol. Sur. Open Report*, OR/13/014.

Pedersen, K., (2000), Exploration of deep intraterrestrial microbial life: current perspectives. *FEMS Microbiol. Lett.* **185**, 9-16.

Poulton, S.W., Krom, M.D. and Raiswell, R., (2004), A revised scheme for the reactivity of iron (oxyhydr) oxide minerals towards dissolved sulfide. *Geochim. Cosmochim. Acta* **68**, 3703-3715.

Reis, M., Almeida, J., Lemos, P. and Carrondo, M., (1992), Effect of hydrogen sulfide on growth of sulfate reducing bacteria. *Biotechnol. Bioeng.* **40**, 593-600.

Reith, F., (2011), Life in the deep subsurface. *Geology* **39**, 287-288.

Santillan, E.U., Kirk, M.F., Altman, S.J. and Bennett, P.C., (2013), Mineral Influence on Microbial Survival During Carbon Sequestration. *Geomicrobiol. J.* **30**, 578-592.

Socolow, R., Hotinski, R., Greenblatt, J.B. and Pacala, S., (2004), Solving the climate problem: technologies available to curb CO_2 emissions. *Environ. Sci. Policy for Sustainable Development* **46**, 8-19.

Stevens, T. O. and McKinley, J. P., (1995), Lithoautotrophic microbial ecosystems in deep basalt aquifers. *Science* **270**, 450-450.

Swart, P. K., Burns, S. J. and Leder, J. J., (1991), Fractionation of the stable isotopes of oxygen and carbon in carbon dioxide during the reaction of calcite with phosphoric acid as a function of temperature and technique. *Chem. Geol.: Isotope Geosci. Sect.*, **86**, 89-96.

Szynkiewicz, A., Moore, C.H., Glamoclija, M. and Pratt, L.M., (2009), Sulfur isotope signatures in gypsiferous sediments of the Estancia and Tularosa Basins as indicators of sulfate sources, hydrological processes, and microbial activity. *Geochim. Cosmochim. Acta* **73**, 6162-6186.

Van Houten, R.T., Pol, L.W.H. and Lettinga, G., (1994), Biological sulphate reduction using gas-lift reactors fed with hydrogen and carbon dioxide as energy and carbon source. *Biotechnol. Bioeng.* **44**, 586-594.

Van Lith, Y., Vasconcelos, C., Warthmann, R. and McKenzie, J., (2000), Role of sulfate reducing bacteria during microbial dolomite precipitation as deduced from culture experiments, *J. Conf. Abst.* 1038.

Van Lith, Y., Warthmann, R., Vasconcelos, C. and Mckenzie, J.A., (2003), Sulphate-reducing bacteria induce low-temperature Ca-dolomite and high Mg-calcite formation. *Geobiology* **1**, 71-79.

Visscher, P.T., Reid, R.P., Bebout, B.M., Hoeft, S.E., Macintyre, I.G. and Thompson, J.A., (1998), Formation of lithified micritic laminae in modern marine stromatolites (Bahamas): the role of sulfur cycling. *Am. Mineral.* **83**, 1482-1493.

Visscher, P.T. and Stolz, J.F., (2005), Microbial mats as bioreactors: populations, processes, and products. *Palaeogeo., Palaeoclimatol., Palaeoecol.* **219**, 87-100.

Warthmann, R., Van Lith, Y., Vasconcelos, C., McKenzie, J.A. and Karpoff, A.M., (2000), Bacterially induced dolomite precipitation in anoxic culture experiments. *Geology* **28**, 1091-1094.

Weisburg, W.G., Barns, S.M., Pelletier, D.A. and Lane, D.J., (1991), 16S ribosomal DNA amplification for phylogenetic study. *J. Bacteriol.* **173**, 697-703.

Werner, B. and Hotchkiss, J., (2006), Continuous Flow Nonthermal CO_2 Processing: The Lethal Effects of Subcritical and Supercritical CO_2 on Total Microbial Populations and Bacterial Spores in Raw Milk. *J. Dairy Sci.* **89**, 872-881.

West, J.M., McKinley, I.G., Palumbo-Roe, B. and Rochelle, C.A., (2011), Potential impact of CO_2 storage on subsurface microbial ecosystems and implications for groundwater quality. *Energy Procedia* **4**, 3163-3170.

White, C.M., Strazisar, B.R., Granite, E.J., Hoffman, J.S. and Pennline, H.W., (2003), Separation and capture of CO_2 from large stationary sources and sequestration in geological formations—coal beds and deep saline aquifers. *J. Air Waste Manag. Assoc.* **53**, 645-715.

Widdel, F., (1988), Microbiology and ecology of sulfate-and sulfur-reducing bacteria. In *Biology of.anaerobic microorganisms* (ed. Zehnder, A.) Wiley, New York, NY. pp. 469-585.

Wilkin, R.T. and DiGiulio, D.C., (2010), Geochemical impacts to groundwater from geologic carbon sequestration: controls on pH and inorganic carbon concentrations from reaction path and kinetic modeling. *Environ. Sci. Technol.* **44**, 4821-4827.

Wu, B., Shao, H., Wang, Z., Hu, Y., Tang, Y.J. and Jun, Y.S., (2010), Viability and metal reduction of Shewanella oneidensis MR-1 under CO_2 stress: implications for ecological effects of CO_2 leakage from geologic CO_2 sequestration. *Environ. Sci. Technol.* **44**, 9213-9218.

Zhilina, T. N., (1986), Methanogenic bacteria from hypersaline environments. *Syst. Appl. Microbiol.* 7, 216-222.

SECTION VI. CHARACTERIZATION OF WATER PROPERTIES AND MICROBIALITES IN THE HYPERSALINE ENVIRONMENT OF STORRS' LAKE, THE BAHAMAS

1. INTRODUCTION

Modern microbialites, such as stromatolites and thrombolites, are organo-sedimentary structures composed of lithified carbonate or siliceous material (Burne and Moore, 1987; Riding, 1991; Dupraz et al., 2009). Representing one of the oldest ecosystems on Earth (~3.5 Ga; Hofmann et al., 1999), microbialites presently occur in a wide range of habitats from coastal marine (e.g., Reid et al., 2000), hypersaline (e.g., Skyring and Bauld, 1990; Glunk et al., 2011), freshwater lakes (e.g., Ferris et al., 1997; Freytet and Verrecchia, 1998; Laval et al., 2000), to deep sea methane seeps (e.g., Bailey et al., 2009). The organic microbial mats are generally present on the top surface of the microbialites and are considered to be the driving force that produces the microbialite mineral structures. These microbial mats often include a diverse microbial community that can be involved in the trapping, binding, and/or precipitation of carbonate minerals. The microbial population, availability of sunlight, microbe-produced exopolymeric substances (EPS), wave/tidal energy in the environment, water depth and the chemistry of the surrounding aqueous environment are some of the key factors that determine the growth and lithification potential of microbialites (Reid et al., 2000; Riding, 2000; Dupraz et al., 2004; Visscher and Stolz, 2005; Dupraz et al., 2006; Braissant et al., 2007; Dupraz et al., 2013).

Microbial mats that have the propensity to form microbialite structures typically consist of six major functional guilds of microorganisms (Van Gemerden, 1993; Dupraz and Visscher, 2005): (i) oxygenic photoautotrophs, such as cyanobacteria that dominate the upper layers of the microbial mats; (ii) oxygenic heterotrophs that gain energy from the breakdown of organics; (iii) anoxygenic photoautotrophs comprising of purple and green bacteria; (iv) anaerobic heterotrophs, such as sulfate reducing bacteria (SRB) capable of oxidizing organic material by coupling an electron transfer process with compounds like SO_4^{2-}; (v) sulfide oxidizing bacteria that oxidize reduced sulfur compounds with O_2 or NO_3^- while fixing CO_2 into organic compounds; and (vi) fermenters, degrading organic carbon to generate energy along with SRB. Among the above listed populations, the activity of oxygenic and anoxygenic phototrophs, and SRB can result in the net precipitation of carbonate minerals (Visscher et al., 2000; Dupraz and Visscher, 2005; Dupraz et al., 2009). In contrast, sulfide oxidizers, and fermentative and aerobic heterotrophs will promote the dissolution of carbonate minerals (Dupraz and Visscher, 2005). Therefore, it is the combined metabolic activities of the microbial mat communities coupled with the environmental conditions that determines the net precipitation potential of the microbialites. Cycling of various organic and inorganic energy sources is also important in the mat functioning. For example, hydrogen production by cyanobacteria and consumption by members of

Chloroflexi and SRB has been shown to be an important metabolic process in the functioning of hypersaline mat community from Guerrero Negro, Mexico (Lee et al., 2014).

The mineralogy constituting modern microbialites can include Mg-calcite, aragonite (Neumann et al., 1989; Reid et al., 2000), to siliceous deposits (Jones et al., 1998). Fossil microbialites may also contain chert and dolomite due to diagenetic changes, with traces of the original carbonate or siliceous minerals sometimes preserved (Sommers et al., 2000). Dolomite has been shown to form diagenetically in microbial mats, especially along anoxic sediment fronts (Furman et al., 1993; Vasconcelos and McKenzie, 1997). Phototrophic communities synthesize EPS, the production of which is directly influenced by the light availability (Decho et al., 2005). Precipitation and lithification are influenced through the decomposition of EPS, which releases bound bicarbonate and calcium ions. Favorable sites within the EPS can serve as nucleation templates for $CaCO_3$ precipitation (Dupraz and Visscher, 2005). Not all microbial mats, however, undergo mineral precipitation and lithification. For example, the hypersaline mats of Guerrero Negro, Mexico, harbor many of the same functional guilds of microbes found in microbialites, yet do not undergo lithification (Ley et al., 2006).

Storrs' Lake is located on the eastern side of Sal Salvador Island, The Bahamas (Section II-Fig. 6). It is a hypersaline lake that formed during a late Holocene sea level rise, when a depression on the east side of the island was flooded, and then subsequent evaporitic conditions caused the lake to become seasonally hypersaline (Neumann et al., 1989; Zabielski, 1991). The lake is shallow, with a maximum depth of ~2 m (Mann and Nelson, 1989), is slightly alkaline, and extremely turbid. The salinity of the lake water fluctuates depending on evaporation rate and the frequency of rain. The turbidity in the lake is caused by floating planktonic material and benthic components that become suspended after they trap gas bubbles released from microbial metabolism (Mann and Nelson, 1989; Neumann et al., 1989). Storrs' Lake is an unusual system due to the growth of microbialites in shallow water with limited light penetration.

Four distinct microbialite morphologies in Storrs' Lake have been previously identified in discreet zones (Mann and Nelson, 1989; Neumann et al., 1989). Moving along a transect from the shore to the lake center, the first morphotype identified is the clotted thrombolytic pie mounds. These microbialites are located close to shore in shallow water, and are periodically exposed to desiccating conditions during low lake levels. The next set of microbialites form a shallow water plateau offshore that consists of calcareous knobs as tall as 15 cm (the 'bulbous crust' of Neumann et al., 1989). The upper parts of the calcareous knobs may also be subaerially exposed during periods of low water. The water depth increases further into the lake at which point the flat topped plateau stromatolites with a hard calcified structure are observed. These are firmly attached to the substrate. Columnar pinnacle mounds are found in yet deeper portions of the lake (club shaped mounds of Neumann et al., 1989) These are up to 70 cm in length. We also describe a new morphotype, the 'multi-cuspate' type that has been discovered. Three weakly lithified microbial mats also occur: (i) near-shore ectoplasmic pie mounds, (ii) an offshore mat that covered the calcareous knobs, and (iii) a thick, leathery, ‘cheesecake’ microbial mat present in between and on top of the deeper water microbialites (Neumann et al., 1989).

Radiocarbon dating of a microbialite encrusted tree root in Storrs’ Lake indicated that the microbialites have been present for at least 2360 +/- 70 years and their growth rates appear to be episodic (Paull et al., 1992). The deeper, larger microbialites have been suggested to be covered under the bottom ooze and may have become inactive (termed a ‘sub-fossil’), and some of them could have started to undergo digenetic alteration (Dupraz et al., 2006; Fowler, 2011; Dupraz et al., 2013). Submerged mats in the lake exhibit a low rate of photosynthesis and nitrogen fixation relative to open marine microbialites (Bebout; 1992; Paerl et al., 2003; Dupraz et al., 2013). Previous morphological studies of the microbial population have identified several taxa within the different mats found in the lake bottom and the shallow calcareous knob microbialite, including cyanobacteria, such as *Scytonema*, *Gloeocapsa, Schizothrix, Phormidium, Microcoleus, Calothrix, Spirulina;* colorless sulfur bacteria, *Beggiatoa,* purple sulfur bacteria *Chromatium,* etc., and diatoms like *Navicula* and *Nitzchia* (Mann and Nelson, 1989; Neumann et al., 1989; Pentecost, 1989). A 16S rRNA gene analysis of the microbial population of the near shore calcareous knob also identified at least five genera of SRB including *Desulfovibrio, Desulfobulbus, Desulfococcus, Desulfobacter* and *Desulfobacterium* (Brigmon et al., 2006). This previous study also indicated that cyanobacteria populations were reported to be dead in the evaporitic mats present in non-photic zone of Storrs’ Lake, whereas non-photosynthetic bacteria were dominant in these regions. Apart from the shallower calcareous knobs, none of the other microbial mats found in the deeper microbialites have been previously analyzed for their microbial diversity by using molecular techniques.

Most modern microbialites are located in shallow and clear water environments, with the notable exception of deep sea occurrences (Bailey et al., 2009) and those at Pavilion Lake (Laval et al., 2000; Lim et al., 2009),. The high turbidity water of Storrs’ Lake limits sunlight availability, especially to the deeper water microbialites, and thus likely affects their phototrophic population. Determining light availability at different depths, water chemistry and the microbial mat composition is critical to understand the complex role of the various biogeochemical components on the development of these microbialites. Here, we present data on several of the lake’s abiotic parameters including water chemistry, intensity of sunlight penetration at depth, and mineralogy of the microbialites. We also applied 16S rRNA gene sequencing to assess the microbial diversity of the surface mats associated with the microbialites mounds.

2. RESULTS

2.1. Water Chemistry Analysis

A water chemistry profile was generated along the Storrs’ Lake transect at different depths and locations during visits to the site over a three-year period (Table 1). The maximum water depth from sediment to the surface increased from ~1 m in April 2011 to ~1.1 and ~1.3 m in June 2012 and June 2013, respectively. Mann and Nelson (1989) reported that depths up to ~ 2.0 m were observed in the lake. These maximum depths could have been observed in other portions of the lake that were not transected during our field visits. Water parameters fluctuated between each sampling visit. For example, the average pH changed from 8.22 ± 0.05 to 8.58 ± 0.08 and back to 8.22 ± 0.2 in the three years of sampling. Water conductivity was measured during cursory visits to the island in May of 2004, 2005 and 2009. The conductivity values during these three years were 98.3 mS/cm (66 ppt), 108 mS/cm (72 ppt) and 40.6 mS/cm (26 ppt), respectively. The corresponding conductivity readings in April 2011, June 2012, and June 2013 were 138 mS/cm (92 ppt), 64 mS/cm (43 ppt) and 59 mS/cm (39 ppt), respectively, while ocean water collected from nearby Dim Bay in 2012 had a conductivity value of 53.9 mS/cm (36 ppt).

Table 1. Water parameters measured over three sampling seasons at Storrs' Lake. Values represent an average and standard deviation of 6 to 20 measurements from different depths and locations. Anions were only analyzed in 2012. Near-shore water measurements for the brackish water zone are not included. Salinity is calculated by multiplying conductivity by 0.667 to obtain the parts per thousand (ppt) concentration (Boyd, 2002).

Parameters	**3/31 to 4/1/2011 15:00 (EST)**	**6/16 to 6/20/12 15:00 (EST)**	**6/3 to 6/3/13 16:00 (EST)**	**Seawater6/16/1 2 14:00 (EST)**
Max. Water Depth	~1 m	~1.1 m	~1.3 m	-
pH	8.22 (± 0.05)	8.58 (± 0.08)	8.22 (± 0.20)	8.26
Eh (mV)	-60 (± 2)	-80 (± 12)	-73 (± 14)	-55
Alkalinity (mg/L as $CaCO_3$)	178 (± 8)	151 (± 1)	140 (± 27)	113
Ca-hardness (mg/L as $CaCO_3$)	-	1328 (± 40)	1150 (± 233)	1060
Mg-hardness (mg/L as $CaCO_3$)	-	6953 (± 296)	6340 (± 466)	5840
Temperature (°C)	27.5 (± 1.0)	28.7 (± 1.2)	24.6 (± 0.2)	28
Conductivity (mS/cm)	138 (± 4.5)	64 (± 1.3)	59 (± 2.3)	53.9
Salinity (ppt)	92.1 (± 3.0)	42.7 (± 0.9)	39.4 (± 1.5)	36.0
Dissolved Oxygen (mg/L)	3.86 (± 1.07)	5.72 (± 1.80)	3.11	4.70
Turbidity (NTU)	169 (± 15)	96 (± 12)	135 (± 12)	5
Calcium (ppm)*	990 (± 32)	503 (± 15)	689 (± 52)	386
Magnesium (ppm)*	2873 (± 84)	1676 (± 43)	2033 (± 108)	1361
Sodium (ppm)*	25,133 (± 275)	14,422 (± 280)	16,692 (± 807)	11,811
Potassium (ppm)*	926 (± 27)	520 (± 15)	629 (± 28)	417
Strontium (ppm)*	22 (± 1.5)	-	-	-
Chloride (ppm)[Ŧ]	-	24,075 (± 624)	-	19,000
Sulfate (ppm)[Ŧ]	-	3910 (± 94)	-	2700

The average 2013 values shown in Table 1 do not include those obtained from the near–shore brackish water inlet to the lake. The source for the brackish water is from the nearby swamp along with surface runoff that drained into the lake through the man-made conduit (Section II-Fig. 7A). The swamp area is separated from Storrs' Lake by a low roadway. There was a distinct delineation seen in the lake (~60 m from the shore during 2013), where the relatively clear and brownish colored-brackish water mixes with the more turbid and hypersaline portion of the lake (Section II-Fig. 7B). The average conductivity near the conduit through which the brackish water entered the lake was 3.77 ± 0.11 mS/cm with a pH of 7.74 ± 0.2. The averaged calcium, magnesium, potassium, and sodium concentrations of the brackish water were 99, 90, 27 and 728 ppm, respectively.

Proceeding from the lake shore to the more offshore locations, the pH, Eh and conductivity values displayed a distinct lateral profile in the near-surface water collected from the top several centimeters of water at these locations in 2013. The pH generally increased (7.73 to 8.47) and the redox conditions become more reduced (-43.3 mV to -87.7 mV) while moving further from shore. The conductivity values also gradually increased towards the lake center, starting at 3.7 mS/cm near the brackish water inlet, rising to 17.5 mS/cm about 23 m away from the shore, 43.3 mS/cm at the mixing zone (~60 meters from shore) and 53.5 mS/cm at the turbid water region. Alkalinity did not change much in the three years, with the highest value in 2011 of 178 ± 8 mg/L and lowest in 2013 of 140 ± 27 mg/L. Calcium and magnesium hardness measured in 2012 and 2013 (diluted lake water 1:100 or 1:20 with deionized water). The average calcium hardness in 2012 was 1328 ± 40 mg/L as $CaCO_3$ (532 ± 16 mg/L Ca), and that of magnesium was 6,953 ± 296 mg/L as $CaCO_3$ (1988 ± 85 mg/L Mg). The respective Ca and Mg concentrations, as detected through ICP-OES were 507 ±16 and 1681 ±49 ppm (mg/L). Elements, including Si, Fe, Mn, Al, Li, and B, were always below 15 ppm and are not reported in Table 1.

Water chemistry was also measured along a vertical profile in several locations along the transect in 2013. These depth analyses at one location (three samples at near-surface, ~64 and ~130 cm depths) of the more visibly turbid region gave pH values of 8.13, 8.35 and 7.85, respectively. The corresponding conductivity and turbidity values increased progressively with for these three depths: 57.0, 58.7 and 62 mS/cm, and 121, 127 and 145 NTU, respectively. This pattern was consistent with two other similar locations where the water was analyzed directly above plateau-mushroom type microbialites (data not shown). Dissolved oxygen consistently decrease from the shallow to deeper waters. For example in 2011, the average dissolved oxygen decreased from 5.0 (± 0.6) mg/L in shallow waters, to 4.1 (± 0.7) mg/L at ~25 cm, 3.3 (± 0.8) mg/L at ~50 cm, 3.4 (± 0.4) mg/L at ~75 cm, and 2.2 mg/L (± 0.1) at ~100 cm. Quantitative readings for dissolved oxygen could not be made in 2012 and 2013 due to error in instrument calibration, though a progressive decrease in the dissolved oxygen content was still detected. Saturation index (SI) values for carbonate minerals were calculated by using the equilibrium based PHREEQ software program and the measured chemical parameters of Storrs' Lake water. The calculated SI values indicated that the water conditions always remained supersaturated with respect to both aragonite and calcite (SI > 0.0). For aragonite, the SI values in 2011, 2012 and 2013 averaged 1.13, 0.94 and 0.95, respectively. The corresponding calcite SI values were 1.27, 1.08 and 1.09. The lower 2012 and 2013 values reflect the influence of a heavy rainfall event that occurred before and during water sampling visits to the lake.

Particulate material in Storrs' Lake water was examined by optical microscopy and found to be dominated by a variety of algae, bacteria, diatoms and dinoflagellates, all of which contributed to the high turbidity. Comparisons made between the settling rates of particulate material from Storrs' Lake versus illite and smectite clay samples suspended in a 5% synthetic seawater solution are shown in Fig. 1. The turbidity values indicated that the lake water sample took ~180 days to reduce from a turbidity value of 121 to 8 NTU. In contrast, illite and smectite clay in the 5% seawater solution, took only 11 and 6 hours, respectively, to go from a starting turbidity of approximately 450 down to 8 NTU.

During the low salinity and high lake level periods of the 2012 and 2013 visit, the lake was also inhabited by a species of fish. Dissection of one specimen revealed stomach and intestinal contents containing calcium carbonate fragments, indicating that the fish had been feeding on the microbialites and/or carbonate sediments.

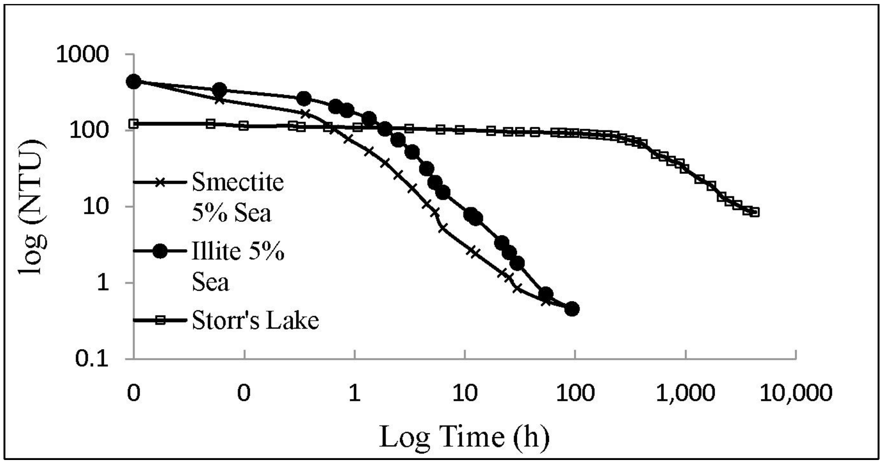

Figure 1. Turbidity measurements comparing Storrs' Lake particle settling rates with smectite and illite clays suspended into a 5% synthetic seawater solution. The relatively flat horizontal settling trends at the beginning of each test reflect the time taken for the suspended particles to move from the top of the water column in the vials to below the level of the light scattering detector. Sample vials were held in complete darkness during measurement. NTU, Nephelometric Turbidity Units.

2.2. Microbialite Morphology and Distribution

A representative transect of the distribution of microbialites identified along the northern section of Storrs' Lake is shown in Fig. 2. Several of the microbialites types have been previously described (Mann and Nelson, 1989; Neumann et al., 1989) and include: calcareous knobs (Fig. 3A), plateau-mushroom shaped (Fig. 3B), pinnacle mound (Fig. 3C), and cauliflower-top mushroom shaped stromatolites (Fig. 3D). Samples of each of these types were collected in both April 2011 and June 2012. The near-shore calcareous knobs or bulbous crust (Neumann et al., 1989) exhibited two distinct features: (i) a lower, darker colored, fused-granular, carbonate structure (~6 to 7 cm in thickness) by which the microbialite was attached to the lake bottom. Occasional gastropods, leaf material and slimy microbial mats were found on the sides and incorporated into the carbonate structure; (ii) an upper, lighter colored carbonate structure (~5 cm thick) that had a smoother, continuous carbonate build up compared to the granular bottom portion. A microbial mat with sporadic eukaryotic algal material was found between the grooves and on the uppermost surface. This upper portion was marked by several knobby growth like patterns, with plenty of cavities on its surface.

It is important to note that the cauliflower-top mushroom and the plateau-mushroom type described here possess the same overall external morphological appearance but varied in certain physical characteristics as described below. Also, the cauliflower-top mushroom described in this report is the same as the 'mushroom type' described by Neumann et al. (1989). The new terminologies, i.e., plateau-mushroom and cauliflower-top mushroom types, was required to differentiate between the two different types of mushroom microbialites identified in our study and distinguish these from previous studies. Both plateau-mushroom and cauliflower-top mushroom types were found at similar depths (70 to 100 cm). The cauliflower-top mushroom microbialite had several bulging calcium carbonate knobs on the top surface, each resembling individual, smaller mounds, similar to the mushroom knobs reported by Neumann et al. (1989). These mounds began to disappear (~3 to 4 cm from the top) and were followed by continuous horizontal calcium carbonate laminations with intermittent branching or thrombolytic nodes. The laminations ended in the bottom stalk, which was very fragile and crumbled easily.

Morphologic features of the plateau-mushroom type varied only slightly from the cauliflower type, with the top crust having a reticulated structure that was more brittle than exhibited by the cauliflower type. The plateau type had a visible gap that was variable in height (~0.2 and 1.0 cm), observed between the more reticulated top crust and the compacted segment located directly below the crust. This microbialite exhibited a highly compacted base with a prominent stalk (also highly cemented) attached to the lake sediment segment, above which, the lithification lacked any prominent, horizontally stratified layers. Occasionally, two individual plateau type microbialites were observed that fused with each other to form a single large unit.

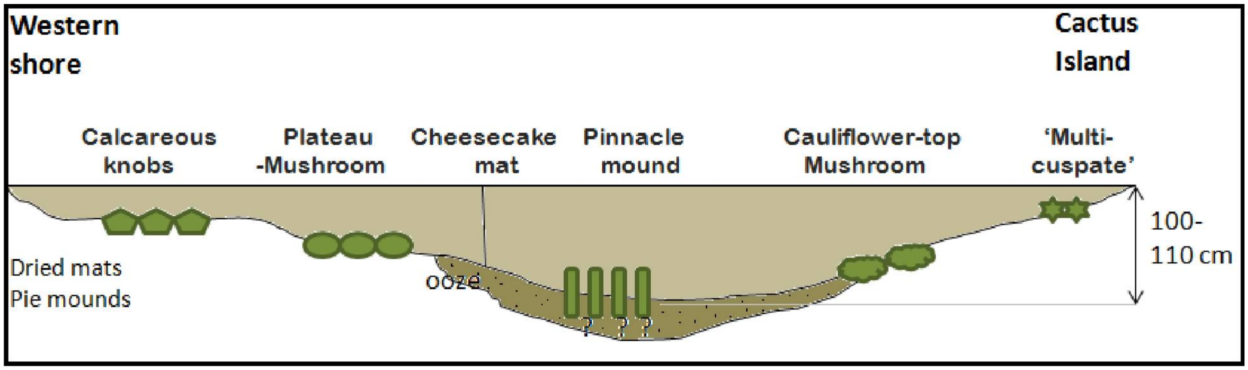

Figure 2. Cross-sectional view of the distribution of microbialites in Storrs' Lake showing the approximate locations where microbialites and water samples were collected (after Mann and Nelson, 1989; Neumann et al., 1989). Vertical scale is exaggerated and the horizontal distance from the western shore to the Cactus Island is ~450 m. The depth that the pinnacle mound microbialites extends into the sediment is unknown.

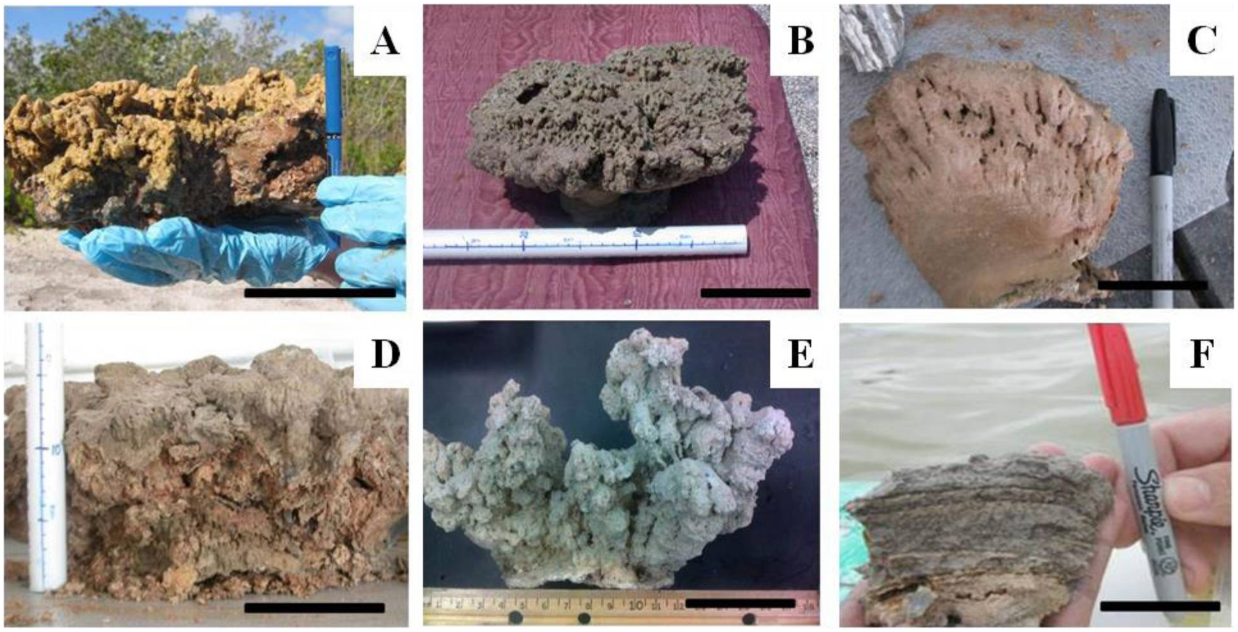

Figure 3. Microbialites and microbial mats collected from Storrs' Lake. (A) calcareous knobs, bar = 12 cm; (B) plateau-mushroom, bar = 10 cm; (C) half-sectioned pinnacle mound, bar = 7.5 cm; (D) cauliflower-top mushroom; bar = 10 cm (E) multi-cuspate type, bar = 5 cm; (F) cohesive, but nonlithified cheesecake mat shown in cross-section profile, bar = 7.5 cm.

The upper most surficial crust of the pinnacle mound microbialite was a continuous layer that was 0.5 to 1 cm thick on which, the microbial mats were found in a scattered manner (Fig. 3C). A thrombolytic morphology involving a combination of branched and massive features that were ~7 to 8 cm thick were observed directly below the upper crust. These thrombolytic features were replaced below by a highly compacted region that extended between 5 and 6 cm. In its bottom most region, the pinnacle mound exhibited stromatolitic layering for 1 to 2 cm. The pinnacle mound was broken off as it was pulled from the sediment at the base of the lake, thus the exact length of this type of microbialite could have been longer than that described here (i.e. ~17 cm). Following the cauliflower-top mushroom shaped microbialite and moving towards Cactus Island, another microbialite morphotype was identified at a depth of about 46 to 50 cm, here referred to as the 'multi-cuspate'. The distribution of the multi-cuspate type was fairly continuous from the point it began to appear, but was less frequent towards the shore of Cactus Island. The multi-cuspate microbialites were morphologically different from the other morphotypes owing to their more distinguished protrusions and sharper edges (Fig. 3E). The closest resemblance was to the calcareous knob microbialite form that was located at similar depths, but on the other end of the transect along the western shore of the lake. The multi-cuspate were well lithified structures and did not crumble easily. The bottom 1 or 2 cm of the multi-cuspate microbialite was layered and seemed to represent the locations by which the microbialite was anchored to the lake bottom sediment. Similar bottom layering was also found in the pinnacle mound microbialite. On top of this layered profile, the multi-cuspate microbialite began to form a massive carbonate structure, which eventually proliferated to result in sharper edges of varying lengths, resembling several fused cusp-like formations. These large (~3 to 5 cm) protrusions distinguished these microbialites from the calcareous knobs. Cross-section profiles of the multi-cuspate type revealed a fairly porous calcified structure. The multi-cuspate microbialites possessed limited microbial mat material on the top surface unlike the other microbialite types found in Storrs' Lake, with occasional gelatinous green and pink material found scattered on the grooves and flatter surfaces. The frequency of lithified microbialite structures decreased in the deepest portions of the lake, except for the occasional, broken calcified knobs that were submerged in ~30 cm thick gelatinous bottom material.

The microbial mat type that most often colonized the surfaces of the microbialite structures ranged from 0.5 – 1.0 cm in thickness. These mats, containing faint laminations, were present either uniformly or scattered on the surface of all the microbialite morphotypes except for multi-cuspate. A well laminated, cohesive, but weakly lithified and flat lying 'cheesecake' microbial mat was found to be present on top of the gelatinous material in most lake bottom locations (Fig. 3F). This mat type was particularly abundant in the region between the plateau-mushroom and pinnacle mounds, and the multi-cuspate microbialite and Cactus Island shore. The laminations in the cheesecake mat extend to about 7 to 8 cm depth from the top of the sediment layer. A loose and friable, calcified layer existed below the laminations. The laminations disappeared below this calcified layer and were replaced by the soft, yet cohesive gelatinous material that extends below for approximately 30 cm, till it reaches the hard, bottom layer of the lake. The cheesecake mat was the only microbial mat collected that was not associated with the lithified microbialite heads.

2.3. Light Penetration in Storrs' Lake Water

Due to the high turbidity of the Storrs' Lake water, it was essential to determine the amount of light available for phototrophs in the microbial mat at different depths in the water. The Secchi disk light penetration method was determined at two similar locations, where the calcareous knob microbialites were identified (June 2012). The white portion of disks was not visible below depths of 17 to 26 cm and the black portion disappeared below depths of 15 to 20 cm. Neumann et al. (1989) reported depths of 46 cm below which the Secchi disk disappeared during their December 1987 study.

Light intensity was also measured by HOBO pendant loggers with results shown in Figs. 4A and B. In 2012, the probe was initially set into the location adjacent to the top of calcareous knob microbialites at a depth of 40 cm. Day 1 was mostly cloudy and recorded a maximum signal of ~1150 to 1200 lumens/ft^2 (107 to 112 lumens/m^2). The probe was removed from the water and exposed to direct sunlight above the water surface during Day 2, where a maximum reading of ~20,000 lumens/ft^2 (1860 lumens/m^2) was obtained. The same day, the probe was then moved and inserted at the same height as the top of a plateau-mushroom microbialite at a depth of about 100 cm and kept in this position for two days. The weather patterns changed from partly cloudy on Days 2 and 3, to scattered rain on Day 4. The light intensity during Days 3 and 4 at the plateau position varied from 200 to 600 lumens/ft^2, or between 1 to 3% of the surface light intensity.

In 2013, the probe was placed at ~95 cm next to the top of the plateau-mushroom shaped microbialite and left in place for six days. The highest intensity of light at this depth was recorded at 12 lumens/ft^2 (1.12 lumens/m^2) relative to the surface, where a maximum intensity of ~5,100 lumens/ft^2 was obtained. This represents a decrease in luminosity with 96 cm of water depth of approximately 99.8%. The lower light intensity values in 2013 as opposed to 2012 were due to the heavy overcast conditions. Unfortunately, the overcast and rainy conditions present during both our 2012 and 2013 sampling intervals prevented us from making any recordings under full sunlight conditions with the HOBO pendants.

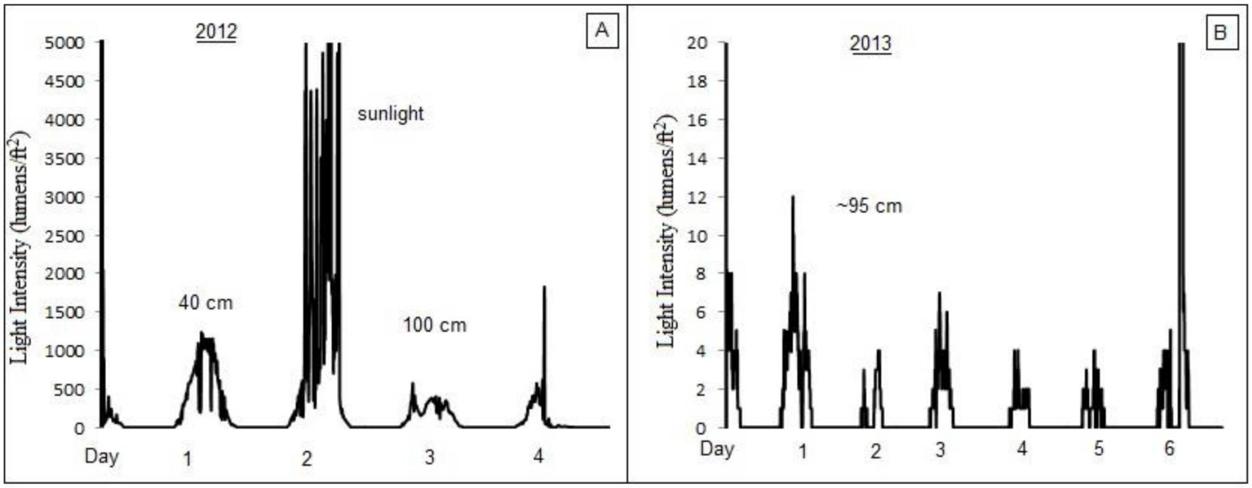

Figure 4. Light intensity data collected using HOBO logger anchored into the bottom sediment and set at a depth of the microbialite heads. The graph shows the data from day and night cycles. (A) 2012; Day 1, probe placed; Day 2, probe exposed to direct sunlight followed by placement next to plateau-mushroom at 100 cm (the y-axis in the plot is cut-off at 5,000 lumens/ft^2, while sunlight reached ~20,000 lumens/ft^2); Day 3, probe left at 100 cm depth; Day 4, probe removed from lake water, the ~1800 lumens/ft^2 peak was due to exposure to surface sunlight under overcast conditions. (B) 2013; the probe was placed at ~95 cm water depth for six days. The y-axis in the plot is cut-off at 20 lumens/ft^2, but the value when exposed to sunlight at day six reached ~5,100 lumens/ft^2.

2.4. Mineralogy and Microscopic Characterization of the Microbialites

In the homogenized microbialite samples prepared for XRD analysis with a composite sample, both Mg-calcite and aragonite were identified as the only precipitated minerals. Mg-calcite was the dominant mineral found in all five microbialite types. Aragonite was detected only in the pinnacle mound, plateau-mushroom, and in smaller quantities (~3%) in the multi-cuspate type. A second set of XRD analyses was conducted with individual samples being collected from multiple positions within the microbialite heads (Fig. 5). These tests were used to determine if the plateau-mushroom and pinnacle mound microbialites displayed any spatial variability with respect to both aragonite and Mg-calcite contents. The pinnacle mound (PM) microbialite contained aragonite in the top one cm surface section (PM-1b-C); however, no aragonite was detected in the sample collected at a 2 cm depth below the surface (PM-2b-C) and in the central core of the sample located 9 cm below the surface. Aragonite percentages were highest at the base of this microbialite (PM-3b-S to PM-4b-C) and at the lateral surfaces (PM-6-S). In the plateau type microbialites, both lateral surficial (Plateau-S) and core (Plateau-C) samples had some of the highest proportions of aragonite detected in Storrs' Lake microbialites, though the aragonite/calcite ratios decreased outward; 76/24 for core *versus* 48/52 for surficial sample, respectively. Although the aragonite/calcite ratios varied from site-to-site within the microbialites, no particular trend was observed with regards to water depth or distance from the shore in the microbialites that were evaluated.

Insoluble components were not detected as residues by visual inspection following a 5% nitric acid digestion step performed on eleven sections of the microbialite heads. Calcium carbonate with variable mole percent Mg (7.5 to 15.6%) was identified as the dominant mineral type in all samples analyzed by using combined ICP-OES (Table 2) and XRD analyses (Fig. 5). Concentrations of Si and Na were at or just above detection limits (i.e., 10 ppm), while Fe, K, Mn, and Al concentrations were all below detection. An inverse correlation was noted in the plateau-mushroom sample, when the aragonite XRD % determinations were compared against mole % Mg (Table 2). For example, considering the mole percent Mg from the top to middle to bottom of this sample, the value becomes lower, albeit gradually; 14.0 to 13.0%. This trend correlated inversely with the XRD analyses, where the aragonite percentage increased with depth from trace detection to 38%. An inverse trend was also observed when the percent Mg-calcite and molar Mg/Ca ratio were compared with the Sr values, and when aragonite percentage was compared with mole percent Mg. The Sr and Mg values obtained from ICP-OES analysis did correlate positively with the XRD aragonite and calcite trends, respectively (Fig. 6). Strontium is an important element with respect to evaluating carbonate mineral polymorph formation as it is preferentially incorporated in the aragonite mineral structure over calcite (aragonite $K_{d\text{-}Sr} = 1.13$ *versus* calcite $K_{d\text{-}Sr} = 0.045$ to 0.14; Morse and Mackenzie, 1990). Thus, if strontium is present, its concentration can be indirectly used to evaluate aragonite/calcite ratios. Conversely, Mg is often enriched in the calcite phase. In both the Sr *versus* percent aragonite plot (Fig. 6A) and the percent Mg versus percent calcite plots (Fig. 6B), the pinnacle mound samples had several points that fitted poorly with the regression line. The squared Pearson's correlation coefficient (R^2) values of 0.0928 and 0.0289, respectively, indicated the poor relationship between the respective parameters, though the plots generally displayed a positive correlation trend. On the other hand, the data from plateau-mushroom samples fitted well with R^2 values of 0.9695 and 0.8186, respectively.

Scanning Electron Microscopy-Energy Dispersive Spectroscopy (SEM-EDS) analysis of the microbialites revealed a variety of internal morphological features (Fig. 7). The microbialites were dominated by calcium carbonate crystals, with 0.5 to 3.9 atomic percent Mg. The morphology of the crystals ranged from irregular to angular, blocky, needle and triangular shaped, with calcium carbonate encrusted cyanobacteria filaments and remains of exopolymeric substances (EPS). Plateau-mushroom and pinnacle mound microbialite exhibited occasional needle shaped structures, suggesting the presence of aragonite (Fig. 7A). Remains of diatoms, such as *Navicula*, were also observed to be present in the microbialites (Fig. 7B).

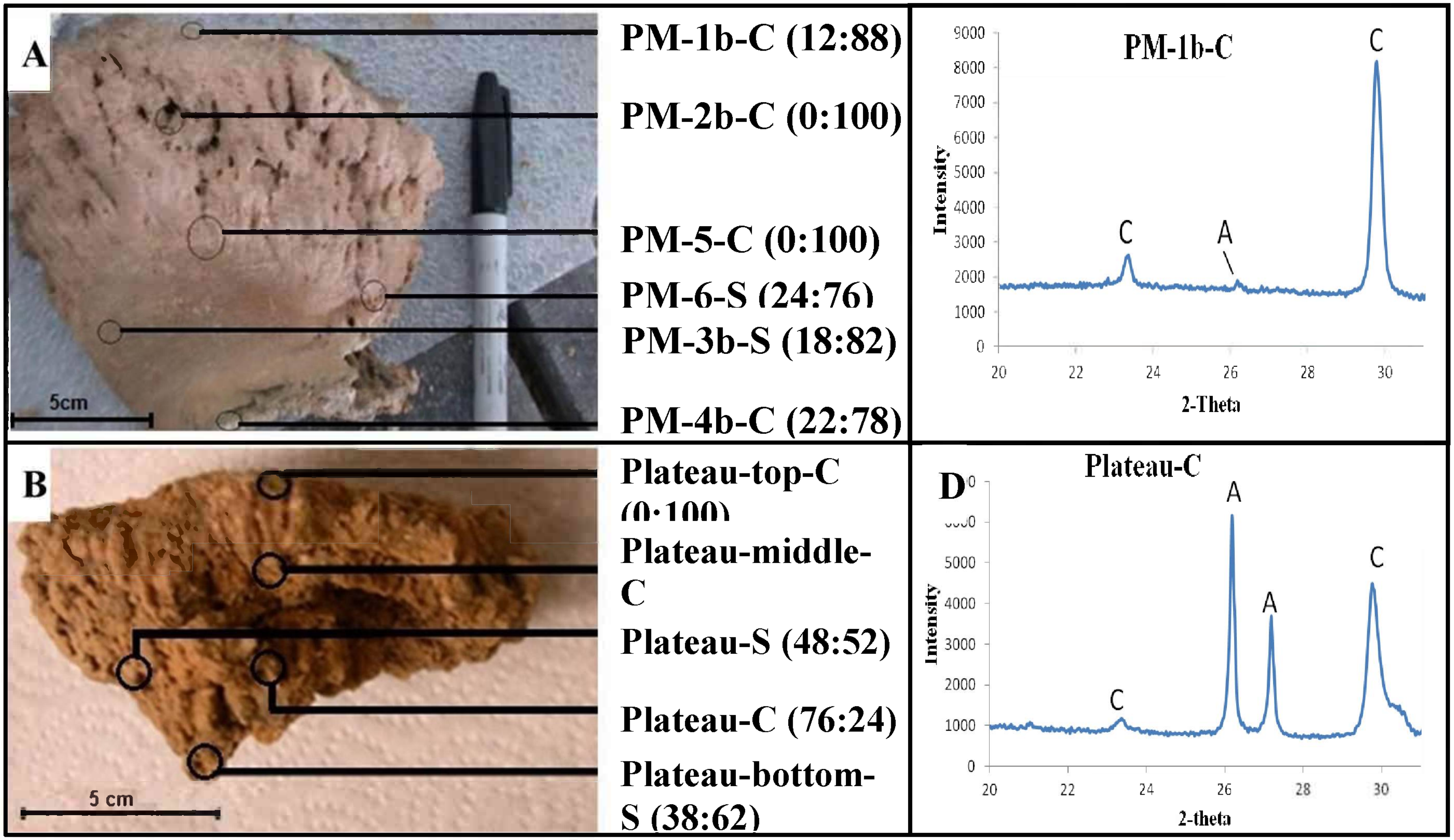

Figure 5. XRD analysis of microbialite mineralogy depicting the various positions where samples were collected for analysis. (A) Half-sectioned pinnacle mound (PM), and (B) half-sectioned plateau-mushroom shaped microbialites. Samples were collected either in the center: C, or at surface: S. Numbers to the right of the sample locations in (A) and (B) correspond to the aragonite: calcite percent ratio as determined by XRD analysis. Examples of XRD pattern for two of the samples, PM-1b-C (C) and Plateau-C (D), show peaks for aragonite and calcite, shown by the letters 'A' and 'C' respectively.

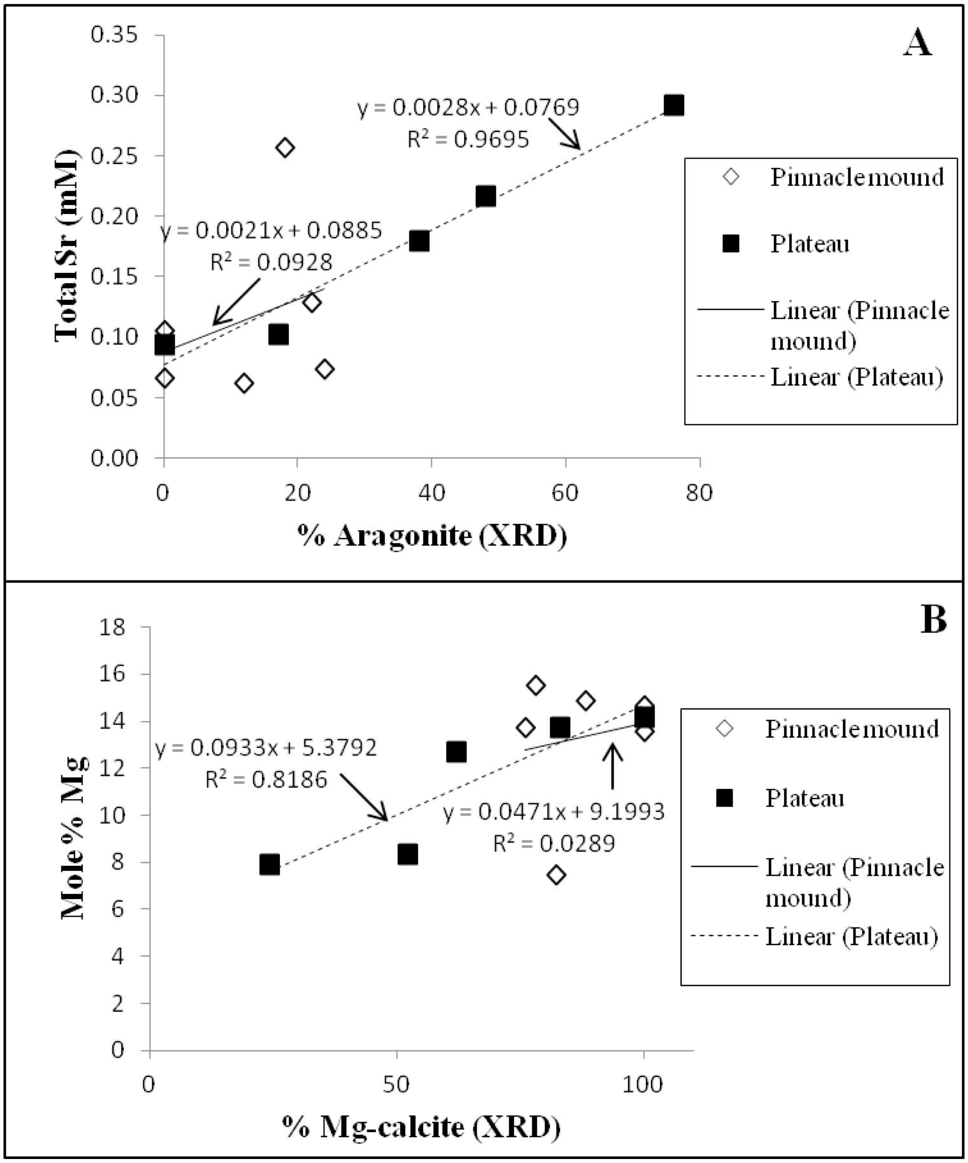

Figure 6. Correlations between elemental concentration and XRD mineralogy for pinnacle mound and plateau type microbialites. (A) Positive correlation between % aragonite, as determined by XRD, and mM of strontium, and (B) Positive correlation between % Mg-calcite, as determined by XRD, and mole % Mg.

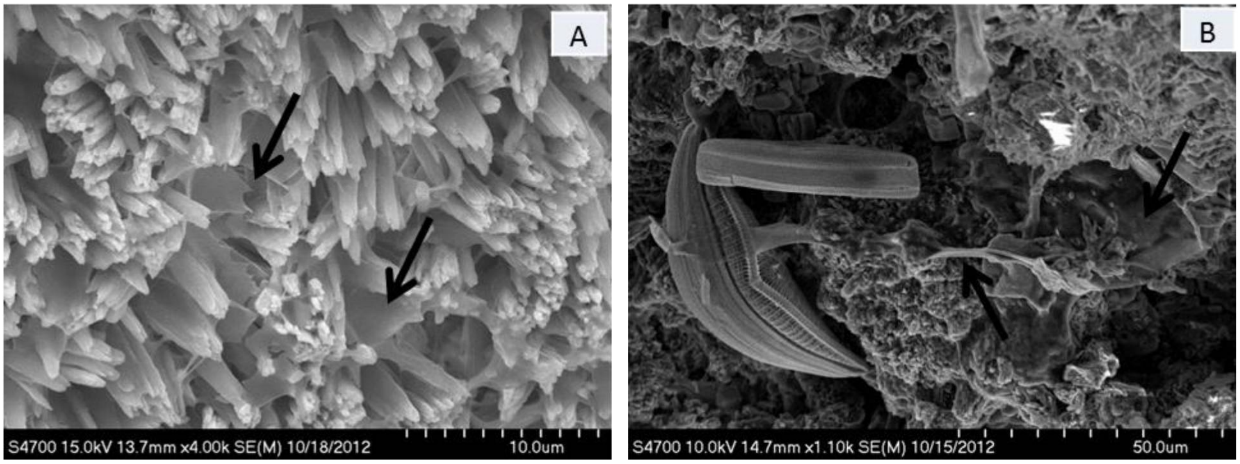

Figure 7. SEM images of the microbialite structures. (A) Acicular crystals found in the lower section of plateau-mushroom microbialite, probably indicating aragonite. Remains of EPS material is indicated by black arrows; (B) Diatoms and remains of EPS (black arrows) in the microbialites of Storrs' Lake.

Table 2. ICP-OES results for the acid digested microbialite solid samples showing the profile positions as noted in Fig. 5, the Σ mM values of Ca, Mg and Sr recovered from the digestion of 0.25 grams of solid in 10 ml of solvent. The molar ratio of Ca:Mg, and the molar Mg percentage in the samples are also shown.

	Sample	mM		Molar Ca:Mg ratio	Molar Mg:Ca ratio	Mole % Mg	Total Sr (mM)
		Ca	Mg				
Pinnacle Mound	PM-1b-C	201	35.2	5.7	0.18	14.9	0.06
	PM-2b-C	212	33.0	6.4	0.16	13.6	0.11
	PM-3b-S	207	16.7	12.4	0.08	7.5	0.26
	PM-4b-C	195	34.7	5.6	0.18	15.6	0.13
	PM-5-C	211	36.2	5.8	0.17	14.6	0.07
	PM-6-S	216	34.6	6.3	0.16	13.7	0.07
Plateau	Plateau-top-C	203	32.9	6.2	0.16	14.2	0.09
	Plateau-middle-C	219	34.5	6.3	0.16	13.7	0.10
	Plateau-bottom-S	217	32.4	6.7	0.15	12.7	0.18
	Plateau-C	215	18.3	11.7	0.09	7.9	0.29
	Plateau-S	227	21.0	10.8	0.09	8.4	0.22
	Vein Calcite	259	0.09	2742	insignificant	Insignificant	Not analyzed

2.5. Microbial Mat Diversity

Cultivation independent microbial diversity analyses were performed on the five different types of microbial mats (i.e., calcareous knob, plateau-mushroom, pinnacle mound, cauliflower-top mushroom shaped and cheesecake) isolated from Storrs' Lake. Amplicon libraries of the partial 16S rRNA genes (V1-V3 region) were sequenced and clustered into operational taxonomic units (OTUs) at 97% similarity or greater. The summary of the data obtained from the pyrosequencing method is shown in Table 3. A total of 126,576 barcoded sequences were recovered after sequence trimming and filtering by using mixed and dots filters. The mixed filter removed reads that occurred as a result of simultaneously sequencing a mixture of different DNA molecules, whereas the dots filter removed sequences with three successive nucleotide flows that recorded no incorporation. The average read length of the sequences was 471 bp. The five different mat types had between 15,782 and 31,862 sequence reads, and were clustered into OTUs by using QIIME software (Caporaso et al., 2010).

Alpha diversity index values (Table 3) were calculated based on equalized sequences and indicated that all five microbial mat types exhibited high diversity. Chao 1 values, used to estimate species richness, indicate that the plateau-mushroom microbial mat had the largest estimated diversity (20,915), whereas the lowest was for the shallow water calcareous knobs (7743). The plateau mat had also the highest Shannon index values (12.03). The Chao1 values were found to correspond well with the Shannon index and observed species values. Estimates of Good's coverage indicate that the calcareous knobs had the highest percent sequencing coverage (90.3%), with the cheesecake, cauliflower-top mushroom and pinnacle mound each showing ~80.0% coverage. The lowest value was observed in the plateau type (73.4%). The distribution of species was most even in the plateau type and closely followed by the other microbial mats as shown by the equitability values.

Among the OTUs identified, only 24% of the recovered sequences were shared between all five microbial mats suggesting each mat type had a distinctive community. The relatedness between the five microbial mat communities was also calculated by using a beta diversity analysis. A distance tree was constructed by using the unweighted pair group method with arithmetic mean (UPGMA). Jackknife analysis allowed repeated subsampling of a subset of data from each sample, providing a final robust distance tree (Fig. 8). The mat on the shallow water calcareous knob was most similar to the plateau-mushroom microbial mat in terms of microbial population, and hence these two clustered together with the cheesecake microbial mat, found on top of the gelatinous material covering the lake bottom at deeper water locations. The deep water pinnacle mound microbialite, grouped closely with the cauliflower-top mushroom microbialite. Both of these latter two types of microbialites are located further away from the western shore of the lake.

Table 3. Summary of the bacterial 16S rRNA gene diversity analysis by pyrosequencing.

	Calcareous Knobs	**Plateau**	**Cheesecake**	**Mushroom**	**Pinnacle Mound**
Sequences	31,862	30,608	28,082	20,242	15,782
OTUs[a]	5636	12,261	9096	6859	4897
Singletons[a]	3083	8118	5872	4493	3075
Doubletons[a]	852	1774	1355	1020	795
Equalized Sequences[b]	14,500	14,500	14,500	14,500	14,500
Chao1[c]	7743 (± 236)	20,915 (± 725)	15,697 (±347)	14,218 (± 262)	10,507 (±183)
Chao1 Confidence[d]	7343/ 8054	20,217/ 22,302	15,209/ 16,213	13,873/ 14,547	10,260/ 10,800
Shannon[c]	10.07 (± 0.02)	12.03 (± 0.02)	11.25 (±0.02)	10.90 (±0.01)	10.49 (± 0.01)
Observed Species[c]	3595 (± 37)	7340 (±41)	5840 (±42)	5501 (±23)	4646 (±14)
Equitability	0.82	0.92	0.88	0.87	0.86
% Coverage[e]	90.3	73.4	79.1	77.8	80.5

[a] Values calculated based on 97% similarity threshold, [b]Number of equalized sequences used to generate the diversity indices, such as Chao1, Shannon, observed species, [c]Average values ± standard deviation of diversity using 10 iterations of randomized sequences, [d]Chao1 lower and upper confidence limits at 95%, and [e]Based on Good's coverage estimator.

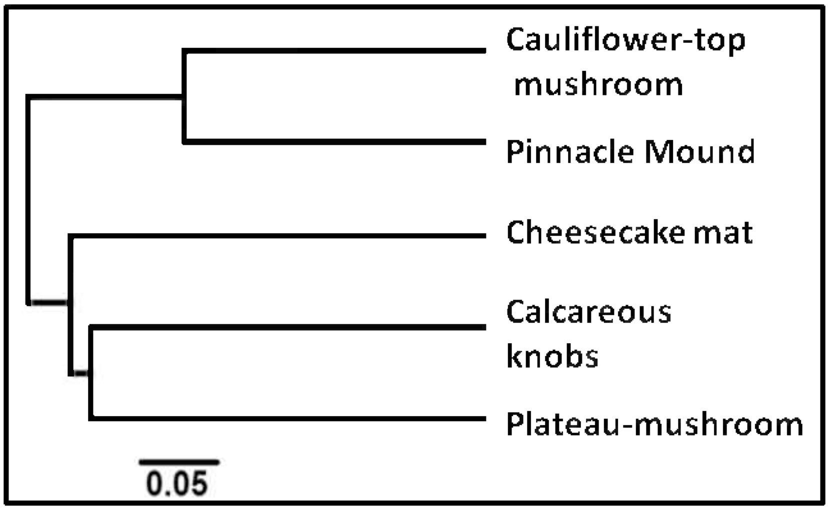

Figure 8. Dendrogram showing the relationship between the different microbial mats in Storrs' Lake acquired by Jackknifed UPGMA clustering method. The scale bar indicates the evolutionary distance between the communities and has a value of 0.05, meaning 0.05 nucleotide substitutions per sequence position.

The bacterial composition of the five mats fell into 12 major bacterial phyla, each distributed in various relative percentages among the mats (Fig. 9). Though a large amount of sequences were recovered, the analysis of only a partial length (V1-V3) of the entire 16S rRNA gene allowed identification only up to the family level of taxonomy, with few sequences reaching only to level of class or order. The cheesecake microbial mat had approximately one third (36%) of its OTUs as unclassified, which was the highest among the five mat types. The least percentage of unclassified bacteria was present in the shallow water calcareous knob (12%). Chloroflexi constituted approximately half (~46%) of the entire bacterial population identified in both the cauliflower-top mushroom and pinnacle mound mats, while calcareous knob, plateau-mushroom and cheesecake types had only 16 to 20% Chloroflexi. Within the phylum Chloroflexi, anaerobic halorespirers, Dehalococcoidaceae made up to 24% in the cauliflower-top mushroom and 21% in the pinnacle mound. Other members included several bacteria under the class Anaerolineae and order Dehalococcoidetes (family Dehalococcoidaceae falls under this order). Members of the yet uncultured OPB11 order, thought to include several green non-sulfur bacteria (Hugenholtz et al., 1998), were present in notable quantity, especially in the pinnacle mound and cheesecake mat (~9% in each). The class Deltaproteobacteria includes several SRB types, were most enriched in the shallow water calcareous knob (21%), then followed by the cheesecake mat (16%). The lowest percentage of Deltaproteobacteria occurred in the deeper water pinnacle mound (5%) and cauliflower-top mushroom (6%) mat types. The SRB family, Desulfobacteraceae, dominated the recovered Deltaproteobacteria sequences. For example, 16% of the 21% of Deltaproteobacteria were represented by Desulfobacteraceae. Other significant SRB members in this class included family Desulfohalobiaceae and Desulfovibrionaceae. The other taxa represented in all mat types included the Spirochaetes, Planctomycetes, Alphaproteobacteria, Gammaproteobacteria, Bacteriodetes and Caldithrix. Purple non-sulfur bacteria of families Rhodospirillaceae and Rhodobacteraceae belonging to the class, Alphaproteobacteria, were detected only in the plateau-mushroom and calcareous knob microbialites.

Several members of the phyla discussed above include halophilic and brackish environment bacteria, with many of them also being photosynthetic (e.g., order Chromatiales and family Chromatiaceae in the Gammaproteobacteria) and able to survive in anoxygenic environments (Imhoff, 2006). Vibrionaceae is yet another anaerobic, phototrophic Gammaproteobacteria that represented ~4% of the total calcareous knob population. Cyanobacteria were detected at low levels in all of the mat types ranging between <1.0 and 3.0%. The highest levels of cyanobacteria were observed in the shallow water calcareous knobs (~3.0%), and included families Cyanobacteriaceae, Pseudanabaenaceae, Phormidiaceae and order Chroococcales. The other mat types had less than 1.0% relative abundance of cyanobacteria. Other taxa, such as Acidobacteria, Verrucomicrobia and Lentisphareae were below 1.0%, while Firmicutes, Actinobacteria, Chlorobi, Elusimicrobia, Betaproteobacteria, and Epsilonproteobacteria were present at less than 0.1% (Supporting information, Table 2). A relatively high proportion of the mat population was classified as candidate phyla, which include bacteria that have not yet been cultured in the laboratory, but whose existence has been observed through 16S rRNA gene analysis. For example, 11 and 8.0% of the cauliflower-top mushroom and pinnacle mound population, respectively, were represented by the order HMMVPog-54, which had been identified in methane-rich biofilm communities, consisting of a high diversity of Deltaproteobacteria (Lösekann et al., 2007). Additionally, bacteria from the phyla WS3 (Dojka et al., 1998) occupied anywhere from ~0.6% in cauliflower-top mushroom shaped to a maximum of ~3.4% in calcareous knobs.

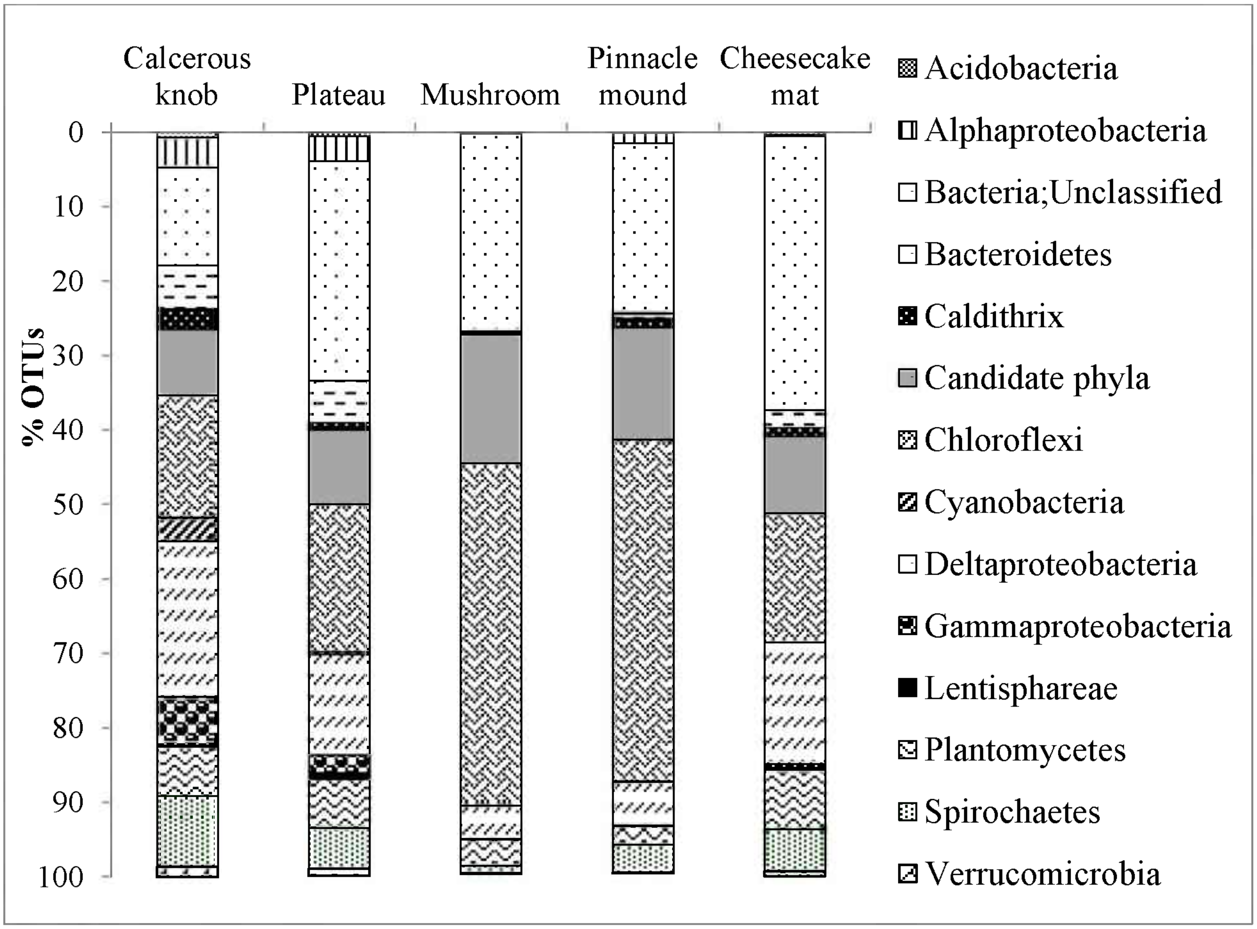

Figure 9. Relative percentage abundance of major bacterial taxa detected in five Storrs' Lake **microbial mats by analysis of partial 16S rRNA gene. Twelve different major taxa are reported along with significant percentages of candidate phyla and unclassified bacteria. Note: Plateau indicates plateau-mushroom microbialite and mushroom indicates cauliflower-top mushroom microbialite.**

3. DISCUSSION

3.1. Physical, Chemical, and Optical Characterization of Storrs' Lake Water

The water parameters, such as depth, salinity, and local turbidity, etc., in Storrs' Lake exhibited high fluctuations, primarily influenced by rainfall events (Table 1). The main body of water was always turbid during field analysis, but during and after periods of heavy rainfall, the lake possessed lower turbidity zones and a relatively clear water brackish lens adjacent to the local regions of the shoreline. The associated brackish to saline mixing zone migrates outwards into the deeper portions of the lake during periods of high meteoric water runoff (Section II-Fig. 7B). Previous studies have reported that rainfall events can cause considerable dilution of the lake water, resulting in lowered salinity and an increase in the metabolism of the phototrophic community in the lake (Pinckney et al., 1995; Paerl et al., 2003). The lowering of salinity following rain events was confirmed in the present study and we believe our May 2009 recording of 26 ppt is the lowest salinity reading ever recorded for Storrs' Lake. This lower salinity can enable gastropods and fish to occasionally colonize the lake (Garrett, 1970). The occasional presence of eukaryotic organisms can also negatively affect the growth and development of the microbialites (Awramik, 1971).

The reddish-brown color in the lake is most likely imparted by two sources: (i) the organic tannins, brought in by the brackish water draining into the lake and from other plant material, and (ii) the presence of planktonic communities of halophilic alga and bacteria, which are usually enriched in carotenoid pigments contribute to the reddish coloration (Mann and Nelson, 1989; Oren and Rodríguez-Valera, 2001). Bacteria, algae, and most organic material have a net negative surface charge, causing these particles to repel from each other, enabling the material to become colloidal and remain suspended rather than settling to the bottom. The ability of this material to remain suspended for long periods of time is demonstrated by the data in Figure 1. Living photosynthetic, planktonic microorganisms seeking sunlight for their metabolism would also swim towards the surface of the water during day. After death, they sink to the bottom, providing organic and nutrient sources to the mat community. Neumann et al. (1989) suggested that oxygen gas released from the gelatinous thrombolytic mounds also carried some of the mat material to the surface. A similar process, possibly involving other gas components as well, could be presumed to occur with the microbial mats at deeper depths. Additionally, high wind activity seen in the lake could possibly agitate the water, thus keeping the particles suspended, although the stratification observed in dissolved oxygen profiles suggests that complete and rapid vertical mixing is hindered. It should be noted that tidal flow has only a minimal effect on the lake due to limited connectivity to the ocean, though abnormal high or low tides could influence the lake parameters (Mann and Nelson, 1989). Density changes due to seasonal or diurnal warming-cooling cycles and evaporative concentration of dissolved components also conceivably play a role in water mixing. In addition to the above factors, freshwater inflow during rain and storm events would also affect the changes seen in turbidity, pH, salinity and other water parameters.

An earlier investigation of the lake water by Mann and Nelson (1989) reported only a minor and gradual stratification in the lake, noting salinities of 92, 93 and 93.5 ppt at surface, 30cm and 60 cm depths, respectively. McNeese (1988) noted that the salinity in the lake ranged from 70 to 100 ppt during the months of December to May. Brigmon et al. (2006) presented a more thorough water chemistry analysis of water samples collected from six locations close to the shore at depths between 0.1 and 0.5 m. The dissolved oxygen content from their study varied from 0 to 5 mg/L. Brigmon et al. (2008) sampled water from 12 locations in the northern section in July 2001, along a similar transect as our current investigation and previous studies (Mann and Nelson, 1989; Neumann et al., 1989). The Brigmon et al. (2008) study reported higher average dissolved oxygen values of 7.05 ± 1.05 mg/L, with salinities of 73.2 ± 4.5 ppt and pH of 8.4 ± 0.9. The salinity and dissolved oxygen were reported to follow an increasing trend from the western shore to the middle of the lake. This salinity trend was consistent with our 2013 readings when the water input from the conduit was prominent because of the heavy rainfall.
The southern sector of Storrs' Lake has been studied for its water and microbialite characteristics (Fowler, 2011; Dupraz et al., 2013). Fowler (2011) analyzed water samples from four different locations and depths in the relatively shallower southern section of the lake during June 2010. The average salinity and temperature of the lake was ~60 ppt and ~40°C, respectively, with the pH ranging from ~8.1 to ~8.6. Our 2013 measured pH values are within the same range (8.2 to 8.6) to those of Fowler's. Averaged values from the Fowler study revealed concentrations of 661 ppm Ca, 6466 ppm Mg, 26,616 ppm Na, 45,050 ppm Cl, and 6204 ppm sulfate for the southern section of the lake, while our 2013 sampling revealed less saline conditions of 727 ppm Ca, 2194 ppm Mg, 18,749 ppm Na, and 24,075 ppm Cl in the northern section.

The average turbidity was 96 (±12) and 135 (± 12) NTU, during 2012 and 2013, respectively. Likewise, the light intensity reaching depths of ~100 cm in both these years were 200-600 and 12 lumens/ft^2, respectively, ranging from 0.2 to 3% of the intensity of sunlight reaching the surface of the lake. The limited sunlight reaching the bottom was likely scattered between particles as it penetrated through the water column (Figs. 4 and 6). The penetration of any amount of sunlight to these depths was unexpected given the high turbidity of the lake water. In one recent study, cyanobacterial mats displayed maximum photosynthetic efficiency under limited light conditions (Al-Najjar et al., 2012). The wavelengths of the penetrating light are also important in governing the phototrophic system. For a cyanobacteria photosynthetic community to function, it requires light of wavelengths between 400 to 700 nm (Jørgensen et al., 1987). However, some photosynthetic communities are capable of surviving in wavelengths of the extended spectrum (ultraviolet and infrared), having developed specialized pigments and enzymes capable of using wavelength fractions (Castenholz and García-Pichel, 2000; Kühl et al., 2005). Phototrophic green sulfur bacteria, for example, contain light-harvesting antennae (chlorosomes) that make them well adapted to survive in low light conditions (Frigaard and Bryant, 2004). In the case of Storrs' Lake, the shorter wavelength UV spectrum would be expected to be more penetrating and thus, extend to deeper sections of the lake. Also, the small amount of light reaching to depths of ~1.0 m appears to be able to support a photosynthetic community on the microbialites based upon our microbial diversity results (Fig. 9).

3.2. Distribution and Mineralogy of Microbialites

The overall distribution of the microbialites and their associated microbial mats in Storrs' Lake, though described by the current and previous studies (Neumann et al., 1989; Mann and Nelson, 1989), still remains poorly understood. This ambiguity is largely a result of the high turbidity in the lake, which greatly hinders any attempt to evaluate microbialite distributions, and dense mangrove thickets that hinder entry into the lake from most shoreline regions. Mann and Nelson (1989) and Neumann et al. (1989) provide a generic base map by which to evaluate this variable in any future studies. The overall external morphology of the cauliflower-top mushroom microbialite identified in our study was similar to the previously reported plateau-mushroom type, but closer observation revealed differences in laminations and appearances. Hence, the cauliflower-top mushroom and plateau-mushroom were separately categorized in this study. In addition to the previously identified microbialites, a new morphotype of the microbialite termed 'multi-cuspate' that had limited microbial mat material is reported here. The lack of prominent microbial mat development on the surface of these multi-cuspate microbialites is not a reflection of water depth since these were located at almost the same water level as the calcareous knobs. Probably the deposition of sediment washout from the nearby Cactus Island during rain or storm events (Pratt, 1982) could have led to the partial destruction of the mats in the multi-cuspate type. However, the exact reason for the limited microbial mat cover on the multi-cuspate microbialite is still unknown.

In addition to the previously reported Mg-calcite mineralogy of the microbialite heads, we also identified considerable amount of aragonite in the pinnacle mound and plateau-mushroom microbialites (Fig. 5). All previous studies of Storrs' Lake microbialites reported only the presence of Mg-calcite and no aragonite (Hattin, 1982; Pentecost, 1989; Neumann et al., 1989; Fowler, 2011). These authors probably investigated the near shore and shallow water bulbous crust (calcareous knob) mounds, the same microbialite that we also found to contain undetectable aragonite contents. Neumann et al. (1989) examined 31 samples including the walls, nodes and laminae of calcified components of the 'heads' by XRD, but the type of the microbialite that was analyzed was not specified.

In the present study, we observed that the mole percent Mg in the carbonate minerals of the pinnacle mound type microbialites, initially decreased from the top to middle positions (PM-1b-C to PM-3b-S) but then increased, moving from the middle towards the bottom of the microbialite (PM-4b-C). The aragonite percentage decreased from PM-1b-C to PM-2b-C and

PM-5-C; and then increased again, reaching the highest values with samples PM-4b-C and PM-6-S (Figs. 7A and 7B; Table 2). Calcite can accept a higher proportion of Mg in its crystal structure relative to aragonite, especially when the calcite is precipitated in biologically mediated reactions (Weiner and Dove, 2003). Aragonite does not readily accept Mg in its crystal structure, thus the aragonite content should be inversely correlated with Mg content. The results obtained generally support this expectation, but there were clear anomalies. For example, both the aragonite percentage and Mg content reach their maximum values with sample PM-4b-C (22% aragonite and 15.1 mole percent Mg; Table 2). Therefore, the Mg/Ca ratios may be controlled by processes associated with calcite formation rather than exclusionary processes arising from the formation of aragonite. The presence of aragonite was further confirmed by the correlation seen between Sr and Mg concentration analyzed. The large radius of Sr^{2+} (1.18 Å) is more readily accepted into the aragonite structure, while the smaller Mg^{2+} ion (0.72 Å) gets preferentially incorporated as a replacement for Ca^{2+} (1.00 Å) in calcite (Krauskopf and Bird, 1967).

Alternating formation of aragonite, calcite and other minerals had been investigated previously in interpreting the formation of the microbialites and the conditions that existed during the different phases of the microbialite growth (Arp et al., 2003; Spadafora et al., 2010). The factors controlling carbonate mineral phase precipitation are complex and often interdependent. For example, oscillations in the Mg/Ca ratio of seawater are reported to induce the formation of low-Mg calcite when the ambient Mg/Ca molar ratio is <1, high-Mg calcite forms when the ratio is between 1 and 2, and high-Mg calcite plus aragonite form when the ratio is > 2 (Füchtbauer and Hardie, 1976; Hardie, 1996; Stanley, 2006). Therefore, aragonite formation should be favored during periods of high evaporation when the precipitation of Ca-enriched minerals leads to an increase in the lake Mg/Ca ratios. Other competing ions, such as sulfate, have been shown to favor aragonite precipitation by decreasing the Mg/Ca ratio to a point where calcite is destabilized and aragonite becomes dominant (Bots et al., 2011). The saturation state of the carbonate minerals in water has also been shown to be an essential component in determining microbialite development (Dupraz and Visscher, 2005). The saturation index values for current Storrs' Lake water samples obtained in the present study were evaluated using PHREEQ program with results indicating that calcite precipitation is favored over aragonite, when only equilibrium considerations are made. Though the microbial mats can drastically alter the availability of ions, such as calcium and bicarbonate in the micro-environment that they create (Dupraz et al., 2009), the characteristics of the water above them are also pivotal in controlling the mineralogy of the microbialites. The calcite and aragonite composition in the microbialites could thus be partially or completely dependent on the past composition of the lake water.

Storrs' Lake began to form around 3100 years ago due to shifting tidal sands that closed inlets. Carbon dating revealed that the microbialites began to form at least 2310 years ago (Zabielski, 1991; Paull et al., 1992). Terrestrial and evaporative processes increasingly influenced the lake water composition after the basin became isolated from direct tidal input. Given the fluctuations observed in the lake water parameters even in this three-year study, it is likely that the lake has experienced similar and possible even more drastic changes in its composition during its 3100 year history. Park (2012) reported that the sedimentation rates were influenced by hurricane and tropical storm events, leading to the 'freshening' events in the southern Fortune Hill Basin portion of the lake. Five sediment over wash episodes were reported due to hurricane events in the past 233 years in this study. Furthermore, the Park study also notes that, gypsum and halite were precipitated in the lake prior to 700 years before present, reflecting more arid conditions and higher lake salinities in the past. In addition to the strong hurricanes (category 3 or higher), the frequency for which averages once every 46.6 years, tropical events and weaker hurricanes could have freshened the lake more frequently. Our May 2009 salinity measurement (26 ppt) following a heavy rain event, indicates that freshening from meteoric water runoff has the capacity to freshen the lake to a great extent and likely occurs more frequently. Perhaps, such environmental changes with accompanied microbial population shifts (Pinckney et al., 1995; Paerl et al., 2003), were responsible for favoring the precipitation of one carbonate mineral over the other in the microbialites. The incorporation of the other calcium carbonate precipitating organisms such as gastropods (Neumann et al., 1989), foraminifera, and diatoms in the microbialite structure could also possibly influence the variation seen in mineral composition. Beach sands are occasionally washed into the lake by hurricanes, especially adjacent to low-lying coastal dunes along East Beach and Dim Bay (Park, 2012). Wind-blown detritus may conceivably be carried across the entire lake during intense storm activity, and thus may include fragments of foraminifera tests which are common in the sediments of East Beach. These external sources thus can possibly contribute to the mineralogy of the microbialites.

In addition to the overlying and pore-water chemistry, other factors influence the mineralogy and morphology of the carbonate material. For example, the extracellular polymeric substances (EPS) produced by the microorganisms within the microbial mat have been identified as a key component in controlling the shape of the crystals (Fig. 7; Braissant et al., 2007). The microbial populations present in microbial mats also control the mineralogy of the microbialites. Both SRB and cyanobacteria, the two main groups of microbes involved in carbonate mineralization are capable of producing a variety of carbonate minerals, such as Mg-calcite, dolomite, aragonite, and intermediate to amorphous forms of some of these minerals (Thompson and Ferris, 1990; Van Lith et al., 2003). Microbialites from Lake Van, Turkey produce both aragonite and Mg-calcite, with the former being suggested to have been directly precipitated by cyanobacterial and heterotrophic bacterial activity (Kempe et al., 1991; López-García et al., 2005).

Diagenesis and recrystallization may also influence the mineralogy of the microbialites. The observed zoning of a Mg-calcite rich core zone surrounded by more aragonite enriched exterior zones (Fig. 5; Table 2) may reflect diagenetic transformation of aragonite to calcite over time, especially if the cores of the pinnacle mound types represent older microbialite growth. Diagenetic changes that occur, if significant, would render the microbialite structures less useful for paleoenvironmental investigations. The deeper, aragonite-containing sections of the pinnacle mound microbialite structure exist near a point where the structure (sample PM-4b-C) could have been buried under the organic-rich sediment ooze at the bottom of the lake and not directly exposed to the water column above. The causes for the variation in microbialite mineralogy in Storrs' Lake thus remain unknown, but may likely involve a combination of diagenesis, alterations in lake water composition, and temporal changes in microbial populations.

3.3. Microbial Mat Diversity

Earlier studies of Storrs' Lake microbialites have described the physical nature of the microbial mat and microbialites (Neumann et al., 1989; Mann and Nelson, 1989; Paerl et al., 2003; Dupraz et al., 2006). Few genetic studies have been performed to investigate the microbial diversity of the mats and even those examinations focused specifically on the near-shore and shallow water calcareous knob (Brigmon et al., 2006). The current effort provided a more comprehensive coverage of the microbial population in mats on the surface of four different microbialites and the cheesecake mat that is associated with the lake bottom sediments not with the microbialite heads. Although funding limitations prevented an analysis of duplicate morphological samples to examine the horizontal variation within a mat type, we were able to generate a more comprehensive survey of the microbes present within the different mat types (Table 3). Clustering analysis revealed that the cauliflower-top mushroom and pinnacle mound clustered together in the UPGMA tree indicating that the bacterial diversity and abundances were phylogenetically comparable between these two types (Fig. 8). The cheesecake mat, not associated with the microbialite heads, was positioned intermediate between these two microbialite pairs in the phylogenetic tree. On the other hand, the calcareous knob and plateau-mushroom type grouped together. The cheesecake mat was collected from a location (labeled as 'ooze' in Fig. 2) between the calcareous knob-plateau and the off shore cauliflower top-pinnacle mound pair, thus potentially representing a transition microbial population between the two groups. The bacterial population in the calcareous knob mat had the highest coverage (90%) indicating that ~10% of the sequences were not identified. A high percentage of the bacterial population (11 to 36%) in all mat types was unknown, suggesting that potentially novel and previously unidentified microorganisms are present in the microbial mats (Fig. 9).

In Storrs' Lake microbial mats, the amount of cyanobacteria detected, especially in the deeper mats was extremely low (e.g., 0.01% in the pinnacle mound). The turbidity in the lake and consequently, the lower amount of sunlight (Fig. 4) reaching the deeper portions, is the most likely explanation for this lack of abundant light dependent cyanobacteria on the pinnacle mounds. Hypersaline conditions could also contribute to the reduced presence of cyanobacteria (Paerl et al., 2003; Marcarelli et al., 2006). Though these phototrophic microorganisms are capable of growing in hypersaline conditions and generally have a wide range of salt tolerance (Green et al., 2008), the activity and population can be negatively affected during times of peak hypersaline conditions (Nübel et al., 2000; Abed et al., 2007). This negative effect of hypersalinity has been shown to occur even in microbial mats (Pinckney and Reid, 1997). Only the shallow water calcareous knob display any appreciable cyanobacterial population in our study (~3%), while they were almost negligible in the deeper cheesecake, cauliflower-top mushroom and pinnacle mound mats. In contrast, anaerobic photosynthesizers of phyla Chloroflexi (e.g., green non-sulfur bacteria) were identified even in these deeper mats in spite of the low amounts of sunlight received at these depths.

The dissolved oxygen content at the deeper sections of Storrs' Lake was low, thus potentially promoting the growth of anoxygenic phototrophic bacteria, even under limited light conditions. Members of purple sulfur bacteria of the class, Gammaproteobacteria are prevalent in the shallow calcareous knobs, can oxidize hydrogen sulfide produced by SRB, and in turn, provide sulfate for use by SRB. The presence of these phototrophs are indicative that light, albeit in low amounts, reached the lake bottom with enough intensity to stimulate their metabolic activity. In addition, both colorless and purple sulfur bacteria can chemosynthesize organic carbon by using CO_2 (Gammaproteobacteria; Van Gemerden, 1993). These organisms can oxidize sulfides produced by SRB respiration, thus cycling sulfur and carbon within the microbial mat system. Fermenters, such as members of class Phycisphaerae (maximum of 7% in the cheesecake microbial mat), and phyla Spirochaetes were also present in the microbial mats, indicating the metabolically diverse population that are present (Magot et al., 1997; Fukunaga et al., 2009; Dubinina et al., 2011; Lee et al., 2014). Fermentation is an important component of the microbialites' carbon cycle as they can obtain energy by oxidizing the organic acids produced by the phototrophs.

In a typical microbial mat, the photosynthetic cyanobacteria act as the primary producer, providing carbon sources for the other inhabitants in the mat (Dupraz and Visscher, 2005). With the apparent lack of cyanobacteria in the deeper mats at Storrs' Lake, organic electron donors for the heterotrophic community members must be provided by other sources. In addition to the anoxygenic photosynthetic bacteria, planktonic microorganisms, along with plant material, eventually fall to the bottom of the lake and microbialite heads. These settling organic carbon particles can serve as sources of energy and carbon to the heterotrophic members of the mat community. For example, fragments of leaf material were found in the gelatinous sediments on the bottom of the lake. Dissolved tannins that color the lake water, could also contribute as a minor carbon source.

3.4. Microbial Influence on Carbonate Mineral Precipitation and Lithification

The microbialites at the deeper locations were suggested to be inactive or 'sub-fossilized' (Dupraz et al., 2006; Fowler, 2011; Dupraz et al., 2013). Though the presence of key carbonate mineral precipitating microbial communities in all mat types including anaerobic phototrophs and sulfate-reducers (except for cyanobacteria) was noted (Fig. 9), whether these microorganisms are actively contributing to the precipitation on the microbialite head is not certain. In the absence of cyanobacteria, carbonate mineralization can potentially occur with the activity of the SRB and anoxygenic phototrophs (Visscher et al., 2000; Dupraz and Visscher, 2005). Considering the possibility that only shallow water calcareous knobs microbialites are the 'actively' forming microbialites, the SRB families in class Deltaproteobacteria (~18%) was still higher than the phylum Cyanobacteria (~3.2%) in these mats. This large representation of Deltaproteobacteria indicates that the SRB may be playing an active role in carbonate mineral precipitation in these mats. As the SRB and anoxygenic phototrophs were present in significant percentages in all mat types, it is possible that these two groups dominantly influence carbonate mineralization. The role of SRB in the precipitation of carbonate minerals in microbialites has been verified by using the $^{35}SO_4^{2-}$ coated Ag-foil technique, where maximum SRB activity has been shown to precipitate aragonite laminae (Visscher et al., 2000). In addition to the abundance of microorganisms capable of carbonate mineral precipitation, knowledge of their metabolic rates is also important to better understand the actual mechanism(s) involved (Dupraz and Visscher, 2005). Our study further highlights the complexity of the microbial mat system in the Storrs' Lake environment, where several biogeochemical components are suspected to play an interactive role in the precipitation and lithification of the microbialites.

4. CONCLUSIONS

Our research builds upon previous analysis and interpretation of: (i) the water parameters, (ii) microbialite distribution and mineralogy, and (iii) the microbial mat composition through the application of molecular tools. One of our main findings was the identification of aragonite as a significant part of the microbialite mineralogical composition in the plateau-mushroom and pinnacle mound microbialites. Secondly, a new microbialite morphology 'multi-cuspate' was discovered near to the Cactus Island and described. Thirdly, our molecular diversity analysis of the microbial mats revealed that the cyanobacterial population was generally low and were almost negligible in certain deeper water microbial mats. The lack of prominent cyanobacteria is likely explained by the less intense sunlight reaching those depths. On the other hand, a plethora of anaerobic phototrophs existed in the deeper mats, indicating that factors along with light, such as oxygen availability or the lack of it at those depths, likely affected the distribution of these phototrophs. Though most microbialites are found in relatively clear waters, the Storrs' Lake microbialites present an anomaly to this trend as they exist under highly turbid and low light conditions. Hence, these and other uncommon examples further necessitate the exploration of potential unique and diverse environments under which microbialites may be found. Investigations on Storrs' Lake microbialites has potential implications for understanding life on other planets, origination of life on earth, and also in applied areas, such as carbon sequestration, where microbial activity could enhance the conversion of CO_2 gas in to carbonate minerals. A better knowledge of the strongly interconnected components in such microbialite systems could also provide useful clues on the development and survival of these structures under changing climatic and environmental conditions in the past and present, and as a possible indicator of local or global climate in the future.

REFERENCES

Abed RM, Kohls K, de Beer D (2007) Effect of salinity changes on the bacterial diversity, photosynthesis and oxygen consumption of cyanobacterial mats from an intertidal flat of the Arabian Gulf. *Environmental Microbiology* **9**, 1384-1392.

Al-Najjar MA, de Beer D, Kühl M, Polerecky L (2012) Light utilization efficiency in photosynthetic microbial mats. *Environmental Microbiology* **14**, 982-992.

Arp G, Reimer A, Reitner J (2003) Microbialite formation in seawater of increased alkalinity, Satonda Crater Lake, Indonesia. *Journal of Sedimentary Research* **73**, 105-127.

Awramik SM (1971) Precambrian stromatolite diversity: reflection on metazoan appearance. *Science* **174**, 825–827.

Bailey JV, Orphan VJ, Joye, SB, Corsetti, FA (2009) Chemotrophic microbial mats and their potential for preservation in the rock record. *Astrobiology* **9**, 843-859.

Bots P, Benning L, Rickaby R, Shaw S (2011) The role of SO_4 in the switch from calcite to aragonite seas. *Geology* **39**, 331-334.

Boyd CE (2002) Specific Conductance, Alternative Salinity Measurement. *The Advocate*, 70-71.

Braissant O, Decho AW, Dupraz C, Glunk C, Przekop KM, Visscher PT (2007) Exopolymeric substances of sulfate-reducing bacteria: Interactions with calcium at alkaline pH and implication for formation of carbonate minerals. *Geobiology* **5**, 401-411.

Brigmon RL, Smith G, Morris P, Byrne M, McKay D (2006) Microbial Ecology in Modern Stromatolites from San Salvador, Bahamas. In *Proceedings of the Twelfth Symposium on the Geology of the Bahamas and Other Carbonate Regions* (eds. Davis RL, Gamble DW), 1-12.

Brigmon RL, Morris P, Smith G (2008) Evaporite microbial films, mats, microbialites and stromatolites. In *Links Between Geological Processes, Microbial Activities & Evolution of Life* (eds. Dilek Y, Furnes H, Muehlenbachs K) Springer, 197-235.

Burne RV, Moore LS (1987) Microbialites: organosedimentary deposits of benthic microbial communities. *Palaios* **2**, 241-254.

Caporaso JG, Kuczynski J, Stombaugh J, Bittinger K, Bushman FD, Costello EK, Fierer N, Pena AG, Goodrich JK, Gordon JI (2010) QIIME allows analysis of high-throughput community sequencing data. *Nature Methods* **7**, 335-336.

Castenholz RW, García -Pichel F (2002) Cyanobacterial responses to UV-radiation. In *The ecology of cyanobacteria* (eds. Whitton BA, Potts M). Kluwer, Dordrecht, 591-611.

Decho AW, Visscher PT, Reid RP (2005) Production and cycling of natural microbial exopolymers (EPS) within a marine stromatolite. *Palaeogeography, Palaeoclimatology, Palaeoecology,* **219**, 71-86.

DeSantis TZ, Hugenholtz P, Larsen N, Rojas M, Brodie EL, Keller K, Huber T, Dalevi D, Hu P, Andersen GL (2006) Greengenes, a chimera-checked 16S rRNA gene database and workbench compatible with ARB. *Applied and Environmental Microbiology* **72**, 5069-5072.

Dojka MA, Hugenholtz P, Haack SK, Pace NR (1998) Microbial diversity in a hydrocarbon-and chlorinated-solvent-contaminated aquifer undergoing intrinsic bioremediation. *Applied and Environmental Microbiology* **64**, 3869-3877.

Dubinina G, Grabovich M, Leshcheva N, Rainey FA, Gavrish E (2011) *Spirochaeta perfilievii sp. nov.*, an oxygen-tolerant, sulfide-oxidizing, sulfur-and thiosulfate-reducing spirochaete isolated from a saline spring. *International Journal of Systematic and Evolutionary Microbiology* **61**, 110-117.

Dupraz C, Fowler A, Tobias C, Visscher PT (2013) Stromatolitic knobs in Storr's Lake (San Salvador, Bahamas): a model system for formation and alteration of laminae. *Geobiology* **11**, 527-548.

Dupraz C, Pattisina R, Verrecchia EP (2006) Translation of energy into morphology: simulation of stromatolite morphospace using a stochastic model. *Sedimentary Geology* **185**, 185-203.

Dupraz C, Reid RP, Braissant O, Decho AW, Norman RS, Visscher PT (2009) Processes of carbonate precipitation in modern microbial mats. *Earth-Science Reviews* **96**, 141-162.

Dupraz C, Visscher PT (2005) Microbial lithification in marine stromatolites and hypersaline mats. *Trends in Microbiology* **13**, 429-438.

Dupraz C, Visscher PT, Baumgartner L, Reid R (2004) Microbe–mineral interactions: early carbonate precipitation in a hypersaline lake (Eleuthera Island, Bahamas). *Sedimentology* **51**, 745-765.

Ferris FG, Thompson JB, Beveridge TJ (1997) Modern freshwater microbialites from Kelly Lake, British Columbia, Canada. *Palaios* **12**, 213-219.

Fowler AJ (2011) Stromatolitic Knobs in Storr's Lake, San Salvador, Bahamas: Insights into Organomineralization, Master's Thesis, University of Connecticut.

Freytet P, Verrecchia EP (1998) Freshwater organisms that build stromatolites: a synopsis of biocrystallization by prokaryotic and eukaryotic algae. *Sedimentology* **45**, 535-563.

Frigaard NU, Bryant DA (2004) Seeing green bacteria in a new light: genomics-enabled studies of the photosynthetic apparatus in green sulfur bacteria and filamentous anoxygenic phototrophic bacteria. *Archives of Microbiology* **182**, 265-276.

Füchtbauer H, Hardie L (1976) Experimentally determined homogeneous distribution coefficients for precipitated magnesian calcites: application to marine carbonate cements. *Geological Society of America Abstracts with Programs* **8**, 877.

Fukunaga Y, Kurahashi M, Sakiyama Y, Ohuchi M, Yokota A, Harayama S (2009) Phycisphaera mikurensis gen. nov., sp. nov., isolated from a marine alga, and proposal of *Phycisphaeraceae* fam. nov., *Phycisphaerales* ord. nov. and *Phycisphaerae classis* nov. in the phylum *Planctomycetes*. *The Journal of General and Applied Microbiology* **55**, 267-275.

Furman FC, Woody RE, Rasberry MA, Keller DJ, Gregg, JM (1993) Carbonate and evaporite mineralogy of Holocene (<1900 RCYBP) sediments at Salt Pond, San Salvador Island, Bahamas: Preliminary study. In *Proceedings of the Sixth Symposium on the Geology of the Bahamas* (ed. White B), 47-54.

Garrett P (1970) Phanerozoic stromatolites: noncompetitive ecologic restriction by grazing and burrowing animals. *Science* **169**, 171-173.

Glunk C, Dupraz C, Braissant O, Gallagher KL, Verrecchia EP, Visscher PT (2011) Microbially mediated carbonate precipitation in a hypersaline lake, Big Pond (Eleuthera, Bahamas). *Sedimentology* **58**, 720-736.

Green SJ, Blackford C, Bucki P, Jahnke LL, Prufert-Bebout L (2008) A salinity and sulfate manipulation of hypersaline microbial mats reveals stasis in the cyanobacterial community structure. *The ISME Journal* **2**, 457-470.

Haas BJ, Gevers D, Earl AM, Feldgarden M, Ward DV, Giannoukos G, Ciulla D, Tabbaa D, Highlander SK, Sodergren E, Methe B, DeSantis TZ, Human Microbiome Consortium, Petrosino JF, Knight R, Birren BW (2011) Chimeric 16S rRNA sequence formation and detection in Sanger and 454-pyrosequenced PCR amplicons. *Genome Research* **21**, 494-504.

Hardie LA (1996) Secular variation in seawater chemistry: An explanation for the coupled secular variation in the mineralogies of marine limestones and potash evaporites over the past 600 my. *Geology* **24**, 279-283.

Hattin DE (1982) Holocene Lithification of carbonate Sediments San Salvador Island, Bahamas, In *Proceedings of the First Symposium on the Geology of the Bahamas*, 41-51.

Hofmann H, Grey K, Hickman A, Thorpe R (1999) Origin of 3.45 Ga coniform stromatolites in Warrawoona Group, Western Australia. *Geological Society of America Bulletin* **111**, 1256-1262.

Hugenholtz P, Pitulle C, Hershberger KL, Pace NR (1998) Novel division level bacterial diversity in a Yellowstone hot spring. *Journal of Bacteriology* **180**, 366-376.

Imhoff J (2006) The Chromatiaceae. *The Prokaryotes* **6**, 846-873.

Jones B, Renaut RW, Rosen MR (1998) Microbial biofacies in hot-spring sinters; a model based on Ohaaki Pool, North Island, New Zealand. *Journal of Sedimentary Research* **68**, 413-434.

Jørgensen B, Cohen Y, Des Marais D (1987) Photosynthetic action spectra and adaptation to spectral light distribution in a benthic cyanobacterial mat. *Applied and Environmental Microbiology* **53**, 879-886.

Kempe S, Kazmierczak J, Landmann G, Konuk T, Reimer A, Lipp A (1991) Largest known microbialites discovered in Lake Van, Turkey. *Nature* **349**, 605-608.

Krauskopf KB, Bird DK (1984) Introduction to geochemistry (third edition). McGraw-Hill New York.

Kühl M, Chen M, Ralph PJ, Schreiber U, Larkum AW (2005) Ecology: a niche for cyanobacteria containing chlorophyll d. *Nature* **433**, 820-820.

Laval B, Cady SL, Pollack JC, McKay CP, Bird JS, Grotzinger JP, Ford DC, Bohm HR (2000) Modern freshwater microbialite analogues for ancient dendritic reef structures. *Nature* **407**, 626-629.

Lee JZ, Burow LC, Woebken D, Everroad RC, Kubo MD, Spormann AM, Weber PK, Pett-Ridge J, Bebout BM, Hoehler TM (2014) Fermentation couples *Chloroflexi* and sulfate-reducing bacteria to Cyanobacteria in hypersaline microbial mats. *Frontiers in Microbiology* **5**, 1-17.

Ley RE, Harris JK, Wilcox J, Spear JR, Miller SR, Bebout BM, Maresca JA, Bryant DA, Sogin ML, Pace NR (2006) Unexpected diversity and complexity of the Guerrero Negro hypersaline microbial mat. *Applied and Environmental Microbiology* **72**, 3685-3695.

Lim DS, Laval BE, Slater G, Antoniades D, Forrest AL, Pike W, Pieters R, Saffari M, Reid D, Schulze-Makuch D, Andersen D, McKay CP (2009) Limnology of Pavilion Lake, BC, Canada-Characterization of a microbialite forming environment. *Fundamental and Applied Limnology/Archiv für Hydrobiologie* **173**, 329-351.

López-García P, Kazmierczak J, Benzerara K, Kempe S, Guyot F, Moreira D (2005) Bacterial diversity and carbonate precipitation in the giant microbialites from the highly alkaline Lake Van, Turkey. *Extremophiles* **9**, 263-274.

Lösekann T, Knittel K, Nadalig T, Fuchs B, Niemann H, Boetius A, Amann R (2007) Diversity and abundance of aerobic and anaerobic methane oxidizers at the Haakon Mosby Mud Volcano, Barents Sea. *Applied and Environmental Microbiology* **73**, 3348-3362.

Lozupone C, Knight R (2005) UniFrac: a new phylogenetic method for comparing microbial communities. *Applied and Environmental Microbiology* **71**, 8228-8235.

Magot M, Fardeau ML, Arnauld O, Lanau C, Ollivier B, Thomas P, Patel B (1997) *Spirochaeta smaragdinae sp. nov.*, a new mesophilic strictly anaerobic spirochete from an oil field. *FEMS Microbiology Letters* **155**, 185-191.

Mann CJ, Nelson WM (1989) Microbialitic structures in Storr's lake, San Salvador Island, Bahama Islands. *Palaios* **4** 287-293.

Marcarelli AM, Wurtsbaugh WA, Griset O (2006) Salinity controls phytoplankton response to nutrient enrichment in the Great Salt Lake, Utah, USA. *Canadian Journal of Fisheries and Aquatic Sciences* **63**, 2236-2248.

McNeese LR (1988) Modern Stromatolites in hypersaline Storr's Lake, San Salvador, Bahamas, Master's Thesis, University of North Carolina Chapel Hill.

Muyzer G, de Waal EC, Uitterlinden AG (1993) Profiling of complex microbial populations by denaturing gradient gel electrophoresis analysis of polymerase chain reaction-amplified genes coding for 16S rRNA. *Applied and Environmental Microbiology* **59**, 695-700.

Neumann C, Bebout B, McNeese L, Paull C, Paerl H (1988) Modern stromatolites and associated mats: San Salvador, Bahamas. In *Proceedings of the Fourth Symposium on The Geology of Bahamas,* (ed. Mylroie JE), 243-254.

Nübel U, Garcia-Pichel F, Clavero E, Muyzer G (2000) Matching molecular diversity and ecophysiology of benthic cyanobacteria and diatoms in communities along a salinity gradient. *Environmental Microbiology* **2**, 217-226.

Oren A, Rodriguez-Valera F (2001) The contribution of halophilic Bacteria to the red coloration of saltern crystallizer ponds (1). *FEMS Microbiology Ecology* **36**, 123-130.

Paerl HW, Steppe TF, Buchan KC, Potts M (2003) Hypersaline cyanobacterial mats as indicators of elevated tropical hurricane activity and associated climate change. *AMBIO: A Journal of the Human Environment* **32**, 87-90.

Park LE (2012) Comparing two long-term hurricane frequency and intensity records from San Salvador Island, Bahamas. *Journal of Coastal Research* **28**, 891-902.

Paull C, Neumann A, Bebout B, Zabielski V, Showers W (1992) Growth rate and stable isotopic character of modern stromatolites from San Salvador, Bahamas. *Palaeogeography, Palaeoclimatology, Palaeoecology* **95**, 335-344.

Pentecost A (1989) Observations on the Scytonema mats of San Salvador, Bahamas. In *Proceedings of the Fourth Symposium on The Geology of Bahamas* (ed. Mylroie JE), 295-302.

Pinckney J, Paerl H, Bebout B (1995) Salinity control of benthic microbial mat community production in a Bahamian hypersaline lagoon. *Journal of Experimental Marine Biology and Ecology* **187**, 223-237.

Pinckney J, Reid R (1997) Productivity and community composition of stromatolitic microbial mats in the Exuma Cays, Bahamas. *Facies* **36**, 204-207.

Pratt BR (1982) Stromatolite decline-a reconsideration. *Geology* **10**, 512-515.

Reid RP, Visscher PT, Decho AW, Stolz JF, Bebout B, Dupraz C, Macintyre I, Paerl H, Pinckney J, Prufert-Bebout L (2000) The role of microbes in accretion, lamination and early lithification of modern marine stromatolites. *Nature* **406**, 989-992.

Riding R (1991) Calcareous algae and stromatolites. Springer-Verlag Berlin.

Riding R (2000) Microbial carbonates: the geological record of calcified bacterial–algal mats and biofilms. *Sedimentology* **47**, 179-214.

Saini-Eidukat B, Yahin A (1999) Web-phreeq: a WWW instructional tool for modeling the distribution of chemical species in water. *Computers and Geosciences* **25**, 347-353.

Skyring G, Bauld J (1990) Microbial mats in Australian coastal environments. *Advances in Microbial Ecology* **11**, 461-498.

Sommers M, Awramik S, Woo K (2000) Evidence for initial calcite-aragonite composition of Lower Algal Chert Member ooids and stromatolites, Paleoproterozoic Gunflint Formation, Ontario, Canada. *Canadian Journal of Earth Sciences* **37**, 1229-1243.

Spadafora A, Perri E, McKenzie JA, Vasconcelos C (2010) Microbial biomineralization processes forming modern Ca: Mg carbonate stromatolites. *Sedimentology* **57**, 27-40.

Stanley SM (2006) Influence of seawater chemistry on biomineralization throughout Phanerozoic time: Paleontological and experimental evidence. *Palaeogeography, Palaeoclimatology, Palaeoecology* **232**, 214-236.

Thompson J, Ferris F (1990) Cyanobacterial precipitation of gypsum, calcite, and magnesite from natural alkaline lake water. *Geology* **18**, 995-998.

Van Gemerden H (1993) Microbial mats: a joint venture. *Marine Geology* **113**, 3-25.

Van Lith Y, Warthmann R, Vasconcelos C, Mckenzie JA (2003) Sulphate-reducing bacteria induce low-temperature Ca-dolomite & high Mg-calcite formation. *Geobiology* **1**, 71-79.

Vasconcelos C, McKenzie JA (1997) Microbial mediation of modern dolomite precipitation and diagenesis under anoxic conditions (Lagoa Vermelha, Rio de Janeiro, Brazil). *Journal of Sedimentary Research* **67**, 378-390.

Visscher PT, Reid RP, Bebout BM (2000) Microscale observations of sulfate reduction: correlation of microbial activity with lithified micritic laminae in modern marine stromatolites. *Geology* **28**, 919-922.

Visscher PT, Stolz JF (2005) Microbial mats as bioreactors: populations, processes, and products. *Palaeogeography, Palaeoclimatology, Palaeoecology* **219**, 87-100.

Weiner S, Dove PM (2003) An overview of biomineralization processes and the problem of the vital effect. *Reviews in Mineralogy and Geochemistry* **54**, 1-29.

Weisburg WG, Barns SM, Pelletier DA, Lane DJ (1991) 16S ribosomal DNA amplification for phylogenetic study. *Journal of Bacteriology* **173**, 697-703.

Zabielski VP (1991) The depositional history of Storr's Lake San Salvador Island, Bahamas, Doctoral dissertation, University of North Carolina-Chapel Hill.

SECTION VII. EDUCATION AND TRAINING IN THE UNDERGRADUATE CURRICULUM: CARBONATE SYSTEMS AND CARBON SEQUESTRATION

1. AQUEOUS CARBONATE PROCESSES OCCURRING AT MARAMEC SPRING PARK, MISSOURI

The Maramec Spring system lends itself as a natural outdoor laboratory to introduce college undergraduate students to both field analytical techniques and carbonate geochemistry. We have taken advantage of this opportunity to bring 157 students to Maramec Spring Park to study this system during the 2010 through 2012 academic years (43 students in 2010, 59 in 2011, and 55 in 2012). Graduate and undergraduate students who had previously taken the course were also employed to assist the new students with the field based activities. Students measured water chemical parameters, evaluated the importance of the carbonate minerals in the carbon cycle, and were posed questions to the importance of this system as an analog in understanding processes influencing the sequestration of anthropogenic carbon dioxide. The concepts and activities associated with the field trip activities have been included in power point lectures for regular classroom lectures. We have also incorporated some simple experiments devised for this project as part of our classroom demonstrations (e.g., measuring pH changes associated with the uncapping of a bottle of seltzer water and the acid neutralizing effect of water-mineral interactions).

Maramec Spring Park is operated by the James Foundation in St. James, Missouri, and is accessed by an 18 mile drive from the Missouri University of Science and Technology campus in Rolla, Missouri. It can thus can be visited and studied by students in a one-day laboratory exercise. This site was used as a research-based laboratory project for students enrolled in introductory geochemistry (GEOL 275), a course that is taught once each year in the spring semester. Enrollment numbers have been increasing over the past half-decade and the class attracts a diverse array of students from different campus programs including Geology & Geophysics, Geologic Engineering, Petroleum Engineering, Environmental Engineering, Mining Engineering, Chemistry, and Biology. Students from all programs take this course following their 1st semester of introductory college chemistry.

Because of the high enrollment numbers, students were divided into two near equal groups each year to visit the laboratory site, using successive Friday and Saturday field trips. Students had been lectured on carbonate geochemistry topics during the semester including topics of aqueous carbonate speciation, interaction of atmospheric CO_2 with aqueous systems, pH changes associate with carbonate chemistry, and saturation limits associated with carbonate minerals. Climate change and methods of investigating the geologic record of long term climate using the principals of isotope chemistry were also lectured upon each semester after the field trip. Students were also introduced to the importance of calcium carbonate precipitation and dissolution processes with respect to CO_2 sequestration efforts.

The student's first objective upon visiting the site was to examine the pH change that occurs following the opening of a bottle of seltzer water (carbonated water). This experiment allows the student to examine a very simplified chemical system under well-controlled conditions where they can observe the effect of losing confining pressure (which they induced by opening the bottle), CO_2 loss (which they see in the bubbling of the system), and pH change (measured with a portable pH meter). Most students can make the analogy between the decrease in pressure in the seltzer water system and the upwelling of water from ≥190 feet at Maramec Spring. Following the preliminary seltzer water experiment, students recorded various water measurements from the Maramec Spring system including pH, Eh, conductivity, temperature, alkalinity, Ca-Mg hardness (concentration), and turbidity of suspended particulate material (Figure 1). All instruments requiring standardization (e.g., pH and conductivity probes) were calibrated with their respective commercial laboratory standards prior to use and then field checked throughout the day by the students so that they can monitor for instrument drift. Students worked in teams of four, taking turns in conducting stream measurements and recording the data. Each group then posted their data set on the class Blackboard site so that all students could observe the data set for all respective groups.

The students were then assigned a series of nine questions (below) following the field component of the exercise. Students then turned their answers as a laboratory report that was graded and returned to them. The answers to the project assignments were discussed in class and student comments were shared and discussed with each subsequent class year.

The questions included:

1) Record your observations on the effect of removing the confining pressure from the seltzer water/tonic water bottle: record both visible changes and pH.
2) Discusses the experimental methods used and how instruments were calibrated.
3) Identify changes that occur in the Maramec Spring water system as the water moves downstream.
4) Compare your observations between the seltzer/tonic water and Maramec Spring.
5) Write a charge and chemical balanced reaction – or coupled series of reactions – that explain pH changes in the seltzer water and Maramec Spring systems.
6) Make a comparison of the calcium concentration in Maramec Spring to saturation levels for calcite and aragonite (use the K_{sp} values from the literature).
7) Record your observations and interpretations on the turbidity of the Maramec Spring water.

8) Had this exercise assisted students in the understanding of the aqueous chemistry of carbonate systems? In what way?
9) Could the information gained in the exercise be applied towards an industrial process to capture and potentially sequester carbon?

Feedback on the class field trip project was gained through a review of student responses from the Missouri University of Science and Technology on-line evaluation that is submitted by the students at the end of each semester. Their responses are submitted voluntarily, anonymously, and using a standard university questioner that asks for strengths and weaknesses in the class, but does not specifically refer to the Maramec Spring field project. Most responses were positive with regards to their participation in the field trip activities, use of analytical instrumentation, and the use of simple experiments in the class lectures and field experiments. The responses from students were more varied when they reflected on the effort that they had to put into completing the written questions for the lab report. Many students accepted the challenge with enthusiasm, while others displayed some resentment in the unstructured nature of the problem. The response from one student is particularly enlightening. This student expressed disappointment in that they had to "*…do a lot of researching and googling to try to answer all of the questions" and "While you may have asked some questions to get us thinking, you did not answer them…*". In retrospect, this student's disappointment in their time commitment and absence of a step-by-step procedure is a reflection of their being forced away from their "academic comfort zone". Students who are required to use their cognitive thinking abilities will often develop a deeper understanding of research activities, similar to the manner in which what may be required of them in their future working careers and/or graduate school research projects.

2. ATTRIBUTES OF THE MIDCONTINENT RIFT SEQUENCE, LAKE SUPERIOR REGION, FOR CARBON SEQUESTRATION

The study of the MCR provided a relatively minor portion of the undergraduate educational component of this carbon sequestration project. Ten students were enrolled in the GEOL 372 Spring Field Studies class at Missouri University of Science & Technology in the spring 2012 semester. Classroom discussions for this class were based on pre-class reading assignments from the literature. The students then discussed in class the multiple geologic processes that are responsible for the formation of the MCR as well as discussing the concept, favorable features, and difficulties in using this geologic basin as a carbon sequestration target. The students then traveled on a nine-day field trip to the Lake Superior region in May 2012 to visit many of the same sites that they had read about and discussed during the semester class meetings. Students were able to visit numerous outcrops displaying the sedimentary and igneous rocks of the rift, and view many of the fine scale features associated with natural carbonate mineralization that had occurred in the rift sedimentary and volcanic rocks in the geologic past. Some of the samples used in the research portion of this study (Section IV of this report) were collected during that field trip.

Figure 1. a) Upper left - Maramec Spring water at the location of upwelling (note small ripples at right of photo and milky blue-white color resulting from the presence of fine-grained colloidal particles. b) Upper right – students conducting Eh-pH measurements. c) Lower left – group photograph at trout hatchery. d) Lower center – students conducting colorimetric titration experiment to determine alkalinity. e) Lower right – students filter water samples for future chemical analysis to be conducted back at the laboratory.

3. CARBONATE GEOLOGY OF THE BAHAMIAN PLATFORM

The Spring Field Studies class on the Bahamian Carbonate Platform was taught during the spring semesters in 2011 and 2013. The two courses had eight and ten students, respectively. Students who enrolled in the course were majors mostly from the Geology and Geophysics Program, but this class also included students from Geological Engineering and Chemistry. Students had met one evening each week for the spring semester prior to the trip to discuss scientific papers that pertain to the biology, chemistry, and geology of the Bahamian Carbonate Platform. The spring 2013 GEOL 372 course was also held in conjunction with a parallel biology course taught by Dr. Melanie Mormile in our Department of Biological Sciences. The two courses meshed together very well as many of the mineralization processes occurring on the island are biogeochemical in nature. The Biology and Geology students meet together for a combined class five times during the semester where they debated topics related to the island biogeochemical system. All combined, the three courses (Geology in 2011, Biology and Geology in 2013) included the participation of 32 college and 2 high school students.

The field course logistics and housing were supplied by the Gerace Research Centre (http://geraceresearchcentre.com). The Gerace center has been hosting visits from researchers and student groups interested in the biology, geology, and anthropology of the Bahamian Islands for nearly 35 years. The island is a wonderful natural laboratory for students to examine many different facets pertaining to the Earth's carbon cycle. Students can wade into the organic rich detritus in Storr's Lake and Salt Pond – sediments that given time, and a sufficient trap rock cover, may form the oil reserves of our distant geologic future. Carbonate precipitation occurs everywhere on the island as a result of inorganic reactions resulting from the upwelling of seawater from the adjacent abyss, through the interaction of multiple biologic organisms that remove CO_2 from the seawater (e.g., coral reefs fringing the island or primitive microbialite communities in Storrs Lake), or in pore spaces between the sediments. Students can also examine the effects of ancient global climate change by standing upon fossilized coral reefs that were stranded some eight feet higher than today's sea level after the polar ice caps melted some 125,000 years ago.

A typical research day on the island involved an examination of ancient carbonate system features on land during the morning, followed by snorkeling trips that examine the same sedimentary structures forming in the modern marine, lagoon or pond environments. Students examined and mapped cross-section profiles of marine to beach transitions (Figure 2a), both modern and ancient aeolianite (wind-blown) dune deposits, peritidal cliff zones and how various organisms colonize these areas in response to moisture in wave splash zones, weathering features of carbonate rocks, how wave energy influences beach profiles, and ancient coralline reef structures. Students determined whether the corals died in a growth-position (sea level regression) or as a result from disease, global warming, and/or deep submergence; all features that would likely lead to ancient corals, especially the branching corals being knocked-down prior to burial and solidification. Students also observed ancient paleosol features including soil textures in carbonate-rich environments root cast structures, and karst-cave features.

Afternoon snorkeling trips brought the students in view of modern patch and barrier reefs plus their associated biologic communities and sediment development (Figures 2b and 2c). Students were also able to observe the carbonate mineral production associated with platform and highly restricted lagoon settings, especially with respect to the various forms of *Thalassia* grass and Codiaceae algae that thrive in these settings, and how these plants as well as mangrove communities trap sediment and convert marine areas into land.

Inland lakes offered students a unique opportunity to examine hypersaline environments as well as a few areas where relatively low-salinity fresh water lenses float upon higher salinity groundwater. Some of these lake systems can be waded, others required snorkeling equipment. Students used various portable field instruments to measure salinity, Eh, pH, dissolved oxygen, alkalinity, and turbidity of the lake systems. They were also able to use soft sediment piston cores to examine shallow sediment profiles in these lakes. Of particular interest on this carbon capture and sequestration theme trip was the examination of the hypersaline Storrs Lake and its associated modern stromatolite and thrombolite mounds (Figure 2d). These microbial communities are actively precipitating carbonate minerals in the lake water. Carbonate mineralization processes in stromatolite-thrombolite communities are typically thought of as resulting from photosynthetic processes upon exposure to sunlight. In Storrs Lake, however, many of these stromatolites receive very limited sunlight due to the high turbidity of the lake water. The ability of these microbial communities to precipitate carbonate minerals in the absence of sunlight and in high salinity water suggests that they may potentially be used in underground carbon capture and sequestration processes to induce and/or accelerate carbonate mineralization. These microbial communities also utilize the high dissolved sulfate concentration in the lake water as a sink for the transfer of electrons as a result of their metabolic activities. The utilization and reduction of sulfate arising from the metabolic activities of these microorganisms also suggests that scrubbing of sulfate from coal-fired power plants may not be required or at least can be completed to lower rates of removal prior to off-gas injection underground. A more detailed discussion of these microbial communities of Storrs' Lake is given in "Section VI, "Characterization of Water Properties and Microbialites in the Hypersaline Environment of Storrs' Lake, The Bahamas", of this report.

4. INDEPENDENT UNDERGRADUATE RESEARCH PROJECTS

Eight undergraduate students were directly involved in research activities where they conducted experiments and gathered data on small segments of the project. These students worked closely with a specific graduate student during their initial laboratory assignment, while four of the students also advanced to the point where they were assigned independent research projects (e.g., pH measurements in association with the Goldich weathering experiments, Section IV).

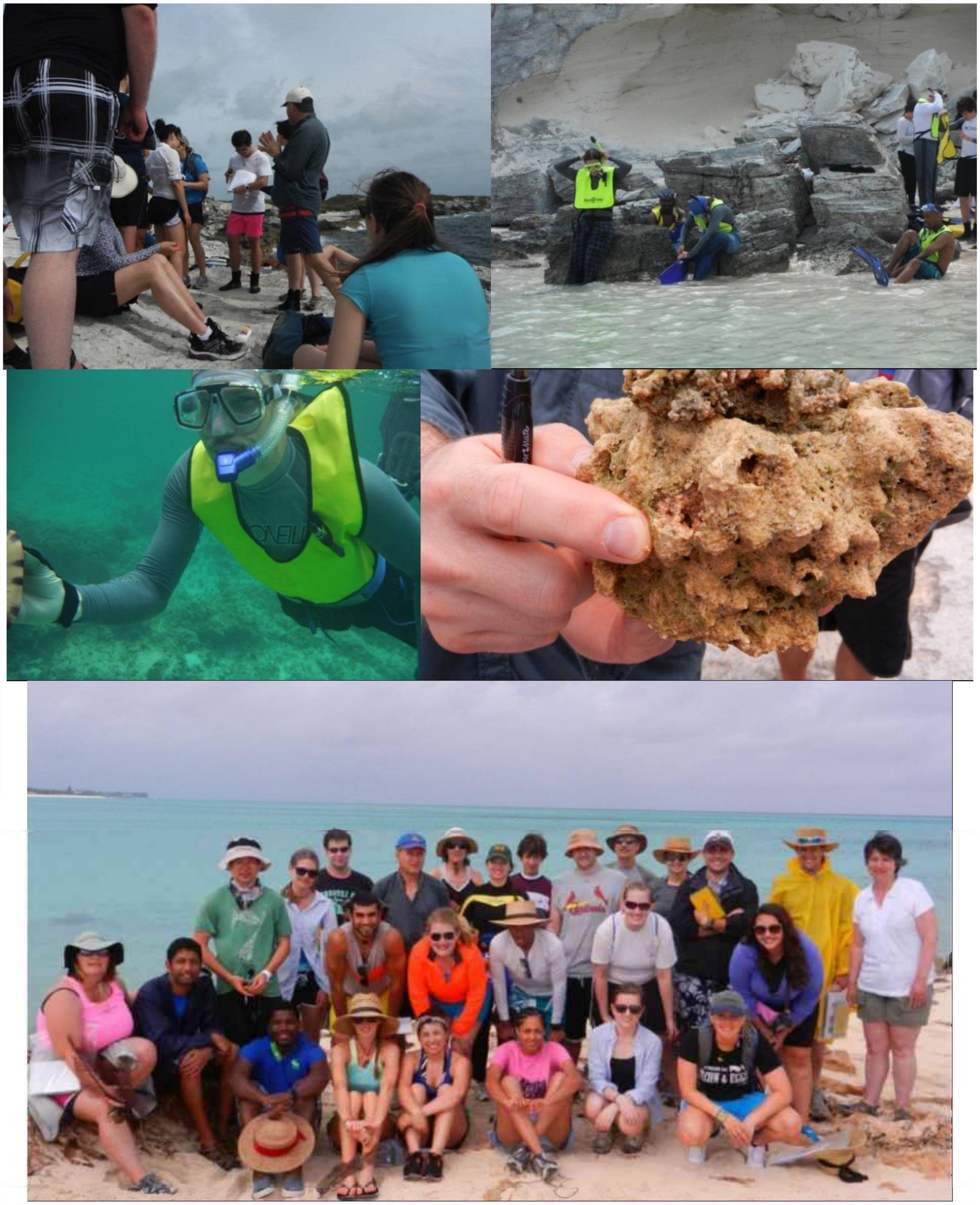

Figure 2. a) Upper left – students and faculty discussing the formation of ancient dune structures, b) upper right – student gear up for dive at Graham's Harbor. c) Middle left – a gastropod gets a closer inspection, d) lower right – students examine the layering in Storrs' Lake with colors ranging from green photosynthetic to pink sulfate reducing bacteria communities, e) bottom – 2013 group photo at Rocky Point, San Salvador Island.